ISSN 1349-0087
SPring-8 Document D2008-009

SPring-8 Research Frontiers

2007

SPring-8
Research Frontiers
2007

Contents 2007

Note: The principal publication(s) concerning each article is indicated with all author's names in italics in the list of references.

Editor's Note

SPring-8 Research Frontiers 2007 covers advances achieved during two consecutive research periods, the second half of 2006 and the first half of 2007. SPring-8 Research Frontiers describes the remarkable scientific achievements obtained at SPring-8 in various fields of basic and applied science including industrial applications, as well as the developments of the accelerators, beamlines and experimental apparatuses and the present status of the facility. This is its tenth issue. Glancing over the ten volumes, it is clear that SPring-8 has made substantial contributions to SR science and technology during the years. We are expecting further outstanding contributions in the next ten years.

Each year we have revised some of the contents and the design of Research Frontiers. This time we have adopted the style of a two-page spread for the reports in Scientific Frontiers so that the readers can read them easily. In the extra spaces left as a result of the page adjustment, photographs of flowers grown at the SPring-8 campus have been inserted.

In the SPring-8 site NewSUBARU, a 1.5 GeV storage ring for industrial applications is under operation. We have decided to include a report from NewSUBARU, even though it is managed by an organization different from SPring-8, since it is playing an important role in the development of SR science and technology.

Copies of SPring-8 Research Frontiers will be sent on request. Its full text is also available on the SPring-8 website (http://www.spring8.or.jp/). For the list of publications of studies by SPring-8 users and staff members, please visit the publications database at https://user.spring8.or.jp/en/pubsch.

We give our appreciation to the many specialists who recommended excellent research results suitable for publication in SPring-8 Research Frontiers. We would also like to express our sincere gratitude to the users and staff members of SPring-8 for contributing their reports to this issue.

Preface

In October 2007 SPring-8 celebrated the 10th anniversary of inauguration. SPring-8 has kept the position of the world largest for a decade because no gigantic facilities were constructed after SPring-8. Furthermore, people have learned from the results of operation of the big three third-generation facilities that the most of the demands to synchrotron radiations can be covered by high-performance medium-energy (~3 GeV) machine, which were materialized by using the vacuum-sealed undulator developed at SPring-8. This recognition led to the construction of such machines, which will probably respond to most of the users' demands in the future.

SPring-8 is the most expensive machine in the world to operate and to maintain, and will be no more competitive to the new medium-energy machine from the economical point of view. SPring-8 is now destined to depend on the extreme quality and/or high energy of the beam. In other words, the gravity center of SPring-8 should be shifted to the experiments that are worthy to utilize the superior beams of SPring-8. We are forced to yield the good result of utilization to convince the public society for holding such expensive beams.

Machine construction team consisting of RIKEN and JASRI scientists already provided extensive plans for improving the beam on the SPring-8 site. The construction of the XFEL (X-ray free electron laser) based on an 8-GeV linear accelerator (LINAC) started in 2006. In the future this LINAC will be connected to the storage ring of SPring-8 to supply the electron beam of lower emittance than the present. Thus, the machine is ready for the upgrade for the future.

Akira Kira
Director General
SPring-8 / JASRI

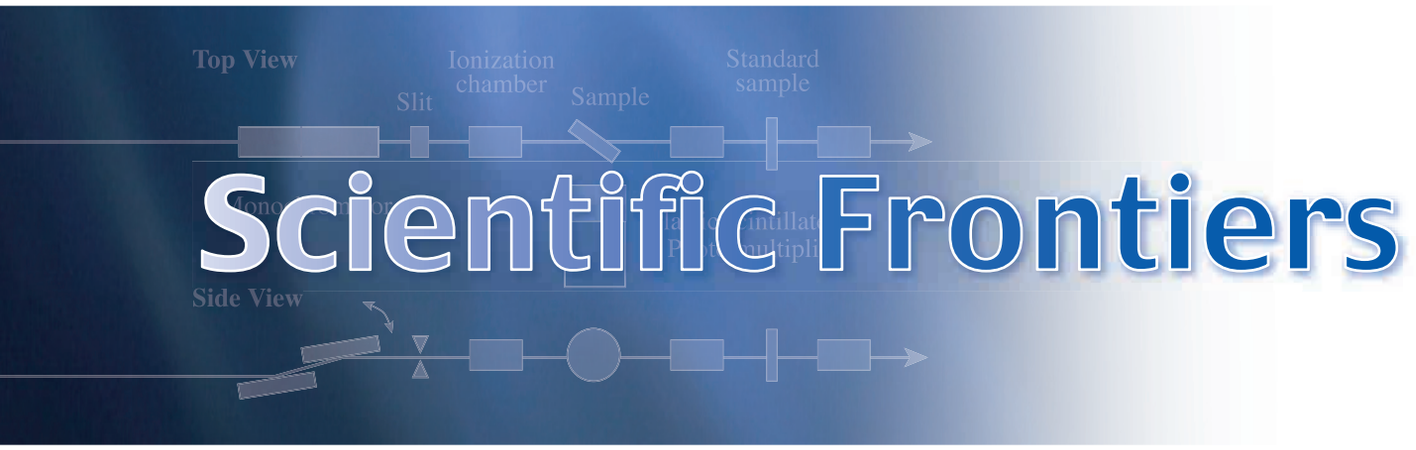

Scientific Frontiers

A Place in the "X-ray" Sun

Endeavors at Frontiers of Research

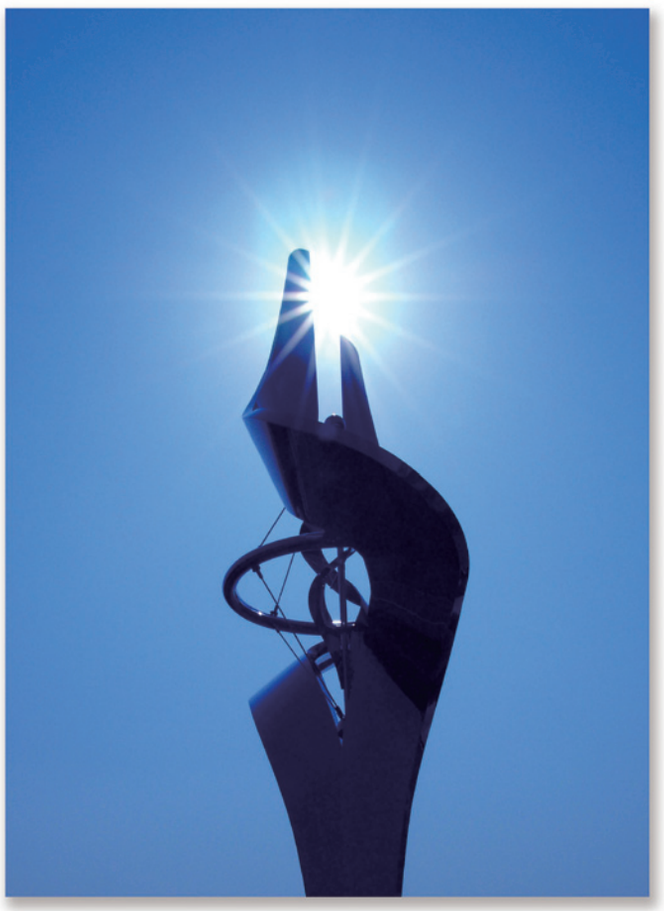

1. Fine Art at SPring-8

The *largest* instrument at SPring-8 is the inelastic X-ray scattering (IXS) spectrometer at BL35XU (Fig. 1). It measures the dynamics of atoms, investigating atomic motions in liquids and glasses, and the relation between phonons and solid-state properties including superconductivity, ferroelectricity and elasticity. Traditionally this has been the domain of inelastic neutron scattering (INS). However, X-rays offer some very significant advantages over neutrons. For disordered materials, a crucial advantage allows X-rays to probe regions of energy and momentum transfer not accessible to INS, and has led to an explosion of research on disordered materials in the last decades. For crystals, the subtle advantages of low background and simplicity (which should never be under-rated) allow phonon measurements essentially as easily as X-ray diffraction. However, perhaps the single biggest advantage of X-rays over neutrons is the *reduction in required sample volume by some 5 orders of magnitude* due to the brilliance of the X-ray source. This makes it possible to consider doing experiments never dreamed of with neutrons, including, for example, investigating phonons in hot new samples, such as MgB_2, now well investigated by IXS (but still not accessible to INS) or the very new iron containing superconductors.

The exquisite design and implementation of the IXS beamline by Baron and co-workers integrates cutting edge instrumentation with the exceptional performance, stability, and the high electron-energy of the SPring-8 storage ring. This year one can find contributions within this volume from the IXS spectrometer, including work on phonons in quasi-crystals (page 78), sound in a metal glass (page 76), and phonons in superconducting diamond (page 82). The metal-glass measurements show the advantages of IXS for disordered materials, the work on superconducting diamond shows the value of IXS for very small sample volumes, while the quasicrystal work is an example of fine art.

"Symmetry" is a common theme in Art, Science and Mathematics. In basic geometry, a plane can be filled periodically by closely packing building blocks with 3-fold, 4-fold, even 6-fold symmetry structure, but not 5-fold "pentagonal" structure (Fig. 2). Thus, about 20 years ago, the scientific community was surprised by the discovery of class of space-filling materials that had 5-fold symmetry. The explanation was that they were not periodic - but only quasi-periodic - having a

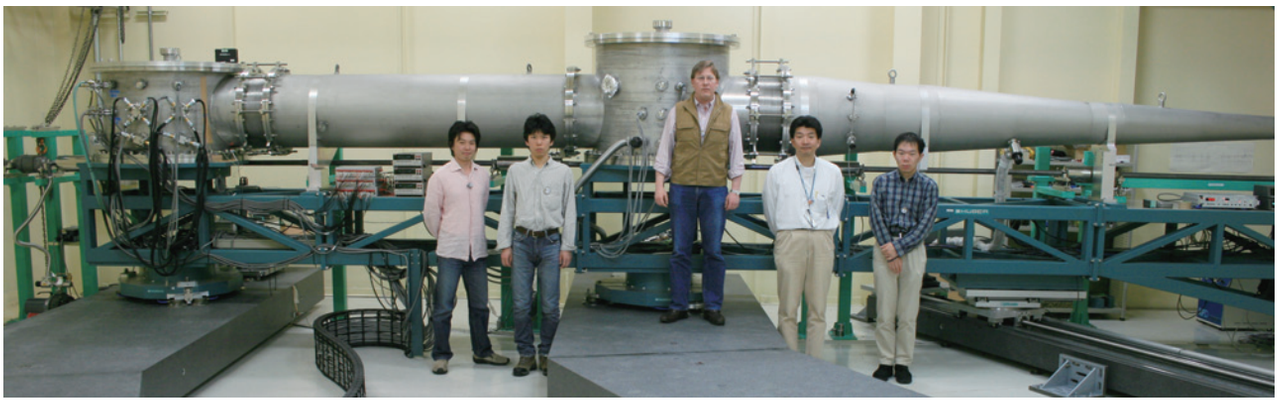

Fig. 1. Alfred Baron's Research Group (JASRI) with high resolution inelastic scattering spectrometer at BL35XU.

structure that repeated, but not with a fixed step size. These beautiful new materials generated artistic and mathematical interest, but also forced a re-examination some basic physical principles, since periodicity is built into the foundations of much of materials science. Their structure is now beginning to be understood with the help of a six-dimensional system for crystallography.

The relevant question is how the symmetry of a quasi-crystal influences the atomic motions. The first part of the answer can be found in [1] as discussed in the contribution on page 78, where inelastic X-ray scattering, inelastic neutron scattering and sophisticated calculations, are used to isolate the effect the quasi-crystal symmetry. In fact, exploring dynamics in unusual symmetries may be the early stage of a fad – note also the work on tiling arrangements in the work on block copolymers using SAXS by Matsushita's group of Nagoya University (see Chemical Science: Mesoscopic tiling patterns of ABC star-shaped terpolymers studied by microbeam small-angle X-ray scattering, page 106).

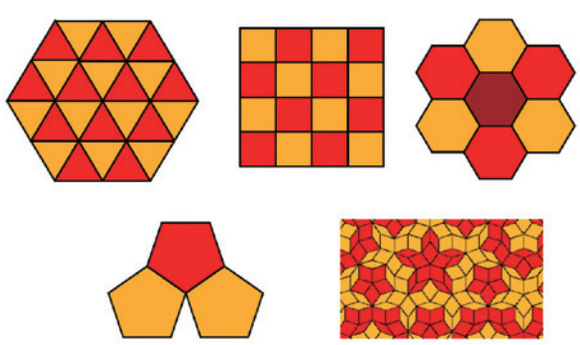

Fig. 2. Close packing of 3, 4 and 6-fold symmetric structures can be used to fill a plane. However, 5-fold structures cannot be stacked that way, one has to introduce an additional shape, and then the plane can be filled without translational symmetry.

[1] Marc de Boissieu, Sonia Francoual, Marek Mihalkovic *et al.*, Nature Materials advanced online publication (2007).

2. Winds of Change

- New type of industrial-academic alliance -

This year, the construction of 4 new beamlines was approved, making a big step toward filling the available synchrotron radiation ports at SPring-8.

Three Contract Beamlines

Frontier Soft Matter Beamline (BL03XU)
(Frontier Soft Matter Beamline Consortium)

University of Tokyo Beamline (BL07LSU)
(Outstation Program of University of Tokyo)

TOYOTA Beamline(BL33XU)
(TOYOTA Central R&D Labs.,Inc)

One RIKEN Beamline

RIKEN Target Proteins Beamline (BL32XU)

In particular, the Frontier Soft Matter Beamline (FSM BL) has a unique consortium organization based on an ***industrial-academic alliance***. The fundamental structure of the consortium consists of 17 corporate groups, including industrial companies and their collaborating academic scientists as shown in Fig. 3. It is also important to note that the Kwansei Gakuin University (private university) join the FSM BL consortium as an independent industry aiming scientist & engineer resource development.

The mission of the FSM BL is to clarify the nano-to-meso scale properties of polymers and soft matter from both industrial and academic points of view. It is aimed at development of next-generation materials for nano- and micro-technology. Construction of the FSM BL will be started in spring of 2008 and it will be opened for the consortium users in the winter of 2009, after commissioning. The academic members will lead the consortium to new science with polymers and soft-matter using synchrotron radiation.

A schematic of the FSM BL is shown in Fig. 4. The first hutch will be used for thin-film structural investigations. The experimental hutch will have systems for time-resolved GIXD and GISAXS to

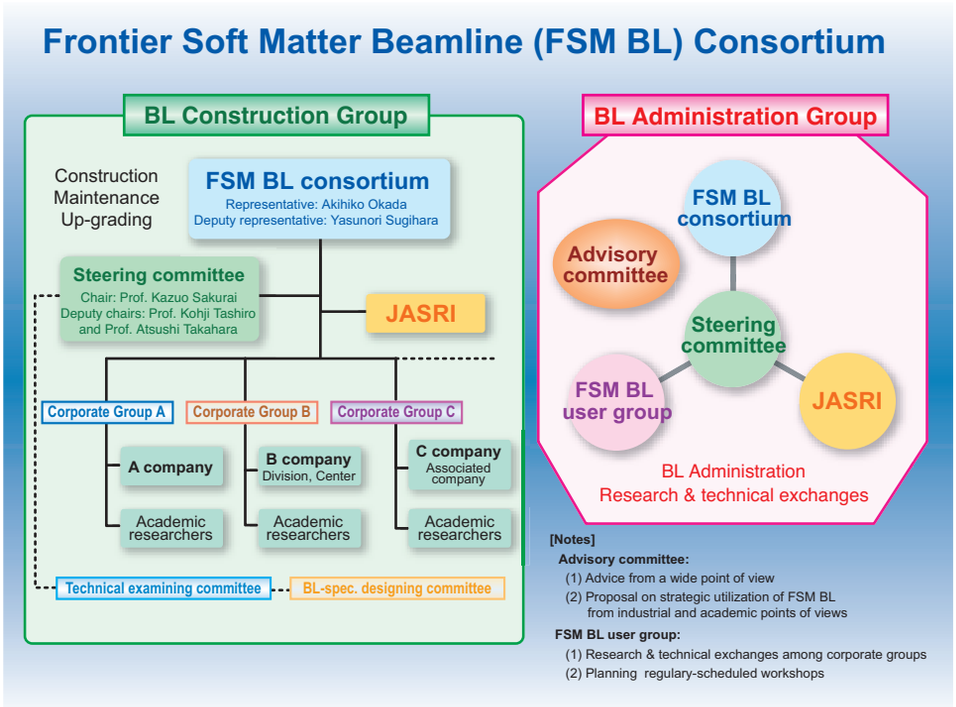

Fig. 3. Organization and participants in the FSM beamline.

conduct measurements on thin films of polymers and soft matter. The second hutch will focus on dynamic nano·meso-structure science. The main specifications of second experimental hutch design are:

- SAXS resolution up to 0.7 μm (1.0 μm).
- Time-resolved WAXS/SAXS measurements and microbeam WAXS and SAXS measurements for bulk samples.
- A large space (3m (l) × 3m (w) × 4 m (h)) for optional equipment at the sample area to conduct new experiments, such as multi-control measurement and manufacturing/processing machine tests.

The planned beamline will bring a wide range of advancements for polymer and soft materials science and their industrial applications. Moreover, the new type of organization, the industrial-academic alliance, will surely create a broad-ranging partnership between industrial and academic communities, bringing new impetus to industrial application of synchrotron radiation.

3. A New Horizon

- Dawn in Asia and Oceania -

The first summer school of the Asia-Oceania Forum of Synchrotron Radiation Research (AOFSRR) was held from 10 to 20 September, 2007, at SPring-8. The AOFSRR was organized in 2006 by the Australian Synchrotron Research Program (Australia), the Chinese Society of Synchrotron Radiation Research (China), the Indus (India), the Japanese Society of Synchrotron Radiation Research (Japan), the National Synchrotron Research Center (Thailand), the National Synchrotron Radiation Research Center (Taiwan), the Pohang Light Source (Korea) and the Singapore Synchrotron Light Source (Singapore). The purpose of the school is to provide useful and

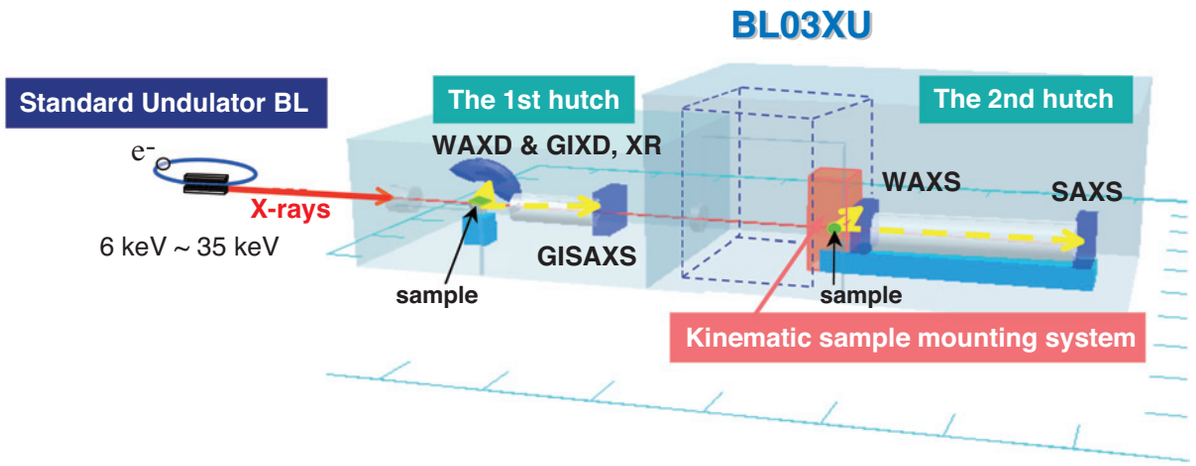

Fig. 4. Schematic of the frontier soft matter beamline (FSM-BL).

basic knowledge, as well as a broad perspective of synchrotron radiation science and technology. It is aimed at graduate students, post-docs, young scientists and engineers in the Asia-Oceania region. Most important is that this summer school should be useful and practical for the Asian Oceania SR facilities. Thus, the school curriculum includes a round table discussion, ***"Meet The Experts,"*** where the students can consult experts for their own problems in SR science, and a practical section, ***"BL Practice."***

The ***Cheiron School*** is named after an immortal gods in Greek mythology who specialized in providing the right knowledge or skill to the right person: Cheiron taught martial art to Hercules, medicine to Aesculapius, horsemanship to Castor, etc. The policy of the school is similar, aiming to teach the needed skill to the right person. It is an important tool to develop engineers and scientists as a resource for synchrotron radiation research in Asia-Oceania region. The ***Cheiron School*** will promote a "person-to-person" network in Asian/Oceania synchrotron radiation community. Further details can be found at http://cheiron2007.spring8.or.jp/index.html.

Masaki Takata

Fig. 5. Poster and school photo of Cheiron School.

Table 1. List of the lecturers

SUBJECT	LECTURER
Overview of SR	Robert N. Lamb (Australian Synchrotron)
Light Source 1&2	Takashi Tanaka (RIKEN)
History of SR	Taizo Sasaki (Japan)
X-ray Monochromator	Shunji Goto (JASRI)
Mirror and Multilayer	Christian Morawe (ESRF)
Micro-focusing Optics	Barry Lai (APS)
Next Generation Sources	Tsumoru Shintake (RIKEN)
Accelerator Physics (Linac)	Yujiro Ogawa (KEK)
Accelerator Physics (Ring)	Greg LeBlanc (Australia)
Diffraction and Scattering	Brendan Kennedy (Univ. of Sydney)
Powder Diffraction	Brendan Kennedy (Univ. of Sydney)
Photoemission(2): PEEM and nanoscience	Bruce Cowie (Australian Synchrotron)
Spectra -a Synchrotron Radiation Calculation Code-	Takashi Tanaka (RIKEN)
Inelastic X-ray Scattering	Ercan Alp (APS)
Protein crystallography	Soichi Wakatsuki (KEK)
Photoemission(1): Spectroscopy	Nobuhiro Kosugi (UVSOR)
VUV & SX Optics 1&2	Takeshi Namioka (Tohoku Univ.)
Detector	Chris Hall (Monash University)
Soft X-ray Absorption Spectroscopy and Resonant Scattering	Di-Jing Huang (NSRRC)
Imaging	Chris Hall (Monash University)
Small-angle Scattering	Moonhor Ree (PAL)
Atomic and Molecular Physics	Akira Yagishita (KEK)
EXAFS	Iwao Watanabe (Ritsumeikan Univ.)
Pump-Probe Experiment	Shin-ichi Adachi (KEK)
Industrial Applications	Norimasa Umesaki (JASRI)
X-ray Fluorescence Analysis	Atsuo Iida (KEK)
LIGA	Linke Jian (SSLS)
High pressure/High temperature	Osamu Shimomura (KEK)
Infrared	Mark Tobin (Australia)
New Scientific Possibilities and Directions	Tetsuya Ishikawa (RIKEN)

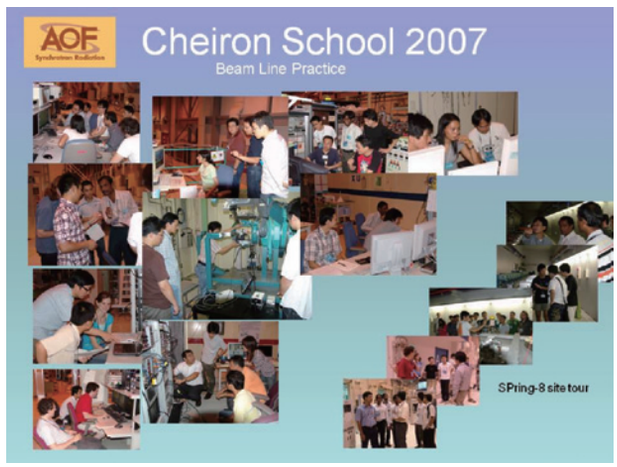

Fig. 6. Practical session.

Fig. 7. Excursion to the Imperial Palace in Kyoto.

LIFE SCIENCE :

"Kiri" - Paulownia

Structural biology propels exhaustive explorations of the structural and functional details of biological macromolecules. For this purpose, the development and upgrade of SPring-8 structural biology beamlines are moving forward and continuing. As a result, the number of structures determined is increasing yearly. Moreover, in this year, we are able to produce many fruitful results in broad biological fields as follows.

The structure of human proteins can be used as basis for drug development. Leukotriene C_4 synthase is embedded in the nuclear membrane and related to allergic reactions. Ago *et al*. determined the structures of its trimeric integrated membrane protein. Its active site located between adjacent subunits and two arginine residues performs an acid-base catalysis. Endotoxin is a material released by the lysis of pathogenic bacteria and causes an immune response. The structure of the complex of the MD-2 protein and its antiendotoxic lipid was determined by Satow *et al*. Their results suggested a principal role of MD-2 in the endotoxin shock mechanism. Reelin is a signaling protein that interacts with lipoprotein receptors and regulates correct cell positioning during brain development. The structures of the repeated portions in reelin were determined by Nogi *et al*. They investigated new insights into a long rod of the entire structure and the candidates of the receptor-binding interface.

STRUCTURAL BIOLOGY

The association and dissociation of any protein unit are clues for investigating biological phenomena. Structural biology provides the observation direct or indirect of these phenomena. Akiyama *et al*. revealed the oscillatory mechanism of the circadian clock using KaiABC proteins by SAXS analysis. The phosphorylation-dependent structural change of KaiC promotes the oscillatory association and dissociation of KaiA and KaiB to KaiC. Fukunaga *et al*. revealed structurally the cysteinyl-tRNA synthesis by SepRS and SepCysS in an archaeal bacterium. This reaction starts uniquely with a noncanonical *O*-phoshoserine, and the formation of the protein complex is essential to prevent mistranslation. This unique secure strategy is also interesting from the viewpoint of evolutional process of the genetic code. Higuchi *et al*. determined the structure of the DIX domain, a component of the Wnt signaling pathway that is a major cancer pathway. Its structure showed an ubiquitin-like fold and seemed to be polymerized with a long helical chain. This dynamic property might be important for regulating the association to partner proteins. Miki *et al*. determined the three structures required in synthesis of complex metal center, $NiFe(CO)(CN)_2$, of [NiFe] hydrogenase. From three independent structures, it is suggested that the HypCD complex captured its Fe atom and forms a ternary complex with thiocyanated HypE to obtain CN ligands. To complete the metal center, thiol redox signaling similar to the ferredoxin:thioredoxin reductase-like cascade is adopted.

Basic biological phenomena were also able to be solved using crystal structures. Imada *et al*. showeded the structure of FliI, a component of the bacterial export apparatus for secreting flagellar axial proteins. Since this component is highly similar to the F_1 portion of F_0F_1 ATP synthase, both machines might have evolved from a common ancestral system. The entry of macromolecules into the cell nucleus is strictly regulated by importin proteins. Transportin is a transport receptor of the system and binds signal sequences of substrate proteins. The structures of substrate-free and -bound forms of transportin were determined by Sato *et al*. Binding/release of substrates might be regulated by the interaction with the signal sequences and RanGTP to the two arches of the superhelical S-like structure of transportin. Magnesium homeostasis is essential for regulating many enzymatic processes including the utilization of ATP. Nureki *et al*. revealed the structure of a magnesium transporter and suggested its selective membrane transport mechanism. A high concentration of magnesium ion mediates the interaction between cytosolic and transmembrane domains, which would close the ion-conducting pore. Endocytosis is a dynamic cellular process for the uptake of materials from the outside of the cell. Shimada *et al*. revealed the structure of the EFC domain that assists in the tubulation of the cell membrane. The diameter of curvature of its spiral/ring structure is consistent with the size of the tubular membrane. This shows that the EFC domain plays a leading role in the invagination step of endocytosis.

Finally, we report over 2000 citations of an article on the structure of bovine rhodopsin determined with a SPring-8 beamline in 2000.

Masaki Yamamoto and Yoshitsugu Shiro

Crystal Structure of Human Membrane-integrated Protein Responsible for Biosynthesis of Cysteinyl Leukotrienes

The human membrane-integrated protein leukotriene C_4 synthase (LTC_4S) embedded in the nuclear membrane is the first enzyme involved in the biosynthesis of cysteinyl leukotriene (Cys-LT), and its inhibitor is expected to be a new therapeutic agent for symptoms caused by proinflammatory acute smooth muscle constriction in conditions such as anaphylaxis, allergy, and asthma. LTC_4S conjugates leukotriene (LT) A_4 and reduced glutathione (GSH) to synthesize LTC_4 (Fig. 1). LTC_4 and its metabolites, LTD_4 and LTE_4, are collectively called Cys-LTs, and Cys-LTs have been known as slow-reacting substance of anaphylaxis (SRS-A) [1,2]. The smooth muscle constriction activity of Cys-LT is one thousand-fold higher than that of histamine, a well-known inflammatory substance. LTC_4S is a potential target in the development of new therapeutic agents for anaphylaxis, allergy, and asthma, and the three-dimensional structure of LTC_4S enables us to apply modern method for drug discovery.

We elucidated the crystal structure of human LTC_4S at 3.3 Å resolution using beamline **BL44B2**, which makes human LTC_4S one of three human membrane-integrated proteins whose structures were determined crystallographically first [3]. Indeed, one of the bottlenecks is the production of a fully active human membrane-integrated protein at crystallographic quality and quantity using a heterologous expression system. We established a heterologous expression system using the fission yeast *Schizosaccharomyces pombe* to obtain a fully active LTC_4S on the milligram scale from a few liters of yeast culture.

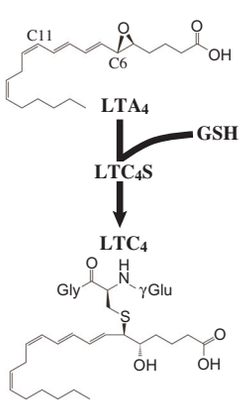

Fig. 1. Biosynthesis of Cys-LT. LTC_4S catalyzes conjugation between LTA_4 and reduced GSH to synthesize LTC_4, which is further metabolized to LTE_4 through LTD_4 by hydrolytic enzymes.

The crystal structure of LTC_4S revealed that trimeric LTC_4S in a three-fold symmetry is a biological functional unit [3]. An LTC_4S monomer is composed of five α-helices, the first four of which are transmembrane α-helices and the fifth α-helix protruding into the bulk solvent from nuclear membrane (Fig. 2(a,b)). The V-shaped cleft surrounded by five α-helices is the substrate binding site. All the five α-helices contribute to the binding of a unique U-shaped GSH to the upper side of the cleft (Fig. 2(c)). For example, the positive charge of Arg51 of α-helix II is essential to the binding of GSH [4]. The remaining space extending from GSH to the bottom of the cleft would be the binding site of LTA_4. The depth and shape of the space fits well to the molecular shape of the aliphatic chain of LTA_4 having two *cis*-double bonds at C11 and C14 (Fig. 3). Indeed, the hexyl moiety of *S*-hexyl glutathione as a weak inhibitor occupies the space in the *S*-hexyl GSH complex crystal (Fig. 2(d)). Furthermore, the aliphatic chain of dodecyl maltoside occupies the space in the GSH complex crystal. Together with these results, the active site is located between the two adjacent monomers in the trimeric LTC_4S, and the trimeric LTC_4S is the biological functional unit.

The crystal structure of LTC_4S shows that the conjugation of LTA_4 and GSH is induced by acid-base catalysis, in which Arg31 and Arg104 are the acid and base, respectively. During the course of the conjugation, LTC_4S activates the thiol group of bound GSH for the nucleophilic attack of the sixth carbon of LTA_4 and provide a hydrogen to the negatively charged oxygen derived from the epoxide group at the fifth carbon. The side chain of Arg104 as the base decreases the pKa of the thiol group of GSH as the reactive species under the physiological condition due to a hydrogen bond between Arg104 and the thiol group of GSH (Fig. 2(c)). When LTA_4 binds to the GSH-binding LTC_4S (Fig. 3), the activated thiol group would attack C6 on the opposite side against the epoxy oxygen of LTA_4, and a negative charge would grow on the epoxy oxygen concurrently with the breaking of the bond between the epoxy oxygen and C6. Finally, Arg31 as the acid provides a proton to the negatively charged oxygen at C5, resulting in LTC_4 as the conjugated product.

The crystal structure of the human membrane-

integrated protein LTC_4S reveals unique features for the strict substrate specificity and the conjugation catalyzed by two arginine residues in an acid-base-catalytic manner. We hope that this work contributes to the advancement of the pathobiology of inflammatory diseases and to the development of new therapeutics.

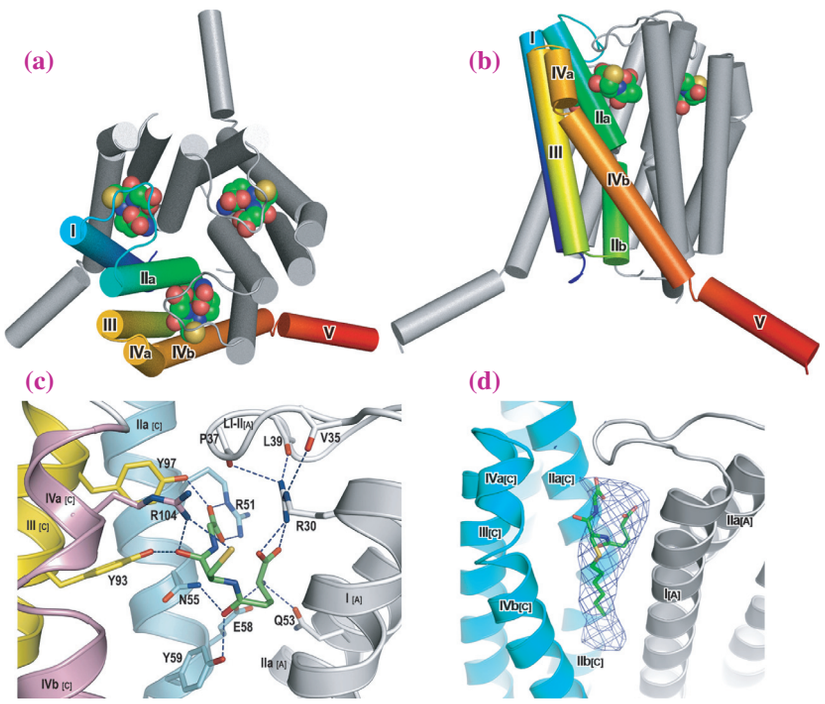

Fig. 2. Crystal structure of LTC_4S. **(a,b)** Schematic representations of trimeric LTC_4S. α-Helices from a monomer are tube models in rainbow color, and the bound GSH is in space-filling model. In all panels, the sequential number on each α-helix is the order of the α-helix from the N-terminus. The small letter following the sequential number means that the α-helix is subdivided. A small capital in square brackets corresponds to the monomer, which contains the α-helix. **(c)** Close-up view of the bound GSH. Dashed lines are polar interactions participating in GSH binding. **(d)** Electron density of inhibitor *S*-hexyl GSH at 5 Å resolution.

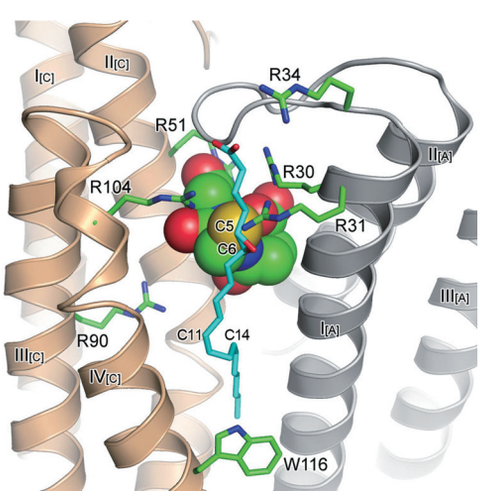

Fig. 3. LTA_4 binding model. The stick model with cyan carbon is the modeled LTA_4, and the CPK model is the bound GSH in which sulfur, carbon, nitrogen, and oxygen are in yellow, green, blue, and red, respectively.

Hideo Ago* and Masashi Miyano

SPring-8 / RIKEN

*E-mail: ago@spring8.or.jp

References

[1] S.-E. Dahlén *et al.*: Nature **288** (1980) 484.
[2] K.F. Austen: Prostaglandins Other Lipid Mediat. **83** (2007) 182.
[3] *H. Ago, Y. Kanaoka, D. Irikura, B.K. Lam, T. Shimamura, K.F. Austen and M. Miyano: Nature **448** (2007) 609.*
[4] B.K. Lam *et al.*: J. Biol. Chem. **272** (1997) 13923.

Structures of Human MD-2 Coreceptor and Its Complex with Antiendotoxic Lipid IVa Preventing Endotoxin Shock

Innate immunity is the first line of defense against microbial infections. Defense responses are activated when microbial components are recognized by a variety of pathogen sensors including the Toll family of receptors and Nod-like receptors. Among microbial components, lipopolysaccharide (LPS) in the outer membrane of Gram-negative bacteria is a potent stimulant of immune responses, and a small difference in LPS structure has a great influence on host responses against the bacteria.

Human MD-2 is a glycoprotein with a 16 amino-acid secretion signal and two *N*-linked glycosylation sites (*1*) and represents a class of MD-2-related lipid recognition (ML) proteins that also include mite allergen proteins. Secreted MD-2 forms a stable receptor complex with Toll-like receptor 4 (TLR4) on the cell surface, and the complex recognizes LPS, reading to activation of innate immune responses (*2*). Excessive responses to the endotoxic LPS frequently cause septic shocks, a rapidly progressing inflammatory disease with high mortality.

Lipid A, the immunostimulatory core of LPS, is diverse in several species, and these variations are discriminated by the TLR4-MD-2 receptor complex as endotoxic or as antiendotoxic. The hexa-acylated form of *Escherichia coli* lipid A acts as a potent agonist in human macrophage cells and in mouse cells. However, its precursor lipid IVa, the tetra-acylated form of lipid A, acts as an antagonist in human cells but as an agonist in mouse cells.

We have determined the crystal structures of human MD-2 itself and of its complex with lipid IVa (*3*). MD-2 was expressed in methyltropic yeast *Pichia pastoris*, and its polysaccharide moieties of MD-2 were trimmed off by endoglycosidase treatment which leaves a single *N*-acetyl-glucosamine (NAG) at each glycosylation site. Crystals of monomeric MD-2 showed severe crystal twinning, but was successfully transformed into single crystals through optimization of cryoprotectant (*4*). The structure of the thus obtained native crystal was determined at 2.0 Å resolution by multiple isomorphous replacement (Protein Data Bank code 2E56). A cocrystal with the lipid IVa complex was also obtained as a twinned form nearly isomorphous to the native crystal. The structure of the complex was refined at 2.2 Å resolution (Protein Data Bank code 2E59). Diffraction datasets were collected at 100 K on beamline **BL38B1**, with a CCD detector.

MD-2 with two *N*-linked NAGs at Asn^{26} and Asn^{114} is folded into a single domain consisting of two β sheets in the immunoglobulin fold conserved among the ML proteins: one sheet consists of three antiparallel β strands, and the other of six anti-parallel strands (Fig. 1). Between these sheets is a large and deep hydrophobic cavity. Both the glycosylation sites are distant from the cavity region, indicating that the glycosylation plays a role, not in ligand binding, but presumably in the secretion and protection of MD-2. In the native structure, unexpected three electron-densities were observed in the cavity; these were attributed to bound myristic acid molecules.

The MD-2 structure of the lipid IVa complex is not significantly altered upon lipid IVa binding. In the complexed structure, electron densities in the cavity were assigned to the parts corresponding to lipid IVa: two glucosamine, two phosphate, and four fatty acid chains (Fig. 1). Residues Phe^{119} to Gly^{123} are important for the LPS recognition (Fig. 2), and these residues, with the exception of Lys^{122}, are conserved in all the species of MD-2. Hydrophobic and electrostatic surface potentials in the vicinities of

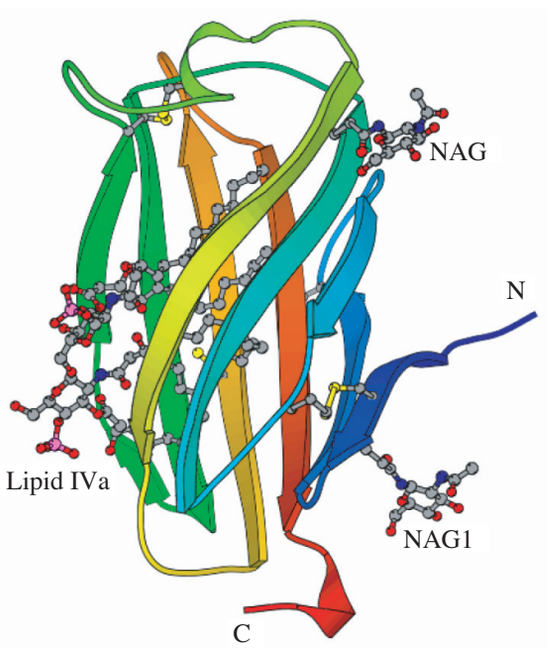

Fig. 1. Ribbon model of human MD-2 in complex with lipid IVa. The lipid IVa moiety is drawn as a ball-and-stick model: O atoms in red, N in blue, C in gray, and P in pink.

the entrance indicate that the entrance is positively charged and the inside of the cavity is highly hydrophobic (Fig. 3). Lysine and arginine residues located in the vicinities of the entrance mainly contribute to the attraction of negatively charged lipid IVa. None of the phosphate groups of lipid IVa are involved in direct hydrogen bonds to MD-2 atoms. Four fatty-acid chains are all deeply confined in the cavity and are packed next to each other through van der Waals contacts.

The complexed structure that confines most of lipid IVa suggests that MD-2 plays a principal role in recognizing LPS. Moreover, it provides a basis for structure-based development of antiseptic drugs that might be effective in preventing endotoxin shock.

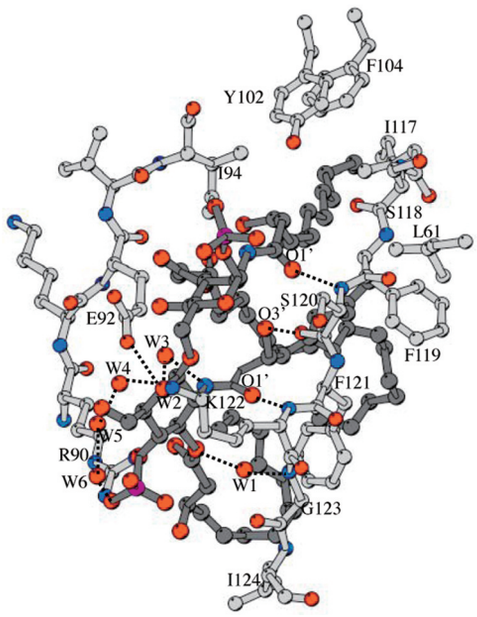

Fig. 2. Close-up view of the binding interface to lipid IVa. Amino acid residues are drawn as ball-and-stick models and the lipid IVa moiety is similarly drawn in darker gray. Water O atoms involved in hydrogen bonds are also depicted.

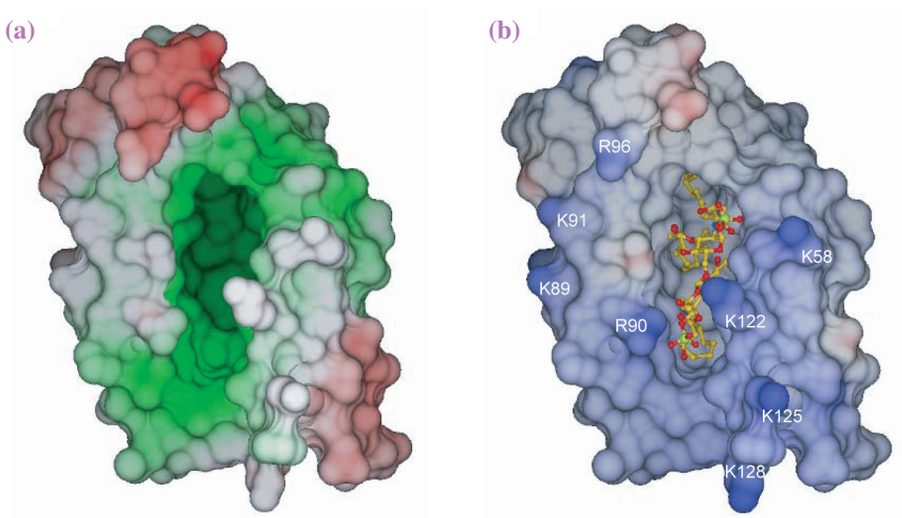

Fig. 3. Binding pocket and surface properties of MD-2. **(a)** Protein surface representing hydrophobicity (green) and hydrophilicity (red), and their extents are indicated by color darkness. **(b)** Electrostatic potential surface. Positive and negative potentials are shown in blue and red, respectively. Bound lipid IVa is drawn as a ball-and-stick representation.

Yoshinori Satow* and Umeharu Ohto

Graduate School of Pharmaceutical Sciences,
The University of Tokyo

*E-mail: satowy@mol.f.u-tokyo.ac.jp

References

[1] M. Gangloff and N.J. Gay: Trends Biochem. Sci. **29** (2004) 294.
[2] Y. Nagai *et al.*: Nature Immunol. **3** (2002) 667.
[3] *U. Ohto, K. Fukase, K. Miyake and Y. Satow: Science* ***316*** *(2007) 1632.*
[4] *U. Ohto and Y. Satow: J. Synchrotron Rad.* ***15*** *(2008) 262.*

Structural Study on the Extracellular Signaling Molecule Reelin Involved in the Cortical Layer Formation

Reelin, a gigantic extracellular glycoprotein produced by Cajal-Retzius neurons and other neurons in the cortex, plays a central role in cortical layer formation during mammalian brain development. Reelin was originally identified as a gene product absent in *reeler* mice exhibiting malformations of the cerebral cortex. Reelin acts on migrating neuronal precursors, and regulates correct cell positioning in the cortex and other brain structures. It is now accepted that reelin binds to the lipoprotein receptors ApoER2 or VLDLR on neurons and initiates a signaling cascade involving phosphorylation of the adaptor molecule Dab-1 (Fig. 1(a)). The biochemical basis for the reelin-receptor interaction, however, has remained poorly understood owing to the lack of structural information.

Reelin is a modular protein composed of a signal sequence, an F-spondin-like region, nine sequentially concatenated repeat units of ~380 amino acids, and a C-terminal basic tail region (Fig. 1(b)). The N-terminal repeat is incomplete and shows a markedly lower similarity to other repeats. Each of eight complete reelin repeats contains a central epidermal growth factor (EGF) module flanked by two homologous subrepeats of 150-190 amino acids. The EGF-like module is ubiquitous among extracellular proteins, but the two subrepeats are unique to reelin and do not show any sequence similarities to other protein families. Therefore, structure determination was indispensable for elucidation of the molecular architecture of reelin.

In this study, we first attempted to obtain structural data on a single reelin repeat. We designed and tested a series of deletion constructs of reelin to find a fragment suitable for structural study. As a result, the third repeat, R3, showed the highest expression level, and was subjected to crystallization. The R3 fragment was produced in the mammalian expression system, and the structure has been solved by the Se-SAD method at 2.05 Å resolution [1]. X-ray diffraction data for phasing and refinement were collected at beamline **BL44XU**. As shown in Fig. 2(a), the resulting structure has a horseshoe-like globular structure, in which the two subrepeats separated by the EGF-like module make close contact. Subrepeats A and B have a common 11-stranded β-jelly roll fold, which shows a structural similarity to carbohydrate-binding proteins. In addition, the subrepeats share a common feature with carbohydrate-binding proteins in metal binding. Many carbohydrate-binding proteins contain a calcium ion, and we also identified a metal ion, presumably a calcium ion, at the corresponding site.

We carried out functional analysis of reelin-receptor interaction, and narrowed down the receptor-binding unit to the R5-6 fragment. Interestingly, neither the R5 nor R6 fragment is capable of binding to the receptor. In addition, we designed an artificial fragment R6-5, an inverted version of R5-6 in which the positions for R5 and R6 were swapped, but it does not bind with the receptor, neither. These observations indicate that the correct positioning of R5 and R6 is critical for receptor binding. Therefore, we next determined the structure of R5-6.

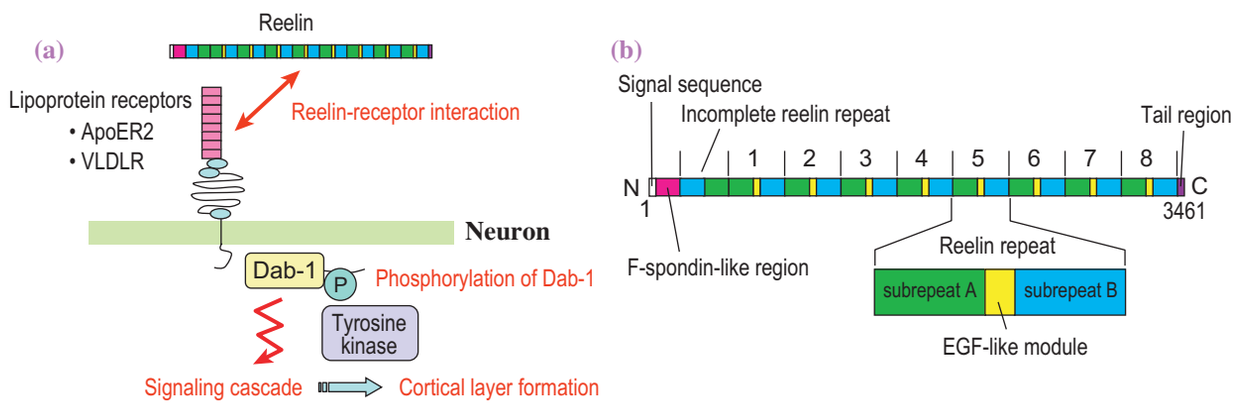

Fig. 1. **(a)** Diagram of reelin signaling on neuron. **(b)** Modular structure of reelin molecule.

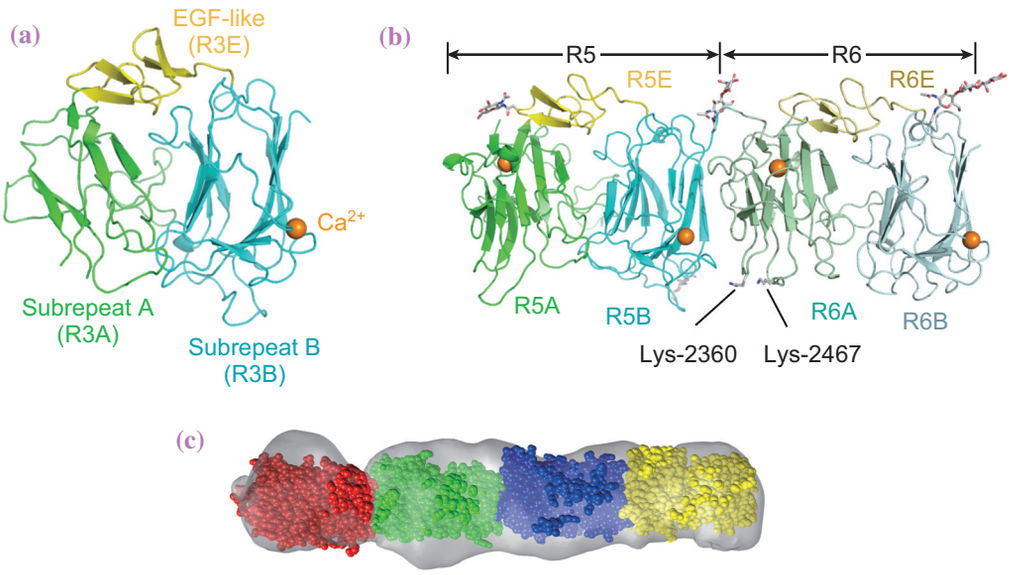

Fig. 2. **(a)** Crystal structure of single reelin repeat R3. The reelin repeat is composed of N-terminal subrepeat A (R3A, green), the central EGF-like module (R3E, yellow), and C-terminal subrepeat B (R3B, cyan). A metal ion presumed to be calcium ion was found in subrepeat B. **(b)** Crystal structure of two-repeat fragment R5-6. Two repeat units are arranged side by side and related by an almost perfect translation. The two lysine residues critical for receptor binding (Lys-2360 and -2467) are highlighted in the stick model. Calcium ions and N-glycans are shown in sphere and stick-model, respectively. **(c)**Averaged electron tomogram of four-repeat fragment R3-6. Space-filling models of four reelin repeats are fitted onto the envelope calculated from electron microscopy.

The recombinant R5-6 fragment was also produced in mammalian cell. For structure determination, we collected diffraction data at beamline **BL41XU**. We solved the structure by the molecular replacement method at 2.0 Å resolution [2] (Fig. 2(b)). The structural features of the R5 and R6 units are almost identical to those of R3, but their spatial arrangement is unique and unprecedented. These homologous R5 and R6 units are positioned side by side and related by an almost perfect translation, without any bends or twists at the junction. R5 and R6 are connected by a short linker, and they make intimate contact through hydrophobic interactions. Electron tomographic imaging also indicated the same type of arrangement of reelin repeats. A four-repeat fragment, R3-6, was subjected to electron microscopy, and was shown to form a rod-like structure (Fig. 2(c)). The longest dimension of R3-6 is almost twice that of R5-6, and the other two-dimensions are almost the same as those of R5-6. Presumably, all four repeats in R3-6 are arranged similarly to those in R5-6.

Subsequently, we attempted to identify the receptor-biding site on reelin. Structural studies of other lipoprotein receptor-ligand systems elucidated the importance of lysine residues of the ligands in the interaction. We designed a series of point mutants, in each of which a single lysine residue was changed to alanine. On the basis of the structure of R5-6, we selected lysine residues located at the molecular surface and close to the boundary between R5 and R6. Finally, we found that Lys-2360 and -2467 are involved in receptor-binding. In addition, the mutation of Lys-2467 to alanine, in the context of either R5-6 or full-length reelin, abolished their ability to induce Dab-1 phosphorylation in neurons, which means that this residue is essential for the signaling. We are now trying to crystallize the reelin fragment in complex with its receptor so as to confirm the involvement of the two lysine residues in the interaction and to further analyze the binding mechanism on the basis of the three-dimensional structure at an atomic level.

Terukazu Nogi*, Norihisa Yasui and Junichi Takagi

Institute for Protein Research, Osaka University

* E-mail: nogi@protein.osaka-u.ac.jp

References

[1] *T. Nogi, N. Yasui, M. Hattori, K. Iwasaki and J. Takagi: EMBO J.* ***25*** *(2006) 3675.*
[2] *N. Yasui, T. Nogi, T. Kitao, Y. Nakano, M. Hattori and J. Takagi: Proc. Natl. Acad. Sci. USA* ***104*** *(2007) 9988.*

Real-time Small-angle X-ray Scattering Observation of Assembly and Disassembly Dynamics of Cyanobacterial Periodosome

Circadian clocks are endogenous timing systems enabling a variety of living organisms to adapt daily alternations of environments on earth. Cyanobacterium *Synechococcus elongatus* PCC 7942 is one of the simplest organism known to possess a self-sustained circadian oscillator composed of three clock proteins termed KaiA, KaiB, and KaiC [1]. KaiA enhances the autophosphorylation of KaiC, whereas KaiB induces the autodephosphorylation of KaiC by antagonizing KaiA activity. Recently, Nakajima *et al.* succeeded in reconstructing the KaiC phosphorylation cycle *in vitro* solely by incubating KaiA, KaiB, and KaiC in the presence of ATP [2]. This pioneering work suggests that the Kai proteins are assembled and disassembled into heteromultimeric Kai complexes (periodosome) to effect a circadian switching of KaiC activity from autophosphorylation to autodephosphorylation and *vice versa*.

In order to elucidate the oscillatory mechanism, much attention has been focused on the structure of the Kai periodosome. To date, the crystal structures of the individual Kai proteins have already been determined independently [3]. However, a potential relationship between the assembly/disassembly dynamics and the KaiC phosphorylation cycle is still poorly understood because of the difficulty in unraveling the underlying mechanisms solely from the static crystal structure of individual clock components. Although it is important to characterize Kai complexes along a reaction coordinate, a blind search for crystallization conditions of oscillatory-transient complexes is not necessarily a promising strategy.

To take a structural snapshot of the Kai periodosome, we followed the assembly/disassembly dynamics of a ternary mixture containing KaiA, KaiB, and KaiC in real-time using small-angle X-ray scattering (SAXS) at beamline **BL45XU** [4]. As shown in Fig. 1, weight-averaged molecular weight (MW^{app}) estimated from forward scattering intensity of measured SAXS curves increased dramatically upon mixing three Kai proteins and peaked at 9 h. After a monotonous decrease from 9 to 18 h, MW^{app} revealed a robust oscillation with a period of 24.4 h. Interestingly, MW^{app} was phase-delayed by approximately 6.6 h (6.6/24.4 = ~π/2) relative to the phosphorylated KaiC fraction ($Phos^{app}$), whereas the period of MW^{app} was nearly identical to that of $Phos^{app}$ (23.8 h). The phase delay of π/2 implies that $Phos^{app}$ is closely related to the time derivative of MW^{app}, and that there is a relationship between reactant and product. The current observations therefore suggest that the assembly/disassembly of the Kai periodosome is not under steady-state conditions, but evidently driven by the phosphorylation status of KaiC.

To investigate the relationship between the Kai complex structure and KaiC phosphorylation, we conducted titration SAXS experiments [4,5] for binary mixtures of KaiA and KaiC, and KaiB and KaiC. Titration data sets of both binary pairs were fitted uniquely to a theoretical curve for a 1:1 binding scheme. The dissociation constant (K_d) of the phosphorylated KaiA:^{P}KaiC complex (4.7 μM) was approximately 40-fold larger than that of the dephosphorylated KaiB:^{NP}KaiC complex (0.12 μM), indicating a greater affinity of KaiB for ^{NP}KaiC than of KaiA for ^{P}KaiC.

On the basis of the binding scheme and K_d, the scattering curves of the binary complexes were estimated by global fitting on the titration data set. Low-resolution envelopes were restored from the deconvoluted SAXS curves (Figs. 2(a) and 2(c)), onto which the crystal structure of each Kai protein was uniquely superimposed (Figs. 2(b) and 2(d)). Our complex models clearly demonstrate that KaiA binds a

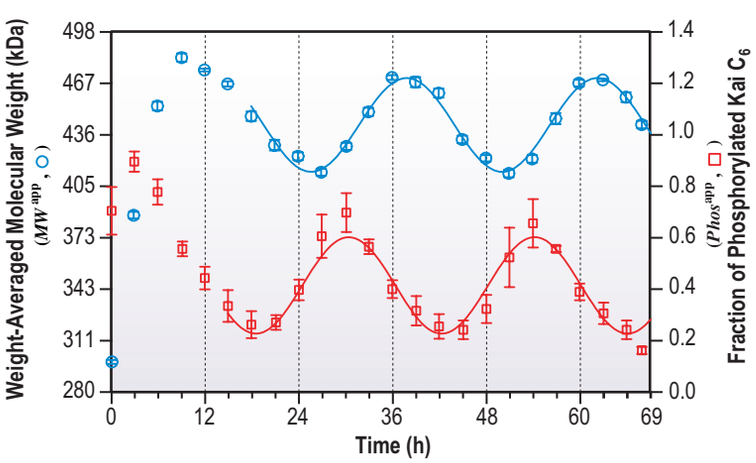

Fig. 1. Assembly/disassembly dynamics of ternary mixture containing KaiA, KaiB, and KaiC in the presence of ATP. Weight-averaged molecular weight (MW^{app}, blue open circle) is phase-delayed by π/2 relative to phosphorylated KaiC fraction ($Phos^{app}$, red open square). The solid lines represent sine-wave functions fitted to the experimental data.

broad interface ranging from the C2 domain to the tail of ^{P}KaiC. Interestingly, KaiB shares a common docking site of the C2 domain with KaiA.

These binary interactions offer a reasonable explanation for the assembly/disassembly of the Kai periodosome in a phosphorylation-dependent manner. Upon mixing three Kai proteins, KaiA immediately binds KaiC to form the KaiA:KaiC complex, thereby enhancing the autophosphorylation of KaiC. KaiB then approaches the KaiA:^{P}KaiC complex to inhibit KaiA activity. Because of the greater affinity of KaiB for the common docking site of the C2 domain than KaiA, KaiB can displace KaiA of the KaiA:^{P}KaiC complex, and thereby switching KaiC activity from autophosphorylation to autodephosphorylation.

It must be noted that the Kai periodosome assembles and disassembles robustly also *in vivo* [1,2]. This is astonishing because assembly/disassembly processes under physiological conditions should be affected to some extent by crowding and higher viscosity. From the crystal structure [3], dual phosphorylation sites of KaiC are localized to the C2 domain. Thus, the resistances against crowding and viscosity will be achieved in the Kai complexes by controlling the timing of assembly/disassembly of KaiA and/or KaiB though phosphorylation-dependent structural changes of the C2 domain of pacemaking KaiC.

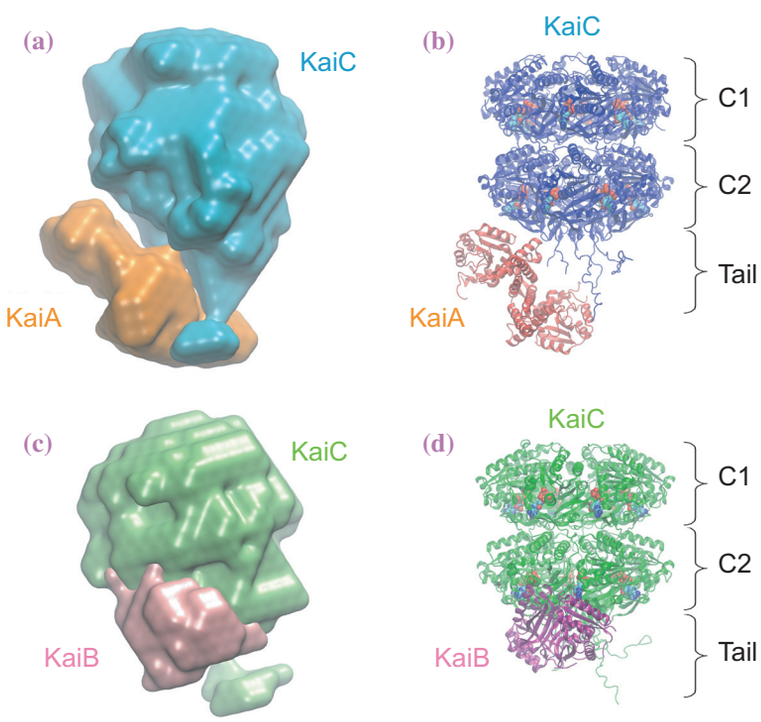

Fig. 2. Low-resolution models of Kai complexes. **(a)** Low-resolution envelope of KaiA:^{P}KaiC complex restored from SAXS data. **(b)** Superimposed crystal structures of KaiA and KaiC to low-resolution model of KaiA:^{P}KaiC complex. **(c)** Low-resolution envelope of KaiB:^{NP}KaiC complex restored from SAXS data. **(d)** Superimposed crystal structures of KaiB and KaiC to low-resolution model of KaiB:^{NP}KaiC complex.

Shuji Akiyama[a,b,*], Atsushi Nohara[c], Kazuki Ito[b] and Yuichiro Maéda[d,e]

[a] PRESTO, Japan Science and Technology Agency
[b] SPring-8 / RIKEN
[c] Division of Biological Science, Nagoya University
[d] Structural Biology Research Center, Nagoya University
[e] ERATO Actin Filament Dynamics Project

*E-mail: akishu@spring8.or.jp

References

[1] M. Ishiura *et al.*: Science **281** (1998) 1519.
[2] M. Nakajima *et al.*: Science **308** (2005) 414.
[3] C.H. Johnson and M. Egli: Nat. Struct. Mol. Biol. **11** (2004) 584.
[4] *S. Akiyama, A. Nohara, K. Ito and Y. Maéda: Mol. Cell* ***29*** *(2008) 703.*
[5] S. Yamada *et al.*: J. Mol. Biol. **362** (2006) 123.

Structural Insights into RNA-dependent Cysteine Biosynthesis in Archaea

The universal genetic code of twenty amino acids is interpreted by the canonical set of aminoacyl-tRNA synthetases (aaRSs), which attach specific amino acids to their cognate tRNAs. However, methanogenic archaea lack the canonical cysteinyl-tRNA synthetase (CysRS) for the "direct" Cys-tRNA^{Cys} formation. In such organisms, Cys-tRNA^{Cys} is produced by the "indirect" pathway, in which non-canonical *O*-phosphoseryl-tRNA synthetase (SepRS) ligates a non-canonical amino acid, *O*-phosphoserine (Sep), to tRNA^{Cys}, and Sep-tRNA:Cys-tRNA synthase (SepCysS) converts the produced Sep-tRNA^{Cys} to Cys-tRNA^{Cys} (Fig. 1). The unique feature of *O*-phosphoserine is that it has divalent negative charges in the side-chain phosphate group, unlike the 20 canonical amino acids. The SepRS/SepCysS pathway is the sole route for cysteine biosynthesis in such organisms. The "indirect" pathway for Cys-tRNA^{Cys} formation by SepRS/SepCysS is ancient and may predate the "direct" pathway by CysRS. Therefore, elucidation of the structure of SepRS and its recognition mechanism for tRNA^{Cys} and *O*-phosphoserine may contribute to our understanding of the evolution of the genetic code table. To gain insight into the evolution of cysteine coding, we determined the crystal structures of the *Archaeoglobus fulgidus* SepRS·tRNA^{Cys}·*O*-phosphoserine ternary complex (Fig. 2 and Fig. 3) [1] and *A. fulgidus* SepCysS (Fig. 4) [2] at 2.6 and 2.4 Å resolutions, respectively, using **BL41XU** beamline.

SepRS forms an α_4 tetramer, which binds two tRNA^{Cys} molecules (Fig. 2(b)). This is the first structure of an aaRS that forms an α_4 tetramer. The SepRS monomer consists of four parts, the N-terminal extension, the catalytic domain, the inserted domain, and the C-terminal anticodon-binding domain, which are connected by linker loops (Fig. 2(a)). No structural neighbors of the inserted domain and the anticodon-binding domain were detected by a DALI search. Therefore, the two domains are novel structures. The aminoacylation catalytic domain recognizes *O*-phosphoserine uniquely (Fig. 3(a)). The phosphate moiety of *O*-phosphoserine is extensively recognized; each of the three non-bridging oxygen atoms is recognized via two hydrogen bonds. The N-terminal end of the conserved central helix, which is positively charged by the dipole moment of the α-helix, contributes to the recognition. Notably, the involvement of protein main-chain groups in the recognition of the amino-acid side chain of the substrate is unique to SepRS, and has never been observed in canonical aaRSs. The GCA anticodon bases of tRNA^{Cys} are located on the edge of the long two-stranded antiparallel β-sheet in the anticodon-binding domain and are recognized in a sequence-

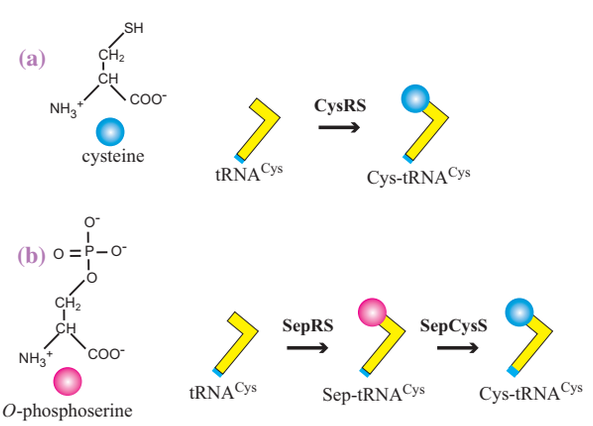

Fig. 1. **(a)** "Direct" Cys-tRNA^{Cys} formation by CysRS in normal organisms. **(b)** "Indirect" Cys-tRNA^{Cys} formation by SepRS and SepCysS in methanogenic archaea.

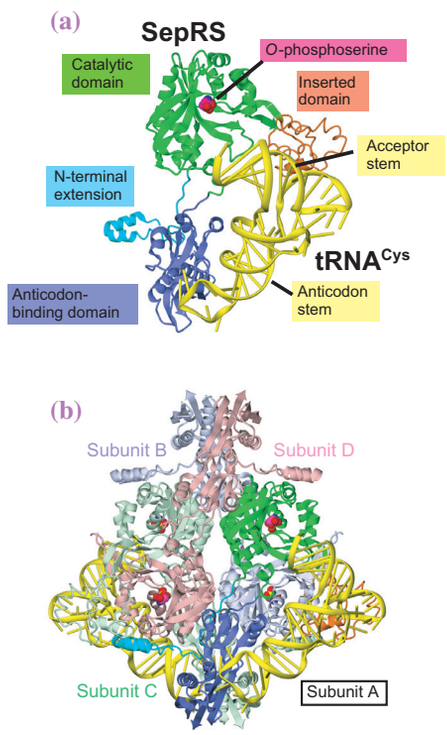

Fig. 2. **(a)** Overall structure of *A. fulgidus* SepRS·tRNA^{Cys}·*O*-phosphoserine complex. The tRNA^{Cys} and *O*-phosphoserine molecules are represented by yellow tubes and magenta ball-and-stick models, respectively. **(b)** *A. fulgidus* SepRS α_4 tetramer complexed with two tRNA^{Cys} molecules and four *O*-phosphoserine molecules. Color coding is as in **(a)** for SepRS subunit A. SepRS subunits B, C, and D are shown in light blue, light green, and light pink, respectively.

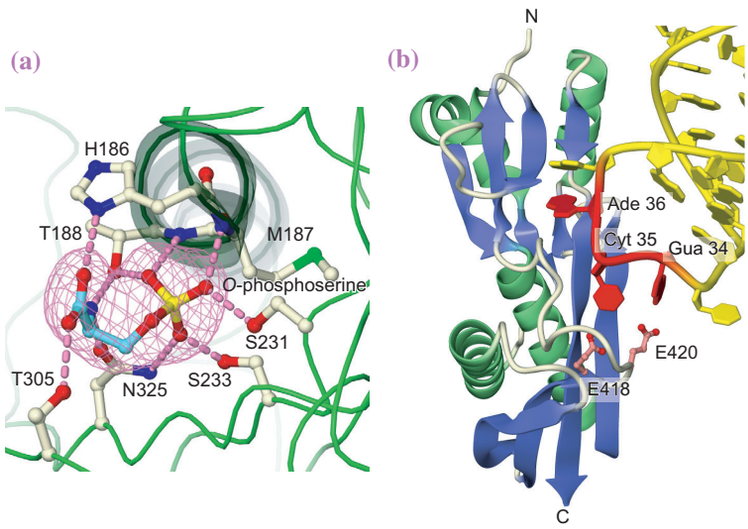

Fig. 3. **(a)** Recognition mechanism for *O*-phosphoserine in SepRS catalytic domain. **(b)** Recognition mechanism for GCA anticodon of $tRNA^{Cys}$ in SepRS C-terminal anticodon-binding domain.

specific manner (Fig. 3(b)).

SepCysS forms an α_2 dimer (Fig. 4(a)). The SepCysS monomer is composed of large and small domains. The large domain has a seven-stranded β-sheet, which is typical of pyridoxal 5'-phosphate (PLP)-dependent enzymes. In the active site, which is located near the dimer interface, PLP is covalently bound to the side chain of the conserved Lys209 by an aldimine bond. Lys209 is located on a short α-helix inserted into the seven-stranded β-sheet. PLP is deeply bound within the active site cleft near the dimer boundary. The active site is sufficiently wide to accommodate the 3'-end of Sep-$tRNA^{Cys}$.

On the basis of the two determined structures, we were able to construct the model structure of the SepRS·$tRNA^{Cys}$·SepCysS ternary complex (Fig. 4(b)). In the ternary complex, the phosphoserylated 3'-terminus of $tRNA^{Cys}$ can be transferred directly from SepRS to SepCysS, for conversion to the cysteinylated form. Such a mechanism may prevent the intermediate Sep-$tRNA^{Cys}$ from being delivered to the ribosome and prevent mistranslation.

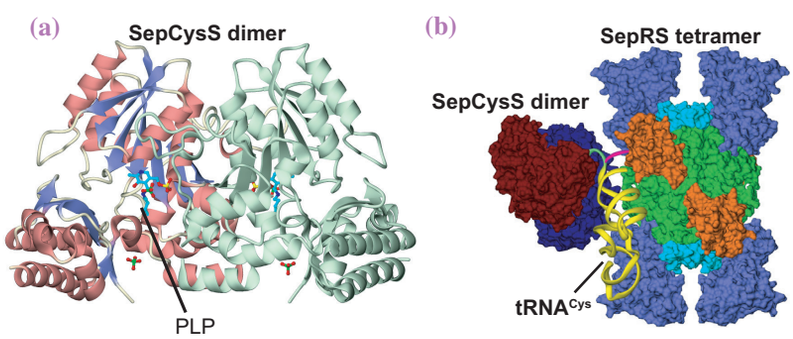

Fig. 4. **(a)** Overall structure of *A. fulgidus* SepCysS dimer. The α-helices and the β-strands of subunit A are shown in pink and blue, respectively. Subunit B is shown in light green. The internal aldimine Lys209-PLP is represented by a cyan ball-and-stick model. **(b)** Modeled ternary complex of SepRS·$tRNA^{Cys}$·SepCysS. The four 3'-terminal nucleotides of $tRNA^{Cys}$ are modeled for the SepCysS active site (green) and SepRS active site (magenta).

Ryuya Fukunaga[a,b,*,†] and Shigeyuki Yokoyama[a,b]

[a] Dept. of Biophysics and Biochemistry, The University of Tokyo
[b] RIKEN Genomic Sciences Center, Yokohama

*E-mail: fukunaga@berkeley.edu

[†] Present address: Dept. of Molecular and Cell Biology, University of California, Berkeley, USA

References

[1] *R. Fukunaga and S. Yokoyama: Nat. Struct. Mol. Biol.* ***14*** *(2007) 272.*
[2] *R. Fukunaga and S. Yokoyama: J. Mol. Biol.* ***370*** *(2007) 128.*

Structural Basis of Dynamic Polymerization of DIX Domains: Revised Model of Wnt Signaling

The Wnt signaling pathway controls numerous cell fates in animal development, and is also a major cancer pathway. A key negative cytoplasmic effector of this pathway is Axin, one of the components of the "destruction complex," which promotes phosphorylation of β-catenin and its subsequent degradation. Another key cytoplasmic effector, Dishevelled (Dvl), a positive effector of this pathway, binds to the Wnt transmembrane receptors, Frizzled and LRP5/6, and interacts with Axin to inhibit phosphorylation of β-catenin. Then, β-catenin is accumulated and translocated to the nucleus where it binds T-cell-specific transcription factor or lymphoid-enhancer factor to activate transcription of Wnt target genes. Axin functions as a tumor suppressor, and mutation of Axin often results in development of various human cancers.

Both Dvl and Axin contain a DIX domain, a functionally important domain whose molecular properties and structure have been unclarified. We have determined the first crystal structure of the Axin-DIX domain at 2.9 Å resolution by the single-anomalous diffraction method using data collected at **BL41XU** beamline [1]. DIX has a ubiquitin-like fold with five β-strands (β1-β5) and one α-helix. DIX interacts with neighboring molecules in a head-to-tail manner through a β-bridge between β2 and β4, forming filaments in the crystal (Fig. 1). Specifically, Y766 and I764 on β2 of one monomer interact with Y793 on β3 and F807 on β4 of the adjacent monomer (Fig. 2), thus forming a hydrophobic cluster.

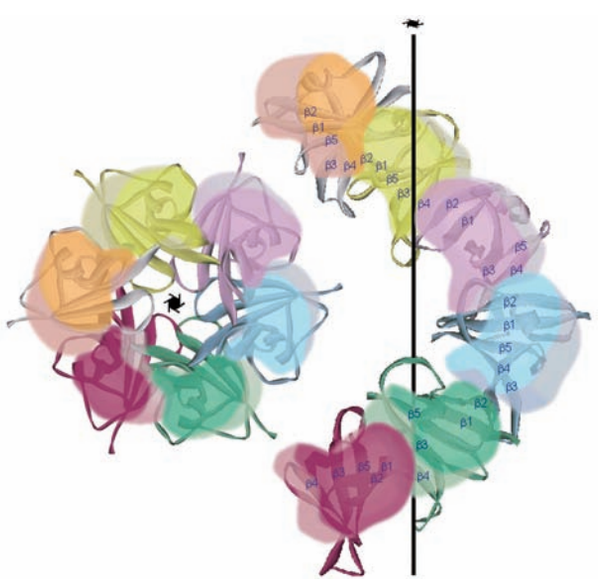

Fig. 1. Helical filament formed by Axin-DIX domain in crystal. Homomeric filament formed by Axin-DIX domain along crystallographic 6_1-axis. The filament is formed by head-to-tail interactions predominantly between β2 and β4 surfaces.

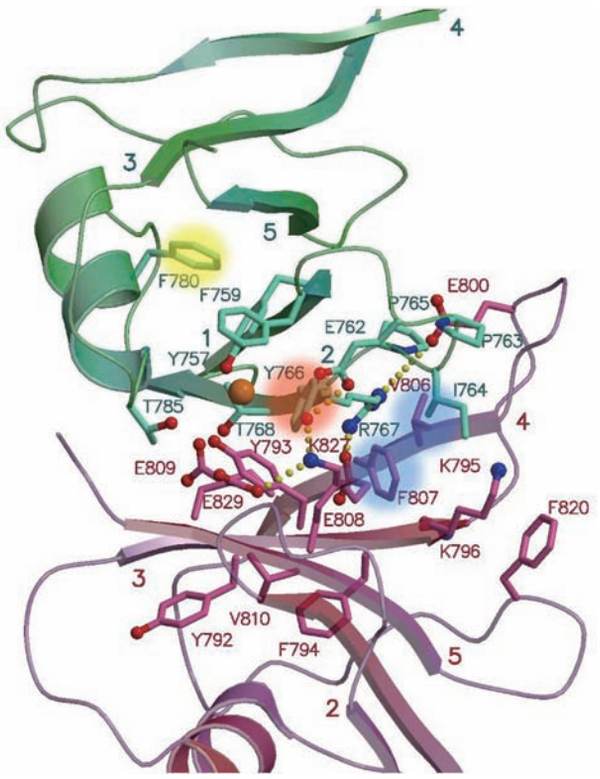

Fig. 2. Residues involved in intermolecular interactions between Axin-DIX domains. The residues corresponding to the mutated residues Y27, F43, and V67/K68 of Dvl2 mutants are highlighted in red, yellow, and blue, respectively. The orange sphere indicates an isolated electron density peak at the molecular interface.

The DIX domain of Dvl2 mediates dynamic polymerization, which is essential for the signaling activity of Dvl2 *in vivo* [1]. The purified DIX domain self-associates *in vivo*, and polymerizes gradually and reversibly in a concentration-dependent manner, ultimately forming fibrils [1]. The sequences of Dvl2 and Axin-DIX domains are highly homologous and both self-associate *in vitro* [2]. Mutation studies of Dvl2 in the DIX domain showed that Y27D (designed from the crystal structure), F43S, and V67A/K68A point mutations, which correspond to Y766, F780, and V806/F807 in Axin, respectively, abolished both Wnt signaling activity and dynamic polymerization ability [1]. Y766, V806, and F807 of Axin are on the

molecular interface between adjacent monomers in the crystal (Fig. 2). The mutation of these residues may weaken β2-β4 interaction. F780 is a core residue of the domain; therefore, it may affect the intra-filamental interaction indirectly.

These studies suggest the crucial role of polymerization of Dvl2 through its DIX domain in the Wnt signaling pathway. Increasing local concentration of Dvl2 by clustering may increase the avidity of Dvl2 for low-affinity binding partners such as Axin and Frizzled (Fig. 3). The DIX domain mediates the formation of a dynamic interaction platform with a high local concentration of binding sites for transient signaling partners.

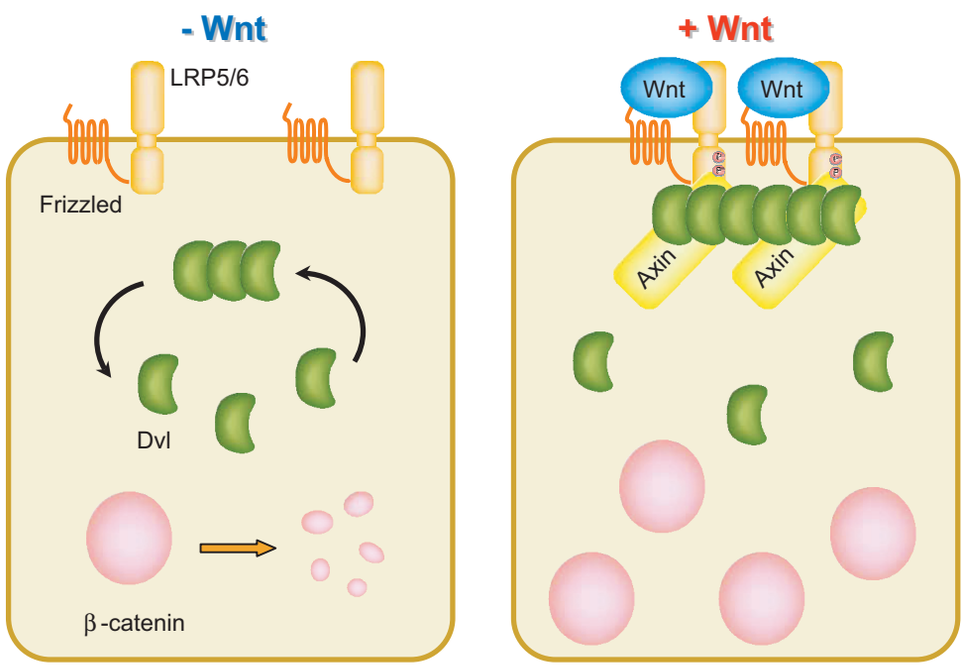

Fig. 3. Revised model of Wnt signaling. Left panel: In the absence of Wnt, Dvl remains cytoplasmic and in equilibrium between monomers and polymers. The destruction complex is active, and β-catenin is degraded. Right panel: Wnt stimulation triggers Dvl recruitment to the plasma membrane by Frizzled receptors, which function with LRP5/6 coreceptors. Dvl polymers at the membrane serve as a dynamic scaffold for Axin recruitment and inactivation. Wnt stimulation also leads to phosphorylation of LRP5/6. Phosphorylated LRP5/6 can interact with Axin, potentially providing another mechanism of recruitment and inactivation of Axin at the membrane.

Naoki Shibata [a,b] and Yoshiki Higuchi [a,b,*]

[a] Department of Life Science, University of Hyogo
[b] SPring-8 / RIKEN

*E-mail: hig@sci.u-hyogo.ac.jp

References

[1] *T. Schwarz-Romond, M. Fiedler, N. Shibata, P.J.G. Butler, A. Kikuchi, Y. Higuchi, M. Bienz: Nat. Struct. Mol. Biol.* ***14*** *(2007) 484.*
[2] C. Sakanaka and L.T. Williams: J. Biol. Chem. **274** (1999) 14090.

Crystal Structures of [NiFe] Hydrogenase Maturation Proteins, HypC, HypD, and HypE

[NiFe] hydrogenases catalyze the reversible formation of molecular hydrogen in a variety of microorganisms. The core enzyme of [NiFe] hydrogenases carries a $NiFe(CO)(CN)_2$ metal center at the active site. The synthesis of this metal center is a complex process, in which specific maturation proteins, six Hyp proteins (HypABCDEF), are required [1]. HypA and HypB are involved in the insertion of the Ni atom into the precursor large subunit. HypE and HypF are involved in the synthesis of the cyanide ligand attached to the active site Fe atom. HypF catalyzes the transfer of the carbamoyl group from a carbamoylphosphate to the C-terminal cysteine residue of HypE coupled with the conversion of ATP to AMP and PPi. An ATP-dependent dehydration by HypE converts HypE-carboxamide to HypE-thiocyanate. HypC and HypD form a complex that is presumably involved in the insertion of the Fe atom coordinated by diatomic ligands. The HypCD complex receives the cyanide ligand from HypE-thiocyanate and is assumed to insert the Fe atom into the precursor large subunit of [NiFe] hydrogenases. However, the mechanism of the CN transfer to the iron atom in the ternary complex remains unclear. In order to gain insight into the mechanism of the cyanation reaction, we have determined crystal structures of HypC, HypD, and HypE from a hyperthermophilic archaeon, *Thermococcus kodakaraensis* KOD1 at 1.8 Å, 2.07 Å, and 1.55 Å resolution, respectively, using beamlines **BL41XU** and **BL44B2** [2].

The overall structure of HypC consists of a β-barrel (oligonucleotide/oligosaccharide binding (OB)-fold) domain and a C-terminal α helix (Fig. 1(a)). N-terminal residues adopt an extended conformation, which allows the essential cysteine residue (Cys2) to make contact with the solvent. Comparison of three HypC monomers in the asymmetric unit has shown that the arrangement of the OB-fold domain and the C-terminal helix differs between the monomers (Fig. 1(b)), suggesting that the C-terminal α helix is very flexible.

The overall structure of HypE consists of two α/β domains (domains A and B) and a C-terminal tail (Fig. 2(a)). This structure is similar to that of other PurM proteins, whose members are characterized by a common motif for ATP hydrolysis. In the crystal, HypE forms a homodimer with a symmetry-related molecule (Fig. 2(b)). The structure of the HypE dimer also resembles that of the PurM dimer. In the HypE dimer, four conserved motifs are assembled at the active site, suggesting that the HypE dimer is a functional unit for ATP-dependent dehydration.

The crystal structure prepared by co-crystallization with ATP shows that the C-terminal tail of HypE exists in an ATP-dependent dynamic equilibrium between outward and inward conformations (Fig. 2(c)). In the

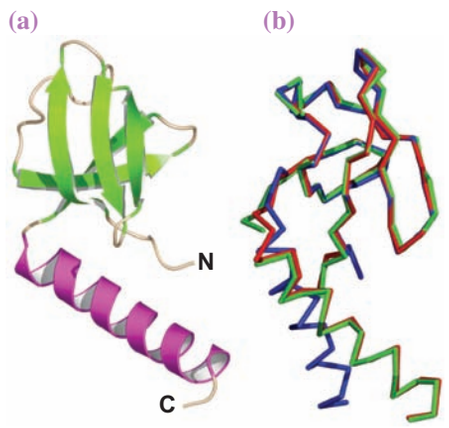

Fig. 1. Crystal structure of HypC. **(a)** Overall structure of HypC in a ribbon representation. The OB fold domain is shown in green; the C-terminal α helix is shown in pink. **(b)** A superposition of the Cα backbone of the three HypC molecules in the asymmetric unit.

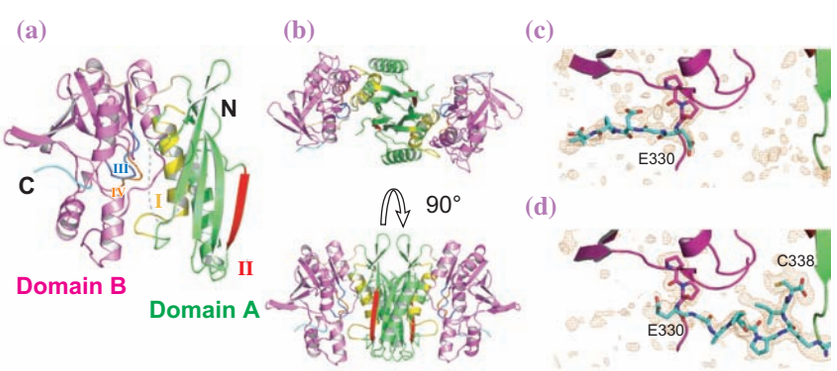

Fig. 2. Overall structure of HypE. **(a)** Ribbon representation of the overall structure of HypE. The two α/β domains A and B, and the C-terminal tail are shown in green, pink, and cyan, respectively. The conserved motifs I, II, III, and IV are colored yellow, red, blue, and orange, respectively. **(b)** Top (upper panel) and side (lower) views of the HypE dimer. **(c** and **d)** Electron density of a simulated annealing omit map (omitting residues 328-338) around the C-terminal tail in the absence of ATP **(c)** or in the presence of ATP **(d)** is shown at 2.5σ (blue).

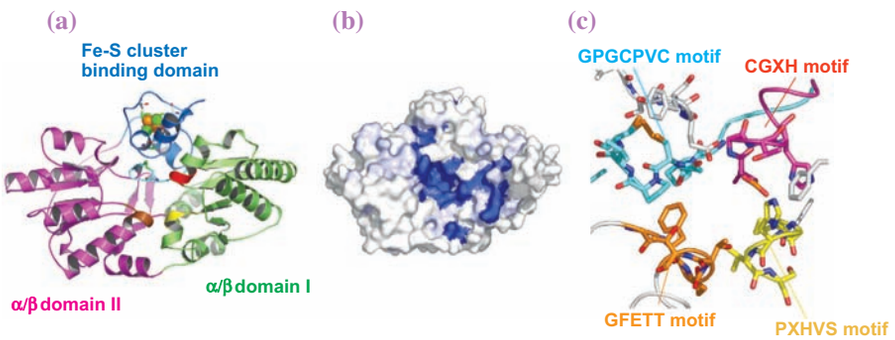

Fig. 3. Overall structure of HypD from *T. kodakaraensis*. **(a)** Ribbon representation of the overall structure of HypD. The two α/β domains I and II, and the Fe-S cluster binding domain are shown in green, magenta, and blue, respectively. Cysteine residues and the [4Fe-4S] cluster are represented in a stick-and-sphere model. **(b)** Surface representation of HypD. Identical and conserved residues among HypD proteins are colored in blue and light blue, respectively. The orientation is identical to that in Fig. 3**(a)**. **(c)** Close view of the assembly of the conserved motifs in a stick representation. The conserved motifs are shown in different colors: CGXH motif, magenta; GPGCPVC motif, cyan; GFETT motif, orange; and PXHVS motif, yellow, respectively.

ATP-unbound state, the C-terminal tail of HypE takes the outward conformation, which is appropriate for receiving carboxamide from a carbamoylphosphate by HypF or for transferring thiocyanate to the HypCD complex. Binding of ATP to HypE will shift the equilibrium toward the formation of the inward conformation, in which HypE dehydrates the S-carboxamide moiety to yield thiocyanate.

The overall structure of HypD consists of three domains: an α/β domain I, an α/β domain II, and an Fe-S cluster binding domain (Fig. 3(a)). The Fe-S cluster-binding domain carries a [4Fe-4S] cluster. The overall architecture of HypD is not similar to any other known structures. These three domains form a cleft at the center of the molecule. Mapping of conserved residues on the molecular surface has shown that residues around the center cleft are highly conserved (Fig. 3(b)). In particular, the four conserved motifs are assembled at the bottom of the cleft (Fig. 3(c)). Therefore, these observations strongly suggest that the active site of HypD is constructed by the four conserved motifs.

The crystal structure of HypD reveals that the disulfide bond SS2 (Cys325-Cys354) is located very close to the [4Fe-4S] cluster (Fig. 4). The sulfur atom of Cys325 in the reduced form makes a close contact with the iron atom. Furthermore, the disulfide bond SS1 (Cys66-Cys69) is located close to SS2. Unexpectedly, the [4Fe-4S] cluster environment of HypD is quite similar to that of ferredoxin:thioredoxin reductase (FTR), suggesting the existence of a redox cascade between the 4Fe-4S cluster and two disulfide bonds.

The present structures of HypC, HypD and HypE provide deep insights into the cyanation reaction. In particular, the assembly of conserved residues of HypD around the center cleft suggests that the coordination of the cyanide ligand to the Fe atom takes place at the conserved motifs (Fig. 3(c)). The interface between HypD and other Hyp proteins is probably the conserved region around the center cleft (Fig. 3(b)). An extended conformation of each conserved motif of HypC and HypE allows the essential cysteine residues of both proteins to interact with the active site of HypD. Revealed FTR-like redox cascade implies that the cyanation reaction is catalyzed by unique thiol redox signaling in the HypCDE complex.

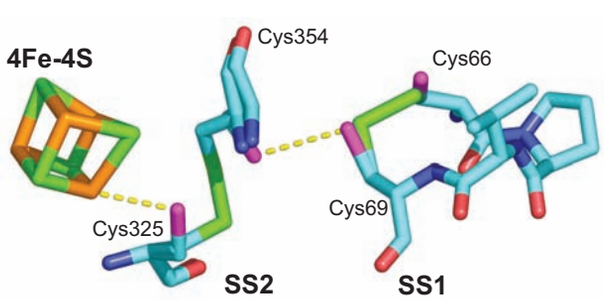

Fig. 4. Redox cascade between the [4Fe-4S] cluster and two disulfide bonds of HypD. Sulfur atoms in the dithiol form of cysteine residues are shown in magenta.

Satoshi Watanabe [a] and Kunio Miki [a,b,*]

[a] Department of Chemistry, Kyoto University
[b] SPring-8 / RIKEN

*E-mail: miki@ kuchem.kyoto-u.ac.jp

References

[1] A. Böck *et al.*: Adv. Microb. Physiol. **51** (2006) 1.
[2] *S. Watanabe, R. Matsumi, T. Arai, H. Atomi, T. Imanaka and K. Miki: Molecular Cell* ***27*** *(2007) 29.*

Extensive Structural Similarity between the Flagellar Type III ATPase FliI and F_1-ATPase Subunits

In response to environmental stimuli, bacteria swim by rotating a filamentous organelle called the flagellum. It is a molecular complex composed of more than 25 kinds of proteins, each in multiple copies from several to several tens of thousands. The flagellar axial proteins and other proteins involved in their assembly and regulation are synthesized in the cytoplasm. They are selectively exported into the central channel of the growing flagellar structure by the flagellar type III export apparatus, and travel through the narrow channel to the growing end for their self-assembly [1]. The flagellar type III export apparatus, which is composed of six integral membrane proteins and three soluble proteins [2] (Fig. 1), is homologous in the quaternary as well as the primary structure level to the virulence type III protein secretion system, which bacterial pathogens use to export its axial component proteins for self-assembly and to secrete effecter proteins into their host cells for invasion. Characterization of these type III protein export systems has been intensively carried out by many groups, and many intriguing features have been revealed, such as export specificity switching for controlling assembly size and selective secretion, involvement of cytoplasmic chaperones, and unfolding of export substrate proteins for export through the channel of about 2 nm in diameter. However, the mechanisms of these functions are still obscure due to lack of structural information.

FliI is a soluble component subunit of the flagellar type III export apparatus and an ATPase that is thought to facilitate the flagellar protein export process. To elucidate the mechanism of type III protein export, we determined the crystal structure of monomeric FliI in complex with ADP at 2.4 Å resolution by using X-ray diffraction data collected at beamline **BL41XU**. Because of the low solubility of native FliI, we prepared a highly soluble variant lacking the first 18 residues, FliI(Δ1-18), crystallized it and solved its structure .

FliI consists of three distinct domains; the N-terminal domain, the ATPase domain and the C-terminal domain (Fig. 2). The central ATPase domain of FliI has a significant similarity in the primary sequence to the α and β subunits of F_oF_1-ATPsynthase [3], but the overall sequence similarity is rather low, and the functions of these two systems are quite different from each other. FliI is involved in protein export and is therefore thought to be a linear motor that unfolds and threads the export substrate proteins through its central channel, while F_oF_1-ATPsynthase is a rotary motor. However, we have

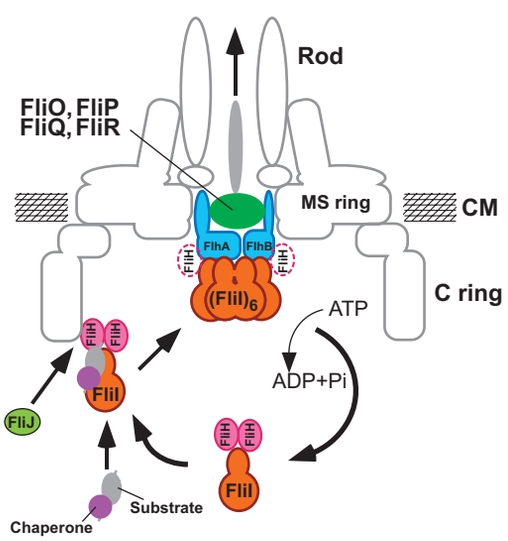

Fig. 1. Schematic diagram of the bacterial flagellar type III protein export apparatus. FlhA, FlhB, FliO, FliP, FliQ and FliR are integral membrane components and FliH, FliI and FliJ are cytoplasmic components. FliI forms a hetero-trimer with the FliH dimer in the cytoplasm and assembles into hexamer upon docking to the cytoplasmic domains of FlhA and FlhB. An export general chaperon FliJ interacts with the FliH/I complex in the cytoplasm.

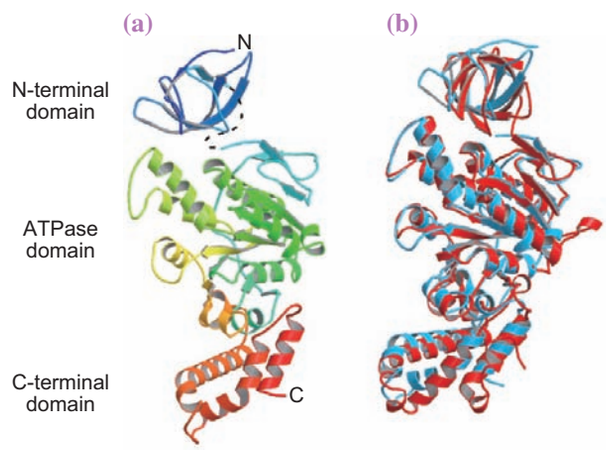

Fig. 2. **(a)** Cα ribbon representation of FliI(Δ1-18). **(b)** FliI(Δ1-18) (cyan) is superimposed to the β_{ADP+Pi} subunit (red) in the ADP-AlF_4 bound form of the F_1-ATPase (PDB code: 1H8E).

found that the entire structure of FliI has a striking similarity to the α and β subunits of F_oF_1-ATPsynthase, both in the conformation of the whole molecule and the ATP binding site. The structure of FliI with ADP exhibited a half closed conformation, which is very similar to the β_{ADP+Pi} subunit of an inhibited form of F_1-ATPase obtained in the presence of aluminium fluoride and Mg-ADP (Fig. 2). Amino acid residues of the F_1-α/β subunits known to be involved in ATP hydrolysis are highly conserved in FliI (Fig. 3). These structural similarities strongly suggest that FliI and F_1-ATPase share a similar catalytic pathway for ATP hydrolysis.

A FliI hexamer model we built by superimposing the atomic model of FliI monomer to each subunit of the $\alpha_3\beta_3$ hexameric ring structure shows that all the differences are found on the outer surface of the ring, while the intersubunit interface and the region surrounding the central channel of the ring are structurally very well conserved (Fig. 4). These results suggest that these two complex molecular machines have been evolved from a common ancestral system and share a common working mechanism albeit the present functions appear to be quite different from each other.

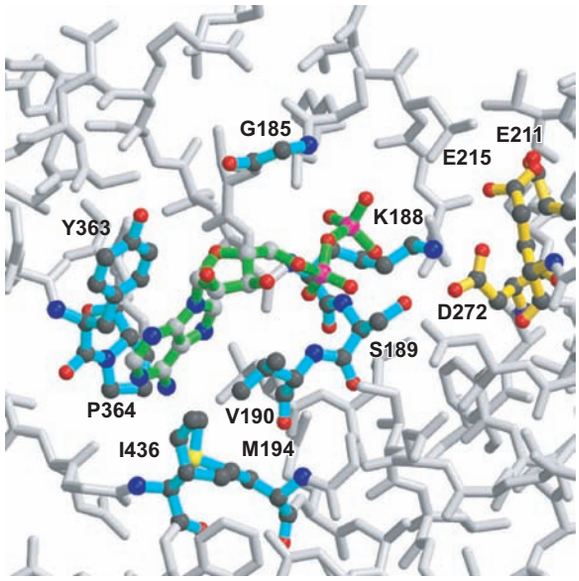

Fig. 3. Close up view of the nucleotide-binding site. The bound ADP is colored green. Residues interacting with ADP are shown in cyan and conserved residues involved in catalysis are colored yellow.

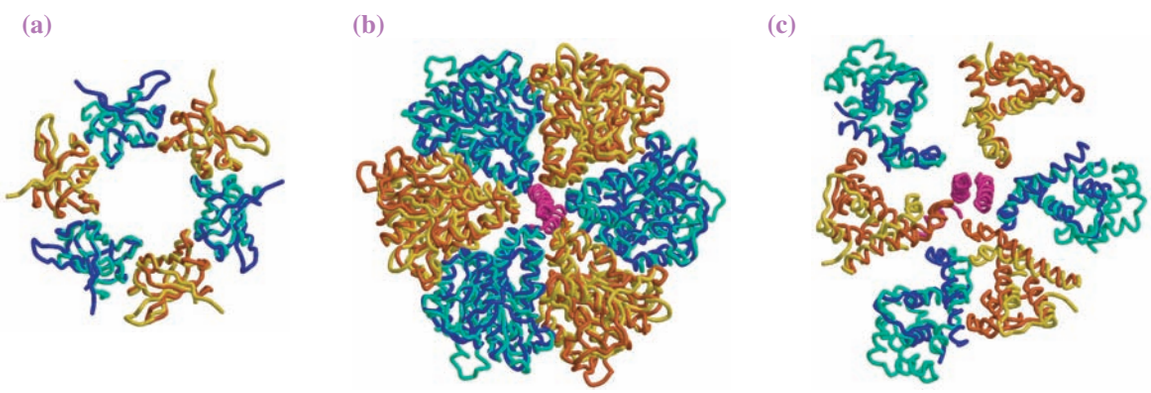

Fig. 4. Superposition of FliI (blue and yellow) to the α (blue green) and β (orange) subunits of F_1-ATPase. **(a)** The N-terminal domain, **(b)** the ATPase domain, and **(c)** the C-terminal domain. The γ subunit of F_1-ATPase at the center is shown in purple.

Katsumi Imada*, Tohru Minamino and Keiichi Namba

Department of Frontier Biosciences, Osaka University

*E-mail: kimada@fbs.osaka-u.ac.jp

References

[1] R.M. Macnab: Annu. Rev. Microbiol. **57** (2003) 77.
[2] T. Minamino and R.M. Macnab: Mol. Microbiol. **35** (2000) 1052.
[3] A.P. Vogler *et al.*: J. Bacteriol. **173** (1991) 3564.
[4] *K. Imada, T. Minamino, A. Tahara and K. Namba: Proc. Natl. Acad. Sci. USA* ***104*** *(2007) 485.*

Structural Basis for Substrate Recognition and Dissociation by Human Transportin 1

The transport of macromolecules between the nucleus and the cytoplasm through nuclear pore complexes (NPCs) is mediated via several transport pathways by transport receptors that are most commonly members of the importin-β family [1]. Transport receptors form complexes with their transport substrates ("cargoes") through cognate nuclear localization signals (NLSs) for import substrates or nuclear export signals (NESs) for export substrates, and target substrates to NPC components. Transportin 1 (Trn1) is a transport receptor that belongs to the importin-β family, and was first identified as the receptor of heterogeneous nuclear ribonucleoprotein A1 (hnRNP A1) [2]. Other substrates whose transport is mediated by Trn1 have since been identified. NLSs of these transport substrates have little sequence similarity, but recent mutational analyses have shown the importance of two successive proline and tyrosine residues (called a PY motif) conserved in the NLSs of hnRNP D, TAP, JKTBP, hnRNP A1, and hnRNP M for recognition by Trn1 [2,3]. Here, we show four crystal structures of human full-length wild-type Trn1 corresponding to Trn1 in a substrate-free form and bound to the following three NLS peptides, which all have a PY motif: hnRNP D NLS (residues 332-355), TAP NLS (residues 53-82), and JKTBP NLS (residues 396-420). We propose a mechanism for NLS recognition and dissociation from Trn1 [4]. Diffraction data for NLS-free Trn1 and Trn1 bound to hnRNP D NLS and JKTBP NLS were collected using an ADSC Quantum 315 CCD detector on **BL41XU** at SPring-8 and those for Trn1 bound to TAP NLS were collected using an ADSC Quantum 210 CCD detector on NW-12 at Photon Factory Advanced Ring (PF-AR).

Trn1 is a superhelical S-like molecule formed by two overlapping arches (N- and C-terminal arches), and is constructed by helical stacking of 20 HEAT repeats (H1-H20) and a long disordered H8 loop (Fig. 1(a)). The structure of the N-terminal arch (HEAT repeats 1-13) is almost the same in the four Trn1 structures, whereas that of the C-terminal arch (HEAT repeats 8-20) changes depending on the NLS to which Trnl is bound (Fig. 1(b)). The overlapping region of the N- and C-terminal arches (HEAT repeats 8-13) show no conformational change. Comparison of the four structures with the structure of the Trn1-RanGTP complex [5] demonstrates that RanGTP binding to the N-terminal arch produces substantial conformational changes in both the N- and C-terminal arches (Fig. 1(b)). Electron density appearance of the three NLSs (Fig. 1(c)) correlates with the dissociation constant for the NLS interaction with Trn1. A NLS with a PY motif is recognized by Trn1 at two sites, Site A (HEAT repeats 8-13) with high affinity and Site B (HEAT repeats 14-18) with low affinity (Fig. 2(a)). Furthermore, three consensus residues (H/R, P, Y) in hnRNP D NLS and TAP NLS and one hydrophobic residue (V) in hnRNP D NLS are recognized at Sites A

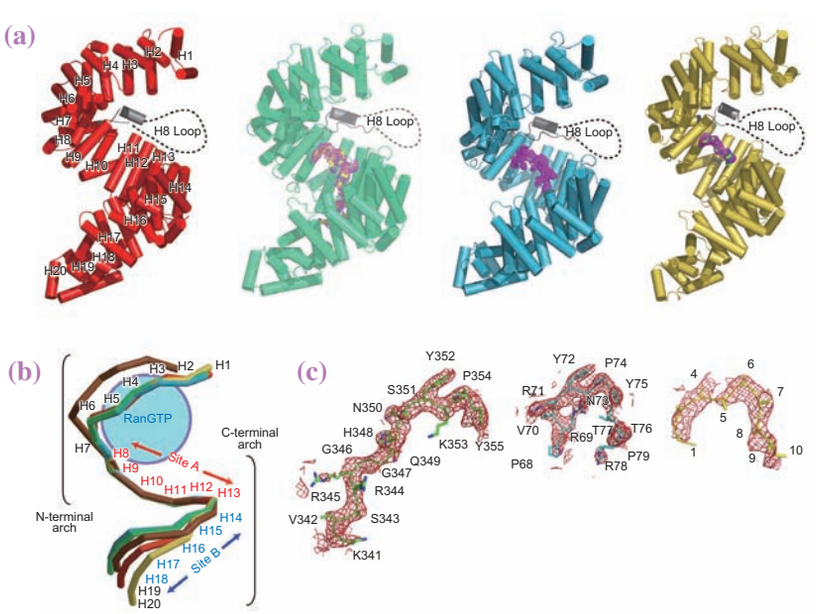

Fig. 1. Structures of Trn1. **(a)** Overall structures of NLS (substrate)-free Trn1 (red) and Trn1 bound to hnRNP D NLS (green), TAP NLS (blue), and JKTBP NLS (yellow), where α helices are represented by cylinders. Twenty consecutive HEAT repeats (H1-H20), each of which is composed of two antiparallel helices, are labeled on the NLS-free Trn1 structure. The H8 loop is represented by a black cylinder (α helix) and a black dotted line (disordered region). **(b)** Trn1 structure showing conformational changes upon either RanGTP or NLS binding. The structures of NLS-free Trn1 (red), Trn1 bound to hnRNP D NLS (green), Trn1 bound to TAP NLS (blue), Trn1 bound to JKTBP NLS (yellow), and Trn1-RanGTP complex (brown) were superimposed in the overlapping region of the N- and C-terminal arches (HEAT repeats 8-13). The 20 consecutive HEAT repeats in each Trn1 molecule are represented by straight lines. The structure of the Trn1-Ran complex was drawn using the refined coordinates deposited in the Protein Data Bank (accession code: 1QBK). **(c)** The CNS composite simulated annealing omit map of the NLS region bound to Trn1. The map was calculated with coefficient $2F_o - F_c$ and contoured at 1.0 σ. NLSs of hnRNP D, TAP, and JKTBP are shown as stick models in green, blue, and yellow, respectively.

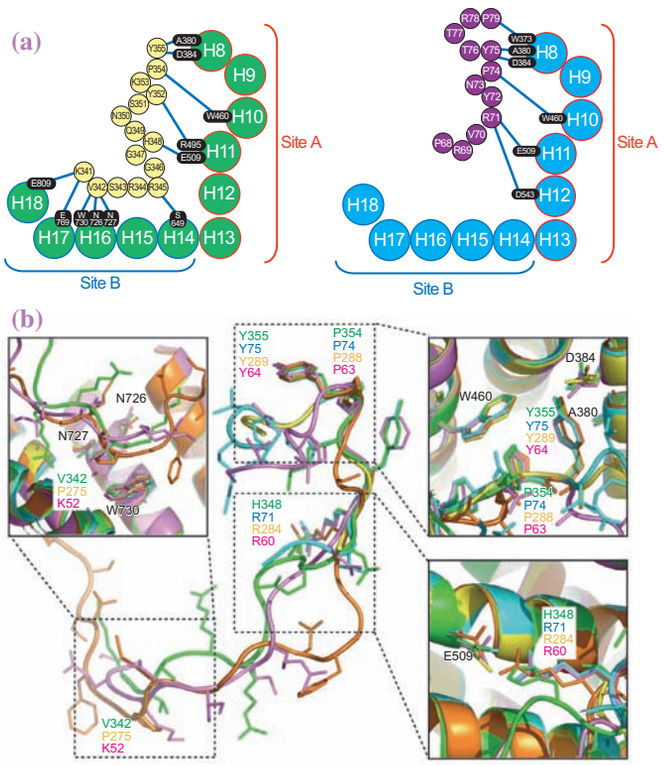

Fig. 2. NLS recognition by Trn1. **(a)** Schematic illustrations of Trn1 interactions with hnRNP D NLS (left) and TAP NLS (right). Trn1-NLS contacts less than 3.8 Å are shown. **(b)** Structures of hnRNP D NLS (green), TAP NLS (blue), hnRNP A1 NLS (orange), and hnRNP M NLS (purple) bound to Trn1. Two close-up views of structures on the right side and one close-up view on the left side show the interactions with Trn1 at Sites A and B, respectively. Structures of hnRNP A1 NLS and hnRNP M NLS bound to a H8 loop-truncated Trn1 mutant were drawn using the refined coordinates deposited in the Protein Data Bank (accession codes: 2H4M and 2OT8).

and B, respectively, in the same manner as that for hnRNP A1 NLS and hnRNP M NLS (Fig. 2(b)).

Figure 3 shows a proposed mechanism for NLS recognition and dissociation from Trn1. In the cytoplasm, Trn1 recognizes the NLS H/R-$X_{(2-5)}$-P-Y motif (X: any residue) at Site A (pre-loaded state). In some cases, Trn1 changes its conformation to make hydrophobic interaction between Site B and the hydrophobic motif of NLS (loaded state). The Trn1-NLS complex is transported through NPC into the nucleus. In the nucleus, RanGTP binding to the N-terminal arch in NLS-bound Trn1 induces a competing interaction from the H8 loop against Site B (pre-unloaded state), resulting in displacement of NLS from Site B. This displacement from Site B is critical for NLSs such as hnRNP D, which interact strongly with Site B. This displacement, however, is not critical for NLSs with weak or no interaction at all with Site B (such as TAP NLS and JKTBP). After the release from Site B, NLS is displaced from Site A by the spatial overlap of the H8 loop with the part of the NLS at Site A, resulting in a complete dissociation from Trn1.

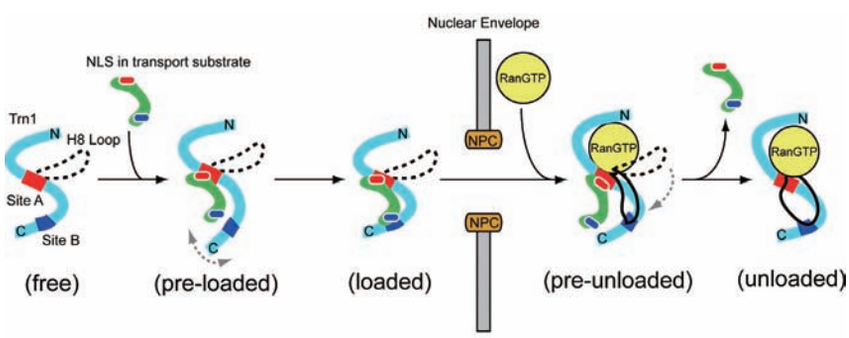

Fig. 3. Proposed mechanism for nuclear import pathway mediated by Trn1. The Trn1 molecule is represented by S-like cyan ribbon labeled with N- and C-termini. NPC is the nuclear pore complex. Red and blue ellipsoids on NLS in the transport substrate show the three consensus residues (red ellipsoid) and one hydrophobic residue (blue ellipsoid).

T. Imasaki, T. Shimizu, H. Hashimoto, M. Yamada and M. Sato*

Field of Supramolecular Biology,
Yokohama City University

*E-mail: msato@tsurumi.yokohama-cu.ac.jp

References

[1] E.J. Tran and S.R. Wente: Cell **125** (2006) 1041.
[2] M. Iijima *et al.*: FEBS Lett. **580** (2006) 1365.
[3] M. Suzuki *et al.*: FEBS J. **272** (2005) 3975.
[4] *T. Imasaki, T. Shimizu, H. Hashimoto, Y. Hidaka, S. Kose, N. Imamoto, M. Yamada, M. Sato: Mol. Cell **28** (2007) 57.*
[5] Y.M. Chook and G. Blobel: Nature **399** (1999) 230.

Crystal Structure of MgtE Mg^{2+} Transporter

Magnesium ion, Mg^{2+}, is one of the most abundant divalent cations in biological systems and vital for all living organisms. For example, Mg^{2+} is essential for ATP utilization and is a cofactor for myriad enzymes, e.g., those in ribosomes. The chemical properties of Mg^{2+} are quite unique among biological cations. Its ionic radius is the smallest whereas its hydrated radius is by far the largest among all cations. Therefore, it has been a mystery how Mg^{2+} transporting proteins selectively recognize and dehydrate the very large fully-hydrated Mg^{2+} cation for its transport.

The MgtE family of Mg^{2+} transporters is ubiquitously distributed in all phylogenetic domains, and human homologues have been functionally characterized and suggested to be involved in magnesium homeostasis. However, its Mg^{2+} transporting mechanism is absolutely unclarified.

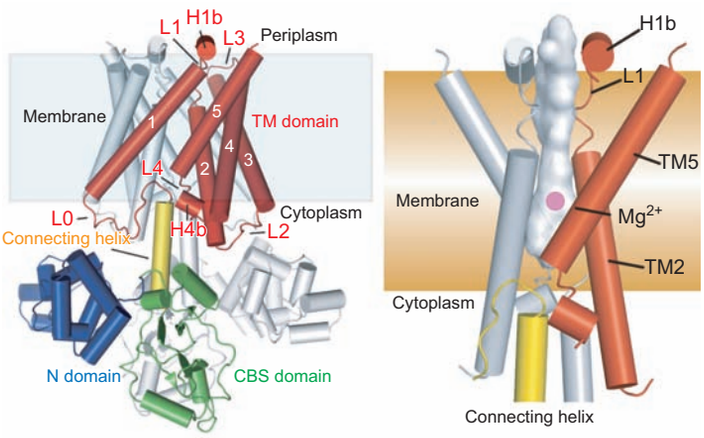

Fig. 1. Structure of MgtE Mg^{2+} transporter. **(a)** The MgtE dimer is viewed in the plane of the membrane, highlighting the N domain (blue), CBS domain (green), connecting helix (yellow), and transmembrane (TM) domain (red) in one subunit. The other subunit is in grey. The transmembrane helices of one subunit are numbered. The membrane surface is indicated. **(b)** Solvent-accessible surface of pore with pore-forming transmembrane helices. The putative Mg^{2+} is shown in purple.

To understand the transport mechanism by MgtE, we determined the crystal structure of full-length *Thermus thermophilus* MgtE at 3.5 Å resolution using beamline **BL41XU** (Fig. 1(a)). The transporter adopts a homodimeric architecture, consisting of the carboxy-terminal transmembrane (TM) domains with five TM helices and the amino-terminal cytosolic domains, which are composed of the superhelical N domain and tandemly repeated cystathionine-β-synthase (CBS) domains. The linker region between the cytosolic and TM domains contains a stretching helix referred to as a 'connecting helix' which is oriented perpendicularly to the membrane interface.

The MgtE structure reveals a putative continuous ion-conducting pathway, formed mainly by the TM2 and TM5 helices (Fig. 1(b)), which does not traverse the membrane at the cytosolic side. The TM5 helices from both subunits close the pore through interactions

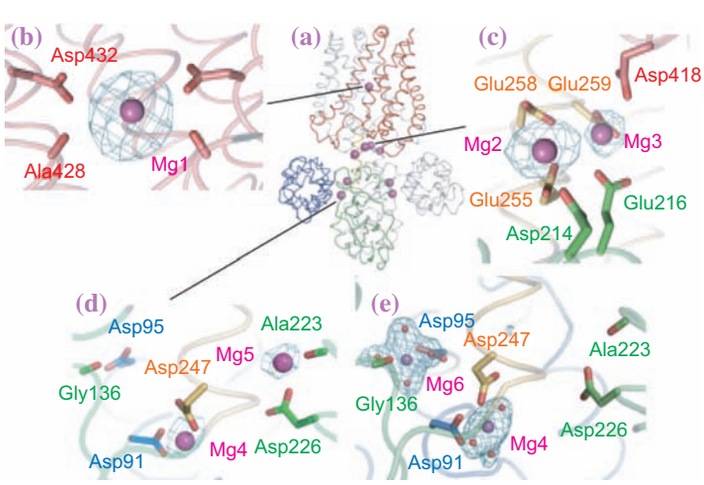

Fig. 2. Putative Mg^{2+} binding sites. The coloring scheme is the same as in Fig. 1. **(a)** Side view of overall structure with bound Mg^{2+}. **(b - d)** Close-up view of respective Mg^{2+} (Mg1-5) binding sites in full-length MgtE structure, with F_o-F_c simulated annealing omit map (contoured at 4.0 σ) calculated with full-length structure excluding Mg^{2+}. **(e)** Close-up view of Mg4 and Mg6 in cytosolic domain with F_o-F_c simulated annealing omit map (contoured at 4.0 σ) calculated with cytosolic domain structure excluding Mg^{2+} and water molecules.

with 'connecting helices'. Therefore, the current structure seems to represent a closed state for ion conduction.

We identified five strong residual electron density peaks (4.0 σ) per MgtE monomer in the full-length MgtE structure (Fig. 2). Considering that the crystallization condition included 40 mM magnesium acetate, and that all of the electron densities are close to the conserved acidic residues, it is reasonable to interpret the densities as Mg^{2+} ions, which are referred to as Mg1-5.

Mg1 is bound to the strictly conserved Asp 432 within the pore, which is presumably critical for the Mg^{2+} transporting activity. The other four putative Mg^{2+} ions (Mg2-5) are bound at the interface between the connecting helices and the other domains, and this may lock the current closed conformation of the pore.

We also determined the cytosolic domain structures in the presence and absence of Mg^{2+} at 2.3 Å and 3.9 Å resolutions, respectively. A structural comparison of the cytosolic domains in the presence and absence of Mg^{2+} revealed that the respective structures of the N and CBS domains are essentially identical, but the domain organization is markedly changed (Fig. 3(a,b)). In particular, the structures of the dimeric CBS domains are significantly changed. On the basis of the structural comparison of the cytosolic domains in two states, we propose here the following transport mechanism. In the presence of Mg^{2+}, the CBS domains tightly dimerize and the following connecting helices are fixed by Mg2-, Mg3- and Mg4-mediated interactions with the cytosolic and TM domains, which close the ion-conducting pore and lock the closed state (Fig. 3(c)). In contrast, in the absence of Mg^{2+}, the dimer interface of the CBS domains is loosened; consequently, the connecting helices are 'unlocked' and rotated by 20° to swing away from each other (Fig. 3(b)). This movement of the connecting helices disrupts the interactions between the connecting helices and the TM domains, thus allowing the rearrangement of the pore-forming TM helices (TM2 and TM5) and leading to the opening of the ion-conducting pore (Fig. 3(d)). Altogether, the cytosolic domain of MgtE may function as a 'Mg^{2+} sensor', which regulates the gating of the Mg^{2+} transporting pore by sensing the intracellular Mg^{2+} concentration, representing a putative negative feedback or Mg^{2+} homeostasis mechanism (Fig. 3(c,d)).

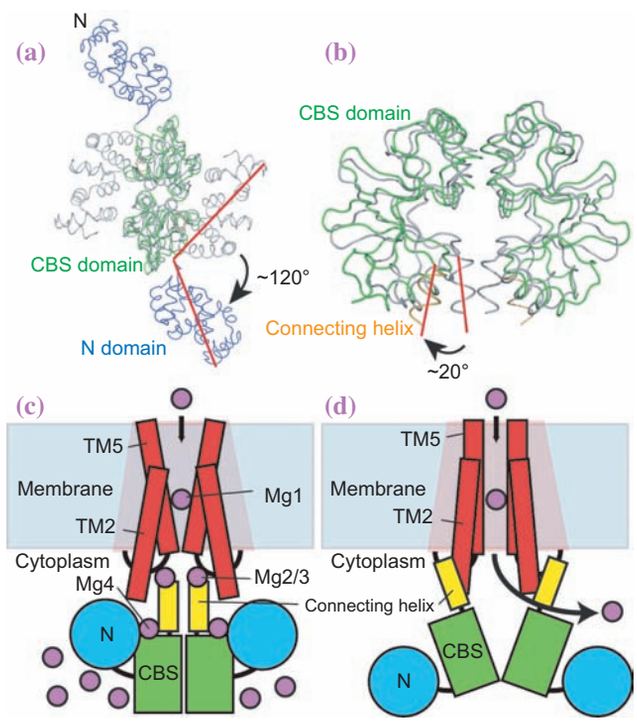

Fig. 3. Proposed Mg^{2+} homeostasis mechanism. **(a, b)** Structural comparison of Mg^{2+}-bound and Mg^{2+}-free cytosolic domains, which are superimposed on CBS domains and viewed from cytoplasm **(a)** and in membrane plane **(b)**. The coloring scheme of the Mg^{2+}-free cytosolic domain is the same as that in Fig. 1. The Mg^{2+}-bound cytosolic domain is in grey. **(c, d)** Proposed gating mechanism. Closed state at high intracellular Mg^{2+} concentration **(c)**. Open state at low intracellular Mg^{2+} concentration **(d)**.

Motoyuki Hattori and Osamu Nureki*

Department of Biological Information,
Tokyo Institute of Technology

*E-mail: nureki@bio.titech.ac.jp

References

[1] *M. Hattori, Y. Tanaka, S. Fukai, R. Ishitani, O. Nureki: Nature* ***448*** *(2007) 1072.*
[2] M. Hattori *et al.*: Acta Crystallogr. F **63** (2007) 682
[3] Y. Tanaka *et al.*: Acta Crystallogr. F **63** (2007) 678.

Crystal Structure of the EFC/F-BAR Domain -Mechanism of Membrane Invagination in Endocytosis-

Endocytosis is a fundamental process for eukaryotic cells to take up molecules from the extracellular space. One of the well-characterized endocytic pathways is clathrin-mediated endocytosis (CME), which is involved in various physiological processes, such as receptor internalization, somatic nutrient uptake, and synaptic vesicle recycling [1]. CME proceeds sequentially with the help of at least twenty different proteins (Fig. 1). Some of the endocytic proteins, such as epsin, amphiphysin, endophilin, and dynamin, directly bind and deform phospholipid membranes into tubules *in vitro* [2]. Their membrane deformation activities are believed to play an important role in the dynamic morphological changes of the plasma membrane in different steps of CME. These proteins utilize several mechanisms for membrane deformation, as shown in Fig. 1 (inset).

Pombe Cdc15 homology (PCH) proteins are involved in various actin-based physiological processes, including CME. They contain a recently identified membrane deformation module, the extended FER-CIP4 homology (EFC) domain, also known as the FCH and BAR (F-BAR) domain [3,4]. The EFC/F-BAR domain is responsible for the induction of tubular membrane invaginations by PCH proteins and tubulates the lipid membrane *in vitro*. The EFC domain shares a weak sequence homology with the BAR domain and induces tubular membranes with diameters several times larger than those of membranes induced by the BAR domain.

To elucidate the mechanism underlying membrane tubulation by the EFC domain and its role in CME, we determined the crystal structures of the EFC domains of human formin-binding protein 17 (FBP17) and Cdc42-interacting protein 4 (CIP4), using the X-ray diffraction data collected at the RIKEN Structural Genomics Beamline I (**BL26B1**) at SPring-8 and the Southeast Regional Collaborative Access Team (SER-CAT) 22-ID beamline at the Advanced Photon Source, Argonne National Laboratory [5].

The structures of the EFC domains of FBP17 and CIP4 revealed an elongated gently curved helical bundle dimer (Fig. 2(a)). Structural and mutational analyses showed that the positively charged concave surface of the EFC domain interacts with the negatively charged phospholipid bilayer by electrostatic interactions, leading to membrane tubulation (Fig. 2(b)). The structure of the EFC domain was similar in topology to that of the BAR domain (Fig. 2(a)). However, the overall structures of these domains differ in length and curvature. The diameter of a tubular membrane that fits the concave surface of the EFC domain was several times larger than that of the BAR domain (Fig. 2(a)). Therefore, the difference in curvature between the two domains correlates well with the fact that the diameters of the EFC-induced tubular membranes are several times larger than those of the BAR-induced membranes.

Interestingly, the EFC dimers of FBP17 and CIP4 formed filaments by end-to-end interactions in the crystals. Introduction of mutations into the residues involved in filament formation abolished the membrane tubulation activity of the EFC domain, suggesting the importance of filament formation in tubulation. The EFC filament seems to be flexible and able to bend at the dimer-dimer interfaces to form spiral/ring-like EFC filaments. On the basis of on these facts, we constructed a mechanistic model of membrane tubulation induced by the EFC domain, in which the curved EFC filaments drive tubulation (Fig. 3(a)). This model was later verified by direct observation of tubular membranes covered with EFC filaments by phase contrast cryo-transmission electron microscopy.

Because the biochemical and structural data strongly

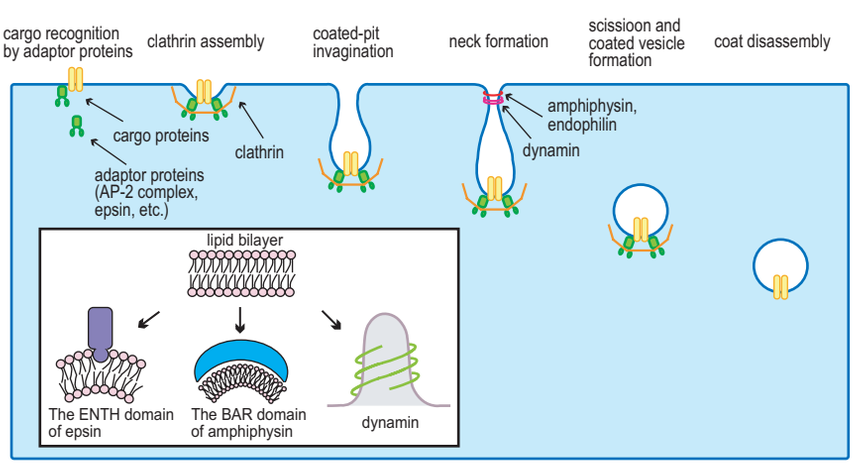

Fig. 1. Schematic diagram of coordinated vesicle formation in CME. Proteins involved in CME are indicated. Short descriptions of the different steps of CME are presented. (inset) Schematic diagram showing mechanisms of membrane deformation by proteins involved in CME.

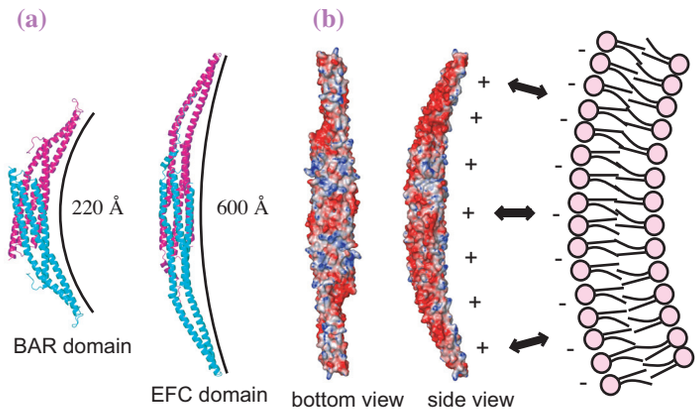

Fig. 2. **(a)** Ribbon diagrams of dimers of BAR domain (left) and EFC domain (right). The structure of the amphiphysin BAR domain and that of the CIP4 EFC domain are shown as representative structures. One molecule of each dimer is colored magenta and the second molecule is colored cyan. The diameter of tubular membranes that fit the concave surfaces of the BAR domain and that of the EFC domain are indicated. **(b)** Electrostatic potential surfaces of EFC-domain dimer with blue indicating positive charges and red negative charge. The bottom view (concave side, left) and the side view (right) are shown. The side view of the EFC domain is accompanied by a cartoon showing its interaction with the phospholipid membrane. The "+" and "–" symbols indicate positive and negative charges on the surfaces of the EFC domain and the phospholipid bilayer, respectively.

suggest that the EFC domain induces tubular membranes with clearly larger diameters than the BAR-induced membranes, we speculated that the EFC domain and the BAR domain may function in distinct steps of CME. The diameters of hemispherical coated pits formed in the early step of CME are typically more than ~700 Å, whereas that of the narrow neck formed at the foot of the coated pits in the late step of CME is ~200 Å. Because the EFC domain induces tubular membranes with more than ~650 Å diameters, it is plausible that the EFC domain plays a role in the invagination step between the initial clathrin assembly step and the neck formation step (Fig. 3(b)). This hypothesis was tested by the real-time imaging of fluorescence-labeled clathrin and FBP17 during CME [5]. It was shown that FBP17 co-localized with clathrin for a period corresponding to that of the invagination step of CME.

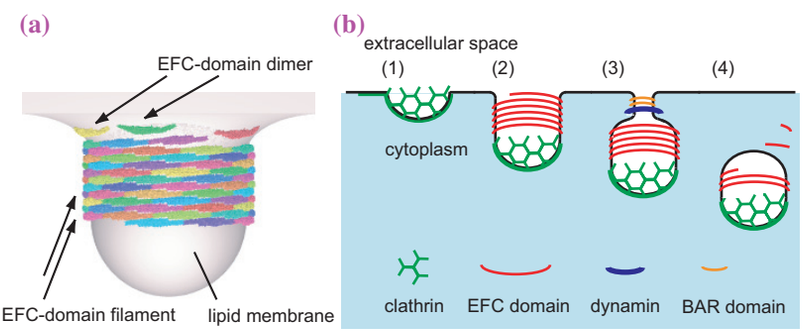

Fig. 3. **(a)** Model for membrane tubulation induced by EFC domain. Each EFC-domain dimer is colored differently. Incoming EFC dimers join end-to-end into a spiral-like filament at the foot of the nascent tubular membrane to drive continuous membrane tubulation. **(b)** Model for coordinated vesicle formation in CME. (1) Clathrin assembly, (2) coated pit invagination, (3) neck formation, and (4) scission steps are shown.

Atsushi Shimada [a,b] and Shigeyuki Yokoyama [b,c,*]

[a] SPring-8 / RIKEN
[b] Systems and Structural Biology Center, RIKEN Yokohama Institute
[c] Department of Biophysics and Biochemistry, The University of Tokyo

*E-mail: yokoyama@biochem.s.u-tokyo.ac.jp

References

[1] D. Perrais and C.J. Merrifield: Dev. Cell **9** (2005) 581.
[2] H.T. McMahon and J.L. Gallop: Nature **438** (2005) 590.
[3] T. Itoh *et al.*: Dev. Cell **9** (2005) 791.
[4] K. Tsujita *et al.*: J. Cell Biol. **172** (2006) 269.
[5] *A. Shimada, H. Niwa, K. Tsujita, S. Suetsugu, K. Nitta, K. Hanawa-Suetsugu, R. Akasaka, Y. Nishino, M. Toyama, L. Chen, Z.J. Liu, B.C. Wang, M. Yamamoto, T. Terada, A. Miyazawa, A. Tanaka, S. Sugano, M. Shirouzu, K. Nagayama, T. Takenawa and S. Yokoyama: Cell **129** (2007) 761.*

LIFE SCIENCE :

"Yamatsutsuji" - Japanese mountain azalea

"Sakura" - Japanese cherry

MEDICAL BIOLOGY

Two experimental methods are discussed in the articles of this section. One is X-ray imaging and the other X-ray diffraction. The experimental data obtained by these methods are quite different, X-ray imaging provides images in real space, whereas X-ray diffraction provides patterns in reciprocal space. However, what is common between these two methods is that both can be used to study biological specimens under native conditions. This enables us to study a function of a biological object. Even though the sizes of the objects are different by three orders of magnitude, the experiments described in these five articles were all carried out for the same purpose: to study physiological functions.

The article by Sasaki describes the most important result obtained by the new diffraction technique that enables us to observe motion of a single protein molecule. This technique was successfully used to observe motion of a potassium channel, which is biologically quite important. Similarly, Pearson and his colleagues studied a function of myosin, which is the motor protein that produces force in cardiac muscle. Both the potassium channel and cardiac muscle are indispensable in our life. X-ray diffraction was also used by Inoue and his colleagues to study the structure of hair cuticle, which is the top layer of human hair. The cuticle plays a major role in controlling penetration of chemicals into hair. Benzyl alcohol, which is used at all hair salons, seems to open a pathway of penetration in the cuticle for dyes.

The other two articles, biological functions are studied at a structural level about 1000 times larger by X-ray imaging. Kondoh studied blood vessels in the mouse brain by angiography. The images clearly demonstrated a change in the diameter of 100-200 μm blood vessels. Hooper and his colleagues studied penetration of air into the lungs using refraction-enhanced imaging. The results are significant in the management of breathing of a baby born preterm.

All these articles demonstrate that SPring-8 is now an established tool to study biological functions at different structural levels.

Naoto Yagi

Twisting Conformational Changes of Single KcsA Potassium Channel upon Gating using Diffracted X-ray Tracking

Ion channels are signal transduction molecules that selectively permeate ions and generate electrical signals through turning on and off of ion permeation pathways. Channels respond to various stimuli, such as membrane voltage and chemical substances. With sensor domains, channel molecules transduce various stimuli into conformational changes of ion permeation pathways, leading to ion-conductive (open) and non-conductive (closed) states. Single-channel current recordings have elucidated the random nature of opening and closing transitions (gating; Fig. 1(a)). Genes of potassium channels exist from bacteria to humans and constitute one of the largest gene family. Ten years ago, the crystal structure of a potassium channel from *Streptomyces lividans* (KcsA channel) was resolved (Fig. 1(b)). The three-dimensional structure provided the architecture of the ion permeation pathway and insights on how ions are selectively permeated. Crystal structures of several other types of potassium channel have been obtained. However, the mechanism underlying the gating has not been elucidated from static images of potassium channels.

Here, we applied the diffracted X-ray tracking (DXT) method to examine conformational changes of single KcsA potassium channels upon gating [1]. Gold nanocrystals were produced (20 nm × 5 nm), which elicit single diffraction spots from the (200)-plane upon irradiation of X-rays. KcsA channels were mutated to have four reaction sites for secure binding of a nanocrystal. Diffraction spots from the nanocrystals were recorded at a video rate, which represents the trajectory of the conformational changes of the channel molecules [2]. To observe the channels from a fixed viewpoint, channels were attached to a glass plate in the same orientation. Here, an upright orientation was taken by attaching the extracellular loop of channel to the plate. A gold nanocrystal was bound to the cytoplasmic domain of the channel and white X-rays (**BL44B2**) were irradiated normal to the glass surface (Fig. 2(a)). In this configuration, radial motions of diffraction spots represent the bending of the channel molecule along the longitudinal axis, and circumferential motions of the spots correspond to rotational changes of the channel around the axis (Fig. 2(b)). KcsA channels show pH-dependent gating, which were exploited in this study to contrast the changes in motion in a different gating status.

When channels were in the closed state at neutral pH, diffraction spots moved radially. This represents bending motions of channels in the range of a few degrees. When channels were actively gated at acidic pH, diffraction spots moved circumferentially (Fig. 3(a,b)). These motions of the spots correspond to the rotation of the channel around the longitudinal axis. Random clockwise and counter-clockwise rotations were recorded. We found that the range of the rotations was several tens of degrees, which are unexpectedly large values. The direction of the rotational motions was sometimes reversed during recordings. We call this type of motion as twisting. This is the first observation of a large twisting in the conformational change of channel molecules upon gating.

The twisting of the channel was confirmed by observing the motion from different viewpoints. The channel was oriented upside-down (Fig. 2(c)), in which the channel molecules were attached to the glass plate through the cytoplasmic domain and the nanocrystal was attached to the extracellular loop. Again, similar twisting motions were detected. In another experiment, channels were laid sideways. The channel was attached to the glass plate at the N-terminus and the nanocrystal was attached to the

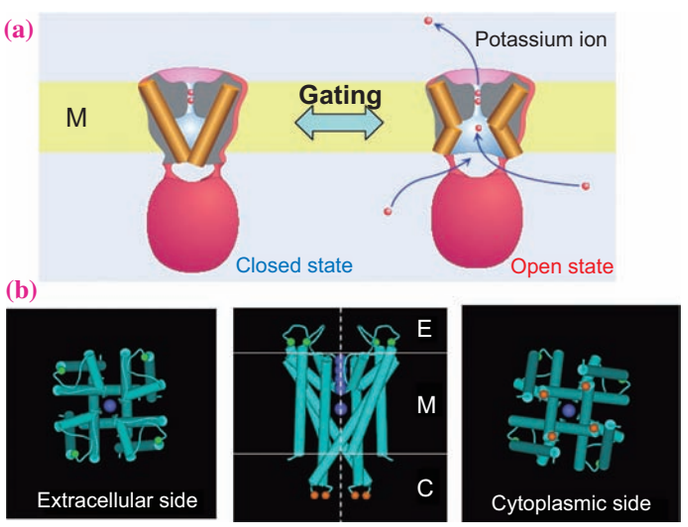

Fig. 1. KcsA potassium channel. **(a)** Cartoons for gating transition of channels. **(b)** Architecture of KcsA potassium channels for transmembrane domain. The potassium channels are tetrameric and composed of two transmembrane helices for each subunit. Inner helices form a bundle crossed at the intracellular side. Dark blue spheres are potassium ions, red spheres are the binding sites for the nanocrystal and green spheres are sites for attaching the glass plate.

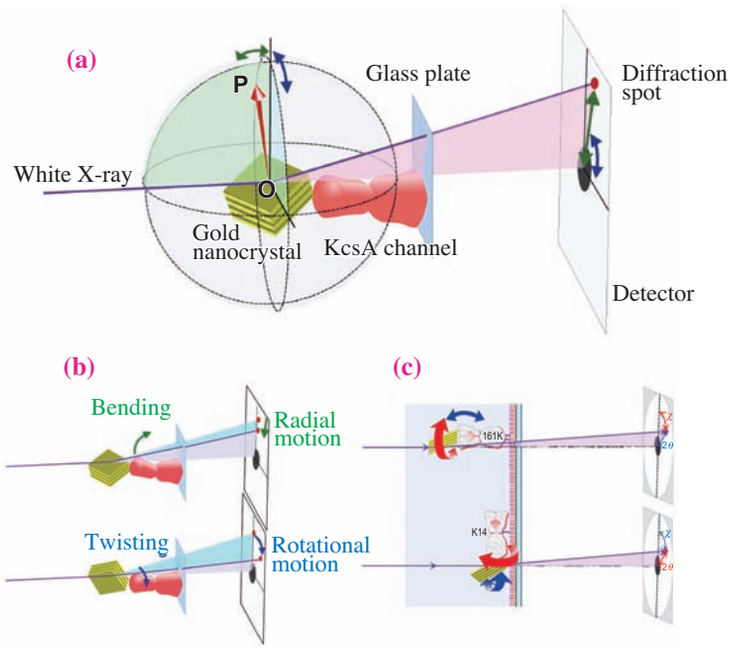

Fig. 2. DXT method. **(a)** Experimental configuration of DXT measurement. The channel was fixed on the glass plate in the upright position. White X-rays were irradiated normal to the glass surface and the diffraction spots were recorded on the detector, which was placed 100 mm from the sample. **(b)** Geometrical relationships of channel motions in real space and spot motions in image plane. **(c)** Different orientations of channel on plate. The upper cartoon shows that the channels were fixed in the opposite orientation. The lower cartoon shows the channel laid sideways.

cytoplasmic domain. In this orientation, the twisting of the channel should result in radial motions of the diffraction spots rather than circumferential motions. We found that no circumferential motions of the diffraction spots were observed even in the actively gated state, and radial motions were enhanced. These results are consistent with the geometrical conversion of the conformational changes of the channels in real space and the motions of the diffraction spots in the image plane. The underlying conformational changes of the channel seem to be invariant, even when the patterns of the motions of the diffraction spots differed significantly from different viewpoints.

In this study we traced the trajectories of the conformational changes of channel molecules upon gating. The clockwise and counter-clockwise twisting of the channel can be related to the helical bundle architecture of the permeation pathway. In the closed conformation, the helical bundle is crossed at the cytoplasmic side, which prevents the permeation of ions. The unwinding of the helical bundle, which allows ions to permeate, was detected as twisting motions (Fig. 3(c)). The twisting mode of conformational changes may prevail for gating of ion channels.

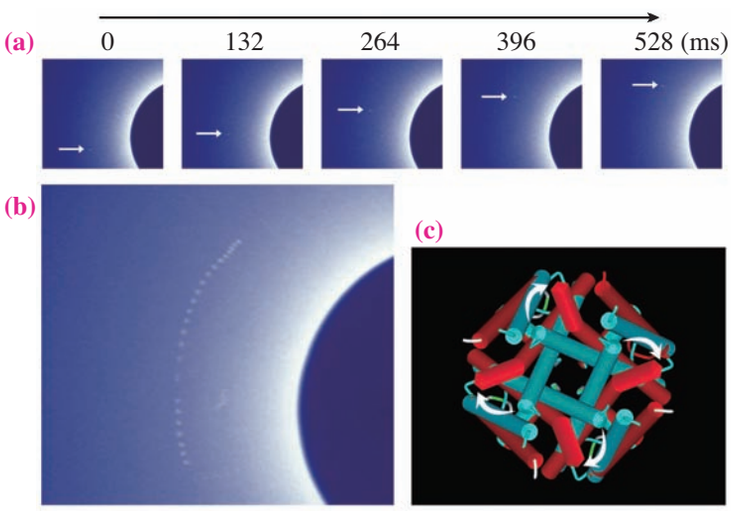

Fig. 3. Trajectories of diffraction spot upon gating. **(a)** Time series of image frames. **(b)** A trajectory of a spot recorded at a video rate was superimposed (24 frames) on an image frame. **(c)** KcsA channel viewed from intracellular side. Blue represents the closed structure and red represents the open structure. Concerted motions of helices lead to twisting of the channel structure.

Hirofumi Shimizu [a,b], Masayuki Iwamoto [a,b], Yuji C. Sasaki [a,c,*] and Shigetoshi Oiki [a,b]

[a] CREST Sasaki-team, Japan Science and Technology Corporation
[b] Department of Molecular Physiology and Biophysics, University of Fukui Faculty of Medical Sciences
[c] SPring-8 / JASRI

*E-mail: ycsasaki@spring8.or.jp

References

[1] *H. Shimizu, M. Iwamoto, T. Konno, A. Nihei, Y.C. Sasaki and S. Oiki: Cell* ***132*** *(2008) 67.*
[2] Y.C. Sasaki *et al.*: Phys. Rev. E **62** (2000) 3843.

Effects of Sustained Length Dependent Activation on *In Situ* Cross-bridge Dynamics in Rat Hearts

Pumping of blood out of the healthy heart is regulated on a beat-to-best basis so that the blood volume ejected from the left ventricle (LV) matches the venous blood volume returning to the heart. When venous blood return is increased acutely the force developed by the LV must increase to enable it to eject more blood. This homeostatic mechanism is the basis of the Frank-Starling law of the heart.

Ca^{2+} release from internal stores is an important determinant of force developed by cardiac muscle. Nevertheless, it has been established that acute stretch of fibers increases force without an increase in the systolic (force generating phase) Ca^{2+} transient. This phenomenon is called length-dependent activation (LDA). Studies with isolated cardiac fibers have shown that Ca^{2+} sensitivity increases with muscle sarcomere length, but the mechanism for the increase in force development remains unclear.

One frequently reported consequence of stretch is that the probability of cross-bridge binding and their transition to strong attachments (force producing state) increases as the distance between myosin and neighbouring actin filaments (interfilament spacing) decreases, as the sarcomere length increases.

We have been applying small angle X-ray scattering to studies of cardiac muscle contractions in the beating hearts of rodents [1,2]. With higher photon fluxes at **BL40XU** beamline it is possible to record very rapid diffraction patterns to analyze events within the cardiac cycle, and therefore also the cross-bridge cycle. This allows us to probe how force generation is regulated *in vivo*. This is important as the beating heart performs 'work', in other words, contraction occurs under a physical load during systole in contrast to isolated muscle in studies implementing isometric contractions. Therefore our objective was to investigate how LDA affects cross-bridge dynamics in the *in situ* heart [3].

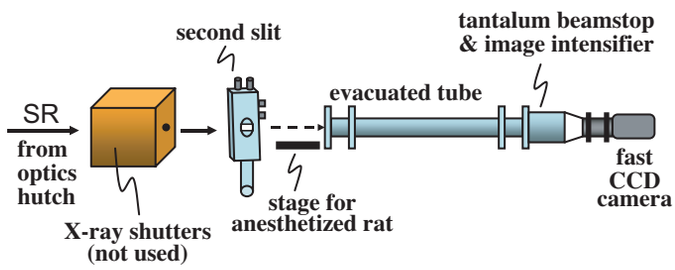

Fig. 1. Experimental set up at the BL40XU hutch for *in situ* whole-heart X-ray diffraction recordings. V5445P image intensifier and C4880-80-24A CCD camera (Hamamatsu Photonics) were used. Camera distance from the beating hearts was *ca*. 3 m during all experiments.

The aim of this study was to determine if sustained increased in venous return to the heart significantly decreases myosin interfilament spacing and increases cross-bridge formation within a localized region of the surface layer of LV muscle (anterior free-wall) of rat hearts. To achieve this we recorded diffraction patterns under baseline conditions and again in the same region during acute volume loading; i.e. an intravenous infusion was given to increase venous return to the heart. Recorded diffraction patterns indicate the proximity of myosin thick filaments to actin thin filaments within the filament lattice of myofibers, due to the large size, abundance and highly ordered arrangement.

We used a narrow collimated quasi-monochromatic beam (0.2 mm × 0.2 mm) provided at BL40XU beamline for X-ray diffraction recordings of spontaneously beating Sprague-Dawley rat hearts (Fig. 1). Beam flux was ~10^{12} photons/s (reduced with 3 mm thick Al bar, 15 keV and ring current 60-100 mA). Beating hearts were continuously exposed for *ca*. 2 s to the X-ray beam and diffraction images recorded at a 15-ms sampling interval (about 8-11 consecutive heart beats per recording). Beam orientation was perpendicular to the fiber direction in the outermost layer of the LV (equatorial position reflections). Anesthetized rat models were prepared as detailed elsewhere [2]. Simultaneous macro-level determinations of LV performance were made using intracardiac catheters to determine LV pressure (LVP) and volume (LVV) changes. Indices of cardiac function and heart work were determined with the aid of pressure-volume (P-V) loops and compared with *in situ* indices of crossbridge dynamics.

An index of myosin mass transfer to actin was determined as the decrease in intensity ratio (intensity of 1,0 reflection over 1,1) during the cardiac cycle (beat-to-beat interval identified from P-V loops). The distance between 1,0 reflections was converted to a lattice spacing between myosin filaments ($d_{1,0}$, nm) using a pixel calibration factor determined from a collagen sample.

Indices of cardiac function and cross-bridge cycling from a typical heart under baseline and volume loading conditions are shown (Fig. 2). As can be seen LVP (force developed) did not increase with stretch, but the volume changes during the cardiac cycle and the rate of pressure development (LVP dP/dtmax) increased significantly. At the same time,

interfilament spacing $d_{1,0}$ and equatorial intensity ratio ($I_{1,0}/I_{1,1}$) changes during the cardiac cycle were larger during volume loading. Notably, not only was the minimum intensity ratio decreased (more myosin heads in close proximity to actin), but the interfilament spacing was decreased by ~0.5 nm. From these 2-s recordings we obtained mean values for each rat. In all the hearts examined we found that the maximum rate of LVP development was significantly correlated with myosin mass transfer index (Fig. 3, top panel).

As expected, we found an inverse relation between $d_{1,0}$ and LV volume over the contractile phase of the cardiac cycle (Fig. 3, bottom panel). This suggests that interfilament spacing increases during fiber shortening in a predictable manner. Interestingly, diastolic relaxation of the LV caused a further 1 nm increase in $d_{1,0}$ at a time when sarcomeres are expected to be lengthening. X-ray diffraction techniques showed that the reduction in interfilament spacing caused by stretch initiated a greater activation of force-producing cross-bridges in early contraction. These findings support a role for interfilament spacing in modulating LDA.

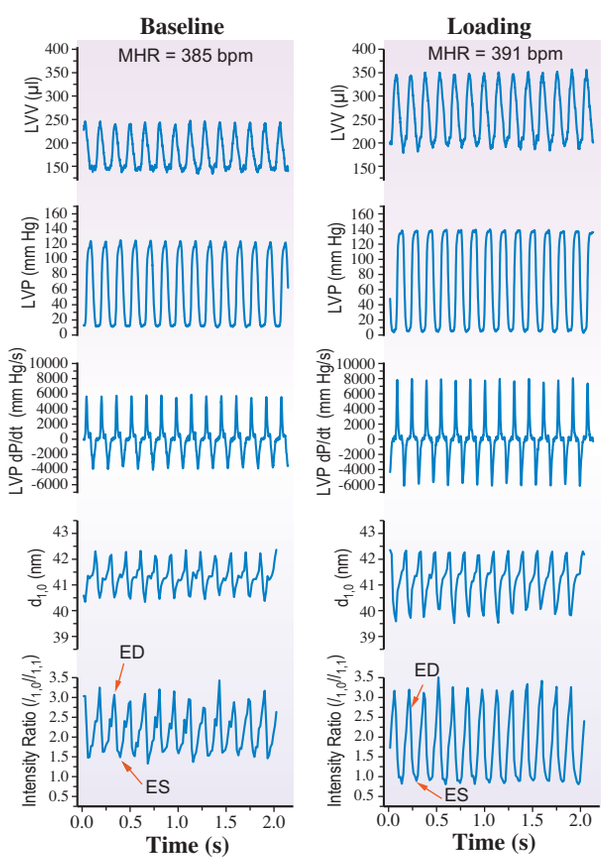

Fig. 2. Examples of the calculated beat-to-beat changes in intensity ratio ($I_{1,0}/I_{1,1}$), $d_{1,0}$, and measures of cardiac function over a series of heart beats under normal baseline conditions and volume loading (60 ml/h intravenous lactate solution).

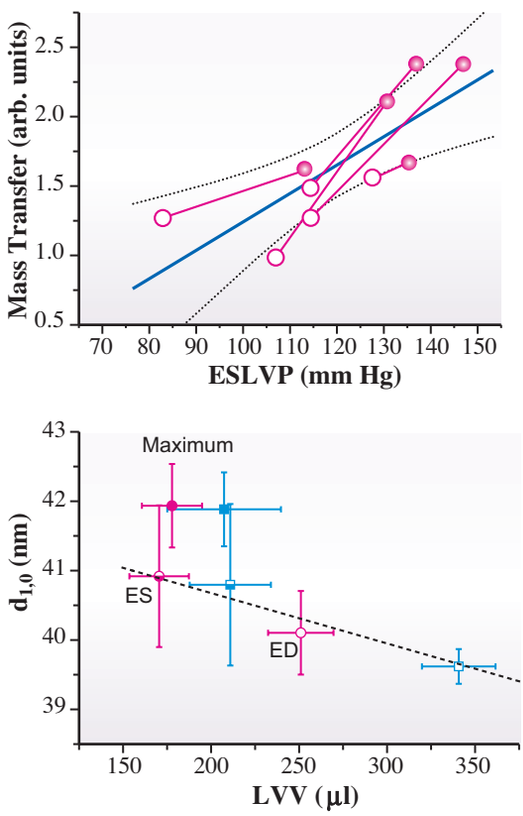

Fig. 3. Relation between the number of cross-bridges (mass transfer) developed locally in the heart wall and the rate of pressure development during contractions of the beating hearts (upper panel) and myosin spacing ($d_{1,0}$) changes in relation to LV volume (LVV) (lower panel). In the upper panel, baseline values are indicated as open circles, connected with volume loading means for the same hearts. In the lower panel, interfilament spacing increased linearly from end-diastole (ED) to end-systole (ES) for baseline (circles) and loading (squares) conditions, but was ~1 nm less than the maximum recorded shortly after the contraction finished.

James T. Pearson [a,†,*], Mikiyasu Shirai [a,††] and Naoto Yagi [b]

[a] Department of Cardiac Physiology, National Cardiovascular Center
[b] SPring-8 / JASRI

* E-mail: james.pearson@med.monash.edu.au

† Present address: Department of Physiology, Monash University
†† Present address: Department of Clinical Radiology, Hiroshima International University

References

[1] J.T. Pearson *et al.*: Circulation **109** (2004) 2976.
[2] R. Toh *et al.*: Biophys. J. **90** (2006) 1723.
[3] *J.T. Pearson, M. Shirai, H. Tsuchimochi, D.O. Schwenke, T. Ishida, K. Kangawa, H. Suga, N. Yagi: Biophys. J.* ***93*** *(2007) 4319.*

Structural Analysis of Human Hair in Aqueous Solutions using Microbeam X-ray Diffraction

In hair beauty treatments such as permanent waving and hair coloring, and in daily treatments using shampoo and hair conditioner, most of the hair care products are used under wet conditions. Therefore, it is important to understand how water-soluble products penetrate into hair. The structural information of hair in aqueous solutions seems essential for understanding the penetration mechanism. However, conventional methods such as electron microscopy are not suitable for hair structural analysis in aqueous solutions. Because X-ray has a characteristic of high transmittance to materials, we have performed small angle X-ray diffraction (SAXD) experiments of hair cuticle in aqueous solutions. From the diffraction patterns, we have estimated the structure of the cell membrane complex (CMC) in the cuticle. The cuticle is the outermost layer of a hair fiber and is composed of a stack of several sheet-like cells. CMC is a substructure of the cuticle composed of three layers; a proteinous layer (δ-layer) is sandwiched between two lipid layers (β-layer), and considered to be an important penetration pathway. We have investigated the effects of penetration enhancers on the CMC structure in aqueous solutions. Penetration enhancers such as benzyl alcohol are used in hair coloring products to enhance coloring ability.

Using a 5 μm high flux beam (λ = 0.083 nm), SAXD experiments were carried out at beamline **BL40XU** (Fig. 1). Hair samples were obtained from Japanese women who had not undergone any chemical treatments. After cutting to a length of 8 cm, each hair fiber was fixed on a hair holder and dipped into aqueous solutions of alcohols. The SAXD patterns from hair cuticle in aqueous solutions were recorded using an imaging intensifier and a charge coupled device detector. The thickness of the β-layer and δ-layer was estimated from X-ray scattering patterns using an electron density model [1,2].

Some alcohols, such as benzyl alcohol, increase the dyeing extent of acidic hair dye. The effects of benzyl alcohol on the CMC structure were estimated by comparison between the structure of hair dipped in 4% benzyl alcohol solution and that in distilled water. The obvious increase in thickness by benzyl alcohol was detected both in the β-layer and δ-layer, indicating that the structural change of CMC induced the penetration-enhancing effect. We compared the effects of alcoholic compounds on the CMC structure. The CMC structure was measured in aqueous solutions of 2% or 4% ethanol, n-propanol, n-butanol, cyclohexanol, benzyl alcohol and cyclohexanediol. The thicknesses of the β-layer and δ-layer are shown in Fig 2. The thickness of the β-layer increased in alcohol solutions except cyclohexandiol. The comparison of structures in 2% and 4% solutions showed that a higher concentration of alcohols

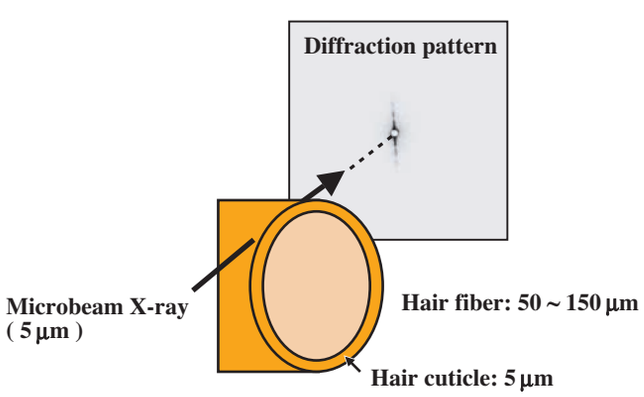

Fig. 1. Illustration of SAXD experiment.

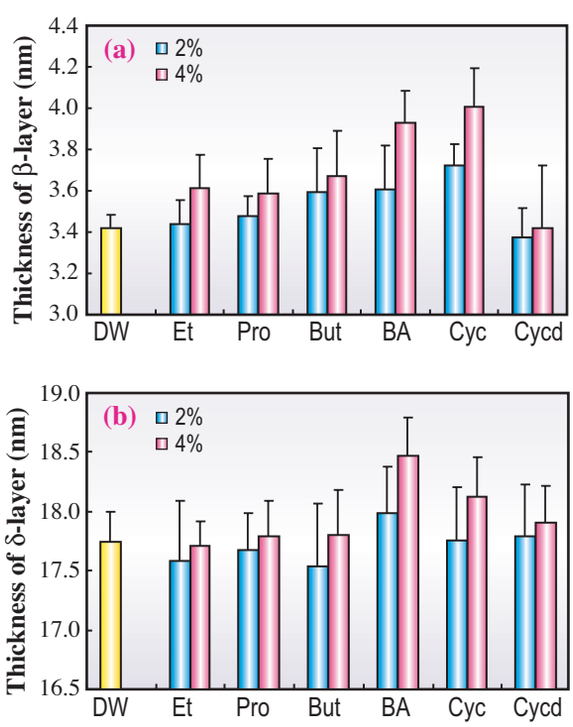

Fig. 2. Effects of alcohols on CMC structure. **(a)** β-layer. **(b)** δ-layer. DW, distilled water; Et, ethanol; Pro, n-propanol; But, n-butanol; BA, benzyl alcohol; Cyc, cyclohexanol; Cycd, cyclohexanediol. Mean ± SD (n=9).

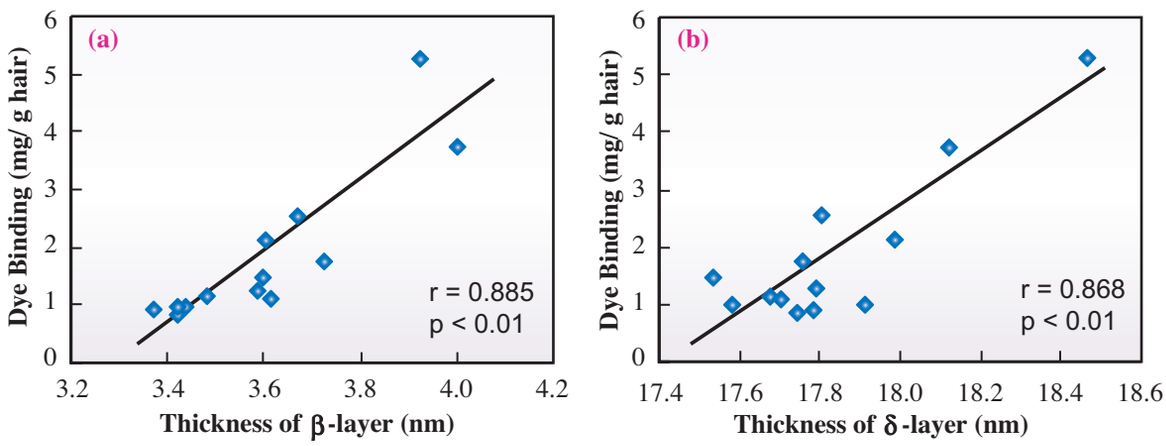

Fig. 3. Relationships between CMC structure and dyeing extent. **(a)** β-layer. **(b)** δ-layer.

produced a larger thickness of the β-layer in each alcohol. The swelling effect was detected in a dose-dependent manner and was marked in cylohexanol and benzyl alcohol. These circular alcohols also induced significant swelling of the δ-layer at 4% concentration. Figure 3 shows the β-layer and the dyeing extent: a larger increase in β-layer thickness resulted in a greater increase in dyeing extent. Similarly, the thickness of the δ-layer shows a correlation with dyeing extent. These correlations agree with the penetration-enhancing mechanism, that is, a penetration enhancer affects directly the penetration pathway to promote mobilization of substances.

Microbeam SAXD provided other structural information regarding CMC. The β-layer is a lipid layer in CMC, and the structural conformation is different from that of ordinary plasma membrane. It is suggested that the β-layer is composed of covalently linked fatty acids and loosely bound lipids [3]. It is unclarified whether the lipids in individual β-layers of CMC are monolayers or bilayers [3,4]. Our analysis showed that the thickness of the β-layer is 3.4 nm in pure water (Fig. 2). The thickness of the β-layer seems too large for a monolayer model. We also detected obvious swelling of the β-layer induced by benzyl alcohol. This observation indicates that the thickness of the β-layer changes in response to the environment the hair fiber is placed. These lines of evidence agree with the bilayer model: that is, the β-layer consists of a bilayer of lipids with a partially interdigitated structure as shown by Robbins *et al.* [4].

Microbeam SAXD is useful for hair structural research. We found changes in the thickness of the β-layer indicating that the β-layer was composed of a partially interdigitated bilayer structure. The structural changes of both the β-layer and δ-layer induced by alcohols correlated with the changes in dyeing extent. This correlation indicates a new penetration enhancing mechanism, that is, alcohols induce structural changes of the penetration pathway.

Takafumi Inoue [a,*], Noboru Ohta [b] and Naoto Yagi [b]

[a] Basic Research Laboratory, Kanebo Cosmetics
[b] SPring-8 / JASRI

* E-mail: inoue.takafumi@kanebocos.co.jp

References

[1] N. Ohta *et al.*: J. Appl. Cryst. **38** (2005) 274.
[2] T. Inoue *et al.*: J. Cosmet. Sci. **58** (2007) 11.
[3] J.A. Swift: J. Cosmet. Sci. **50** (1999) 23.
[4] C. Robbins *et al.*: J. Cosmet. Sci. **55** (2004) 351.

In Vivo X-ray Angiography of Mouse Brain using Synchrotron Radiation

X-ray angiography using a contrast agent has the main advantage of being able to simultaneously demonstrate the anatomy of vessels and changes in morphology. In rats, morphological changes and different vasoreactivities have been studied by angiography; however, the spatial resolution has not been sufficient to detect detailed changes in vessel diameter. Furthermore, owing to the relatively large volume of contrast agent (300-500 μl) required for such studies, imaging studies could not be repeated in each rat. We previously developed an angiography technique using SPring-8, a third generation synchrotron radiation facility. With highly monochromatic synchrotron radiation as an X-ray source and a newly developed X-ray direct-conversion-type VIDICON camera, our previous study showed rat cerebral perforating arteries [1]. We, then, for the first time, performed *in vivo* X-ray angiography of the mouse brain using beamline **BL28B2** [2].

A thin PE-50 tube was placed in the unilateral external carotid artery in adult male C57Black/6J mice. While maintaining the blood flow in the internal carotid artery, 33 μl of contrast agent was injected, and then selective angiography of the hemisphere was performed. The average diameters of cerebral artery were as follows: 142.5 ± 7.90 in the middle cerebral artery, 138.3 ± 9.35 in the anterior cerebral artery, 120.5 ± 5.53 in the posterior cerebral artery, and 162.6 ± 10.87 in the internal carotid artery (μm, n=5). To demonstrate the changes in diameter, we induced hypercapina and detected the dilatation of the vessels between 121 and 124 % of the original diameters (n=5). We also repeated angiography in the mice before and after intracarotid injection of vasodilatation drugs: papaverine hydrochloride, adenosine 5'-triphosphate disodium, and fasudil hydrochloride hydrate. We demonstrated the chronological changes in diameter in each artery 1, 5, 15, and 30 minutes after injection (n = 1 for each drug). As a result, using only a minimum volume of the contrast agent, synchrotron radiation enables us to conduct X-ray angiography of the mouse brain. The morphology of the vessels can be clearly observed under physiological conditions. The diameter of vessels and changes in diameter can also be successfully determined *in vivo*.

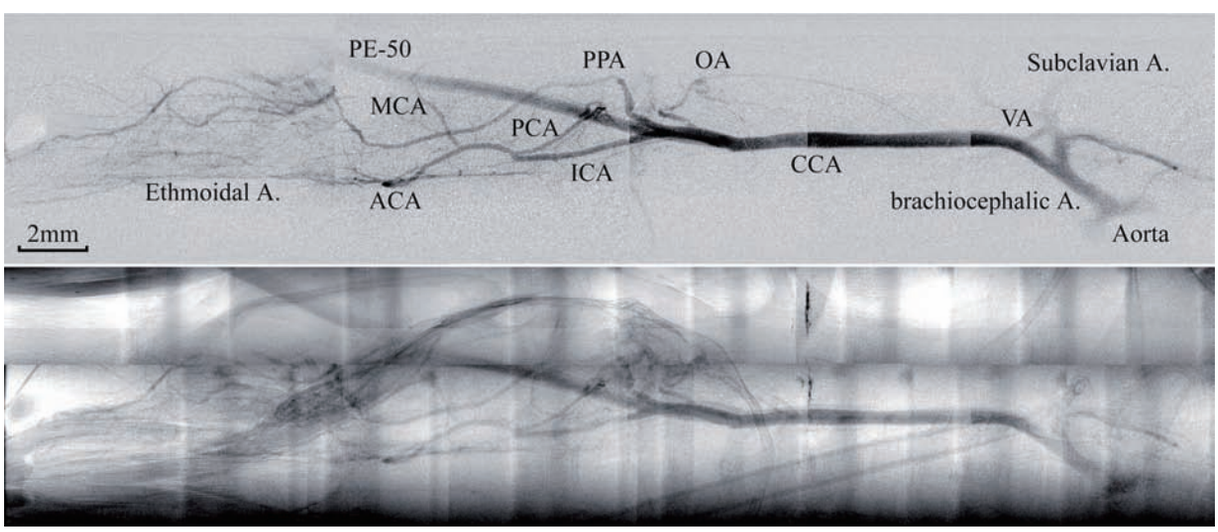

Fig. 1. Synchrotron radiation X-ray angiography of mouse showing anatomy of cerebral arteries in brain hemisphere and neck. Note that selective imaging was performed in the ICA territory. A subtraction image of the vessels (*upper*) and the original image with the skull (*lower*). Assembled with 4 to 8 images for each. CCA, common carotid artery; ECA, external carotid artery; ICA, internal carotid artery; OA, occipital artery; PPA, pterigopalathine artery.

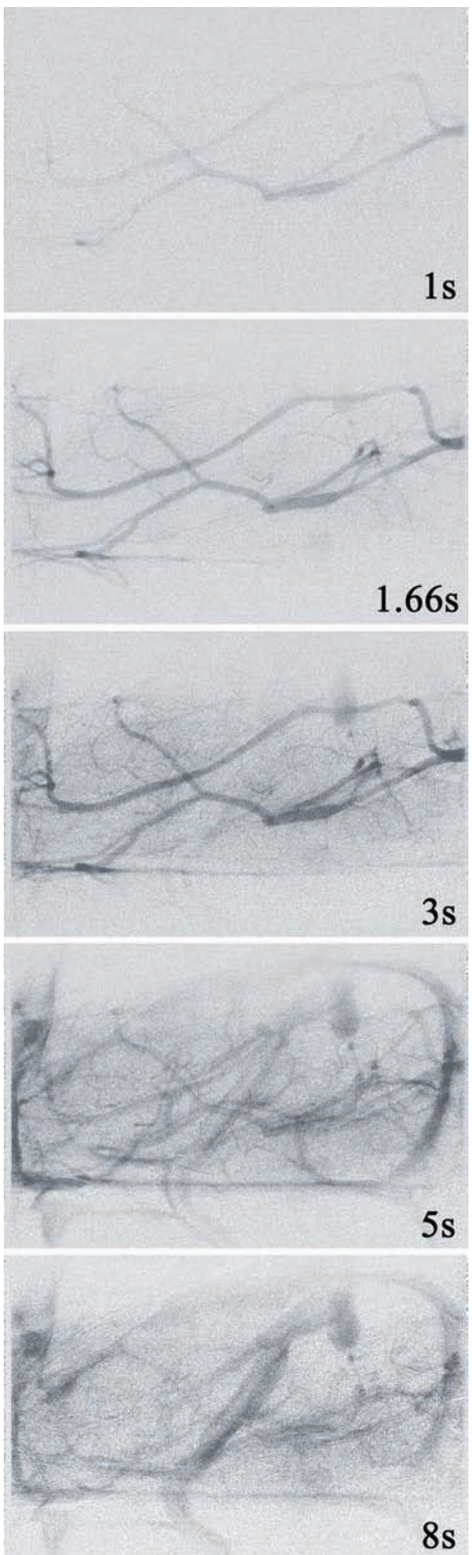

Fig. 2. Serial images from arterial phase to venous phase 1.0, 1.66, 3.0, 5.0, and 8.0 seconds after the start of contrast agent injection.

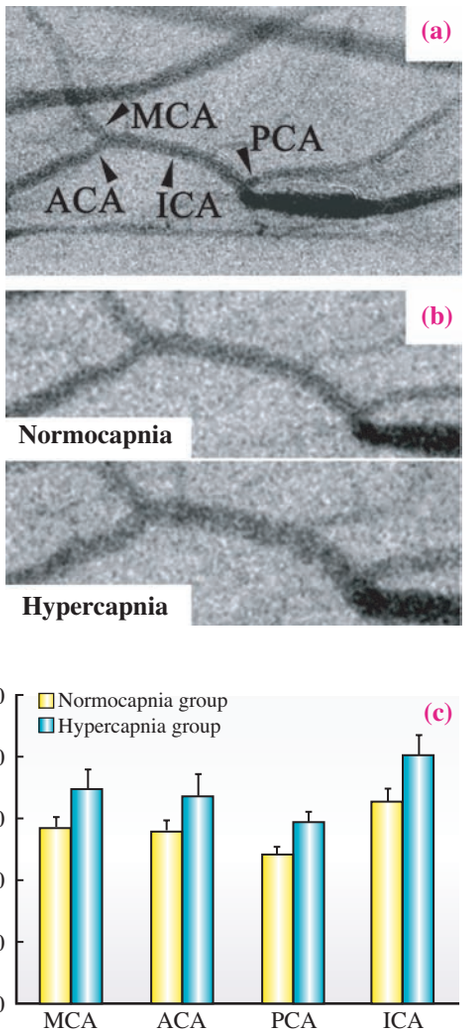

Fig. 3. **(a)** Image showing points for measurement of diameter of each artery. **(b)** Images showing distension of arteries under hypercapnia. **(c)** Comparison of diameters of cerebral arteries of mouse brain under normocapnia and under hypercapnia.

Takeshi Kondoh

Department of Neurosurgery,
Kobe University Graduate School of Medicine

E-mail: tkondo@med.kobe-u.ac.jp

References

[1] A. Morishita *et al.*: Neuroreport. **17** (2006) 1549.
[2] *K. Kidoguchi, M. Tamaki, T. Mizobe, J. Koyama, T. Kondoh, E. Kohmura, T. Sakurai, K. Yokono, K. Umetani: Stroke* ***37*** *(2006) 1856.*

Imaging Lung Aeration at Birth Identifies Better Strategies for Ventilating Very Premature Babies

The transition to air-breathing at birth is crucial for the survival of all newborn infants. To make this transition, the liquid that fills the airways during fetal life must be cleared to allow the entry of air and the onset of pulmonary ventilation [1]. However, a thin film of liquid must remain to protect the inner surface of the lung from desiccation, leading to the formation of an air/liquid interface and the creation of surface tension within the lung which increases lung recoil. This process initiates many changes in lung physiology that allow it to become the sole organ of gas exchange [2]. For instance, the onset of pulmonary ventilation is closely associated with a dramatic increase in pulmonary blood flow (PBF) and the closure of vascular shunts that allow blood to by-pass the lungs during fetal life [2]. However, airway liquid clearance is restricted in infants that are born very preterm (<28 weeks of gestation) and, therefore, these infants commonly suffer from airway liquid retention. This reduces the lung's gas volume, increases the risk of lung injury and impedes the changes required for the lung to transform into an efficient gas exchange organ. It is not surprising, therefore, that respiratory failure at birth is the greatest cause of morbidity and mortality in newborn infants.

Despite the fundamental importance of lung aeration to survival at birth, little is known about this process because until recently, it could not be observed or measured. As a result, the ventilation procedures that most effectively aerate the lung are unknown, although this information is vital for the resuscitation and ventilation of infants that are born preterm. Using phase contrast (PC) X-ray imaging we can now observe and measure the rate and pattern of lung aeration from birth. PC X-ray imaging utilises refractive index variations (phase information) in addition to conventional absorption information to greatly improve image contrast of the lung [4,5]. As the air-filled lung is predominantly comprised of air (~80% by volume), surrounded by thin tissue structures (predominantly water), a marked difference in refractive index exists between the airways and surrounding tissue. When X-rays pass through the lung, the refractive index differences between air and water cause phase shifts in the propagated wavefronts and a change in their direction. The phase shifted wavefronts interfere with adjacent waves producing strong edge enhancement of the boundaries between air and tissue [4]. As the fetal lung is liquid-filled, it is not visible using phase contrast X-ray imaging, but rapidly becomes visible as the lung aerates after birth.

Our aim was to identify ventilation procedures that promote uniform lung aeration and facilitate pulmonary ventilation without causing injury to the very immature lung. In particular, we have examined the benefits of applying a positive end expiratory pressure (PEEP) to the lungs immediately following birth during the resuscitation period. Although the international guidelines for the resuscitation of very preterm infants does not recommend the application of PEEP, we hypothesised that PEEP is essential for proper lung aeration.

Rabbit pups were delivered prematurely (at 27 days of a 32 day gestation) by Caesarian Section, placed in a water-filled plethysmograph (head out) and were imaged while they were being ventilated. Pups were ventilated from birth using a set peak inspiratory pressure (PIP) and either no PEEP or a PEEP of 5 cmH_2O. The increase in tidal volume and lung gas volume at end expiration were observed and measured using PC X-ray imaging and plethysmography. In the absence of PEEP, all pups gradually developed an increasing tidal volume, but no pups were able to accumulate an end expiratory gas volume within their lung during the period examined (10-15 mins) (Figs. 1 and 2). As a result, the lungs collapsed at the end of each

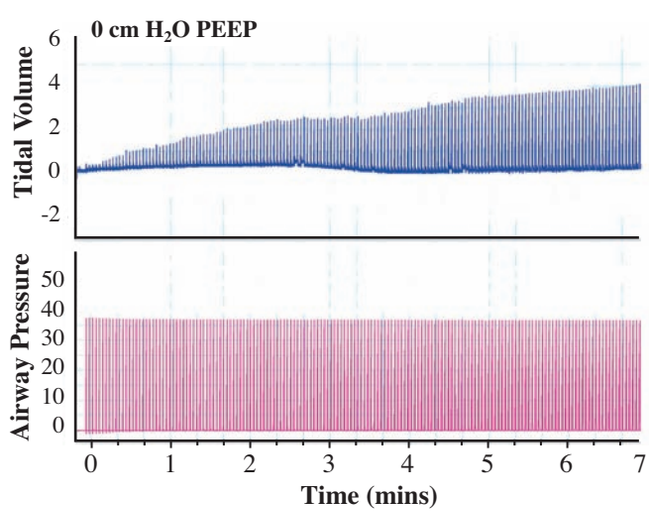

Fig. 1. Change in lung gas volume (top panel), measured using a water-filled plethysmograph, from birth in a mechanically ventilated prematurely delivered newborn rabbit pup. The pup was ventilated with a peak inspiratory pressure (PIP) of 35 cmH_2O and no (0 cmH_2O) positive end expiratory pressure (PEEP; bottom panel).

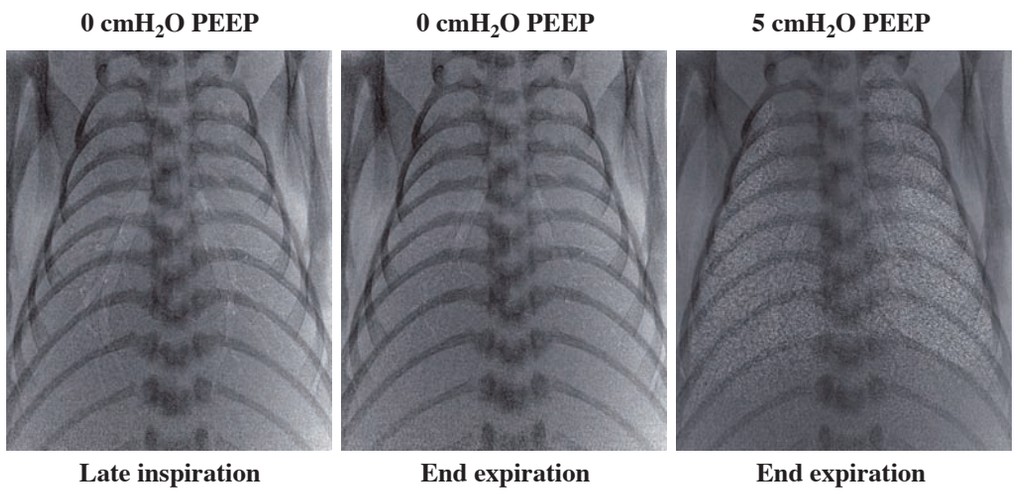

Fig. 2. Phase contrast X-ray images of prematurely delivered newborn rabbits mechanically ventilated from birth using a peak inspiratory pressure of 35 cmH_2O and either no (0 cmH_2O) positive end expiratory pressure (PEEP; left and middle images) or 5 cmH_2O of PEEP (right image). The two images (let and middle) acquired from a pup ventilated with 0 cmH_2O of PEEP where acquired at late inspiration (left) and end expiration (middle) and demonstrate lung collapse at the end of each breath.

expiration which is known to be very injurious to the lung; closure of the airways at end-expiration (vs mid inspiration) is clearly evident in the PC images (Fig. 2). In contrast, all pups ventilated with 5 cmH_2O of PEEP gradually accumulated an end-expiratory gas volume within the lung and, importantly, the lungs did not collapse at end expiration (Figs. 2 and 3); the increase was very similar to the increase measured previously in spontaneously breathing term pups [5].

Our observations demonstrate that the application of PEEP to very preterm infants that require ventilation at birth prevents lung collapse at end-expiration and, therefore, is less injurious to the lung than the application of no PEEP. These data will be used to change the International guidelines for the resuscitation and ventilation of very preterm infants.

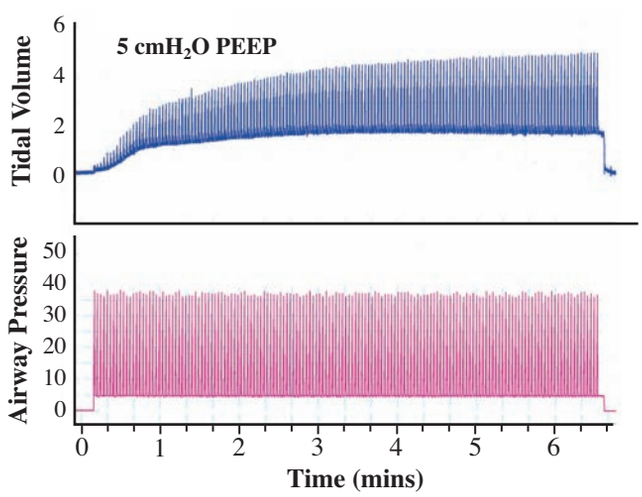

Fig. 3. Change in lung gas volume (top panel), measured using a water-filled plethysmograph, from birth in a mechanically ventilated prematurely delivered newborn rabbit pup. The pup was ventilated with a peak inspiratory pressure (PIP) of 35cmH_2O and 5 cmH_2O positive end expiratory pressure (PEEP; bottom panel)

Stuart B. Hooper [a,*], Marcus Kitchen [b], Naoto Yagi [c] and Robert Lewis [d]

[a] Department of Physiology, Monash University, Australia
[b] School of Physics, Monash University, Australia
[c] SPring-8 / JASRI
[d] Centre for Synchrotron Science, Monash University, Australia

*E-mail: stuart.hooper@med.monash.edu.au

References

[1] S.B. Hooper and R. Harding: Clin. Exp. Pharmacol. Physiol. **22** (1995) 235.
[2] S.B. Hooper and R. Harding: Current Resp. Med. Rev. **1** (2005) 185.
[3] M.J. Kitchen *et al.*: Brit. J. Radiol. **78** (2005) 1018.
[4] R. A. Lewis *et al.*: Phys. Med. Biol. **50** (2005) 3031.
[5] *S.B. Hooper, M.J. Kitchen, M.J. Wallace, N. Yagi , K. Uesugi, M.J. Morgan, C. Hall, K.K.W. Siu, I.M. Williams, M. Siew, S.C. Irvine , K. Pavlov and R.A. Lewis: FASEB J.* ***21*** *(2007) 3329.*

MATERIALS SCIENCE :

"Mokusyungiku" - Marguerite

"Matsubaunran" - Linaria canadensis

STRUCTURE

Various unique structures were reported in Materials Science at SPring-8 this year. Fujihisa *et al*. succeeded in determining the incommensurate structure generated under high pressure, "Incommensurately Modulated Phase of Phosphorus under Pressure" by high pressure X-ray powder diffraction analysis. Their discovery, the displacive modulated incommensurate structure with only one atomic site position, was the third case after the reports on iodine and chalcogens in 2003. As shown in this article, the quality and reliability of powder data is increasing as well as making the complicated structure model building possible. The research and development in basic techniques for the high quality control of powder diffraction data at SPring-8 carried out in "Long-Term Proposal" and "Power(experienced) User Project" has been achieved in the following studies: "Direct observation of oxygen stabilization in layered ferroelectric $Bi_{3.25}La_{0.75}Ti_3O_{12}$" by Moriyoshi *et al*. and "Unique structures in yttrium trihydride at high pressure" by Machida *et al*. In these studies, accurate structure analyses for complicated structural systems were achieved. In addition, the direct observation of ferroelectric $Bi_4Ti_3O_{12}$ crystal growth using the Piezoresponce Force Microscopy (PFM) by Noguchi *et al*. was indirectly but strongly supported by the results of precise powder diffraction structure analysis, which indicates the evidence of no significant lattice change under the various oxygen pressure relating to crystal growth.

As studies representing the progress in data accuracy for structural study, the two articles are selected from the research area of surface and interface structure. One is "Structural characterization of Ar^+-irradiated $SrTiO_3$ showing room-temperature blue luminescence" by Shimakawa *et al*. and the other is "Multilayer relaxation of Ru studied by surface X-ray diffraction" by Nakamura *et al*. The importance and demands of the utilization of SPring-8 in this research area should increase in materials science and its industrial applications.

Five other emerging and unique studies are also selected this year as research frontiers of 2007. These research studies shall bring a new breakthrough to Materials Science in SPring-8 and may attract growing end user demands, which is not yet on the horizon.

Masaki Takata

Incommensurately Modulated Phase of Phosphorus under Pressure

Black phosphorus phase I (orthorhombic, *Cmca*), which is stable under ambient temperature and pressure, transforms to high pressure phase II (rhombohedral, $R\bar{3}m$) at 4.2 GPa, phase III (simple cubic, $Pm\bar{3}m$) at 10 GPa as shown in Fig. 1(a), intermediate phase IV at 107 GPa, phase V (simple hexagonal, *P6/m mm*) at 137 GPa, as shown in Fig. 1(c), and phase VI (bcc, $Im\bar{3}m$) at 262 GPa [1]. The structure of intermediate phase IV remains unsolved. Recently, Ishikawa *et al.* proposed a structural model for phase IV by first-principles calculations using the metadynamics simulation method [2]. They reported a monoclinic structure that has atomic displacement with an A-B-A-C pattern and a unit cell that is 4 times longer along the *c* axis than that of phase III or V. The purpose of this study is to determine the crystal structure of phosphorus phase IV by an angle dispersive powder X-ray experiment and Rietveld analysis.

Powder diffraction patterns of black phosphorus samples at pressures up to 150 GPa were measured using a diamond-anvil high-pressure cell (DAC) with 150 μm culet diamonds and an imaging plate detector (IP) at beamline **BL10XU**. The X-ray wavelength was 0.49654 Å. The X-ray beams were collimated by a 10-μm-diameter pinhole. The typical exposure time was 20 minutes. A one-dimensional powder pattern was obtained by averaging the whole intensities along the Debye-Scherrer rings recorded on the IP.

The diffraction patterns of phase IV were observed from 107 GPa to 137 GPa. By indexing the pattern at 125 GPa, we obtained a C-centered orthorhombic lattice as a possible candidate cell, as shown by blue dashed rectangle in Fig. 1(d). This lattice had a *c* axis length that was 11 times longer than that of phase III or V. After fitting the observed pattern by optimizing the atomic coordinates, a transverse wave along the *c* axis appeared, as shown in Fig. 1(d). However, some peak positions calculated by this model were found to be slightly shifted from the observed positions. Therefore, the structure of phase IV was considered to have an incommensurate modulation. By dividing the length of the *c* axis by 11, the fundamental lattice was obtained as shown by red rectangles in Figs. 1(b) and 1(d). The superspace group of this modulated structure was assigned to be $Cmmm\ (00\gamma)s00$. By the Rietveld refinement based on the incommensurate model in Fig. 2, the lattice parameters and its volume were determined to be a = 2.772±0.001 Å, b = 3.215±0.001 Å, and c = 2.063±0.001 Å, and V = 18.39±0.02 Å^3, respectively. The modulation wavenumber was also refined to be γ = 0.2673±0.0003, 1/γ = 3.741±0.004. The modulation amplitude corresponds to *xsin1* = 0.148±0.001 in a fractional coordinate and 0.410 Å in real space. The green dotted rectangle in Fig. 1(d) shows the theoretical prediction, that is, the Ishikawa's 4 times supercell [2]. Since the value of 4 is 7% larger than the experimental value for 1/γ, a misfit of the peak

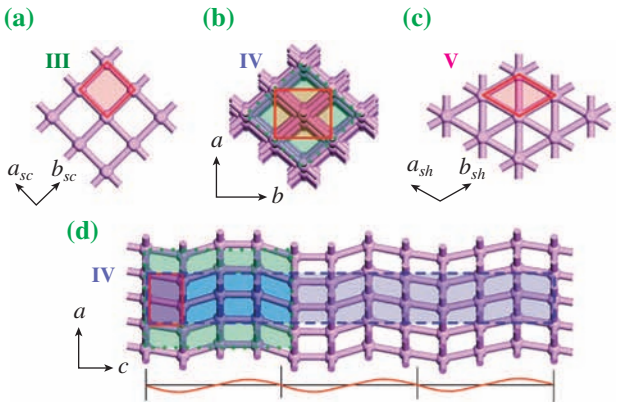

Fig. 1. Crystal structures of phosphorus **(a)** phase III, **(b)** phase IV, **(c)** phase V in *ab* plane, and **(d)** phase IV in *ac* plane with a commensurate approximation. The dashed blue rectangle in **(d)** represents the 11 times supercell. The solid red rectangles in **(b)** and **(d)** show the fundamental lattice for the *Cmmm* (00γ)*s* 00 model. The dotted green rectangle in **(d)** shows a monoclinic lattice predicted by Ishikawa *et al.* [2].

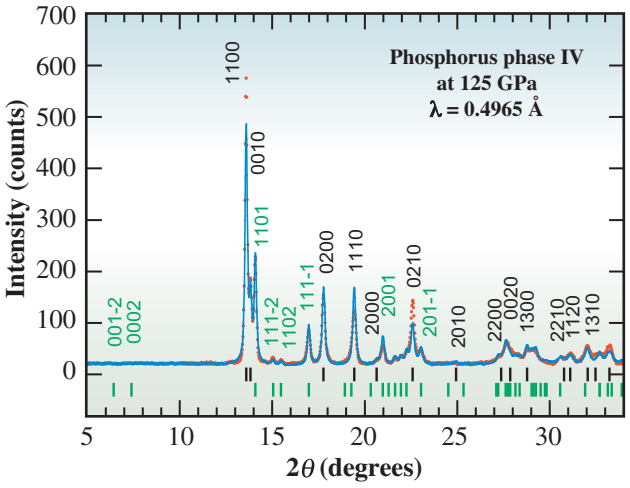

Fig. 2. Diffraction pattern of phosphorus phase IV observed at 125 GPa (brown dots) and the Rietveld fit with the proposed *Cmmm* (00γ)*s* 00 model (blue curve). The upper and lower tick marks show the peak positions of the fundamental and satellite reflections, respectively.

positions indeed exists between the observed data and the pattern calculated from the Ishikawa's model. However, their model is essentially consistent with our experimental result from the viewpoint of forming a particular superlattice structure.

Figure 3 shows the pressure dependence of the lattice parameters for phases III, IV, and V. The nearest interatomic distance for phase III (a_{sc}) was connected continuously to that for phase IV in the *ab* plane, written as $\sqrt{a^2+b^2}/2 \cdot \sqrt{2}\,a_{sc}$ for phase III split into *a* and *b* in phase IV. The coordination number of 6 for phase III was maintained in phase IV. As a result of the modulation, the interatomic distances along the *c* axis were distributed from 2.06 Å to 2.15 Å at 125 GPa. The *a* length of 2.74 Å in phase IV at around 140 GPa shrunk to a_{sh} 2.18 Å in phase V. The coordination number increased from 6 to 8 at the IV-V transition. Consequently, our proposed model of the phase IV structure suggests the meaningful explanation for the mechanism of the phase transition from phase III to V.

An incommensurate displacive modulation by only one site of the atomic position was first discovered in a high pressure phase of iodine [3] as a superspace group $Fmmm\,(00\gamma)s00$. The second one was $I'2/m\,(0q0)s0$ for chalcogens [4]. The present $Cmmm\,(00\gamma)s00$ for phosphorus phase IV is the third incommensurate displacive modulation. Comprehensive studies regarding pressure-induced incommensuration are needed.

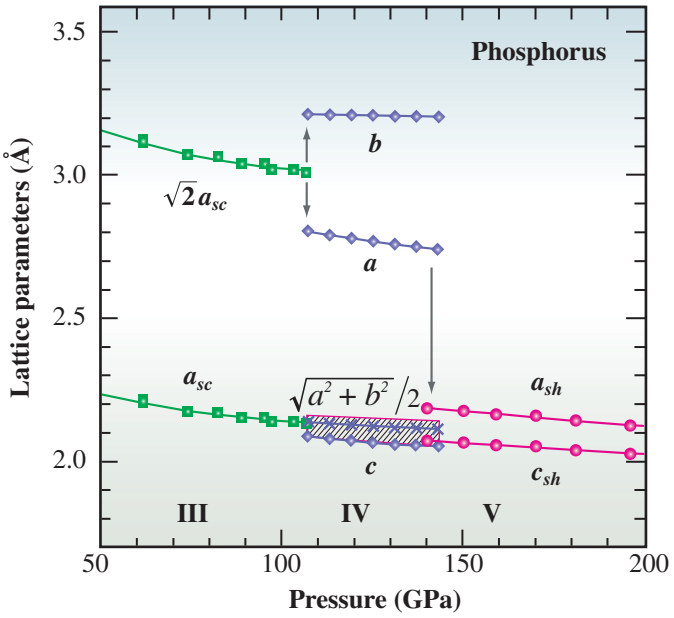

Fig. 3. Pressure dependence of the lattice parameters for phosphorus phases III, IV, and V. The squares, diamonds, and circles denote the lattice parameters for each phase. The crosses correspond to the nearest distance in the *ab* plane in phase IV. The pink-hatched area above the *c* axis length shows the nearest distance along the *c* axis, which is elongated by the modulation.

Hiroshi Fujihisa [a,*], Yuichi Akahama [b] and Yasuo Ohishi [c]

[a] Research Institute of Instrumentation Frontier, AIST
[b] Graduate School of Material Science, University of Hyogo
[c] SPring-8 / JASRI

*E-mail: hiroshi.fujihisa@aist.go.jp

References

[1] Y. Akahama *et al.*: Phys. Rev. B **61** (2000) 3139.
[2] T. Ishikawa *et al.*: Phys. Rev. Lett. **96** (2006) 095502.
[3] K. Takemura *et al.*: Nature **423** (2003) 971.
[4] C. Hejny and M.I. McMahon: Phys. Rev. Lett. **91** (2003) 215502.

Direct Observation of Oxygen Stabilization in Layered Ferroelectric $Bi_{3.25}La_{0.75}Ti_3O_{12}$

Ferroelectric crystals have several polarization states under zero electric field, which can be switched by applying an electric field. Recently, this has been utilized in ferroelectric random access memory (FRAM), which is one type of nonvolatile memory. Bismuth titanate, $Bi_4Ti_3O_{12}$ (BiT), has been regarded as a promising material for FRAM because BiT shows a high Curie temperature T_C of 675 °C and a large spontaneous polarization [1]. However, BiT has a small remanent polarization P_r, and exhibits "polarization fatigue", with P_r decreasing with the polarization switching [2]. It has been reported that La-substituted BiT, $Bi_{3.25}La_{0.75}Ti_3O_{12}$ (BLT), shows a relatively large P_r and a high endurance to polarization fatigue [3].

It is widely recognized that the small P_r and polarization fatigue are attributed to domain clamping, i.e., a decrease in the number of domains that can be switched by applying an electric field. The domain clamping is caused by the strong interaction between domain walls and defects such as oxygen vacancies [4]. Since the stability of oxygen ions strongly depends on the local crystallographic environment, it is essential to investigate the chemical bonding in BiT and BLT to elucidate the role of La and to develop designs for high-performance BiT-based-devices.

The aim of the present study is to clarify the role of La in BLT on the stability of oxygen ions in terms of the chemical bonding obtained by electron charge density analysis. Analyzing X-ray diffraction data using the maximum entropy method (MEM)/Rietveld method allows us to get information about the nature of chemical bonding directly from the electron density map. We performed high-energy synchrotron radiation (SR) powder diffraction measurements on BiT and BLT. The electron density distributions show clear evidence of the stabilization of oxygen ions in the perovskite layer in BLT [5]. Powder samples of BiT and BLT were prepared by a solid-state reaction. The SR diffraction experiments were performed at 300 K in the ferroelectric phase of BiT and BLT using a large Debye-Scherrer camera with an imaging plate installed at beamline **BL02B2**. We used high-energy SR with a wavelength of λ = 0.35639(2) Å (E = 35 keV) to reduce absorption by the samples because BiT and BLT contain heavy atoms such as Bi and La.

Figure 1 shows the crystal structure and the equidensity map of the electron density distribution of

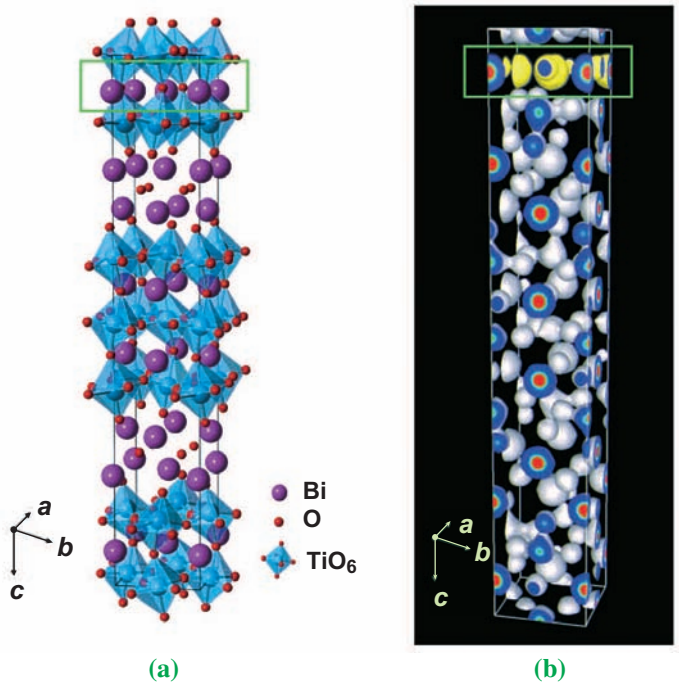

Fig. 1. Structure of ferroelectric BiT at 300 K. **(a)** Crystal structure determined by Rietveld analysis. **(b)** Equidensity map of electron charge density distribution derived by MEM/Rietveld analysis. The surface level is 1.0 eÅ^{-3}. The perovskite layer shown in Fig. 2 is indicated by the green rectangle in the figure.

BiT. The structure has alternate stacking of Bi_2O_2 layers and perovskite $Bi_2Ti_3O_{10}$ layers along the *c* axis. In BLT, it is found that most La occupies the Bi sites in the perovskite layers, one of which is indicated by the green rectangle in Fig. 1. As a result, the substitution of La leads to a significant change in the chemical bonding of Bi–O in the perovskite layer. Figures 2(a) and 2(b) exhibit the Bi–O and Bi/La–O planes in the perovskite layer viewed along the *c* axis in BiT and BLT, respectively. It is clear that, in BiT, the chemical bonding of Bi–O along the *a* axis (polarization direction) is stronger than that of Bi–O along the *b* axis. Note that the chemical bonding around Bi/La in BLT is quite different from that around Bi in BiT. The La substitution provides an additional chemical bond of Bi/La–O along the *b* axis in addition to that along the *a* axis. It is natural to think that fewer oxygen vacancies occur in BLT than in BiT because the oxygen ions are stabilized by the newly formed Bi/La–O bonds in BLT. Thus, the high endurance to polarization fatigue achieved for BLT can be ascribed to the stabilization of oxygen ions by La substitution in the perovskite layer due to the isotropic chemical bonding of Bi/La–O.

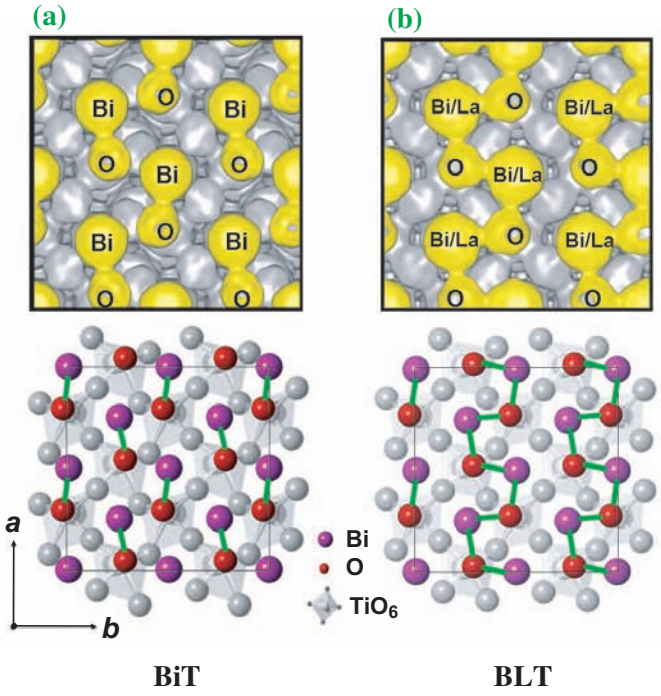

Fig. 2. Ferroelectric structures of BiT and BLT in the perovskite layer at the *c* axis coordinate ~0.07*c*. In each figure, the lower section is the crystal structure and the upper section is the equidensity map of the electron density distribution (surface level 0.55 eÅ^{-3}) derived by the MEM/Rietveld analysis. The depicted cell size is $2a \times 2b$. The oxygen ions in BLT are connected by Bi/La–O chemical bonding along the *a* and *b* axes.

Chikako Moriyoshi [a,*], Yoshihiro Kuroiwa [a,c] and Yuji Noguchi [b]

[a] Department of Physical Science, Hiroshima University
[b] Research Center for Advanced Science and Technology, The University of Tokyo
[c] CREST/JST

*E-mail: moriyosi@sci.hiroshima-u.ac.jp

References

[1] S.E. Cummins and L.E. Cross: J. Appl. Phys. **39** (1968) 2268.
[2] P.C. Joshi and S.B. Krupanidhi: J. Appl. Phys. **72** (1992) 5827.
[3] B.H. Park *et al.*: Nature (London) **401** (1999) 682.
[4] M. Soga *et al.*: Appl. Phys. Lett. **84** (2004) 100.
[5] *S.J. Kim, C. Moriyoshi, S. Kimura, Y. Kuroiwa, K. Kato, M. Takata, Y. Noguchi and M. Miyayama: Appl. Phys. Lett.* ***91*** *(2007) 062913.*

Unique Structures in Yttrium Trihydride at High Pressure

In rare-earth metal hydrides, it is an important problem to determine the roles interstitial hydrogen (H) atoms play in structural and electronic properties. For yttrium hydrides, YH_x, as a prototypical example, various studies have been performed. Yttrium trihydride, YH_3, exhibits a hexagonal metal lattice, which contains three H atoms per metal atom in the interstitial spaces under ambient conditions. Two H atoms are located at the tetrahedral (T) sites and the remaining H atom is located near the Y metal plane in the octahedral (O) sites. On the other hand, dihydride YH_2 has an fcc metal lattice in which the T sites are filled with H atoms. YH_x exhibits a gradual opening of the band gap during hydrogenation over x=2 with a structural change from cubic to hexagonal. Hexagonal YH_3 eventually becomes transparent at a gap of 1.8 eV. Upon dehydrogenation into YH_2, insulating YH_3 transforms into metallic YH_2 with a reversible hexagonal-cubic structural transition. It is considered that the interstitial H atoms, especially the O-site H atoms, play a dominant role in the hydrogen-induced band-gap opening as well as in the structural transition. Band structure calculations have been performed in an attempt to give a clear-cut explanation for the unusual metal-insulator transition, but the origin of the large band-gap opening seems still controversial.

At a highly densified state, which is realized under high pressure, the hydrogen-metal (H-M) and H-H interactions are thought to play an essential role in the structural and physical properties. Previous high-pressure X-ray diffraction experiments have revealed that hexagonal YH_3 sluggishly transforms into cubic YH_3 upon an increase in pressure from about 10 to 20 GPa, suggesting the existence of an intermediate structure bridging the hexagonal and cubic structures [2]. On the other hand, a rapid decrease in the optical gap on compression has been observed for this intermediate phase by optical absorption measurements in the visible region [3]. The electronic band structure of the intermediate phase is very sensitive to pressure. This is in strong contrast to the behavior of insulating hexagonal YH_3, which has a band gap that remains approximately constant with changing pressure. The structural investigation of the intermediate phase is crucial for understanding the mechanism of the hexagonal-cubic structural transition and the band gap closing mechanism for YH_3. In this work, we propose a candidate structural model for the intermediate state [1].

A diamond anvil cell (DAC) was used for the high-pressure hydrogenation of Y metal and successive X-ray diffraction measurements on the hydride. Synchrotron radiation X-ray diffraction patterns were measured at pressures of up to 30 GPa at ambient temperature using a diffractometer for the DAC that was constructed at beamline **BL22XU**. The diffraction pattern of hexagonal YH_3 exhibits significant changes at about 12 GPa on compression. Some of the reflection peaks split into several peaks and new peaks appear. The diffraction pattern becomes simple with gradual peak merging on further compression, and the observed major reflection peaks are eventually indexed with an fcc lattice above 22 GPa. Hexagonal YH_3 transforms to the cubic structure through an intermediate state that exists over a wide pressure range of 10 GPa. These structural changes are reversible; the fcc structure reverts to the hexagonal structure through the intermediate phase with hysteresis as the pressure is released.

The diffraction patterns of the intermediate state are complicated, as shown, for example, in the pattern obtained at 14.0 GPa on the top of Fig. 1, and cannot be interpreted using the two-phase coexisting model or other structures reported for rare-earth metals such as Sm-type (9R) or dhcp (4H) structures. We speculate that the intermediate structure consists of stacked metal layers with partial hexagonal-type and fcc-type sequences along the c-axis of the hexagonal unit cell. Starting with this structural model, we searched for a suitable candidate structure.

Powder diffraction profiles are simulated for various candidate structural models by systematically changing the numbers of hexagonal-type (*ABA*-type) and fcc-type (*ABC*-type) layers contained in a unit cell.

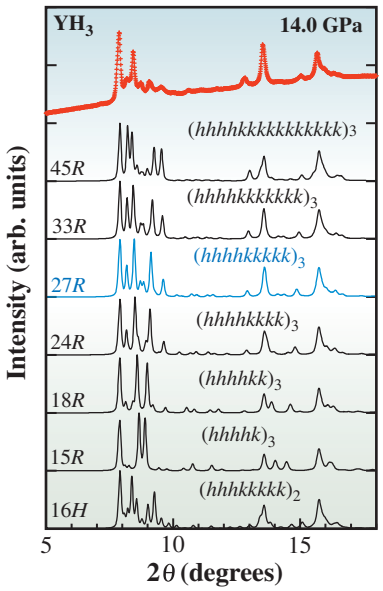

Fig. 1. Simulated patterns of the long period stacking structures (solid curves). Top pattern is the experimental one measured at 14.0 GPa (crosses).

Here, we adopt the Jagodzinski notation to describe the stacking sequence: symbols *h* and *k* denote the layers with hexagonal and cubic arrangements, respectively. According to Jagodzinski notation, the Sm-type (*ABABCBCAC*) and dhcp (*ABAC*) structures are described as $(khh)_3$, and $(kh)_2$, respectively. The subscripts indicate the number of times the sequence of layers must be repeated to complete the unit cell in the structure. The number of metal layers considered in the unit cell ranged from 9 to 51. In our simulation, only the lattice of Y metal is taken into account, because the contribution of the hydrogen atoms to the diffraction profile is neglected due to the small atomic scattering factor of hydrogen. Figure 1 shows typical examples of the simulated patterns. From 15*R* to 45*R*, the stacking sequences systematically change: the number of *k*-layers varies from 1 to 11 while the number *h*-layers remains unchanged. The profiles from 24*R* to 45*R* show good agreement with the experimentally obtained pattern, particularly in the high angle region. The high-angle peaks are less affected by extrinsic factors such as preferred orientation. By comparison with the simulated and experimental patterns, we find that the 27*R* $(hhhhkkkkk)_3$ structure well reproduces the overall profile.

The structural parameters are further refined by Rietveld analysis using RIETAN-2000 program. Figure 2 shows the results of Rietveld refinements using the 27*R* structural model. The space group *R*-3*m* is chosen and is assumed to be unchanged in the pressure range of 12-22 GPa in the fitting analysis. For 14.0 and 17.9 GPa patterns, different stacking sequences are examined. We correct the preferred orientation parameters as well as the atomic coordinates. The observed diffraction patterns are satisfactorily reproduced from the refined parameters.

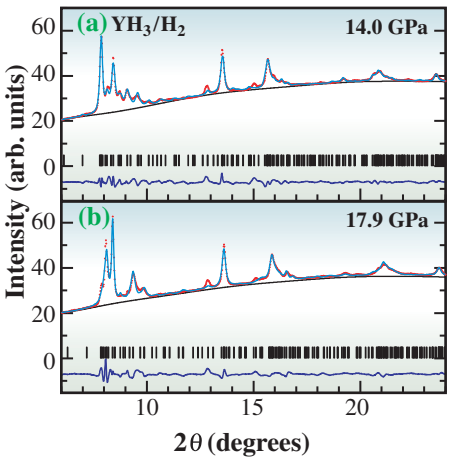

Fig. 2. X-ray diffraction patterns of YH_3 measured at 14.0 and 17.9 GPa. Solid curves are results of Rietveld refinements with the 27R structure models.

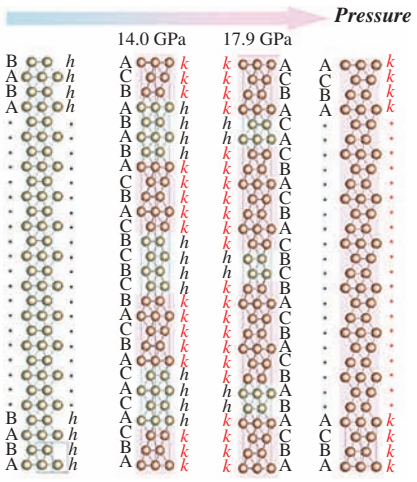

Fig. 3. Schematic illustrations of the long-period structures of the yttrium sublattices at 14.0 and 17.9 GPa. The hexagonal and cubic structures are also shown.

The intermediate structure is most likely to be a long-period metal lattice with a stacking sequence that successively changes toward the fcc structure upon compression.

Schematic illustrations of the long-period structures of the yttrium sublattices at 14.0 and 17.9 GPa are shown in Fig. 3. The hexagonal and cubic structures are also shown. Such stacking structures can be regarded as periodic arrangements of *h*-layer and *k*-layer domains. The 14.0-GPa structure consists of 4 *h*-layers and 5 *k*-layers, while the 17.9-GPa structure consists of 2 *h*-layers and 7 *k*-layers. The number of *k*-layers shows a tendency to increase with pressure as expected, and the full fcc stacking sequence is realized at about 22 GPa. In contrast with the parent metal, the hexagonal-cubic transition of YH_3 is slow and proceeds via an intermediate state in which the metal layer sequence gradually changes with increasing pressure. Such a transition process is considered to be characteristic of rare-earth metal hydrides and should be interpreted in terms of the H-H interactions and H-M bonding.

Akihiko Machida

SPring-8 / JAEA

E-mail: machida@spring8.or.jp

References

[1] *A. Machida, A. Ohmura, T. Watanuki, K. Aoki and K. Takemura: Phys. Rev. B* **76** *(2007) 052101.*
[2] A. Machida *et al.*: Solid State Commun. **138** (2006) 436.
[3] T. Kume *et al.*: Phys. Rev. B **76** (2007) 024107.

High-oxygen-pressure Crystal Growth of Ferroelectric $Bi_4Ti_3O_{12}$ Single Crystals

Ferroelectric bismuth titanate ($Bi_4Ti_3O_{12}$, BiT) has been regarded as a promising material for innovative semiconductor-based applications such as nonvolatile memories, electro-optic devices and uncooled infrared detectors because of its high Curie temperature, large spontaneous polarization (P_s) and large electro-optic coefficient [1]. The control of polarization states is the underlying basis of these functional devices, and polarization switching is achieved through the nucleation of domains and the following domain-wall motion by applying an electric field (E). Leakage current arising from defects, however, interferes with the polarization switching of BiT-based materials [2]. In addition, oxygen vacancies are known to act as an obstacle to the polarization switching, and a resultant remanent polarization (P_r) is suppressed by the clamping of the domain walls by oxygen vacancies [2]. The leakage current and domain clamping by oxygen vacancies make BiT unsuitable for the practical applications. Thus, a guiding principle of defect control is required to be established for obtaining high-quality BiT-based devices with a large P_r as well as a low leakage current. Here, we show that high-oxygen-pressure crystal growth is an effective process for obtaining high-quality BiT crystals with a large P_r and a low coercive field (E_c) as well as low leakage current [3].

Synchrotron radiation powder diffraction experiments on the crushed powder of the crystals were performed using a large Debye-Scherrer camera installed at **BL02B2** to investigate the precise crystal structure of BiT synthesized by the processing method. We used high-energy SR with a wavelength of λ = 0.035639(2) nm (E ~ 35 keV) to reduce absorption by the samples. The BiT crystals under different Po_2 atmospheres had almost the same lattice

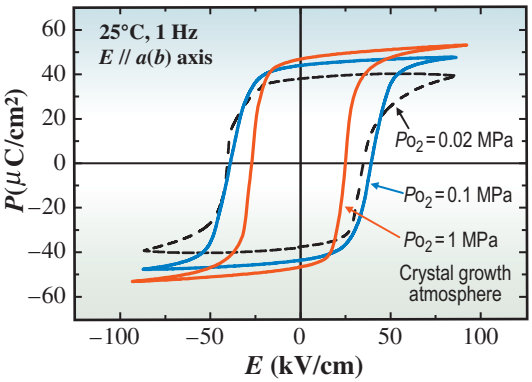

Fig. 1. Polarization hysteresis loops along the ***a***(***b***)-axis for the BiT crystals grown at a Po_2 of 0.02, 0.1, and 1 MPa. These crystals were annealed at 900°C for 10 h in air. The measurements were conduced at 25°C using an E at a frequency of 1 Hz.

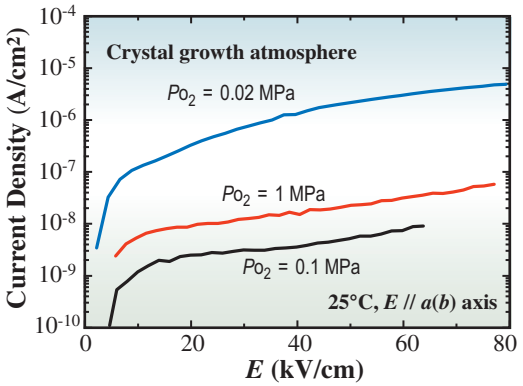

Fig. 2. Remanent polarization (P_r) and coercive field (E_c) as a function of Po_2 during crystal growth (25°C, 1 Hz). The values of P_r and E_c are average in positive and negative regions in the polarization hysteresis loops (Fig. 1).

parameters: a = 0.54505(5) nm, b = 0.54108(4) nm, c = 3.2834(3) nm. Rietveld analyses demonstrated that there was no significant difference in crystal structure in crystals grown under different pressures [3]. These experimental results indicate that high-oxygen-pressure crystal growth is suitable for obtaining defect-controlled ferroelectric crystals without any significant change in the main crystal structure.

Domain observations by piezoresponse force microscopy (PFM) demonstrate that the clamping of 90° domains deteriorates P_r for the crystals grown at 0.02 MPa oxygen, which is suggested to originate from the strong attractive interaction between 90° domain walls and oxygen vacancies. The vacancy formation of Bi and O during crystal growth at high temperatures is suppressed at a higher oxygen pressure, leading to a larger P_r of 47 μC/cm^2 and a lower E_c of 26 kV/cm for the crystals grown at 1 MPa oxygen [3].

Figure 1 shows the polarization hysteresis loops measured along the ***a***(***b***)-axis (25°C, 1 Hz) [3]. The crystals (Po_2 = 0.02 MPa) exhibited hysteresis with P_r = 38 μC/cm^2 and an E_c = 38 kV/cm. The high-Po_2-grown crystals had larger values of P_r of 44 μC/cm^2 (Po_2 = 0.1 MPa) and 47 μC/cm^2 (Po_2 = 1 MPa). Note that the crystals grown at Po_2 = 1 MPa exhibited well-saturated polarization hysteresis with E_c = 26 kV/cm. This E_c value was much lower than those of the other crystals. Figure 2 shows P_r and E_c as a function of Po_2 during crystal growth [3]. With increasing Po_2, P_r monotonically increased, while the decrease in E_c was marked over Po_2 = 0.1 MPa.

Figure 3 shows the leakage current density (J) as a function of E along the ***a***(***b***)-axis (25°C) [3]. The

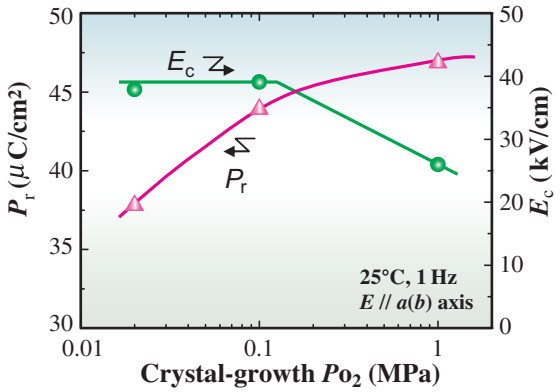

Fig. 3. Leakage current density (J) as a function of E along the $a(b)$-axis for the BiT crystals (25°C, 1 Hz).

crystals (Po_2 = 0.02 MPa) exhibit a high J of the order of 10^{-7} to 10^{-6} A/cm^2. The increase in Po_2 to 0.1 MPa led to a drastic decrease in J to the order of 10^{-9} A/cm^2. The crystals grown at Po_2 = 1 MPa exhibited a relatively low J of the order of 10^{-8} A/cm^2.

Here, we discuss the mechanism of domain clamping during the polarization switching along the ***a***(***b***)-axis. Figure 4 shows the PFM images observed on the ***a***(***b***)-***c*** surface of the crystals grown at Po_2 = 0.02 MPa [3]. The in-plane PFM image of the as-annealed (nonpoled) crystals (Fig. 4(a)) exhibits 180° DWs parallel to the ***a***-***b*** plane. After an E of 100 kV/cm was applied along the ***a***(***b***)-axis at 25°C, the out-of-plane PFM image of the poled crystals was observed (Fig. 4(b)). A single domain state was not established for the poled crystals even though the applied E (100 kV/cm) is much higher than the E_c value (38 kV/cm). Domains with $P_{s(a)}$ parallel to the poling direction were found. This is direct evidence that 90° domains are switched by applying an E of 100 kV/cm. Note that unswitched regions, i.e., 90° domains with $P_{s(a)}$ normal to the poling direction remained, and 90° DWs with an irregular structure appeared. The irregular-shaped 90° DWs have been reported to originate from the attractive interaction between $V_O^{\cdot\cdot}$ and the electric field established near the 90° DWs due to the discontinuity of the P_s component normal to the DWs. In the domains with $P_{s(a)}$ parallel to the poling direction, a small number of 180° domains with $P_{s(a)}$ antiparallel to the poling direction were observed. These 180° domains are a result of the domain backswitching due to the depolarization field. Our PFM observations lead to the conclusion that the clamping of 90° DWs plays a detrimental role in the $P_{s(a)}$ polarization switching in the BiT crystals. The vacancy formation at high temperatures is suppressed under a higher-Po_2 atmosphere, and then [$V_O^{\cdot\cdot}$] becomes lower for the crystals grown at a higher Po_2. The larger P_r observed for the crystals (Po_2 = 1 MPa) is found to originate from suppressed 90° domain clamping because of a lower [$V_O^{\cdot\cdot}$].

In summary, the effects of Po_2 during the crystal growth of BiT on domain-switching behavior have been investigated through polarization measurements and domain observations by PFM. The crystal structure is investigated by high energy synchrotron radiation powder diffraction. The crystals grown at a high Po_2 of 1 MPa showed a large P_r of 47 μC/cm^2 and a low E_c of 26 kV/cm. PFM observations demonstrate that the clamping of 90° DWs plays a detrimental role in polarization switching, leading to a low P_r. High-Po_2 sintering is proposed as an effective process for suppressing the formation of vacancies of Bi and O without any change in the main crystal structure, leading to the realization of high-quality BiT-based devices with enhanced polarization-switching properties as well as low leakage current.

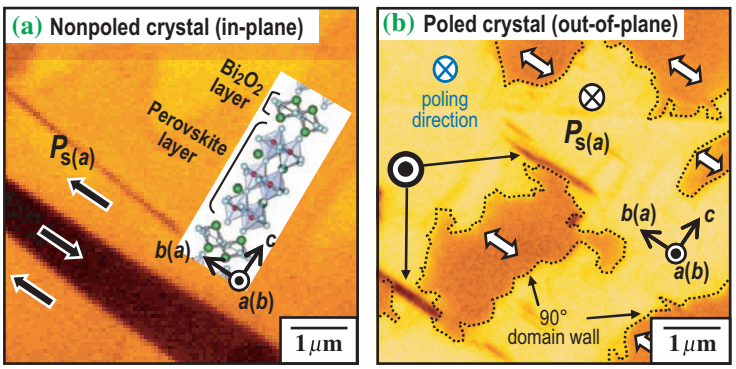

Fig. 4. PFM images of the $a(b)$-c surface of the BiT crystals grown in air (Po_2 =0.02 MPa); (**a**) in-plane image of the nonpoled (as-annealed) crystal, and (**b**) out-of-plane image of the poled crystal. The poling was conducted by applying an E of 100 kV/cm along the $a(b)$-axis at 25°C.

Yuji Noguchi [a], Masaru Miyayama [a] and Yoshihiro Kuroiwa [b]

[a] Research Center for Advanced Science and Technology, The University of Tokyo
[b] Department of Physical Science, Hiroshima University

*E-mail: ynoguchi@crm.rcast.u-tokyo.ac.jp

References

[1] M. Soga *et al.*: Appl. Phys. Lett. **84** (2004) 100.
[2] *S.-J. Kim, C. Moriyoshi, S. Kimura, Y. Kuroiwa, K. Kato, M. Takata, Y. Noguchi and M. Miyayama: Appl. Phys. Lett.* ***91*** *(2007) 062913.*
[3] *K. Yamamoto, Y. Kitanaka, M. Suzuki, M. Miyayama, Y. Noguchi, C. Moriyoshi and Y. Kuroiwa: Appl. Phys. Lett.* ***91*** *(2007) 162909.*

Structural Characterization of Ar^+-Irradiated $SrTiO_3$ Showing Room-temperature Blue Luminescence

$SrTiO_3$ is a transparent insulator and is widely used as an artificial gem. Recently we found that oxygen-deficient metallic $SrTiO_3$ shows blue (430 nm) emission at room temperature. This is not observed for stoichiometric $SrTiO_3$ [1]. The blue luminescence originates from radiative recombination of conduction electrons and excited holes located in the band gap. Thus, the electron carriers doped by the oxygen deficiency play an important role in this emission. Oxygen vacancies can be introduced into the $SrTiO_3$ crystal by Ar^+-irradiation, resulting in the blue luminescence. We investigated structural changes of an Ar^+-irradiated $SrTiO_3$ single crystal by analyzing the intensity of the X-ray diffraction pattern, and propose a model where the lattice constants are modified by the oxygen deficiency [2].

The Ar^+-irradiation was performed at room temperature at 500 V and an Ar gas flow of 3 cc/min for 10 min. The irradiated crystal showed the room-temperature blue luminescence as well as metallic conductivity. X-ray diffraction measurements on stoichiometric and Ar^+-irradiated $SrTiO_3$ crystals were performed, at room temperature, with a four-cycle diffractometer installed at beamline **BL13XU**. An X-ray beam with a photon energy of 11.9 keV (0.104 nm) and a size of 0.1 × 0.1 mm was incident on the samples.

Figure 1(a) shows the reciprocal-lattice map around (114) $SrTiO_3$ Bragg reflection, on a logarithmic intensity scale, for the non-irradiated crystal. Crystal truncation rod (CTR) scattering is visible along the [11*L*] direction due to the highly two-dimensional (i.e., atomically flat) surface structure. After the Ar^+-irradiation, Fig. 1(b), the sample showed additional intensity in the lower *L* direction region of the (114) reflection. This additional intensity was not observed for the non-irradiated $SrTiO_3$, suggesting that the surface layer modified by the Ar^+-irradiation gave rise to slight lattice expansion along the *c*-axis due to the oxygen-deficiencies in the $SrTiO_3$. Note that the in-plane lattice constant of the Ar^+-irradiated $SrTiO_3$ was fixed by the non-irradiated region so that the surface layer was under compressive strain.

As shown in Fig. 2(a), (00*L*) scans around the (002) Bragg reflection of the Ar^+-irradiated $SrTiO_3$ shows an asymmetric profile. This asymmetry is explained by the surface-lattice structure expansion model illustrated in Fig. 2(b). In the model, the following form for the distribution in the lattice parameter of the *k*-th Ar^+-irradiated tetragonal region ($Z > 0$) along (00*L*) is introduced.

$$c(k) = 3.905 + \Delta c(k) = 3.905 + \alpha \cdot \exp(k/\beta) \quad (k \geq 1).$$

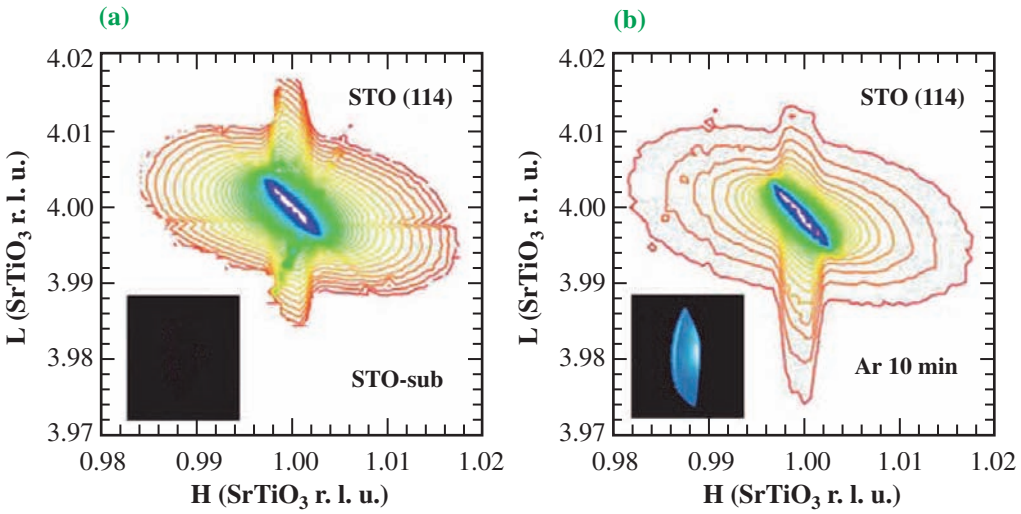

Fig. 1. Logarithmic intensity reciprocal-lattice map around (114) $SrTiO_3$ Bragg reflection for **(a)** non-irradiated and **(b)** Ar^+-irradiated crystals. Inset is a photo of luminescence from each crystal.

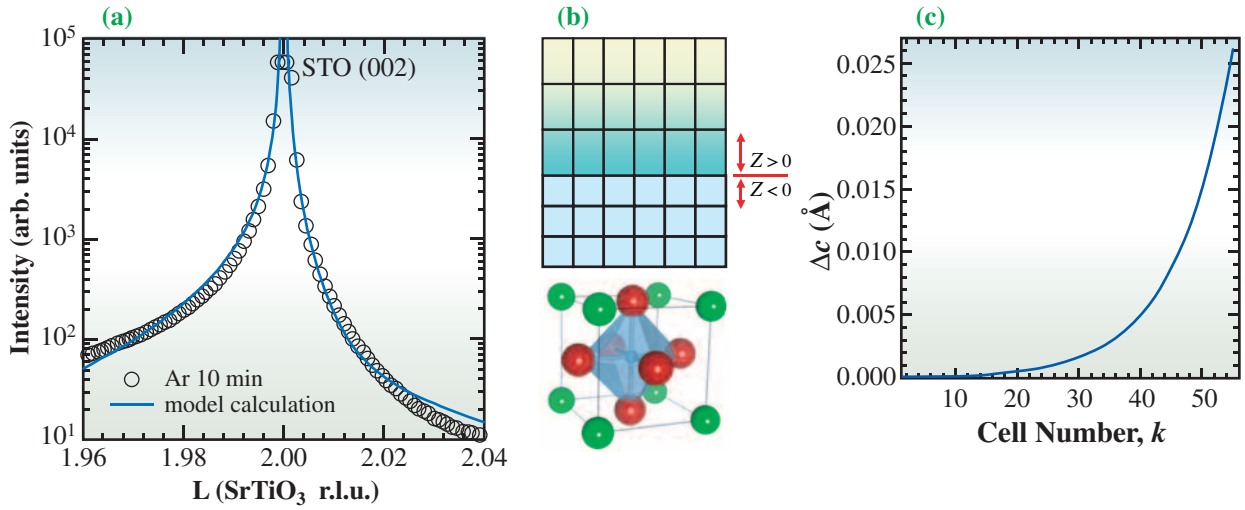

Fig. 2. **(a)** (00*L*) scan around (002) $SrTiO_3$ Bragg reflection of Ar^+-irradiated crystal and the result of the model calculation. **(b)** Schematic illustration of a structural model. **(c)** Variation of the lattice parameter *c* in the surface layer.

By using the atomic positions along the *z* axis for the constituent atoms and atomic scattering factors, the structure factors of the Ar^+-irradiated region, $F_{Ar\text{-}ir}(00L)$ ($Z > 0$) and the non-irradiated bulk region, $F_{Non\text{-}ir}(00L)$ ($Z \leq 0$), are given by

$$F_{Ar-ir}(00L) = \sum_{k=1}^{n}\left[f_{Sr}\exp(-2\pi iLc^*(Z_1(k)-c(k)/2))+f_{Ti}\exp(-2\pi iLc^*Z_1(k)) + f_O\left\{2\exp(-2\pi iLc^*Z_1(k))+\exp(-2\pi iLc^*(Z_1(k)-c(k)/2))\right\}\right],$$

and

$$F_{Non-ir}(00L) = \left[f_{Sr}\exp(-2\pi iLc^*(-a_0/2)) + f_{Ti}+f_O\left\{2+\exp(-2\pi iLc^*(-a_0/2))\right\}\right]\sum_{k\leq 0}^{-\infty}\exp(-2\pi ikLc^*a_0),$$

respectively. Thus the scattering intensity $I(00L)$ should be

$$I(00L) = A\cdot\left|F_{Ar-ir}(00L)+F_{Non-ir}(00L)\right|^2,$$

where the coefficient *A* is a scale factor.

With this model, the observed Bragg peak is well reproduced with α = 0.00006, β = 9.05, and n = 55. Figure 2(c) shows the results of variation in $c(k)$ as a function of k. The number of cells, n = 55, corresponds to the total thickness of the Ar^+-irradiation modified region of about 21 nm. The maximum lattice expansion reached about 0.67%. Our finding shall give a better understanding for the mechanism of room temperature blue luminescence from oxygen deficient surface layer of $SrTiO_3$ and may lead to novel high performance photo device.

Yuichi Shimakawa [a,*], Daisuke Kan [a] and Osami Sakata [b]

[a] Institute for Chemical Research, Kyoto University
[b] SPring-8 / JASRI

*E-mail: shimak@scl.kyoto-u.ac.jp

References

[1] D. Kan *et al.*: Nature Materials **4** (2005) 816.
[2] *D. Kan, O. Sakata, S. Kimura, M. Takano and Y. Shimakawa: Jpn. J. Appl. Phys.* ***46*** *(2007) L471.*

Multilayer Relaxation of Ru Studied by Surface X-ray Diffraction

The structure and composition of solid surfaces affect the chemical reactivity of heterogeneous catalysts. The elucidation of the structure of oxygen on metal surfaces is important for understanding electrochemical phenomena such as corrosion, oxidation, and oxygen reduction. In particular, adsorbed oxygen or hydroxyl groups on Ru surfaces play an important role in electrocatalysis of the oxidation of carbon monoxide (CO) by Pt/Ru catalysts in the direct methanol fuel cell (DMFC). The platinum surface is poisoned by CO formed during methanol oxidation. ($CH_3OH \rightarrow CO_{ad} + 4H^+ + 4e^-$) Adsorbed CO is easily oxidized to CO_2 by adsorbed oxygen atoms on the Ru surface (Fig. 1).

Surface relaxation influences electronic states, work functions, surface energy, and catalytic reactivity significantly. Detailed understanding of the structure of deeper layers is required to provide a realistic description of the surface electron structure. It is well-known that low-energy electron diffraction (LEED) is an excellent technique for determining the atomic arrangement on the metal surface. However, LEED measurement cannot precisely detect relaxation below the surface because low-energy electrons do not penetrate deep into a material. Surface X-ray diffraction is a powerful tool for investigating the relaxation of subsurface areas as well as the reconstruction of the topmost layer. The structure of a Ru(001) surface after adsorbed-oxygen-induced surface relaxation was determined by surface X-ray diffraction using the UHV chamber on the (2 + 2) diffractometer at beamline **BL13XU**.

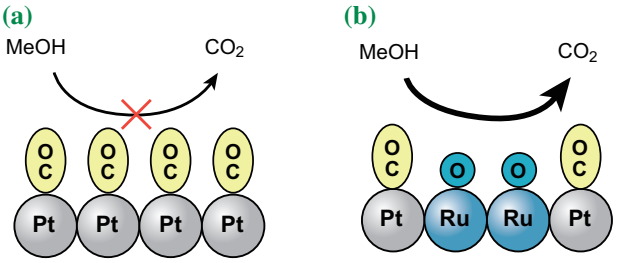

Fig. 1: Schematic model of methanol oxidation on **(a)** Pt and **(b)** Pt/Ru.

Oxygen is absorbed on the Ru(001) surface at hollow sites and forms an ordered (2 × 2) structure. Figure 2 shows the structure factors of diffraction rods at (0 0.5), (0.5 0), (0 1), and (1 0). Bragg peaks appear at integers *L* for the (1 0) and (0 1) crystal truncation rods (CTRs). Fractional-order rods also give rise to periodic peaks near integer values. Without substrate relaxation, the fractional-order rods

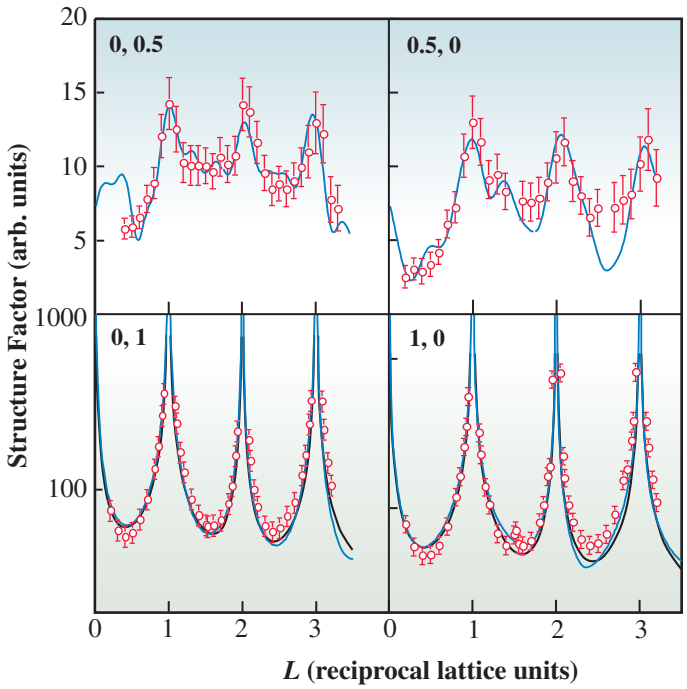

Fig. 2. Structure factors obtained from the crystal truncation rods and fractional-order rods. The blue lines are calculated structure factors obtained from the optimized model. The black lines are calculated ones for a perfectly terminated Ru(001) surface.

do not yield sharp peaks. This indicates that the deviations of Ru atoms from the bulk-phase positions in response to oxygen adsorption occur not just at the topmost surface, but also in the deeper layers. The structural refinement was performed considering the p3ml symmetry. The 9 outermost substrate Ru layers, including 36 Ru atoms and an oxygen atom were subjected to structural refinement. Each substrate layer included four Ru atoms in a (2 × 2) unit cell. In the original paper we present the analysis procedure in detail and the atomic parameters [1].

Figure 3 shows the optimized structural model of oxygen adsorbed on the Ru(001) surface. Atomic oxygen adsorbs at the hcp hollow sites. The Ru-O bond length is 0.203(5) nm, which is consistent with the value determined by the dynamical LEED analysis [2]. The other structural parameters of the lateral and vertical displacements in the first and second layers are also consistent with DFT calculations [3] and LEED results [2]. The atomic rearrangement of the substrate reached the sixth layer. Although it is reported that adsorbate-induced surface relaxation often occurs, the displacement from the bulk position is usually damped at the third layer in a close-packed low-index surface. Oxygen adsorption remarkably enhances the distortion of the atomic arrangement of the internal layers. Atomic displacement decreases exponentially with depth below the second layer. Previous LEED-based analyses have reported adsorbate-induced surface relaxation in the first and second layers on a number of metal surfaces with (2 × 2)-O structures. The lateral expansion (0.006 nm) of Ru atoms (red arrows in Fig. 3) in contact with oxygen in the first layer is significantly larger than that of the others. The binding energy of O on Ru is much higher than on Pt, Pd, Ir, Ni, and Rh. The high binding energy causes the large displacement in the first layer and the large multilayer relaxation of Ru(001)-(2 × 2)-O. The high brilliance SR surface X-ray diffraction conclusively reveals that adsorbed oxygen markedly perturbs the surface electronic structure of a metal.

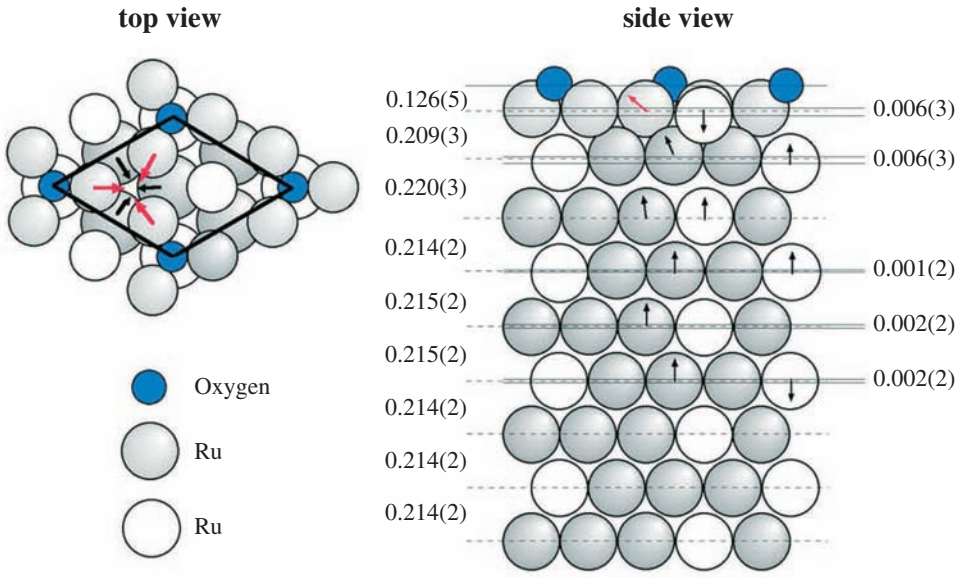

Fig. 3. Optimum surface structure for oxygen adsorbed on Ru(001). Small circles represent adsorbed oxygen atoms. Gray and white circles represent equivalent and independent Ru atoms, respectively. The dashed line indicates the position of the center of gravity in each layer.

Masashi Nakamura [a,*] and Osami Sakata [b]

[a] Department of Applied Chemistry and Biotechnology, Chiba University
[b] SPring-8 / JASRI

*E-mail: mnakamura@faculty.chiba-u.jp

References

[1] *M. Nakamura, H. Kato, N. Hoshi, K. Sumitani and O. Sakata: J. Phys. Chem. C* ***111*** *(2007) 977.*
[2] M. Lindroos *et al.*: Surf. Sci. **222** (1989) 451.
[3] C. Stampfl and M. Scheffler: Phys. Rev. B **54** (1996) 2868.

Instability of Electron Gas in an Expanding Metal

The properties of dilute electron gas have attracted attention since Wigner predicted that it crystallizes in its dilute limit [1]. The behavior of electron gas is often discussed in terms of its ground-state energy, given as a function of the expansion parameter r_s (the Wigner-Seitz radius in units of the Bohr radius). r_s increases with decreasing density and scales approximately as the ratio of the electron interaction energy to the average kinetic energy. As the interaction energy dominates the kinetic energy (r_s increasing), various phase transitions or instabilities such as ferromagnetism or superconductivity have been predicted. Among the various properties of electron gas, compressibility is an intriguing property deduced from the ground-state energy. It becomes negative when $r_s > 5.25$ [2], implying an instability in low-density electron gas. Theoretically, a negative compressibility results in a negative static dielectric function (DF) of the electron gas, $\varepsilon(\mathbf{q}, 0)$, for small $|\mathbf{q}|$. This has interesting consequences, including the possibility that test charges of the same sign might attract. However, the existence of a negative DF in a three-dimensional system has not yet been confirmed.

Expanded fluid alkali metals [3] are good systems for investigating the problem of electron gas instability for several reasons. First, alkali metals are a natural realization of the electron gas because of the nearly spherical Fermi surface of the conducting electrons. Second, a continuous and substantial reduction in electron density is possible by volume expansion along the liquid-vapor saturation line as shown in Fig. 1. Third, positive ions in fluids can readjust their positions more easily than those in solids; thus structural changes might be clearer in fluids through the coupling of electrons and ions.

We have recently fabricated a sample cell with X-ray windows made of single-crystalline molybdenum, which is resistant to the high reactivity of hot alkali metals. By combining this cell with a high-pressure apparatus, we have succeeded in measuring the X-ray diffraction and small-angle X-ray scattering (SAXS) of fluid rubidium over a wide range of temperatures and pressures from the triple point up to supercritical regions [4]. X-ray diffraction measurements were carried out in a dispersive mode at beamline **BL28B2** using an incident white beam and an energy resolving germanium detector. Small-angle X-ray scattering measurements were performed at beamline **BL04B2** using monochromatic 38 keV X-rays, with the scattered X-rays detected using an imaging plate. For the first time, stable and precise measurements were carried out from the triple point up to 2123 K and 22.0 MPa, beyond the critical point of rubidium.

The variation of the position of the first maximum, R_1, is shown as a function of density in Fig. 2(a). R_1 corresponds to the nearest-neighbor distance and it is located at approximately 4.85 Å at 373 K. It decreases slowly with decreasing density to about 1.1 g·cm^{-3}, and then drops more rapidly. In Fig. 2(b), the density dependence of the S(0) of fluid Rb is shown. Below the density of 1.1 g·cm^{-3}, S(0) starts to increase substantially with decreasing density, which indicates the appearance of spatial atomic fluctuations in the fluid.

The change in character of the SAXS results

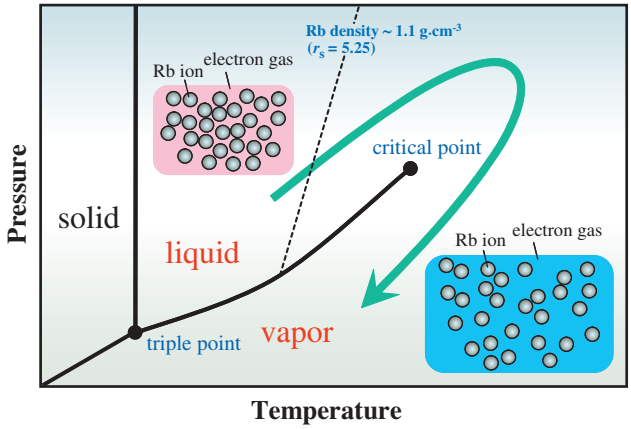

Fig. 1. Schematic illustration of the phase diagram of rubidium (T_c = 2017 K, P_c = 12.45 MPa) [3]. A continuous and substantial reduction in *electron* and ion density is possible by volume expansion along the liquid-vapor saturation line.

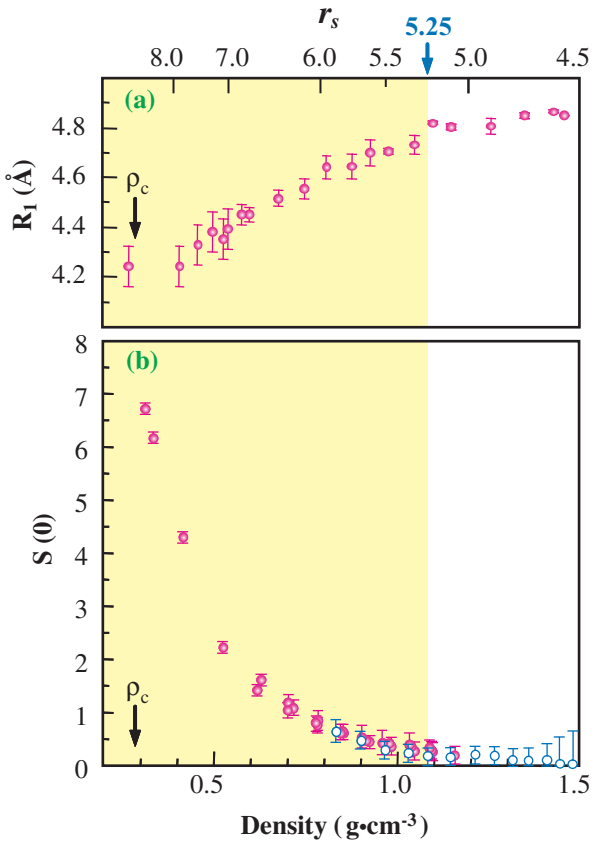

Fig. 2. Density dependence of the structural parameters of fluid rubidium. **(a)** Density dependence of interatomic distance R_1 and **(b)** density dependence of S(0). Dots represent the data measured from 373 K - 1.0 MPa up to 2123 K - 22.0 MPa along the liquid-vapor saturation line. Open circles indicate the data measured from 373 K up to the point near the saturation line at a constant pressure of 5 MPa. The critical density is denoted by ρ_c. The corresponding scale of r_s is shown on the upper axis of the graph of R_1.

occurs at a density, r_s, of between 5 and 5.5, near the critical value of r_s (= 5.25), beyond which the static electron DF becomes negative [2]. The negative electron DF generates an attractive Coulomb interaction among test charges with the same sign. Therefore, the structural features of expanded fluid Rb, such as local contraction and the appearance of the density fluctuation in the metallic state below 1.1 g·cm^{-3}, might be caused by the enhancement in the attractive interaction among the ions in the medium of the electron gas with a negative DF. This also suggests a possible connection to electron pairing. A close connection between the negative static DF and superconductivity has been suggested [5] in the doped cuprates [6]. Expanded fluid alkali metals may show superconductivity at low temperatures if their structural response to the negative electron DF can be frozen.

Kazuhiro Matsuda [a,*], Kozaburo Tamura [a] and Masanori Inui [b]

[a] Graduate School of Engineering, Kyoto University
[b] Graduate School of Integrated Arts and Sciences, Hiroshima University

*E-mail: kazuhiro-matsuda@mtl.kyoto-u.ac.jp

References

[1] E.P. Wigner: Phys. Rev. **46** (1934) 1002.
[2] G. Giuliani and G. Vignale: Quantum Theory of the Electron Liquid (Cambridge University Press, Cambridge, England, 2005).
[3] F. Hensel and W.W.Warren Jr.: Fluid Metals, The Liquid-Vapor Transition of Metals (Princeton University, Princeton, NJ, 1999).
[4] *K. Matsuda, K. Tamura and M. Inui: Phys. Rev. Lett.* ***98*** *(2007) 096401.*
[5] O.V. Dolgov *et al.*: Rev. Mod. Phys. **53** (1981) 81; O.V. Dolgov and E. G. Maksimov: Sov. Phys. Usp. **25** (1982) 688.
[6] M. Tachiki *et al.*: Phys. Rev. B **67** (2003) 174506.

A Peculiar Fluctuation in the Metal-nonmetal Transition Observed in the Supercritical Fluid Mercury

More than half a century ago, Landau, the winner of the 1962 Nobel Prize in physics, predicted that fluid Hg may undergo a first-order metal-nonmetal (M-NM) transition with volume expansion [1]. The M-NM transition in fluid Hg was later confirmed by electrical conductivity and thermopower measurements by Hensel and Frank in 1966. Fluid Hg is now known to undergo the M-NM transition with decreasing density, ρ, from 13.6 g·cm^{-3} under ambient conditions to 9 g·cm^{-3} near the critical point at a high temperature and high pressure (see the phase diagram in Fig. 1). However many experiments have indicated a gradual M-NM transition, *without* evidence of the first-order phase transition. Figure 1 shows the phase diagram of pressure-temperature plane for fluid Hg indicating the relation of the thermodynamic states between the M-NM transition and the critical point (critical data of Hg: T_C = 1751 K, P_C = 167.3 MPa, ρ_C = 5.8 g·cm^{-3}).

Here we report on our recent small-angle X-ray scattering (SAXS) measurements of fluid Hg under extreme conditions, where we found a fluctuation inherent to the M-NM transition [2] consistent with a first-order phase transition. The work was carried out at the high energy X-ray diffraction beamline **BL04B2** [3]. A monochromatized beam of X-rays at 37.8 keV energy was incident on the sample, and scattered

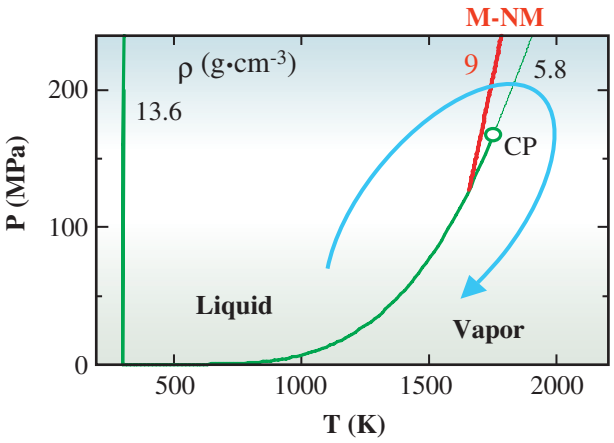

Fig. 1. Phase diagram of fluid Hg on pressure-temperature plane. The bold solid curve denotes the saturated-vapor pressure curve and the open circle at the end is the critical point. Also shown are the isochors of 13.6 g·cm^{-3} (thin solid line), 9 g·cm^{-3} (red bold line) and 5.8 g·cm^{-3} (thin solid line). Continuous volume expansion from liquid to vapor is possible through the supercritical region, as indicated by the light blue arrow.

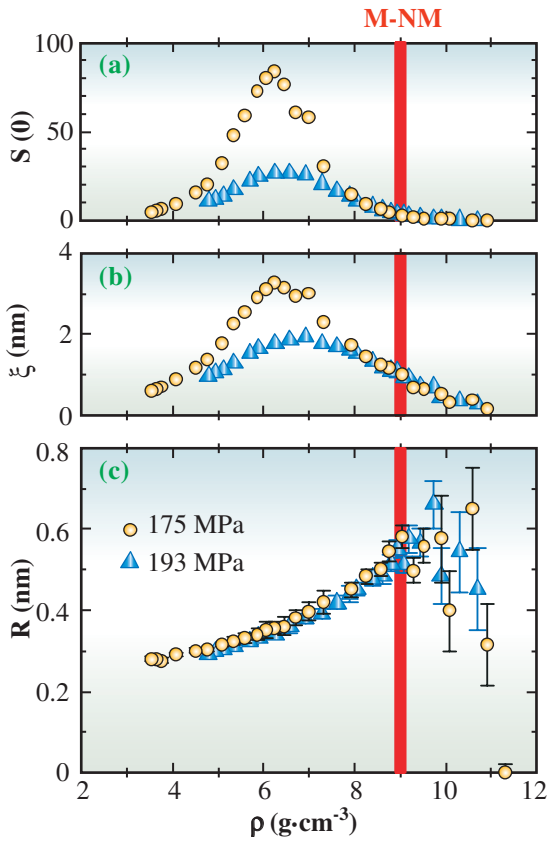

Fig. 2. Density fluctuation *S(0)* **(a)**, correlation length of the fluctuation ξ **(b)** and short-range correlation length *R* **(c)** of fluid Hg at 175 MPa and 193 MPa as a function of density ρ. The red band denotes the M-NM transition region at 9 g·cm^{-3}.

X-rays were detected by an imaging plate at a distance of approximately 3 m. The observable modulus of the scattering vector was from 0.4 nm^{-1} to 4 nm^{-1}. Details of the experiments have been described in [2].

A clear increase of SAXS intensity was observed at the M-NM transition region at 9 g·cm^{-3} for the first time. This means that a medium-range inhomogeneous structure appears at the M-NM transition. We analyzed the observed spectra using Ornstein-Zernike theory to understand the structure. Figures 2(a) and 2(b) show the density fluctuation *S(0)* and the correlation length of the fluctuation ξ as functions of density, ρ. Near the critical point of around 6 g·cm^{-3}, *S(0)* and ξ depend on pressure, and their values become small as the pressure is increased beyond the critical point. However in the M-NM transition region at 9 g·cm^{-3}, *S(0)* and ξ are nearly independent of pressure, which hints that the inhomogeneous structure has an origin different

from the critical fluctuation. Actually, the short-range correlation length R, which is deduced from $S(0)$ and ξ, indicates an anomaly in the M-NM transition as seen in Fig. 2(c). While ξ diverges as it approaches the critical point, R does not change much near the critical point at around 6 g·cm^{-3}. This is consistent with the central assumption in Ornstein-Zernike theory, that the direct correlation between particles is short-range. In contrast, R exhibits a maximum value in the M-NM transition while $S(0)$ and ξ decrease as the M-NM transition is approached. These results suggest that the fluctuation in the M-NM transition is different from the critical fluctuation and that the large R is strongly related to the first-order phase transition.

Further analysis shows that the fluctuation in the M-NM transition consists of slightly dense and slightly rarefied domains approximately 1 nm in diameter, and that these domains have a lifetime of several picoseconds [2]. The dense and rarefied domains have metallic and nonmetallic properties, respectively. Figure 3 shows a snapshot of the atomic configuration in expanded fluid Hg at (a) the M-NM transition and (b) near the critical point, obtained from Monte Carlo simulations using the effective pair potentials deduced from the measured static structure factors. Magenta and light blue particles in the figure show high and low density regions, respectively, calculated as an average over 1 nm spheres. In Fig. 3(a), the aggregates are mixed, as indicated by the yellow and white broken circles in the M-NM transition. This suggests that the first-order M-NM transition occurs as a fluctuation on a ~1 nm length scale. In contrast, the aggregates in Fig. 3(b) are almost all light blue, which suggests a nonmetallic property of the critical fluctuation. Thus, the present study clarifies that the M-NM transition in expanded fluid Hg exhibits the property of the first order phase transition as predicted by Landau.

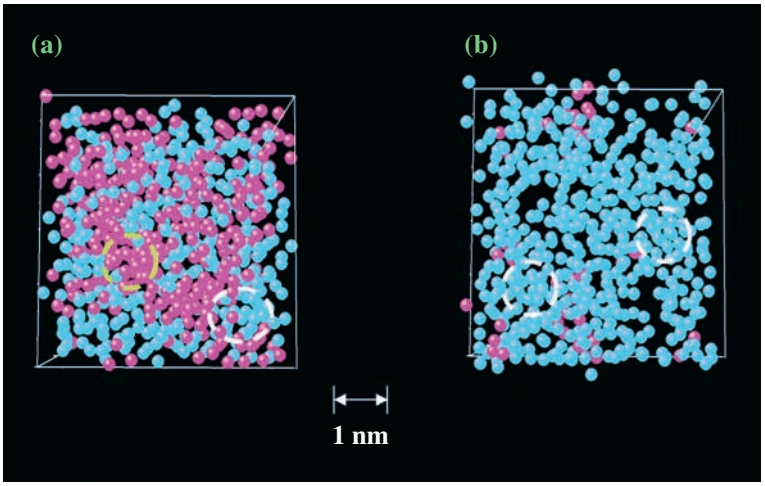

Fig. 3. Snapshot of atomic configuration in the M-NM transition **(a)** and near the critical point **(b)** in expanded fluid Hg. Magenta and light blue particles denote local densities higher and lower than 9 g·cm^{-3}, respectively.

M. Inui [a,*], K. Matsuda [b] and K. Tamura [b]

[a] Graduate School of Integrated Arts and Sciences, Hiroshima University
[b] Graduate School of Engineering, Kyoto University

*E-mail: inui@minerva.ias.hiroshima-u.ac.jp

References

[1] L. Landau and G. Zeldovich: Acta Phys. Chem. USSR **18** (1943) 194.
[2] *M. Inui, K. Matsuda, D. Ishikawa, K. Tamura and Y. Ohishi: Phys. Rev. Lett.* ***98*** *(2007) 185504.*
[3] M. Isshiki *et al.*: Nucl. Instrum. Meth. Phys. Res. A **467-8** (2001) 663.

Mesoscopic Structure Analysis of Metallic Materials by Coherent X-ray Diffraction Microscopy

Coherent X-ray diffraction microscopy [1] (CXDM) is a novel technique for reconstructing the electron density of a sample. Figure 1 shows a schematic illustration of CXDM. By illuminating an isolated sample with coherent X-rays through an aperture, one observes its Fraunhofer diffraction patterns. The finely sampled diffraction intensities are measured by a two-dimensional X-ray detector. The phases of scattered X-rays are retrieved using an iterative algorithm, e.g., Fienup's hybrid input-output (HIO) algorithm [2], allowing the density of the sample to be reconstructed in two- or three-dimensions (2D or 3D).

CXDM has great potential as a technique for structural studies of metallic materials because it can be applied to micron-thick samples and is nondestructive. At present, the best image resolutions that have been achieved are 7 nm for a 2D image and less than 50 nm for a 3D image. The resolutions of transmission electron microscopy (TEM) and 3D atom probe (3DAP) microscopy are currently better than that of CXDM, but a TEM specimen must be less than 0.5 μm in thickness, while 3DAP destroys the specimen during the measurement. CXDM provides mesoscopic structure information about a micrometer sample. For example, precipitates in some aluminum alloys in practical use are a few tens of nanometers in size. CXDM is thus perfectly suited for the study of the exact 3D configuration of precipitates in a micrometer alloy sample. In the present study, the validity of CXDM for this kind of observation is demonstrated with an age-hardened aluminum alloy in practical use [3].

The chemical composition of the aluminum alloy was 96.376 at. % Al, 0.763 at. % Si, 0.010 at. % Fe, 1.887 at. % Cu, 0.431 at. % Mn, 0.515 at. % Mg, <0.005 at. % Cr, 0.004 at. % Zn, 0.006 at. % Ti, and <0.003 at. % Zr. Particles of the alloy of about 1 μm diameter were prepared and mounted on a 30-nm-thick Si_3N_4 membrane. A well-isolated particle was selected by optical microscopy. The CXDM measurement was carried out at beamline **BL29XUL** [4]. The membrane with the aluminum alloy particles was placed in vacuum. Incident X-rays of 5 keV irradiated the selected particle through a 20 μm aperture. Forward X-ray diffraction was collected by a charge-couple device detector placed 1.32 m downstream of the sample. Diffraction profiles were measured as a function of the sample rotation angle (α) around the horizontal axis perpendicular to the incident direction. The α value was changed from –70° to 70° in 5° steps. Each step took 2 hours.

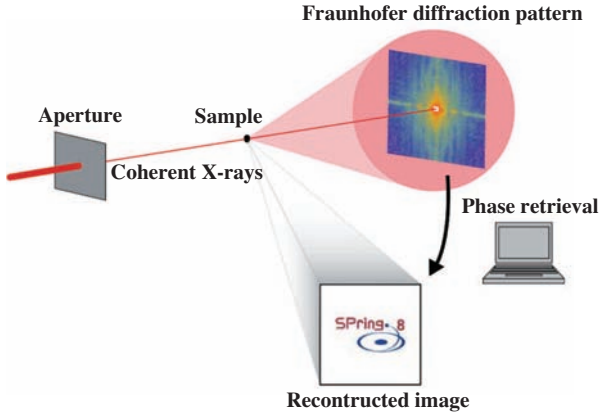

Fig. 1. Schematic illustration of coherent X-ray diffraction microscopy.

Figure 2(a) shows the diffraction pattern at $\alpha = 0°$. The fine structures in the diffraction pattern include information about both the shape of the sample and its internal structure. The sample image was reconstructed by the iterative normalization algorithm [5], which is a kind of HIO algorithm. Figure 2(b) shows the image reconstructed from the diffraction pattern shown in Fig. 2(a). The pixel size is 20.4 nm in both x and y directions. The sample image is displayed in gray scale, with darker colors corresponding to higher electron densities. In this image, the contrast results not only from variations of the sample thickness but also from the distribution of precipitates in the sample. To clarify the internal structure, a 3D image was reconstructed. The 29 diffraction patterns at different α values were normalized by the sum of the 2D reconstructed intensities at each α. A 3D diffraction intensity distribution with $561 \times 561 \times 561$ pixel resolution was made from the normalized 2D diffraction patterns shown in Fig. 3(a). Figure 3(b) shows the 3D reconstructed image. The dark blue area shown in Fig. 3(b) represents the surface figure of the reconstructed 3D image. The voxel size is 29.1 nm on each side. The particle size is about $1280 \times 850 \times 1080$ nm^3. According to Silcock [6], the *S*-phase, which has the composition of Al_2CuMg, precipitates in this aluminum alloy. Thus, we identified the high-electron-density regions resulting from *S*-phase precipitates based on the electron densities of Al and Al_2CuMg calculated from their atomic structures, which are 7.8×10^2 and 1.0×10^3 electrons/nm^3, respectively. Assuming that the voxel with a maximum value in the 3D reconstruction corresponds to pure Al_2CuMg, we trace the region with more than

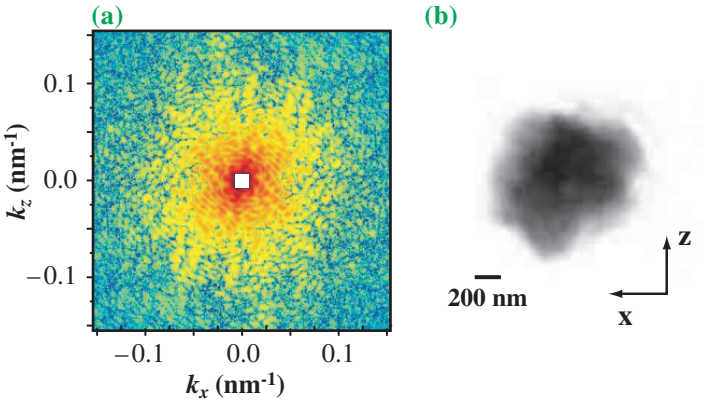

Fig. 2. **(a)** Coherent X-ray diffraction pattern of the Al alloy particle in 801×801 pixels at α=0°. The region of the central 37×37 pixels is an unmeasurable area due to the direct beam stop. **(b)** Image reconstructed from the diffraction pattern of **(a)**. The pixel size is 20.4 nm.

77% of the maximum density, corresponding to the border of the precipitates. The surface image of the high-electron-density region is drawn inside the particle image in Fig. 3(b). The high-electron-density region is about 780×480×220 nm^3 in size.

In conclusion, the internal structure and the shape of a micrometer-sized sample of a precipitation-hardened aluminum alloy were visualized by three-dimensional CXDM, and the spatial distribution of *S*-phase precipitates was evaluated. To examine the shape of each nanometer-sized precipitate, or the interface between the Al and the precipitates, it is necessary to improve the resolution of CXDM by using more brilliant X-rays. This will be realized using a next-generation light source such as an X-ray free electron laser (XFEL). By using an XFEL, *in situ* observation during heating might be realized with nanometer resolution.

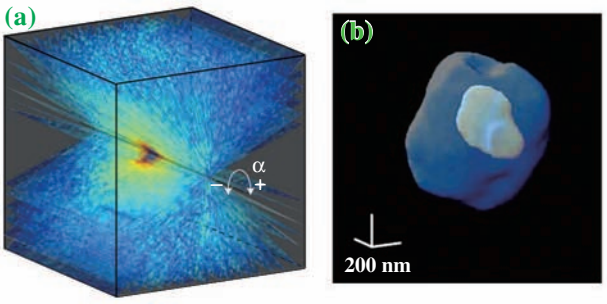

Fig. 3. **(a)** Three-dimensional diffraction array of 561×561×561 pixels made from 29 diffraction patterns of the Al alloy particle within –70° ≤ α ≤ 70° with 5° steps. **(b)** Three-dimensional surface figure of the Al alloy particle reconstructed from the diffraction array. A high-electron-density region resulting from Al_2CuMg precipitates, which is derived using the known electron density, is drawn inside the particle image.

Yukio Takahashi [a,*], Yoshinori Nishino [b], Tetsuya Ishikawa [b] and Eiichiro Matsubara [c]

[a] Graduate School of Engineering, Osaka University
[b] SPring-8 / RIKEN
[c] Department of Materials Science and Engineering, Kyoto University

*E-mail: takahashi@wakate.frc.eng.osaka-u.ac.jp

References

[1] J. Miao *et al.*: Nature **400** (1999) 342.
[2] J. R. Fienup: Appl. Opt. **21** (1982) 2758.
[3] *Y. Takahashi, Y. Nishino, T. Ishikawa, E. Matsubara: Appl. Phys. Lett.* ***90*** *(2007) 184105.*
[4] K. Tamasaku *et al.*: Nucl. Instrum. Meth. Phys. Res. A **467-468** (2001) 686.
[5] Y. Nishino *et al.*: Phys. Rev. B **68** (2003) 220101(R).
[6] J.M. Silcock: J. Inst. Met. **89** (1960) 203.

How Can We Determine a Non-crystalline Structure from Diffraction Data?

The determination of liquid and amorphous structures from diffraction data is by no means trivial. Diffraction data are given as a function of momentum transfer, or equivalently, wavenumber, k. Hence, to extract information as to structures it is necessary to convert the data from the wavenumber space to the real space. Since the diffraction data obtained from diffraction experiments yield structural information in a limited k range, we have to best estimate the missing information outside the k range so as to minimize the effects of finite truncation as far as an ordinary Fourier inversion is adopted. In this article, we report a new method for determining non-crystalline structures that relies on the maximum entropy principle.

We chose a molecular liquid, SnI_4, as a sample for developing the new method, since the intra-molecular atomic configuration of SnI_4 is well-known and we are not aware of any structural data on liquid SnI_4 at ambient pressure. The high-energy synchrotron X-ray diffraction measurement on liquid SnI_4 was performed at the high-energy X-ray diffraction beamline **BL04B2**. The scattered X-ray intensity from the sample in a glass tube measured at 433 K and that of an empty tube are shown by the black and red lines, respectively, in the inset of Fig. 1. The normalized structure factor, $S(k)$, is shown as a blue line in Fig. 1. Note that the oscillation originating from intra-molecular correlation is significant beyond 20 Å^{-1}. The feature of the structure factor can be satisfactorily captured by our molecular dynamics (MD) simulations [1] (as shown in the lower inset), in which the molecules were treated as rigid tetrahedra interacting via the van der Waals potential acting between the vertices. This modeling is justified because the central tin atom within a molecule is completely enveloped by the surrounding iodine atoms located at the vertex sites so that the iodine is electronically regarded as an inert gas atom. The first little peak observed at around k = 1 Å^{-1}, which is characteristic to the system, was found, by RISM calculations to the model, to be ascribed to the Sn-Sn correlation [1].

The distribution of molecules in real space as a function of radial distance, r, called the reduced radial distribution function (RRDF), $G(r)$, can be derived from $S(k)$ by a Fourier inversion, as mentioned above. The radial distribution function (RDF), which statistically describes how molecules are packed around one another in the radial direction, will be obtainable from the RRDF if the density of the liquid is known. Although our wavenumber window is as wide as ~ 25 Å^{-1}, significant oscillation can be observed up to a maximum k value of 25 Å^{-1} (see Fig. 1), suggesting that ordinary inversion would produce spurious peaks in the RRDF.

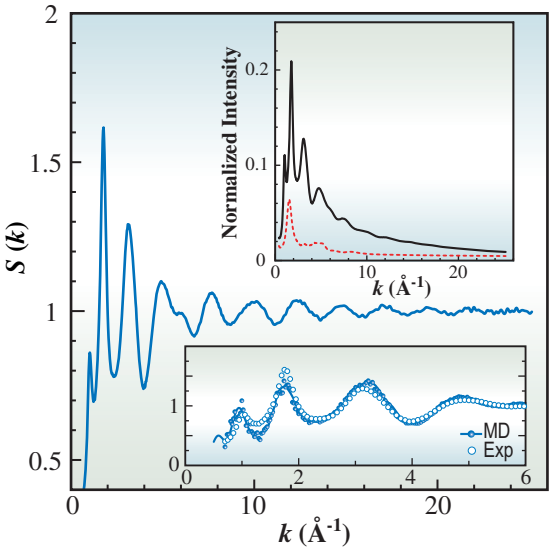

Fig. 1. Structure factor of liquid SnI_4 at 433 K and ambient pressure plotted as a function of wavenumber. The upper inset shows the normalized scattered X-ray intensities of the sample contained in a glass tube (solid black line) and from an empty tube (dashed red line). The lower inset shows a comparison of the main part of the structure factors obtained through the experiment (open circles) and our MD simulations (closed circles).

To prevent artifacts from appearing in the RRDF, a powerful inversion technique based on the maximum entropy method (MEM) has been newly devised. Here, the new method is outlined (refer to Fig. 2) emphasizing the striking differences from existing MEMs (summarized in [2]). The new inversion

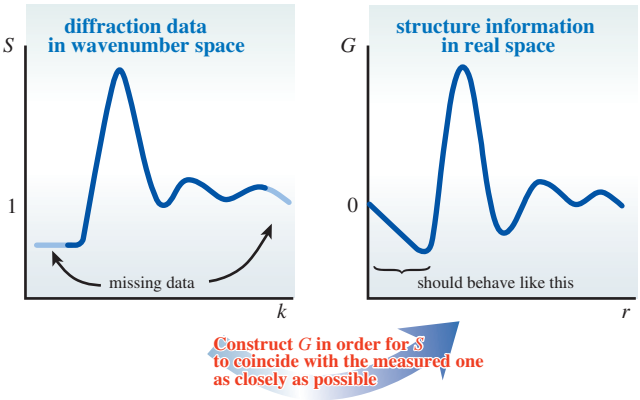

Fig. 2. Schematic diagram of the conversion from structure factor, $S(k)$, to RRDF, $G(r)$. The former information is not necessarily complete. The latter is estimated using the MEM in such a way that S predicted by G mimics the measured one as closely as possible.

process consists of two steps. In the first step, the MEM is used to transform $S(k)$ to $G(r)$ by making an unbiased estimation of the latter so that the structure factor approaches the observed $S(k)$ as closely as possible. The resultant $G(r)$ of this step obtained from $S(k)$ in Fig. 1 is delineated by a pink line in Fig. 3. The anomalies appearing below the first peak are due to systematic errors contained in $S(k)$, which were not removed even by the MEM. The true RRDF, however, should have a linear dependence on r around the region with a slope being proportional to the density. Kaplow, Strong and Averbach (KSA) claimed that an observed $S(k)$ involves ambiguity due to the finiteness of k and suggested that $S(k)$ should be modified in such a way that $G(r)$ has an initial linear part [3]. In the second step, our MEM can naturally incorporate KSA's suggestion by self-consistently determining the density within the procedure. To this end, two useful mathematical relationships were derived in which the RRDF is directly or indirectly connected with the density [2]. It becomes clear from these expressions for a reliable estimate of the density to widen the accessible k range in the experiments. The high-energy synchrotron X-ray diffraction measurements play an essential role in this context. The blue line in Fig. 3 shows the final RRDF resulting from the second step. The mass density was estimated from the initial gradient to be 3.0 g/cc, which almost coincides with the value obtained from our MD simulations, as evident from the excellent agreement between the experimental and simulated (light blue line) RRDFs. (Since SnI_4 molecule was modeled as a rigid tetrahedron in the MD simulations, the first and second peaks, which exhibit the Sn-I and I-I intra-molecular correlations, respectively, assume the form of a delta function.) The principal peaks in the RDF obtained from the final RRDF assuming the aforementioned value for the density are at 2.67 and 4.35 Å. The ratio of these distances, 1.63, implies that the liquid is truly a molecular liquid, consisting of molecules with a regular tetrahedral symmetry. For further discussion on the details of the microscopic structure, refer to [1,2].

From the above explanation, it is evident that our MEM is different from the existing MEMs in the following respects: (i) our target distribution for the maximum entropy estimator is not the RDF but the RRDF, which is not positive definite (that is, the entropy cannot be defined for the latter without an ingenious trick); (ii) the density is assumed to not be given at the outset. Finally, it should be stressed that the RRDF thus obtained through the least-biased estimation is not the final product but an initial trial,

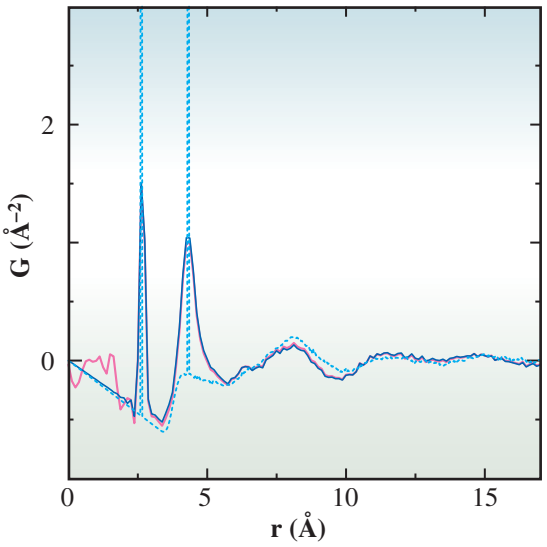

Fig. 3. RRDFs obtained using the MEM inversion in the first step (pink line) and the built-in correction procedure in the second step (blue line), and the RDF obtained from the MD simulations (light blue line) plotted against radial distance.

which must be interpreted using other means such as MD simulations and RISM calculations. This technique was successfully applied to the analysis of a liquid under high temperature and high pressure [4], where there are significant limitations in diffraction data, e.g., attainable k range and the reliability of background subtraction.

Kazuhiro Fuchizaki [a,b]

[a] Department of Physics, Ehime University
[b] Theoretical and Computational Molecular Science, Institute for Molecular Science

E-mail: fuchizaki@phys.sci.ehime-u.ac.jp

References

[1] K. Fuchizaki *et al.*: to be published.
[2] *K. Fuchizaki, S. Kohara, Y. Ohishi and N. Hamaya: J. Chem. Phys.* ***127*** *(2007) 064504.*
[3] R. Kaplow *et al.*: Phys. Rev. **138** (1965) A1336.
[4] K. Fuchizaki *et al.*: to be published.

MATERIALS SCIENCE :

"Taranoki" - Japanese angelica tree

Spectroscopic measurement and diffraction are key techniques for investigating the properties of various kinds of materials. Materials Science focusing on electronic and magnetic properties continues to play one of the major roles at SPring-8. This chapter is organized into four parts in terms of the methods: (1) the dynamical properties of materials studied by inelastic X-ray scattering and nuclear forward scattering, (2) studies of electronic structures using Compton scattering, angle-resolved photoelectron spectroscopy (ARPES), and infrared reflectivity methods, (3) the charge density distributions of materials obtained using diffraction methods, and (4) studies on magnetism by soft X-ray magnetic circular dichroism (MCD) and magneto absorption spectroscopy under a high magnetic field. From the materials point of view, on the other hand, this chapter contains the topics of superconductivities, strongly correlated and heavy electron systems, materials with a lack of translational invariance, and magnetic and electric materials geared towards device applications.

ELECTRONIC & MAGNETIC PROPERTIES

Inelastic X-ray scattering and spectroscopic experiments at SPring-8, in common with other third-generation synchrotron facilities, have become powerful tools for investigating momentum- and energy-dependent charge and lattice dynamics, and electronic structures. In the last SPring-8 Research Frontiers, inelastic X-ray scattering studies mostly focused on superconductivities. This issue, however, highlights not only superconductivity, but also the study of lattice dynamics on nanoscale inhomogeneity materials and quasicrystals in order to investigate how lattice dynamics are affected by local order and long-range order, and by nanoscale inhomogeneities. Diamond and β-ZrNCl are both band insulators. However, they show superconductivity when carriers are doped. The effect of phonons on superconductivity is always helpful for understanding its mechanism. In this chapter, we report the investigation of the longitudinal optical phonon dispersion of the highest phonon branch in both non-superconductor and superconductor diamonds by inelastic X-ray scattering, and the isotope effect on superconductivity in Li_XZrNCl to clarify how the electron-phonon interaction is important for superconductivity. In general, boron-doped diamond is categorized as a *p*-type semiconductor with a wide band gap. (LaO)CuS is also known to be a transparent *p*-type semiconductor with a wide band gap of 3.1 eV. Since it is essential to know the direct electron density distributions in the host material (LaO)CuS to understand its unique electrical and optical properties, a work was conducted to analyze the charge density distribution using powder diffraction. Another material that is geared towards device applications is FePt thin film, which shows perpendicular magnetization. The MCD measurement on this system was performed in order to determine the relationship between the thickness and the perpendicular magnetization.

Since SPring-8 has a Compton dedicated beamline, this kind of experimental activity is quite high. In this issue we present a study on ice I_h by a Compton scattering experiment to observe temperature-induced changes in the ground-state electron momentum density.

The *f*-electron system, such as that of lanthanide and actinide compounds, shows fruitful magnetic and electronic properties probably due to the itinerant and localized behavior of *f*-electrons. Therefore, one of the central issues regarding this system is whether 4*f* and 5*f* electrons are itinerant or localized and how this affects the magnetic and electric properties of various compounds. In this chapter we show some interesting results related to this issue for various *f*-electron materials obtained by ARPES, infrared reflectivity measurement, nuclear forward scattering, and magneto-absorption spectroscopy under a high magnetic field.

Please enjoy our showcase studies on materials science.

Jun'ichiro Mizuki

Nanoscale Elastic Inhomogeneity in a Pd-based Metallic Glass Observed by Inelastic X-ray Scattering and Ultrasonic Experiments

The structures of vitreous substances are one of the attractive subjects of ongoing research in glass science. In general, glasses roughly fall into two classes, "strong" and "fragile" glass-forming liquids, from the viewpoint of their deviation from the Arrhenius behavior in the temperature dependence of viscosity. It is known that strong glasses such as those formed from SiO_2 and GeO_2 consist of a network of covalently bonded clusters. In contrast, the structure of fragile glasses is still unclear, and they exhibit aspects in their physical properties that are not yet understood. In general, the microstructure frequently governs physical properties, but the microstructure of fragile glasses has not been established yet, despite the fact that several models have been proposed to date. In a series of recent experiments using inelastic X-ray scattering (IXS) and ultrasonic (US) techniques [1,2], we have shown that the sound velocity of nanometer-order wavelengths "exceeds" that of millimeter-order wavelengths. This fact indicates that elastically harder and softer regions coexist in the glass matrix, i.e., there is nanoscale elastic inhomogeneity in a metallic glass.

An intriguing behavior of metallic glasses that we have reported is that their structural stability is significantly deteriorated under radio-frequency ultrasonic perturbation at relatively low temperatures near or below the glass transition temperature T_g, even in thermally stable glasses such as Pd-Ni-Cu-P, Pd-Ni-P and Zr-Al-Ni-Cu bulk metallic glasses [3]. Similar instability phenomena have been observed in other metallic glasses (see the references in [3]), but the mechanism causing the instability was unclear. Our mechanical spectroscopy analysis indicates that the instability is caused by atomic motion resonant with the dynamic ultrasonic-strain field and such that atomic jumps are associated with β relaxation, which is usually observed for low frequencies of the order 1 Hz at temperatures far below T_g. Figure 1(a) shows the microstructure observed by transmission electron microscopy for a Pd-Ni-Cu-P sample subjected to ultrasonic annealing near/below T_g, in which the crystallized region is colored yellow and the remaining amorphous region is colored blue. Such atomic motion at temperatures lower than the so-called "kinetic freezing temperature T_g" is considered to originate from the relatively weakly bonded (and/or low-density) regions in the microstructure of glass with nanoscale inhomogeneities. On the basis of this result, we have proposed a plausible microstructural model of fragile glasses, shown in Fig. 1(b), which consists of strongly bonded regions (SBRs) surrounded by weakly bonded regions (WBRs).

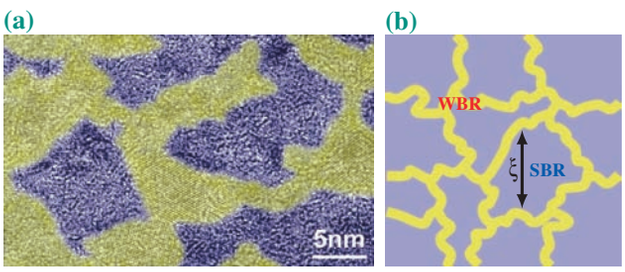

Fig. 1. **(a)** Partially crystallized microstructure of a Pd-based metallic glass obtained by annealing under ultrasonic vibrations slightly below the glass transition temperature. It was found that amorphous regions (blue) are surrounded by the crystallized wall (yellow). **(b)** On the basis of the inhomogeneous microstructure, a two-component microstructural model shown in the right figure is inferred; the blue parts denote strongly bonded regions and the yellow parts denotes weakly bonded regions.

If this structural model is correct, it is predicted that the sound velocity for the nanometer-order wavelength, which mainly represents the elasticity of SBRs, should be faster than that of millimeter-order wavelength, which reflects the macroscopic elastic stiffness of the overall substance including SBRs and WBRs, although the longer-wavelength wave in a homogeneous solid is usually faster. To obtain these sound velocities, two measurement techniques are available: the IXS method for the former sound velocity and the US measurement for the latter. Near the Q value corresponding to the typical domain size ξ, the phonon-dispersion relation is expected to branch positively and negatively from the US line due to the SBR and WBR elasticities, respectively, as shown in Fig. 2(a). To confirm the existence of a "static" structural inhomogeneity, however, we have to eliminate any effects of the hardening/softening due to the relaxation processes that frequently appear in glass substances. Then, in the present work, using one of the most stable bulk metallic glasses (Pd-Ni-Cu-P), we performed the IXS and US measurements far below the glass transition temperature (about 0.5 T_g). As shown in Fig. 2(b), in this metallic-glass system, most of relaxation processes are expected to be excluded from the MHz-ultrasonic measurement and, of course, this is also the case for much higher frequencies such as those in the THz region. Namely, the two kinds of sound velocities (US: MHz, IXS: THz) measured at such a low temperature are both at the high-frequency limit, so that the velocity difference caused in this situation, if present, is limited only to what is caused by the difference between the wavelengths of the probes. We can, thereby, discuss

the "static structure" of the glass through the IXS and US "dynamic" measurements.

The IXS measurement was performed at the high-resolution IXS beamline **BL35XU**. Figure 3(a) shows the typical IXS spectra measured at very low Q values. To obtain the excitation energy, the present IXS spectra were fitted to the damped harmonic oscillator (DHO) function. Figure 3(b) shows the phonon-dispersion relation (lower panel) and compares the phase velocity of longitudinal sound obtained from the IXS data with the US velocities (upper panel). Usually, the US velocity (λ ~ 1 mm) in homogeneous solids is substantially equivalent to the fastest sound velocity at the long-wavelength limit. However, as shown in Fig. 3(b), the sound velocities in the low-Q region are found to be apparently higher than the US velocity in this case. The sound velocity at Q ~ 4 nm^{-1} is virtually equal to the US velocity, indicating that the plots at Q < 4 nm^{-1} deviate positively from the US linear function. For consistency, the sound-velocity plots in the low-Q region should be connected to the long-wavelength limit as shown by curve "A" in the figure. If we had

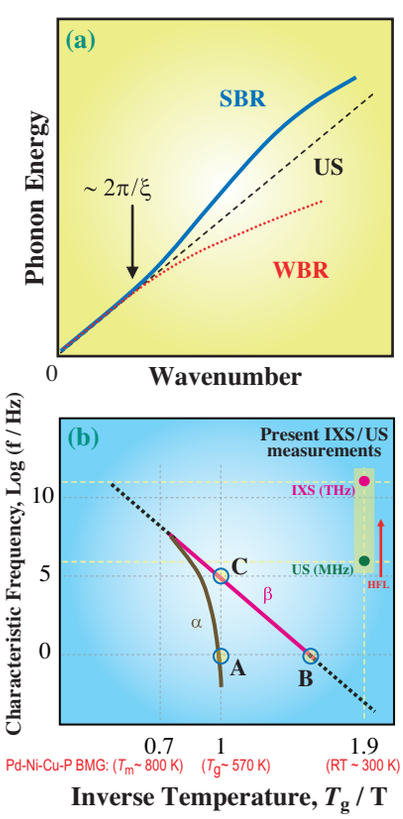

Fig. 2. Schematic illustrations showing **(a)** phonon-dispersion relation in a very small Q region predicted from the model, and **(b)** inverse-temperature dependence of the characteristic frequencies of α and β relaxations. The set of characteristic temperatures in **(b)** is an example for the case of Pd-Ni-Cu-P metallic glass; Point A denotes the glass transition, B and C are obtained from the experiments.

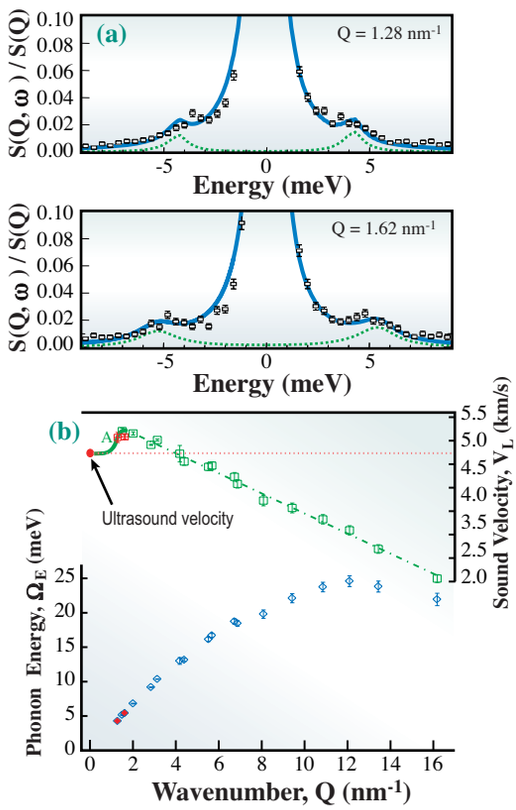

Fig. 3. **(a)** IXS spectra at very low Q values and **(b)** phonon-dispersion curve obtained from the IXS data for a $Pd_{42.5}Ni_{7.5}Cu_{30}P_{20}$ bulk metallic glass (lower), and comparison of the velocity of longitudinal sound obtained from the IXS data and the US velocities (upper).

obtained a critical point that deviated from the US line by measuring the excitation energy at Q values less than 1.28 nm^{-1}, we would know the typical domain size ξ in Fig. 1(b). Finally, we remark that a higher-energy mode is present in this metallic glass and that it should be further investigated in detail.

Tetsu Ichitsubo [a,*], Eiichiro Matsubara [a], Shinya Hosokawa [b] and Alfred Q.R. Baron [c]

[a] Department of Materials Science and Engineering, Kyoto University
[b] Center for Materials Research using Third-Generation Synchrotron Radiation Facilities, Hiroshima Institute of Technology
[c] SPring-8 / JASRI·RIKEN

*E-mail: tichi@mtl.kyoto-u.ac.jp

References

[1] T. Ichitsubo *et al.*: Phys. Rev. Lett. **95** (2005) 245501.
[2] *T. Ichitsubo, S. Hosokawa, K. Matsuda, E. Matsubara, N. Nishiyama, S. Tsutsui and A.Q.R. Baron: Phys. Rev. B* ***76*** *(2007)140201(R).*
[3] T. Ichitsubo *et al.*: J. Chem. Phys. **125** (2006) 154502.

Lattice Dynamics of the Zn-Mg-Sc Icosahedral Quasicrystal and Its 1/1 Periodic Approximant

The discovery, more than 20 years ago, of a new class of materials named quasicrystals for which atoms are arranged in a long range ordered way but without periodicity has immediately attracted the attention of mathematicians, physicists, chemists and even artists. Indeed the diffraction pattern of quasicrystals present sharp Bragg peaks, as a signature of long range order, but with symmetries, such as 5-fold rotations, incompatible with lattice periodicity (see [1] for an introduction).

The question 'where are the atoms in a quasicrystal?' could be answered only recently thanks to the discovery of the binary i-$Cd_{5.7}Yb$ icosahedral quasicrystal [2]. The quasicrystal structure has been solved using the knowledge gained from the 1/1 periodic approximant and sophisticated high dimensional analysis [3]. The atomic structure of the QC and its approximant is described by the same building block, a large atomic cluster made of 158 atoms and whose successive shell are shown Fig. 1. Clusters are connected along the 2-fold and 3-fold directions and are packed on a body centre cubic lattice in the 1/1 approximant whereas they form a quasiperiodic network in the QC as shown Fig. 1.

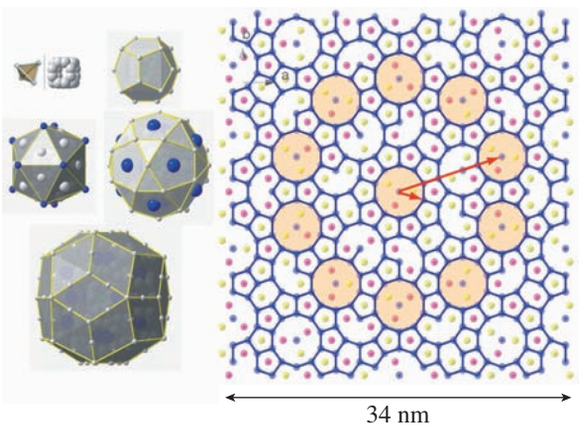

Fig. 1. Atomic structure of the CdYb quasicrystal. The left panel displays the shell decomposition of the atomic cluster. White and blue color stand for Cd and Yb atoms respectively. The cluster network in a large portion of the QC (only cluster centers are displayed) is shown in the right panel.

Understanding the effect of quasiperiodicity on physical properties remains a challenge since most solid state physics results are based on the notion of periodicity and the Bloch theorem. To tackle this problem we have studied the lattice dynamics of the Zn-Mg-Sc icosahedral QC and its 1/1 approximant. This system is isostructural to the CdYb (Zn being equivalent to Cd and Sc to Yb), with thus a detailed understanding of their atomic structure allowing simulation. Moreover the QC and 1/1 approximant allow to study the respective effect of local order (atomic clusters) and long range order (periodic or quasiperiodic) on the lattice dynamics. Within an international collaboration gathering teams from France, Japan, Slovakia, Germany and USA, the response function S(**Q**,ω) has been measured on single grain samples using X-ray (**BL35XU**, SPring-8) and neutron (LLB and ILL) inelastic scattering [4].

From the measured response function, the position, intensity and width of the observed excitation is extracted and reported on the dispersion relation shown Fig. 2 for longitudinal modes, measured on BL35XU. As for other QC, there are well defined acoustic modes in a limited q region, the signal then broaden rapidly. We also observe in both the QC and the approximant well defined dispersion-less excitation located around 6, 8, 16 meV. Besides the similarities, significant differences between the QC and its approximant have been observed. As a general trend, the 'separation' between the acoustic and optic like signal is larger in the approximant than in the QC. In some sense, the long range quasiperiodic order brings in a blurring of the S(**Q**, ω) response function. This can be understood, using the concept of quasi Brillouin zone

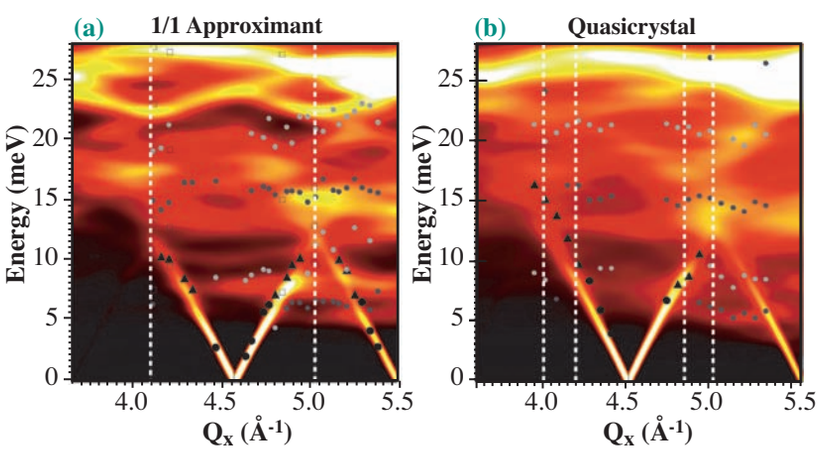

Fig. 2. Longitudinal dispersion relation measured by inelastic X-ray scattering in the approximant and the QC (symbols). The colored coded background stands for the simulation.

boundary in the QC shown as a vertical dashed line.

Those results have been compared to atomic simulations using the known structure and oscillating pair potentials for the Zn-Mg system derived from a data base of *ab initio* calculations. The quasicrystal has been simulated by a large periodic crystal containing about 3000 atoms in a unit cell and whose structure has been derived from the known QC structure. Results of the simulation, superimposed on the experimental data are shown Fig. 2. As can be seen, the simulation reproduces both the similarities and differences of the dispersion relation. The comparison has also been made on a quantitative way, which is a much stronger constraint. A few measured inelastic X-ray spectrums are compared to the simulation on the Fig. 3. The position, width and the relative intensity of the excitations are perfectly reproduced by the simulation, thus validating the model. These results open up the way for a detailed understanding of lattice dynamics of quasicrystal but also to tackle the fascinating question of why they form.

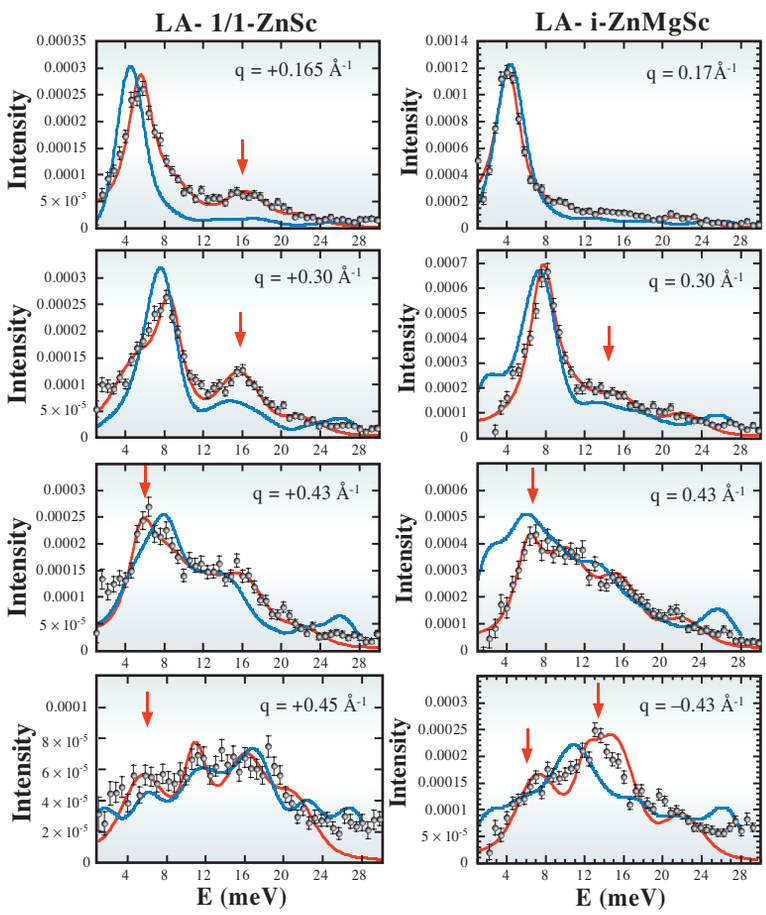

Fig. 3. Series of measured inelastic X-ray spectra in longitudinal geometry in the 1/1 approximant (left) and quasicrystal (right). The distance q from the Bragg peak or zone center is indicated in insert. The dots are for the measurements and the red line for the fit. The blue line is the simulation.

Marc de Boissieu

Sciences et Ingénierie des Matériaux et Procédés, CNRS, Grenoble-INP, UJF, France

E-mail: Marc.de-Boissieu@simap.inpg.fr

References

[1] T. Janssen *et al.*: Aperiodic Crystals. From modulated phases to quasicrystals. Oxford University Press, 2007.
[2] A.P. Tsai *et al.*: Nature **408** (2000) 537.
[3] H. Takakura *et al.*: Nat. Materials **6** (2007) 58.
[4] *M. de Boissieu, S. Francoual, M. Mihalkovic, K. Shibata, A.Q.R. Baron, Y. Sidis, T. Ishimasa, D. Wu, T. Lograsso, L.P. Regnault, F. Gähler, S. Tsutsui, B. Hennion, P. Bastie, T.J. Sato, H. Takakura, R. Currat and A.P. Tsai: Nat. Materials* ***6*** *(2007) 977.*

Isotope Effect in Li_xZrNCl Superconductors

Layer-structured β-ZrNCl is a band insulator and has been found by Yamanaka *et al.* [1] to become a superconductor when electrons are doped through alkali-metal intercalation. The schematic crystal structure of Li-doped ZrNCl is displayed in Fig. 1(a). Recent band calculations have predicted that the doped electrons are accommodated into double-honeycomb ZrN layers and form a rather simple, two-dimensional electronic state. The highest values of the superconducting transition temperature T_c reported thus far are 15.2 K and 25.5 K for the Zr-based material and its Hf analogue, respectively. The specific heat measurement of a $Li_{0.12}ZrNCl$ sample clearly showed [2] that the density of states at the Fermi level and the electron-phonon coupling constant are both very small for the T_c value (=12.7 K). Another interesting feature of this system is that the T_c value increases as the doping concentration is reduced and the band insulator is approached, takes the maximum value of 15.2 K at x = 0.06, and the system suddenly becomes an insulator at x = 0.05. On the basis of these experimental observations, it has been proposed that bosonic fluctuations other than phonon may also contribute to the pairing interaction among the electrons.

It is generally recognized that the measurement of the isotope effect on T_c (namely, the dependence of T_c on the phonon frequency) is very useful for clarifying the role played by the phonon in the pairing interaction. The purpose of the present research is to clarify the isotope effect in the Li_xZrNCl system to address the possible contribution of bosonic fluctuations other than phonon.

The N isotope effect on T_c has already been measured by Tou *et al.* [4] for the $Li_x(THF)_yHfNCl$ system, which is very similar to the present Zr-based system, and was found to be very small [4]. However, the number of samples studied is not very large, and it might be the case that the difference in T_c was small by chance. Therefore, we have prepared a large number of Li_xZrNCl samples containing ^{14}N and ^{15}N isotopes, and have investigated the N isotope effect on T_c in this system [5]. Since the intercalation compounds generally have a strong tendency towards phase separation, all the samples used in this study were carefully examined by X-ray diffraction at beamline **BL02B2**, and were confirmed to consist of a single phase. The deduced lattice constants (*a* and *c*) are plotted in Figs. 1(b) and 1(c), respectively, as a function of Li concentration *x*, which was determined by ICP analysis. We also plotted the data for previously reported ^{14}N compounds, in which undoped ZrNCl powders were prepared by a two-steps procedure as opposed to the one-step process adopted in this study. Clearly, all the ^{14}N and ^{15}N samples show very similar lattice constants, which are also in excellent accord with the previous results. This result indicates that the prepared samples are structurally almost identical to each other and should be investigated in terms of phonon frequencies and T_c in more detail. High-resolution experiments using synchrotron radiation were crucial for obtaining such systematics in the lattice parameter of Li-intercalated ZrNCl.

In Fig. 2, we show the Raman scattering spectra of $Li_{0.18}Zr^{14}NCl$ and $Li_{0.18}Zr^{15}NCl$ at room temperature. Five phonon lines (A-E) are clearly observed in this frequency range. Phonons A and B are ascribed to the normal modes, in which all the Zr, N and Cl atoms have similar vibration amplitudes according to a recent lattice dynamics calculation. Phonon C is mainly due to the motion of Zr along the *c*-axis, whereas higher frequency phonons D and E are basically vibration modes of N. The frequencies of phonons A, B, and C show little change whereas phonons D and E exhibit considerable softening upon ^{15}N substitution for ^{14}N. The shift of frequency is as large as 19 and 20 cm^{-1} for phonons D and E, respectively, as shown in the inset of Fig. 2. The shifts amount to 3.3% of the

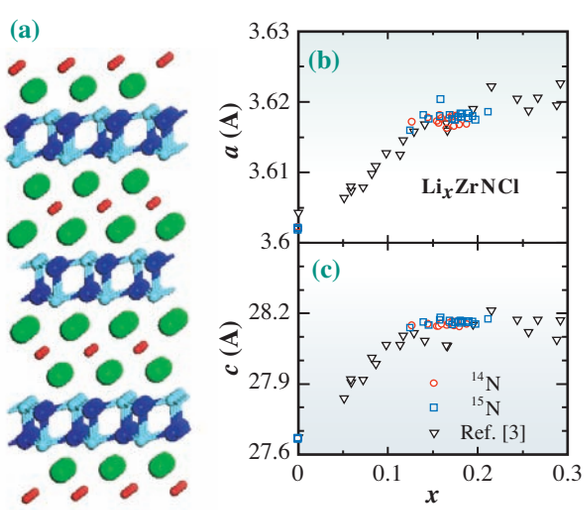

Fig.1. **(a)** The crystal structure of Li_xZrNCl is schematically shown. Red, light blue, blue, and green spheres represent Li, Zr, N, and Cl atoms, respectively. **(b)** *a*-axis and **(c)** *c*-axis lattice constants deduced from the diffraction measurements at BL02B2 are plotted as a function of *x*.

frequency, which is very close to, but certainly smaller than 3.5%, which is expected when the modes are completely due to N vibration.

In Fig. 3, we show a magnified view of the temperature variation of the magnetization near T_c for three representative samples of ^{14}N and ^{15}N. Although the difference between ^{14}N and ^{15}N samples is very small, it is clear that ^{15}N samples have a lower T_c than ^{14}N samples in accord with expectations. For a more quantitative discussion on the isotope effect on T_c , we obtained the T_c values of all the samples indicated in Fig. 3, and plotted them as a function of x in the inset of Fig. 3. The arrow in the inset indicates the expected change in T_c if the relative change in T_c were equal to the relative change in the phonon frequency of the N vibration mode. Clearly, the experimentally observed change is much smaller than the expected change. The solid line and dashed line correspond to two different fits to the data, and the relative change in T_c is estimated to be –(0.5±0.3)%. If we calculate the isotope shift coefficient α ($T_c \propto M^{-\alpha}$) for N, we have α = 0.07±0.04 as an upper limit. This value is in excellent accord with the value reported for the Hf system by Tou *et al.* [4].

Our experimental observation that the shift of T_c is much smaller than that of the phonon frequency strongly indicates that T_c in this system is not dominated by the phonon alone, but that bosonic fluctuations other than phonon also contribute to the pairing interaction in this class of layered superconductors.

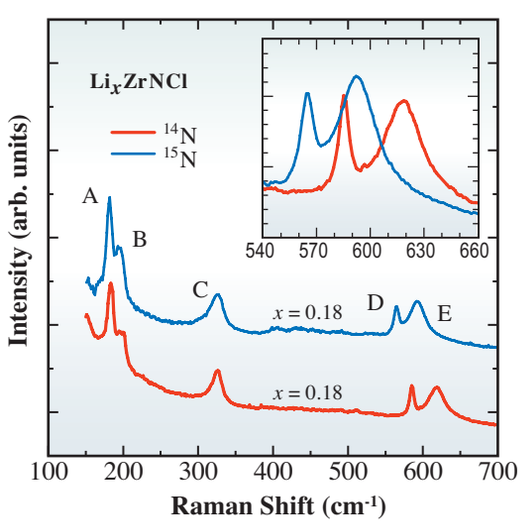

Fig. 2. Raman scattering spectra of $Li_{0.18}Zr^{14}NCl$ and $Li_{0.18}Zr^{15}NCl$ compounds at room temperature. The inset shows a magnified view of the N vibration modes.

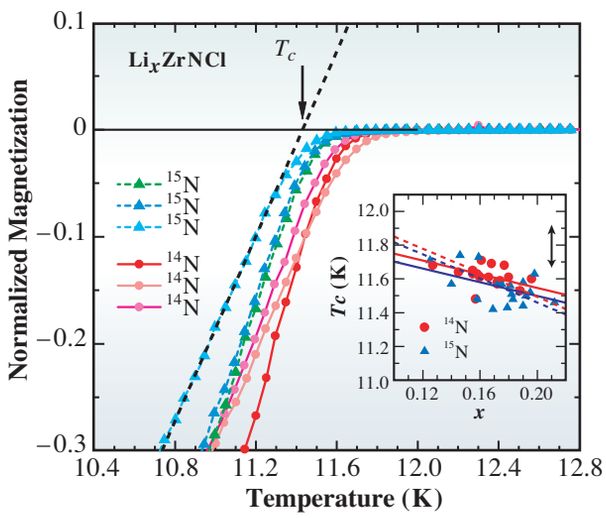

Fig. 3. Temperature dependence of normalized magnetization near T_c for representative ^{14}N and ^{15}N samples. The inset shows the doping dependence of T_c for both isotope samples. The solid line and dashed line represent linear fits to the data based on two different analyses. The solid arrow corresponds to the expected change in T_c if the relative change in T_c were equal to that in the frequency of the N vibration mode.

Y. Taguchi [†,*] and Y. Iwasa

Institute for Materials Research, Tohoku University

*E-mail: y-taguchi@riken.jp

[†] Present address: Cross-correlated Materials Research Group, RIKEN, Wako

Reference

[1] S. Yamanaka *et al.*: Adv. Mater. **8** (1996) 771.
[2] Y. Taguchi *et al.*: Phys. Rev. Lett. **94** (2005) 21700.
[3] Y. Taguchi *et al.*: Phys. Rev. Lett. **97** (2006) 107001.
[4] H. Tou *et al.*: Phys. Rev. B **67** (2003) 100509(R).
[5] *Y. Taguchi, T. Kawabata, T. Takano, A. Kitora, K. Kato, M. Takata and Y. Iwasa: Phys. Rev. B* ***76*** *(2007) 064508.*

Phonon Softening in Superconducting Diamond

Superconductivity in highly boron doped diamond has been reported in 2004 [1]. Pure diamond is an insulator with a large band-gap of 5.5 eV. It is a clear, colourless material of extreme hardness, which makes it attractive for jewellery after sophisticated polishing. At low doping, boron forms an acceptor level of 370 meV binding energy, thus the material becomes a hole-doped semiconductor. This electronic level is also responsible for the colour of the famous blue diamond. At very high doping above the metal-to-insulator transition (MIT), at a doping level $n \approx 3 \times 10^{20}$ cm^{-3}, B-doped diamond becomes metallic. The colour changes to a dull grey, but the metallic state makes it interesting for scientific research. Superconductivity was reported above $n \approx 1 \times 10^{21}$ cm^{-3}. The transition temperature T_c depends on the doping level and on the growth conditions. The highest T_c reported so far is a CVD grown sample with a doping of $n = 8.4 \times 10^{21}$ cm^{-3} and an onset of superconductivity at 11.4 K [2].

To understand this rather high superconducting transition temperature at quite low carrier concentrations of less than 0.05 holes per atom two questions have to be addressed: (i) What is the nature of the metallic carriers in B-doped diamond? (ii) How do the holes couple to form Cooper pairs, the key ingredient of the superconducting state? Question (i) has been addressed by optical spectroscopy and by electron spectroscopy [3]. To address question (ii) the coupling of the metallic holes to the lattice vibrations (phonons) of diamond was investigated in this work. This interaction can then account for the coupling in between the holes that is needed to form the superconducting charge carriers.

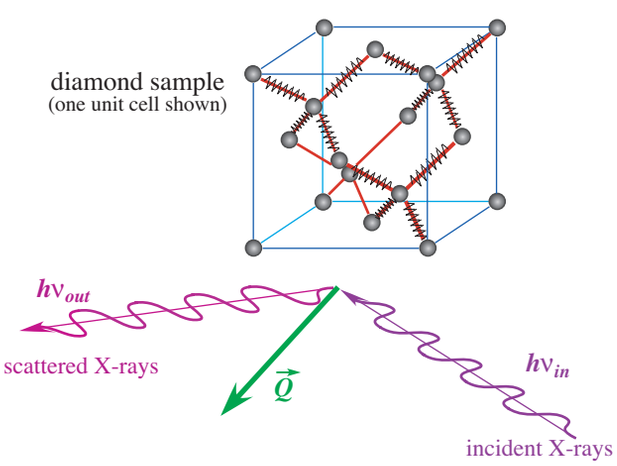

Fig. 1. Schematic view of an IXS experiment. X-rays are scattered with a given momentum transfer Q and excite lattice vibrations in the sample that lead to an energy loss of the X-ray photons.

The hole-hole coupling must be rather strong in the B-doped diamond to lead to such high T_c.

In our experiment we studied the coupling of the metallic charge carriers to the lattice vibrations through the measurement of the dispersion of the phonons. The lattice vibrations are excited when an X-ray photon is scattered in the crystal and looses a small portion of its photon energy according to the frequency of the phonon (see Fig. 1). Measurements at various momentum transfers allow one to trace the dispersion, i.e, the momentum dependence of the phonon frequencies. In diamond, both steeply dispersing acoustic and weakly dispersing optical phonons are present. The frequency of the optical phonon is extremely high (164 meV at the Brillouin zone centre for pure diamond), which reflects the hardness of the material due to the strong short bonds. The experiment was performed at the inelastic X-ray scattering spectrometer (IXS) at beamline **BL35XU**. All measurements were performed at room temperature.

It is difficult to make samples of highly boron doped diamond. In particular single crystals cannot be grown by any standard techniques. In this experiment two samples grown by microwave assisted chemical vapour deposition (CVD) were used. A growth time of over 100 hours leads to a thickness of around 100 μm. The diamond was deposited on a specially prepared silicon substrate with a SiC buffer layer that provides a high degree of epitaxial orientation of the diamond grains. The silicon was etched away to expose only a free-standing diamond layer to the X-ray beam. The samples are shown in Fig. 2(b). A sample of superconducting diamond was grown with a boron concentration of $n = 4.8 \times 10^{21}$ cm^{-3}. It exhibits superconductivity with an onset at 6.4 K as shown in Fig. 2(c). A second sample of nitrogen doped diamond served as a reference for the insulating state and was found to be equivalent to pure diamond for all practical purposes of this experiment. Rocking curves of X-ray diffraction are shown in Fig. 2(d). At a width of around 1° (FWHM) the crystallite orientation is good enough to allow for a well-defined momentum transfer in the experiment.

The presence of metallic charge carriers changes the lattice dynamics and the electron-phonon coupling can shift the phonon frequencies to lower values (softening). The measured dispersion of the phonons along two high symmetry directions of the crystal lattice is shown in Fig. 3. The acoustic phonons show no difference between B-doped metallic diamond and

N-doped insulating diamond. Their dispersion is in good agreement with the well-known results for pure diamond. The optical phonons on the other hand show a strong softening as B-doping is introduced. Close to the zone boundary (X-point and L-point) the softening is constant at about 2 meV over a certain momentum range. Close to the zone centre it becomes stronger with an extrapolated value of ~8 meV at the Γ-point. The softening-curve, i.e. the momentum dependent peak shift between N-doped and B-doped diamond is shown in the top part of Fig. 3.

The observation of strong softening is a clear indication of electron-phonon coupling in diamond. Theoretical predictions (e.g. Ref. [4]) have related this coupling to the superconductivity and found that it can account for the observed transition temperatures. The increased softening close to the zone centre is compatible with the existence of a "spheroid" Fermi surface of the metallic holes as observed in Ref. [3]. For phonon momenta smaller than the diameter of this Fermi surface the coupling is stronger because momentum conserving electronic excitations are possible. For larger momenta the phase space of coupling is reduced and a smaller and constant coupling results.

This result shows that electron-phonon coupling is a good candidate to explain the formation of superconducting hole-hole pairs in a BCS theory.

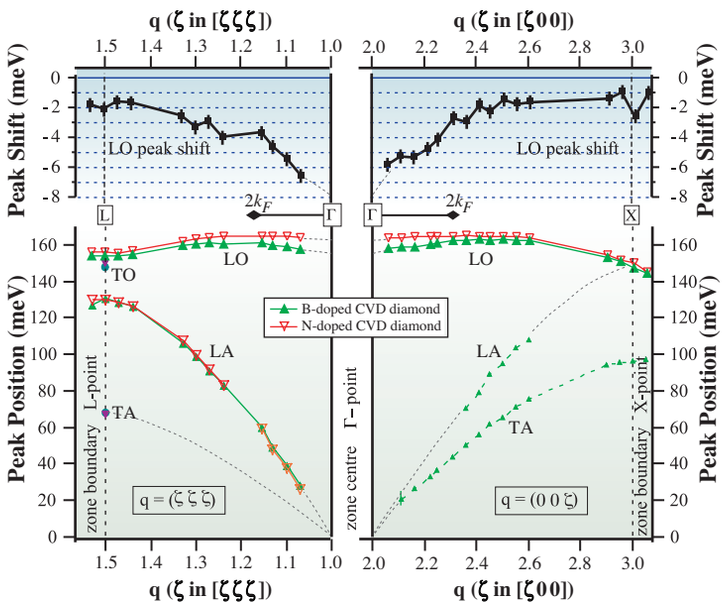

Fig. 3. Measured phonon dispersion in N-doped (open triangles) and B-doped (closed triangles) diamond in two different high-symmetry directions of the diamond lattice. The top part shows the difference of the dispersions of the optical phonons, i.e. the momentum dependent softening. The maximum spanning of the Fermi surface is marked as $2k_F$. It coincides with the range of strong softening. The acoustic phonons are not softened.

Based on the softening, a quantitative estimate of the electron-phonon coupling strength is possible. The extremely high frequency of the optical modes in diamond provides the strong coupling that is needed to form a superconducting state at low carrier concentrations but with remarkably high transition temperatures.

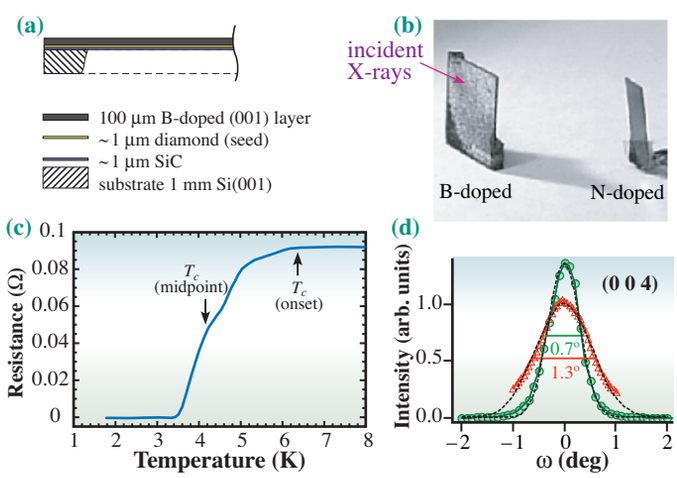

Fig. 2. Samples of CVD grown diamond. **(a)** Schematic view of the B-doped sample. **(b)** Photograph of both the B-doped and the N-doped sample. **(c)** Electrical resistance *vs.* temperature in the region of the superconducting transition in the B-doped sample. **(d)** Rocking curves of X-ray diffraction for the B-doped sample (circles) and the N-doped sample (triangles). The widths of the rocking curves (FWHM) are indicated.

Moritz Hoesch †,* and Tatsuo Fukuda

SPring-8 / JAEA

*E-mail: moritz.hoesch@esrf.fr

† Present address: ESRF, France

References

[1] E.A. Ekimov *et al.*: Nature **428** (2004) 542.
[2] H. Umezawa *et al.*: cond-mat/0503303
[3] T. Yokoya *et al.*: Nature **438** (2005) 647, see also report by T. Yokoya in the 2005 edition of SPring-8 Research Frontiers.
[4] L. Boeri, J. Kortus, O.K. Andersen, Phys. Rev. Lett. **93** (2004) 237002.
[5] *M. Hoesch, T. Fukuda, J. Mizuki, T. Takenouchi, H. Kawarada, J.P. Sutter, S. Tsutsui, A.Q.R. Baron, M. Nagao and Y. Takano: Phys. Rev. B* ***75*** *(2007) 140508(R).*

Charge Density Study of Transparent *p*-type Semiconductor (LaO)CuS

The application of transparent materials into electrically industrial materials had been limited to just electrodes for a long time because wide-gap semiconductors as transparent materials have strong monopolarity. Indeed, almost all transparent conductive oxides such as SnO_2 and In_2O_3 are *n*-type; thus, the lack of transparent *p*-type semiconductors has hindered the realization of transparent *p*-*n* junctions. Recently several *p*-type semiconductors such as $CuAlO_2$ and $SrCu_2O_2$ have been discovered, and considerable effort has been devoted to the fabrication of transparent devices such as a transparent light-emitting device. The further exploration of new *p*-type materials is still in progress.

The rare earth oxysulfide (LaO)CuS is also a transparent *p*-type semiconductor with a band gap of 3.1 eV. This material has various attractive functionalities, for example, it exhibits good luminescent properties in terms of photoluminescence [1,2] and room temperature ferromagnetism when La and Cu are simultaneously replaced by Ca and Ni, respectively [3]. More functionalities are expected to be added to (LaO)CuS by substitution. It is necessary to understand the chemical bonding and the ionic state of (LaO)CuS. Therefore, we have performed a charge density study with synchrotron radiation powder diffraction at beamline **BL02B2** using a large Debye-Scherrer camera equipped with an imaging plate as a highly sensitive X-ray detector [4].

Figure 1 shows the crystal structure of (LaO)CuS with the space group of *P*4/nmm [5]. The salient feature of this structure is that a Cu atom is surrounded tetrahedrally by four S atoms, as shown in Fig. 1(a). Figure 1(b) is the view from the *a*-axis which includes total eight unit cells. Zigzag layers of CuS and LaO are stacked alternately along the *c*-axis alternately and this semiconductor is considered having layered structure. Figure 2 shows the raw data obtained from the large Debye-Scherrer camera, the diffraction profile using a high energy X-ray with an incident wavelength of 0.4969 Å, and the fitting result obtained by Rietveld analysis. Uniform Debye-Scherrer rings are found in the data and this reveals that the data are sufficient reliable for the analysis, for the data up to 70° (d > 0.4332 Å) were used. The calculated result with reliability factors of 4.73 % in R_{wp} and 1.35 % in R_F is in good agreement with the experimental result up to higher 2θ range. The lattice constants obtained by this analysis were 3.99425 Å and 8.51046 Å for the *a* axis and *c* axis, respectively. The charge density distributions of (LaO)CuS were analyzed by the maximum entropy method (MEM)/Rietveld method to obtain information on the bonding nature. Figure 3 shows a three-dimensional view of the charge density distribution at the equi-density level of 0.4 e/Å^3. Contour lines are also added to the cross-sectional view, where the lines are drawn at intervals of 0.1 e/Å^3 from 0.4 to 0.7 e/Å^3 and the black color indicates the region with higher density region than 1.0 e/Å^3. A finite electron density is found between the Cu and S atoms and between the La and O atoms. Consequently, covalent characteristics are found in both the Cu-S bond and the La-O bond, even though the full-potential linear-augmented plane wave band calculation predicted that the Cu-S bond has a covalent character, whereas the La-O bond was ionic [6]. For the interlayer space between the CuS layer and the LaO layer, there is no marked charge density. This is the first evidence showing that this transparent semiconductor has a layered structure. The electron number is counted in the region surrounded by the minimum charge-density surfaces adopting the Mulliken scheme. The electron numbers for La, O, Cu, and S are 55.6, 9.3, 29.3, and 15.8, respectively. The ionic state is defined by subtracting the electron number from the atomic number. The results are +1.4 for ^{58}La, -1.3 for ^{2}O, -0.3 for ^{29}Cu, and +0.2 for ^{16}S. According to these values, the charges of the CuS layer and the LaO layer are electrically almost neutral. Furthermore, the Cu-S chemical bonding is perfectly covalent, whereas the La-O bonding has both ionic and covalent characteristics. These distinctive features such as the charge neutrality of each layer and the covalent

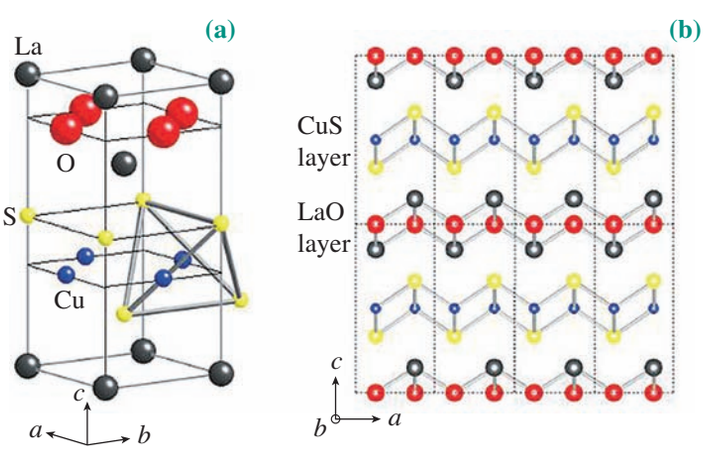

Fig. 1. Crystal structure of (LaO)CuS. Unit cell **(a)** and the view from *a*-axis **(b)**.

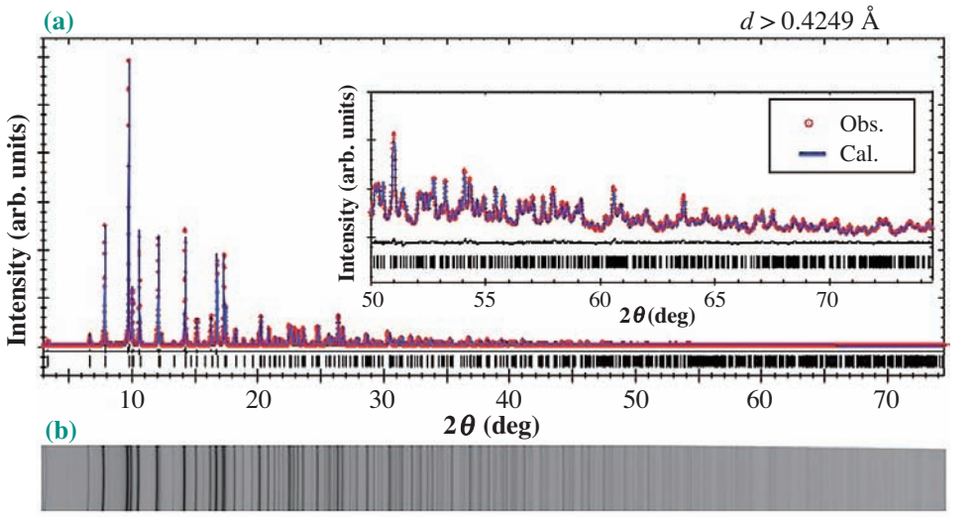

Fig. 2. **(a)** Powder diffraction profile and **(b)** raw data. The dots are experimental results and the solid line is the pattern fitted by the Rietveld method with reliability factors 4.73 % in R_{wp} and 1.35 % in R_F.

character of the La-O bond may provide fascinating functionalities.

In summary, we have studied the charge density distributions of the transparent *p*-type semiconductor (LaO)CuS using synchrotron powder diffraction, whose data were analyzed by the MEM/Rietveld method. The Cu-S bonding was found to have a strong covalent character and the La-O bonding seems to have both covalent and ionic characteristics. The estimated ionic states of each element suggest that each layer has charge neutrality. The charge density distribution provides direct evidence of the layered structure.

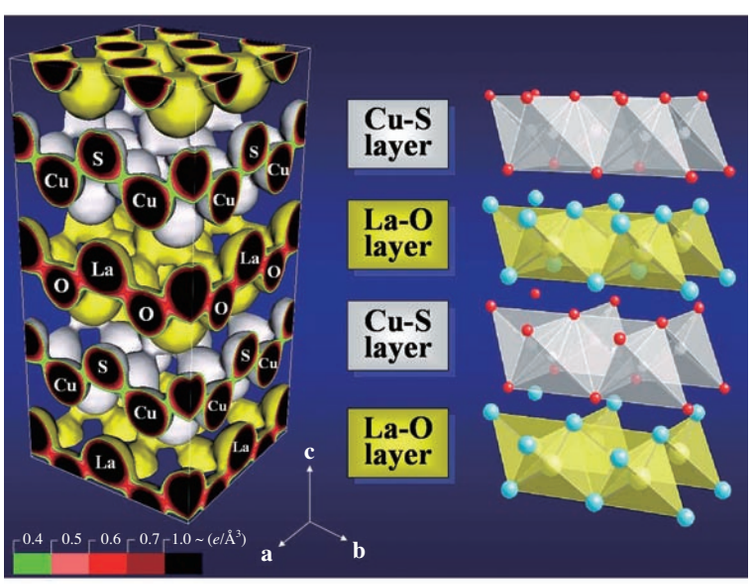

Fig. 3. Three-dimensional view of charge density distributions of (LaO)CuS at 0.4 e/Å^3 equi-density surface accompanying by contour lines, drawn from 0.4 to 0.7 e/Å^3 with an interval of 0.1 e/Å^3.

Kouichi Takase [a,*] and Yoshihiro Kuroiwa [b]

[a] Department of Physics, Nihon University
[b] Department of Physical Science, Hiroshima University

*E-mail: takase@shotgun.phys.cst.nihon-u.ac.jp

References

[1] K. Takase *et al.*: Solid State Comm. **123** (2002) 531.
[2] K. Ueda *et al.*: Appl. Phys. Lett. **77** (2000) 2701.
[3] K. Takase *et al.*: Physica B **329-333** (2003) 961.
[4] *K. Takase, K. Sato, O. Shoji, Y. Takahashi, Y. Takano, K. Sekizawa, Y. Kuroiwa and M. Goto: Appl. Phys. Lett.* ***90*** *(2007) 161916.*
[5] M. Palazzi: C. R. Acad. Sci., Paris **292** (1981) 789.
[6] S. Inoue *et al.*: Phys. Rev. B **64** (2001) 245211.

Perpendicular Magnetization of 1-nm-Thick Epitaxial FePt Films Probed by Soft X-ray Magnetic Circular Dichroism

Perpendicular magnetization makes it possible to magnetize a much smaller area of a magnetic film than in-plane magnetization. This is why perpendicular magnetization has become an essential technology for hard disks, storage capacity of which is growing rapidly. It might also be applicable to spintronic devices, which are a new technology of data processing using the spin of electrons. Epitaxial FePt film with the $L1_0$ crystal structure, which is characterized by alternately stacked of Fe and Pt monatomic-layer sheets, shows stable perpendicular magnetization. Epitaxial FePt film is therefore attracting much attention from the viewpoint of its applications. For such applications, it is crucial to determine how thin the magnetic layer can be made while maintaining perpendicular magnetization at room temperature. Since ferromagnetism is a collective phenomenon, it could be weakened when the thickness is reduced, leading to lower Curie temperatures and possibly to the disappearance of perpendicular magnetization even in the ferromagnetic phase. The verification of such hypotheses is important from the viewpoints of both applications and fundamental research.

In order to determine the thinnest limit for epitaxial FePt films to have perpendicular magnetization, ultrathin films of FePt sandwiched by Pt, as shown in Fig. 1, were fabricated by the alternate monatomic layer (ML) deposition of Fe and Pt [1]. When the thickness of the magnetic layer is a few ML, it is extremely difficult to measure magnetization precisely by conventional techniques such as SQUID because of a large magnetic background due to the substrate. Therefore, we utilized the soft X-ray magnetic circular dichroism [2] of Fe 2*p*→3*d* photoabsorption (Fe 2*p*→3*d* XMCD), which can yield an accurate Fe 3*d* magnetic moment even for Fe coverage of below 1 ML.

Fe 2*p*→3*d* XMCD was measured at beamline **BL25SU** by the total electron yield method in the Faraday configuration, in which the soft X-ray is incident parallel to the magnetic field applied to the sample. The magnetic field was applied perpendicularly to the sample films. The XMCD spectrum was measured by switching the photon spin of the incident light between +1 and –1. The magnetic moments due to spin and orbital angular momenta, μ_{spin} and $\mu_{orbital}$ were estimated by applying the XMCD sum rules to the observed XMCD spectrum.

In Fig. 2 is shown the temperature and thickness dependence of the perpendicular Fe 3*d* magnetic moment [3] in Pt/(Fe 1ML/Pt 1ML)$_n$/Pt(100) under a magnetic field of 1.4 T (a) and under remanent magnetization (b). In the latter, samples were first subjected to a magnetic field of 1.4 T and were then measured without a magnetic field. The drastic decrease from n = 2 to 1 of the moment at room temperature (RT) under 1.4 T (see Fig. 2(a)) might suggest that the Curie temperature T_C is above RT for n ≥ 2 and below RT for n=1. On the other hand, the perpendicular remanent magnetization at RT reaches zero when n = 2. Let us define the temperature at which the perpendicular remanent magnetization drastically increases as T_{rem}. T_{rem} is between 250 K and 300 K for n=2 and T_{rem} ~ 160 K for n=1. These results, characterized by the decrease in both T_C and T_{rem} with the reduction of thickness n, agrees well with the expectation that ferromagnetism should be weakened as the thickness is reduced.

A possible mechanism for the absence of remanent magnetization between T_{rem} and T_C is the formation of stripe domains characteristic of perpendicular magnetization. However, one cannot exclude other possibilities such as the spin reorientation transition to in-plane magnetization. In order to clarify the actual mechanism, it will be

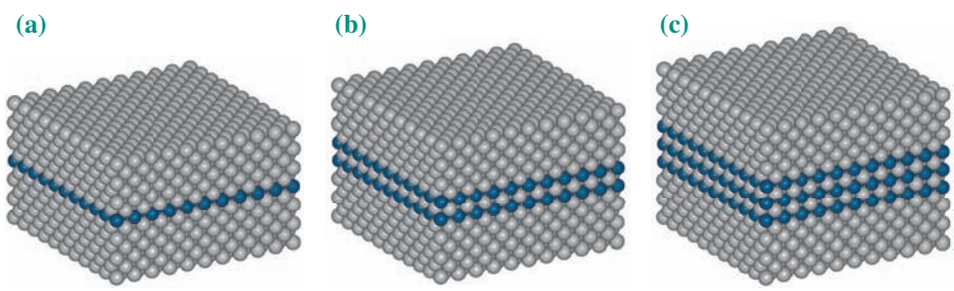

Fig. 1. Schematic view of ultrathin FePt films sandwiched by Pt, where gray and blue spheres represent Pt and Fe atoms, respectively, for Pt/(Fe 1ML/Pt 1ML)$_n$/Pt(100) with n=1 **(a)**, n=2 **(b)**, and n=3 **(c)**.

necessary to investigate magnetic domain structures by methods such as XMCD microscopy.

The magnetic hysteresis loop of Pt/Fe 1ML/Pt (001), i.e. only one atomic layer of Fe sandwiched by Pt, was successfully observed with satisfactory precision, as shown in Fig. 3. This demonstrates the usefulness of XMCD for the study of potentially applicable magnetic ultrathin films. It was observed that the perpendicular remanent magnetization is as large as about 80% of the saturated value and that the coercivity is about 0.1 T at 25 K.

In summary, Pt/(Fe 1ML/Pt 1ML)$_3$ /Pt (001) was found to exhibit perpendicular remanent magnetization at room temperature, which is expected to enable the development of applications in the field of magnetic storage and spintronics. Samples with a thinner FePt layer exhibited perpendicular remanent magnetization at lower temperatures. The thickness dependence of perpendicular magnetization can be attributed to the decreasing in T_C with reduced thickness because ferromagnetism is thought to be weakened due to the crossover from three dimensions to two dimensions.

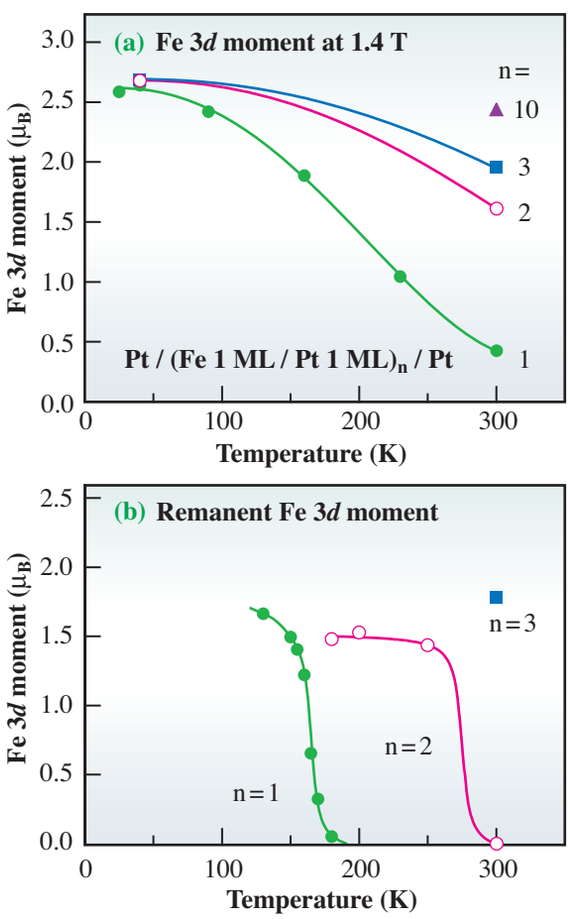

Fig. 2. Temperature and thickness dependence of the perpendicular Fe 3*d* magnetic moment per atom in Pt/(Fe 1ML/Pt 1ML)$_n$ /Pt(100) under a magnetic field of 1.4 T **(a)** and under remanent magnetization **(b)**. The markers represent measured values and the solid lines are guides for the eyes.

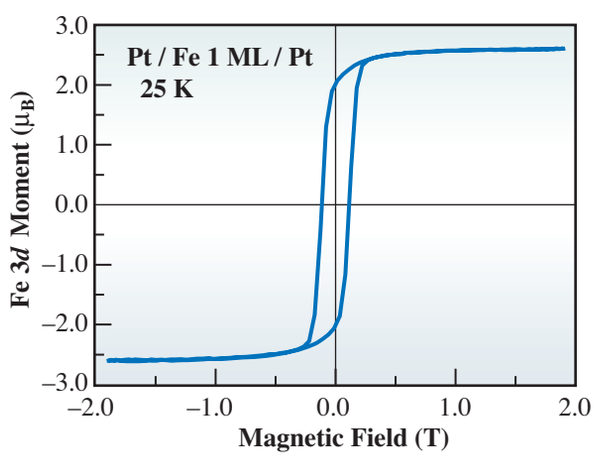

Fig. 3. Magnetization hysteresis loop of Pt/Fe 1 ML/Pt(001) at 25 K obtained by magnetic field dependence of the XMCD intensity.

Shin Imada †

Graduate School of Engineering Science, Osaka University

E-mail: imada@se.ritsumei.ac.jp

† Present address: College of Science and Engineering, Ritsumeikan University

References

[1] T. Shima *et al.*: Appl. Phys. Lett. **80** (2002) 288.
[2] S. Imada *et al.*: Phys. Rev. B **59** (1999) 8752.
[3] *S. Imada, A. Yamasaki, S. Suga, T. Shima and K. Takanashi: Appl. Phys. Lett.* ***90*** *(2007) 13250.*

Infrared Study of the Valence Transition Compound $YbInCu_4$ using Cleaved Surfaces

The physical properties of intermetallic compounds containing rare earth elements, most typically Ce or Yb, are often strongly influenced by the electrons in the 4*f* orbital of the rare earth elements. At high temperatures of the order of room temperature, the *f* electrons are basically localized at the rare earth atom, since the wave function of the 4*f* orbital is strongly confined in the inner portion of the atom. However, at low temperatures of the order of ~10 K or lower, the *f* electrons may become itinerant (delocalized) through hybridization with the conduction electrons. The resulting hybridization state generally has a much larger effective mass m^* than the rest electron mass due to a strong Coulomb interaction acting on the *f* electrons. For many such "heavy fermion" compounds, the crossover from the localized to the itinerant characteristics of *f* electrons occurs gradually and continuously as the temperature is lowered. $YbInCu_4$, however, shows a first order phase transition at T_v ~ 42 K, where a sudden change in the Yb valence is observed from ~3 above T_v to ~2.9 below T_v. Many physical properties such as the lattice constant, electrical resistivity and magnetic susceptibility also show sudden changes at T_v. $YbInCu_4$ has attracted a great deal of attention for showing such a first-order transition between localized and itinerant regimes, since most other heavy fermion compounds show only a gradual crossover as mentioned above.

We carried out an infrared (IR) reflectivity study of $YbInCu_4$ to probe the changes in the microscopic electronic structure associated with this transition [1]. Hancock *et al.* [2] previously reported a detailed IR reflectivity study on $YbInCu_4$ using mechanically polished samples. They clearly observed large spectral changes between the reflectivity spectra [$R(\omega)$] below and above T_v. Below T_v, the optical conductivity obtained from $R(\omega)$ showed a pronounced mid-infrared peak, which was attributed to optical excitation within the hybridization state of the *f* electrons [2]. However, the data showed a gradual evolution of the optical spectra with temperature, in contrast to the result expected for a first-order phase transition. There have also been interesting photoemission results [3] reported on $YbInCu_4$, which showed that the electronic structures and the valence in this compound are extremely sensitive to surface conditions. Motivated by these developments, we used *cleaved* samples to measure $R(\omega)$ of $YbInCu_4$. Since $YbInCu_4$ does not yield a large flat surface by cleaving, we needed to measure the $R(\omega)$ on small specular surfaces on cleaved (fractured) pieces of $YbInCu_4$. The typical dimensions of the specular surfaces were 0.1–0.5 mm. We carried out the measurement at the IR beamline **BL43IR**. Owing to the high brilliance of the IR synchrotron radiation from SPring-8 and using an IR microscope available at BL43IR, a spot size of ~15 μm was obtained at the sample position. This allowed us to measure the $R(\omega)$ of the cleaved surfaces very easily.

Figure 1 shows the measured $R(\omega)$ spectra of both cleaved and polished surfaces of $YbInCu_4$ single crystals taken from the same batch. The $R(\omega)$spectra and their temperature evolutions are qualitatively similar for both cases. However, the cleaved sample data show larger spectral changes between below and above 50 K. In addition, the magnitude of $R(\omega)$ is much lower for the cleaved sample than for the polished one. Figure 2 shows the detailed evolution of $R(\omega)$, integrated over 0.2–0.5 eV, as a function of temperature. For the polished sample, a gradual temperature change is seen, in agreement with a

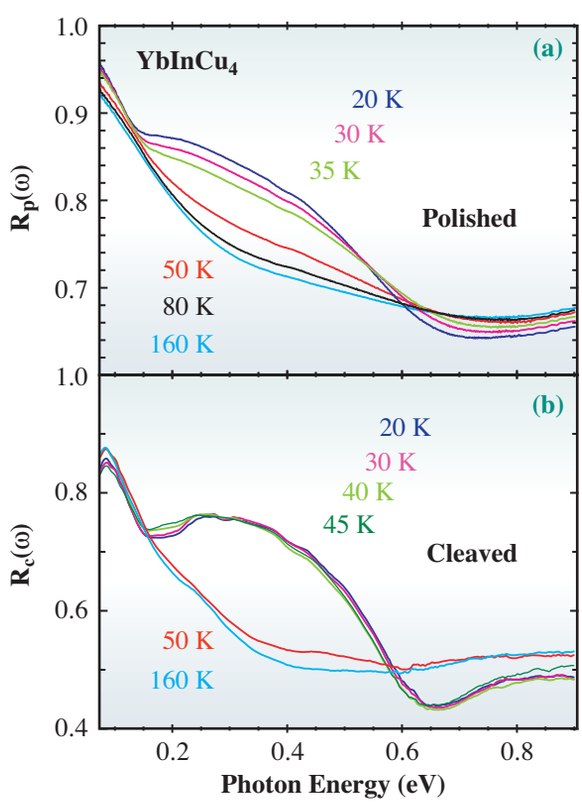

Fig. 1. Temperature dependence of reflectivity spectra $R(\omega)$ for **(a)** polished and **(b)** cleaved $YbInCu_4$.

previous report [2]. However, the cleaved sample data undergoes a sudden change at ~45 K, during which the change in $R(\omega)$ occurs within a temperature range of about 2 K. In addition, a hysteresis of about 1 K was observed between the cooling and warming data (not shown here). These results for the cleaved surfaces are consistent with the sudden changes observed for other physical properties at T_v. They also demonstrate that the microscopic electronic structure indeed undergoes a first-order transition in this compound. The gradual temperature evolution observed for the polished sample is probably due to the compositional and/or site disorder, since it was previously reported that the transition temperature in this compound is very sensitive to even a small deviation from the ideal 114 composition, and to a site disorder between the In and Yb sites.

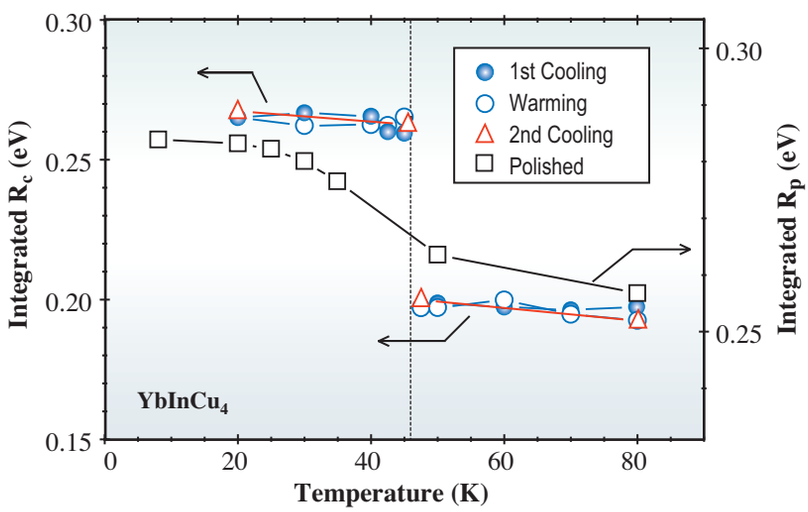

Fig. 2. Detailed temperature dependences of the reflectivity for cleaved and polished samples. The polished sample shows a much more gradual evolution with changing temperature than the cleaved sample.

Hidekazu Okamura

Graduate School of Science and Technology,
Kobe University

E-mail: okamura@kobe-u.ac.jp

References

[1] *H. Okamura, T. Watanabe, M. Matsunami, N. Tsujii, T. Ebihara, H. Sugawara, H. Sato, Y. Onuki, Y. Isikakwa, T. Takabatake, T. Nanba: J. Phys. Soc. Jpn.* ***76*** *(2007) 023703.*
[2] J.N. Hancock *et al.*: Phys. Rev. Lett. **92** (2004) 186405; Phys. Rev. Lett. **92** (2004) 186405.
[3] H. Sato *et al.*: Phys. Rev. Lett. **93** (2004) 246404.

Itinerant to Localized Transition of *f*-Electrons in Heavy Fermion Superconductor UPd_2Al_3

Electrons in solids are conventionally classified as either band-like itinerant ones or atomic-like localized ones. However, *f* electrons in heavy Fermion (HF) compounds show both itinerant and localized behaviors depending on the temperature. Above the characteristic temperature T^*, which is typically few K to a few tens K, their magnetic properties are well described by the ionic *f*-electron model, suggesting that they behave as 'localized' *f*-electrons. On the other hand, at temperatures well below T^*, their Fermi surfaces (FSs) are generally well explained by the 'itinerant' *f*-electron model. The temperature dependence of the electronic structure of HF compounds has never been explored, and their precise behaviors and their origin have remained unknown since their discovery 30 years ago. We have experimentally studied the band structure of the HF superconductor UPd_2Al_3 at temperatures well below and above T^* by angle-resolved photoelectron spectroscopy (ARPES) to clarify how the *f*-electrons change their characteristics around T^*. ARPES is one of the most powerful experimental methods for exploring the electronic structure of solids. By performing ARPES experiments in the soft X-ray region (SX-ARPES), bulk-sensitive and 5*f*-dominant band structures and FS's can be obtained [1]. Figure 1 shows the crystal structure of UPd_2Al_3 which exhibits an antiferromagnetic transition at T_N = 14 K and undergoes a transition into the superconducting state at T_C = 2 K. Its FSs at low temperatures were investigated by de Haas-van Alphen experiments [2], and the result was well explained by the itinerant electron model [3]. On the other hand, the magnetic susceptibility follows the Curie-Weiss law above 50–70 K, suggesting the existence of localized magnetic moments at high temperatures [4]. Therefore, the T^* of UPd_2Al_3 is considered to be about 50–70 K. Photoemission experiments were performed at beamline **BL23SU**. The photon energy used was 595 eV, and the total energy resolution was 120 meV.

Figure 2(a) shows the temperature dependence of the SX-ARPES spectra of UPd_2Al_3 measured at 20 K and 100 K, which were considerably lower and higher than T^*. The position of the measurement in the Brillouin zone is also indicated. Although the essential structures of the spectra were very similar at 20 K and 100 K, noticeable differences between them were clearly observed. Between 20 K to 100 K, the peak structure located around the Fermi level (E_F) shows strong temperature dependence. Changes in the

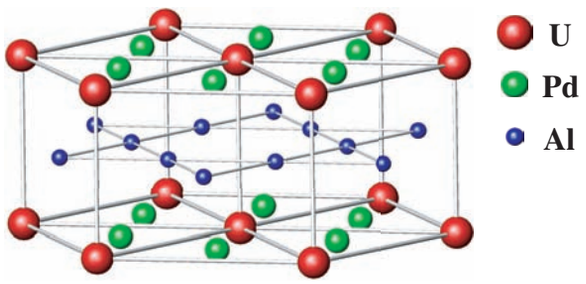

Fig. 1. Crystal structure of UPd_2Al_3.

spectral functions were also observed at the higher-binding-energy sides. However, the changes is E_B>1.5 eV are mainly changes in the peak intensity, and their positions are not changed. This suggests that they are not intrinsic changes of the electronic structures. We also measured the temperature dependence of the ARPES spectra of UNi_2Al_3, whose characteristic temperature is higher than 300 K. Figure 2(b) shows the comparison of the APRES spectra of UNi_2Al_3 measured at 20 K and 100 K. It is clear that the spectra are not different at these two temperatures. Therefore, the temperature dependence of the ARPES spectra of UPd_2Al_3 at around $E_B = E_F$ - 1.5 eV originates from the changes in the electronic structure of UPd_2Al_3 below and above T^*.

We further analyzed the temperature dependence of these ARPES spectra of UPd_2Al_3. Figure 3 shows the second derivatives of the ARPES spectra of UPd_2Al_3 measured at 20 K and 100 K. Before taking the second derivative, the ARPES spectra were divided by the Fermi-Dirac function convoluted with the Gaussian function to reveal the behaviors of the quasi-particle bands in the vicinity of E_F. In these figures, the bright parts correspond to the peaks in the ARPES spectra. The temperature dependence of quasi-particle bands is well recognized in these figures. At 20 K, the quasi-particle bands below E_F disperse to above E_F, suggesting that they are itinerant electrons. On the other hand, at 100 K, they move toward the higher-binding-energy side, and form less dispersive bands around E_B = 0.1 eV, suggesting that they are localized electrons. These changes imply that the quasi-particle bands of U 5*f* origin at low temperatures, which form the itinerant HF states, are excluded from the FSs at high temperatures. On the other hand, the temperature-induced changes in the deeper binding energy region (E_B < 1 eV) were also

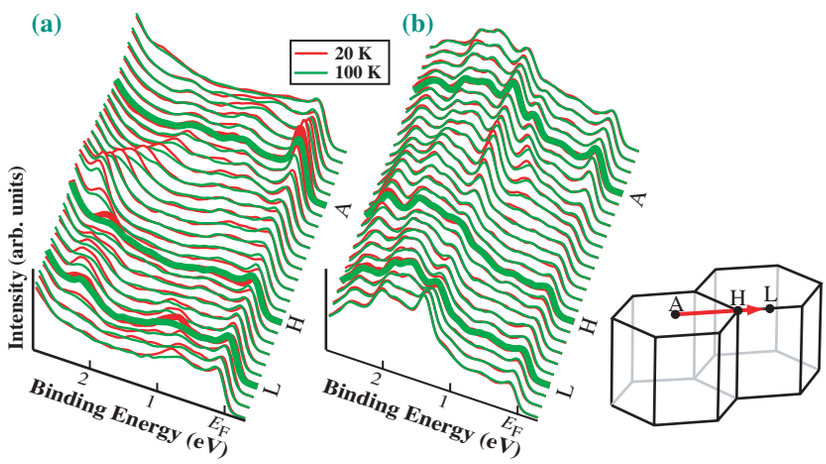

Fig. 2. Temperature dependence of ARPES spectra of **(a)** UPd_2Al_3 and **(b)** UNi_2Al_3.

discerned in these figures. For example, in the circles labeled 1 in Fig. 3, the structure located at E_B = 1 eV moves toward E_B = 1.1 eV as temperature increases from 20 K to 100 K. In addition, the complicated band structures indicated in the circles labeled 2 also have significant temperature dependences. Thus, the transition is accompanied with changes in the band structure with an energy order of 1 eV (~10^4 K), which has never been predicted previously. The result demonstrated for the first time the behaviors and the details of the itinerant and localized states and the transition between them in energy-momentum space. The present result will give new, deeper insight into not only heavy-electron superconductivity but also various types of unconventional superconductivity in solids [5].

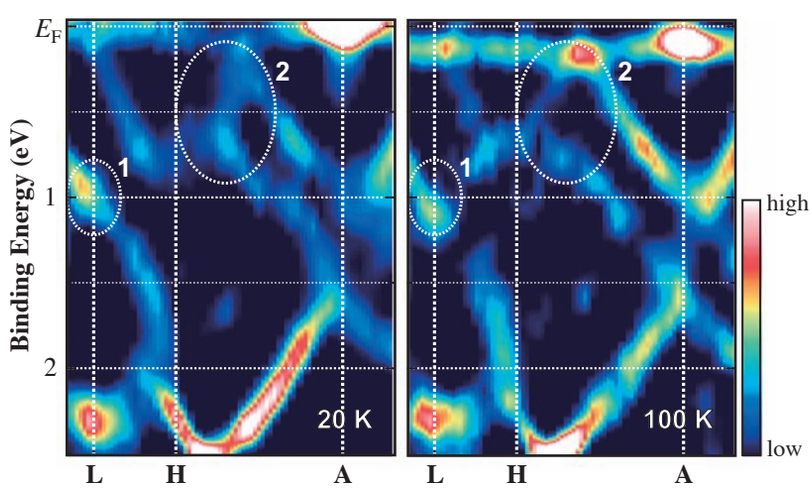

Fig. 3. Temperature dependence of band structure of UPd_2Al_3.

Shin-ichi Fujimori

SPring-8 / JAEA

E-mail: fujimori@spring8.or.jp

References

[1] S. Fujimori *et al.*: Phys. Rev. B **73** (2006) 125109.
[2] Y. Inada *et al.*: J. Phys. Soc. Jpn. **68** (1999) 3643.
[3] K. Kopfle *et al.*: J. Phys. Condens. Matter **8** (1996) 901.
[4] A. Grauel *et al.*: Phys. Rev. B **46** (1993) 5818.
[5] *S. Fujimori, Y. Saitoh, T. Okane, A. Fujimori, H. Yamagami, Y. Haga, E. Yamamoto and Y.Ōnuki: Nature Physics* ***3*** *(2007) 618.*

Probing Bulk Three-dimensional Fermi Surfaces of a Strongly Correlated Material by Soft X-ray Angle-resolved Photoemission

The topology of Fermi surfaces (FSs), the momentum distribution of the electrons with the highest energy on the occupied side (Fermi level, E_F), dominates the macroscopic properties of solids such as electric resistivity, specific heat and magnetic susceptibility. Quantum oscillation measurements based on the de Haas-van Alphen (dHvA) or the Shubnikov-de Haas effect are useful techniques for detecting bulk FSs. The dHvA measurement has so far been applied to many strongly correlated rare-earth materials [1]. However, their electron- or hole-like character and their shape cannot be experimentally revealed by these measurements alone. In addition, these techniques require low temperatures and almost defect-free single crystals. FSs may change their shapes in accord with possible phase transitions at higher temperatures of the order of a few tens of K, where the dHvA measurement is inapplicable. Angle-resolved photoemission (ARPES) is a powerful tool for simultaneously detecting electronic dispersions and FSs. Nowadays it is recognized that high-resolution high-energy photoemission spectroscopy can probe bulk electronic states. In addition, high-energy soft X-ray ARPES has an advantage that it clearly resolves the momentum perpendicular to the sample surface, k_z, owing to a long photoelectron mean free path. Therefore, the soft X-ray ARPES with controlling excitation energy $h\nu$ in addition to polar and azimuthal angles has the potential to detect three-dimensional bulk FSs at high and low temperatures. We have succeeded in probing the three-dimensional FSs of a strongly correlated Ce-based material $CeRu_2Ge_2$ in the paramagnetic phase at 20 K [2], at which it is difficult to experimentally examine the FSs by the dHvA measurement.

The soft X-ray ARPES measurements were performed at beamline **BL25SU**. A clean surface of $CeRu_2Ge_2$ was obtained by cleaving *in situ* at the measuring temperature of 20 K providing a [001]

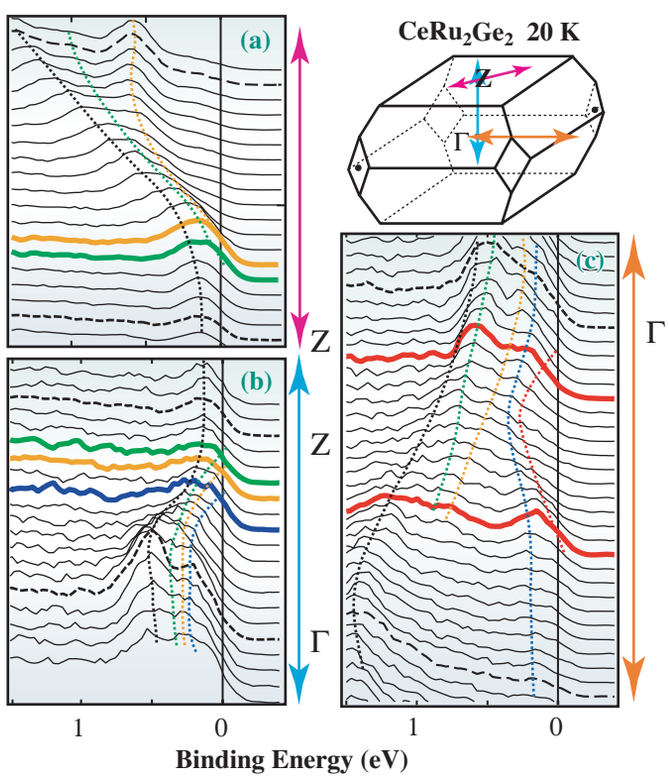

Fig. 1. High-energy soft X-ray ARPES spectra of $CeRu_2Ge_2$ measured at $h\nu$ = 735-840 eV in the paramagnetic phase at 20 K. **(a)** Spectra from point Z in the (110) direction at a fixed $h\nu$ of 755 eV. **(b)** Spectra along line from Z in the $\Gamma(k_z)$ direction obtained by changing $h\nu$. **(c)** Spectra from point Γ in the (100) direction at a fixed $h\nu$ of 820 eV. The spectra with solid color bold lines indicate those on the Fermi surfaces. The dotted lines represent the electronic dispersions as a guide for the eyes. The Brillouin zone for $CeRu_2Ge_2$ is also shown.

plane. A Gammadata-Scienta SES200 analyzer was used, which covers more than a whole Brillouin zone along the direction of the analyzer slit. The energy resolution was set to 200 meV for FS mappings. The angular resolutions were ±0.1° and ±0.15° in the perpendicular and parallel directions to the analyzer slit, respectively. These values correspond to the momentum resolutions of 0.024 $Å^{-1}$ and 0.035$Å^{-1}$ at $h\nu$ = 700 eV.

Figure 1 shows the high-energy soft X-ray ARPES spectra of $CeRu_2Ge_2$ in the paramagnetic phase. The energy positions of many peaks and shoulders in the spectra are changed depending on not only the detection angle (Figs. 1(a) and 1(c)) but also the excitation energy (Fig. 1(b)). Namely, these structures disperse three-dimensionally in the momentum space, which is an indication of the dispersions originated from the bulk electronic. From the ARPES measurements, we obtained intensity maps in the vicinity of E_F, which are equivalent to the cross sections of the FSs, for $CeRu_2Ge_2$ at 20 K along the [110] and [001] planes, as shown in Fig. 2. From these cross sections, small and large ellipsoidal Fermi surfaces centered at Z, and small cylinder-like Fermi surfaces centered at X, are expected.

Based on these results, we can obtain the

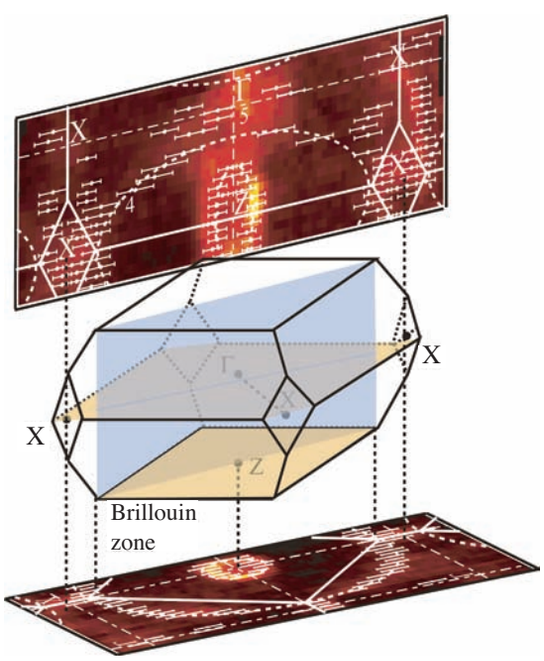

Fig. 2. ARPES intensity maps at E_F ± 100 meV and estimated Fermi wave vectors corresponding to the cross sections of the Fermi surfaces of $CeRu_2Ge_2$. The upper panel shows the cross-sectional Fermi surfaces cut by the [110] plane in the momentum space. The middle panel represents the Brillouin zone. The lower panel shows the cross sections of the same Fermi surfaces, but cut by the [001] plane including point Z.

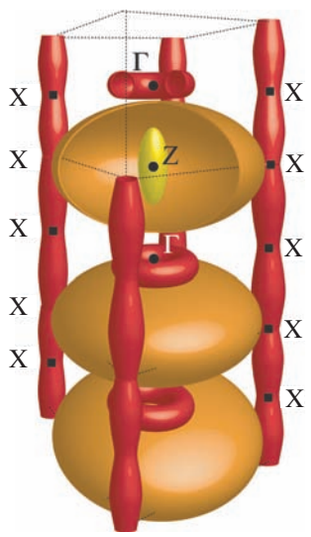

Fig. 3. Schematically drawn and qualitative image of the three-dimensional Fermi surfaces of $CeRu_2Ge_2$ based on our ARPES results.

qualitative shapes of the three-dimensional Fermi surfaces for $CeRu_2Ge_2$ in the paramagnetic phase, as shown in Fig. 3. Although the ellipsoidal Fermi surfaces are similar to those in the magnetic phase below T_c ~ 8 K [3] and those in a theoretical result based on a localized 4*f* model [4], it was found that the cylindrical Fermi surfaces are qualitatively different from those in the magnetic phase and in those the theoretical result.

In summary, we have directly examined the FS topology of $CeRu_2Ge_2$ at a "high" temperature in the paramagnetic phase. We are convinced that the use of high-energy soft X-ray ARPES demonstrated here will become another complementary and powerful technique for probing the bulk FSs in solids in near future.

Akira Sekiyama*, Masao Yano and Shigemasa Suga

Graduate School of Engineering Science, Osaka University

*E-mail: sekiyama@mp.es.osaka-u.ac.jp

References

[1] Y. Onuki *et al.*: J. Phys. Soc. Jpn. **73** (2004) 769.
[2] *M. Yano, A. Sekiyama, H. Fujiwara, T. Saita, S. Imada, T. Muro, Y. Onuki and S. Suga: Phys. Rev. Lett.* ***98*** *(2007) 036405.*
[3] H. Ikezawa *et al.*: Physica B **237** (1997) 210.
[4] H. Yamagami and A. Hasegawa: J. Phys. Soc. Jpn. **63** (1994) 2290.

Nuclear Forward Scattering Study of Relaxation in the Geometrically Frustrated Ferromagnet $Dy_2Ti_2O_7$

$Dy_2Ti_2O_7$ is a pyrochlore in which the Dy^{3+} ions lie on the vertices of a network of corner-sharing tetrahedra. Spins arranged in such a configuration cannot minimize all of their exchange interactions simultaneously if these are antiferromagnetic. This phenomenon, called "geometrical frustration," results in a highly degenerate ground state and exceptionally complex dynamics. $Dy_2Ti_2O_7$ [1], along with similar pyrochlores $Ho_2Ti_2O_7$ [2] and $Ho_2Sn_2O_7$ [3], are ferromagnetic. However, in these materials, strong crystal fields constrain the rare-earth ion spins to lie along the (1 1 1) directions that connect the corners of each tetrahedron to its center, and so they too demonstrate geometrical frustration.

Nuclear forward scattering (NFS) probes the hyperfine fields created at each resonating nucleus by the electrons surrounding it. Thermal fluctuations of the electron spins affect the hyperfine fields and thus the observed NFS spectra. We used NFS at the undulator beamline **BL35XU** to measure the Dy ion spin-flip rate in a 98-μm-thick $Dy_2Ti_2O_7$ crystal foil [4]. We collected NFS time spectra showing the intensity of the resonantly emitted photons as a function of time after the arrival of the initial synchrotron radiation pulse. The nuclear resonance used here is that of ^{161}Dy (natural abundance 19%) with energy 25.65 keV and natural lifetime 42 ns.

The foil was inserted in a cryostat, and its NFS time spectra were collected over a temperature range from 8 to 287.3 K by an array of 16 thin avalanche photodiodes with time resolution below 200 ps and efficiency ~17%. Previous experiments done without such a fast detector (Ref. 15 of [4]) could not capture the fast NFS oscillations caused by the large hyperfine splittings of the ^{161}Dy nucleus. The bandwidth of the beam incident on the foil was limited to about 0.5 meV by a high-resolution monochromator, which passed a flux of about 2×10^8 photons/s. The beam ran parallel to the foil's (1 1 1) direction and was polarized within 3° of its (1 –2 1) axis. NFS data were typically available 4 ns after the exciting pulse, but a correction to the detector efficiency (~20%) was needed at times before 8 ns after the excitation. This has been applied.

Figure 1 shows selected NFS time spectra. At temperatures below about 45 K, the beats due to the magnetic splitting remain clear. The spin flips broaden the resonance linewidths, resulting in the observed faster decay. At intermediate temperatures, the spin-flip rate is high enough to collapse the resonance spectrum into a single broad line, as reflected in the rapid decay observed in our sample at 55 K. Finally, at high temperatures, the average time between spin flips is much less than the nuclear resonance lifetime. Thus the nuclei see only an average hyperfine magnetic field of zero, and only the electric field gradient affects the decay.

The NFS time spectra from 8 to 90 K and at 287.3 K permitted definite determination of the hyperfine fields and spin-flip relaxation times. The hyperfine fields were assumed to consist of a magnetic field **H** and a parallel electric field gradient with a single component, V_{zz}. The relaxation was included by using the model of Blume and Tjon [5]. Theoretical fits to selected spectra are shown in Fig. 2.

The relaxation times τ from 30 to 90 K could be well fit to an Arrhenius equation, $\tau = \tau_0 \exp(E_a/k_BT)$, where T is the absolute temperature in deg K. Figure 3 shows the Arrhenius plot. The high-temperature limit τ_0 of the relaxation time is $15.76^{+3.03}_{-2.53}$ ps, and the activation energy is 271.9±8.1 K. While the activation

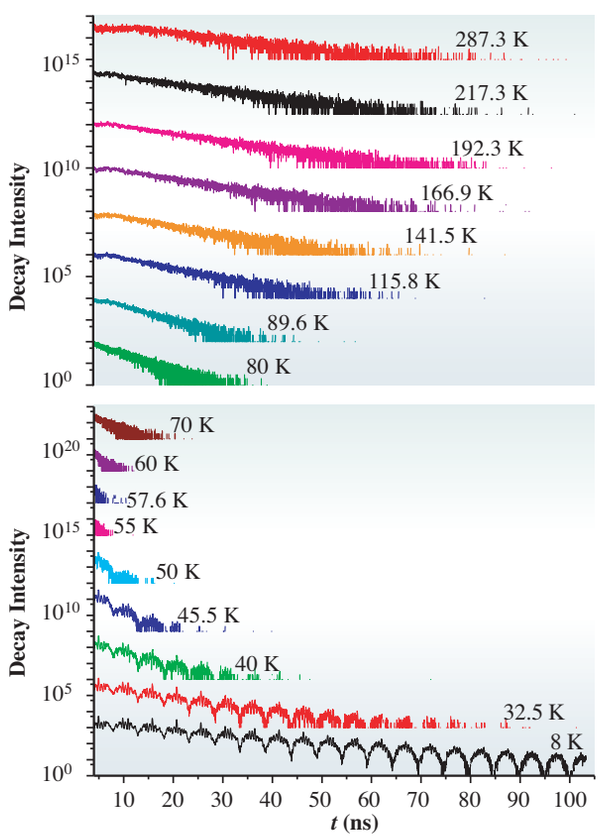

Fig. 1. Selected nuclear forward scattering time spectra collected from $Dy_2Ti_2O_7$ sample foil at various temperatures.

energy of $Dy_2Ti_2O_7$ is similar to those of $Ho_2Ti_2O_7$ and $Ho_2Ru_2O_7$, the τ_0 value for $Dy_2Ti_2O_7$ is about three times its value for the Ho pyrochlores [4]. One possible reason for this difference is that the effective exchange interaction is only 1.1 K in $Dy_2Ti_2O_7$, but is 1.8 K for $Ho_2Ti_2O_7$.

We find that |**H**| and V_{zz} are flat throughout the low-temperature region, with their uncertainties increasing with temperature. |**H**| lies between 559 and 583 T (765-798 MHz) up to 90 K, with uncertainties not exceeding 2.4 T or 3.3 MHz. eQV_{zz}, where Q is the electric quadrupole moment of the ^{161}Dy nucleus, lies between 1160 and 1294 MHz up to 60 K, with uncertainties not exceeding 100 MHz. Our values at 8 K are |**H**| = 561.74±0.01 T and eQV_{zz} = 1293.63±0.09 MHz, in good agreement with previous measurements as discussed in [4]. The spectrum at 287.3 K yields a value of 493 T (675 MHz) for |**H**|, with a large uncertainty of 114 T (156 MHz) consistent with a high spin-flip rate. The value for eQV_{zz} at this temperature, 364.8±3.5 MHz, differs sharply from that found at low temperatures, perhaps because the Dy ions here enter a crystal field excited state in which a different electric field gradient is exerted on the nuclei.

The NFS spectra taken from 100 to 220 K did not yield unique values for the hyperfine fields and relaxation times, though we could obtain reasonable fits by extrapolating these parameters from the low-temperature data. These spectra could be approximated by simple exponential decays with decay lifetimes increasing from 9.6 to 12.6 ns from 115.8 to 192.3 K, falling slightly again to 12.0 ns at 217.3 K.

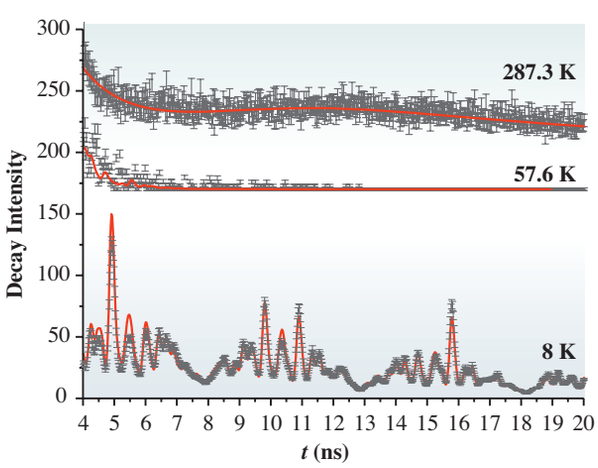

Fig. 2. Best fits of selected spectra from 4 to 20 ns. The data are given by the individual points with error bars. The red curves are the best-fit spectra. For clarity, the 8 K spectrum is scaled down by a factor of 50 and the one for 57.6 K is expanded by a factor of 3.

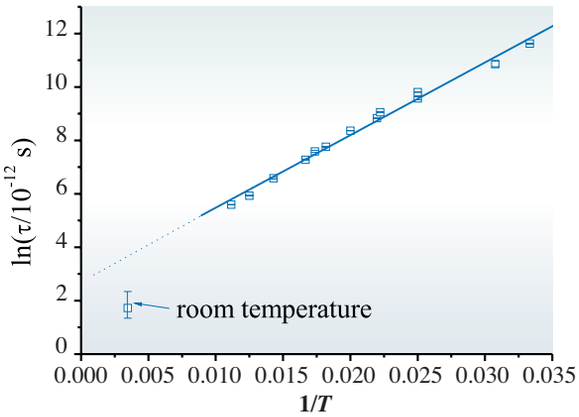

Fig. 3. Arrhenius plot of τ *versus* T in $Dy_2Ti_2O_7$. For the low-temperature data, the error bars lie within the squares. The solid line is the best-fit Arrhenius function (see text). The dotted line is the extrapolation of this best fit to room temperature.

In sum, we have studied spin relaxation in $Dy_2Ti_2O_7$ using nuclear forward scattering of synchrotron radiation by ^{161}Dy. A new fast and efficient detector showed that the NFS technique can be applied to this isotope in a practical way. The activation energy of $Dy_2Ti_2O_7$ appears characteristic of titanate pyrochlores, but the high-temperature limit of the relaxation time is about three times that of Ho pyrochlores. The hyperfine fields agree well with previous measurements at low temperatures and are essentially independent of temperature up to 90 K.

John P. Sutter [a,*], Alfred Q.R. Baron [b,c], Ryuji Higashinaka [d] and Satoshi Tsutsui [b]

[a] Optics & Metrology, Diamond Light Source, United Kingdom
[b] SPring-8 / JASRI
[c] SPring-8 / RIKEN
[d] RIKEN, Magnetic Materials Laboratory, Wako

*E-mail: John.Sutter@diamond.ac.uk

References

[1] A.P. Ramirez *et al.*: Nature (London) **399** (1999) 333.
[2] M.J. Harris *et al.*: Phys. Rev. Lett. **79** (1997) 2554.
[3] K. Matsuhira *et al.*: J. Phys.: Condens. Matter **12** (2000) L649.
[4] *J.P. Sutter, S. Tsutsui, R. Higashinaka, Y. Maeno, O. Leupold and A.Q.R. Baron: Phys. Rev. B. **75** (2007) 140402.*
[5] M. Blume and J.A. Tjon: Phys. Rev. **165** (1968) 446.

Configurational Energetics in Ice I*h* Probed by Compton Scattering

The ubiquitous water and ice exhibit various unusual macroscopic properties, which can be attributed to the local intra- and intermolecular interactions (i.e., both covalent and hydrogen bonding, cf. Fig. 1). Consequently, the ensuing configurational energies are of fundamental importance. Whereas calorimetric data - including both vibrational and configurational contributions - is readily available, experimental information on configurational energies is not easily obtainable. In fact, such information has hitherto been obtained only indirectly by somewhat simplistic modeling of spectroscopic data (see, e.g., Ref. [1]).

Compton scattering, which is inelastic X-ray scattering at large energy and momentum transfers, provides information on the ground-state electron momentum density. The technique has recently been shown to provide fundamental information on both intra- and intermolecular bonding (see, e.g., Refs. [2,3]). Interestingly, a formal connection between the Compton scattering data (the so-called Compton profile) and the total electronic energy has been known to exists for more than 30 years [4]. However, experimental limitations have so far hindered the experimental utilization of this unique property.

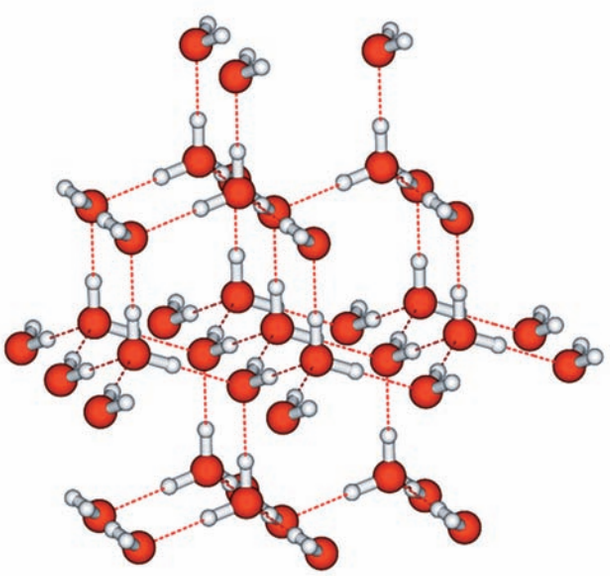

Fig. 1. Structure of ice I*h*.

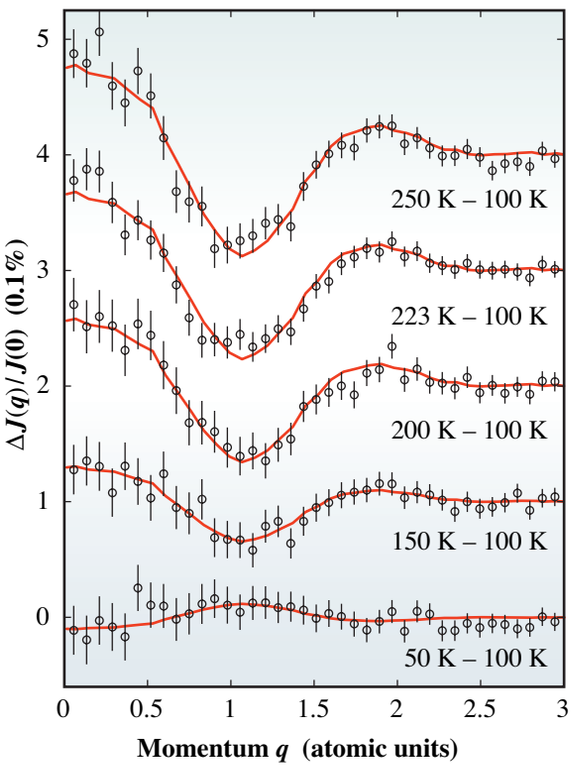

Fig. 2. Temperature-induced changes in the Compton profiles of polycrystalline ice I*h*. The reference Compton profile is acquired at T = 100 K.

We have studied the temperature-induced changes in the ground-state electron momentum density of polycrystalline ice I*h* by Compton scattering at beamline **BL08W** [5]. The experimental data is shown in Fig. 2. Due to the unprecedented accuracy and consistency currently obtainable, the experimental data can be directly interpreted in terms of configurational enthalpies (see Fig. 3). The configurational enthalpy is found to evolve linearly with respect to temperature above T = 100 K, leading to a

constant configurational heat capacity c_p = 0.44±0.11 $Jg^{-1}K^{-1}$ in this temperature regime. Obtaining these fundamental quantities experimentally is important e.g. for assessing the accuracy of molecular-dynamics simulations schemes.

It should be noted that the present experimental approach is, in principle, limited by neither the specific binding (e.g., ionic, covalent, or hydrogen bonding) nor the thermodynamic state of the system (Compton scattering being applicable to solids, liquids, and gases, alike). Combined with the current experimental accuracy, as demonstrated in the present study, energetic studies on a variety of different systems should be feasible by means of Compton scattering.

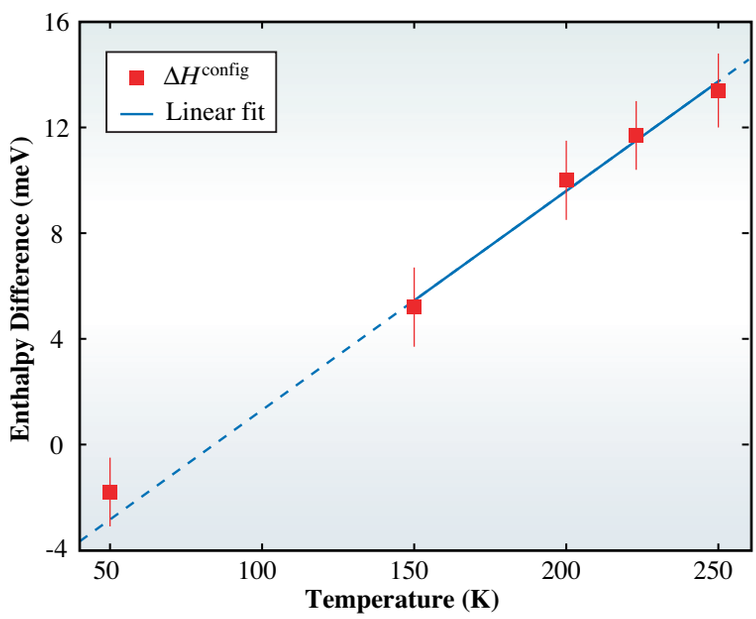

Fig. 3. Temperature-induced changes in the configurational enthalpy (per molecule) as determined from Fig. 2.

Kim Nygård [a, †,*], Mikko Hakala [a] and Keijo Hämäläinen [a]

[a] Department of Physical Sciences, University of Helsinki, Finland

*E-mail: kim.nygard@psi.ch

[†] Present address: Laboratory for Micro- and Nanotechnology, Paul Scherrer Institut, Switzerland

References

[1] J.D. Smith *et al.*: Science **306** (2004) 851.
[2] E.D. Isaacs *et al.*: Phys. Rev. Lett. **82** (1999) 600.
[3] K. Nygård *et al.*: Phys. Rev. E **74** (2006) 031503.
[4] I.R. Epstein: Phys. Rev. A **8** (1973) 160.
[5] *K. Nygård, M. Hakala, S. Manninen, M. Itou, Y. Sakurai and K. Hämäläinen: Phys. Rev. Lett.* ***99*** *(2007) 197401.*

High Field X-ray Magnetoabsorption Spectroscopy of Valence Transition in $YbInCu_4$

The correlation between itinerant electrons and localized electrons induces a variety of exotic properties in solids such as high-T_c superconductivity, the formation of the heavy fermion state and valence fluctuation phenomena. The materials that show these phenomena are so-called strongly correlated materials. Since the localized electrons (*d*- or *f*-electrons) can have large magnetic moments, the investigation of the interplay between the magnetic and electronic properties is crucial for the study of strongly correlated materials. The magnetic field is thus one of the most important external fields in experiments. It is particularly intriguing to study the magnetic-field-induced phase transitions found at low temperatures. At low temperatures, thermal excitation is suppressed and only the change in the ground state due to the quantum mechanical effects can be observed.

$YbInCu_4$ is a typical valence fluctuation material. A sharp first-order valence transition from $Yb^{\sim 3+}$ to $Yb^{\sim 2.85+}$ occurs at about 40 K with decreasing temperature. The valence fluctuates at low temperatures and the localized 4*f* magnetic moments are compensated by the conduction electrons. The ground state is thus non-magnetic below ~ 40 K. As mentioned above, the magnetic-field-induced valence transition at a low temperature is also very interesting. The field-induced valence transition in $YbInCu_4$ was observed by magnetization and magnetostriction measurements [1]. The metamagnetism and the anomaly in the striction were observed and the transition field was found to be around 30 T (Tesla) at 4.2 K.

Synchrotron X-ray spectroscopy plays an important role for the study of the valence fluctuation. The X-ray absorption due to the inner-shell transition of rare-earth ions with different valence states occurs at different energies because the Coulomb repulsive energy between the 4*f* electrons and the core holes (created by the incident X-rays) considerably depends on the number of 4*f* electrons in the shell. The valence transition in $YbInCu_4$ induced by changing the temperature has been investigated intensively by several X-ray spectroscopic techniques. Although it would be interesting to perform an X-ray absorption experiment on $YbInCu_4$ in high magnetic fields exceeding 30 T, such an experiment has not previously been performed because of technical difficulties.

In this article, we present our recent results of a pulsed-high-magnetic-field X-ray absorption experiment on the valence transition in $YbInCu_4$. The portable pulsed field generator allows us to measure X-ray absorption spectra in magnetic fields up to 41 T at 5 K [2]. The significant field dependence of the Yb valence was directly observed for the first time.

The experiment was carried out at beamline **BL22XU**. A single crystal of $YbInCu_4$ was powdered and brushed onto a piece of Scotch tape for the transmission measurement. A very small pulsed magnet (*D*, *L*, *d* = 30 mm, 30 mm, 3 mm, where *D* is the outer diameter, *L* is the length and *d* is the inner diameter) was used to generate a high magnetic field. Since this small magnet can be readily installed into conventional apparatus such as a cryostat or a diffractometer, various experiments can be performed easily in high magnetic fields over 30 T [2,3]. In this study the magnet is installed into a He-flow cryostat and is cooled to the lowest temperature together with the sample. Figure 1 shows a photograph of the small magnet attached on the bottom of the inner rod of the cryostat.

Figure 2 shows the X-ray absorption spectra near the L_{III} edge of Yb at 0 and 41 T. The absorption band at ~ 8.94 keV is due to the transition of Yb^{2+} and that at ~ 8.95 keV is due to Yb^{3+} [4]. Although the Yb^{2+} absorption band is clearly observed at 0 T, it is weaker at 41 T. The Yb^{3+} band is correspondingly stronger at

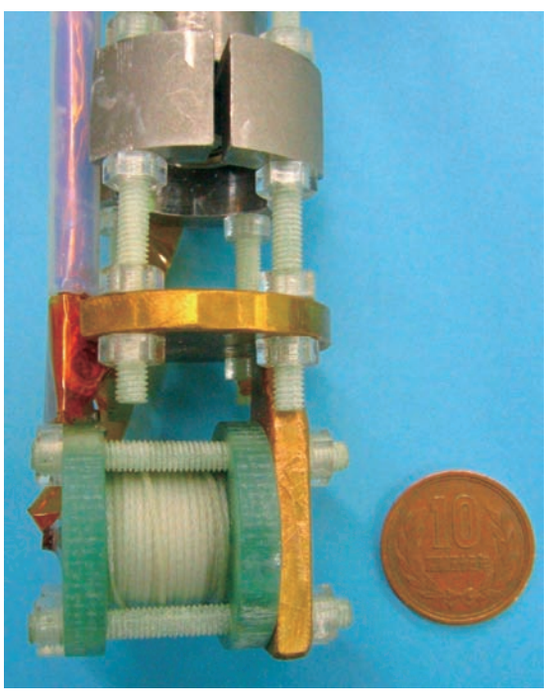

Fig. 1. Photograph of the solenoid-type miniature magnet used for the X-ray absorption measurement.

41 T. Since it is generally accepted that the absorption intensity corresponds to the probability of the existence of each valence state, the valence v^* can be deduced by $v^* = 2I_2/(I_2+I_3)+3I_3/(I_2+I_3)$, where I_2 and I_3 are the absorption intensities of Yb^{2+} and Yb^{3+}, respectively. The solid, dashed and dotted curves in Fig. 2 are the results of the curve fitting using the Lorentzian and the arctangent. It was found that the fitted solid curve accurately reproduces the experimental result. From the fitting, I_2 and I_3 are deduced and the valence v^* can be obtained.

The obtained valences are plotted as a function of the magnetic field in Fig. 3. The temperature variation at 0 T deduced from the X-ray absorption spectra is also shown in the inset. It was found that the valence significantly increases beyond 30 T and becomes saturated at approximately 40 T. Note that the saturated valence ($v^* = 2.96\pm0.02$) is nearly the same value as that at high temperatures ($v^* = 2.97\pm0.02$), as shown in the inset. This fact suggests that the compensated 4*f* moments recover to be localized completely at 40 T. Since the thermal excitation can be disregarded at 5 K, the small deviation of the valence from 3.0 may be due to the effect of final state (the effect of the core-hole). However, further studies are required to allow further discussion.

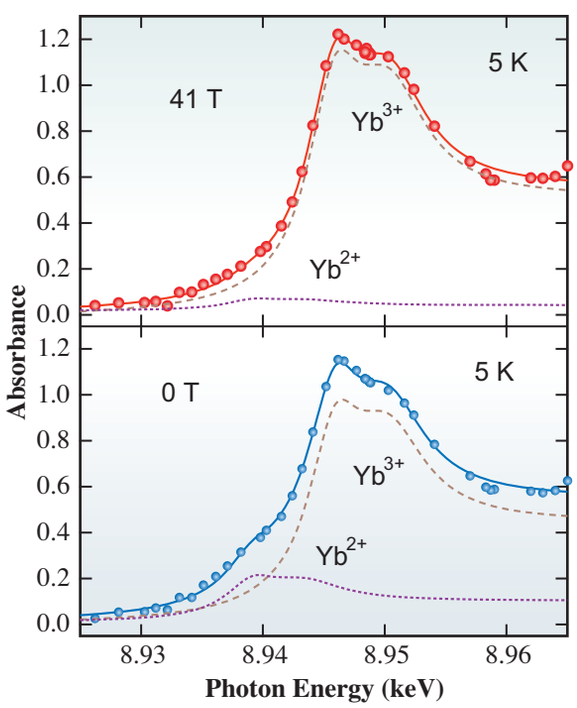

Fig. 2. X-ray absorption spectra at 0 and 41 T. The solid, dashed and dotted curves show the results of the curve fitting.

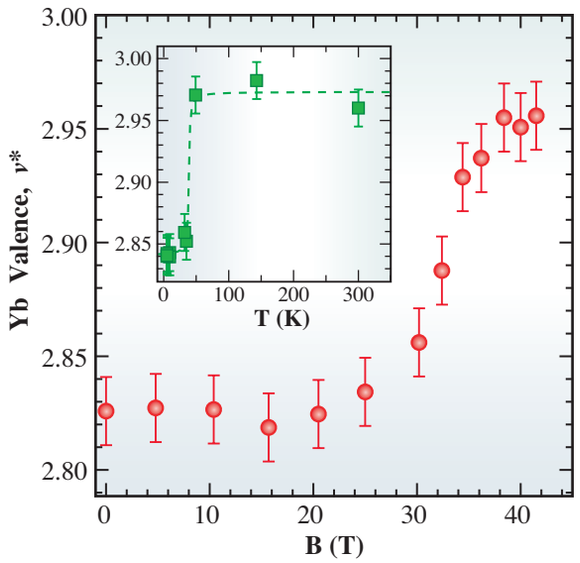

Fig. 3. Magnetic field dependence of the valence at 5 K. The inset shows the temperature dependence of the valence at zero magnetic field.

In the present work, high-magnetic-field X-ray absorption spectroscopy has been established as a unique tool for examining the valence state in very high magnetic fields. This technique can also be applied to various types of magnetic-field-induced phase transitions found in strongly correlated materials.

Yasuhiro H. Matsuda [a,*] and Toshiya Inami [b]

[a] Institute for Materials Research, Tohoku University
[b] SPring-8 / JAEA

*E-mail: matsuda@imr.tohoku.ac.jp

References

[1] K. Yoshimura *et al.*: Phys. Rev. Lett. **60** (1988) 851.
[2] Y.*H. Matsuda, T. Inami, K. Ohwada, Y. Murata, H. Nojiri, Y. Murakami, H. Ohta, W. Zhang, and K. Yoshimura: J. Phys. Soc. Jpn.* ***76*** *(2007) 034702.*
[3] Y.H. Matsuda *et al.*: J. Phys. Soc. Jpn. **75** (2006) 024710.
[4] I. Felner *et al.*: Phys Rev. B **35** (1987) 6956.

CHEMICAL

"Hosobaunran" - Yellow toadflax

"Jaketsuibara" - Yellow bird of paradise

SCIENCE

The needs of SPring-8 for studies in Chemical Science have been steadily extending from diffraction and scattering experiments for structure characterization to spectroscopy as well as inelastic scattering. The work "Exiton properties of organic molecules revealed by inelastic X-ray scattering" by Dr. K. Yang *et al*. is the epoch-making and first successful application of inelastic X-ray scattering (IXS) to an organic molecular crystal. Up to now, IXS has been mainly applied to solid state physics and condensed matter. Thus, Yang's achievement will open the door to various uses of IXS in chemical science.

A wide range of materials are of interest in chemical science, such as organic crystals, polymers, fibers, Langmuir-Blodgett films, etc. Among them, the study by Prof. M. Hasegawa "Correlation between molecular arrangement and emission mechanism of Melem on Languir-Blodgett films of lanthanide(III) complex with stearic acid" revealed the role of lanthanide in an innovative use of existing film technology for new type of thin film display. Her achievement was reported in major newspapers and has attracted considerable attention from industrial companies in Japan.

The discovery of a peculiar quasiperiodic structure in polymeric materials by Prof. Y. Matsushita's group, reported in "Mesoscopic tiling pattern of ABC star-shaped terpolymers studied by microbeam small-angle X-ray scattering" generated intense public interest and was reported in newspapers as a fresh reminder of chemistry in nature.

In addition, seven other papers reporting distinguished attainments were selected this year. There is growing recognition that the highly parallel and high brilliance characteristics of synchrotron beam are powerful tools in advanced chemical science.

Masaki Takata

Structural Investigation of the Charge-transfer Transition in Two-dimensional Cyanide Complex

A charge-transfer (CT) transition that is a cooperative charge-transfer between neighboring molecular units is frequently observed in organic compounds and transition metal complexes, such as halogen-bridged gold complex ($Cs_2Au_2X_6$ (X=I, Br, Cl)) and cyanide complex ($RbMn[Fe(CN)_6]$, $NaCo[Fe(CN)_6] \times H_2O$). The characteristics of the CT transition are that the transition is accompanied by a significant change in the spin state and in the lattice structure. Kato *et al.* have performed electron-level structural analysis of $RbMn[Fe(CN)_6]$, and clarified the variation in the bonding between the Mn ion and the CN ligands [1]. From this viewpoint, the investigation of structural properties, especially the configuration of both metal ions, is indispensable for deeper comprehension of the CT transition as well as of the physical properties.

We chose $Cs[Co(3\text{-}CNpy)_2]W(CN)_8 \cdot H_2O$(CoW cyanide) with 2-dimensional CoW sheet as the target compound. The compound is stoichiometric and is suitable for precise structural analysis with the maximum entropy method (MEM) analysis. The CoW compound shows the thermally-induced CT transition at T_{CT} = 216 K from the Co3+(S=0)-W4+(S=0) configuration to the Co2+(S=3/2)-W5+(S=1/2) configuration. The same CT transition is further induced by photo-irradiation with visible light (600-750 nm, 12.5 mW/cm^{-2}) at 5 K, which causes photo-induced magnetization [2].

The CoW compound consists of cyano-bridged CoW sheets stacked in the *b* direction. Among the eight CN moieties of the octacyanotungsten $[W(CN)_8]$, four are linked to the neighboring Co atoms to form a zigzag sheet, as shown in Fig. 1.

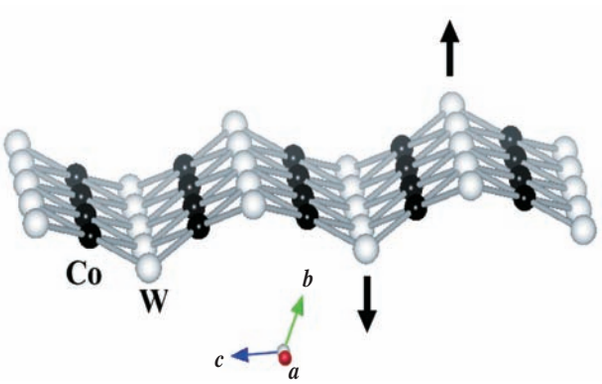

Fig. 1. Cyano-bridged Co-W layer of $Cs[Co(3\text{-}CNpy)_2]W(CN)_8 \cdot H_2O$. White and black circles represent W and Co, respectively. Arrows indicate the out-of-plane movement of the W atoms.

In order to investigate the structural properties of the CoW compounds in the thermally- and photo-induced CT transitions, we measured the powder X-ray pattern at **BL02B2** beamline. The high-energy X-rays reduce the absorption effect even in CoW compounds. The powder diffraction method is free from the mosaicness, which is inevitably introduced at the first-order CT transition. The experiment was carried out with the large Debye-Scherrer camera in the powder X-ray diffraction beamline BL02B2. The wavelength of the incident X-ray was 0.82866 Å. The powder sample was sealed in a 0.1 mmϕ capillary. The temperature was controlled in the range from 90K to 300K by a cooling system of flowing a nitrogen gas. The exposure time was 5 min (60 min) for the photo-induced phase (HT phase and LT phase). In the photo-excitation measurements, the sample powders were thinly attached to the inner surface of the capillary to enable uniform photo-excitation. The excitation laser was a CW green laser (532 nm)

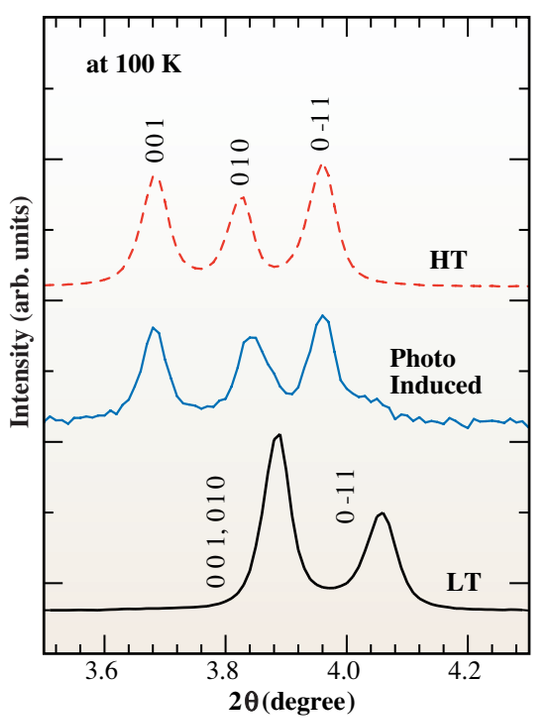

Fig. 2. Magnified X-ray diffraction patterns of $Cs[Co(3\text{-}CNpy)_2]W(CN)_8 \cdot H_2O$. The wavelength of the X-ray was 0.82866 Å. LT and HT represent the low-temperature phase and high-temperature phase, respectively. The photo-induced phase was obtained after irradiation by a continuous-wave laser (532 nm, 10 mW/mm^2) for 30 min. The exposure time was 5 min (60 min) for the photo-induced phase (HT phase and LT phase).

operating at 50 mW. The laser spot size was 1mmϕ at the capillary. The temperature rise at the photo-excitation was estimated to be 30 K.

Figure 2 shows the X-ray diffraction pattern of the high temperature phase (HT), low temperature phase (LT), and photo-induced (PI) phase obtained at 100K. We have analyzed the HT and LT patterns by the Rietveld analysis with the triclinic (*P*-1, *Z*=2) space group. We analyzed the PI pattern with the two phase model and were not able to refine the atom positions. The obtained cell parameters are listed in Table 1. The lattice parameter *a*(*c*) of the HT phase increased by 3% (5%) over the LT phase, while the angles do not change significantly. We found that the cell parameters of the PI phase are close to those of the HT phase. We conclude that the photo-induced magnetization of the CoW compounds is due to the photo-induced structural change to the HT-like metastable structure.

To investigate the detailed structure changes of HT and LT phases, we list the Co-W bond lengths and the Co-W-Co bond angle in Table 2. At the CT transition, the Co-W bond length elongates by ≈0.21 Å. This elongation shows up as an increase in the cell parameters. Indeed, the *y* coordinate of the W atom in the HT phase increased 5% over the LT phase. Yokoyama *et al*. reported that the distance of Co2+(Co3+)-W is 5.37±0.02(5.15±0.02) by means of X-ray absorption fine structure (XAFS) spectroscopy [3]. This elongation of the Co-W bond is consistent with the value determined in this investigation.

In summary, we have investigated the structural properties at the thermally- and photo-induced CT transitions of $Cs[Co(3\text{-}CNpy)_2]W(CN)_8 \cdot H_2O$. A charge density-level structural analysis as well as an electrostatic potential analysis [4] is in progress, which will clarify the nature of the CT transition of the CoW compound.

Table 1. The cell parameter with triclinic setting. υ is the cell volume. The reliable factors are defined as

$$R_{wp} = \left[\frac{\sum_i w_i (y_i - u_{i,calc})^2}{\sum_i w_i y_i^2} \right]^{1/2} \quad R_I = \left[\frac{\sum_K |I_{K,calc} - I_K|}{\sum_K I_{K,calc}} \right]$$

	LT	HT	PI
a (Å)	7.1245(2)	7.3157(2)	7.3067(7)
b (Å)	13.8479(4)	13.9564(4)	13.844(1)
c (Å)	13.6980(4)	14.3791(4)	14.336(1)
α (deg)	116.854(2)	116.223(2)	116.379(8)
β (deg)	90.008(2)	90.010(2)	89.997(6)
γ (deg)	97.702(3)	97.068(3)	96.598(8)
υ (Å^3)	1192.00(7)	1304.48(15)	1288.4(2)
R_{wp} (%)	4.57	4.64	2.71
R_I (%)	4.85	5.12	13.86

Table 2. The bond distance and angles in Co-W. The atomic positions, Co1(-1/2, 0, 1/2), Co2(-1/2,0,0), and W(x,y,z) are also shown

$d_{Co1\text{-}W}$(Å)	5.136(2)	5.334(2)
$d_{Co1\text{-}W}$(Å)	5.160(2)	5.372(2)
$d_{Co2\text{-}W}$(Å)	5.151(2)	5.354(3)
$d_{Co2\text{-}W}$(Å)	5.175(2)	5.390(3)
average(Å)	5.155(2)	5.362(3)
$\theta_{Co1\text{-}W\text{-}Co2}$(deg)	146.85(6)	146.01(6)
x	0.0338(3)	0.0334(4)
y	0.1204(1)	0.1264(2)
z	0.3058(2)	0.3052(2)

J. E. Kim [a,*] and Y. Moritomo [b]

[a] SPring-8 / JASRI
[b] Department of Physics, University of Tsukuba

*E-mail: kimj@spring8.or.jp

References

[1] K. Kato *et al.*: Phys. Rev. Lett. **91** (2003) 255502.
[2] Y. Arimoto *et al.*: J. Am. Chem. Soc. **125** (2003) 9240.
[3] T. Yokoyama *et al.*: Phys. Rev. B **65** (2002) 064438.
[4] H. Tanaka *et al.*: Phys. Rev. B **74** (2006) 172105.
[5] *J.E. Kim and Y. Moritomo et al.: Phys. Rev. B* ***76*** *(2007) 172105.*

Correlation between Molecular Arrangement and Emission Mechanism of Melem in Langmuir-Blodgett Films of Lanthanide(III) Complex with Stearic Acid

Control of molecular arrangements, which have been extended to 2 and 3 dimensions, is one of the key approaches to functional progress on molecular devices at the nanoscale. Research has been concentrated on metal-organic coordination compounds because their various coordination modes lead to multi-functional properties. However, in the case of the solid state or in solution, it is difficult to control their proper arrangements. For these molecular systems, we have proposed an innovative application of an existing film technology to make a molecular base functional control. A technique using Langmuir-Blodgett (LB) films [1] that consist of layers of organic molecules is susceptible to controlling the orientation and density of the molecules. The films are built-up one layer at a time until the desired number of layers is obtained. For this system, we used two different layers. One layer contains the organic compound melem, which is capable of emitting light at specific wavelengths. The other layer contains a metal ion of the lanthanide series, namely praseodymium (Pr(III)), complexed with long-chain fatty acids [2]. Since the first application of LB film techniques in the 1930s, our investigation into metal complexes and molecular interactions will uncover new optical properties for the first time. Consequently, a new possibility has been found by combing an established method and coordination chemistry [3].

Knowing the exact position of these molecules is essential to understanding a profound effect on their optical behavior, that is, a basic structural model of the LB film is important for the description of emission phenomena. In order to get structural information about the thin-films, we have carried out X-ray diffraction measurements on beamline **BL02B2** [4]. Because of the low emittance and high brilliance of SPring-8, we succeeded in reliable and precise data collection even at lower angle diffraction from LB films approx. 25 nm thick. The XRD data were interpreted to indicate that the lanthanides (Ln(III)) are arranged in a plane coordinated to stearic acid (SA, $CH_3(CH_2)_{16}COOH$), whereas melem is intercalated into the film without complexation to Pr(III) (Fig. 1(a)). In the PrSA film, melem is located between alkyl chains of SA at intervals of 54.4 Å, which is different from melem in the SA film without Pr(III). From the Bragg peaks the metal-metal interlayer distance was calculated as 48.6 Å, regardless of the presence of melem. However, EXAFS spectroscopy at the Pr(III) L_3-edge, carried out at beamline **BL01B1** [5], which provides information about the coordination number, showed that the coordination structure around Pr(III) is changed by the presence of melem in the film (Fig. 1(b)). In the case of the film with melem, the coordination structure around Pr(III) is almost the same as that of the Pr(III) coordinated to SA in the solid state.

The emission spectra of the films were also studied in detail. In the PrSA film, two distinct fluorescence bands of melem with different polarity were observed

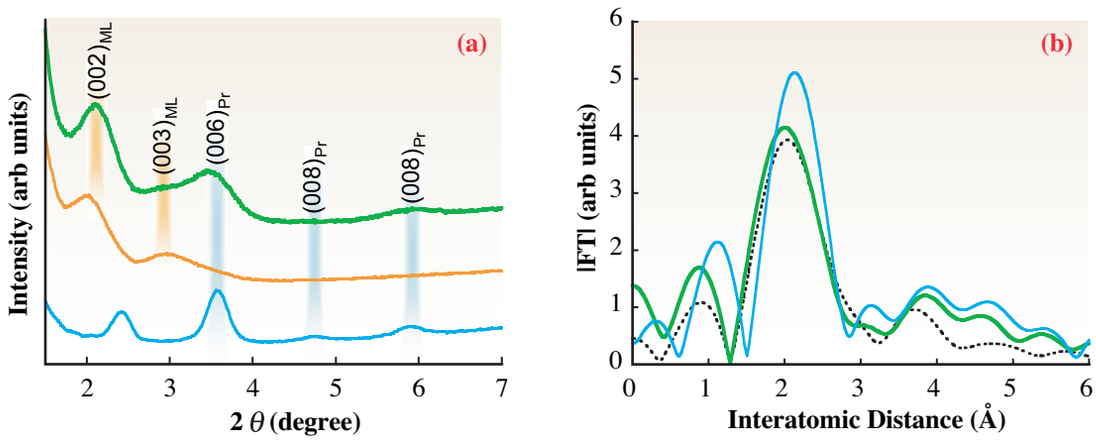

Fig. 1. **(a)** Synchrotron X-ray diffraction patterns of the PrSA-melem film (green), the SA-melem film (red), and the PrSA film (blue), together with assignments of the Bragg reflections. **(b)** Fourier transforms of EXAFS spectra of Pr L_3-edge for the PrSA-melem film (green) and the PrSA film (blue) compared with that for $[Pr(SA)_3(H_2O)]$ in the solid state (dotted line).

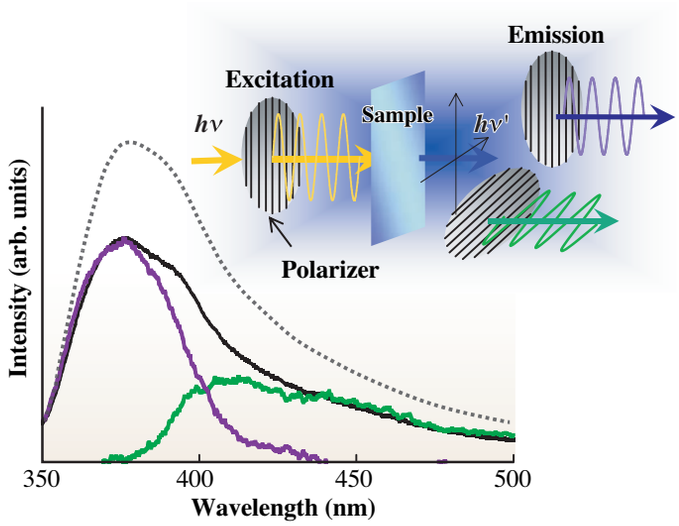

Fig. 2. Fluorescence (dotted line) and the polarized fluorescence spectra of melem in the PrSA film (λ_{ex} = 280 nm) with the vertical or the horizontal emission polarizer, which can be resolved into two components (blue and green).

at 375 nm and 405 nm (Fig. 2 and Fig. 3), polarized at an angle of 0° and 30°, respectively. Interestingly, the dual polarized emissions of melem obtained from the thin film have not been observed in a mixture of the two compounds in the solid state nor in solution. That is, the arrangement and orientation of the molecules using the LB film technique has led to novel emission properties. The present finding may lead to the application of the development of duplex fiber-optic communication systems using this film.

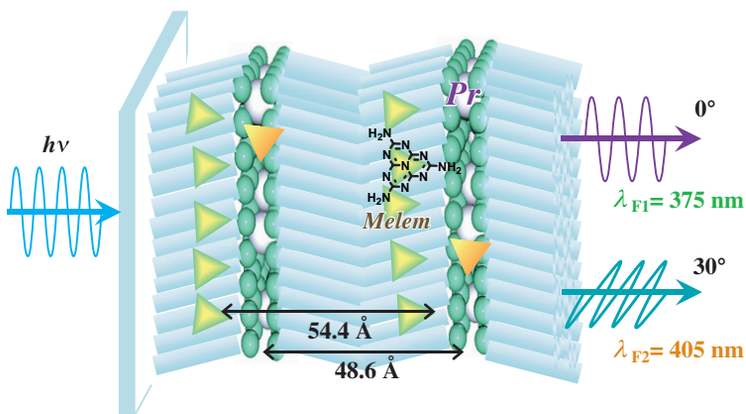

Fig. 3. Illustration of dual polarized emissions of melem arranged in the PrSA film.

Ayumi Ishii [a] and Miki Hasegawa [a,b,*]

[a] College of Science and Engineering, Aoyama-Gakuin University
[b] Research Center for Advanced Science and Technology, The University of Tokyo

*E-mail: hasemiki@chem.aoyama.ac.jp

References

[1] I. Langmuir: J. Am. Chem. **39** (1917) 1848; K.B. Blodgett: J. Am. Chem. **57** (1935) 1007.
[2] *A. Ishii, K. Habu, S. Kishi, H. Ohtsu, T. Komatsu, K. Osaka, K. Kato, S. Kimura, M. Takata, M. Hasegawa and Y. Shigesato: Photochem. Photobiol. Sci.* ***6*** *(2007) 804.*
[3] M. Hasegawa *et al.*: J. Photochem. Photobiol. A **178** (2006) 220; M. Hasegawa *et al.*: Sci. Technol. Adv. Mater. **7** (2006) 72; A. Ishii *et al.*: Chem. Phys. Chem. **8** (2007) 1345.
[4] H. Ohashi *et al.*: Appl. Phys. Lett. **84** (2004) 520; M. Takata *et al.*: Adv. X-ray Anal. **45** (2002) 377.
[5] T. Uruga *et al.*: J. Synchrotron Rad. **6** (1999) 143.

Mesoscopic Tiling Patterns of ABC Star-shaped Terpolymers Studied by Microbeam Small-angle X-ray Scattering

It is known that block copolymers with incompatible components exhibit periodic nanophase-separated structures in condensed states due to the strong repulsion forces among different chemical components. Among the block copolymers, ABC star-shaped terpolymers tend to form characteristic cylindrical structures whose cross-sections reveal tiling patterns because the three different polymer components are connected at one junction point which must be aligned one-dimensionally due to geometrical restrictions (Fig. 1). We have found a variety of mesoscopic tiling patterns formed by ISP star-shaped terpolymers composed of polyisoprene (I), polystyrene (S), and poly(2-vinylpyridine) (P) using transmission electron microscopy (TEM) and small-angle X-ray scattering (SAXS) [1-5].

By conventional SAXS measurements for which the typical size of the X-ray beam is 0.5 mm × 0.5 mm or larger, typical block copolymer samples give powder patterns because the grains with an average size of a few microns are oriented randomly. This fact has made it difficult to characterize the complex tiling patterns for the ISP star-shaped terpolymers in reciprocal space. In this study, therefore, microbeam SAXS technique is used to probe only one or a few grains oriented along the same crystal axes. The microbeam SAXS measurements were performed for annealed sample films cut into thin sections *ca.* 30 μm thick using beamline **BL40XU**. The wavelength of the X-ray used was 0.12 nm and the size of the collimated beam was approximately 5 μm × 5 μm (FWHM) with a camera length of about 3 m.

The ISP star-shaped terpolymers adopt various tiling patterns depending on their volume fractions. For example, Fig. 2 shows TEM images of the $I_{1.0}S_XP_{2.0}$ series (X = 1.3, 1.6, 2.3, and 2.7) where the volume ratio of I:S:P is 1.0:X:2.0. Because the samples were stained with osmium tetroxide and iodine for TEM observation, the black, white, and gray

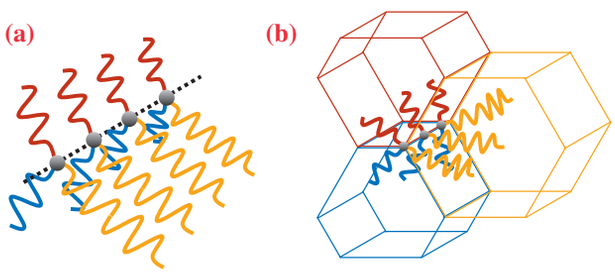

Fig. 1. Schematic drawings of the intramolecular phase separation of ABC star-shaped terpolymer chains **(a)** in bulk and **(b)** their nanodomain assembly.

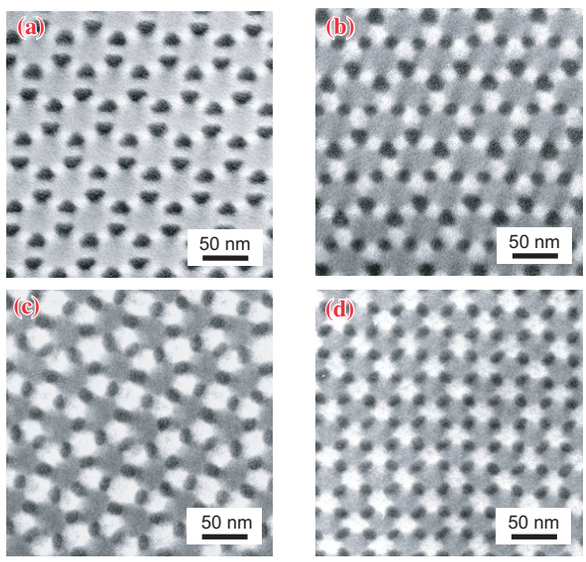

Fig. 2. TEM images of the $I_{1.0}S_X P_{2.0}$ series: **(a)** X = 1.3, **(b)** X = 1.6, **(c)** X = 2.3, **(d)** X = 2.7.

domains represent the components I, S, and P, respectively. For the tiling pattern in Fig. 2(a), the components S, I, and P form the 4-, 6-, and 12-coordinate domains, respectively, and the three kinds of domains contact at every vertex, so it is classified as (4.6.12) Archimedean tiling pattern. In addition to the TEM observation, the (4.6.12) pattern was also characterized by microbeam SAXS. Figure 3(a) shows the microbeam SAXS pattern of $I_{1.0}S_{1.3}P_{2.0}$ and the corresponding d-spacing in real space. This SAXS pattern has 6-fold symmetry, which is consistent with the (4.6.12) tiling pattern having a hexagonal lattice. The $d_{\{10\}}$-spacing, 47 nm, determined by the SAXS pattern agrees well with the value of approximately 50 nm estimated from the TEM image. On the other hand, in the tiling pattern for $I_{1.0}S_{2.3}P_{2.0}$ (Fig. 2(c)), the component I has two types of 4-coordinate domains, the component S consists of 6- and 8-coordinate domains, and the component P has identical 10-coordinate domains. Figure 3(b) shows the microbeam SAXS pattern of $I_{1.0}S_{2.3}P_{2.0}$ and the corresponding d-spacing drawn in a schematic model for the complex pattern. In the SAXS pattern, the {20} and {21} reflections clearly show a 4-fold symmetry, whereas the {10} reflections cannot be confirmed, which suggests the complex tiling pattern has a *P*4*gm* plane group. By applying the imaginary square-triangle tiling manner shown in Fig. 4(a), this complex pattern has been assigned as (3.3.4.3.4), which represents another Archimedean tiling pattern with *P*4*gm* symmetry [2,4].

It should be noted that the (3.3.4.3.4) structure is known as the σ phase in the Frank-Kasper complex crystalline alloy family and is a crystalline analog of a dodecagonal quasicrystal. The quasicrystalline state with non-crystallographic rotational symmetry now represents a new class of ordered state distinct from crystal and amorphous material states. In fact, by exploring a composition range in the vicinity of the (3.3.4.3.4) pattern, we have reached an aperiodic tiling pattern for $I_{1.0}S_{2.7}P_{2.5}$ (Fig. 4(b)) [5]. The square-triangle tiling superimposed on the TEM image has no periodicity, which makes it significantly different from the (3.3.4.3.4) tiling pattern in Fig. 4(a). A microbeam SAXS pattern of $I_{1.0}S_{2.7}P_{2.5}$ is shown in Fig. 4(c). A twelve-fold symmetry pattern up to the higher order can be recognized, suggesting that the square-triangle tiling pattern is a dodecagonal quasicrystal. The length of the sides of the triangles and squares is estimated to be 47.0 nm from the magnitude of the {111100} scattering vector. This result indicates the universality of the dodecagonal symmetry pattern, covering a wide variety of materials including metallic alloys (0.5 nm), chalcogenides (2 nm), organic dendrons (10 nm), and star-shaped polymer (50 nm) herein. We expect that this finding will open a new epoch in self-organization within the field of polymer science and consequently in research on quasicrystals.

In conclusion, the microbeam SAXS technique produces spot-like diffraction patterns, which were never obtained by conventional SAXS measurements, due to scattering from one or a few grains in the polymer samples. These microbeam SAXS patterns enable us to elucidate the complex tiling patterns including the dodecagonal quasiperiodic pattern in reciprocal space. In the future, microbeam SAXS measurements will be widely used to characterize more complex three-dimensional structures such as bicontinuous structures formed by block copolymers.

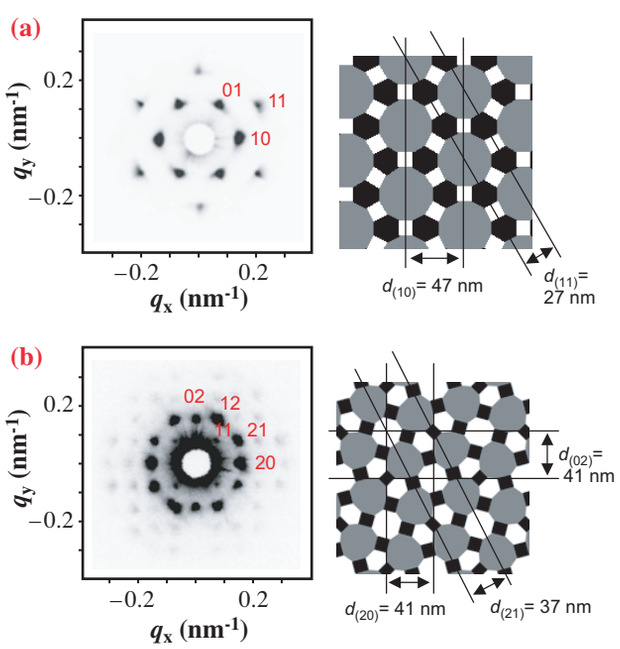

Fig. 3. Microbeam SAXS patterns (left) and the corresponding schematic tiling structures (right): **(a)** $I_{1.0}$ $S_{1.3}$ $P_{2.0}$, **(b)** $I_{1.0}$ $S_{2.3}$ $P_{2.0}$.

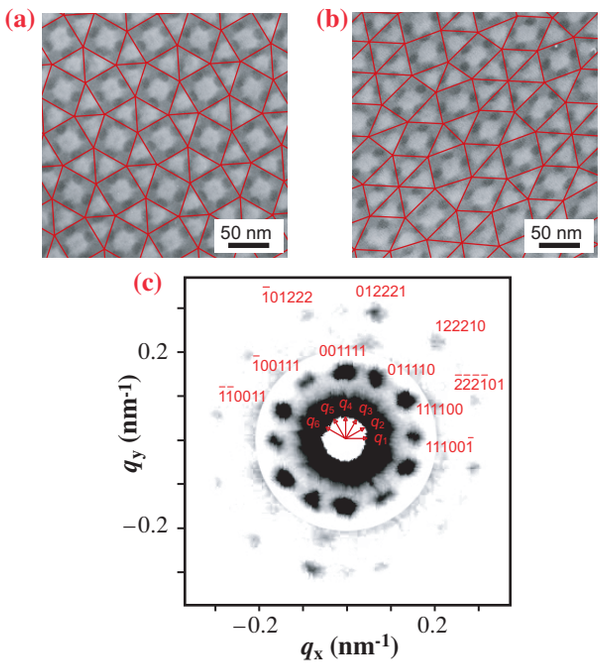

Fig. 4. TEM images of the two ISP samples. The polymer samples are **(a)** $I_{1.0}S_{2.3}P_{2.0}$ and **(b)** $I_{1.0}S_{2.7}P_{2.5}$. An imaginary triangle and square are superimposed on the images. **(c)** Microbeam SAXS pattern obtained for $I_{1.0}S_{2.7}P_{2.5}$. The intensities of the outer twelve diffraction peaks are scaled-up by a factor of 10.

Kenichi Hayashida *, Atsushi Takano, Yushu Matsushita

Department of Applied Chemistry, Nagoya University

*E-mail: hayashid@grace.ocn.ne.jp

References

[1] A. Takano *et al.*: Macromolecules **34** (2004) 9941.
[2] A. Takano *et al.*: J. Polym. Sci. Part B Polym. Phys. **43** (2005) 2427.
[3] K. Hayashida *et al.*: Macromolecules **39** (2006) 4869.
[4] K. Hayashida *et al.*: Macromolecules **39** (2006) 9402.
[5] *K. Hayashida, T. Dotera, A. Takano and Y. Matsushita: Phys. Rev. Lett.* ***98*** *(2007) 195502.*

Degree of Supercooling (ΔT) Dependence and Mass Distribution Function $Q(N,t)$ of Nano-nucleation of Polymers by SAXS

"Nucleation" was assumed to be the early stage of crystallization in classical nucleation theory (CNT) proposed by Becker and Döring [1] in 1930s. Since it is known that the nucleus has a size on the nm order, i.e., that nucleus includes 2 – 10^6 particles or repeating units, we call it a "nano-nucleus." However, it has been too difficult to observe directly nano-nucleation because of the technical issues.

So far, observations with an optical microscope (OM) or a bubble chamber have mainly been done to trace macroscopic nucleation at a scale larger than 1 μm (= macro-crystal). In these studies, it is assumed that both nano-nucleation and macro-crystallization are predominantly controlled by the "critical nano-nucleation," which is an important but unsolved problem. In the CNT, the critical nano-nucleation corresponds to the activated state in the free energy of the nucleation process.

We succeeded in direct observation of nano-nucleation by small-angle X-ray scattering (SAXS) for the first time in 2003 [2] and obtained the size distribution $f(N,t)$ of nano-nuclei in 2007 [3], where N is the size of a nucleus counted by the number of repeating units and t is crystallization time. But these results were obtained only for one case of the degree of supercooling, ΔT. In the nucleation study, it is important to obtain dependence of nano-nucleation on ΔT, as ΔT is proportional to the free energy of melting which is the driving force of nucleation. ΔT is defined as $\Delta T \equiv T_m^\circ - T_c$, where T_m° is the equilibrium melting temperature and T_c is crystallization temperature.

In this study, we obtained dependence of nano-nucleation on ΔT and then compared it with the dependence of macro-crystallization on ΔT to confirm the predominant contribution of the critical nano-nucleation in macro-crystallization. Second, we observed the "mass distribution function $Q(N,t) \propto Nf(N,t)$" directly. The $Q(N,t)$ should exhibit the real image of nano-nucleation, which cannot be described by $f(N,t)$. Finally, we proposed a new nucleation theory by introducing $Q(N,t)$ in order to solve the serious problem in CNT that the kinetic equation with respect to $f(N,t)$ does not satisfy the mass conservation law [4].

We used polyethylene (PE) (NIST, SRM1483a, M_n = 32 × 10^3, M_w/M_n =1.1, T_m° = 139.5°C), where M_n and M_w are the number-average and the weight-average molecular weight, respectively, and M_w/M_n is the index of dispersion. The nucleating agent of sodium 2,2'-methylene-bis-(4,6-di-t-butylphenylene) phosphate (ADEKA Corp., NA-11SF) was mixed with PE. The sample was melted at 160°C for 5 min within a thin evacuated glass capillary (ϕ1mm) and then isothermally crystallized at ΔT = 10.5 – 13.0 K. The SAXS experiment was carried out at beamline **BL40B2**. The range of the scattering vector (q) was (7– 214) × 10^{-3} Å^{-1} and the wavelength (λ) was 1.50 Å.

Figure 1 shows typical $f(N,t)$ against t as a parameter of ΔT for N = 2.2 × 10^4 [rep. unit] which is larger than the size of a critical nano-nucleus (N^*= 450 [rep. unit]). The $f(N,t)$ was obtained by applying an "extended Guinier plot method" to excess scattering intensity $I_X(q,t)$ which was obtained by subtracting background intensity [3]. In the figure, it was found that $f(N,t)$ increases rapidly with an increase of t for larger ΔT, while it increases slowly for smaller ΔT. We determined τ for each ΔT by the onset time of the linearly increasing $f(N,t)$, where τ is the induction time for nucleation.

The inverse of τ is plotted as a function of ΔT^{-1} in Fig. 2. This indicates the relationship as $\tau^{-1} \propto \exp[-\gamma/\Delta T]$ (1), where γ is a constant. Thus, it is clear that nano-nucleation does not occur when ΔT becomes significantly small. This indicates that the "induction period" of crystallization is not controlled by a so-called "spinodal decomposition" process [5] but rather by nucleation process. ΔT dependences of nucleation rate (I) of a macro-crystal and "net flow ($\boldsymbol{j}$)" of nano-nucleation are also shown in Fig. 2. I is defined by the variation of the number of macro-crystals per unit volume and time. We have observed I of macro-crystals larger than 1 μm by OM and obtained the experimental formula, $I \propto \exp[-C'/\Delta T]$ (2), where C' is a constant. When the critical nano-nucleation is the rate-determining process, it is well known in CNT that $\boldsymbol{j}$ is given by $\boldsymbol{j} \propto \exp[-\Delta G^*(N^*)/kT] \propto \exp[-C/\Delta T]$ (3), where $\Delta G^*(N^*)$ is the free energy of

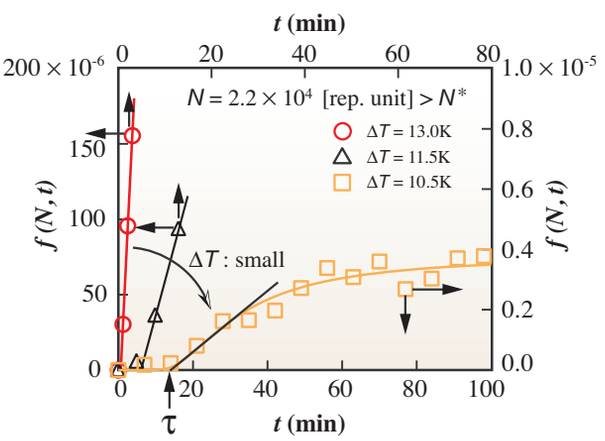

Fig. 1. Plots of $f(N,t)$ against t as a parameter of ΔT for N, 2.2 × 10^4 [rep. unit] > N^*. It clarified that nano-nucleation becomes impossible as ΔT decreases.

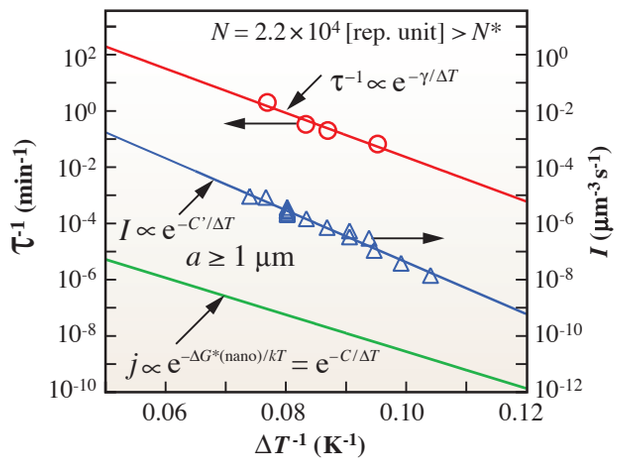

Fig. 2. Plots of τ^{-1}, I and theoretical j against ΔT^{-1}. The observed N of nano-nucleus was $N = 2.2 \times 10^4$ [rep. unit]>N^* and the lateral size of macro-crystal was larger than 1 μm. Since $\tau^{-1} \propto I \propto j$, it clarified that critical nano-nucleation mainly controls macro-crystallization.

critical nano-nucleation, $\Delta G^*(N^*) \propto \Delta T^{-1}$ for two-dimensional nucleus, kT is thermal energy, and C is a constant. It is to be noted that j is the theoretical formula. Since $\tau^{-1} \propto I \propto j$ (4) was obtained, it clarified that the critical nano-nucleation mainly controls the macro-crystallization. Thus it is concluded that OM is a useful tool for convenient routine work in studies of nucleation.

Plots of log$Q(N,t)$ (right axis) and log$f(N,t)$ (left axis) against log$N$ as a parameter of t for $\Delta T = 10.5$ K are shown in Fig. 3. It was found that $f(N,t)$ decreased monotonously but $Q(N,t)$ showed a minimum with a magnitude similar to N^* and increased with an increase of N for each t.

We plotted $Q(N,t)$ against N as a parameter of t in Fig. 4. As $Q(N,t)$ showed a minimum with the similar magnitude of N^* for each t, it was clearly shown that the critical nano-nucleation is the activated state in the nucleation process. $f(N,t)$ cannot describe this entire situation at all. Therefore, we focus the discussion on phenomena in the range of $N \geq N^*$. $Q(N,t)$ had a maximum and became to 0 at N_{max} with the increase of N for each t, where N_{max} is the maximum size of N for a finite time. We obtained N_{max} for each t by extrapolating observed $f(N,t)$ to larger N. N_{max} increases with as t increases. The maximum of $Q(N,t)$ increased and shifted to larger N with the increase of t. Consequently, we found that the total mass of nano-nuclei increases for $N \geq N^*$. Our finding indicates that the crystallinity increases with the increase in t in the nucleation process. We showed that $Q(N,t)$ satisfies the mass conservation law which is demanded by the basic equation of a stochastic process [4].

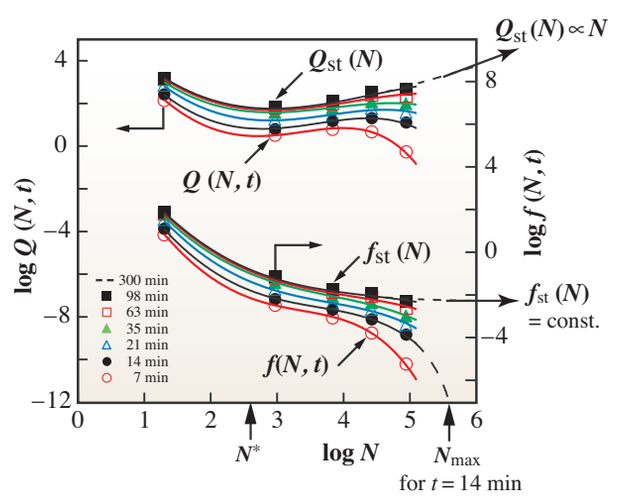

Fig. 3. Plots of log$Q(N,t)$ (left axis) and log$f(N,t)$ (right axis) against log$N$ as a parameter of t for $\Delta T = 10.5$ K.

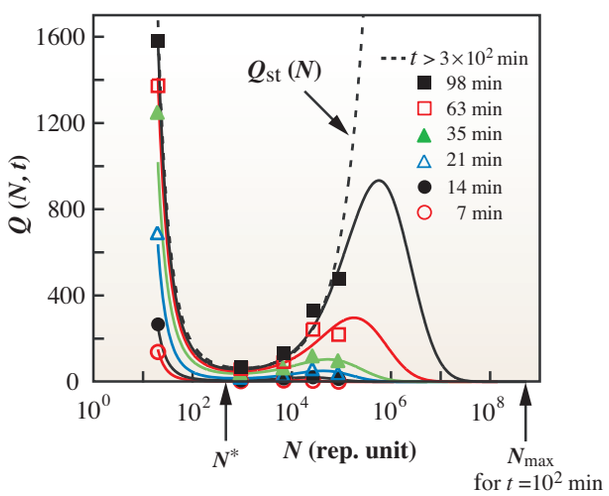

Fig. 4. Plots of $Q(N,t)$ against N as a parameter of t for ΔT = 10.5 K. The total mass of nano-nuclei for $N \geq N^*$ increases. This behavior indicates that crystallinity increases with the increase of t in the nucleation process.

Kiyoka Okada [a], Sono Sasaki [b] and Masamichi Hikosaka [c,*]

[a] Collaborative Research Center, Hiroshima University
[b] SPring-8 / JASRI
[c] Graduate School of Integrated Arts and Sciences, Hiroshima University

*E-mail: hikosaka@hiroshima-u.ac.jp

References

[1] V.R. Becker, W. Döring: Ann. Phys. **24** (1935) 719.
[2] M. Hikosaka *et al.*: J. Macromol Sci. Phys. **B42** (2003) 847.
[3] K. Okada *et al.*: Polymer **48** (2007) 382.
[4] *K. Okada, K. Watanabe, A. Toda, S. Sasaki, K. Inoue, M. Hikosaka: Polymer **48** (2007) 1116.*
[5] M. Imai *et al.*: Polymer **33** (1992) 4457.

Structure-magnetic Properties of Rare-earth Metals Confined in Carbon Nano-spaces

Atoms and molecules confined in nano-sized spaces could have properties which are distinctly different from those of bulk solid or fluid. Carbon nano-space is an interesting space, which can confine atoms and molecules not only by van der Waals force but also by charge transfer interactions. Among them and of particular interest is the rare-earth metal atom confinement in carbon nano-space, namely, endohedral metallofullerenes and fullerene nano-peapods; fullerene nano-peapods are carbon nanotubes encapsulating fullerene molecules inside 1-dimensional channel (Fig. 1). These species of carbon nano-materials have attracted a wide range of researchers not only because of their specific structure and properties but also for various applications including gas sensors, optical devices, and field effect transistors [1,2]. Furthermore, in the case of nano-peapods, we expect novel transport properties correlated with the packing structure and the order-disorder of the orientated structures of encapsulated fullerene molecules. However, in the current stage, the synthetic yield of endohedral metallofullerenes (especially di- and tri-metallofullerenes) and therefore fullerene nano-peapods is very low, which presents an intrinsic difficulty for characterization of structure and properties of these novel compounds. Characterization using high brilliance synchrotron radiation is a very powerful method, which needs only a small amount of sample. Here we report the first structure-magnetic property characterization of Dy-metallofullerene (Dy@C_{82}) and the corresponding nano-peapods using synchrotron soft X-ray magnetic circular dichroism spectroscopy (SXMCD) and X-ray diffraction (XRD) [3].

Single wall carbon nanotubes (SWNTs) were synthesized using laser ablation method, in which a rotating graphite target containing Co/Ni catalyst was irradiated with Nd:YAG laser (wavelength is 532 nm) at 1200 °C. Dy@C_{82} was synthesized using arc-discharge and purified by multi-step high performance liquid chromatography. Nano-peapods were synthesized by gas-phase doping, in which SWNTs and purified Dy@C_{82} were vacuum-sealed in a Pyrex tube and heated at 500 °C for 2 days.

Figure 2 shows the X-ray diffraction pattern of nano-peapods and empty SWNTs measured at beamline **BL02B2**. As clearly illustrated in the figure, the XRD pattern changes drastically after the encapsulation of Dy@C_{82} molecules. Assuming SWNTs and Dy@C_{82} are represented by cylindrical and double spherical electron density, respectively, we can simulate the diffraction patterns that give the filling ratio and mean-intermolecular distance of encapsulated Dy@C_{82} ; the filling ratio is 60% and the intermolecular distance is 10.6 Å, which is much shorter than that of a bulk crystal of Dy@C_{82}. The fact that we can reproduce the observed XRD pattern of nano-peapods by a simple structure model means that the orientation of encapsulated Dy@C_{82} is random.

The temperature dependence of MCD spectra of metallofullerenes and nano-peapods clearly shows that the reciprocal magnetization of encapsulated lanthanide ions is proportional to temperature and the follows Curie-Weiss law (Fig. 1, measured at beamline **BL25SU**). The Weiss temperature of these ions is relatively low (11.6 and 5.2 K for nano-peapod and Dy@C_{82}, respectively), which means that magnetic interaction between encapsulated ions is weak. Curie constants are also different between nano-peapods

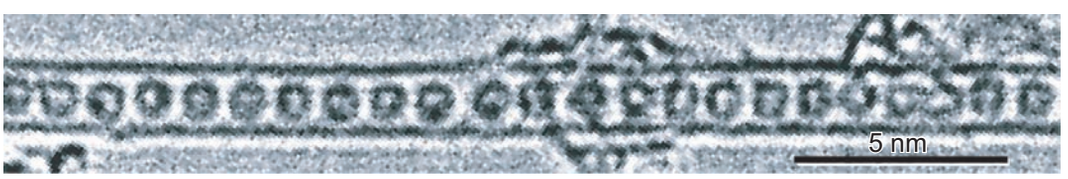

Fig. 1. High-resolution transmission electron microscope image of Dy@C_{82} encapsulating single walled carbon nanotubes. (scale bar corresponds to 5 nm).

and Dy@C_{82}, at 55.1 and 38.0 μ_BK for nano-peapods and Dy@C_{82}, respectively. The calculated effective magnetic moment of Dy ions based on Curie constants is 9.5 and 11.4 μ_B for the nano-peapods and Dy@C_{82}, respectively. This indicates that the encapsulation by nanotubes affects not only inter-Dy magnetic interactions but also the electronic structure of the Dy ion. Crystal field analysis of Dy^{3+} ions reveals that C_{2v} point symmetry with 10 meV energy splitting can represent the difference between nano-peapods and Dy@C_{82}. This means that the electric field acting on Dy^{3+} ions is different, which probably results from charge transfer between encapsulated Dy@C_{82} and carbon nanotubes.

This study has shown that the interaction between SWNTs and encapsulated Dy@C_{82} is not just a weak van der Waals interaction but a strong interaction, probably charge transfer, which means that we can expect novel properties that cannot be understood by a simple sum of contributions from SWNTs and encapsulated fullerene molecules.

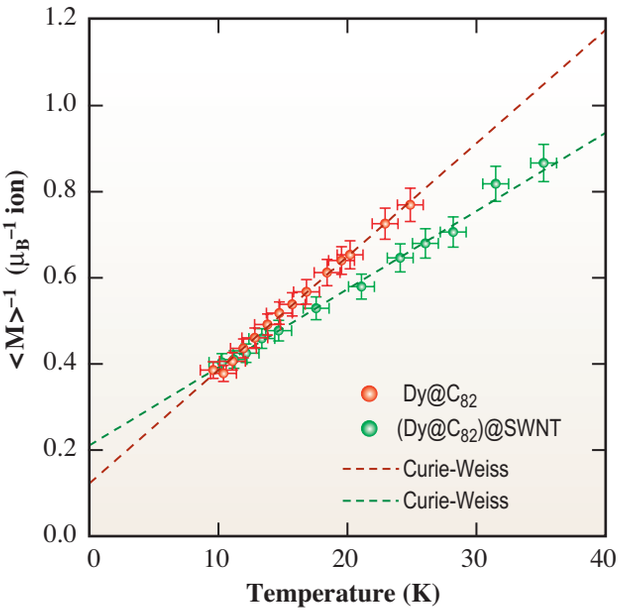

Fig. 3. Temperature dependence of reciprocal magnetization calculated from MCD measurements.

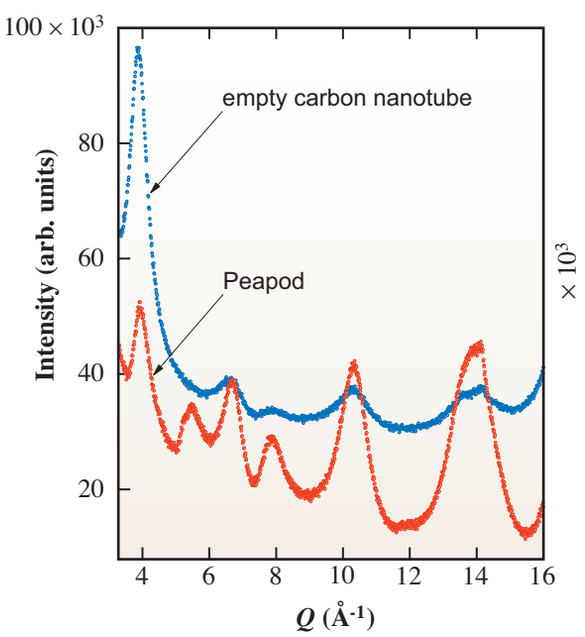

Fig. 2. XRD patterns of empty nanotubes and nano-peapods.

Ryo Kitaura

Department of Chemistry, Nagoya University

E-mail: kitaura@nano.chem.Nagoya-u.ac.jp

References

[1] R. Kitaura *et al.*: Chem. Asian J. **1** (5) (2006) 646.
[2] R. Kitaura *et al.*: Jpn. J. Appl. Phys. **46** (2007) 881.
[3] *R. Kitaura, H. Okimoto, H. Shinohara, T. Nakamura and H. Osawa: Phys. Rev. B* ***76*** *(2007) 172409.*

Femtosecond Nuclear Dynamics at Core-valence Doubly Excited States

Excitation of a core-electron in molecules can be accompanied by promotion of one or more valence electrons, due to electron relaxation (valence polarization) and the correlation effect. Such core-valence doubly excited states lie above the corresponding core ionization thresholds. They are accordingly embedded in the electronic continua, and relax via resonant Auger decay as well as autoionization. The time scale for their electronic decays is comparable to low-frequency vibrational periods; thus the decay processes can be subject to competition with nuclear motion in the femtosecond regime. A novel mechanism of femtosecond nuclear dynamics is unveiled here for the first time using advanced photoelectron spectroscopy. The experiment was performed using a high-resolution electron energy analyzer (Gammadata-Scienta SES-2002) at the soft X-ray photochemistry beamline **BL27SU**.

More than one hundred photoelectron spectra have been measured for molecular nitrogen in the photon energy region of 412.5-417.3 eV at small photon energy intervals of 50 meV [1] to investigate all the autoionization features of doubly excited states. For effective presentation of the photoelectron spectra obtained, they were assembled in a two-dimensional (2D) map as shown in Fig. 1. The 2D map shows remarkable vibrational features of $N_2^+(1\sigma_{g/u}^{-1})$, particularly in the photon energy range of 415-416.5 eV. Such vibrational excitations result from the autoionization of doubly excited states, because the direct inner-shell ionization brings few vibrational excitations to the formed $N_2^+(1\sigma_{g/u}^{-1})$ states.

Our *ab initio* configuration-interaction calculation yields three doubly excited states in the corresponding photon energy range, and their theoretical potential energy curves are plotted in Fig. 2(a). The potential energy curves imply that photoexcitation in the Franck-Condon region populates the doubly excited states above their dissociation asymptote. The doubly excited states, therefore, start dissociating immediately after photoexcitation. The vibrational excitation feature of $N_2^+(1\sigma_{g/u}^{-1})$, observed on the 2D map, manifests the relative rates for nuclear motion and autoionization. In the limit of very fast autoionization, the autoionizing molecule has the same geometry as the initial state of $N_2(X^1\Sigma_g)$, and few vibrational excitations determined by the Franck-Condon factor between $N_2(X^1\Sigma_g)$ and $N_2^+(1\sigma_{g/u}^{-1})$ should be given. At the other extreme (very slow autoionization), the molecule undergoes Auger decay before autoionization, and the autoionization feature should disappear in the 2D map. In the intermediate case, which is equivalent to the present situation, the average geometry of the molecule at a time corresponding to the mean lifetime for autoionization determines the vibrational structure of $N_2^+(1\sigma_{g/u}^{-1})$.

The vibrational excitations up to 3 eV for $N_2^+(1\sigma_{g/u}^{-1})$ can be seen around a photon energy of 416 eV in Fig. 1. This value of vibrational excitation corresponds

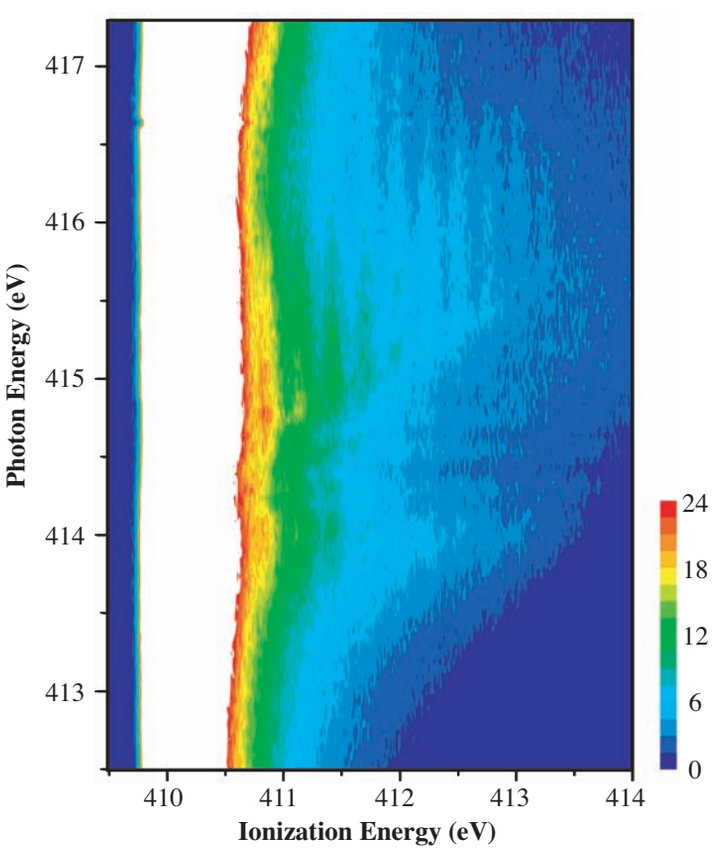

Fig. 1. Two-dimensional map of the inner-shell photoelectron yields from molecular nitrogen as a function of photon energy and ionization energy. The intensities on the 2D map are plotted on a linear scale, while the intensities of low vibrational levels of the $N_2^+(1\sigma_{g/u}^{-1})$ formed are truncated to clarify weak structures.

to autoionization around an internuclear distance of about 1.4 Å [see Fig. 2(a)]. The classical mechanical simulation indicates that it takes about 4 fs to reach an internuclear distance of 1.4 Å after the Franck-Condon transition [see Fig. 2(b)]. This time scale is comparable to that of the resonant Auger decay of the doubly excited states, which exhibits the possibility of competition between autoionization and resonant Auger decay by moving on the dissociative potential energy curve.

This work clearly demonstrates, for the first time, femtosecond nuclear dynamics of core-valence doubly excited states interacting with electronic continua. Extension of this work using short-wavelength free electron laser sources with inherently short pulses, that can be done in the near future, would provide us more details about nuclear-electronic dynamics in core-excited states.

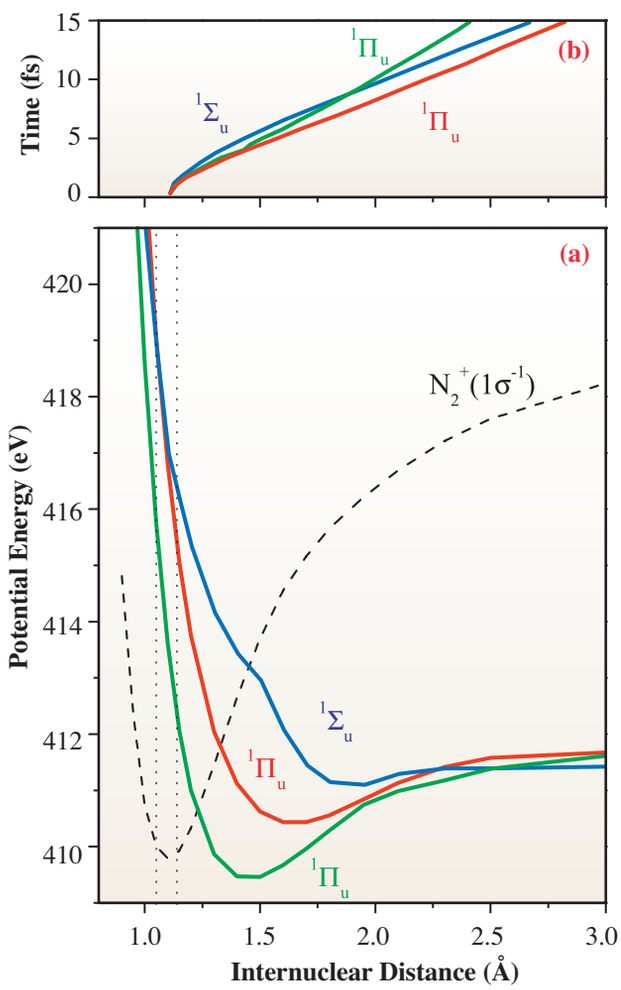

Fig. 2. **(a)** Potential energy curves calculated for the doubly excited states of N_2 lying at 413-416 eV, as well as that for $N_2^+(1\sigma^{-1})$. **(b)** Results of a classical mechanical simulation of the nuclear motion on the potential energy curves in **(a)**. Time measured from the photoexcitation at the equilibrium internuclear distance of the neutral ground state is plotted as a function of the internuclear distance elongated by the nuclear motion.

Y. Hikosaka*, E. Shigemasa and N. Kosugi

Institute for Molecular Science

*E-mail: hikosaka@ims.ac.jp

References

[1] *Y. Hikosaka, T. Kaneyasu, E. Shigemasa, Y. Tamenori and N. Kosugi: Phys. Rev. A* ***75*** *(2007) 042708.*

Young's Double-slit Experiment using Core-level Photoemission from N_2

The Young's double-slit experiment (YDSE) provides the simplest and most fundamental example in which the superposition of two coherent waves of light leads to interference oscillations of the light intensity. Photoionization of homonuclear diatomic molecules represents conceptually a similar phenomenon for the electron waves. The interference of the coherent electron waves emitted from two indistinguishable atoms leads to intrinsic interference oscillations. Cohen and Fano [1] were the first to derive the equation for the total photoionization cross section for the H_2 molecule including this YDSE effect. Subsequent theoretical [2] and experimental studies of ionization of H_2 and D_2 molecules with different projectiles were performed.

Core-level photoemission from molecules like N_2 provides a new opportunity to investigate coherent emission of photoelectron waves [3,4]). For core-level photoionization of these molecules, an additional complication appears due to the presence of the gerade and ungerade 1σ bound orbitals with a slight energy gap between them. This gap is 0.1 eV and is even smaller than the vibrational splitting of ~0.3 eV.

The experiment was carried out at the high-resolution soft X-ray photochemistry beamline **BL27SU**. The light source of the beamline is a figure-8 undulator which provides linearly polarized radiation. The photoelectron spectra were recorded using a high resolution Scienta SES-2002 analyzer. The analyzer bandwidth was set to ~31 meV. The overall bandwidth was determined separately by measuring Xe 5*p* photoelectrons at the same monochromator and analyzer settings.

Figure 1 shows the N 1*s* photoelectron spectrum recorded at photon energy of 831 eV. The experimental spectra were decomposed by least-squares curve fitting into $1\sigma_g$ and $1\sigma_u$ components with the individual vibrational progressions.

The partial cross section ratios of σ_g /σ_u for the photoionization of the 1 σ_g and 1 σ_u shells corresponding to the 0 → 0 and 0 → 1 vibrational transitions and are plotted in Fig. 2 as a function of the photoelectron momentum ***k*** in atomic unit (a.u.) in order to display clearly the oscillations. The results of previous measurements [5] are also included. The *ab initio* calculations using RPA method are compared with measurement.

At low momenta ***k*** < 1.5 a.u. the ratios are defined by the σ^* shape resonance, and only at ***k*** > 1.5 a.u. the CF oscillations become apparent. There is a good qualitative agreement between the theory and the experiment for both vibrational transitions.

The main difference between the $1\sigma_g$ and $1\sigma_u$ shells is connected with the symmetry of these states. From the dipole selection rules, only odd partial waves contribute to the photoionization of the $1\sigma_g$ shell, and only even partial waves to the $1\sigma_u$ shell. The interference modulation is mainly connected with the onset of transitions to the states of increasing orbital angular momentum at increasing photon energies, while the different parity of the photoelectron partial waves for the $1\sigma_g$ and $1\sigma_u$ shells causes the shift of interference modulation for these shells by π. Due to this, the cross section ratio $1\sigma_g$ / $1\sigma_u$ observed experimentally is greatly enhanced, although generally the interference modulation is expected to be relatively small. And the sum of the contributions from the $1\sigma_g$ and $1\sigma_u$ shells will not display any CF

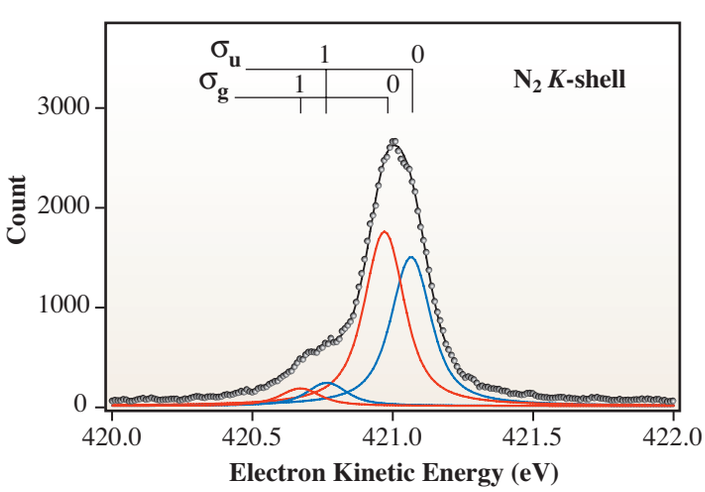

Fig. 1. Photoelectron spectrum at photon energy of 831 eV, parallel to the polarization vector.

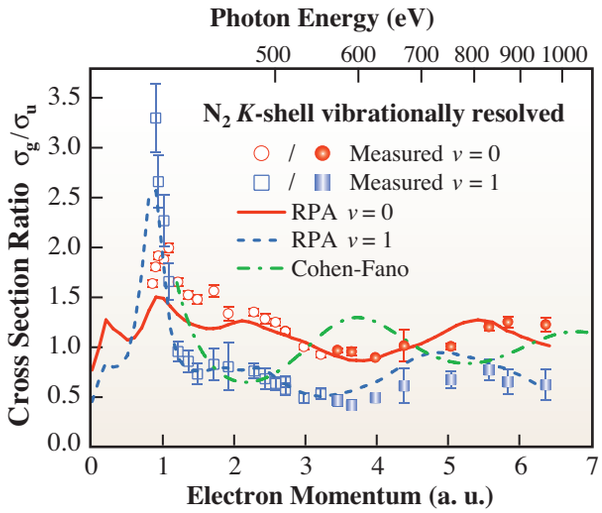

Fig. 2. Comparison of experimental cross section ratios with *ab initio* calculations.

oscillations.

From another point of view, at high electron kinetic energy with the plane wave approximation, the original CF interference pattern is shown in Fig. 2 as the dash-dotted line. Apparently, the phase of the interference pattern is shifted from both the experimental and *ab initio* ones.

To explain this disagreement, we take the sum over the vibrational components for the experimental spectra and obtain the ratios as shown in Fig. 3. By the multiple scattering theory, the Cohen-Fano interference pattern is shifted by twice the phase of the photoelectron scattering by the neighboring N atom. Taking the reported value of phase shift, we obtain the dash-dotted line in Fig. 3. The agreement with the experiment is improved in comparison with the original Cohen-Fano approach but it is still far from being fair. We can obtain the improved value of the scattering phase using a least-squares fitting, shown as the solid line in Fig. 3.

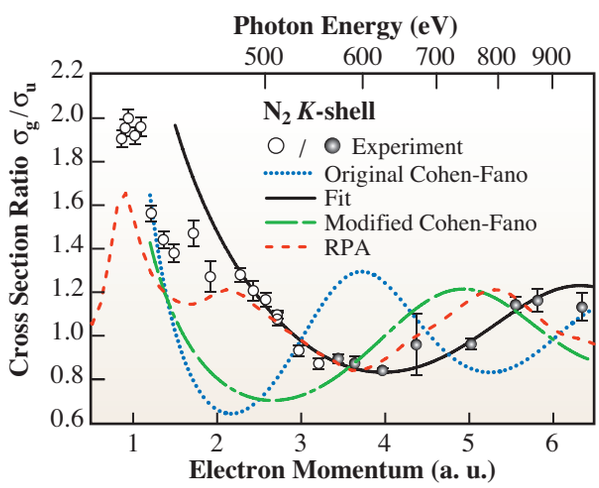

Fig. 3. Ratios of $1\sigma_g$ and $1\sigma_u$ partial photoionization cross sections of N_2 summed over the vibrational components.

X.-J. Liu*, N.A. Cherepkov, F. Gel'mukhanov and K. Ueda

Institute of Multidisciplinary Research for Advanced Materials, Tohoku University

*E-mail: xiliu@mail.tagen.tohoku.ac.jp

Reference

[1] H.D. Cohen and U. Fano: Phys. Rev. **150** (1966) 30.
[2] O.A. Fojón *et al.*: J. Phys. B: At. Mol. Opt. Phys. **37** (2004) 3035.
[3] D. Rolles *et al.*: Nature **437** (2005) 711.
[4] *X.-J. Liu, N.A. Cherepkov, S.K. Semenov, V. Kimberg, F. Gel'mukhanov, G. Prümper, T. Lischke, T. Tanaka, M. Hoshino, H. Tanaka and K. Ueda: J. Phys. B* ***39*** *(2006) 4801.*
[5] M. Ehara *et al.*: J. Chem. Phys. **124** (2006) 124311.

Discontinuous Reorientation of Crystal Lattice and Its Relation to Higher-order Structure Changes in Drawing Process of Polyethylene Fibers

Crystalline polymers, in general, show a complicated aggregated structure composed of stacked lamellae in a hierarchical structure system. It is important to know how such complicated structure changes their features in the deformation process for a deeper understanding of the mechanical properties of polymer materials. So far, the most polymer structural studies for deformation had been about materials with a random distribution of crystalline lamellae [1], and the results, therefore, had not enabled us to reach a conclusive explanation about the mechanical deformation mechanism. It is a good idea to employ a polymer sample with preferentially-oriented lamellar structure to trace the behavior of each lamella in the deformation process. One typical polymer giving such preferential orientation is a polyethylene (PE) sample produced by spinning the melt during the natural cooling process. This sample possesses a relatively high degree of the crystallographic *a*-axial orientation along the fiber axis. We carried out *in situ* and simultaneous measurements of wide-angle (WAXD) and small-angle X-ray scatterings (SAXS) and Raman scattering at beamline **BL40B2**. Consequently, we discovered discontinuous *a*-to-*c*-axial reorientational behaviors of the orthorhombic crystal lattice and its relation to the higher-order structural changes in the cold drawing process of preferentially-oriented PE fibers.

Figure 1 shows time-resolved WAXD and SAXS patterns during the deformation of an *a*-axially-oriented low-density PE (LDPE) sample. The intensity distributions of WAXD are also shown for 110 and 200 reflections as a function of azimuthal angle. As seen in the figure, the *a*-axis oriented along the fiber direction (90°) before stretching. But when a sample was stretched slightly, the intensity distribution was swapped in the direction perpendicular to the fiber axis (0°). During stretching, X-ray intensities were observed around only 0° and 90° direction areas and no intermediate state was observed. This is the first experimental evidence of a discontinuous transition between the two types of crystal lattice with mutually perpendicular orientation structure (refer to Fig. 2). It should be noted that such a discontinuous

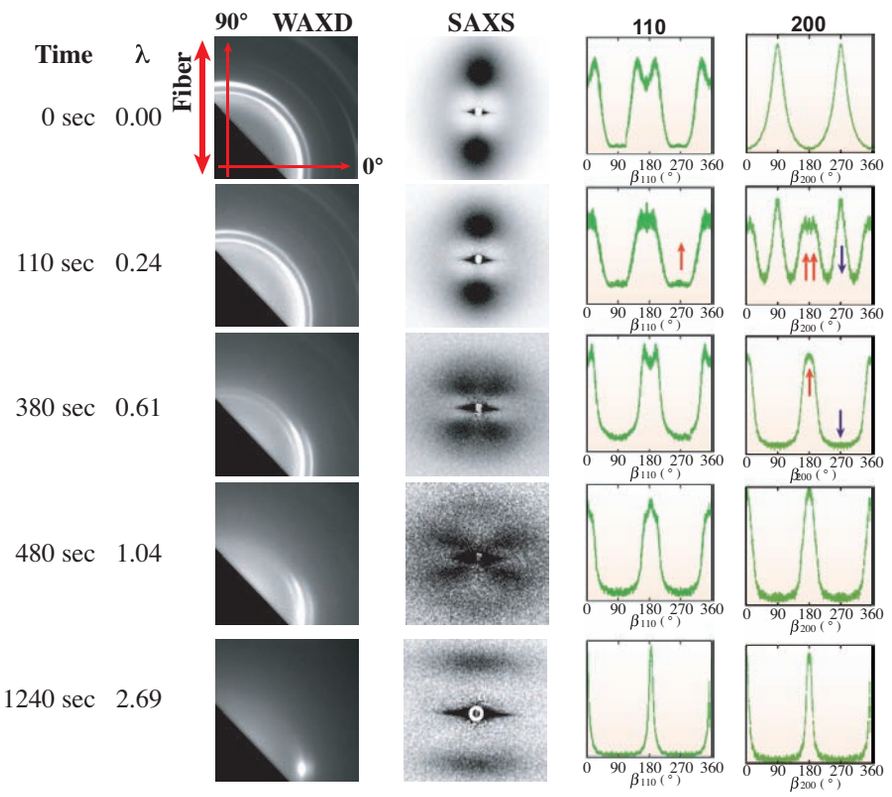

Fig. 1. WAXD and SAXS patterns change of the *a*-axially-oriented low-density polyethylene fiber during the mechanical deformation process under tension. The intensity changes of 200 and 110 X-ray reflections are also indicated with respect to the azimuthal angle β, where β = 0° and 180° correspond to the fiber direction.

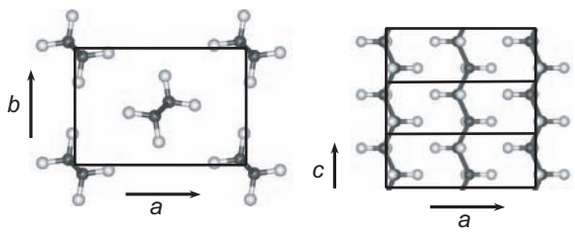

Fig. 2. Crystal structure of orthorhombic polyethylene.

reorientation of the crystal lattice occurs before the start of a remarkable deformation of lamellar stacking structure as seen in the observed SAXS patterns.

In the middle stage of sample stretching, the SAXS pattern changed from a 2-point meridional pattern to a 4-point scattering pattern, indicating the slippage of the neighboring lamellae by shearing stress. This slippage angle was increased up to 60° (see Fig. 3). In the mean time, the long period of the lamellar sequence increased continuously from 160 Å to 360 Å.

In the final stage of stretching, a necked zone appeared in the fiber sample, and then the additional outer 4-point pattern was observed in SAXS pattern.

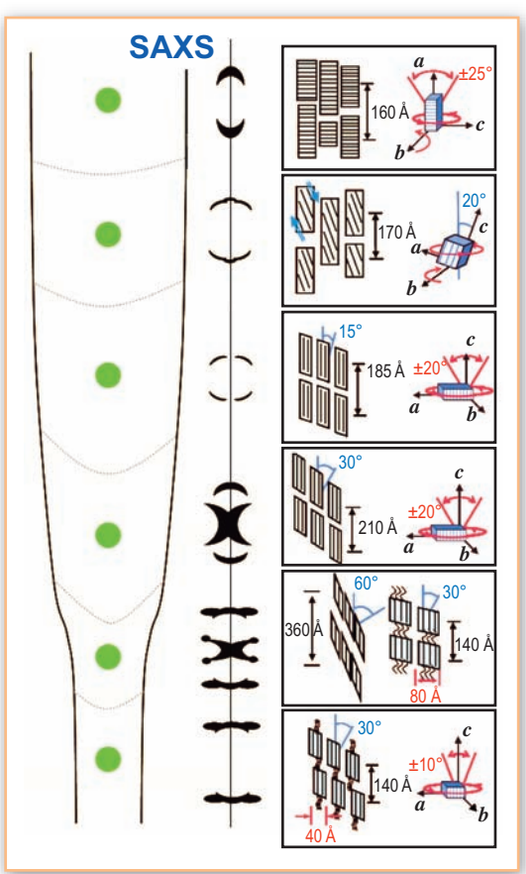

Fig. 3. Schematic illustration of the reorientation of crystal lattice and the stacked lamellar structure change in the cold drawing process of the *a*-axially-oriented low density polyethylene fiber. The SAXS pattern change is also given for reference.

These outer peaks correspond to a lamellar long period of 140 Å, which has no longer systematic relationship with the long period found at the middle stage. We, therefore, interpret these observations as an indication that the already-existing lamellar structure is melted, followed by recrystallization as a new fibrillar structure under the tensile force.

Figure 3 shows a schematic illustration determined from this experiment for the structural changes in the crystal lattice and stacked lamellar structure at various positions in the necked sample. In the proposed structural model, the *discontinuous and almost perpendicular* reorientation from the *a*-axis to the *c*-axis is shown at an early stage of stretching where the magnitude of lamellar deformation is quite slight. One of the promising scenarios to explain this deformation mechanism is that a kinked structure in the extended zigzag chains might be formed through the trans-to-gauche exchange motion under shearing stress as illustrated in Fig. 4. The scenario we suggested shall have an outcome in which this kinked part grows gradually to form the crystal lattice domain with a *c*-axial orientation along the stretching direction with an increase of strain.

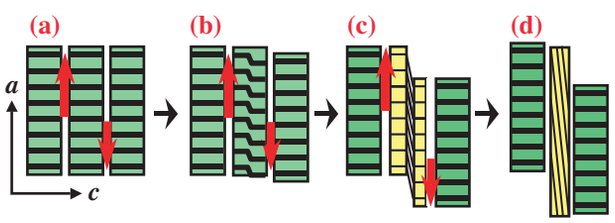

Fig. 4. Schematic illustration of the transformation from the *a*-axially-oriented structure to the *c*-axially-oriented structure in the tensile deformation process, which is assumed to be caused by a generation of kinked structures within the lamella by the action of shearing stress.

Kohji Tashiro*, Shinichi Takeda and Makoto Hanesaka

Department of Future Industry-Oriented Basic Science and Materials, Toyota Technological Institute

*E-mail: ktashiro@toyota-ti.ac.jp

References

[1] T. Sakurai *et al.*: Polymer **46** (2005) 8846.
[2] *K. Tashiro, S. Takeda, M. Hanesaka, H. Masunaga, S. Sasaki, K. Ito and M. Takata: Polym. Prepr. Jpn.* ***56*** *(2007) 3953.*

Liquid Structure of Room Temperature Ionic Liquids Revealed by High-energy X-ray Diffraction and Molecular Dynamics Simulation

Room temperature ionic liquids (RTILs), which are solely composed of ions and have melting points below 100 °C, have environmentally friendly properties, such as that they are practically non-volatile and non-flammable. Thus, RTILs have attracted attention as the alternative to volatile organic solvents. In addition, they are expected to be superior materials for electrochemical devices with high-energy density due to their high conductivity and wide electrochemical window [1]. On the other hand, from the viewpoint of fundamental science, the understanding of structure and dynamics is still insufficient, although the studies on their physics and chemistry have been rapidly in progress. It is thus necessary to reveal the liquid structure at a molecular level.

X-ray diffraction is an essential tool to probe atomic arrangements in liquid and amorphous materials. However, it is not easy to reveal complicated structures in RTILs with enough real-space resolution using low energy X-rays from conventional X-ray sources. In fact, little has been published on the RTILs study by X-ray diffraction [2]. A high-energy X-ray diffraction experiment (HEXRD) covering a wide scattering vector and thus achieving high real-space resolution is one of the solutions to overcoming the problem [3]. Moreover, one can extract chemically valuable atom-atom correlations from the experimental correlation function with the aid of reliable molecular simulations [4]. It is also necessary to clarify in advance the flexibility of the ions [5]. We demonstrated the liquid structure of typical RTILs, 1-ethyl-3-methylimidazolium bis-(trifluoromethanesulfonyl) amide EMI^+TFSA^- and *N*-propyl-*N*-methylpyrrolidinium bis-(trifluoromethanesulfonyl) amide $P_{13}^+TFSA^-$ (Fig. 1) as revealed by a combination of HEXRD experiments and molecular dynamics (MD) simulations.

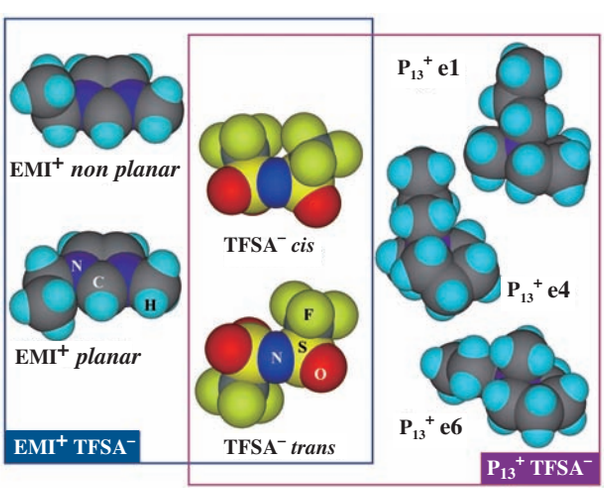

Fig. 1. Optimized geometries at the B3LYP/6-311G(d,p) level of theory for the isomers of ions composing RTILs examined in this study. All isomers exist in equilibrium in the respective ionic liquid as revealed by Raman spectroscopy, DFT calculations, and MD simulations. (Ref. [4] and Ref. [5])

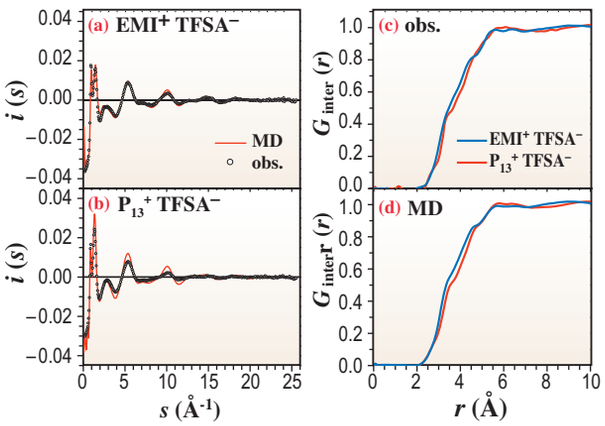

Fig. 2. X-ray structure factors **(a)** for EMI^+TFSA^- and **(b)** for $P_{13}^+TFSA^-$, and **(c)** X-ray weighted inter-molecular correlation functions obtained from HELAXS experiments (window function $W(s) = \exp(-Bs^2)$; B = 0.011 was used in Fourier transformation) and **(d)** derived from MD simulations with an *NTP* ensemble, $N = 256$ ion pairs, $T = 298$ K, and $P = 1$ atm.

The HEXRD experiments were carried out at **BL04B2**. Observed total X-ray interference functions $i^{HEXRD}(s)$ for the respective ionic liquids are shown in Fig. 2. The total X-ray interference functions can be expressed as the sum of the intra-molecular $i^{HEXRD}_{intra}(s)$ and the inter-molecular X-ray interference functions $i^{HEXRD}_{inter}(s)$; $i^{HEXRD}(s) = i^{HEXRD}_{intra}(s) + i^{HEXRD}_{inter}(s)$. $i^{HEXRD}_{intra}(s)$ can be estimated by knowing appropriate geometries and distributions of the conformational isomers of the ions (see Ref. [5]). By subtracting thus estimated $i^{HEXRD}_{intra}(s)$ from $i^{HEXRD}(s)$, $i^{HEXRD}_{inter}(s)$ was evaluated and Fourier transformed to yield the inter-molecular correlation function $G^{HEXRD}_{inter}(r)$. As shown in Fig. 2, $G^{HEXRD}_{inter}(r)$ for both ionic liquids shows bumps around 3.4 Å ascribable to the first neighbor atom-atom correlations (except proton) between cation and anion. It should be noted that $G^{HEXRD}_{inter}(r)$ for the EMI^+TFSA^- appears on the evidently shorter side relative to that for the $P_{13}^+TFSA^-$. This fact suggests that the inter-molecular interaction between EMI^+–$TFSA^-$ is stronger than that between P_{13}^+–$TFSA^-$. More favorable ion-ion interaction in the imidazolium ionic liquids relative to the pyrrolidinium ones has been proposed in terms of dynamics by Watanabe *et al.* [6]. HEXRD provides the direct structural evidence for this at a molecular level.

Total X-ray interference functions derived from the simulations $i^{MD}(s)$ for both ionic liquids are also shown in Fig. 2. The interference functions are in good agreement with experimental ones, indicating that the liquid structure can be satisfactorily reproduced by simulations. X-ray weighted inter-molecular pair correlations derived from simulations $G^{MD}_{inter}(r)$ are

shown in Fig. 2. It is clearly shown by $G^{MD}_{inter}(r)$ that peaks at *ca.* 3.5 Å define the closest atom–atom distance between the cation and anion.

Figure 3 displays the partial atom-atom pair correlation functions between the carbon in the cation and the oxygen $g_{Cn\text{-}O}(r)$ or the fluorine $g_{Cn\text{-}O}(r)$ in the anion. As clearly shown in Fig. 3, for both ionic liquids, the cations favor the oxygen rather than the fluorine as an interaction site on the anion. This fact suggests that the electrostatic force predominantly operates in the ion-ion interaction with the oxygen in $TFSA^-$, while van der Waals force contributes significantly to the inter-molecular interaction at the fluorine rather than the electrostatic one.

With EMI^+TFSA^-, the most intense peak appears in the $g(r)$ of C6–O, followed by the sharpest one with the lowest position in the $g(r)$ of C2–O. It should be emphasized that the *N*-methyl group in EMI^+TFSA^- has a significant role in the inter-molecular interaction. On the other hand, the fluorine in $TFSA^-$ favors the C6 and the C9 carbons. With P_{13}^+, most intense peak is found in the correlation between the *N*-methyl carbon and the oxygen in $TFSA^-$. It should be noted that the inter-molecular atom-atom correlations of the *N*-methyl group and oxygen for both ionic liquids are similar to each other.

The spatial distribution function (SDF) shown in Fig. 4 is useful to reveal the ion–ion interactions from the other aspect. Significantly, the spatial distributions for EMI^+TFSA^- are found to be more or less asymmetric compared with those for $P_{13}^+TFSA^-$. An asymmetric spatial distribution in the ion-ion interaction may increase the configuration entropy in the liquid state, which causes a lowering of the melting point. Actually, the melting point for EMI^+TFSA^- (–20 °C) is lower than that for the other (10 °C), although the ion–ion interaction for EMI^+TFSA^- is stronger in the liquid state. It is also clearly found in the SDFs that the liquid structure of the respective ionic liquid is different from each other. The structural differences may be related to the diverse dynamic properties of the ionic liquids such as larger diffusion coefficients for the imidazolium ionic liquids relative to the pyrrolidinium ionic liquids [6]. However, the liquid structure – dynamics relationship of the ionic liquids is not clear at the present stage. Thus, further investigation is now in progress.

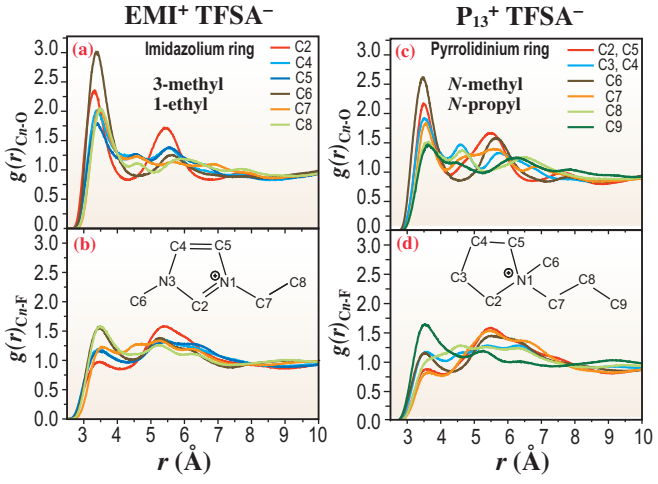

Fig. 3. Partial atom-atom pair correlation functions **(a)** of C*n* - O and **(b)** C*n* – F for EMI^+TFSA^-, and **(c)** and **(d)** for $P_{13}^+TFSA^-$. Panels **(c)** and **(d)** represent the same pair as panels **(a)** and **(b)**.

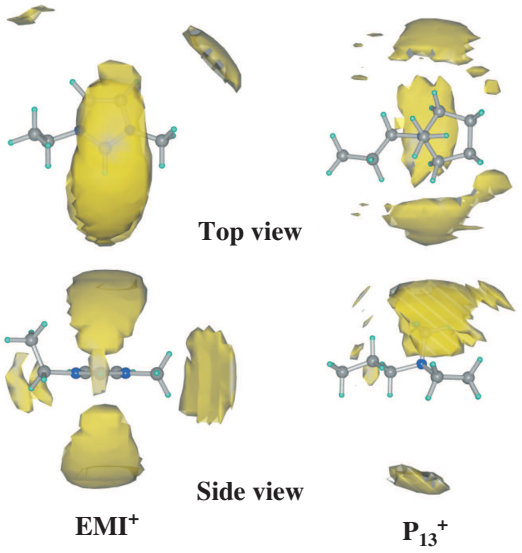

Fig. 4. Spatial distribution functions of the center of mass of $TFSA^-$ around C2 of EMI^+TFSA^- (right) and around the nitrogen of $P_{13}^+TFSA^-$ (left). Yellow clouds around the cation correspond to the isoprobability surface for the center of mass of $TFSA^-$.

Yasuhiro Umebayashi [a,*], Shuhei Fukuda [a], Yasuo Kameda [b], Shinji Kohara [c]

[a] Department of Chemistry, Kyushu University
[b] Department of Material and Biological Chemistry, Yamagata University
[c] SPring-8 / JASRI

*E-mail: yumescc@mbox.nc.kyushu-u.ac.jp

References

[1] H. Ohno: Electrochemical Aspects of Ionic Liquids, John & Wiley Sons, Inc., Hoboken, New Jersey, (2005).
[2] M. Kanakubo *et al.*: J. Phys. Chem. B **109** (2005) 13847.
[3] R. Hagiwara *et al.*: J. Non-Cryst. Solids **312-314** (2002) 414.
[4] K. Fujii *et al.*: J. Phys. Chem. B **112** (2008) 4329.
[5] J.N.C. Lopes *et al.*: J. Phys. Chem. B **112** (2008) 1465.
[6] H. Tokuda *et al.*: J. Phys. Chem. B **110** (2006) 2833.
[7] *Y.Umebayashi, S. Fukuda, T. Yamagichi, K. Fujii, S. Seki, J.N.C. Lopes, A.A. H. Padua, S. Kohara, Y. Kameda, S. Ishiguro: J. Phys. Chem. B, to be submitted.*

Exciton Properties of Organic Molecules Revealed by Inelastic X-ray Scattering

Organic optical materials attract much attention because of their important applications in light emitting devices, biosensors, and nonlinear optical devices among many others [1]. As the optical processes are largely dominated by excitonic excitations in these materials, it would greatly benefit the material design if one knew the location of excitons in molecules, and how the movement of an exciton is correlated with the local structure. To study these properties, one needs momentum resolved information. For the first time, we have performed inelastic X-ray scattering (IXS) on an organic molecular crystal using beamline **BL12XU** [2]. IXS is one of most powerful experimental method for investigating electronic excitations. Unlike conventional techniques such as absorption and Raman scattering, IXS can provide both energy and momentum resolved information. Moreover, unlike electron energy loss spectroscopy, IXS can work well in the high *q* region. These advantages are crucial for studying exciton behavior in organic molecules with complex local structures. The present target material is the open-ring photomerocyanine form of spirooxazines (Py-SO, $C_{21}N_4O_2H_{22}$). One unit cell of the Py-SO crystal is shown in Fig. 1.

Figure 2(a) shows the IXS data with momentum transfer *q* along the a axis. After Raleigh background subtraction, three distinct features were found around 2.2 eV (I), 4.6 eV (II) and 6.6 eV (III) as shown in Figs. 2(b) and 2(c). A weak feature II' also can be observed in Fig. 2(c). The spectral features are identified as the optically excited singlet excitons (I, II, II') and interband transitions (III). Based on the ZINDO/SCI method [3,4], the calculated IXS spectra are shown in Fig. 2(d) for a molecular aggregate of a six-unit-cell stack with the shortest intermolecular separations. There is almost a one-to-one correspondence between the experimental features I-III and theoretical features A-C. The energy centroid positions of features B, B' and C coincide with those of features II, II' and III, respectively. Both feature C and D involve many excitations. Correspondingly, the spectra in the experiment exhibit a very broad feature III followed by rising spectral weight. The experimental feature I disperses from 2.2 eV to 2.07 eV. This is well reproduced in the theoretical spectra, except that the calculated position is about 0.48 eV higher. The small exciton dispersion reflects the weak intermolecular coupling. In the aggregate calculation, the strongest intermolecular coupling is estimated to be 55 meV. Therefore, the excitons are still Frenkel excitons that are confined mostly in a single molecule. As a result, single molecule excitations could be computed to study the local distribution of the electrons and holes. Figure 2(e) shows the IXS spectra calculated for molecular excitations of a single Py-SO molecule, where energy levels of excited states are indicated by straight lines. As expected, the spectra are very similar to the aggregate calculations. The energy gap between LUMO and HOMO is calculated to be 5.62 eV, denoted by the dashed line. Moreover, calculation shows that feature A corresponds to a discrete exciton. Feature B contain mostly two excitons, and features C and D are made up of tens of excitations above the gap. For further confirmation, IXS spectra were also measured for momentum transfer perpendicular to the *a* direction in the *ac* plane, which also shows good agreement with the theoretical calculation. The fact that the theoretical calculation based on a single molecule shows good agreement with the experimental data indicates that the exciton distribution within the molecule is well captured as a result of the weak coupling between the molecules.

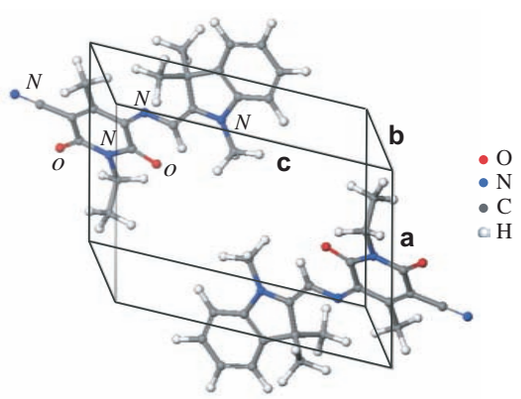

Fig. 1. A unit cell of a Py-SO molecular crystal.

Figures 3(a) – 3(e) are exciton wave functions presented in a way that the false color scale indicates the possibility P(x, y) for finding an electron at atom site x and a hole at atom site y. The gray scale of the solid circles in the inset shows the possibility P(x) = Σ_yP(x, y) of finding the electron or hole at site x on the Py-SO molecule. For feature A, the exciton is mostly situated in the middle region. For feature B, on the other hand, both of the two main excitons are extended over the entire molecule and are much larger than the lowest energy exciton (Figs. 3(e) and 3(f)). For comparison, the two main inter-gap excitations of feature III are shown in Figs. 3(g) and 3(h): one is considerably localized in the phenyl ring; the other is extended.

We have exploited IXS to study exitons in an

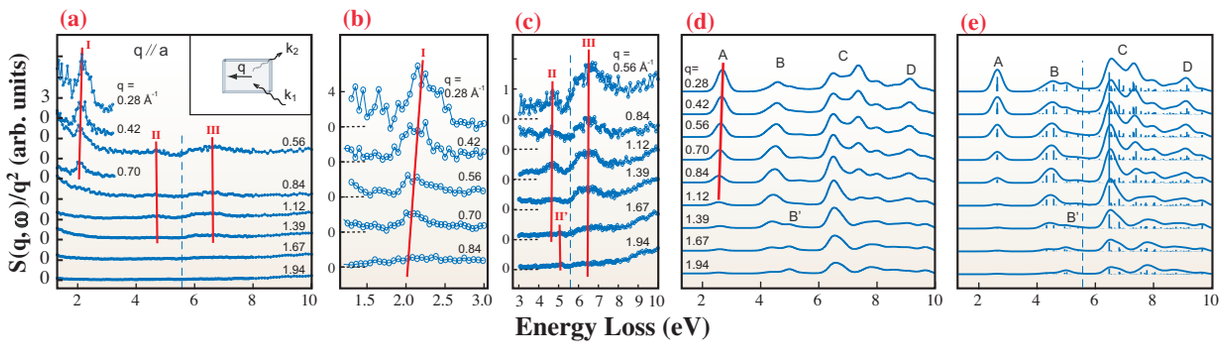

Fig. 2. **(a)** IXS data of Py-SO with q along the a axis. The spectral intensities are divided by q^2. **(b)**, **(c)** enlargements of spectra shown in **(a)** with the elastic line removed. ZINDO/SCI simulated spectra for q along the a axis based on **(d)** the aggregate and **(e)** a single molecule. The dashed lines in panels **(a)**, **(c)**, and **(e)** indicate the calculated HOMO-LUMO gap energy.

organic molecular crystal for the first time. The experimental results are free of multiple scatterings and therefore can be directly compared with theory. The dispersion of the exciton is retrieved from IXS for the first time and gives a good measure of the strength of intermolecular coupling. Combined with suitable quantum chemical calculations, reliable and comprehensive properties of excitons can be obtained, which are crucial for understanding their optical properties and for designing materials of desired optical properties based on exciton transfer or dissociation properties.

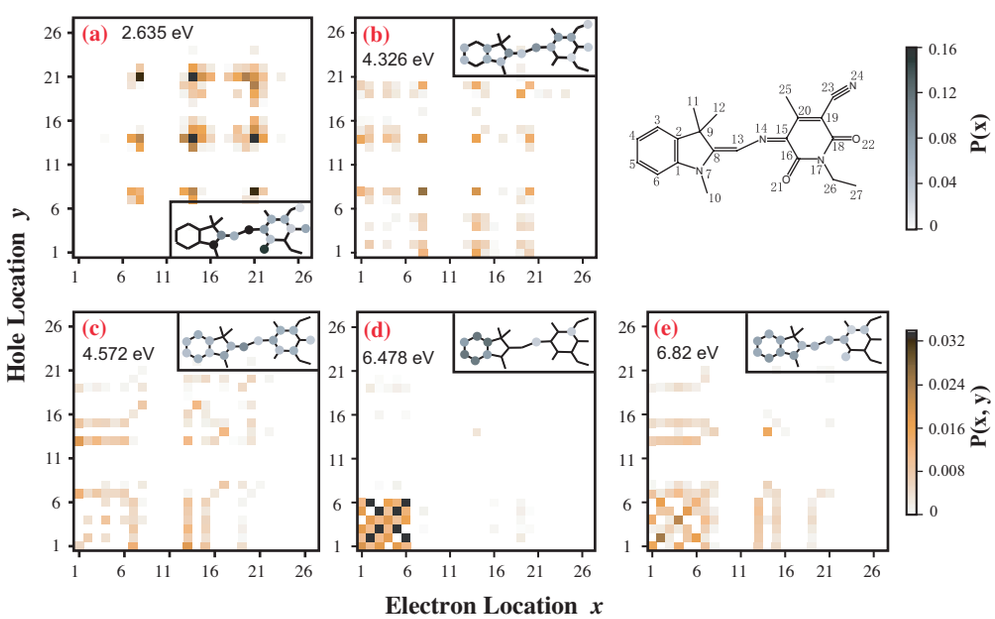

Fig. 3. False color plots for the calculated possibility P(x,y) for **(a)** the lowest energy exciton; **(b, c)** two main excitations of feature B; **(d, e)** two main excitations of feature C. The atom sites are numbered in the top right corner. The atoms plotted in gray scale in the inset represent P(x).

Ke Yang [a,†], Donglai Feng [a,*] and Yong Q. Cai [b]

[a] Department of Physics, Fudan University, China
[b] National Synchrotron Radiation Research Center, Taiwan ROC

*E-mail: dlfeng@fudan.edu.cn

† Present address: SPring-8 / JASRI

References

[1] J.J.M. Halls *et al.*: Nature (London) **376** (1995) 498; C.J. Brabec *et al.*: Adv. Funct. Mater. **11** (2001) 15.
[2] *K. Yang, L.P. Chen, Y.Q. Cai, N. Hiraoka, S. Li, J.F. Zhao, D.W. Shen, H.F. Song, H. Tian, L.H. Bai, Z.H. Chen, Z.G. Shuai and D.L. Feng: Phys. Rev. Lett.* ***98*** *(2007) 036404.*
[3] G.R. Hutchison *et al.*: J. Phys. Chem. A **106** (2002) 10596.
[4] L.P. Chen *et al.*: Synthetic Metals **157** (2007) 670.

EARTH & PLANETARY

"Nemunoki" - Persian silk tree

"Noibara" - Multiflora rose

SCIENCE

Synchrotron radiation techniques available at SPring-8 have opened new directions of research in Earth and Planetary Sciences ranging from the solar system to Earth's core, and outstanding results, including numerous breakthroughs, have been achieved since the beginning of public use in 1997. The rapid growth in research on Earth and planetary materials has been made possible by the development and upgrading of X-ray techniques, and analytical methods based on third-generation synchrotron radiation such as diffraction, spectroscopy, scattering, and imaging. All the scientific instrumentation and techniques at the beamlines have also been constantly upgraded for each specific application to their current state-of-the-art level.

In the present issue, we have chosen some representative studies in the categories of Earth and Planetary Science: volcanology and high-pressure research on Earth's core. The first topic by Nakamura *et al*. is volcanic textures studied by three-dimensional X-ray microtomography. They observed networks of shear-induced bubbles in a sheared rhyolitic sample. The result can provide an understanding of the mechanism of degassing that controls the type of volcanic eruption. The next two topics on the high-pressure and high-temperature research of Earth/planetary core materials are presented by Tsuno *et al*. and Sata *et al*., who carried out X-ray radiography observations using the multianvil apparatus and X-ray diffraction experiments in a laser-heated diamond-anvil cell, respectively. The last topic by Murakami *et al*. is a study on a newly developed simultaneous measurement system using a laser-heated diamond-anvil cell, which consists of X-ray diffraction and Brillouin scattering spectroscopy. This developed system enables us to investigate the elastic properties and seismic wave velocity data of materials deep in the Earth because it provides strong constraints for the global seismic model of the Earth.

Yasuo Ohishi

Microstructure of Bubbles in Flowing Magma

Since bubble growth and expansion in magmas are the driving forces of violent volcanic eruptions, the mechanism of degassing (outgassing) has been a central topic in volcanology. In the last two decades, the permeable gas-flow hypothesis has been widely accepted as an explanation of the degassing of viscous silicic magmas, in which bubbles scarcely rise in the time scale of eruptions. As magma ascends, the solubility of volatiles decreases and the bubbles expand due to decompression, resulting in an increase in magma vesicularity and the formation of foam. This foam should be highly permeable for effective degassing. A recent experimental study showed, however, that the simple decompression process yields very low permeability ($<10^{-16}$ m^2) until the vesicularity reaches *ca.* 70% (i.e., until the magma rises to a depth of a few hundred meters), because the melt films separating the bubbles remain unbroken and hinder the coalescence of bubbles [1]. Compared with the results of conduit flow modeling, this depth may be too shallow to result in nonexplosive eruptions. This suggests that an additional mechanism is necessary for vesiculated magmas to become permeable in deeper volcanic conduits. In this study, we experimentally investigated the effect of shear strain on the bubble microstructure and found that the interconnectivity of the bubbles is drastically enhanced by shear strain in flowing magmas.

We have performed a series of deformation experiments of vesiculated rhyolitic melts using an originally developed, torsion-type, high-temperature deformation apparatus [2,3]. Cylindrical obsidian samples (0.5 wt% water content) of *ca.* 4.7 mm in diameter were placed in a graphite container and sandwiched between the upper and lower pistons. The sample was then heated to 975°C in 50 minutes, kept at this temperature for 3 – 5 minutes for vesiculation, twisted by rotating the lower piston at 0.3 – 0.5 rpm for up to 10 rotations (R) and quenched. The vesicularity of the sample was increased from *ca.* 15 to 45% by adjusting the length of the obsidian cylinder in a fixed-volume container. The melt viscosity of the sample, the maximum shear strain and the strain rate in the experiments are 2.2×10^6 Pa·s, 30 and 0.025 s^{-1}, respectively, which are comparable to those under natural conditions. Three-dimensional images of the sheared samples were obtained by X-ray microtomography at beamline **BL20B2**. The photon energy and exposure time applied were 25 keV and 0.8 s, respectively, and 750 projections were obtained in each imaging. The images are composed of 1344×1344×1024 voxels of 4.34 μm^3. Geometrical analyses of the CT images were performed for the bubbles >10 μm using an algorithm similar to that described in Ikeda *et al.* (2000) [4]. The smaller bubbles may have been affected by relaxation during quenching.

The reconstructed 3D images of the experimentally obtained products are shown in Fig. 1. With increasing strain, the coalescence of the bubbles proceeds as well as elongation of each bubble. The strain rate does not affect the results significantly, as inferred from the large capillary number of the experimental sample. An interconnected tube-like structure was formed from the outside of the sample, at which shear strain is larger than inside the sample.

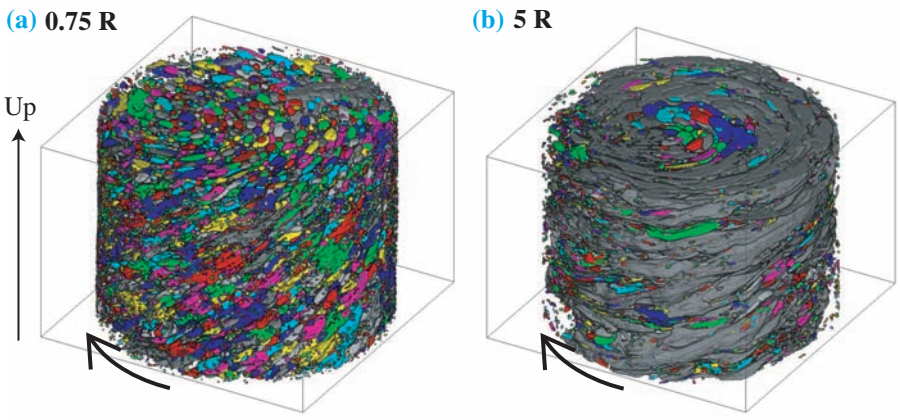

Fig. 1. 3D CT images of the samples undergoing **(a)** 0.75 and **(b)** 5 rotations (R) at 0.5 rpm. Neighboring bubbles that are not interconnected are colored differently. The gray bubble shows the largest interconnection.

The interconnectivity of the bubbles was quantified using a connectivity parameter, *C*, which is the ratio of the largest bubble volume to the total bubble volume [3]. *C* becomes unity when all the bubbles are interconnected and is potentially related to the permeability [5]. As shown in Fig. 2, *C* for the whole sample with >2.5 R begins to increase steeply at a critical vesicularity of 20 – 30% and reaches >0.8 at 40% vesicularity. The inner half of the same sample has a smaller *C* and a higher critical vesicularity than the whole sample, showing that the bubble connectivity increases with strain. The rhyolitic magma with 5 wt% initial water content achieves 40% vesicularity at a depth of *ca*. 1300 m, which is *ca*. 1000 m deeper than that in the case of isotropic vesiculation. These results suggest that the shear-induced networking of bubbles may provide a degassing pathway in deep volcanic conduits, and that the conduit geometry, which governs the shear strain, is an important factor in controlling the mode of volcanic eruption (Fig. 3).

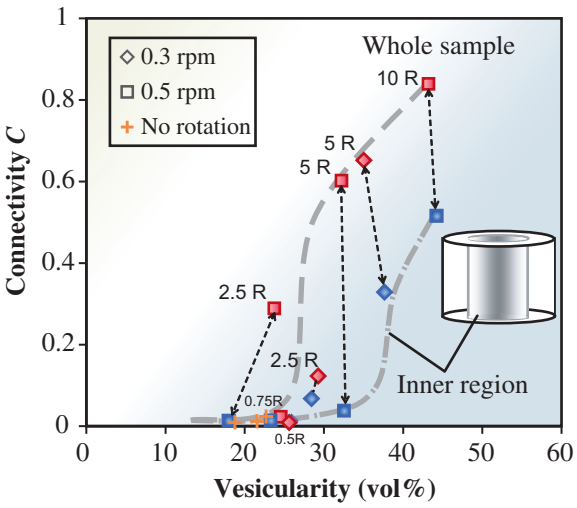

Fig. 2. The bubble connectivity starts to increase at a critical vesicularity of 20 – 30 vol% for the whole sample, whereas it is >35% for the inner region. The dashed arrows show the inner and whole regions for the same run.

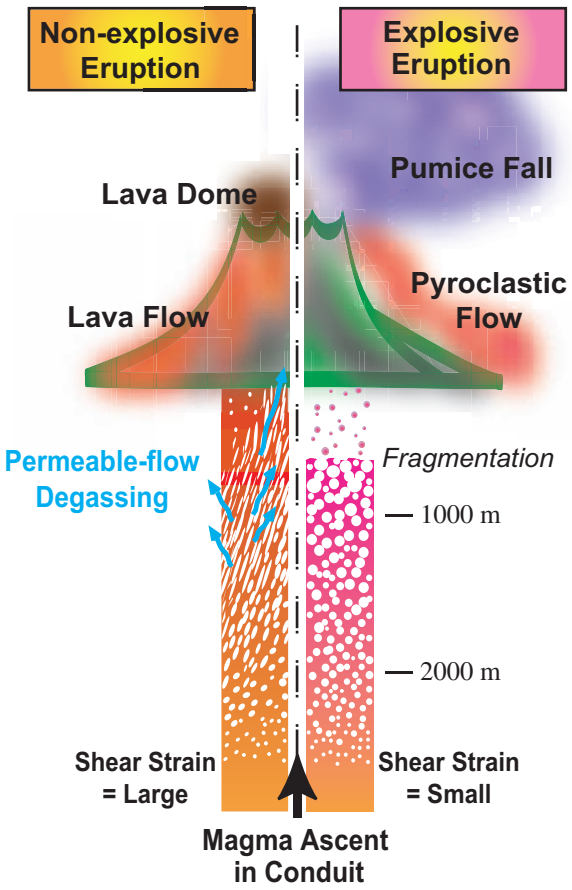

Fig. 3. A schematic diagram showing that non-explosive eruptions such as the formation of lava domes may result from permeable flow degassing through interconnected bubble networks in the flowing magma. The foamed magma under small shear strain has low permeability, which may result in fragmentation and explosive eruptions.

Michihiko Nakamura[a,*], Satoshi Okumura[a] and Akira Tsuchiyama[b]

[a] Department of Earth Science, Tohoku University
[b] Department of Earth and Space Science, Osaka University

*E-mail: nakamm@mail.tains.tohoku.ac.jp

References

[1] S. Takeuchi *et al.*: Geophys. Res. Lett. **32** (2005) L10312.
[2] S. Okumura *et al.*: Geophys. Res. Lett. **33** (2006) L20316.
[3] *S. Okumura, M. Nakamura, A. Tsuchiyama, T. Nakano and K. Uesugi.: J. Geophys. Res., doi:10.1029/2007JB005362, (2008) - in press.*
[4] S. Ikeda *et al.*: Mineral. Mag. **64** (2000) 945.
[5] M. Nakamura *et al.*: J. Volcanol. Geotherm. Res., doi:10.1016/j.jvolgeores.2008.04.011, (2008) - in press.

In situ Observation of Liquid Immiscibility in the Fe-O-S System at High Pressures and Temperatures

The Earth's liquid outer core consists of a liquid Fe-Ni alloy with 10% comprising light elements. Oxygen and sulfur are possible elements in the outer core according to geochemical arguments. Recently, seismological observations show P-wave velocity reduction 100 km underneath the core-mantle boundary, which means that an outermost layer may exist at the top of the outer core (Fig. 1) [1]. The layer may have formed if excess oxygen had been exsolved from an Fe-O-S liquid as an Fe-O ionic liquid during the cooling of the Earth. Experimental studies on phase relations in the Fe-O-S system show liquid immiscible regions at high pressures [2,3] that are composed of Fe-S metallic and Fe-O ionic liquids. The outermost core layer is closely related to the evolution of the growing Earth and the flow of the core is associated with the geodynamo.

In previous studies on the Fe-O-S and Fe-O systems (e.g., Refs. [2,3]), investigations of liquid immiscibility were based on the textural observations of the quenched products. Liquid immiscibility should be interpreted carefully because a miscible liquid passes through the stability field of immiscible liquids during quenching (e.g., Ref. [4]). Therefore, it is important to directly determine the stability fields of immiscible and miscible liquids at high pressures and temperatures. In this study, we have performed an X-ray radiography observation at a high pressure to precisely determine the immiscibility gaps of an Fe-O-S system at 3 GPa and a temperature of up to 2203 K.

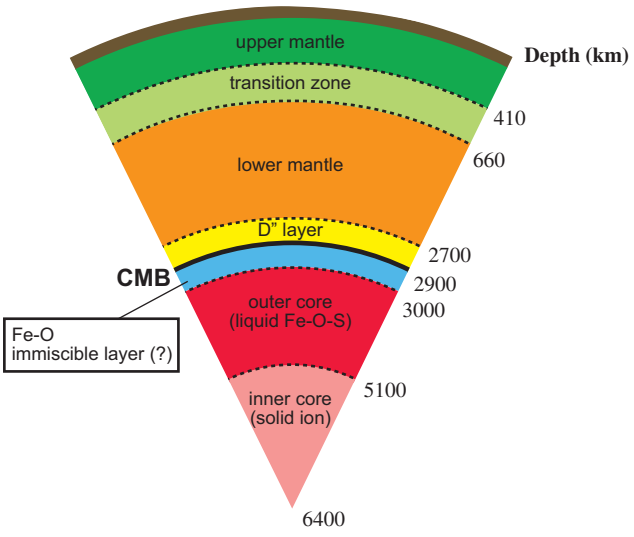

Fig. 1. The internal structure of the Earth. A 100 km layer underneath the core-mantle boundary (CMB) was suggested from a seismological observation [1].

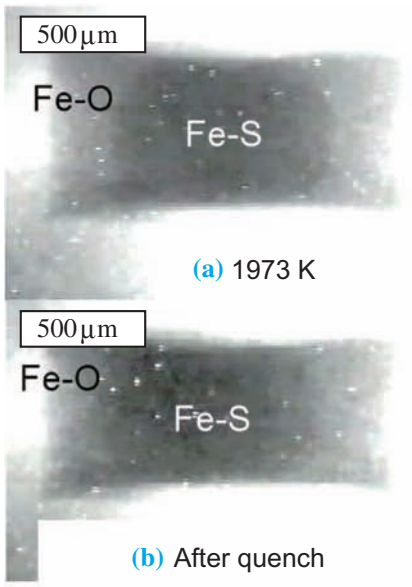

Fig. 2. X-ray radiographic images for a starting composition of $Fe_{65}O_{27}S_8$. **(a)** At 1973 K, Fe-S metallic liquid (dark gray) and Fe-O ionic liquid (light gray) were observed. **(b)** After quenching from 1973 K, two separated phases were observed.

Experiments were performed using an X-ray radiography technique, together with a 1500 ton Kawai-type multianvil apparatus (SPEED-1500) at beamline **BL04B1**. A transmitted X-ray from a sample is converted into visible light using a YAG scintillator and detected by a CCD camera. The starting materials were mixtures of Fe, FeS, and $Fe_{0.91}O$ powders with compositional ranges of 13-27% oxygen and 8-33% sulfur (in atomic ratio). A sintered Al_2O_3 capsule was used because it is less reactive with the samples than sintered MgO and hBN capsules, which are commonly used to study the reactions of liquid Fe with light element(s). Real time radiographic images were recorded as a digital file during heating and quenching. In this paper, we give the results of two representative experimental runs with starting compositions of $Fe_{65}O_{27}S_8$ and $Fe_{62}O_{23}S_{15}$ at 3 GPa.

Figure 2 shows the radiographic images for the starting composition of $Fe_{65}O_{27}S_8$. Immiscible liquids were observed at 1973 K, and two separated phases quenched from this temperature were observed. The dark and gray areas in Fig. 2 correspond to Fe-S metallic and Fe-O ionic liquids, respectively. This result shows that primary immiscible liquids can be quenched as two separated phases.

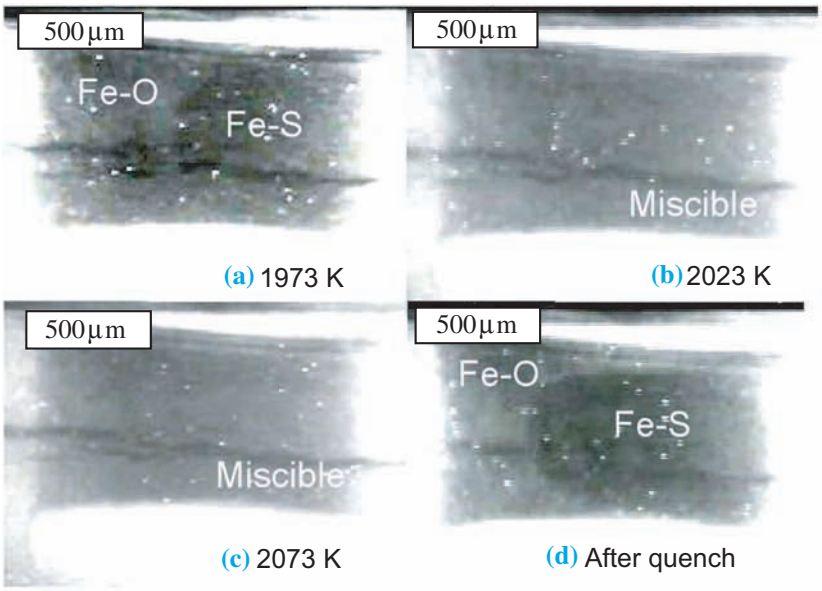

Fig. 3. X-ray radiographic images for a starting composition of $Fe_{62}O_{23}S_{15}$. **(a)** At 1973 K, Fe-S metallic liquid (dark gray) and Fe-O ionic liquid (light gray) were observed. **(b)** At 2023 K, a miscible liquid was observed. **(c)** At 2073 K. **(d)** After quenching from 2073 K, two separated phases that correspond to Fe-S metallic and Fe-O ionic compositions appeared.

Figure 3 shows the radiographic images for the starting composition of $Fe_{62}O_{23}S_{15}$. Immiscible liquids can be observed at 1973 K and these liquids became miscible at 2023 K (Fig. 3), indicating that the liquid miscibility gap closes between these temperatures. During quenching from 2073 K, the miscible liquid was suddenly separated into two phases (Fig. 3). This may be because the miscible liquid passed through the stability field of immiscible liquids during quenching.

Our results indicate that the two phases of the quenched products can be interpreted as either primary immiscible liquids or a single miscible liquid at high temperatures. Therefore, it is necessary to perform *in situ* observations to determine the precise liquid immiscibility gap. Both radiographic observations and the chemical analysis of samples from additional quenching experiments show that the liquid immiscibility gap decreases with increasing temperature at 3 GPa [5].

The light elements potentially in the Earth's core are not only oxygen and sulfur, but also silicon and carbon. In future, melting experiments in other systems, such as Fe-S-Si and Fe-S-C, will also be important for obtaining a better understanding the properties of the Earth's outer core and confirming the existence of the outermost layer in the outer core.

Kyusei Tsuno [a,b,*], Hidenori Terasaki [a] and Eiji Ohtani [a]

[a] Institute of Mineralogy, Petrology, and Economic Geology, Tohoku University
[b] Bayerisches Geoinstitut, Universität Bayreuth, Germany

*E-mail: kyusei.tsuno@uni-bayreuth.de

References

[1] S Tanaka: Earth Planet. Sci. Lett. **259** (2007) 486.
[2] S Urakawa *et al.*: Geophys. Monogr. Ser. **39** (1987) 95.
[3] *K Tsuno, E Ohtani, H Terasaki: Phys. Earth Planet. Inter.* ***160*** *(2007) 75.*
[4] V.C. Kress: Contrib. Mineral. Petrol. **127** (1997) 176.
[5] *K. Tsuno, H. Terasaki, E. Ohtani, A. Suzuki, Y. Asahara, K. Nishida, T. Sakamaki, K. Funakoshi, T. Kikegawa: Geophys. Res. Lett.* ***34*** *(2007) L17303, doi: 10.1029/GR030750.*

High-pressure B2 Phase of FeS: New High-pressure Polymorph under the Earth's Core Conditions

Properties of FeS under high pressure have been of great interest in both condensed matter physics and Earth and Planetary science. Since considerable amount of sulfur is possibly incorporated in iron-rich Earth's core (e.g. [1]), pressure-induced structural phase transitions in FeS have been extensively studied. Stoichiometric FeS has a NiAs-type (B8) related hexagonal structure (troilite, FeS I) at ambient condition. Previous experimental studies demonstrate a series of phase transitions with increasing pressure at room temperature; troilite transforms to a MnP-type structure (FeS II) above 3.4 GPa, and further to a monoclinic structure (FeS III) above 6.7 GPa. The structural change from FeS II to III involves magnetic disordering, spin transition of iron, and metal-semiconductor transition. FeS IV (hexagonal structure) and FeS V (NiAs-type structure) are also known to exist at high pressure and high temperature. Most recently, a phase transition to FeS VI was found to occur above 30 GPa and 1300 K. FeS thus exhibits a rich polymorphism, but all the known structures are closely related to the NiAs-type (B8) structure. Here we report the XRD measurements of FeS to 270 GPa and demonstrate the first experimental evidence for a structural phase transition to the B2 [2,3].

The synchrotron XRD experiments were conducted at high pressures using a diamond-anvil cell (DAC) at beamline **BL10XU**. We used synthesized polycrystalline sample of stoichiometric FeS (troilite) as the starting material. A rhenium gasket was pre-indented to 16-μm in thickness, and a hole (*ca.* 20-μm in diameter) was drilled in the center of the indentation as a sample chamber. A pelletized sample was placed between the pressure medium of MgO, which also served as thermal insulator and internal pressure standard. They were compressed by a pair of double-beveled 60-μm culet anvils up to 270 GPa. After each pressure increment, the sample was heated to less than 1300 K for *ca.* 30 minutes by a Nd:YLF laser. A monochromatic X-ray beam with a wavelength of *ca.* 0.4133 Å (30 keV) was collimated to 15- or 20-μm in diameter. Angle-dispersive X-ray diffraction (XRD) spectra were collected with an imaging plate (IP) detector or a charge coupled device (CCD) detector with a typical exposure time of 10 and 1 min, respectively. We obtained the XRD data only at room temperature.

We have collected the XRD data on FeS repeatedly with increasing pressure to 270 GPa. Below 215 GPa, the patterns were dominated by FeS VI. A new peak (2θ = 13.6°) first appeared at 186 GPa after heating approximately at 1300 K (Fig. 1). With further compression and heating at 198 and 215 GPa, the peak became more intense, although FeS VI was still dominant in these spectra. They further grew when the sample was re-pressurized at room temperature to 270 GPa. Upon subsequent heating, the pressure dropped to 233 GPa, and three other new peaks were found (Fig. 1), whereas the diffraction lines of FeS VI almost completely disappeared.

The four new peaks (Fig. 1) observed in the diffraction pattern obtained at 237 GPa can be indexed by a CsCl-type (B2) cubic unit-cell (a =

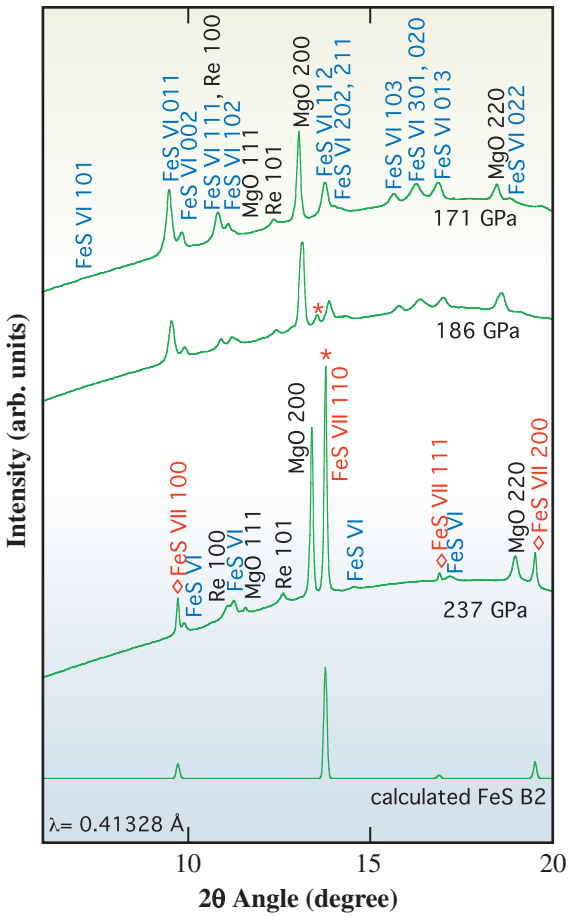

Fig. 1. XRD patterns of FeS at high pressure and room temperature. FeS VI was only observed with pressure medium (MgO) and gasket (Re) at 171 GPa. The most intense 110 peak of B2 phase first appeared at 186 GPa after heating at 1300 K. See text for details.

2.4339(3) Å). The peak intensities are also consistent with the CsCl-type structure (Fig. 1). Since the most intense 110 peak of B2 phase was not found below 171 GPa and first appeared at 186 GPa, the transition pressure from FeS VI to B2 phase (called FeS VII hereafter) was estimated to be around 180 GPa and 1300 K.

The phase transition from FeS VI to VII involves an increase in a coordination number from six to eight, and therefore a significant volume reduction is expected (Fig. 2). The volumes of FeS VII are remarkably smaller by 3.0% than those of FeS VI around 200 GPa. The Fe-S and Fe-Fe interatomic distances are 2.145 and 2.477 Å, respectively, in FeS VII at 186 GPa. These are even slightly longer than those in FeS VI; the Fe-S and Fe-Fe distances are 2.007 and 2.446 Å in average, respectively. On the other hand, the S-S distance is 2.477 Å in FeS VII, which is much shorter than that in FeS VI (2.819 Å).

Recently, a body-centered cubic (bcc) phase of Fe0.9Ni0.1 alloy was found at 225 GPa and 3400 K [4], suggesting that the Earth's inner core consists of the bcc phase. In addition, *ab initio* molecular dynamics calculations also demonstrated that the bcc phase is stabilized at the core conditions with Si or S impurity in iron. Since the bcc iron-rich Fe-Ni alloy and CsCl-type (B2) FeS adopt very similar structure, it is expected that sulfur is easily soluble in the Fe-rich bcc phase. The maximum solubility of sulfur in solid iron is limited to about 1 atomic % at 25 GPa [5] but would increase to more than 10 atomic % in bcc iron at inner core pressures (> 330 GPa), which is required to account for the seismologically observed density deficit from a pure iron at the inner core [1].

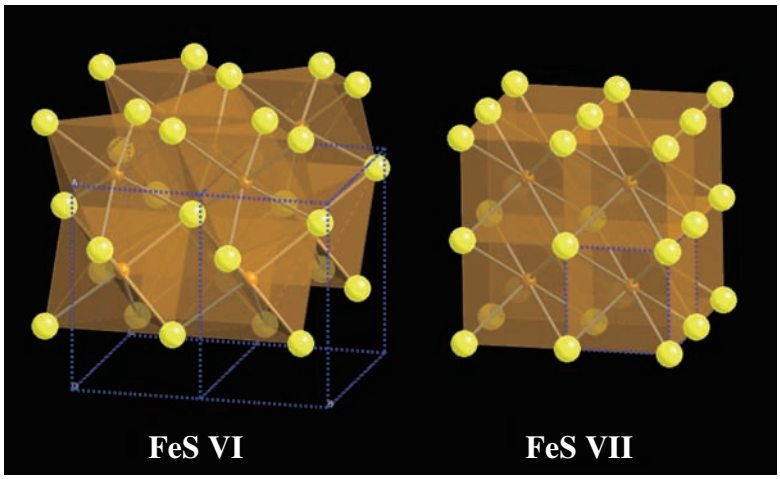

Fig. 2. Structure of FeS VI (left) and FeS VII (right). Yellow and orange spheres indicate sulfur (S) and iron (Fe), respectively. Blue dashed line indicates the unit cell. Coordination number of S to Fe increase from six in FeS VI to eight in FeS VII.

Nagayoshi Sata [a,*], Kei Hirose [b,a] and Hisao Kobayashi [c]

[a] Institute for Research on Earth Evolution, Japan Agency for Marine-Earth Science Technology
[b] Department of Earth and Planetary Sciences, Tokyo Institute of Technology
[c] Graduate School of Material Science, University of Hyogo

*E-mail: sata@jamstec.go.jp

References

[1] A. Jephcoat and P. Olson: Nature **325** (1987) 332.
[2] H. Ohfuji *et al.*: Phys. Chem. Minerals **34** (2007) 335.
[3] *N. Sata, H. Ohfuji, K. Hirose, H. Kobayashi, Y. Ohishi and N. Hirao: Am. Mineral.* ***93*** *(2008) 492.*
[4] L. Dubrovinsky *et al.*: Science **316** (2007) 1880.
[5] J. Li *et al.*: Earth Planet. Sci. Lett. **193** (2001) 509.

Development of *In Situ* Brillouin Spectroscopy at High Pressure and Temperature using Synchrotron Radiation and Infrared Laser Heating System: Application to the Earth's Deep Interior

One of the longstanding challenges in mineral physics has been the experimental determination of reliable acoustic wave velocities of deep-Earth materials under relevant high-pressure and high-temperature conditions, because the precise knowledge of sound velocity (elasticity) is essential for the interpretation of seismic observations and development of global seismological models of the Earth's interior. Considerable effort has thus been focused on the development of measurement techniques for use in high-pressure apparatuses to determine the sound velocities at high pressures and high temperatures. Recently developed and improved techniques include ultrasonic interferometry impulsive stimulated scattering, inelastic X-ray scattering and nuclear resonance inelastic X-ray scattering. However, there have been few studies on sound velocities under lower mantle conditions (above ~25 GPa in pressure and ~1900 K in temperature) because of the experimental difficulties.

A combined diamond anvil cell with Brillouin spectroscopy and synchrotron radiation X-ray diffraction enables the simultaneous measurements of sound velocities and materials density at a high pressure and temperature. This information allows us to determine elastic properties such as bulk and shear moduli, and their pressure and temperature derivatives. Simultaneous measurements under pressure and temperature conditions of the lower mantle and, in particular, achieving the high temperature, are, however, still a technical challenge. The application of resistive heating in a DAC, which is the conventionally used technique for the Brillouin method, normally works well below 10 GPa and 1000 K for simultaneous measurements [1]. A major disadvantage for resistive heating, which can produce temperatures of ~1500 K at most, is generating the higher temperatures of the lower mantle. An infrared laser heating technique, which can potentially generate temperatures over 3000 K at higher pressures, would be a more suitable alternative.

In order to meet all the requirements for simultaneous sound wave velocity measurements and sample characterization under lower mantle conditions, a Brillouin scattering measurement system that uses an infrared laser heating technique was recently installed at beamline **BL10XU** [2]. This system consists of three optical components used for Brillouin spectroscopy, X-ray diffraction and infrared laser heating (temperature measurement). For the simultaneous measurements, all optical probes for these three components must converge on the sample without optical and physical interference. The data obtained from each component is extracted by simultaneous and independent detector/analyzing systems. In this measurement system, a DAC mounted on a XYZθχαβ multiaxial stage is placed in the corner with a 150° angle of a pentagonal optical bench of a Brillouin measurement system (Fig. 1). An incident diode-pumped laser focused to ~20 μm in diameter is introduced into the sample and the scattered light is analyzed by a Fabry-Perot interferometer. A symmetric ~50° scattering angle is adopted in all experiments. The incident X-ray path in the experimental hutch is initially fixed. For simultaneous XRD measurements, the position of the DAC, which is aligned to the symmetric geometry in the optics for the Brillouin scattering measurements, must, therefore, be suitably adjusted to the X-ray independently of the Brillouin optics. For this purpose, the pentagonal optical bench used for Brillouin measurements is mounted on heavy-duty linear translation stages allowing vertical and horizontal motion (Figs. 1 and 2). This stage-scanning system enables a precise search of the exact position of the ~20 μm collimated X-ray beam and the adjustment of the sample to the X-ray position with a resolution

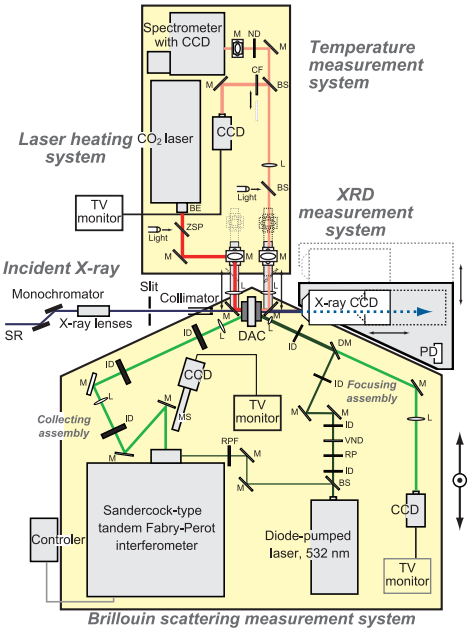

Fig. 1. Schematic layout of the Brillouin scattering measurement system combined with synchrotron radiation and infrared laser heating system of BL10XU beamline.

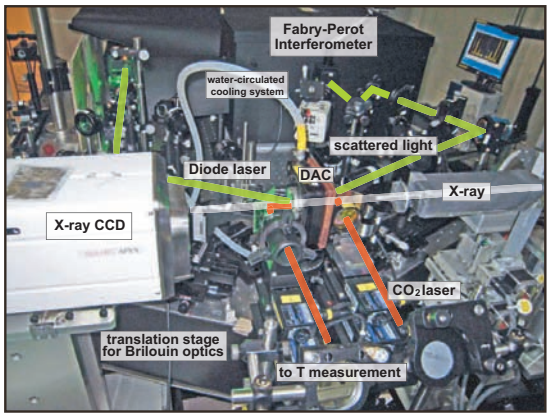

Fig. 2. View of the whole Brillouin scattering measurement system combined with synchrotron X-ray diffraction and laser heating systems at BL10XU. Green, white and red lines indicate the schematic optical paths for Brillouin scattering measurement, X-ray diffraction measurement and the laser heating system, respectively.

better than ~3 μm. A transparent sample is required for high-quality Brillouin spectra. Therefore, a carbon dioxide (CO_2) laser with a 10.59 μm wavelength is employed for the laser heating system, which can heat the transparent (colorless) oxide and silicate materials.

To evaluate the system performance and the potential capacity of this *in situ* Brillouin scattering measurement system, experiments were performed on polycrystalline, single-crystal and fluid-phase samples at high pressure and high temperature. Here we demonstrate experiments on polycrystalline MgO as a proxy of dominant mantle minerals. The experimental configuration of the DAC in this experiment is almost the same as that described in Ref. [3]. The sample mixture, placed in a rhenium gasket hole (100 μm in size), was compressed at a pressure of 45 GPa using 300 μm culet diamond anvils to, and then heated at ~2300 K for 2.5 hours to carry out Brillouin scattering measurements during heating. The sample position, once adjusted for the Brillouin scattering and X-ray diffraction measurements and CO_2 laser heating, was stable owing to the water-circulated cooling jacket used for the DAC. The size of the heating spot emitted by the visible radiation in the present experiment was a substantial proportion of the whole sample, as shown in Fig. 3. The Brillouin spectrum of polycrystalline MgO at 49 GPa and ~2300 K is shown in Fig. 4. We can recognize the shear acoustic modes of MgO and the longitudinal acoustic modes of NaCl together with the shear acoustic modes of diamond.

The infrared laser heating system is found to be highly suitable for use with this combined measurement system. Preliminary results in the present study indicate that a large variety of materials

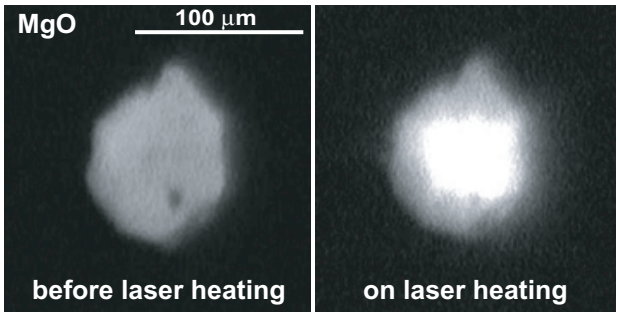

Fig. 3. Photomicrographs of polycrystalline MgO in a DAC before laser heating (at 45 GPa) and during laser heating (at ~2300 K).

such as oxides, glasses and fluids can be investigated regardless of their form (polycrystalline or single-crystal) at pressures up to 1 Mbar and temperatures up to 2300 K using our system. The present measurement system is thus a very powerful tool for providing direct information on acoustic sound velocity and elasticity data, and resolving remaining issues in mineral physics.

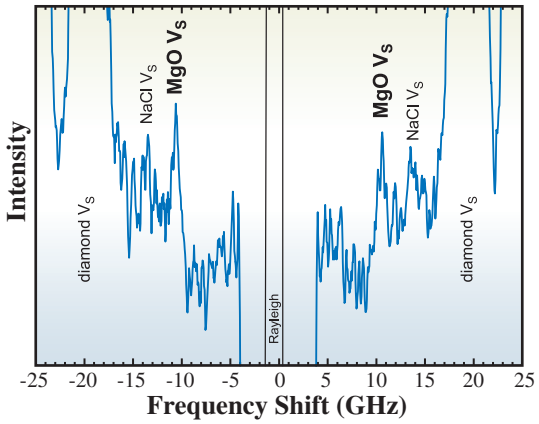

Fig. 4. Brillouin spectrum of polycrystalline MgO at 49 GPa and ~2300 K.

Motohiko Murakami †

Institute for Study of the Earth's Interior, Okayama Univ.

E-mail: motohiko@m.tains.tohoku.ac.jp

† Present address: Department of Earth and Planetary Materials Science, Tohoku University

References

[1] S.V. Sinogeikin *et al.*: Rev. Sci. Instrum. **77** (2006) 103905.
[2] *M. Murakami, Y. Asahara, Y. Ohishi, N. Hirao and K. Hirose: to be published in Phys. Earth Planet. Int. (2008).*
[3] M. Murakami *et al.*: Earth Planet. Sci. Lett. **259** (2007) 18.

ENVIRONMENTAL

"Nagamihinageshi" - Long-headed poppy

This section covers the research area concerning environmental pollutants, artificial materials used for environmental protection, such as catalysts and extractants, and natural minerals of interest in geochemistry. Since many of the samples mentioned above are in an amorphous structure, X-ray absorption fine structure (XAFS) methods can be used most effectively. In fact, all the topics in this section involve investigations by XAFS methods. The number of proposals in this research area have gradually increased, and also higher-level information about the structure and chemical state of actual

SCIENCE

samples has been increasingly required. To address this situation, more sophisticated experimental techniques have been developed and practically applied to samples as described below.

The first topic concerns Sb compounds, which are considered to be pollutants of priority interest but their geochemical and environmental behaviors were largely unknown. Mithunobu *et al*. clarified the chemical states of dilute Sb in both solid and water phases to clarify the reaction of Sb in a soil-water environment in comparison with that of As.

In the second topic, Ikeda *et al*. investigated the mechanism of adsorption and separation by resin extractants for chemical substances such as trivalent actinides (An(III)) and lanthanides (Ln(III)). An(III)/Ln(III) intergroup separation using pyridine resin depends on the counter anions in the solute. They showed that this dependence was caused by the difference in the interaction between pyridine groups with An(III) and Ln(III) ions at the atomic scale using highly reliable Ln *K*-edge XAFS spectra.

The third topic concerns the surface reaction mechanism on Pt/C cathode catalysts in a fuel cell. Tada *et al*. developed a novel time-gating quick XAFS method for *in situ* time-resolved measurements. They succeeded in determining all the kinetic parameters for the electron transfer processes and redox structural changes during the rapid voltage operating processes for the first time.

The fourth topic concerns the anti-aging mechanism of Pt-supported CeZrY (Pt/CZY) catalysts, which extract harmful components from automotive exhausts such as NO_x and CO. Nagai *et al*. clarified that the formation of rigid Pt-O-Ce bonds on CZY suppresses the sintering of Pt and maintains its high catalytic activity after aging.

The fifth topic concerns the state-selective XAFS study of a Au/TiO_2 catalyst for low-temperature CO oxidation. Izumi *et al*. clarified the reason for the critical difference in catalytic activity depending on the Au particle size using a Au $L\alpha_1$-selecting Au L_3-edge XANES method, which selectively gave chemical state information for each Au site, such as anionic, neutral, and cationic sites.

The last topic concerns basic geochemistry for the age evaluation of materials by radiogenic ^{187}Re- ^{187}Os decay in molybdenite. Takahashi *et al*. examined the local structure around ^{187}Os using Os L_3-XAFS spectra, which were extracted by removing the intense X-rays from coexisting elements of Re and Mn using a fluorescence analyzer. They found that the valence and local structure of Os reflect the higher mobility of Os in molybdenite, which is related to the reliability of Re-Os dating.

Tomoya Uruga

XAFS Study on the Comparison of Soil-water Distribution of Antimony with that of Arsenic under Various Redox Conditions

Antimony (Sb) is the 9th most exploited metal worldwide being mined each year. It is heavily used (> 10^5 tons annually worldwide) in non-metal products such as antimony trioxide (Sb_2O_3), primarily in flame retardants, but it is also used as a catalyst in the production of plastics, a fining of glassware, and a pigment in paints and lacquers [1]. Antimony compounds are considered to be pollutants of priority interest by the United States Environmental Protection Agency and the European Union. However, the geochemical and environmental behaviors of Sb are largely unknown. Antimony belongs to group 15 in the periodic table below arsenic (As), and the most frequently observed species are Sb(III) and Sb(V) in the environment. The behavior and toxicity of Sb in the environment depend on its oxidation state as is similar to that of As. The toxicity of Sb(III) compounds is 10 times higher than that of Sb(V) species [1]. Therefore, Sb analysis in environmental samples requires quantitative measurement of Sb(III) and Sb(V). The aim of this study is the speciation of Sb and As in both solid and water phases to understand the reaction of Sb in soil-water environment and to compare the Sb behavior with As examined in mine tailings in a natural system and in a soil-water system synthesized in laboratory [2].

Natural soil and soil water samples containing Sb and As were collected around the Ichinokawa mine pithead, Ehime, Japan, which was formerly one of the largest Sb mine (stibnite: Sb_2S_3) in the world. To observe the Sb and As species under various redox conditions, the soil and soil water samples were collected at four different depths. It was found that the Eh (redox potential expressed in voltage) value decreased with the depth. In laboratory experiments, soil containing Sb and As was incubated for 7 days at 25°C to observe their oxidation states under various redox conditions by changing the total amount of water in the soil. The Eh value decreased with the increase of the water amount. Antimony *K*-edge XAFS spectra were measured at beamline **BL01B1** in SPring-8 in fluorescence mode, while *K*-edge XAFS spectra of As, Fe, and Mn at beamline BL12C in KEK-PF. The oxidation states of Sb and As in soil water were determined by high performance liquid chromatography (HPLC)-ICP-MS.

In both Ichinokawa and laboratory experiment systems, Sb XANES analysis shows that Sb in the soil was dominantly present as Sb(V) and slight Sb(III) was observed in soil under reducing condition or at lower Eh (Fig. 1(a)). On the other hand, most of As was as As(III) (reduced species) under reducing condition (Fig. 1(b)). These results show that Sb(V) is stable form in the environment and that Sb is oxidized under more oxic condition than As. Local structure of Sb and As were examined by EXAFS to obtain direct information on the host phases of Sb and As in the soil. All radial structure functions (RSFs) for Sb and As were quite similar within soil profiles. The RSF of

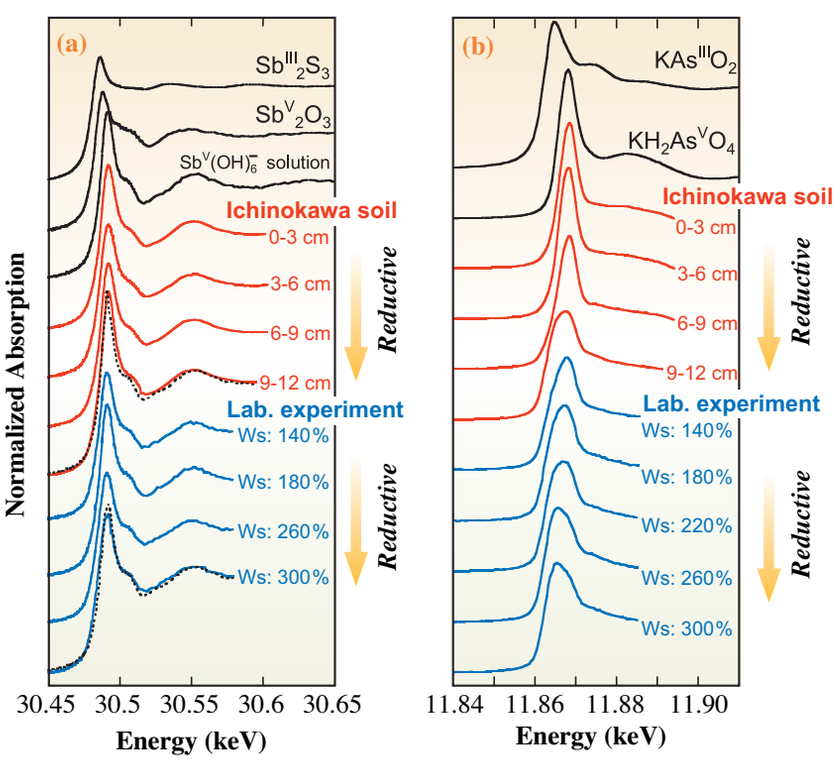

Fig. 1. **(a)** Normalized Sb *K*-edge XANES spectra of the reference materials (Sb_2S_3, Sb_2O_3, and $Sb(OH)_6^-$ solution), Sb in soil samples in the laboratory experiments, and in the Ichinokawa soil samples. Some spectra were overlapped with the spectrum of $Sb(OH)_6^-$ shown by dotted curves for comparison. **(b)** Normalized As *K*-edge XANES spectra of the reference materials ($KAsO_2$ and KH_2AsO_4), As in solid samples in the laboratory experiments, and in the Ichinokawa soil samples.

Sb(V) adsorbed on Fe hydroxide (ferrihydrite) has second prominent peak near 2.85 Å in addition to Sb-O shell near 1.5 Å (Fig. 2(a)). These features in RSFs and EXAFS spectra are similar to all the soil samples for Sb and As (Fig. 2), suggesting that Sb and As in the soil is mainly associated with Fe(III) hydroxide at all the depths [2].

Under reducing condition, concentration of As in the soil water increased with Fe and Mn concentrations in both Ichinokawa and laboratory experiment systems. These results suggest that As release from soil depends on (i) the reductive dissolution of Fe(III) hydroxide, host-phase of As in soil, and (ii) the reduction of As(V) to As(III), since As(III) is more mobile than As(V) [3,4]. On the other hand, Sb abundance in soil water decreased under reducing condition and Sb in the soil water was predominantly in the oxidized form, Sb(V), opposite to findings of As. In addition, Fe XANES analysis shows that Fe(III) hydroxide in the soil keeps its potential as adsorbent and host-phase for Sb even under reducing condition, which suggests that the decline of Sb abundance in reducing soil water may be due to a change of Sb species. It is reported that the solubility of Sb(III) is much lower than that of Sb(V) [5], and the Sb(III) was also slightly observed in both soil and soil water phases under reducing condition in present study. Therefore, it is considered that Sb reduced to Sb(III) was precipitated on the mineral surface due to its low solubility and that the precipitates containing Sb(III) like Sb_2O_3 cause the fixation of Sb to solid phase under reducing condition. These findings suggest that the different behavior of Sb and As under reducing condition is one of important factors controlling the partition behavior of Sb and As in soil-water systems.

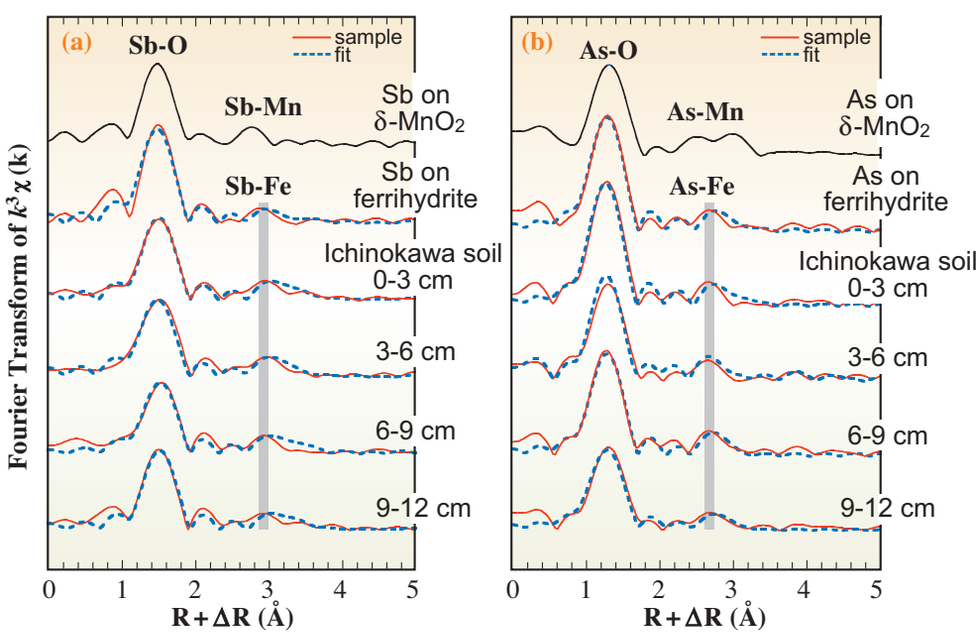

Fig. 2. Fourier-transformed EXAFS spectra of Sb **(a)** and As **(b)** in the Ichinokawa soil samples and model compounds (Sb and As adsorbed on ferrihydrite and δ-MnO_2 in **(a)** and **(b)**, respectively).

Satoshi Mitsunobu* and Yoshio Takahashi

Department of Earth and Planetary Systems Science, Hiroshima University

*E-mail: mitsunobu@hiroshima-u.ac.jp

References

[1] M. Krachler *et al.*: Trends Anal. Chem. **13** (2001) 79.
[2] *S. Mitsunobu, T. Harada and Y. Takahashi: Environ. Sci. Technol.* ***40*** *(2006) 7270.*
[3] P.L. Smedley and D.G. Kinniburgh: Appl. Geochem. **17** (2002) 517.
[4] Y. Takahashi *et al.*: Environ. Sci. Technol. **38** (2004) 1038.
[5] M. Filella *et al.*: Earth-Sci. Rev. **57** (2002) 125.

EXAFS Investigation of Adsorption and Separation Phenomena of Metal Ions in Organic Resin – Specific Coordination Properties in Micropores

Organic resin extractants, such as ion-exchange resins, are simple but powerful materials for separating, removing, and purifying chemical substances. Hence, they are widely employed not only in basic and applied research but also in various industrial fields. The practical application of organic resin extractants utilizes a unique property of the solid-liquid interface formed between the resin surface and the solution phase. That is, the chemical environment formed at the resin-solution interface is significantly different from that in bulk solution. For instance, the hydration of ions is weakened and, consequently, other complexation is enhanced in organic resins. This special effect in organic resins has been recognized for a long time; nevertheless, it has still not been sufficiently substantiated by experimental evidence because of the experimental difficulty in investigating such a limited minimal field in the resin. Accordingly, the chemical phenomena occurring inside organic resins remain conjectural, and they are still open to debate for the most part. To investigate the chemical phenomena in resins, extended X-ray absorption fine structure (EXAFS) spectroscopy is a very powerful tool. This technique is highly element-selective and can qualitatively distinguish different chemical species such as bulk species in the solution phase and adsorbed species formed at the resin-solution interface. In this study, we employ EXAFS spectroscopy to investigate the adsorption and separation phenomena of lanthanides (Ln(III)) by a tertiary pyridine resin [1]. The tertiary pyridine resin (Fig. 1) is an effective extractant for the separation of trivalent actinides (An(III)) and Ln(III) and, interestingly, its adsorption and separation behavior depends on the counter anions in the solute [2].

The tertiary pyridine resin used in this study was synthesized by the copolymerization of 4-vinylpyridine and *m/p*-divinylbenzene. The cross-linking and porosity of the resin were reduced as much as possible (i.e., 10 wt% cross-linking with 20 vol% porosity) to increase the number of pyridine functional groups and to decrease the volume of solution in the resin. The synthesized resin was washed, dried, and equilibrated with HCl/MeOH or HNO_3/MeOH solution containing Ln(III). After achieving the adsorption equilibrium, the resin was filtered to remove excess solution and placed in a polystyrene cuvette or polyethylene bag for the EXAFS measurement.

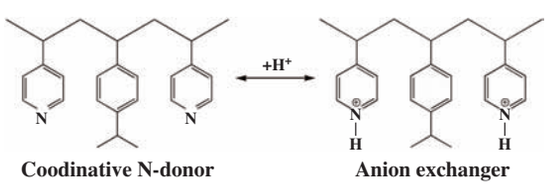

Fig. 1. Structure of tertiary pyridine resin and its protonation reaction.

The *K*-edge X-ray absorption spectra of Ln(III) were collected at the high-energy undulator beamline **BL11XU** using a Si(311) monochromator. The L_{III}-edge X-ray absorption spectra of Ln(III) always suffer from the multielectron excitation effect (MEE), which causes another oscillation in their EXAFS spectra [3], which deteriorates the accuracy of data analysis. However, there is no disturbance due to MEE in the *K*-edge region. Therefore, we can obtain more reliable results by measuring the *K*-edge spectra. All the measurements were performed in transmission mode at ambient temperature.

Figure 2 shows the Fourier transforms (FTs, = radial structural functions) of the *K*-edge EXAFS spectra for La(III) in different chemical environments containing chloride ions (Cl^-). The results of curve fitting reveal that La(III) ions are hydrated by 9-10

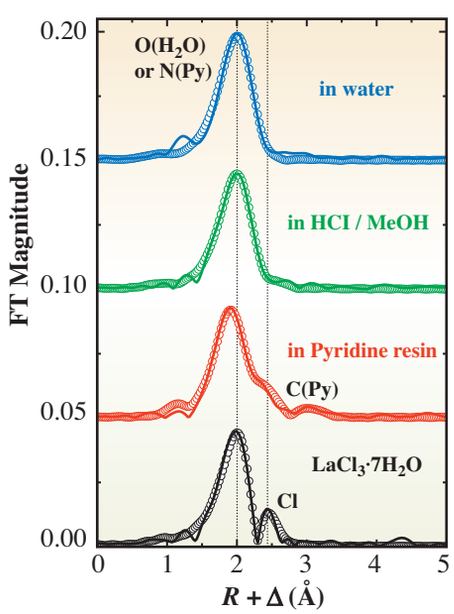

Fig. 2. Fourier transforms of La *K*-edge EXAFS spectra for La(III) in water, in HCl/MeOH mixed solution, adsorbed in the tertiary pyridine resin from HCl/MeOH solution, and in hydrated $LaCl_3$ crystal: solid lines; experimental data, circles; theoretical fit. Solvent composition of HCl/MeOH mixture: 6.0 M HCl (solute)/50 vol% MeOH in solvent.

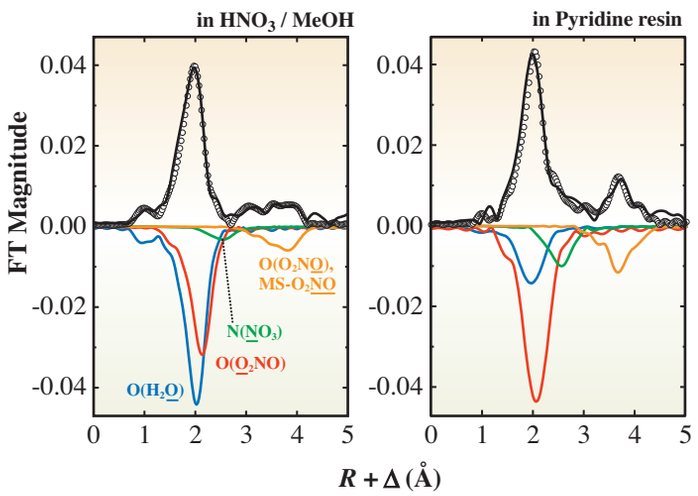

Fig. 3. Fourier transforms of Nd *K*-edge EXAFS spectra for Nd(III) in HNO_3/MeOH mixed solution and adsorbed in the tertiary pyridine resin from HNO_3/MeOH solution: solid lines; experimental data, circles; theoretical fit. Solvent composition of HNO_3/MeOH mixture: 6.8 M HNO_3 (solute) / 50 vol% MeOH in solvent.

water molecules in water and HCl /MeOH solution, while the hydration becomes weaker and, consequently, the Cl^- complexation is enhanced in the resin phase. Also, the FT for the resin sample shows an additional distinguishable peak at around $R + \Delta$ = 3.0 Å, which corresponds to the single scattering of C atoms of directly coordinating pyridine groups. This suggests that the pyridine groups in the resin directly coordinate to Ln(III) ions in the chloride solution system. In the HSAB theory by Pearson *et al.* [4], pyridine is classified as a soft donor ligand. In fact, soft donor ligands bind An(III) more strongly than Ln(III) and exhibit high selectivity for An(III) over Ln(III). Therefore, the observed An(III)/Ln(III) intergroup separation by the pyridine resin in chloride solutions [2] is considered to originate from the direct interaction of pyridine groups with An(III) and Ln(III) ions in the resin phase.

On the other hand, Fig. 3 shows the FTs of the *K*-edge EXAFS spectra for Nd(III) in HNO_3 / MeOH mixed solution and that adsorbed in the pyridine resin. The results of curve fitting indicate that Nd(III) ions are coordinated by two nitrate ions (NO_3^-) with a bidentate mode in the solution phase, forming a cationic nitrate complex of $[Nd(NO_3)_2(H_2O)_m]^+$, whereas the nitrate complexation is further enhanced in the resin phase, resulting in the formation of an anionic nitrate complex, $[Nd(NO_3)_4(H_2O)_n]^-$. The actual adsorption and separation behavior of An(III)/Ln(III) by the pyridine resin in nitrate solutions differs from that in the previous chloride solution system [2] but it is analogous to the behavior of that by anion exchange resins [1]. In fact, as illustrated in Fig. 1, the tertiary pyridine resin can also function as an anion exchanger by protonating pyridine groups. Considering these facts, we can conclude that the adsorption and separation of An(III)/Ln(III) in the nitrate solution system is caused by an "anion exchange" interaction, in which the protonated pyridine groups interact with the negatively charged metal-nitrate complexes. The proposed adsorption mechanism of An(III)/Ln(III) ions by the tertiary pyridine resin is illustrated in Fig. 4.

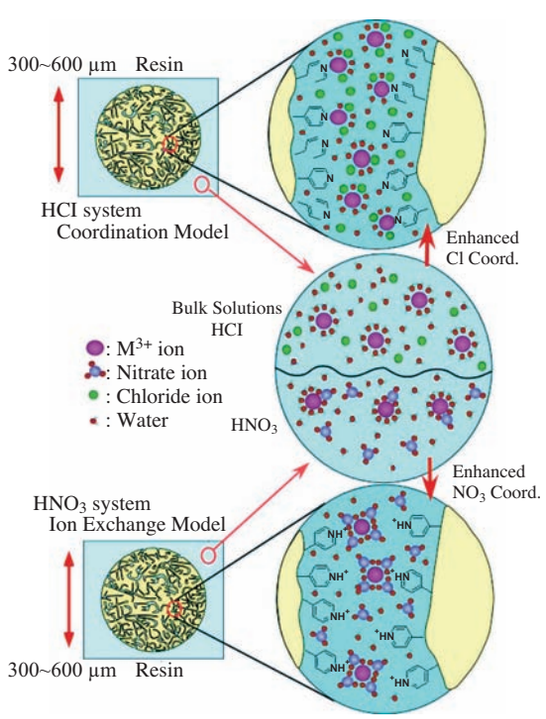

Fig. 4. Proposed adsorption mechanism of An(III)/Ln(III) ions by the tertiary pyridine resin.

Atsushi Ikeda, Hideaki Shiwaku and Tsuyoshi Yaita*

SPring-8 / JAEA

*E-mail: yaita@spring8.or.jp

References

[1] *A. Ikeda, T. Yaita, Y. Okamoto, H. Shiwaku, S. Suzuki, T. Suzuki, Y. Fujii: Anal. Chem.* ***79*** *(2007) 8016.*
[2] A. Ikeda *et al.*: J. Alloys Compd. **408-412** (2006) 1052.
[3] J.A. Solera *et al.*: Phys. Rev. B **51** (1995) 2678.
[4] R.G. Pearson: J. Am. Chem. Soc. **85** (1963) 3533.

In Situ Time-resolved Time-gating Quick XAFS Study for Dynamic Surface Events on Pt/C Cathode in a Fuel Cell

Environmentally friendly proton-exchange-membrane fuel cells (PEMFC) can be used in both fuel-cell automobiles and energy systems to address the serious environmental and energy problems faced by society. For the commercial applications of fuel-cell systems to automobiles, power-on/off processes with a large energy transfer are indispensable. However, the surface atoms of the active metal particles tend to dissolve into the electrolyte in contact with the cathode catalyst layer when we repeatedly rapidly change cell voltages to alter a car's speed. We have developed a novel time-gating quick XAFS method (TG-QXAFS) for *in situ* time-resolved XAFS measurements of Pt/C cathode catalysts in fuel cells and succeeded in determining all the kinetic parameters of the 8 elementary steps involved in rapid voltage-operating processes. Significant time lags between the electrochemical reactions and the structural changes of the Pt catalysts were observed for the first time.

The acquisition of QXAFS spectra at a Pt L_{III} edge requires at least 15 s due to the slow mechanical rotation of a monochromator; however, the time resolution of 15 s is too slow to observe the reaction mechanism of a Pt/C cathode in a fuel cell for rapid voltage-operating processes completed within a few seconds. We developed TG-QXAFS, whose schematic is illustrated in Fig. 1(a), at beamline **BL01B1**. The QXAFS system was synchronized with a potentiostat connected to a homemade electrode XAFS cell (Fig. 1(c)), and the cell voltage was rapidly changed between 0.4 V and 1.0/1.4 V (t = 0) while the current in the fuel cell was recorded in real time. A trigger signal was initially sent from the potentiostat to the QXAFS system, and a series of QXAFS measurements with delay time *t* shifted by 1 s for each measurement (Fig. 1(a)) were repeated. The obtained QXAFS spectra with the different delay times were divided into 15 fragments in *k* space, and the 15 fragments of the EXAFS oscillations obtained from the 15 different QXAFS measurements were combined into one interval. Thus, we can obtain a TG-QXAFS spectrum with a time resolution of 1 s, which is much faster than the conventional QXAFS method (15 s). H_2 for the anode and N_2 or air for the cathode were dewed through deionized water baths and introduced into the XAFS cell at 333 K (Fig. 1(b)).

Figure 2(a) shows the series of time-resolved TG-QXAFS Fourier transforms for a voltage-stepping process from 0.4 V to 1.0 V under H_2-N_2 gas conditions. Analysis of XANES, EXAFS and electrochemical data recorded on the potentiostat revealed the valence of Pt nanoparticles, the coordination numbers (CN) and distances of Pt-O and Pt-Pt bonds, and the electron transfer in the fuel cell, respectively. Such structural parameters for active metal nanoparticles cannot be obtained by other spectroscopic techniques, and the operando measurements of both structural and electronic kinetics of a Pt/C fuel-cell catalyst were successfully performed for the first time.

We have succeeded in determining the eight rate constants for the oxidation and reduction processes, which are related to the electron transfer, structural change, and d-electron density change at the Pt/C cathode catalyst, which are significantly different from each other. The TG-QXAFS analysis revealed a

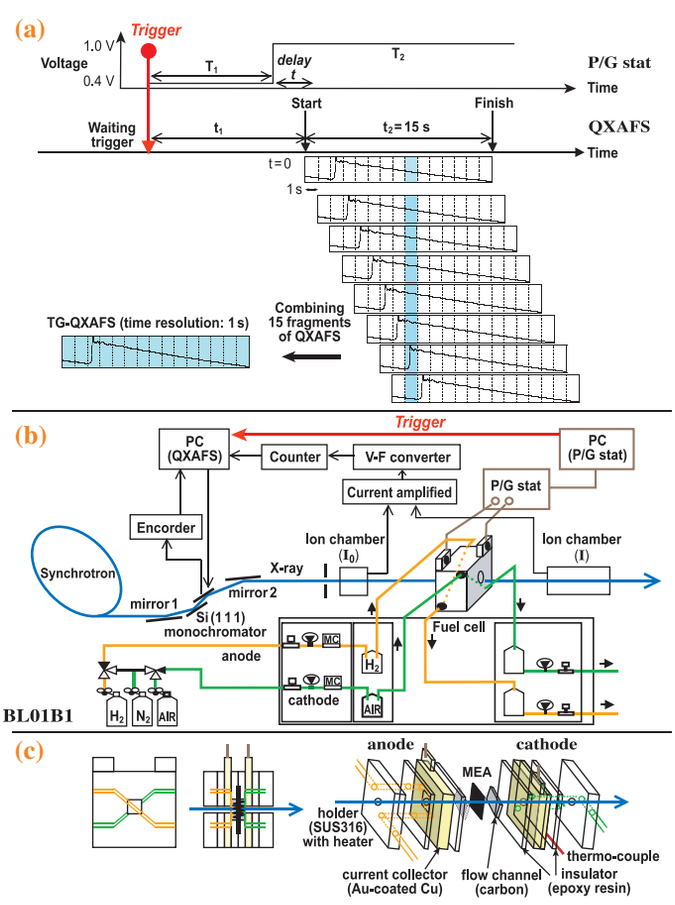

Fig. 1. **(a)** Procedure for TG-QXAFS with a time resolution of 1 s. **(b)** Schematic of the fuel cell and in situ time-resolved TG-QXAFS system at BL01B1 beamline. **(c)** Homemade in situ XAFS cell.

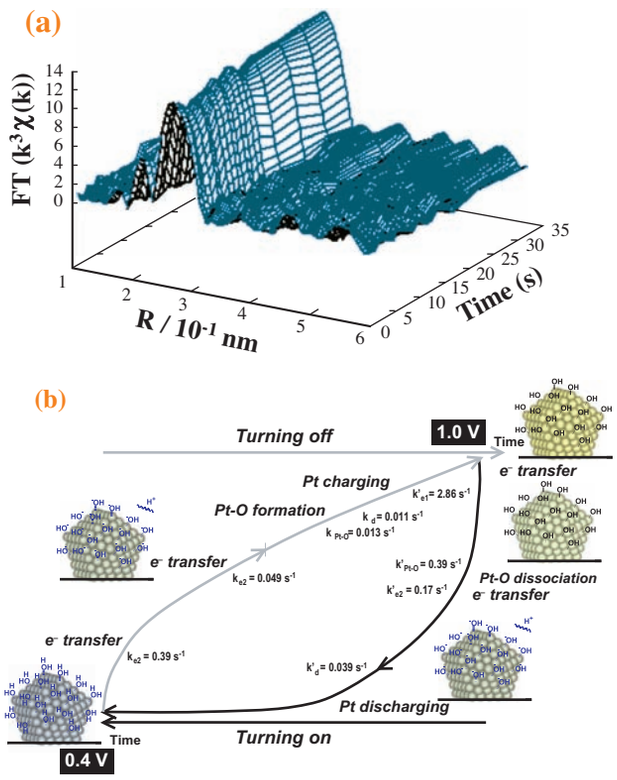

Fig. 2. **(a)** Series of TG-QXAFS Fourier transforms at Pt L_{III} edge for a voltage-operating process from 0.4 V to 1.0 V. **(b)** Reaction mechanism for structural and electronic changes in the Pt/C fuel-cell catalysts at cell voltages of 0.4/1.0 V under H_2 (anode) and N_2 (cathode) at 333 K.

hysteresis loop for the structural changes in the Pt particles in both processes (Fig. 2(b)). It should be noted that there is a significant time lag between the four processes on the cathode surface. In the oxidation process from 0.4 V to 1.0 V, the first dramatic electron transfer (k_{e1} = 0.39 s^{-1}) was 8 times faster than the subsequent second electron transfer (k_{e2} = 0.049 s^{-1}). After the first electron transfer, the Pt particles were only slightly charged, and there were no chemical bonds with oxygen on the Pt surface. Then Pt-O bonds slowly formed ($k_{Pt\text{-}O}$ = 0.013 s^{-1}) in conjunction with Pt charging with k_d = 0.011 s^{-1}, which was monitored through the *d*-electron density of states. On the other hand, the CN of Pt-Pt particles remained constant at about 9 between 0.4 V and 1.0 V, which indicates that no decomposition of the Pt catalyst or significant leaching to the electrolyte occurred.

When the cell voltage was increased to 1.4 V, the Pt particles were gradually oxidized and the CN of Pt-Pt bonds decreased, the reaction mechanism for which is presented in Fig. 3. The 20% decrease in the CN of Pt-Pt bonds and the CN of 0.8 for Pt-O bonds demonstrate that oxygen atoms enter the subsurface of the Pt particles at 1.4 V. Repeated voltage manipulations did not cause any decrease in electric charges, and the number of Pt-Pt bonds returned to its original value when the cell voltage returned to 0.4 V. Thus, the Pt ions do not dissolve in the electrolyte under N_2, although the voltage (1.4 V) exceeds the threshold voltage for H-O-H bond dissociation and promotes the penetration of oxygen into the Pt subsurface. However, when the cell voltage was increased to 1.4 V in air, the Pt-Pt bonds immediately broke, and the Pt nanoparticles disintegrated. The CN of the Pt-Pt bonds did not recover when the cell voltage was returned to 0.4 V. If a local inclination of electric potential forms on the electrode surfaces, the dissolution of Pt ions gradually occurs, resulting in the serious deterioration of Pt-cathode catalysts.

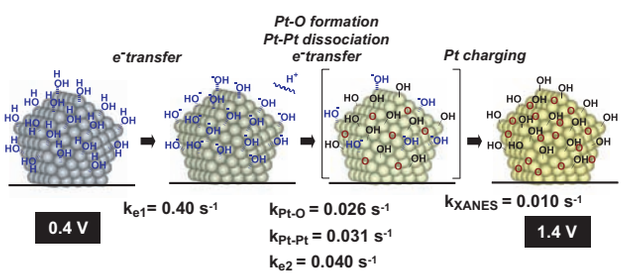

Fig. 3. Structural model of the Pt nanoparticles for the voltage-operating process from 0.4 V to 1.4 V suggested by *in situ* time-resolved QXAFS.

In conclusion, we have succeeded in the *in situ* observation of the reaction mechanisms occurring on a Pt/C catalyst surface in a fuel-cell cathode for the first time. The reaction kinetics of the electron transfer processes and redox structural changes, which involve eight elementary steps, on the Pt-cathode catalysts were determined. The significant time lag between the electron transfer, the redox structural changes and the Pt charging of the Pt/C catalysts characterizes the property of Pt nanoparticles on a carbon support as well as the population of the bound OH species, which are crucial for the performance of a Pt/C catalyst in a fuel cell [1].

Mizuki Tada* and Yasuhiro Iwasawa

Department of Chemistry, The University of Tokyo

*E-mail: mtada@chem.s.u-tokyo.ac.jp

References

[1] *M. Tada, S. Murata, T. Asaoka, K. Hiroshima, K. Okumura, H. Tanida, T. Uruga, H. Nakanishi, S. Matsumoto, Y. Inada, M. Nomura and Y. Iwasawa: Angew. Chem. Int. Ed.* ***46*** *(2007) 4310.*

Sintering Inhibition Mechanism of Platinum Supported on Ceria-Based Oxide for Automotive Catalysts

Three-way catalysts (TWCs) can efficiently purify harmful automobile emissions. Since being commercialized in the USA and Japan in 1977 [1], TWCs have played an important role in environmental protection. Recently, due to the increasing demand for global environmental protection, more stringent regulations have been imposed on the automobile industry. As a result, automobile companies are striving to purify automobile exhaust emissions. Consequently, there is a strong demand for the development of more advanced TWCs through technical innovations. Figure 1 shows a brief overview of the TWC. An automotive TWC is placed under the floor or beside the engine of a vehicle. TWCs are composed of three components, namely, a precious metal such as Pt or Rh, a support such as Al_2O_3, and an oxygen storage/release component. The precious metal functions as a source of active sites that extract harmful components from automotive exhausts such as nitrogen oxides (NOx), carbon monoxide (CO) and unburned hydrocarbons (HC). The precious-metal particles are a few nanometers in diameter and are dispersed on a support oxide. When a TWC is exposed to a high temperature of about 800 °C or greater, the precious-metal agglomerates and is sintered, reducing the active surface area of the catalyst. Generally, the sintering of precious-metal particles during operation is considered to reduce the catalytic activity, that is, it degrades the catalyst. In addition, the exhaust from an automotive gasoline engine fluctuates between an oxidizing and a reducing atmosphere during vehicle operation. Specifically, the activity of Pt-supported catalysts decreases to a considerably lower extent during high-temperature ageing in an oxidizing atmosphere than in a reducing atmosphere due to the sintering of the Pt particles [2]. Thus, the development of highly durable catalysts that do not undergo Pt sintering in an oxidizing atmosphere is a current goal of automotive industrial research. Although it is known that ceria-based oxides stabilize precious-metal dispersion [3], the interaction between Pt and ceria is very complicated and is still not fully understood. Here, we present the sintering inhibition mechanism of Pt particles on a ceria-based oxide at the atomic level based on the results of X-ray absorption spectroscopy at **BL01B1** and **BL16B2** [4].

In this work, we prepared Pt/Al_2O_3 and Pt/Ce-Zr-Y mixed oxide (referred to as CZY). Pt/Al_2O_3 and Pt/CZY samples are considered as models of conventional and newly developed catalysts, respectively. The samples were aged in air for 5 h at 800 °C. This ageing treatment involved to an accelerated test for durability in an oxidizing atmosphere. Figure 2 shows the Fourier transforms (FTs) of Pt L_3-edge EXAFS spectra for the aged catalysts and reference samples. The FT spectrum of Pt/Al_2O_3 after ageing is clearly different from that of Pt/CZY. For the aged Pt/Al_2O_3, only an intense peak at 2.76 Å, which corresponds to the Pt-Pt bond, was observed. The FT spectrum of Pt/Al_2O_3 was similar to that of Pt foil. The coordination number of the Pt-Pt shell in the aged Pt/Al_2O_3 was 11.5. This indicates that the Pt metal particles on Al_2O_3 after ageing are at

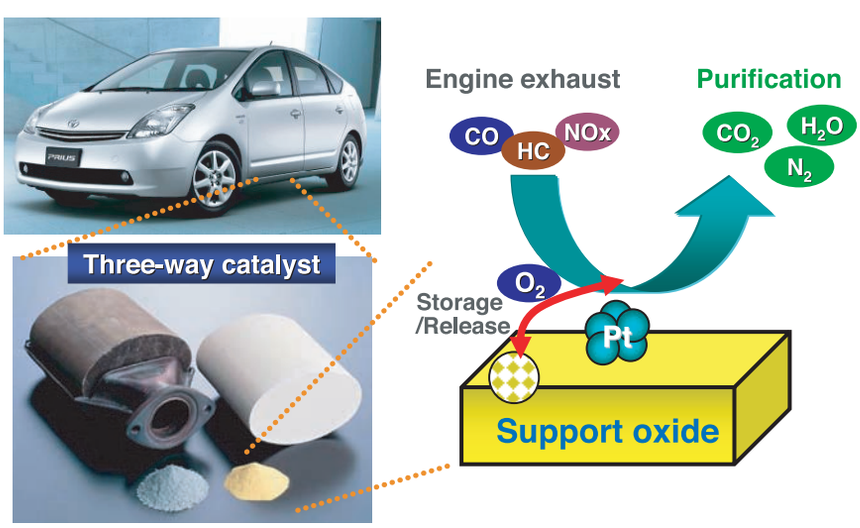

Fig. 1. Automotive three-way catalyst used for emission control.

least 20 nm in size. Actually, the average particle size in the aged Pt/Al_2O_3, determined by the CO pulse method, was 24 nm. The FT spectrum of Pt/CZY after ageing was different from the spectra of both Pt foil and PtO_2 powder. The position of the first peak at 2.02 Å in Pt/CZY was close to that of PtO_2, and this peak was fitted with the Pt-O bond. It should be noted that the second peak in the spectrum, which was absent in the spectra of both Pt foil and PtO_2 powder, was at 3.01 Å. A curve-fitting simulation of this second peak was carefully performed. An excellent fitting result for the simulation of a Ce atom could be obtained. This result leads to the conclusion that Pt atoms strongly interact with the CZY support during ageing and form Pt-O-Ce bonds. The value of the coordination number of the Pt-Ce shell in the aged Pt/CZY was 3.5. This is lower than 12, which is the saturated coordination number for the cubic fluorite structure. This indicates that Pt ions exist on the surface of the CZY support.

On the basis of the above observation, we propose the sintering inhibition mechanism of Pt supported on CZY shown in Fig. 3. In the case of Pt/Al_2O_3, since the interaction between Pt and Al_2O_3 is weak, Pt particles migrate across the surface of the Al_2O_3 support and are sintered during 800 °C ageing treatment in an oxidizing atmosphere. In contrast, Pt supported on CZY strongly interacts with the CZY support. Therefore the CZY support stabilizes the high-oxidation state of Pt, and the formation of a rigid Pt-O-Ce bond acts as an anchor. The formation of Pt-O-Ce bonds on CZY suppresses the sintering of Pt. Generally, Pt^0 (metal) is considered to be the active

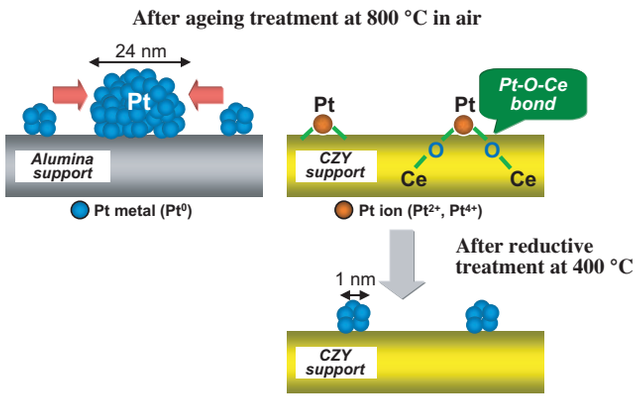

Fig. 3. Schematic illustration of the Pt sintering inhibition mechanism for a Pt/ceria-based catalyst and a conventional Pt/Al_2O_3 catalyst.

site for the catalytic reaction in automotive exhaust conditions. The CZY support can stabilize a high-oxidation state of Pt after aging. Therefore, Pt on the CZY support must be reducible during the catalytic reaction. In another experiment, we confirmed that the Pt-O-Ce bond easily breaks by reductive treatment and that Pt metal particles are highly dispersed on the CZY support. According to the results from the CO pulse method, the estimated average size of Pt metal particles in the reduced Pt/CZY after the aging is *ca.* 1 nm. The Pt particle size is the same as that in the fresh catalyst. This indicates that Pt in the Pt/CZY catalyst did not sinter at all during the ageing treatment.

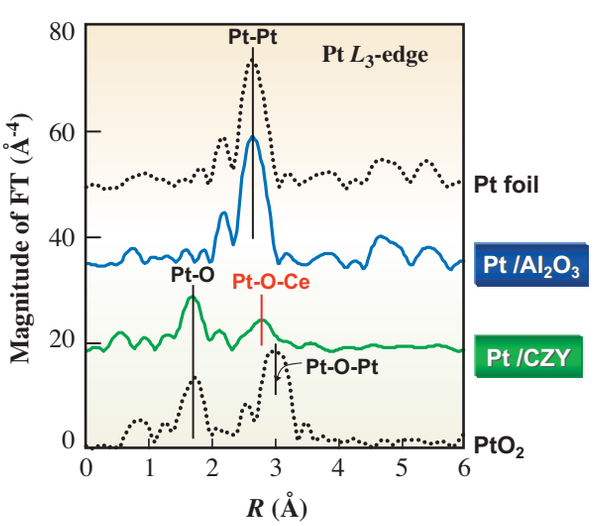

Fig. 2. Fourier-transformed $k^3\chi$ data of Pt L_3-edge EXAFS for supported Pt catalysts after 800 °C ageing in air and the standard samples of Pt foil and PtO_2 powder.

Yasutaka Nagai [a,*], Kazuhiko Dohmae [a] and Nobuyuki Takagi [b]

[a] TOYOTA Central R&D Labs., Inc.
[b] TOYOTA Motor Corporation

*E-mail: e1062@mosk.tytlabs.co.jp

References

[1] S. Matsumoto: Catal. Today **90** (2004) 183.
[2] P.J F. Harris: J. Catal. **97** (1986) 527.
[3] L.L. Murrell *et al.*: Stud. Surf. Sci. Catal. **71** (2001) 275.
[4] *Y. Nagai, T. Hirabayashi, K Dohmae, N. Takagi, T. Minami, H. Shinjoh and S. Matsumoto: J. Catal.* ***242*** *(2006) 103.*

Why Gold Becomes Active When in Form of Dispersed 3 nm Particles? Reaction Intermediate Detected at SPring-8*

Since ancient times, gold has been a symbol of wealth and power because of its eternal brightness due to its poor chemical reactivity. However, Au becomes chemically active when it is in the form of dispersed 3 nm particles, e.g., for the catalysis of low-temperature CO oxidation [1]. The reason for the contrasting reactivity of Au between the nanometer and centimeter scales is not yet known.

Various possibilities have been proposed as the active site of Au nanoparticles: anionic Au cluster sites, the interface sites between Au and the supporting metal oxide, and lower-coordination step-edge sites [1]. It is difficult to determine the active site because the site structure of Au nanoparticles cannot be determined individually from the various chemical states of Au.

X-ray diffraction (XRD) is insensitive to 3 nm particles because there is insufficient repetition of lattices of Au particles. Also, XRD does not discriminate between different chemical states. In contrast, X-ray photoelectron spectroscopy (XPS) can be used to monitor chemical states and provides the population of each state near the surface of the sample. However, XPS does not give structural information. X-ray absorption fine structure (XAFS) provides local structural information. However, the information is in the form of a statistical average if more than two chemical states are present in the element in the sample. A heterogeneous catalyst is a typical example of such a mixture of chemical states for the active element, particularly during catalysis.

To determine each Au site structure in Au nanoparticles on a porous, complex surface of TiO_2, we applied state-sensitive XAFS spectroscopy [2]. State-sensitive XAFS, which is an evolved version of general XAFS spectroscopy [3]. The statistical disadvantage of XAFS that it gives average information is not applicable to state-sensitive XAFS because the chemical states of Au can be distinguished by high-energy-resolution X-ray fluorescence spectrometry. XAFS data for each chemical state of Au was obtained by selecting X-ray fluorescence signals originating from anionic, neutral, and cationic Au sites independently [2].

A homemade Rowland-type fluorescence spectrometer [3] was set in the undulator beamline **BL37XU**. With the excitation energy set to 11943 eV, the Au $L\alpha_1$ emission from the sample was analyzed using a Johansson-type Ge(555) crystal. The Rowland radius was 220 mm. The measured energy resolution of this fluorescence spectrometer was 2.9 eV at 9.7 keV including the contribution of the beamline.

The fluorescence spectrometer was tuned to each emission energy and the Au L_3-edge XANES (X-ray absorption near-edge structure) spectra were measured. By tuning the energy to 9713.3 eV (peak of emission spectrum, Fig. 1, inset), Au $L\alpha_1$-selecting Au L_3-edge XANES spectra were measured for Au metal (Fig. 1, solid red line). The absorption edge at 11921.2 eV was steeper and the peaks at 11923.3, 11935.3, 11941.3, and 11948 eV were sharper and more resolved than those in the corresponding spectrum measured in transmission mode (Fig. 1, dotted blue line). This sharpening effect is derived from identical rationale used to discriminate between chemical states in XANES combined with high-energy-resolution fluorescence spectrometry [4].

The particle size of Au nanoclusters on TiO_2 was controlled between 2.9 and 8.7 nm by changing the deposition-precipitation synthesis conditions of the catalyst: the pH (NaOH or urea), the surface area of TiO_2 (60 - 1200 m^2g^{-1}), the reaction temperature, and the duration of the deposition-precipitation reaction [2]. The Au particle size distribution was very narrow (standard deviation ≈26%).

The reason why there is critical difference in low-temperature CO oxidation reactivity depending on the

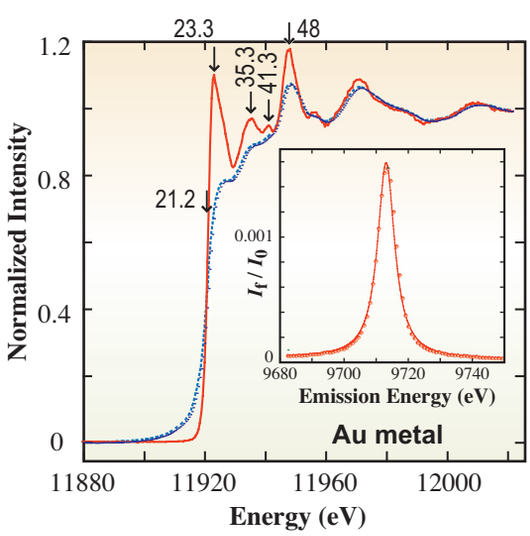

Fig. 1. Au $L\alpha_1$-selecting Au L_3-edge XANES spectrum tuned to Au $L\alpha_1$ peak (solid red line) and XANES spectrum measured in transmission mode (dotted blue line). (Inset) Au $L\alpha_1$ emission spectrum.

*Part 27 in the series.

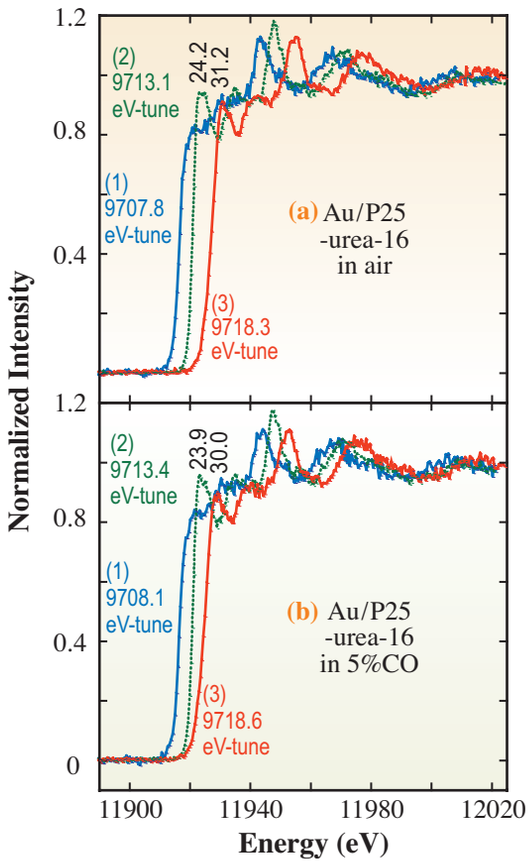

Fig. 2. Au $L\alpha_1$-selecting Au L_3-edge XANES spectra measured for Au/TiO_2(P25) of 2.9 nm nanoclusters synthesized at 353 K using urea in air **(a)** and in 5% CO (balance gas: Ar) **(b)**. 0.93 wt% Au. The energies were tuned to 9707.8, 9713.1, and 9718.3 eV **(a)** and 9708.1, 9713.4 and 9718.6 eV **(b)**.

Au particle size [1] was clarified on the basis of the Au $L\alpha_1$-selecting Au L_3-edge XANES spectra obtained by tuning the fluorescence spectrometer to 9708, 9713 and 9718 eV. The measured sample was a Au/TiO_2 catalyst of 2.9 nm nanoparticles synthesized using urea at 353 K for 16 h on TiO_2 (Degussa P25) in air and in CO(5%)/Ar.

The Au L_3-edge energy and spectral pattern of XANES tuned to 9713 eV (Figs. 2(a-2) and 2(b-2)) resembled those for XANES measured for Au metal (Fig. 1, solid red line). Thus, the neutral Au^0 site located on upper side of Au nanoparticles on TiO_2 was selected at 9713 eV (Fig. 3). When the energy was tuned to 9708 eV on the lower-energy side of Au $L\alpha_1$ emission, the Au L_3-edge energy shifted by -4.6 to -4.7 eV toward the lower-energy side. The first intense peak became a weak shoulder at 11922 eV (Figs. 2(a-1) and 2(b-1)). These trends indicated greater Au 5*d* occupation [5]. Thus, the formation of the anionic $Au^{\delta-}$ site was suggested (Fig. 3(b)). The population of $Au^{\delta-}$ site was greater for Au nanoparticles of 2.9 nm than for those with average size of 8.7 nm. However, this $Au^{\delta-}$ site was not affected whether in air or in 5% CO.

Finally, the fluorescence spectrometer was tuned to 9718 eV on the higher-energy side of Au $L\alpha_1$ emission. The Au L_3-edge energy shift was +6.8 eV for Au/TiO_2(P25)-urea-16 of nanoparticles of 2.9 nm in air (Fig. 2(a-3)), greater than that in 5% CO (+3.9 eV, Fig. 2(b-3)) and that of nanoparticles of 8.7 nm (average) in air (+3.7 eV) [2]. Thus, it is suggested that O_2 molecules are activated on the cationic $Au^{\delta+}$ site, probably near the interface with the TiO_2 surface terminated with Ti atoms (the so called SMSI effect; Fig. 3(a)) by the further negative charge transfer from $Au^{\delta+}$ to the adsorbed O_2. The charge donation observed in Fig. 2(a-3) is a snapshot of the reaction intermediate of CO oxidation that proceeds on Au nanoparticles of 2.9 nm, but does not occur on larger Au nanoparticles [1].

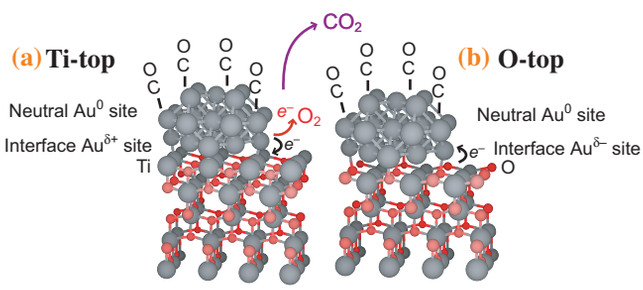

Fig. 3. Au_{26} cluster models on anatase-type TiO_2(001) surface terminated with Ti atoms **(a)** and O atoms **(b)**.

Yasuo Izumi

Graduate School of Science, Chiba University

E -mail: yizumi@faculty.chiba-u.jp

References

[1] A. Cho: Science **299** (2003) 1684.
[2] *Y. Izumi, D.M. Obaid, K. Konishi, D. Masih, M. Takagaki, Y. Terada, H. Tanida and T. Uruga: Inorg. Chim. Acta* ***361****(4) (2008) 1149.*
[3] Y. Izumi *et al.*: J. Electron Spectrosc. Relat. Phenom. **119** (2001) 193.
[4] Y. Izumi *et al.*: Anal. Chem. **77** (21) (2005) 6969.
[5] N. Weiher *et al.*: J. Am. Chem. Soc. **129** (8) (2007) 2240.

Atomic-Scale Environment of Re and Radiogenic ^{187}Os in Natural Molybdenite Mineral Related to Reliable Re-Os Dating

The age of terrestrial and extraterrestrial materials is determined by the ratio of parent to daughter nuclides, which can vary as a function of time due to radioactive decay [1]. The radiometric dating method assumes the retention of both parent and daughter nuclides in the samples since their formation. The chemical properties of the daughter nuclides often differ from those of the parent, which may result in the separation of the parent and daughter nuclides. Therefore, their retention in the sample may depend on the chemical environment of both nuclides, which affects their stabilities against various processes such as metamorphism, alteration, and diffusion within a crystal. Therefore, the chemical states of parent and daughter nuclides in mineral or rock samples is important for accurate dating.

Recently, Os geochemistry has attracted considerable interest due to the variation of Os isotopes related to the ^{187}Re-^{187}Os decay system [2]. In particular, molybdenite (MoS_2) is known as a robust geochronometer resistant to regional deformation and metamorphism, as demonstrated by a trial of the ^{187}Re-^{187}Os system for the dating of molybdenite [3]. In this method, however, it has been indicated that successful dating requires the careful selection of a representative sample from a specific geologic occurrence with a sufficient volume of the sample for the analysis to overcome the decoupling of ^{187}Os and Re in the molybdenite after their formation. This decoupling of Re and Os has been attributed to the high mobility of radiogenic ^{187}Os relative to Re in molybdenite. In this study, we examine the local structure of Re and radiogenic ^{187}Os at the atomic scale in molybdenite using their X-ray absorption fine structure (XAFS) to clarify the atomic-scale environment and chemical state of the parent and daughter nuclides (Fig. 1) [4]. The XAFS for Os in molybdenite is considered to originate from radiogenic ^{187}Os produced by the β-decay of ^{187}Re (half life: 4.4 × 10^{10} years), since it is well known that the abundance of common Os initially contained in molybdenite is negligible. Thus, the local atomic structures of Re and radiogenic ^{187}Os in molybdenite from the Onganja Mine (Namibia) were examined by XAFS, which was conducted at beamlines **BL37XU** and **BL01B1**.

Rhenium L_{III}-edge XANES (X-ray absorption near-edge structure) and EXAFS (extended X-ray absorption fine structure) showed that the oxidation state of Re, the interatomic distances between Re and the neighboring atoms, and the coordination number of Re to S are very similar to those of Mo in molybdenite.

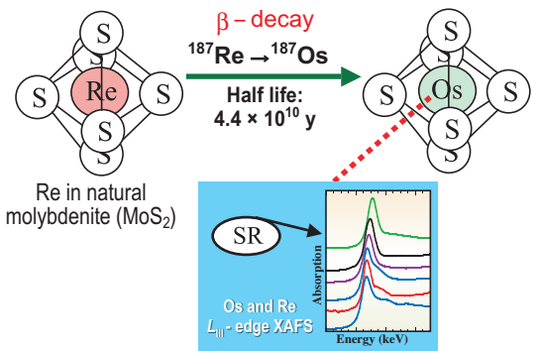

Fig. 1. Schematic representation of this study illustrating the importance of determining the chemical environment of the daughter nuclide (^{187}Os in this study) in the mineral (molybdenite in this study) for the reliable dating of natural samples.

The results confirm that Re is substituted at the Mo site in molybdenite.

We successfully measured the L_{III}-edge XANES and EXAFS of the small quantity (8.55 ppm) of radiogenic Os in molybdenite in fluorescence mode by removing the interference of X-rays from Re and other elements using a crystal analyzer system at BL37XU (Fig. 2) [4,5]. The XANES data indicate that the oxidation state of radiogenic Os is either Os(IV) or Os(III), similar to Re(IV) and Mo(IV), but not Os(II), the state in $Os^{II}S_2$ (= erlichmanite), naturally occurring stable Os sulfide (Fig. 3). XANES data also suggest that radiogenic Os does not form a secondary Os phase, such as OsS_2 or Os metal, in molybdenite.

The EXAFS of radiogenic Os in molybdenite was successfully simulated assuming that Os is present at the Mo site in molybdenite using the parameters

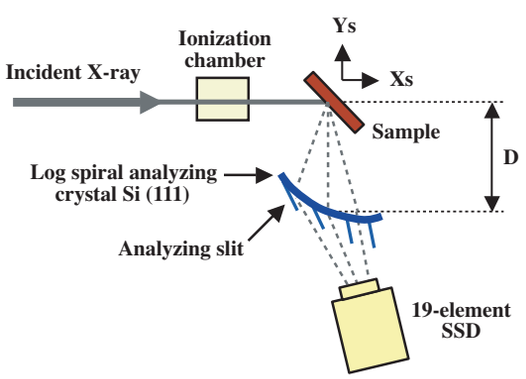

Fig. 2. Schematic of experimental setup of the fluorescence XAFS using a crystal analyzer system at BL37XU.

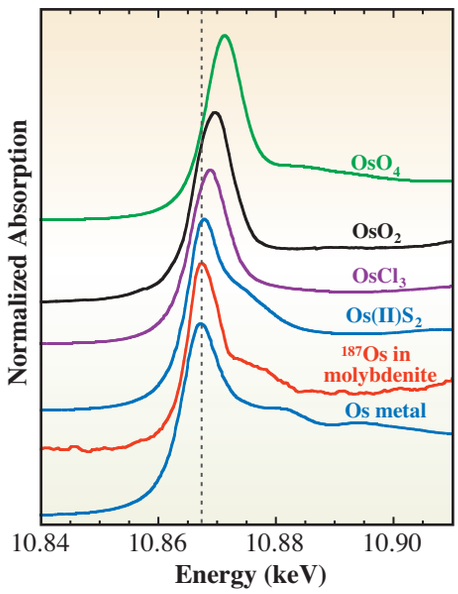

Fig. 3. Osmium L_{III}-edge XANES for Os in molybdenite and reference materials such as Os metal, $Os^{II}S_2$, $Os^{III}Cl_3$, $Os^{IV}O_2$, and $Os^{VIII}O_4$.

generated by FEFF (Fig. 4). EXAFS data are not consistent with the presence of Os phases such as Os metal and OsS_2. The EXAFS simulation showed that the interatomic distance between Os and S is 2.27 Å, which is 0.12 Å smaller than those of Re-S and Mo-S (2.39 Å) in the molybdenite. This shorter distance between radiogenic Os and S may be explained by the relatively small ionic radii of Os(IV) and Os(III). The interatomic distance of Os-S is 2.35 Å in $Os^{II}S_2$, and Os(III) or Os(IV) should have a shorter interatomic distance with S than that in $Os^{II}S_2$ due to the larger charge. The similar valence and ionic radius between Re and Mo in molybdenite obtained from our XAFS data support the fact that a large amount of Re can be incorporated into the Mo site, as was indicated in previous studies (e.g., [3]), while the different geochemical properties of Os compared with Mo and Re suggested here are evidence for the much lower abundance of common Os in molybdenite [3]. This makes molybdenite an ideal mineral for the Re-Os geochronometer. However, the shorter distance between radiogenic Os and S compared with those of Re-S and Mo-S in molybdenite suggests that Os diffuses faster than Re and Mo ions in molybdenite, which may induce the decoupling of Re and radiogenic Os in molybdenite. This is consistent with the higher mobility of Os than Re in molybdenite suggested in previous studies.

To our knowledge, this is the first study to clarify the chemical environment at atomic scale for the daughter nuclide produced by radioactive decay in natural samples. Atomic scale information is essential for every decay system to elucidate reliable dating data to understand the evolution of the solar system and the earth.

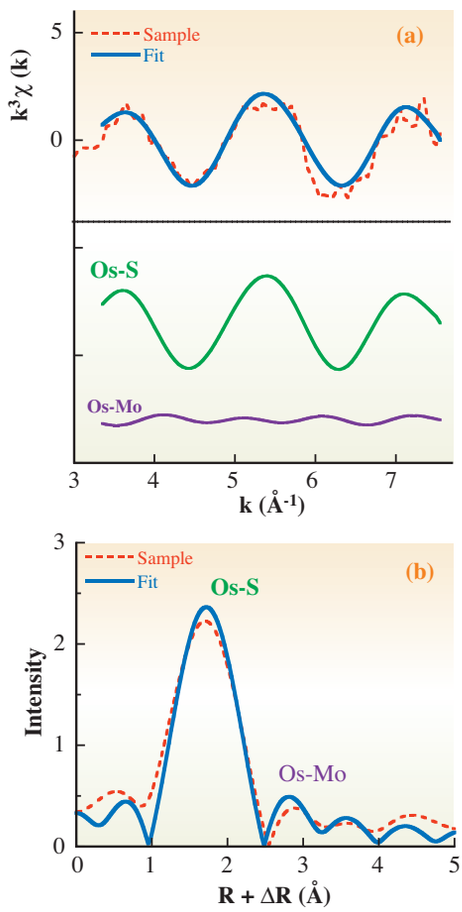

Fig. 4. EXAFS results for Os in molybdenite including **(a)** k^3-weighted $\chi(k)$ with the simulated spectrum with the contribution of Os-S and Os-Mo shells considered therein and **(b)** radial structural function (RSF) for Os with the simulation curve.

Yoshio Takahashi

Department of Earth and Planetary Systems Science, Hiroshima University

E-mail: ytakaha@hiroshima-u.ac.jp

References

[1] G. Faure and M.T.G. Mensing: Isotopes: Principles and Applications (Wiley 2004).
[2] Y. Yamashita *et al.*: Geochim. Cosmochim. Acta **71** (2007) 3458.
[3] W. Herr and E. Merz: Z. Naturforschg **10a** (1955) 613.
[4] *Y. Takahashi, T. Uruga, K. Suzuki, H. Tanida, Y. Terada, and K.H. Hattori: Geochim. Cosmochim. Acta **71** (2007) 5180.*
[5] Y. Takahashi *et al.*: Anal. Chim. Acta **558** (2006) 332.

INDUSTRIAL

"Nankinhaze" - Chinese tallow tree

A great strength of SPring-8 is the fact that this facility is highly focused on increasing the number of users from industry. Whereas most overseas facilities are focused on protein structure analysis and long-term large-scale businesses, SPring-8 is more pragmatic about its development. In fact, SPring-8 has a good track record of developing industrial applications in various fields, such as electronics, materials, energy, chemical, and environment-related companies, and was used by more than 170 companies in 2007. Applications in areas directly related to everyday life, such as cosmetics, hair care, and dental drug products, have also recently increased. The most important factor contributing to our success in attracting a wide range of industries is the implementation of various utilization propulsion programs at public beamlines, which have been improved continuously. In particular, the dramatic increase in the number of research experiments for industrial users in 2005 was clear due to the Strategic Use of Advanced Large-scale Research Facilities (SUALRF) program (FY2005-FY2006), supported by the Ministry of Education, Culture, Sports, Science and Technology.

APPLICATIONS

The system for industrial use needs more flexibility regarding the carrying out of experiments, such as allowing the immediate use of a beamline after the submission of a proposal and regular use at short intervals. Thus, after the SUALRF program was completed, JASRI implemented a new utilization propulsion program from FY2007 at public beamlines: the Priority Research Proposal (priority field: industrial application). In this program, to better reflect the needs of industrial users, the application system was also improved. For example, in deference to those companies who have indicated that applications twice a year do not match their development cycles, applications can now be submitted 4 times a year for the use of some public beamlines dedicated to industrial research. In view of the patenting process, which is very important for companies, the publication of results in this program will also be postponed for up to two years when a postponement request is accepted. When the postponement ends, companies have an obligation to submit a report to JASRI on the consequences of the postponement.

As of December 2007, SPring-8 accommodates two public beamlines dedicated to industrial use. One is the Engineering Science Research I (BL19B2) beamline, a standard bending magnet beamline, for grazing-incidence X-ray scattering, X-ray reflectivity measurements, powder X-ray diffraction, and X-ray imaging experiments. The other is the Engineering Science Research II (BL14B2) beamline, a brand-new bending magnet beamline dedicated to XAFS measurements. In addition to the two public beamlines, there are three contract beamlines under companies' operation in SPring-8: Industrial Consortium ID (BL16XU), Industrial Consortium BM (BL16B2), and Pharmaceutical Industry (BL32B2). In addition, Hyogo BM (BL08B2) and Hyogo ID (BL24XU), contract beamlines under the local government, are running independent programs for industrial use.

In the present issue, eight topics have been chosen to represent the outstanding work carried out in the various fields of industrial applications from 2006A through 2007A. The topical experiments introduced here were performed using the following techniques: hard X-ray photoelectron spectroscopy (HAXPES; BL47XU), X-ray magnetic circular dichroism and photoemission electron microscopy (XMCD-PEEM; BL25SU and BL17SU), grazing-incidence X-ray diffraction (GIXD; BL19B2), infrared microspectroscopy (BL43IR), X-ray section topography (BL24XU), X-ray microtomography (BL20XU), and X-ray tomography (BL19B2).

Yoshio Watanabe

Effect of Interface Layers on Phase-change Recording Material Analyzed by HX-PES Method

Phase-change storage technology has been developed for rewritable optical media and recently for the nonvolatile semiconductor memory. The history of the technology is long and began with the discovery of reversible electrical switching in a chalcogenide compound by Ovshinsky [1]. Kolobov *et al*. recently proposed a novel phase-change model for GeSbTe (GeTe-Sb_2Te_3: GST) based on an X-ray absorption fine structure (XAFS) study [2]. On the other hand, research for industrial application is more advanced than fundamental research, i.e., the understanding of the fast phase-change mechanism. Two main types of materials have already been used practically for phase-change recording media. One is the pseudobinary compound GeSbTe (GST). The other is a eutectic alloy, which is typically an SbTe alloy that has been known for a long time to be a compound semiconductor having a narrow band gap. On the basis of various evidence, it is also known that the crystallization mode of a pseudobinary phase-change material is different from that of a eutectic alloy phase-change material. In addition, the interface layer, which is a very thin dielectric layer located immediately above the recording layer, is important for the practical use of phase-change media. The effect of the interface layer material on the phase-change recording material is only understood phenomenologically. The development of high-speed phase-change material is crucial for the high-speed operation of the media, because the erase process of rewritable media corresponds to the crystallization process. In other words, it is necessary for both the development of high-speed phase-change materials and the understanding of the effect of the interface layer on the recording layer from a microscopic viewpoint, including the characterization of the chemical and electronic states of the phase-change recording material in actual media. However, the analysis of the actual media presents various challenges. For example, the recording layer is buried beneath other films. The thickness of a protection layer is over 30 nm. On the other hand, the detection depth of conventional X-ray photoelectron spectroscopy (XPS) is below a few nm [3]. An etching process is required to detect the signal from the recording layer using conventional laboratory XPS, because conventional XPS is only sensitive to the surface. The etching process alters the interface between the two films. Thus, it is difficult to detect the detailed chemical state of samples having a structure used in actual media. However, hard-X-ray photoelectron spectroscopy (HX-PES), which has a large probing depth, has been developed [4].

The effect of the interface layer on the pseudobinary material and the eutectic alloy used as phase-change recording materials was investigated at room temperature for the first time by HX-PES to clarify the high-speed phase-change recording mechanism. The HX-PES experiments were performed at beamline **BL47XU**. GeBiTe (GeTe-Bi_2Te_3: GBT) and SbTe alloys were adopted as the pseudobinary compound and eutectic alloy, respectively. GBT is used for high-speed rewritable HD DVD media, as shown in Fig. 1(a). Samples

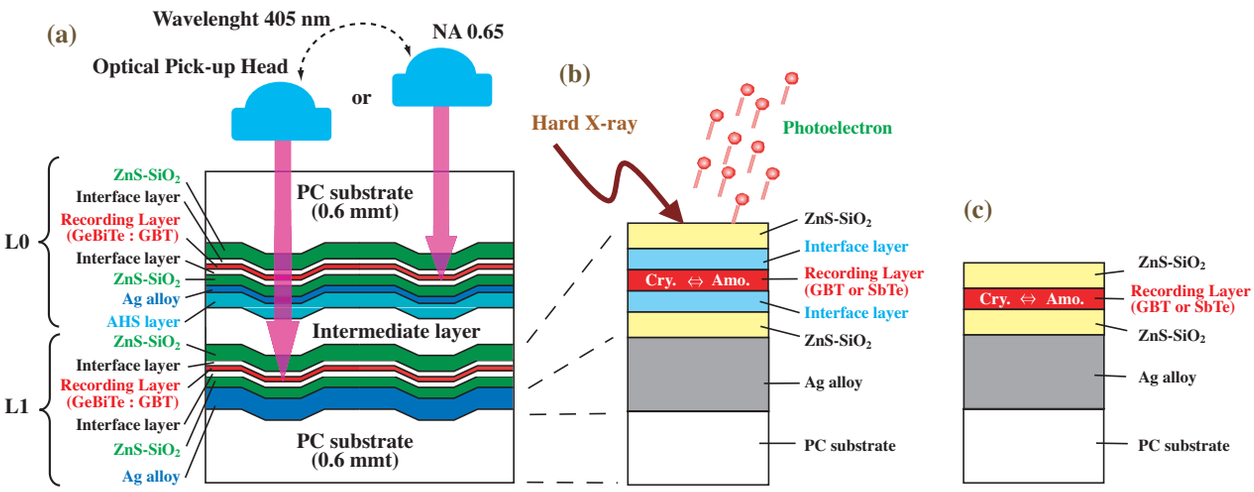

Fig. 1. **(a)** Cross-sectional view of the dual-layer rewritable HD DVD media and the sample used for HX-PES: **(b)** with interface layers and **(c)** without interface layers.

having a structure used in actual media were prepared with interface layers on both sides of the recording material (Fig. 1(b)) and without interface layers (Fig. 1(c)) for comparison. We used GBT and SbTe films with a thickness of 5 nm, which is similar to that used in actual media. The interface layers were oxide-based and nitride-based compounds with a high crystallization acceleration function. We did not include Ge, Sb, Te, or Bi in the interface layers. We also used other interface-layer materials that had similar crystallization acceleration functions. However, the obtained results from HX-PES were similar for all samples having interface layers. The film stack was deposited on a 0.6-mm-thick PC substrate using manufacturing-scale sputtering equipment (OCTAVA-II: Shibaura Mechatronics). Along with a sample having an as-deposited amorphous recording film, a sample with a crystalline recording film was prepared. The recording film was crystallized using the same initialization equipment as that used for the initialization of rewritable HD DVDs.

Figure 2 shows photoemission spectra for the valence band of GBT with and without interface layers obtained by HX-PES. They are almost equivalent to the density of states (DOS) for the valence band of GBT. The DOS for the amorphous state without interface layers is smaller than that of the crystalline GBT. The band-edge energy of the amorphous state without interface layers is lower than that of the crystalline state by about 0.5 eV. On the other hand, the DOS of the valence band and the band-edge energy of the amorphous GBT with interface layers are almost same as those of the crystalline state. This result may lead to almost the same carrier density required for the electrical conduction of the crystalline and amorphous states, which is completely unexpected and thus very interesting because the atomic arrangements should differ from each other. This is confirmed by investigating actual media

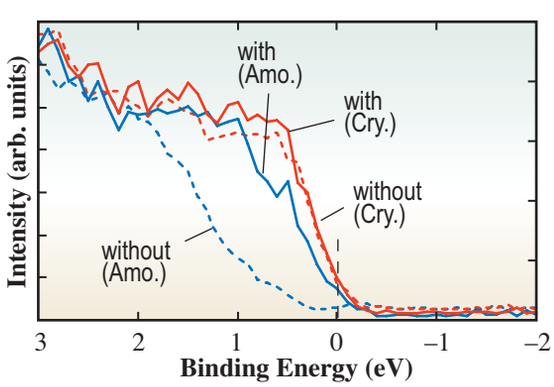

Fig. 2. Photoemission spectra for valence band of the GBT film without and with interface layers.

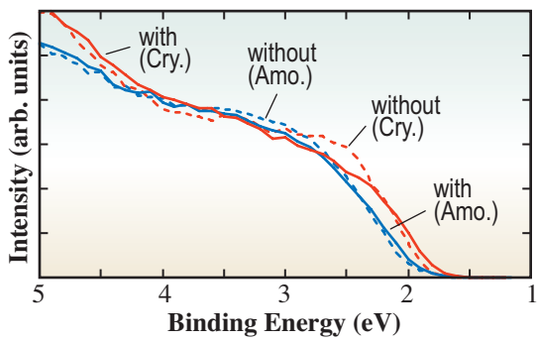

Fig. 3. Photoemission spectra for valence band of the SbTe film without and with interface layers.

nondestructively by EXAFS analysis at beamline **BL16B2** [5]. We speculate that this effect is a factor required for high-speed crystallization.

The photoemission spectra from the valence band of the crystalline SbTe films showed very little difference from those of the amorphous SbTe films regardless of whether or not they were in contact with the interface layers (Fig. 3). This behavior is similar to the results for the pseudobinary recording films with the interface layers, but is in contrast with the pseudobinary recording films without interface layers. These results suggest a difference in the crystallization mode between the pseudobinary alloy and the eutectic compound.

These findings are useful for understanding the phase-change mechanism of optical recording media. Also, they can be applied for the research of semiconductor devices such as phase-change random access memories (PRAMs).

Tsukasa Nakai* and Masahiko Yoshiki

Corporate Research & Development Center,
Toshiba Corporation

*E-mail : tsukasa.nakai@toshiba.co.jp

References

[1] S. Ovshinsky: Phys. Rev. Lett. **21** (1968) 1450.
[2] A.V. Kolobov *et al.*: Nature Materials **3** (2004) 703.
[3] T. Nakai, M. Yoshiki and N. Ohmachi: Jpn. J. Appl. Phys. **46** (2007) 3968.
[4] For example, K. Kobayashi: BUTSURI **60** (2005) 624 [in Japanese].
[5] *T. Nakai, M. Yoshiki and Y. Satoh: Proc. SPIE* ***6620*** *(2007) 66202c-1.*

Application of XMCD-PEEM to the Magnetic-domain Structural Analysis of Nd-Fe-B Sintered Magnets

Nd-Fe-B sintered magnets have been widely applied for various motors, particularly in recent years, such as motors for hybrid electric vehicles, where higher coercivities are required compared with other applications. The microstructure of Nd magnets consists of polycrystalline $Nd_2Fe_{14}B$ with aligned magnetic easy axes. Each grain is surrounded by complementary phases such as an Nd-rich nonmagnetic phase. In order to understand the coercivity mechanism more clearly, it is important to elucidate the relation between these microstructures and the characteristics of magnetic reversal. X-ray magnetic circular dichroism and photoemission electron microscopy (XMCD-PEEM) can provide such information on these characteristics simultaneously, which is one of the most promising methods for the analysis of complicated domain structures and heterogeneous morphologies such as those in Nd magnets. Since the XMCD-PEEM imaging technique has been developed, it has been utilized for various investigations of mainly soft magnetic materials. To the authors' knowledge, there have been few such investigations on hard magnetic materials; thus, this work might be the first reported application of XMCD-PEEM to Nd-Fe-B sintered magnets. The aim of this study is to establish experimental methods for the domain analysis of Nd magnets using XMCD-PEEM techniques. We focused on the difference in domain structures between the thermal demagnetized and DC field-demagnetized states of Nd-Fe-B magnets.

Our experiments on XMCD-PEEM were performed at beamlines **BL25SU** and **BL17SU**. A schematic of the XMCD-PEEM imaging method is illustrated in Fig. 1.

Each beamline is equipped with a helical undulator, which generates circular polarized X-rays. The X-rays are monochromatized into the absorption edge energy of the magnetic elements present in the sample using varied-line spacing plane gratings (VLSPG), then is focused by the optical system. The core electrons of the sample are excited by the incident X-rays, which generate photoemission electrons. These photoelectrons are accelerated by a high voltage to form the XMCD-PEEM image on the screen. The core absorption intensities of the polarized X-rays vary according to the angle between the helicity and the magnetization vectors in the domains, which results in the contrast in the image due to the magnetic domains.

Nd-Fe-B magnets were prepared by powder metallurgical processing. The as-sintered samples were in the thermally demagnetized state. The DC field-demagnetized samples were prepared by a superconducting quantum interference device (SQUID; manufactured by Quantum Design Inc.). The thermally demagnetized samples were fully magnetized once in the positive direction followed by demagnetization in the reverse field, as can be seen from the minor loop in the second and third quadrants of the 4πI-H curve, in Fig. 2. The surface regions of the field-demagnetized samples were mechanically removed to exclude their individual coercivity characteristics. These samples were elementally analyzed by field-emission scanning electron microscopy and energy-dispersive spectroscopy (FE-SEM/EDS) prior to the XMCD-PEEM experiments. As a result, the complementary phases were identified as Nd oxides and Nd-rich regions (Fig. 3(a)). Figures 3(b) and 3(c) show the PEEM images obtained at the

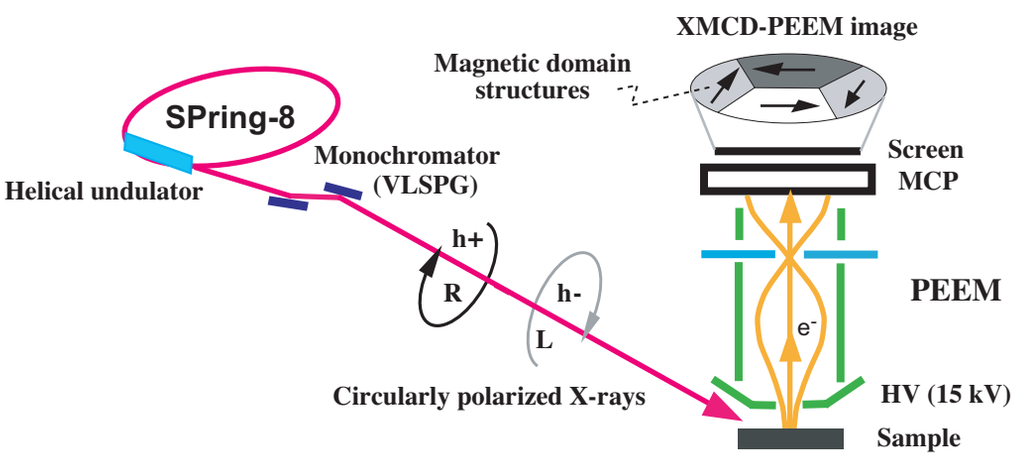

Fig. 1. Schematic illustration of XMCD-PEEM imaging.

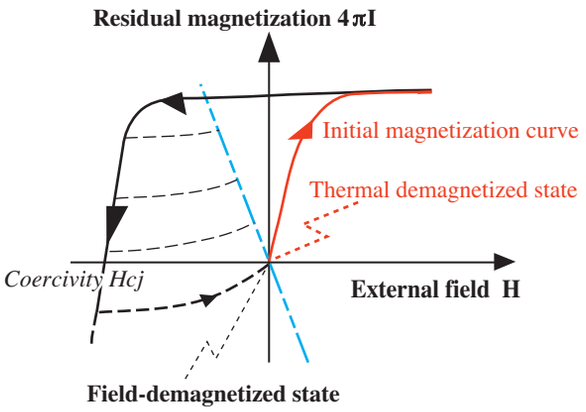

Fig. 2. Schematic magnetic hysteresis of Nd-Fe-B magnets during sample preparation starting from thermal demagnetized state to field-demagnetized state.

energies of the Nd-M_4 and Fe-L_3 edges, which were taken within the yellow- and blue-circled areas in Fig. 3(a), respectively. These images provide information on the elemental distribution upon selecting light with a suitable energy. Figure 3(d) shows the XMCD image of the same area as that shown in Fig. 3(c), which was taken at the energy of the Fe-L_3 edge. The structure appears to have a striped pattern in the lateral direction. In the thermally demagnetized state, each grain sample exhibits a multidomain structure, which is magnetically coupled across the grain boundaries over a wide range of length scales along

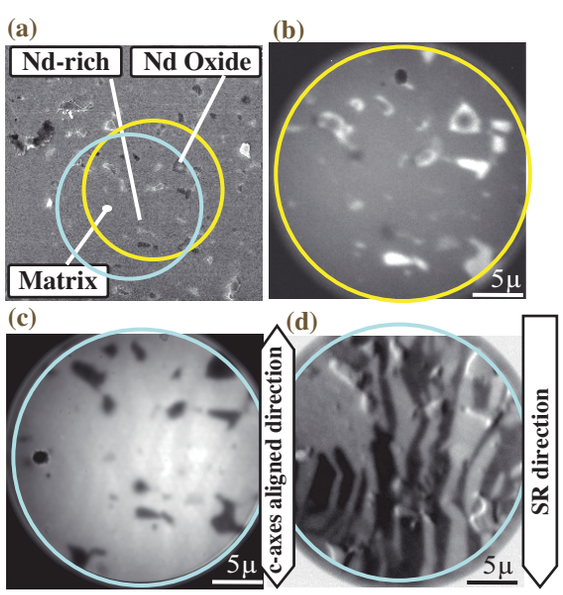

Fig. 3. Structures of magnetic domains and complementary phases of Nd-Fe-B sintered magnet in the thermally demagnetized state; **(a)** FE-SEM image (phases identified by EDS), **(b)** PEEM image of Nd-M_4 within yellow-circled area in Fig. 3 **(a)**, **(c)** PEEM image of Fe-L_3 within blue-circled area in Fig. 3 **(a)**, **(d)** XMCD image of Fe-L_3.

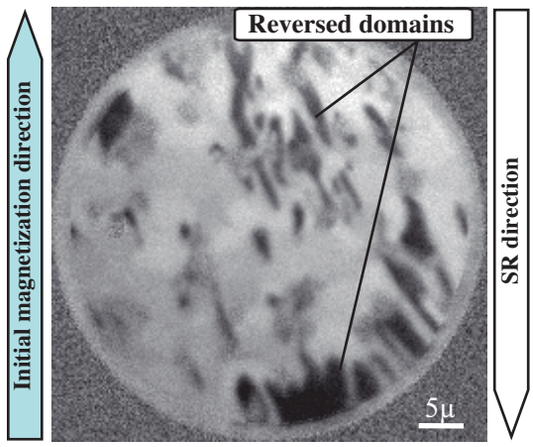

Fig. 4. Structures of magnetic domains of Nd-Fe-B sintered magnet in the field-demagnetized state: XMCD image, SR//c-axis (antiparallel); arrows: examples of reversed domains.

the easy-axis-aligned direction. This may be because of the requirement for preventing the generation of magnetic poles in the domain structure, so that the magnetostatic energy is minimized.

Figure 4 shows the XMCD image in the DC field-demagnetized state, which was taken with the incident X-rays antiparallel to the initial magnetization direction. In this domain image, the white region consists of mainly single domains, and is primary magnetized area, in contrast with the black region of reversed domains that belong to multidomain structures. These reversed domains exhibit a needle-like morphology in some areas, which agglomerate in other areas. Thus, the magnetic domain structures markedly changed after the DC field demagnetization.

The average width of the typical domains and the size of fine Nd-rich regions are approximately 1 μm and of submicron order, respectively. Since these sizes match the resolution of PEEM, XMCD-PEEM is an appropriate method for analyzing such complicated domain structures and the elemental distribution in the microstructures of Nd magnets.

Sukeyoshi Yamamoto[a,*], Mitsuharu Yonemura[a] and Toyohiko Kinoshita[b]

[a] Corporate R&D Labs, Sumitomo Metal Industries, Ltd.
[b] SPring-8 / JASRI

*E-mail: yamamoto-sky@sumitomometals.co.jp

Study of Correlation between LC Display Quality and Degree of Crystallinity at Surface of Alignment Film

The market for liquid crystal (LC) displays has been growing with the strong global demand for flat-panel displays such as those used in televisions. Rubbed polyimide films called alignment films are widely used in LC displays to uniformly align LC molecules. Therefore, understanding the mechanism of the alignment of LC on rubbed polyimide surfaces is one of the most important issues from both fundamental and industrial viewpoints. However, no clear-cut explanation of the mechanism has yet been given. We found that the capability of aligning LC molecules is correlated with the crystallinity of the polyimide film at the surface [1].

Figure 1 shows the typical structure of LC displays. The LC molecules are sandwiched between two glass substrates that are coated with a polyimide alignment film that has been unidirectionally rubbed with a cotton or rayon cloth. The LC molecules are aligned in a direction by this rubbing process. The brightness of LC displays is controlled by the direction of LC molecules, which are switched by the electric field. Therefore, the alignment of LC molecules is important for insuring the quality of LC displays, as shown in Fig. 2.

Up to now, we have developed many types of alignment films using many kinds of polyimides in order to control the alignment of LC molecules. Our studies have indicated that the alignment of LC was strongly affected by the molecular structure of the polyimide. Additionally, we have found that there is a correlation between the LC alignment capability and the degree of crystallinity of the polyimide. Grazing incidence X-ray diffraction (GIXD) is a unique technique for separately detecting the crystallinity at the surface and in the bulk. Thus, we investigated the relationship between the degree of crystallinity of the polyimide and the LC alignment capability using GIXD.

We prepared three types of polyimide films that have different LC alignment capabilities. PI-A, PI-B and PI-C polyimides have excellent (○), good (△) and poor (×) LC alignment capabilities, respectively. Thin polyimide films were prepared by curing spin-coated polyamic acid on a Si substrate. The thickness of the films obtained after curing was about 100 nm. GIXD experiments were performed using a multiaxis diffractometer installed in the 2nd hutch of the beamline **BL19B2**. The incident X-ray energy was set at 10 keV.

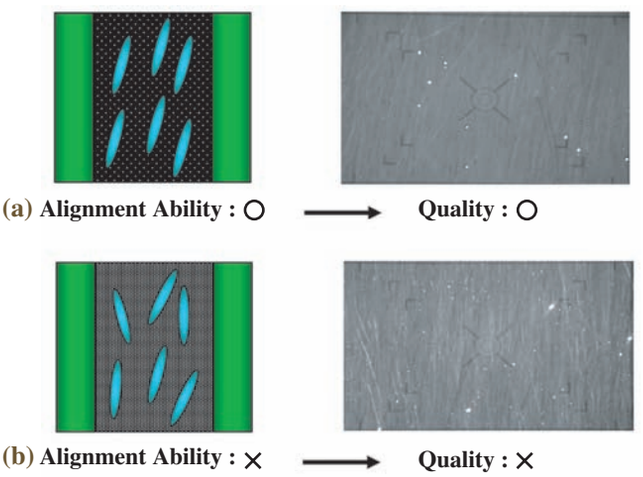

Fig. 2. Relationship between the capability of aligning LC molecules and the quality of LCD. **(a)** When all LC molecules are unidirectionally aligned, the LC quality is high. **(b)** If each LC molecule has a different direction, the brightness varies from area to area. That results in poor LC quality.

Figure 3 shows plots of the observed in-plane θ-2θ profiles of the rubbed films when the scattering vector is parallel to the rubbing direction with an incident angle of 0.16° (over the critical angle of the films). In this condition, we were able to obtain bulk-sensitive information on the films, since the incident X-ray penetrated deep into the polyimide films. For all films, we observed one sharp diffraction peak at around 4° and one broad diffraction peak around at 15°, as shown in the figure. These observed profiles suggest that there was no significant difference in the degree of crystallinity between the bulk films. That is, there is no relationship between the crystallinity of the bulk and the LC alignment capability.

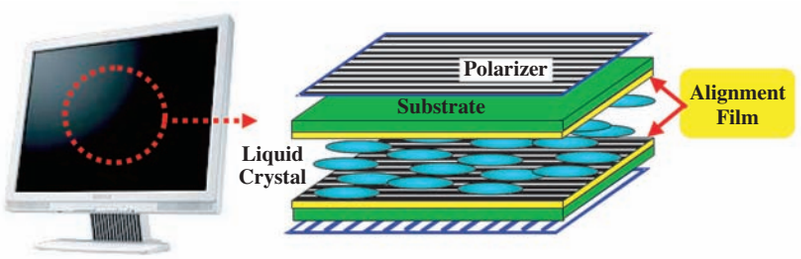

Fig. 1. Typical structure of LCD.

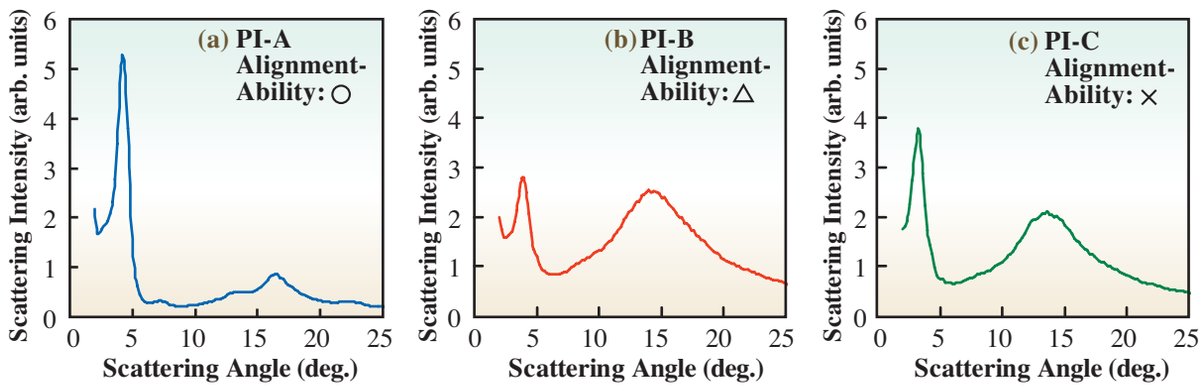

Fig. 3. Observed diffraction profiles obtained from **bulk**-sensitive measurements.

On the other hand, surface-sensitive profiles were obtained from in-plane θ-2θ scans by setting the incident angle at 0.12° (below the critical angle). In this condition, the X-ray penetration depth was estimated to be about 8 nm. The surface-sensitive profiles show important differences in the intensities of the diffraction peak at around 4° among the three films, as shown in Fig. 4. A sharp and intense peak was observed in the case of PI-A, which has excellent alignment capability (○). However, the surface-sensitive peak of PI-B (alignment capability: △) is weak. Furthermore, there appears to be no surface-sensitive peak in the case of PI-C (alignment capability: ×) despite the fact that the bulk-sensitive peak of PI-C was clearly observed. These facts indicate that there is a clear correlation between the LC alignment capability and the degree of crystallinity at the surface of the polyimide films.

In conclusion, we investigated the crystallinity of polyimide films having different alignment capabilities using GIXD and found a correlation between the LC alignment capability and the crystallinity at the surface. As mentioned above, the LC alignment capability is directly related to the LCD quality. Thus, we have obtained a result that can act as a guide for the development of films with excellent alignment that have the capability of realizing excellent LCD quality.

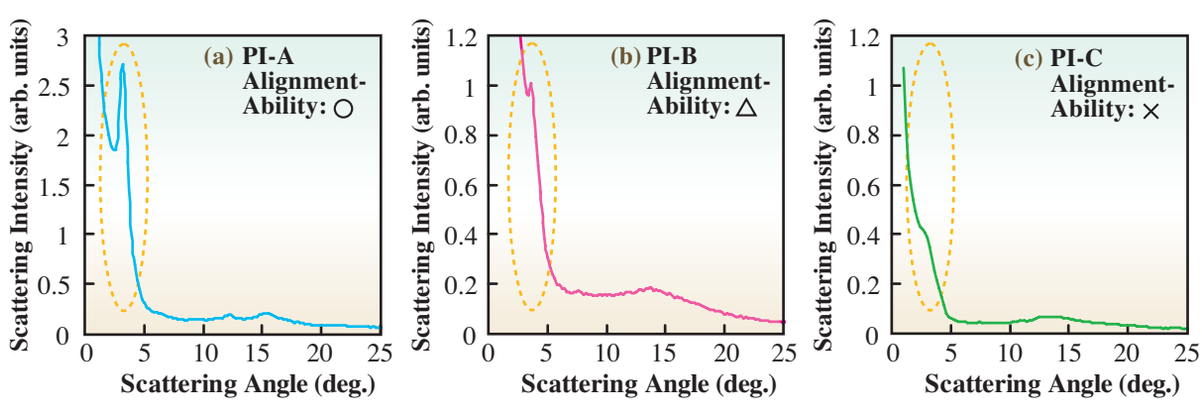

Fig. 4. Observed diffraction profiles obtained from **surface**-sensitive measurements.

Takahiro Sakai[a,*,†], Hidenori Ishii[a] and Ichiro Hirosawa[b]

[a] Electric Materials Research Laboratories, Nissan Chemical Industries, LTD.
[b] SPring-8 / JASRI

*E-mail: sakai_takahiro@mrc.co.jp

[†] Present address: Materials Science and Analysis Res. Center, Mitsubishi Rayon Co., Ltd.

References

[1] *T. Sakai: Kinou Zairyou (Function & Materials)* ***27*** *(2007) 69 (in Japanese).*

Three-dimensional Topography using an X-ray Microbeam and Novel Slit Technique

X-ray section topography is a powerful tool for the nondestructive crystallographic analysis of semiconductor materials. In such analysis, however, recent requirements are beyond the capability of conventional section topography due to the development of microstructured semiconductor devices. Not only is submicron resolution required, but also the cross sections to be examined are often parallel or perpendicular to the device surface or along a dislocation line. Three-dimensional (3D) X-ray topography is intended for the quick measurement of topography for such various cross sections of devices with submicron resolution [1]. In this article we describe the application of this new method to the defect analysis of a SiC diode.

Experiments were conducted at the undulator beamline **BL24XU**. A monochromatic X-ray beam (E = 15 keV) was focused on a sample using a bent cylindrical mirror. The half widths (at 1/e of the maximum) of the focused beam were 1.16 μm and 1.04 μm in the horizontal and vertical directions, respectively. We used a special slit with a V-shaped crevice (V-slit) for microbeam X-ray diffraction (Fig. 1). The V-slit is a metal contact made of stainless steel with polished slanted edges and an opening angle of 4°, that has a sharp-pointed exponential transmission curve [1]. The diffraction beam impinges on the V-slit, through which a thin beam passes to reach a scintillation counter (SC). We can thus observe a small region Q, where the incident beam crosses the extended line (broken arrow) of the beam passing through the slit, and scanning the sample position provides 3D topography. Although the image obtained involves blurring caused by the tailed transmission curve of the slit, deconvolution can effectively restore the image [1].

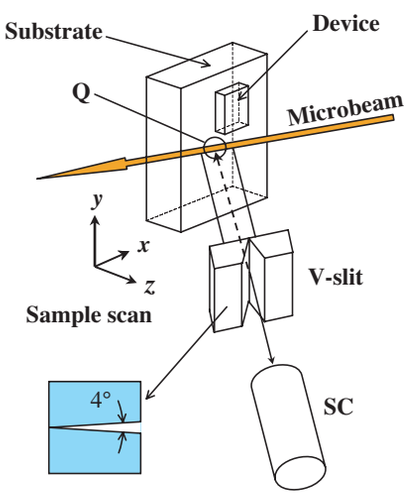

Fig. 1. Experimental setup. An X-ray microbeam penetrates a sample and a diffraction beam impinges on the V-slit, through which a thin beam passes to reach a scintillation counter (SC). Scanning the sample produces 3D topography. The V-slit is a metal contact made of stainless steel with polished slanted edges.

The sample examined is a 200 × 200 μm^2 p-n diode fabricated on an 8°-off-cut (0001) 4H-SiC wafer (Fig. 2(a)). As shown in Fig. 2(b), slice topographs (SiC 0 0 20 reflection) were obtained by performing a z (depth) scan and an x-y scan at each z position. Figure 3(a) shows a slice image (log scale), in which we observed three screw dislocations (SD1, SD2, and SD3). To examine the depth distribution of the SDs, x-z-section topographs along the SDs were reconstructed (Figs. 3(b), 3(c), and 3(d)). The broken lines indicate the interface between the epilayer and the substrate (epi/sub interface). Since the z scale is six times greater than the x scale, the slight slant of the sample is exaggerated. These figures clearly indicate that the SD lines penetrate the epi/sub interface.

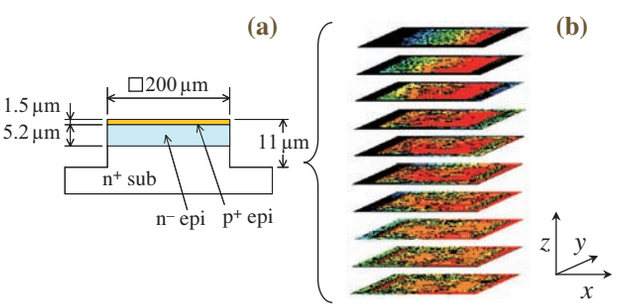

Fig. 2. Cross-sectional view of the sample SiC diode **(a)** and its slice topographs **(b)**. The diode was fabricated on an 8°-off-cut (0001) 4H-SiC wafer **(a)**. The slice topographs were obtained by performing a z (depth) scan and a 2D scan at each z position **(b)**.

Figure 4(a) shows a slice topograph (linear scale) of a similar diode with a SiC 0 0 16 reflection, where we observe an SD located on an upwardly winding grain boundary. We performed an x-y-z scan in a small region including this SD and obtained the x-y and x-z topographs shown in Figs. 4(b) and 4(c), respectively. For the x-z cross-sectional images, we performed a deconvolution [1] to restore the image. Note that the two boundaries as well as the wafer surface become clear in the restored image Fig. 4(d). These boundaries are in good agreement with the p/n junction and epi/sub interface (broken lines). The image restoration can improve the spatial resolution from about 2 μm to 0.5 μm or less.

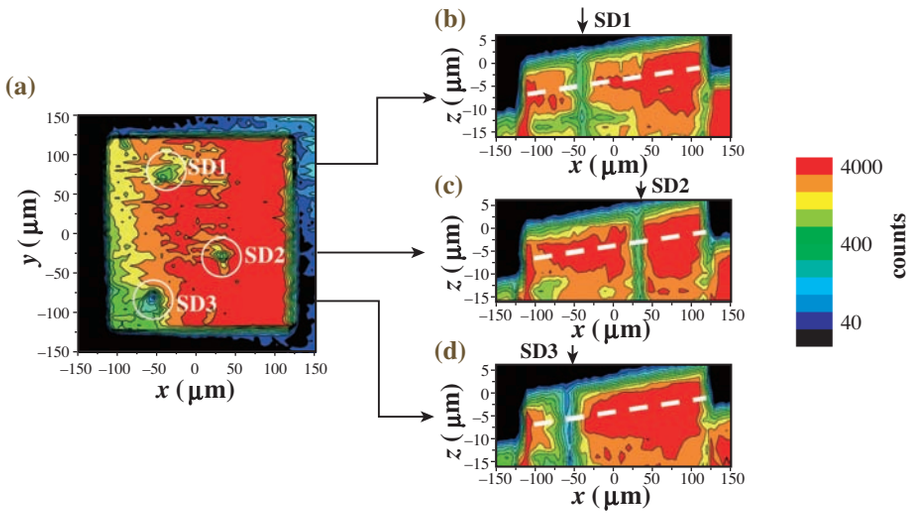

Fig. 3. Analysis of screw dislocations in a SiC diode. The *x*-*y* slice topograph **(a)** and *x*-*z* section topographs **(b)**-**(d)** were obtained from a 3D scan over the device region. The topographs show three screw dislocations (SD1, SD2, and SD3) that penetrate the epi/sub interface (broken lines).

We thus clarified that the V-slit method can provide a submicron-depth-resolved diffraction image. Such analysis is valuable for SiC devices because it is important to examine whether a defect is generated during epilayer growth, or is replicated from the substrate. The new method also meets various requirements in semiconductor analysis. In particular, its nondestructive, cross-sectional imaging is useful in the crystallographic analysis of recently developed layer-structured devices.

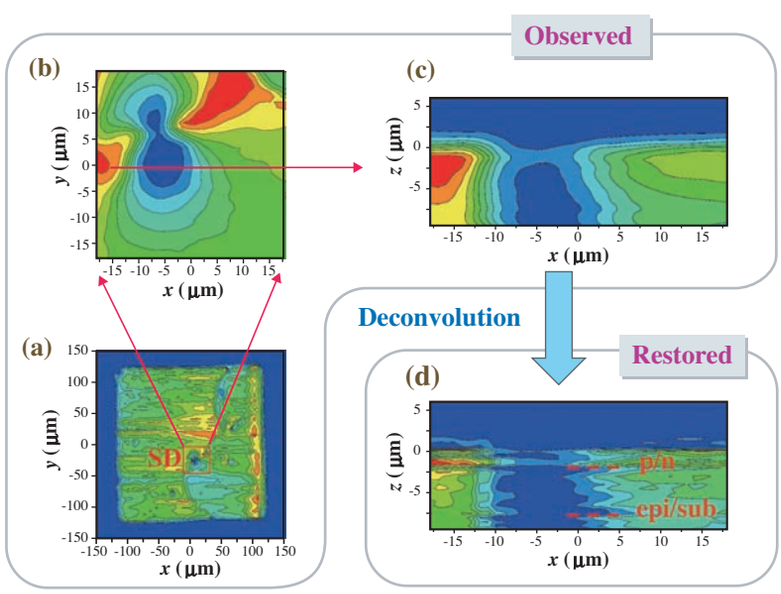

Fig. 4. High-resolution defect analysis of a SiC diode. The slice topograph shows a screw dislocation (SD) **(a)**. An *x*-*y*-*z* fine scan around the SD was performed to obtain the *x*-*y* and *x*-*z* topographs **(b)(c)**. Deconvolution provides the restored image, in which the two boundaries of the dislocation as well as the wafer surface become clear **(d)**. These boundaries are in good agreement with the p/n junction and epi/sub interface (broken lines).

Ryohei Tanuma* and Tae Tamori

Fuji Electric Advanced Technology Co., Ltd.

*E-mail: tanuma-ryohei@fujielectric.co.jp

References

[1] *R. Tanuma, T. Kubo, F. Togoh, T. Tawara, A. Saito, K. Fukuda, K. Hayashi, Y. Tsusaka: Phys. Stat. Sol. (a)* ***204*** *(2007) 2706.*

Application of X-ray Microtomography to Evaluate Thermal Fatigue Crack Propagation and Lifetime in Flip Chip Interconnects

In high-density packaging technology, one issue of particular importance is the enhancement of reliability in micrometer-sized joints connecting LSI (large scale integrated circuit) chips to PCBs (printed circuit boards) electrically and mechanically. A microstructure approach is required to evaluate the reliability of these so-called microjoints, which are significantly affected by fatigue damage (microstructure evolution or fatigue cracks, etc.). To evaluate the microstructure damage due to fatigue, the development of a nondestructive inspection technology is highly desirable for industries producing electronic devices and components. However, none of the microstructure images of the joints obtained by industrially used nondestructive inspection methods such as ultrasonic flaw detection, X-ray radiography or X-ray tomography have sufficient spatial resolution. In this work, an X-ray microtomography system called SP-μCT with a spatial resolution of about 1 μm [1] was applied to the evaluation of thermal fatigue crack propagation and lifetime of solder microbumps in flip chip interconnects.

The specimens have a flip chip structure in which an LSI chip is mounted on an FR-4 substrate by joining Sn-37wt%Pb eutectic solder bumps 100 μm in diameter. A thermal cycle test was carried out under accelerated conditions with upper temperature 125°C, lower temperature –40°C and holding time 30 min. The specimens were picked up after various numbers of test cycles and the solder bumps were observed by using SP-μCT at **BL20XU**. Under typical measurement conditions 1800 projections were taken in 0.1° steps during 180° rotation, and the exposure time for each projection was 0.2 sec. The refraction-contrast imaging technique was applied to visualize fatigue cracks in the solder bumps. That is, the distance between the X-ray beam monitor and the specimen was optimized so as to maximize the contrast of the crack edges imaged by Fresnel diffraction.

Figure 1 shows a three-dimensional image of a specimen loaded for 300 cycles under the accelerated conditions. For convenient observation of the inner structure, the Si chip and some components are not shown in the image. The microstructure of the bumps and the fiber orientation of the FR-4 substrate are clearly identified.

The CT images in Fig. 2 show the process of microstructure change and crack propagation on the same cross section of the same solder bump due to the thermal cyclic loading [2]. After 100 cycles, no thermal fatigue cracks were observed and the microstructure maintained its initial characteristic state with fine, dispersed Pb-rich phases. After 300 cycles, fatigue cracks appeared at the corners of the interface between the solder bump and the Cu pad. This number of cycle corresponds to the mean lifetime of fatigue crack initiation determined by SEM (scanning electron microscope) destructive observation.

As the number of thermal cycle increases, the cracks gradually propagate to the inner region of the solder bump. The lengths of the same fatigue cracks were measured consecutively from CT images obtained at the centers of the same bump. Figure 3 shows the crack propagation process for some solder bumps in terms of the relationship between the fatigue crack length and the number of cycles *N*. The fatigue crack propagation is characterized by the average propagation rate being approximately constant even though transient acceleration or stopping is observed in each solder bump. The average propagation rate was calculated to be 0.058 μm/cycle, and the total fatigue crack lifetime to failure N_f was estimated as N_f = 1800 cycles. This estimate is relatively precise because the mean fatigue lifetime to failure determined by SEM observations was less than 2000 cycles.

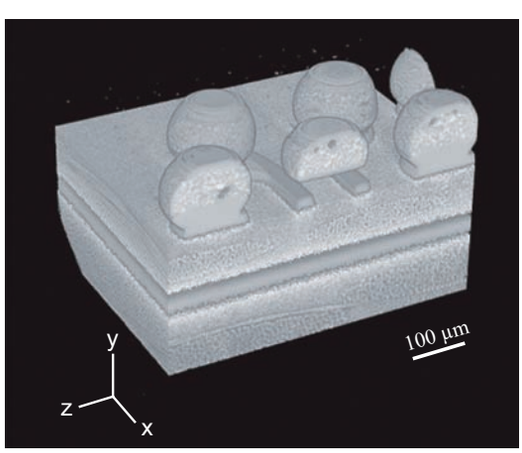

Fig. 1. Volume-rendered image of a flip chip specimen.

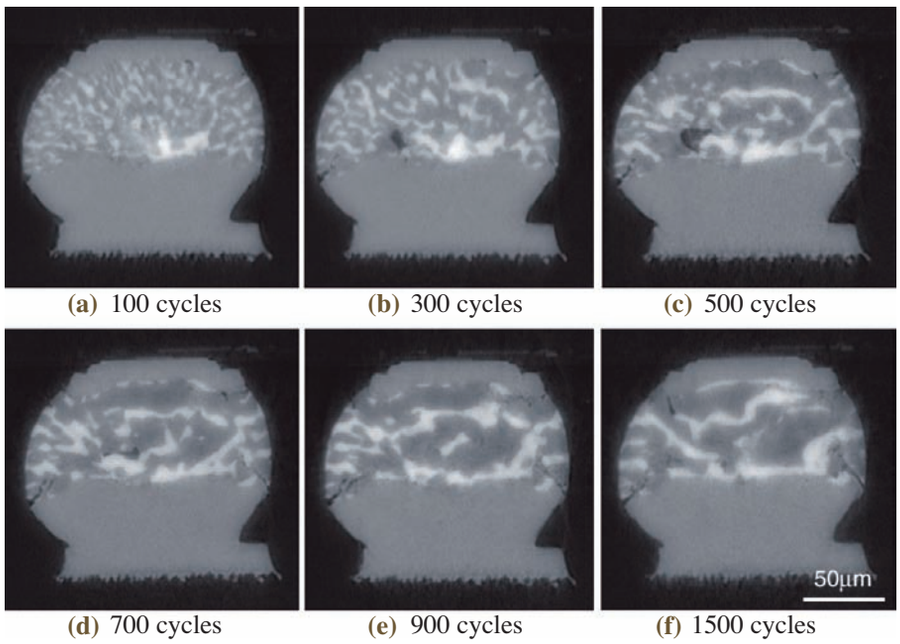

Fig. 2. CT images of the same solder bump showing fatigue crack propagation induced by thermal cyclic loading.

These results were not obtained by industrially used nondestructive inspection systems, and show that nondestructive testing by a synchrotron radiation X-ray micro-CT system is useful for evaluating the thermal fatigue lifetime in microjoints.

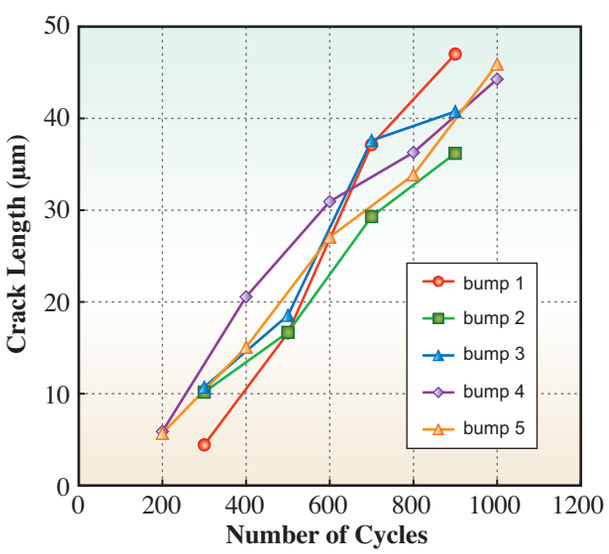

Fig. 3. Crack propagation process in solder bumps during thermal cyclic loading.

Hiroyuki Tsuritani [a], Takeshi Takayanagi [b,*] and Toshihiko Sayama [a]

[a] Toyama Industrial Technology Center
[b] Cosel Co., Ltd.

*E-mail: takayanagi@cosel.co.jp

References

[1] K. Uesugi *et al.*: Nucl. Instr. Method. A **467-468** (2001) 853.
[2] *H. Turitani, T. Sayama, Y. Okamoto, T. Takayanagi, K. Uesugi and T. Mori : Proc. IPACK2007, ASME InterPACK'07, IPACK2007-33170, Vancouver, Canada.*

Detection of Cracks due to SCC in Ni-base Alloys by Synchrotron Radiation CT Imaging

Stress corrosion cracking (SCC) is an intergranular failure that takes place in structures such as austenitic stainless steels and nickel-base alloys exposed to high-temperature and high-pressure water. SCC is an important engineering issue for the structural integrity of light water reactors.

For the inspection of cracking in structural components, ultrasonic testing (UT) is recognized as an important and useful technique. However, it is generally not easy to detect the defects and obtain correct information on cracks in the welding metal by UT. This is due to the fact that the anisotropic and inhomogeneous microstructure of the welding metal leads to direction-dependent sound propagation, which is related to sound velocity, polarization, sound reflection and absorption at interfaces. The accuracy of crack size and depth data obtained by UT are sometimes evaluated by other methods such as a cross-sectioning examination. As the cracks due to SCC are complex with a 3-dimensional (3D) distribution, the numerical data obtained by 2-dimensional (2D) techniques such as the cross-sectioning method may results in errors. A numerical simulation technique to interpret the UT signal and data is under development [1].

In this study, we aimed to demonstrate the applicability of X-ray computer tomography (CT) with refractive contrast to the 3D imaging of minute cracks produced in weld metals of nickel-base alloy caused by SCC. Whilst the X-ray CT technique has already been applied to fatigue cracks of light metals such as Al alloys, no trial has yet been performed to evaluate the SCC in steels or Ni alloys [2]. Although X-ray attenuation is high for the Ni alloy specimen due to its large mass absorption coefficient, 3D images are successfully reconstructed by the X-ray CT technique using highly parallelized brilliant X-rays from SPring-8. Accurate crack size and depth data were obtained.

The SCC test specimens were prepared from a weld metal of nickel-base alloy (Ni-15Cr-7Fe-0.15C) after it was exposed to tetrathionic acid solution for few days. The crack depth was fixed by controlling the corrosion potential. The specimen employed was rod-shaped with a diameter of about 0.7 mm, as shown in Fig. 1, and was made so that the top of the rod was on the original material surface. The CT imaging experiments were performed at beamline **BL19B2**. The experimental setup is schematically shown in Fig. 2. The X-ray energy was adjusted to 37 keV using a Si double-crystal monochromator. The distance between the bending magnet (X-ray source) and the sample was about 110 m. The area detector (cooled CCD camera) was set 0.41 m or 0.8 m behind the specimen to obtain refractive contrast imaging. Projection data of 1024 × 1024 pixels was recorded every 0.5° from 0 to 180°. The effective pixel size of the detector was about 6 μm. Slice images were reconstructed by a standard algorithm used for filtered-back projection.

Reconstructed slice images for a crack due to SCC in the Ni-base weld metal obtained at a camera length of 0.41 m are shown in Figs. 3 and 4. A typical bent or twisted crack with a complex structure is observable in Fig. 3. The width of the crack is narrow. The crack propagation is considered to depend on the orientation of the crystal and solidified structures. On the other hand, another type of crack with a flat or plane structure similar to a fatigue crack can be observed in Fig. 4. Although the SCC conditions were the same, it is clear that the crack structure and distribution may change depending on the base-metal condition such as its grain orientation, grain boundary and precipitates. The resolution of the crack image is about 10 μm near the surface.

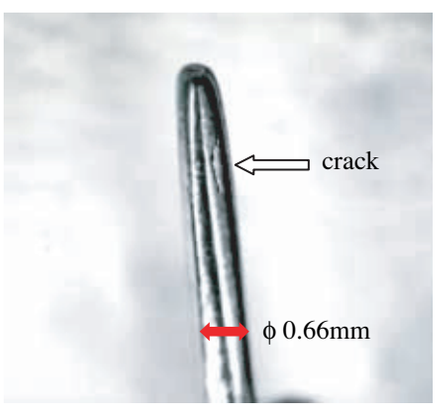

Fig. 1. Appearance of test sample.

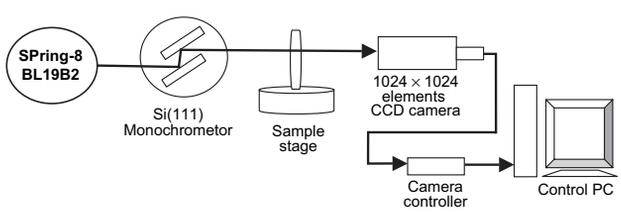

Fig. 2. Schematic illustration of measurement system.

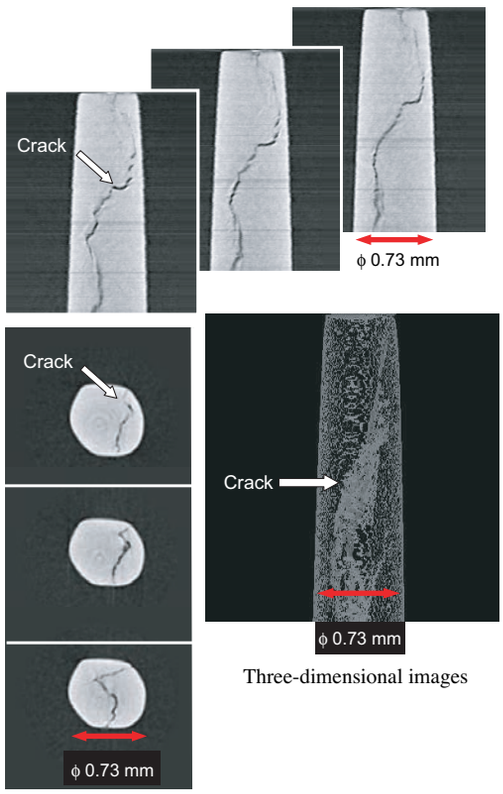

Fig. 3. Reconstructed slice images (sample 1).

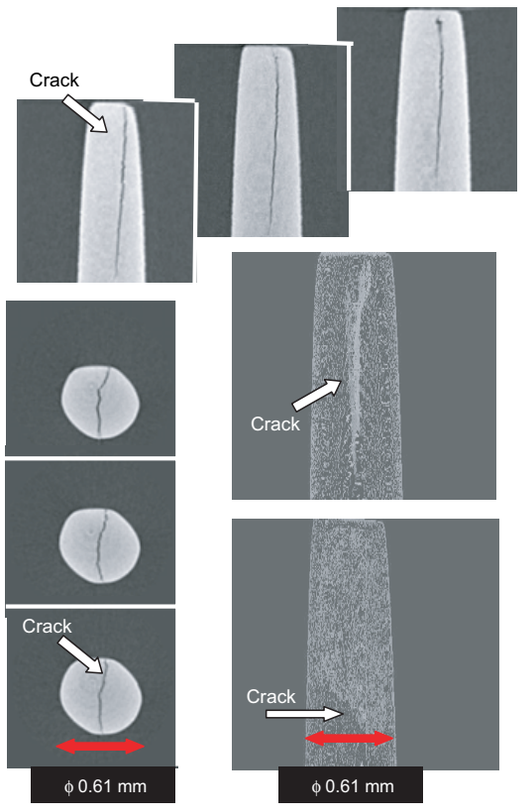

Fig. 4. Reconstructed slice images (sample 2).

The results of crack length measured by a crack depth gage, cross-sectioning examination and CT imaging are compared in Table 1. The values of crack length obtained by cross-sectioning examination are shorter than those obtained by X-ray CT imaging. This is expected since an internal crack cannot be observed by cross-sectioning examination. Although the difference is not large in this case, it should be noted that X-ray CT imaging is a nondestructive technique.

In summary, clear images of fine cracks in nickel-based metal due to SCC were successfully obtained by synchrotron radiation CT imaging.

Table 1. Comparison of the crack depth obtained by crack depth gage, cross-sectioning examination and CT imaging

Sample	Crack depth gage	Sectioning	CT imaging
No. 1	3.2 mm	1.2 mm	1.6 mm
No. 2	1.6 mm	0.7 mm	0.9 mm

Shigeo Nakahigashi [a,*], Mititaka Terasawa [b], Atsushi Yamamoto [b] and Kentaro Kajiwara [c]

[a] Japan Power Engineering and Inspection Corporation
[b] University of Hyogo
[c] SPring-8 / JASRI

*E-mail : nakahigashi-shigeo@ japeic.or.jp

References

[1] I. Komura *et al.*: 2nd Int. Conf. NDE, New Orleans, May 24-26, 2000, B 221-231
[2] H. Toda *et al.*: Acta Metall. **52** (2004) 1305.

Infrared SR Analysis of Trace Vitamin E in an Artificial Joint made of Ultrahigh Molecular Weight Polyethylene (UHMWPE)

Artificial joint substitution for the elderly has been increasing in accordance with their desire for independent living and the recovery of functional use. Also, orthopedic implantations have been increasing in recent years.

In the case of knee joint substitution, a joint made of ultrahigh molecular weight polyethylene (UHMWPE) connected with titanium or Co-Cr-Mo alloy components is placed between the thigh bone and the shin bone. The life of an artificial joint depends on the degree of deterioration of UHMWPE, and the average life is recognized as being 15-20 years. The joint is slowly ablated, oxidized and deteriorated by the weight load and friction. Increased oxidation stability and wear resistance are key features in extending the life of an artificial joint. UHMWPE has good wear resistance but poor oxidation stability to free radicals [1] and low wear resistance to heat treatment [2]. An example of a failed UHMWPE knee component is shown in Fig. 1(a). Many materials have been tested as functional additives to UHMWPE, and vitamin E has been recognized as a promising material. UHMWPE with added vitamin E has similar mechanical properties to pure UHMWPE [3] but also exhibits high oxidation stability [4], high wear resistance [4] and ease of molding.

In this study, we aimed to evaluate the oxidation stability and wear resistance of UHMWPE with added vitamin E by infrared SR analysis.

A tibial component used in total knee arthroplasty (High-Tech Knee II, Nakashima Medical) made of UHMWPE with added vitamin E as shown in Fig. 1(b), was prepared by the direct compression molding (DCM) technique. An accelerated oxidation was conducted by the method of Sun as follows. We first irradiated the sample with 25 kGy gamma rays in air at atmospheric pressure at 80°C. After irradiation, we kept the sample at 23°C for 7 days. The six-station four-axis knee joint simulator (Fig. 2(a)) (AMTI, Boston, MA) was then applied to the sample. The waveform for the simulation was that of normal walking and a 5,000,000-cycle test was carried out, which simulates 7-10 years of use in real life. After the 5,000,000-cycle simulation, the sample lost 30% of its weight as shown in Fig. 2(b).

We carried out measurements of the samples at the infrared microspectroscopy beamline **BL43IR** before (=control) and after applying the accelerated oxidation and the knee joint simulator. Two hundreds spectra were accumulated at a wavenumber resolution of 4 cm^{-1}. The mapping area was 2000 μm × 75 μm wide along the X and Y axial directions, respectively, and the stepping pitch was 25 μm × 25 μm. The quantity of added vitamin E was trace, which was why we used infrared synchrotron radiation instead of FT-IR with a conventional light source. We chose a 500-μm-thick sample to ensure that we obtained the absorption intensity of the trace vitamin E. A sample of this thickness cannot easily be measured by conventional FT-IR, and the highly brilliant synchrotron radiation at SPring-8 is ideal for the measurement.

Figure 3 shows the infrared absorption spectra of UHMWPE with vitamin E concentrations of 0, 0.3, 1

Fig.1. **(a)** Failed UHMWPE knee component due to lack of oxidation stability. **(b)** Test sample (top), control (bottom) and HTK II knee joint.

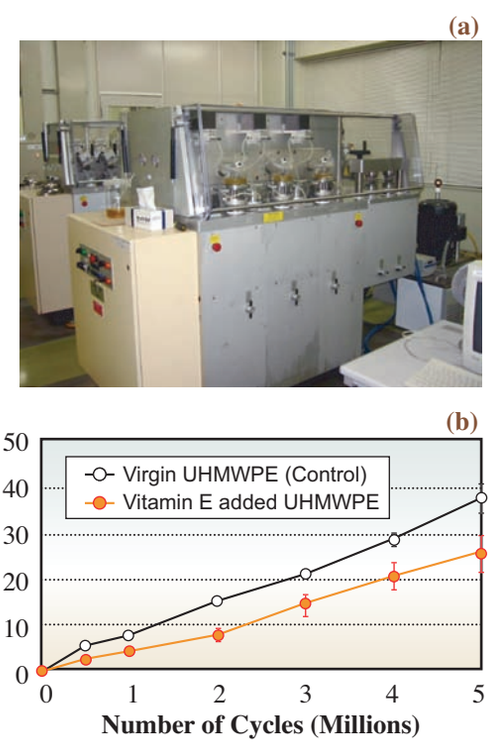

Fig. 2. **(a)** AMTI knee joint simulator. **(b)** Weight loss of the samples during the simulation.

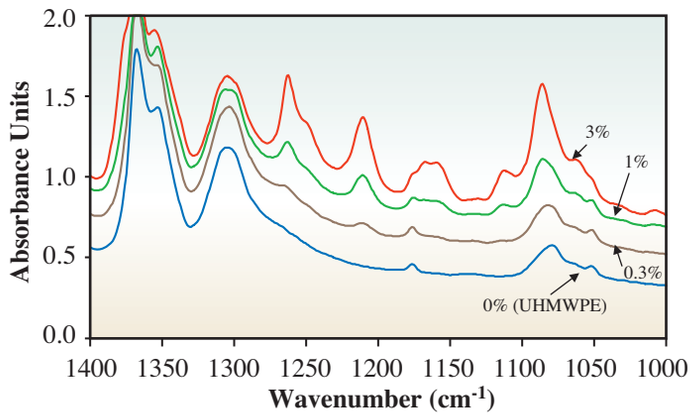

Fig. 3. Infrared absorption spectra of UHMWPE with various concentrations of added vitamin E.

and 3%. In the spectra, we confirmed the presence of -OH and -C-O-C- functional groups in the chromane ring of vitamin E at *ca*. 1050 - 1300 cm^{-1}. In the mapping images shown in Fig. 4, we found vitamin E distributed near the surface before (=control) (Fig. 4(b)) and even after applying the accelerated oxidation and the knee simulator (Fig. 4(a)), which suggests that vitamin E in UHMWPE plays an important role in preserving the joint under conditions simulating oxidation, weight load and friction that occur in daily use.

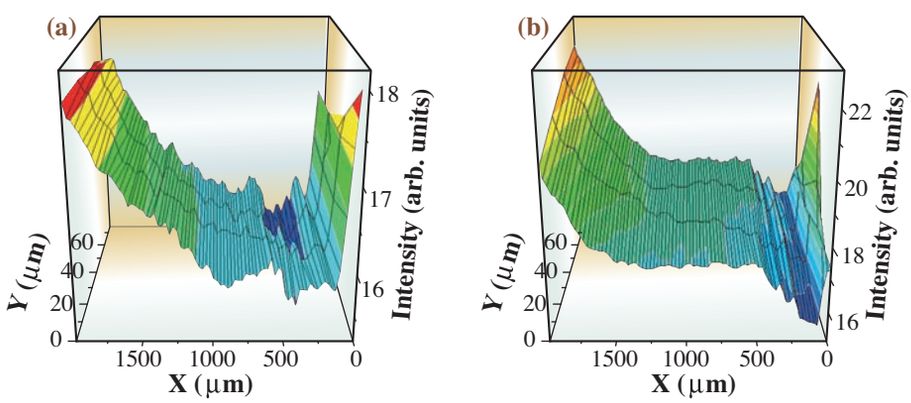

Fig. 4. Mapping images of the ⁻OH functional group of the chromane ring in vitamin E. The X axis is along the depth direction and the Y axis is along the surface of the artificial joint. **(a)** After accelerated oxidation and knee simulator. **(b)** Before accelerated oxidation and knee simulator (control).

N. Nishimura [a,*], E. Fukuda [a], Y. Yamazaki [a], Y. Ikemoto [b] and T. Moriwaki [b]

[a] Nakashima Medical Division, Nakashima Propeller Co., Ltd.
[b] SPring-8 / JASRI

*E-mail: nishimura@nakashima.co.jp

References

[1] Currier *et al.*: 51st Ann. Mtg. Orthopaedic Res. Soc. (2005) 1128.
[2] Oral *et al.*: 51st Ann. Mtg. Orthopaedic Res. Soc. (2005) 1712.
[3] Mori *et al.*: 47th Ann. Mtg. Orthopaedic Res. Soc. (2001) 1017.
[4] Mori *et al.*: 48th Ann. Mtg. Orthopaedic Res. Soc. (2002) 1041.

Analysis of Ingredients that Penetrate into the Inside of Hair by Infrared Microspectroscopy

Japanese women have come to enjoy various hair color tones and hairstyles that accompany changes in fashion with the diversification of lifestyles in recent years. Although the black hair coloring boom of several years ago may be on the wane, hair dying still remains popular among young people as a way of changing their image. Many senior citizens are also concerned about gray hair. Therefore, their interest in hair dyes remains strong and the market for such products is gradually increasing. Hair-dying products contain hydrogen peroxide to adjust the color of the dye substances and induce a chemical reaction between the hair and the dye. For this reason, repeated use may result in damaged hair, such as changes to the hydrophilicity of the hair surface and to the internal structure of the hair.

The use of hair treatments for preventing such damage, and for hair protection and easy styling has been increasing in recent years. These formulations contain ingredients such as proteins, amino acids, oils, polymers, minerals, surfactants and moisturizers, and the control of the penetrability of these ingredients is an important factor for the effective realization of their functions. Therefore, an analysis of the penetrability of these functional substances is important for the development of highly effective formulations.

One conventional method for confirming the penetrability of a substance into hair is to dye the hair with a pigment and afterwards make an indirect estimate of penetrability by measuring the degree of color difference. Regarding direct measurement, one method of analysis is to employ a substance labeled with a radioisotope or fluorescent material. However, such labeling may cause changes in the chemical and physical properties of the tested substances, and thus may not be a completely accurate method for evaluating the penetrability of a substance.

Similarly, small-angle X-ray scattering experiments have been carried out using the X-ray microbeam of the high flux beamline **BL40XU** to analyze the structure of the cell membrane complex (CMC) at the hair's cuticle, which is considered to be a penetration route for applied substances, and the contribution of the CMC to substance penetration has previously been examined. Nevertheless, regarding penetrability, analysis has been limited to the indirect method in color-difference measurements, and the penetrabilities of the ingredients in hair treatment product have not been confirmed directly [1].

We have focused our attention on a particular high-molecular weight (HMW) phospholipid-derived polymer that exhibits excellent styling performance. Generally, the HMW polymer does not react inside hair. However, it has been surmised from our initial observations that a close relationship exists between the polymer's penetrability into the inside of hair and the styling performance. Thus, we decided to confirm the penetrability of this polymer by determining the infrared absorption properties of the phospholipid-derived polymer, which differs from other components in hair.

The experimental methods and their results are described below. Two types of hair bundles (healthy and damaged by bleaching) were immersed in a phospholipid-derived polymer water solution for 72 hours, and then the bundles were extracted and dried. The dried bundles were then embedded in resin, and cross sections (with thickness about 3 μm) of each bundle were prepared for the measurement. The samples were placed in the microspectroscopy beamline **BL43IR**, and one quarter of the cross-

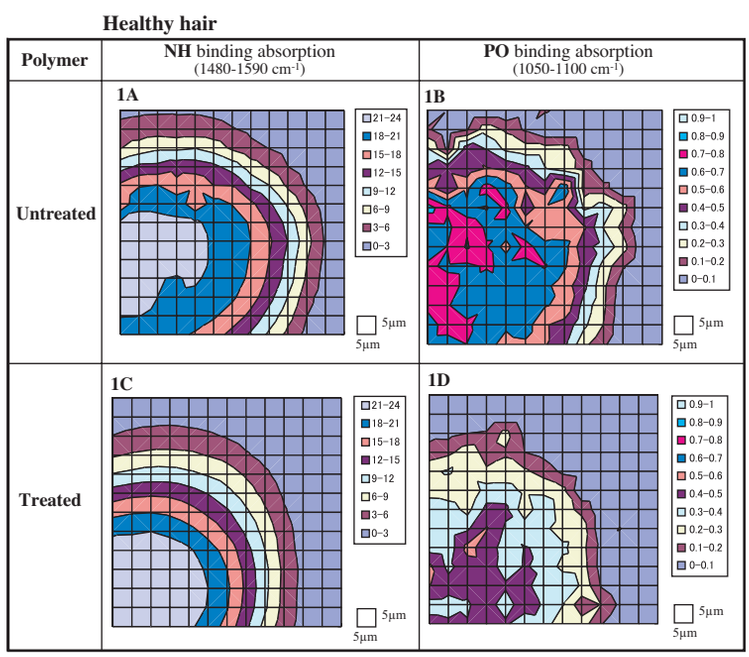

Fig. 1. Comparison of absorption intensity image mapping data (healthy hair). Higher absorption intensity represents higher values in each graph. Spatial resolution: 5 μm. Wave number range: 8000-450 cm^{-1}.

sectional area (roughly 70 μm × 70μm) was measured by the transmission method while moving the mapping stage every 5 μm in the wave number range from 8000 to 450 cm^{-1}.

On the basis of the measurement results, we created an image map of the NH binding absorption peak (Figs. 1A, 1C, 2A and 2C) derived from keratin protein amide, and the PO binding absorption peak (Figs. 1B, 1D, 2B and 2D) derived from the phosphate components of the hair and the phospholipid-derived polymer.

As a result, we could capture the hair contours by image mapping the NH binding absorption peak (healthy hair: Figs. 1A and 1C, damaged hair: Figs. 2A and 2C). Moreover, from the results of the hair untreated with the polymer, it became evident that damage to the hair led to an apparent decrease in the PO binding absorption peak (Figs. 1B and 2B) of the hair itself. When each hair bundle was treated with polymer, the following results were obtained. In the case of healthy hair, there was no major change in the PO binding absorption intensity (i.e., no penetration of the polymer was observed). In the case of damaged hair, a high rate of PO binding absorption was observed over a wide range of the internal part of the hair, particularly at the intermediate part (i.e., a high rate of penetration into the hair). It was also confirmed that the target polymer selectively penetrated deeper into the damaged hair.

From the experimental results, we concluded that an analytical method for assessing the penetrability of the target substance into hair had been established. In the future, we plan to realize the widespread application of this method by analyzing other target substances.

From the results of experiments using fluorescence-labeled compounds, the phospholipid-derived polymer's excellent hair styling performance is considered to be closely related to the polymer's ability to penetrate into hair. In the current experiment, we clarified this penetration phenomenon directly and confirmed the relationship between penetration and styling performance. In other words, this polymer may achieve its excellent styling performance by penetrating into the inside of hair and affecting its internal structure.

We have already carried out a structural analysis of the CMC in the cuticle layers of hair using BL40XU, and examined its contribution to substance penetration. In combination with the new method for analyzing penetration by IR microspectroscopy established in this experiment, it is expected that the relationship between structural changes in the cuticle CMC and a substance's penetration ability will become clearer, enabling the development of more effective hair treatment products.

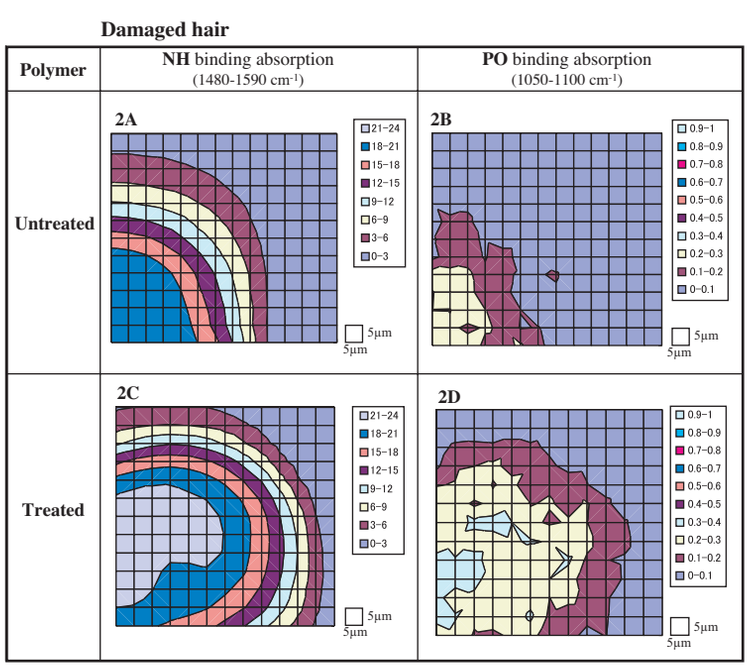

Fig. 2. Comparison of absorption intensity image mapping data (damaged hair). Higher absorption intensity represents higher values in each graph. Spatial resolution: 5 μm. Wave number range: 8000-450 cm^{-1}.

Satoshi Inamasu [a,*], Taro Moriwaki [b] and Yuka Ikemoto [b]

[a] Beauty Care Laboratory, Kracie Home Products, Ltd.
[b] SPring-8 / JASRI

*E-mail: s.inamasu@khp.kracie.co.jp

References

[1] T. Inoue *et al.*: J. Cosmet. Sci. **58** (2007) 11.

INSTRUMENTATION &

"Kobushi" - Magnolia

"Fuji" - Wisteria

METHODOLOGY

Although the 10th anniversary of the SPring-8 inauguration was celebrated in October 2007, the development of new instrumentation and methodology are still continuing. Ten years of operation has accumulated a wide variety of instrumentation, yet some new instrumentation would be required to devise because of and (i) possible transplantation of new devices developed in other fields than the synchrotron radiation science, (ii) possible combination of existing instrumentation for more advanced and/or efficient data acquisition, and (iii) continuing improvement of the light source performance which includes the reduction of the horizontal emittance of the electron beam as well as the increase of the time-averaged intensity with the top-up operation. In addition, as reported in this volume, the construction of a new X-ray free electron laser (XFEL) facility started in 2006 to complete in 2010. Some new instrumentations and methodologies for XFEL are being developed using SPring-8 beams.

We have selected six excellent articles among many candidates for the Instrumentation & Methodology chapter of this volume.

Five articles describe new instrumentation/methodology which combines two or more techniques to make a new unique technique. Dr. Hiroyasu Masunaga and coauthors presented a WAXD/SAXS simultaneous measurement system applied to polymer samples. Dr. Takaya Mitsui presented a Mössbauer spectroscopy under ultrahigh-pressure by combining the ultrahigh-pressure technique with nuclear Bragg diffraction with synchrotron radiation. Dr. Tomoya Uruga and coauthors combined fast oscillation mechanism with a crystal monochromator to realize quick EXAFS using a pink beam from an undulator. Dr. Akira Saito and coauthors has been trying to devise an element-sensitive STM by combining STM with hard X-ray excitation with a micerobeam. Dr. Yoshiki Kohmura presented the combination of X-ray in-line holography with shearing interferometry which can give the complete information of the complex transmissivity of samples.

The approaching coherent X-rays from the coming X-ray free electron laser urged to open up a new methodology of X-ray non-linear optics. Dr. Kenji Tamasaku and coauthors presented a new finding in parametric down-conversion of X-rays.

We hope some of the instrumentation introduced in this volume will be used by wider scientific communities in the near future.

Tetsuya Ishikawa

Application of WAXD/SAXS Simultaneous Measurements to Study Aggregation Structure of Polyvinylfluoride in Ferroelectric Phase Transition Process

Polymeric materials consist of complicated aggregation state of chains. In semicrystalline polymers, for example, these chains gather together to form the crystalline region or a crystalline lamella. These lamellae are stacked together to construct a spherulite. It is essentially important to clarify the evolution process of this complicated hierarchical structure of polymers from the various viewpoints on angstrom-to-micrometer scale in order to design and control their physical and structural properties.

The time-resolved measurements of the wide-angle X-ray diffraction (WAXD) and small-angle X-ray scattering (SAXS) allow us to trace the hierarchical structural evolution process of polymers in the heating or cooling process, for example. There were many reports on the WAXD and/or SAXS experimental data [1,2]. The WAXD and SAXS measurements are usually performed separately for a sample by assuming the reproducibility of the experimental conditions. Strictly speaking, however, we have no guarantee for the reproducibility of the experimental conditions in the WAXD and SAXS measurements, since the polymeric material has a large hysteresis concerning the thermal or mechanical treatment. It is ideal to perform the simultaneous measurement of WAXD and SAXS for one sample under the completely same conditions.

A simultaneous 2D-WAXD/SAXS measurement system was installed for the public use at beamline **BL40B2**. We measured the temperature dependences of WAXD, SAXS and enthalpy change to investigate the crystal phase transition of poly(vinylidene fluoride) (PVDF) using this system combined with DSC equipment for the study of thermally-induced structural change in the heating or cooling process of polymers [3].

Figure 1 shows a photograph of the DSC/WAXD/SAXS measurement system built at BL40B2. The system is using a CMOS FP detector for WAXD, while a CCD detector coupled with X-ray imaging intensifier for SAXS, which can trace the change of the hierarchical structure of polymeric materials every few seconds. The data collection timing can be controlled by an external trigger which can synchronize the FD detector and II+CCD detector with the external instrument such as a DSC.

The uniaxially-oriented vinylidene fluoride-trifluoroethylene random copolymers are well known to show the ferroelectric phase transition between the polar form I crystal (I) and nonpolar crystalline phases (HT) in the heating and cooling processes. This allows us to speculate that PVDF form I may show a phase transition to the HT phase in much higher temperature region close to the melting point. However, the samples sometimes melted before the observation of the phase transition. We need to confirm the observation of form I -to- HT phase transition during the heating process at relatively fast rate to avoid the local sample melting. We were challenged to perform the simultaneous DSC/WAXD/SAXS measurement using the above-mentioned synchrotron system.

Figure 2 shows the 2-D WAXD and SAXS patterns measured for the uniaxially-oriented PVDF form I sample at 154.5°C and 164.6°C. The WAXD pattern at 154°C corresponds to that of pure form I crystal. The SAXS was the four-points scattering pattern, indicating a tilt of stacked lamellae about 50° from the

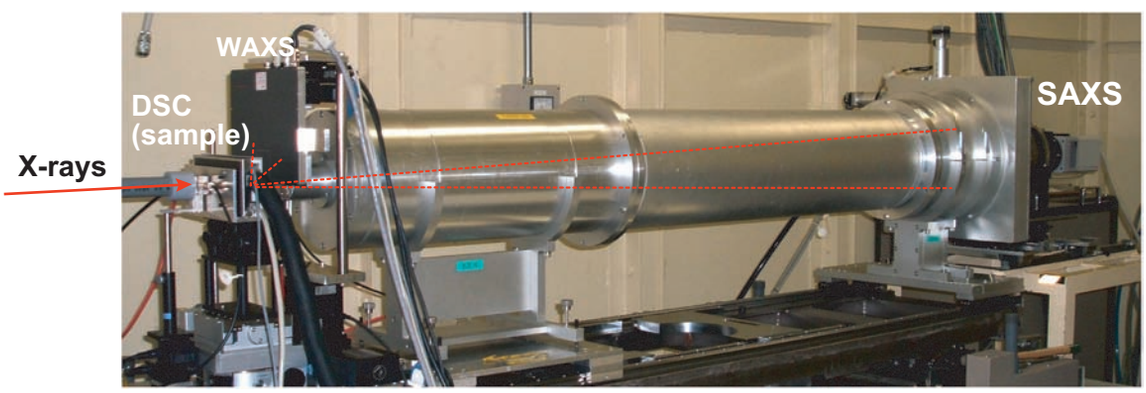

Fig. 1. Photograph of the DSC/WAXD/SAXS simultaneous measurement system built-up at beamline BL40B2.

draw axis. As the temperature increased, the intensity of form I reflections became weaker. In the WAXD pattern taken at 164.7°C, the new pattern was found to appear, which corresponded well to the X-ray diffraction pattern of HT phase. The SAXS pattern was found to change also drastically from the four-points scattering pattern to the meridional two-points scattering pattern. These changes in patterns suggested the tilting angle of lamellae became almost zero, and the long period increased remarkably from 10 nm to 53 nm.

Figure 3 shows the temperature dependences of X-ray reflection intensity estimated for form I and HT phase and that of the long period and lamellar tilting angle in comparison with the DSC thermogram. A shoulder detected in the lower temperature side of DSC peak corresponds to the phase transition from form I to HT phase.

In this way we succeeded in confirming the phase transition of PVDF form I occurring in the temperature region close to the melting point. The newly installed DSC/WAXD/SAXS measurement system has enabled us to detect these phase transition phenomena satisfactorily. As a result, we have been able to establish the important universal phenomenon common to many crystalline polymers: the morphological change of stacked lamellae occurs in strong association with the crystalline phase transition. The system will be improved regarding data collection and analysis.

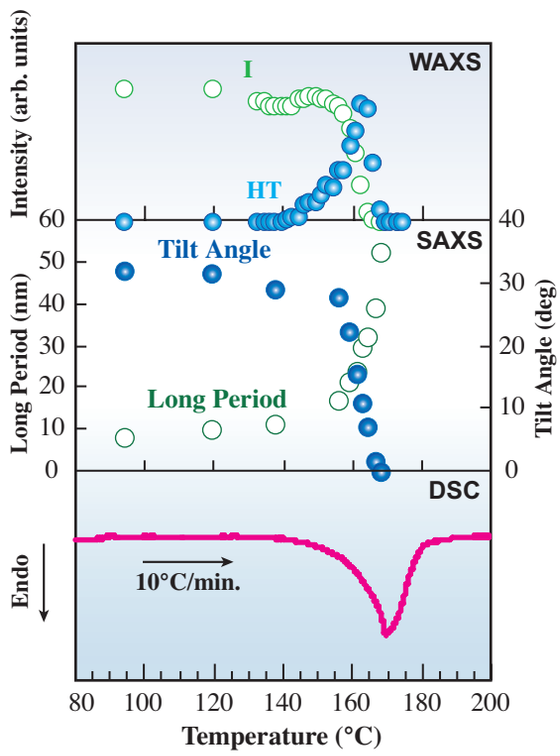

Fig. 3. Temperature dependences of long period and tilting angle of stacked lamellae, peak intensity of the (001)I and (002)HT reflections and DSC thermogram measured for the uniaxially-oriented PVDF form I in the heating process at 10.0 °C/min.

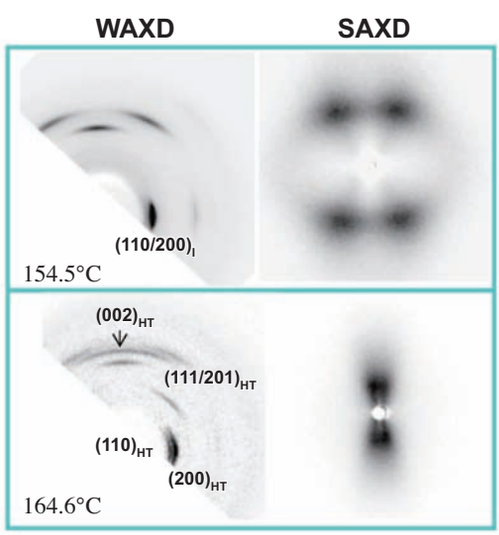

Fig. 2. WAXD and SAXS patterns measured simultaneously for oriented PVDF sample at 154.5 °C and 164.5 °C. The meridional direction is parallel to the oriented direction of sample.

Hiroyasu Masunaga[a,*], Sono Sasaki[a] and Kohji Tashiro[b]

[a] SPring-8 / JASRI
[b] Dept. of Future Industry-oriented Basic Science and Materials, Graduate School of Engineering Toyota Technological Institute

*E-mail: masunaga@spring-8.or.jp

References

[1] K. Tahiro and S. Sasaki: Prog. Polym. Sci. **28** (2003) 451.
[2] Y. Nozue *et al.*: Macromolecules **40** (2007) 2036.
[3] *H. Masunaga, S. Sasaki, K. Tashiro, M. Hanesaka, M. Takata, K. Inoue, N. Ohta and N. Yagi: Polym. J. **39** (2007) 1281.*

Ultrahigh-pressure Synchrotron Radiation ^{57}Fe-Mössbauer Spectroscopy using Single-line Pure Nuclear Bragg Reflection

Pure nuclear Bragg reflection of a $^{57}FeBO_3$ single crystal at the Néel temperature can select single-line ^{57}Fe Mössbauer radiation from synchrotron radiation (SR) [1,2]. This fully recoilless single-line is a very attractive probe beam for various applied researches using energy-domain SR Mössbauer spectroscopy because it has high directivity, small beam size, and pure linear polarization. In particular, SR Mössbauer spectroscopy using single-line pure nuclear Bragg reflection combined with a focusing X-ray optics has enabled us to easily achieve micron-scale small-target researches. As a typical example of such experiment, the Mössbauer transmission spectra were observed for polycrystalline iron metal and hematite under multimegabar pressures (> 200 GPa) in a diamond anvil cell (DAC) for the first time [3].

The nuclear diffraction optics for ultrahigh-pressure SR Mössbauer spectroscopy is shown in Fig. 1. The experiments were performed at beamline **BL11XU** (JAEA). A σ-polarized X-rays with an energy width of 2.5 meV at 14.4 keV nuclear resonance of ^{57}Fe were produced by a liquid-nitrogen-cooled Si (111) double-crystal pre-monochromator and a high-resolution monochromator (HRM). A bent elliptical multilayer mirror focused the incidence X-rays were horizontally with a focal size of 400 × 36 μm^2 at the sample position. Downstream of a Doppler vibrating sample mounted on a velocity transducer, the transmission X-rays were ultimately monochromatized into a 15.4 neV bandwidth by the electronically forbidden (333) pure nuclear Bragg reflection of a $^{57}FeBO_3$ single crystal near the Néel temperature (75.8°C) in a 150 Oe external magnetic field [2]. Behind a slit, the nuclear Bragg diffracted X-rays were detected by a NaI(Tl) scintillation detector. The peak photon counting rate of $^{57}FeBO_3$ (333) reflection was 2.4 × 10^3 cps, and the noise level was below 8.0%. In this optics, the Mössbauer spectrum was measured by counting the intensity of single-line nuclear Bragg reflection as a function of velocity. The measurement scheme is shown in Fig. 2.

As the first demonstration of ultrahigh pressure SR Mössbauer spectroscopy, a micron-sized polycrystalline iron metal (^{57}Fe 95%) placed in a DAC was measured in the multimegabar range. The specimen and small platinum (Pt) chip were enclosed in a hole of 18 μm diameter in a rhenium (Re) gasket between the flat parallel faces of two oppositely facing diamond anvils, without a pressure medium. The pressure was estimated at 252 GPa from the X-ray diffraction profile of Pt. The Mössbauer spectrum was observed using a vibrating DAC mounted on a velocity transducer at sample position of Fig. 1. The result is shown in Fig. 3.

The statistically sufficient spectrum of a polycrystalline iron metal under the ultrahigh pressure of 252 GPa was obtained in a short measurement time of 2.0 h. It clearly showed a single-line absorption profile, which was a typical Mössbauer spectrum of paramagnetic α-Fe. As for the quadrupole interaction of α-Fe, no significant change was observed in the spectrum. However, the isomer

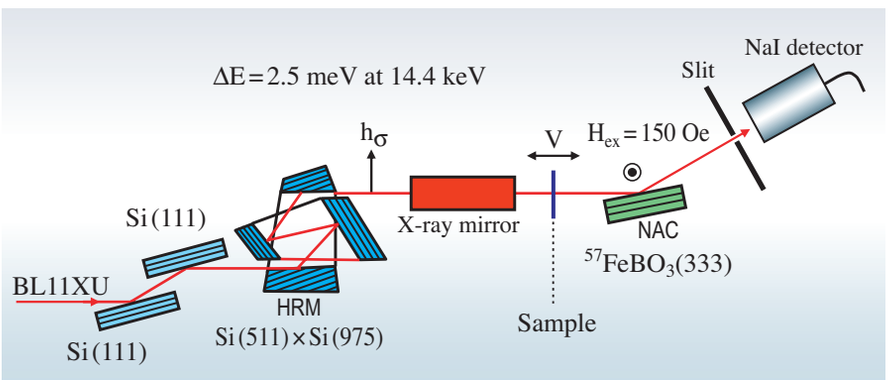

Fig .1. Optics for the energy domain SR Mössbauer spectroscopy using single-line pure nuclear Bragg scattering. (HRM: high-energy-resolution monochromator; NAC: nuclear analyzer crystal).

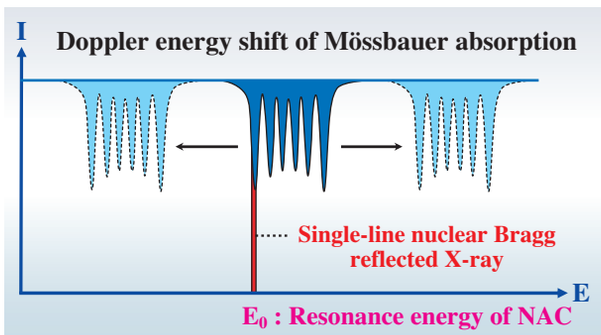

Fig. 2. Conceptual diagram for the energy domain SR Mössbauer spectroscopy with single-line pure nuclear Bragg scattering.

shift showed a marked energy shift (-0.85 mm/s) at 252 GPa. This is attributed to the considerable increase in the s-electron charge density at the ^{57}Fe nucleus owing to the decrease in atomic volume at 252 GPa.

Figure 4 shows the high-pressure Mössbauer spectra of a hematite (^{57}Fe 95%) polycrystal measured in the multimegabar range. The measured spectra show the clear dependence of hyperfine magnetic field and electric quadrupole splitting under pressure. This method will become a powerful tool for high-pressure science and geophysics.

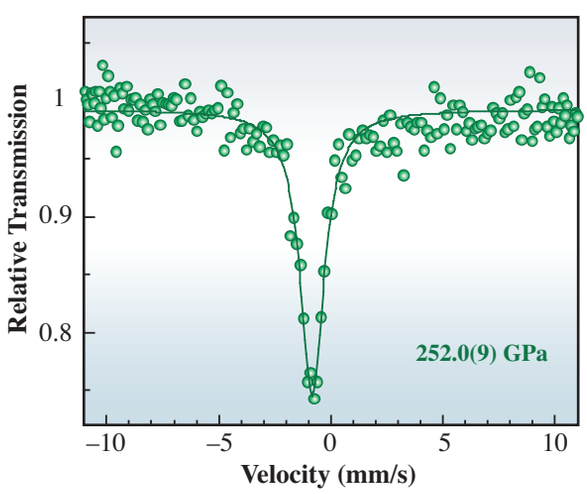

Fig. 3. SR Mössbauer spectrum of a polycrystalline iron metal (^{57}Fe 95%) in DAC at ultrahigh pressure of 252 GPa. The solid line is fit with Lorenzian line.

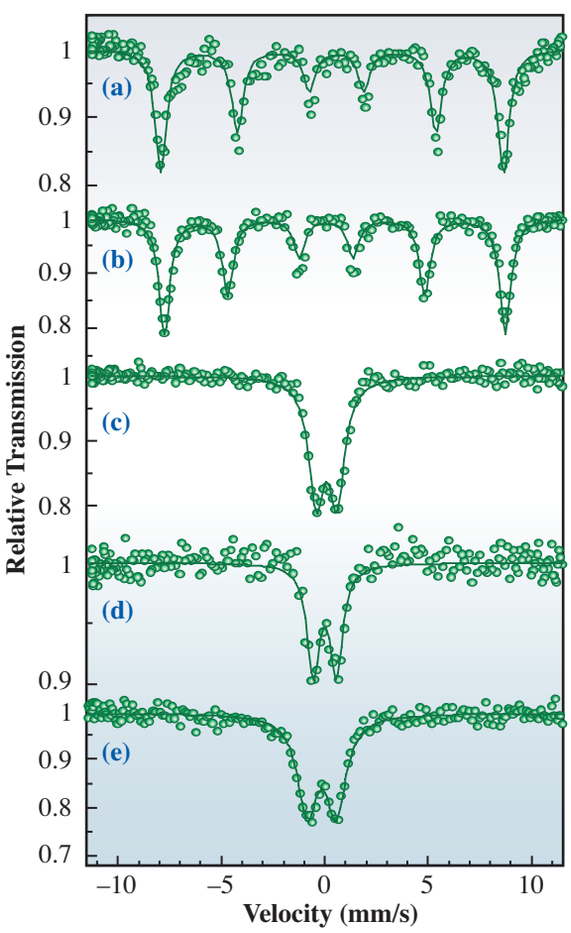

Fig. 4. SR Mössbauer spectra of $^{57}Fe_2O_3$ at different pressure conditions. **(a)** 0 GPa, **(b)** 43 GPa, **(c)** 91 GPa, **(d)** 121 GPa and **(e)** 204 GPa. The solid lines are fits with Lorenzian lines.

Takaya Mitsui

SPring-8 / JAEA

E-mail: taka@spring8.or.jp

References

[1] G.V. Smirnov *et al.*: Phys. Rev. B **55** (1997) 5811.
[2] T. Mitsui *et al.*: Jpn. J. Appl. Phys. **46** (2007) 821.
[3] *T. Mitsui, M. Seto, N. Hirao, Y. Ohishi, Y. Kobayashi, S. Higashitaniguchi and R. Masuda: Jpn. J. Appl. Phys.* ***46*** *(2007) L382.*

Milliseconds Quick XAFS System using Quasimonochromatic Undulator Radiation

Time-resolved X-ray absorption fine structure (XAFS) technique is a powerful tool for investigating local structure and electronic state of materials in both crystalline and non-crystalline state during chemical or physical reaction process. Recently, dilute or thin film samples in transient reaction states have been highly interested in many research fields, such as catalysts, functional devices, environmental materials and so on. In this report, we describe the newly developed milliseconds time-resolved XAFS measurement system adapted for actual dilute or film samples in transient reaction states [1].

Two major techniques are used in time-resolved XAFS measurements for transient reactions: energy dispersive XAFS (DXAFS) and quick XAFS (QXAFS). In DXAFS measurement, polychromatic X-rays are focused on the sample by a bent-crystal, which have different energies depending on the diffraction angle. It is capable of measuring XAFS spectra with a one-shot exposure of several-tens microsecond using a position sensitive detector. DXAFS can only be used in transmission mode, which is adapted mostly for concentrated samples. QXAFS is carried out by quick scanning of a monochromator to obtain XAFS spectra within a short time, of which time resolution is seconds in most beamlines. QXAFS has a big advantage in that it can be applied to the fluorescence mode, which enables the measurements of dilute or thin film samples.

To achieve faster QXAFS, a higher X-ay flux on the sample and faster scanning monochromator are needed. We used helical undulator radiation in **BL40XU** [2,3]. This undulator generates on-axis fundamental radiation in the energy range from 8 - 17 keV. The total power was reduced to 7 - 15 W by eliminating off-axis higher harmonics radiation in the front end without significant loss of the fundamental radiation, which greatly mitigated the heat load on the X-ray optics. Low heat load radiation allowed the cooling devices to be removed and the monochromator to be downsized.

We newly developed a compact Si(111) channel cut monochromator (size: 27 (l) × 13 (w) × 14 (t) mm). The monochromator crystal was mounted on a galvano scanner stage (Fig. 1) which repeatedly oscillate a Bragg angle of crystal with up to 100 Hz in the EXAFS range. The height of the exit beam from the channel cut monochromator changed during an XAFS measurement but was reduced to about 40 - 5 μm at 8 - 17 keV due to a small gap of 3 mm between the reflecting surfaces of the crystal. Detectors were the ionization chambers for the transmission mode and a photomultiplier with a plastic scintillator for the fluorescence X-ray detection. The monochromator, detectors and a sample were arranged on an experimental stage placed in an experimental hutch (Fig. 2). The energy at each data points was calculated from the angle of the galvano scanner, and was corrected with simultaneously measured XAFS spectrum of a standard sample using the beam

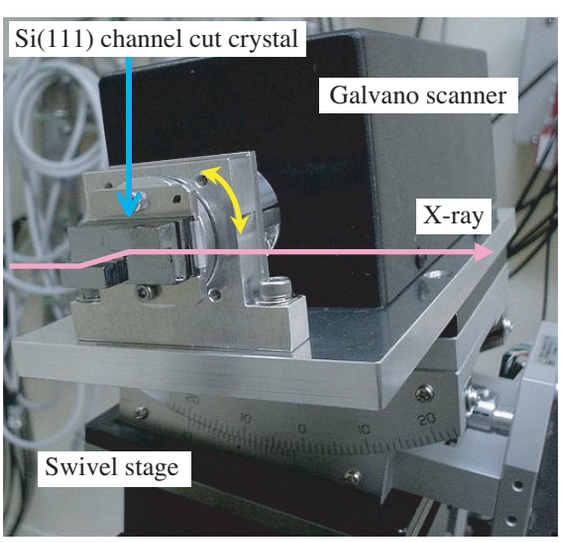

Fig. 1. Si(111) channel-cut monochromator mounted on galvano scanner stage.

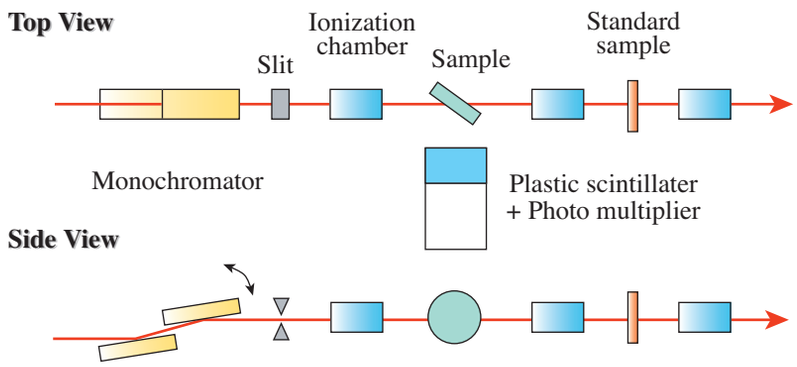

Fig. 2. Layout of monochromator, sample and detectors on experimental stage.

transmitted through the target sample.

Figure 3(a) shows an XAFS spectrum around the Pt-L_3 edge (11.6 keV) of Pt foil in the transmission mode together with the incident X-ray intensity. The peak of the fundamental radiation from the undulator can be set to the maximum energy of the target energy region. We set it at 12.5 keV to measure spectra with a high S/N ratio up to k = 15 A^{-1}. The intensity of the incident beam gradually decreased toward the lower energy region but was still higher than that of the bending magnet source in SPring-8. Such an incident beam profile of the helical undulator is adequate for XAFS measurements because the EXAFS spectrum in the high k region requires a high incident X-ray flux.

Figure 3(b) shows a $k^3\chi(k)$-XAFS spectra of Pt foil in the fluorescence mode measured in BL40XU in comparison with that measured at the bending magnet beamline BL01B1. The data were not corrected for the self-absorption effect. Good quality spectra were obtained in 30 msec. We have adapted so far milliseconds quick XAFS measurement system to dilute samples, such as fuel cell catalysts and automotive exhaust catalysts, with collaborators, and successfully measured spectra with the time resolution of 50 - 100 msec. The results will be published in the near future.

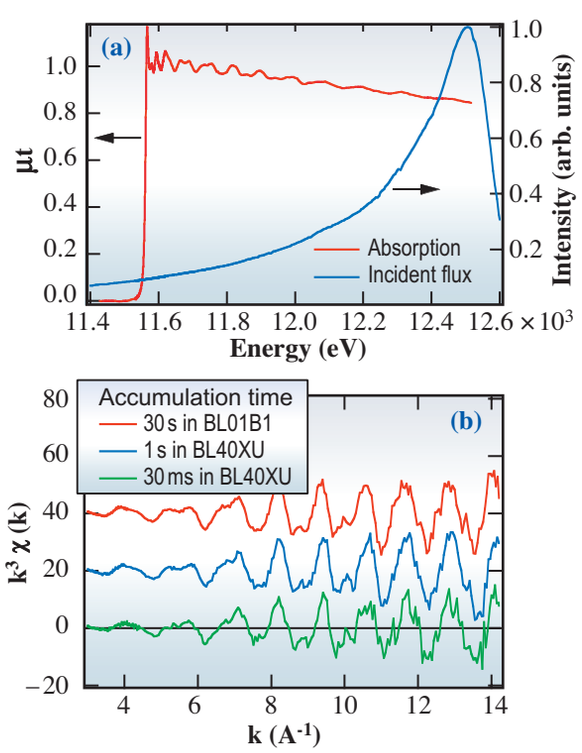

Fig. 3. **(a)** Pt-L_3 edge (11.6 keV) XAFS spectrum of Pt foil in transmission mode together with incident beam intensity, and **(b)** $k^3\chi(k)$-XAFS spectra in fluorescence mode measured in BL40XU and BL01B1.

Tomoya Uruga*, Hajime Tanida and Hiroshi Yamazaki

SPring-8 / JASRI

*E-mail: urugat@spring8.or.jp

References

[1] *T. Uruga, H. Tanida, K. Inoue, H. Yamazaki and T. Irie: AIP Conf. Proc.* ***882*** *(2007) 914.*
[2] T. Hara *et al.*: Nucl. Instrum. Meth. A **467-468** (2001) 165.
[3] K. Inoue *et al.*: Nucl. Instrum. Meth. A **467-468** (2001) 674.

Development of a Scanning Tunneling Microscope for *In Situ* Experiments with a Synchrotron Radiation X-ray Microbeam

An attempt to combine scanning tunneling microscopy (STM) with X-rays appears attractive because it contains various possibilities for original and important applications. Inner-shell excitation of a specific level under STM observation provides a possibility to analyze elements or to control local reactions with the spatial resolution of STM. However, the number of studies to combine STM with X-rays is quite limited. This may be because of difficulties specific to X-rays. To overcome a small efficiency of core-excitation by X-rays, we installed an STM system at beamline **BL19LXU** that is providing the world's-highest brilliance of X-rays from a 27 m long undulator, and focused the beam two-dimensionally to increase the photon density. To solve problems derived from the high brilliance (thermal and electrical noise, damage around the STM scanner, instability of the system such as thermal drift, etc.), we developed a special STM system dedicated to the *in situ* observation under the irradiation of X-rays from synchrotron radiation (SR)[1].

Our strategy is not to collect the emitted electrons that come from a wide irradiated area and can damage the spatial resolution of the analysis. It is essential to acquire the tunnelling signal to obtain the locality, thus we need to measure a tip current modulation caused by core-excitation under the tunneling condition, by avoiding collection of the widely emitted electrons. The technical point is how to adjust the incident X-rays as small as possible at the observation point of STM in order to avoid the excessive irradiation. The *in situ* STM measurements were enabled by developing an accurate alignment system (Fig. 1): the small X-ray beam of ϕ 10 μm in diameter was aligned at the STM observation point

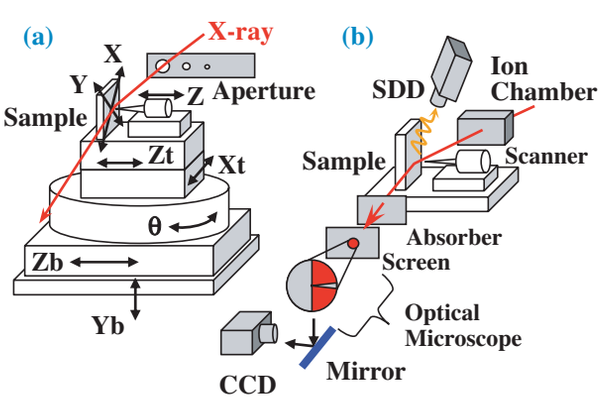

Fig.1. Schematic view of **(a)** alignment and **(b)** monitoring system. Under a conventional STM scanner, an independent four-axis stage is set, whereas the height Yb is controlled by an air dumper.

with accuracy of 1 μm in ultra-high-vacuum. A system to monitor the STM tip and sample in the X-rays was developed to realize a prompt alignment. In order to obtain high signal to noise (S/N) ratio and record a small signal, we developed a detection system of the tunnelling signal using an optical chopper and lock-in amplifier [2]. Also a special tip coated by an insulator (Fig. 2) was developed using focused ion beam (FIB) etching to remove the electrons coming from wide irradiated area [3].

Despite the noisy condition and radiation load around the tip, STM images were successfully obtained with atomic resolution. After thermal noise was effectively removed, the tip current modulation was successfully obtained on Ge nanoislands on a clean Si (111) surface, by changing the incident photon energy across the Ge absorption edge. Figure 3 shows the topographic (left) and beam-induced current images (right), which were obtained simultaneously, at higher (11.114 keV) and lower (11.090 keV) energies than the Ge absorption edge. The tip current image at higher photon energy shows the Ge island darker than the surrounding area. The emitted electrons cannot explain the decrease in current on the Ge island, because the emitted electrons must increase the current on the Ge island, in which the Ge atoms are richer than in the surrounding area. The decrease of the tip current on the Ge island was not observed at lower photon energy, which indicates that the dark Ge island is not an effect of the modulated tunneling gap that is based on the tip motion. The above results indicate that the difference between on and out of the Ge island was detected across the absorption edge with spatial resolution of STM. In consideration of the cross-sectional profile in Fig. 3(e), the spatial resolution in this analysis is estimated to be ~ 4 nm.

After the first successful elemental identification at a nanometer scale for a semiconductor hetero-interface (Si(111)-Ge nanoisland), we succeeded in obtaining a second result stably on another sample, which is composed of metal and a semiconductor (Cu nano-domain on a Ge(111) clean surface) [4]. The spatial resolution was found to be ~2.5 nm by the same estimation as shown in Fig. 3(e). These results mean that the "single nanometer scale" elemental analysis was successfully achieved for "two systems" that have essentially different composition from each other, even though both of them have "extremely dilute" surface atomic concentration (total amount of the deposited element is ~0.3 monolayer for both).

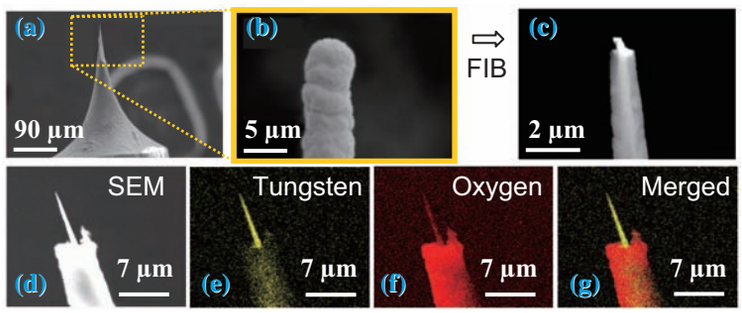

Fig. 2. **(a)**~**(g)** SEM images of the fabricated insulator coat tips. [upper] SEM images before **(a**,**b)** and after **(c)** FIB etching. [lower] SEM **(d)** and EDX images to distinguish the tungsten core **(e)** and coated SiO_2 film **(f)**. Merged image is shown **(g)**.

Practically, this STM system was found to serve as a realistic tool for element-identification. For example, our STM system enables clear recognition of a boundary between Cu and Ge nano-domains on a coarse surface terrace [5], which was roughly treated and rather common than well-defined surfaces. Such boundary is generally difficult to distinguish by the conventional STM because of the roughness. This SR-based STM study will also provide new information on basic science by investigation on an interaction of surface atoms and the hard X-rays. Also this system will serve to local reaction control with STM resolution.

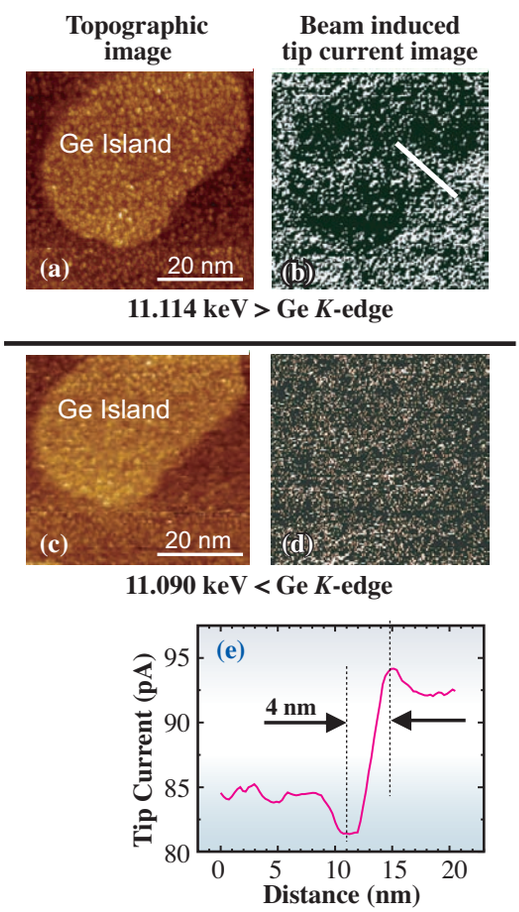

Fig. 3. Energy dependence of tip current images **(b**, **d)** and simultaneously obtained conventional topographic STM images **(a**, **c)**. (50 × 50 nm^2, -2 V, 0.5 nA for all). Cross-sectional profile along white line in **(b)** is shown in **(e)**.

A. Saito [a,b,c,*], Y. Kuwahara [a,b], M. Aono [d]

[a] Dept. of Precision Science and Technology, Osaka University
[b] SPring-8 / RIKEN
[c] PRESTO, JST
[d] WPI Center, NIMS

*E-mail: saito@prec.eng.osaka-u.ac.jp

References

[1] *A. Saito, J. Maruyama, K. Manabe, K. Kitamoto, K. Takahashi, K. Takami, Y. Tanaka, D. Miwa, M. Yabashi, M. Ishii, Y. Takagi, M. Akai-Kasaya, S. Shin, T. Ishikawa, Y. Kuwahara, M. Aono: J. Synchrotron Rad.* ***13*** *(2006) 216; Chap. 27 in "Handbook of Surface Phys. and Engineer.," Maruzen Inc., Tokyo (2007).*
[2] A. Saito *et al.*: Jpn. J. Appl. Phys. **45** (2006) 1913.
[3] A. Saito *et al.*: Surf. Sci. **601** (2007) 5294.
[4] A. Saito *et al.*: J. Surf. Sci. Soc. Jpn. **28** (2007) 453; A. Saito *et al.*: Surf. Interface Anal. **40** (2008) 1033.
[5] A. Saito *et al.*: Chap. 4.2 in "Nano-Imaging," NTS Inc., Tokyo (2008) p.278.

Unique Recovery of Complex Transmissivity using X-ray In-line Holography and Two-beam Interferometry

In-line holography is most promising in the hard X-ray region because it requires only one propagation-based phase contrast image and no optical elements. Difficulty in the in-line holography is the overlapping of conjugate images, which is known as the twin image problem. The elimination of the conjugate image is usually achieved either by (i) using multi-holograms at different distances between samples and recording media [1] or by (ii) giving up the in-line scheme and employing two-beam off-axis holography [2]. Both of these are inapplicable to the objects having larger size than the field of view of the detector. The above problems, however, can be solved by a combined use of the in-line hologram and the shearing interferograms [3,4]. By recording them at the fixed sample and detector positions, the missing phase of the in-line hologram is determined. Deconvolution of the propagation from the sample to the detector, uniquely determines the exit-face wave field, in other words the complex transmissivity, of the sample without the overlap of conjugate images. The samples larger than the field of view of detector are measurable with a high precision.

The experiments were performed at the undulator beamline **BL20XU**, using 12.4 keV X-rays. By placing the 20 μm-width cross slits about 200 m upstream of the experimental station, the coherence length of ~1 mm was achieved in two dimensions. The in-line holography mode and the shearing interferometry mode can be switched by insertion and retraction of an X-ray prism into the beam (Figs. 1(a) and 1(b)). In the X-ray shearing interferometry, the X-ray prism was inserted in the beam at L = 6 m and the sample was placed in the overlap of the two beams in the proximity of the detector at z = 0.1 m (Fig.1 (b)). The deflection angle of the X-rays was adjusted to $\Delta\theta$ = 23 μrad for observing fringes with the spacing of 4.4 μm, which gives the width of the interference region of $L\Delta\theta$ = 140 μm. The phase was determined by the fringe scanning method using the translational movement of the prism. The used detector was a modified version

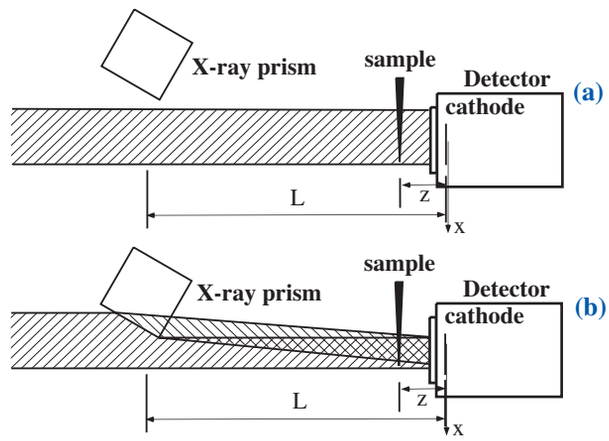

Fig. 1. Schematic experimental setup of **(a)** the X-ray in-line holography mode and **(b)** the X-ray shearing interferometry mode.

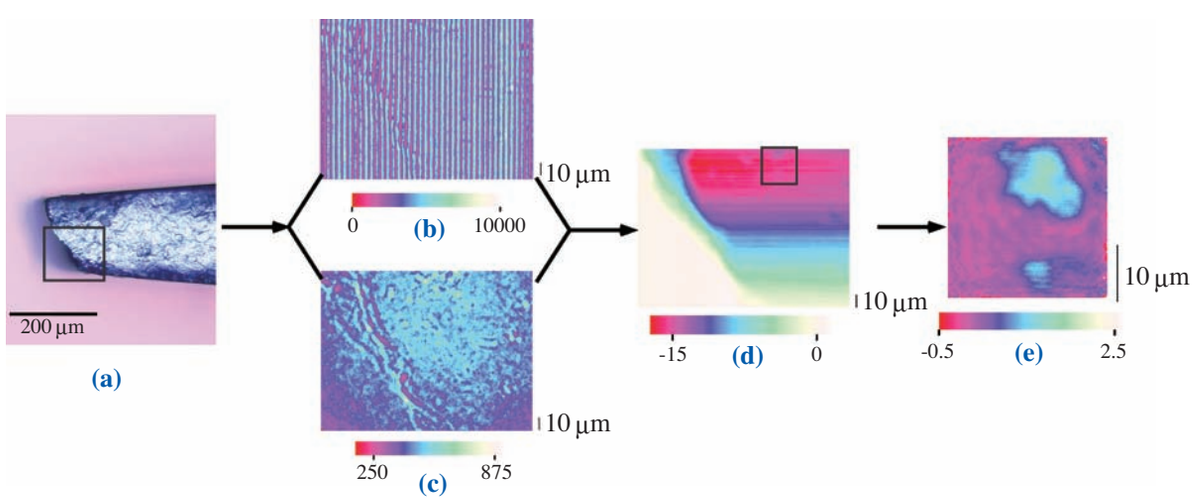

Fig. 2. Images of beryllium foil A. **(a)** Visible microscope image, **(b)** shearing interferogram, **(c)** in-line hologram, **(d)** phase image at the detector in wide field of view and **(e)** exit-face phase image for the box region in Fig. 2**(d)**. The units of the phase images are radians. Bright spots in **(e)** correspond to defects with reduced thicknesses.

of Hamamatsu C5333 zooming tube having the spatial resolution higher than 1 μm. Samples were beryllium (Be) foils including defects, partly because the defects in them affect the coherence of the X-ray beam in the beamlines [5]. The size and the density of defects were quantitatively measured for (*A*) a hot-pressed powder Be foil (240 μmt) and (*B*) an ingot Be foil (180 μmt) from Brush Wellman Electrofusion Products, U.S.A.

Figures 2(b) and 2(c) show the X-ray shearing interferogram and the in-line hologram of the foil A. From the phase integrated from the differential phase (Fig. 2(b)), and the amplitude (derived from Fig. 2(c)), the complex amplitude at the detector plane is derived. By deconvoluting the propagation along distance *z*, the exit-face wave field (or the complex transmissivity) of the sample is uniquely determined (Fig. 2(e)). In Fig. 2(e), two defects with the size of around 4 and 7 μm (FWHM) are observed. The change of optical thickness at these two defects correspond to the reduced thickness of 6 and 12 μm assuming $\delta = 2.2 \times 10^{-6}$ for beryllium. Similar analysis was done for the foil *B*. Figure 3(d) shows the exit-face phase image where several defects are observed with reduced thickness. The size of typical defect is around 3 μm (FWHM). The change of optical thickness correspond to the reduced thickness of 3 ~ 7 μm at the defects assuming the same δ. The observed defects are generally smaller and thinner for the ingot foil than for the hot-pressed powder foil.

The simple experimental setup enabled us to uniquely determine the exit-face wavefield (or complex transmissivity) of samples larger than the field of view of detector. This method is applicable to samples with size variations, due to the tunable field of view of the zooming tube and the adjustable interference region size. The method is powerful for visualizing the phase objects such as the defects in low-Z material as in this research. We are planning to improve this technique for measuring more uniform foils such as the beryllium foils recently developed by the physical-vapor-deposition (PVD) method [5].

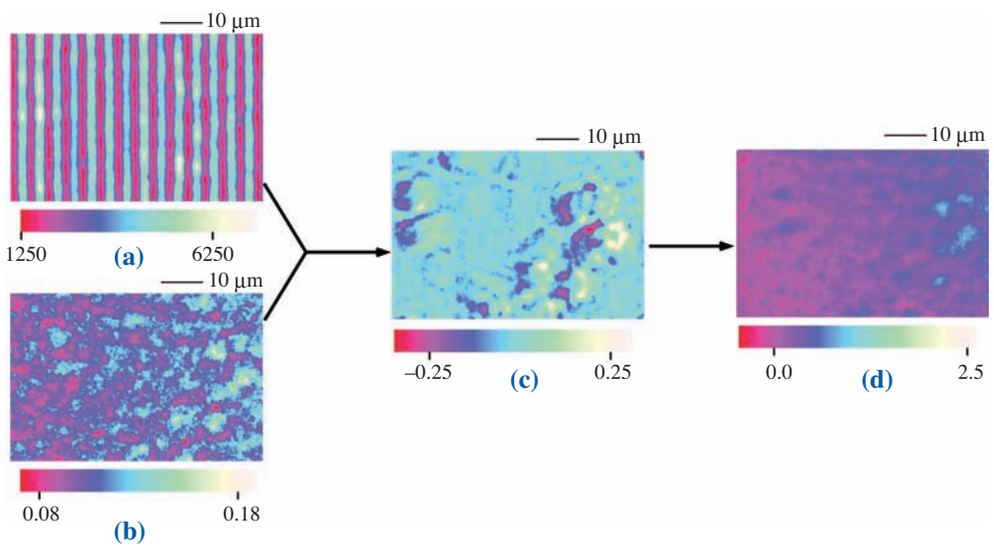

Fig. 3. Images of beryllium foil B. **(a)** Shearing interferogram, **(b)** in-line hologram, **(c)** differential phase image on detector plane and **(d)** exit-face phase image. The units of the phase images are radians. Bright spots in **(d)** correspond to defects with reduced thicknesses.

Yoshiki Kohmura* and Tatsuyuki Sakurai

SPring-8 / RIKEN

* E-mail: kohmura@spring8.or.jp

References

[1] P. Clothens *et al.*: Appl. Phys. Lett. **75** (1999) 2912.
[2] Y. Kohmura *et al.*: J. Appl. Phys. **96** (4) (2004) 1781.
[3] Y. Kohmura *et al.*: J. Appl. Phys. **93** (4) (2003) 2283.
[4] *Y. Kohmura, T. Sakurai, T. Ishikawa, A. Takeuchi, Y. Suzuki and S. Goto: J. Appl. Phys.* ***102*** *(2007) 023101.*
[5] S. Goto *et al.*: AIP Conf. Proc. **879** (2007) 1057.

X → X+EUV Parametric Conversion Interfered with by Compton Scattering

The following year of the invention of laser in 1960, optical nonlinear response was demonstrated by generating the second harmonic of light. Now, nonlinear optics becomes an indispensable tool for science and engineering. On the other hand, there is little knowledge of nonlinear optics in the hard X-ray region to date. Scientists considered that nonlinearity in the X-ray region is too small to investigate and to find applications without X-ray lasers. Here, we show that some process in X-ray nonlinear optics is observable with sufficient accuracy for quantitative analysis by the currently available X-ray sources.

We investigated parametric down-conversion of X-rays into extreme ultraviolet (EUV), the lowest order nonlinear process. The X-ray pump photon decays spontaneously into the X-ray signal photon and the EUV idler photon, i.e., X→X+EUV, when both energy and momentum are conserved. The momentum conservation is usually referred to as phase-matching condition. The phase matching is realized by using a reciprocal lattice vector, **Q**, resulting in nonlinear diffraction (Fig. 1(a)). When the idler photon is in the EUV region, it was predicted that the efficiency of parametric down-conversion is determined by the **Q**-th Fourier component of the bond charge density [1,2], as is shown schematically in Fig. 1(b).

The experiment was performed at the 27-m in-vacuum undulator beamline **BL19LXU**. The pump energy was 11.0 keV, whereas the signal (idler) energy was changed from E_s = 10.96 keV (E_i = 40 eV) to 10.87 keV (130 eV) by a bent crystal analyzer (Fig. 2). Figure 3 shows the rocking curves of the 111 nonlinear diffraction of diamond. Rocking the crystal corresponded to scanning the phase-matching condition.

First we discuss the rocking curve at E_i = 100 eV [3]. On the exact phase-matching angle, there observed small enhancement of the signal intensity by ~10 counts/sec due to the X→X+EUV parametric conversion. We note that the incidence was eleven orders of magnitude higher. To our surprise, the measured rocking curve was asymmetric, having not only a peak but also a distinct dip. If there had been no interaction between the X→X+EUV parametric conversion and the Compton scattering, there should be a Lorentzian peak on the smooth Compton background. The high signal-to-noise ratio measurement made it clear for the first time that the Compton scattering interferes with the nonlinear process.

The rocking curve depended strongly on the signal and the idler energies [4]. The line shape, which was Lorentzian-like, became asymmetric, and finally characterized by a dip, as E_i (E_s) decreased (increased). The energy dependence is considered to relate to E_i, because there is no internal excitation in diamond around 11.0 keV, e.g., the nearest core excitation energy is 290 eV.

The physical picture of the interference is not clear at present. We pointed out similarity to the Fano effect, which is observed when a discrete state is buried in a continuum. The phase-matched parametric conversion and the Compton scattering may be regarded as the discrete transition and the

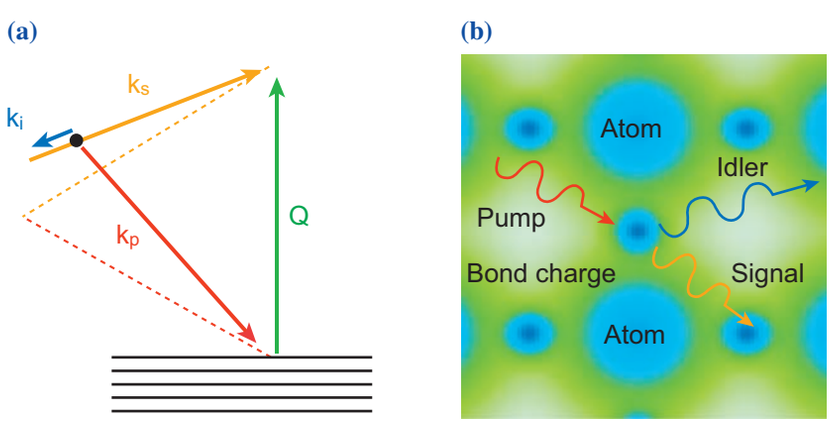

Fig. 1. Schematic view of **(a)** nonlinear (solid line) and linear (dashed line) diffraction, and **(b)** the X→X+EUV parametric conversion due to the bond charge.

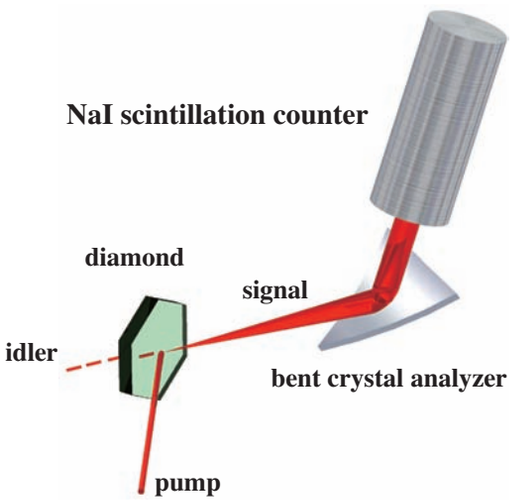

Fig. 2. Schematic view of the experimental setup. The signal photon was measured, whereas the idler photon was absorbed in the nonlinear crystal.

continuous transition, respectively. The difficulty of this picture is that quantum mechanical interference, such as the Fano effect, requires the identical final state for both the transitions. However, the final state of the parametric down-conversion is different from that of the Compton scattering, e.g., the number of photon is two in the former case, and one in the latter case. Further experimental and theoretical investigation is needed to understand the X→X+EUV parametric conversion and to apply it to structural analysis of the bond charge density.

The experimental findings shown here imply that the X-ray nonlinear optics has large frontiers. Also, the results show that the part of frontiers can be explored with the present X-ray sources.

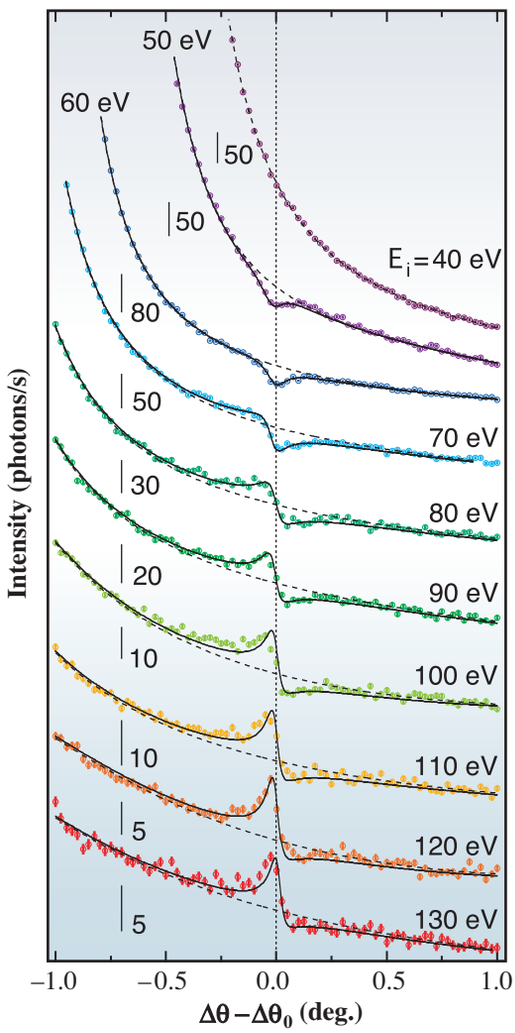

Fig. 3. Rocking curves of the 111 nonlinear diffraction of diamond for several combinations of E_i and E_s. The vertical dashed line indicates the exact phase-matching angle. The solid and the dashed line are the best fitting with the Fano formula and the estimated background, respectively.

Kenji Tamasaku

SPring-8 / RIKEN

E-mail: tamasaku@spring8.or.jp

References

[1] I. Freund: Chem. Phys. Lett. **12** (1972) 684.
[2] H. Danino and I. Freund: Phys. Rev. Lett. **46** (1981) 1127.
[3] *K. Tamasaku and T. Ishikawa: Phys. Rev. Lett.* ***98*** *(2007) 244801.*
[4] *K. Tamasaku and T. Ishikawa: Acta Crystallogr. A* ***63*** *(2007) 437.*

NUCLEAR

"Fuji" - Wisteria

"Rindou" - Marsh gentian

PHYSICS

A linearly polarized photon beam is produced by the backward Compton scattering of laser photons from 8 GeV electrons at BL33LEP. At the current LEPS facility, the photoproduction of hadrons in forward angles is studied, where the high linear polarization plays an essential role to decompose various reaction processes.

The beam polarization is high and can be changed easily by changing the laser polarization. The LEPS covers the photon energy region from 1.5 GeV to 2.9 GeV, which is suitable for studying creation of strange quark and anti-quark pairs near the production thresholds, in such process like as photoproduction of the ϕ meson and hyperons. Since we cannot extract a free quark from a hadron, detailed studies of its production and decay are essential for revealing the structure of hadrons in terms of quarks and their interactions governed by QCD.

The first topic we report is ϕ photoproduction near the production threshold. The aim of the experiment is to shed light on the interaction between a ϕ meson and a nucleon. Since a ϕ meson is composed of a strange quark and an anti-strange quark, meson exchange contributions in the interaction are highly suppressed. Multi-gluon exchanges such as Pomeron exchange and glueball exchange processes have become very important to understand the mechanism of the production process. By studying the correlation between the spin polarization of a ϕ meson and linear polarization, we can get information about the spin and parity of the exchanged particles.

The second topic reported is meson photoproduction, which is a powerful tool for obtaining deeper insight into baryon resonances. We observed anomalous behavior in both the cross-section and the spin observable in backward π^0 production. This may indicate a hint for the existence of a missing resonance, which has been predicted by a quark model but not yet observed. A theoretical investigation to understand the new data obtained from LEPS is now in progress.

Takashi Nakano
Research Center for Nuclear Physics
Osaka University

Coherent φ-Meson Photoproduction from Deuterium

The common behavior of high-energy diffractive processes of hadron-hadron and photon-hadron interactions is traditionally interpreted as the exchange of a Pomeron. The physical particles responsible for Pomeron exchange have not been conclusively identified, but such particles can exist in the strong interaction as glueballs, composite particles of gluons. The behavior of Pomeron exchange at low energies is not well understood because meson-exchange processes appear and become comparable near threshold.

A particularly interesting and unique way of studying the possible Pomeron exchange is φ(1020)-meson photoproduction from hadrons. In this reaction pseudo-scalar π-meson exchange is suppressed. Furthermore, with the use of an iso-scalar deuteron target, the coupling between iso-vector π-mesons and deuterons is forbidden due to iso-spin conservation. Accordingly, the coherent photoproduction of φ mesons from deuterons, $\gamma d \rightarrow \phi d$, becomes an excellent source of information for Pomeron dynamics at low energies.

We measured the differential cross sections and decay asymmetries of coherent φ-meson photoproduction from liquid deuterium target near threshold in the very forward direction with linearly polarized photons using the LEPS spectrometer in **BL33LEP**. Highly polarized photons were produced by backward Compton scattering with an ultra-violet Ar laser from 8 GeV electrons in the storage ring of SPring-8. The photon energy was determined by measuring the recoil electrons with a tagging spectrometer event by event. A liquid deuterium target with an effective length of 16 cm was employed. Charged particles produced at the targets were detected at forward angles with the LEPS spectrometer which consisted of a dipole magnet, a silicon-strip vertex detector, three multi-wire drift chambers, a plastic scintillator behind the target, and a time-of-flight hodoscope placed downstream of the tracking detectors.

The production of φ mesons was identified via the charged kaon decay mode with the detection of K^+ and K^- in the final state. A clear signal of φ mesons was seen in the invariant mass of K^+K^- pairs, for photon energy of 1.5-2.4 GeV as shown in Fig. 1(a). The separation of coherent ($\gamma d \rightarrow \phi d$) and incoherent ($\gamma d \rightarrow \phi pn$) interactions could not be performed on an event-by-event basis. Instead, the individual yields were disentangled by fitting the distributions of missing mass where the reaction of coherent production from deuterons, $\gamma d \rightarrow \phi d$, has a structure peaking at the mass of deuterons 1.875 GeV/c^2, as shown in Fig. 1(b). This distribution is nicely reproduced by the sum of individual ones generated by Monte Carlo simulations.

The cross section of coherent production at zero degree shows a strong increase with photon energy. A very large decay asymmetry of 0.48±0.07(stat)±0.07(sys) was observed, contrasting with a value of 0.2 from the proton. Within errors, our measurement reaches the maximum boundary corresponding to a pure natural-parity exchange process, showing that coherent φ-meson production from deuterons is predominantly from natural-parity processes. It is found that deduced $\gamma N \rightarrow \phi N$ cross sections for isoscalar t-channel exchange at zero

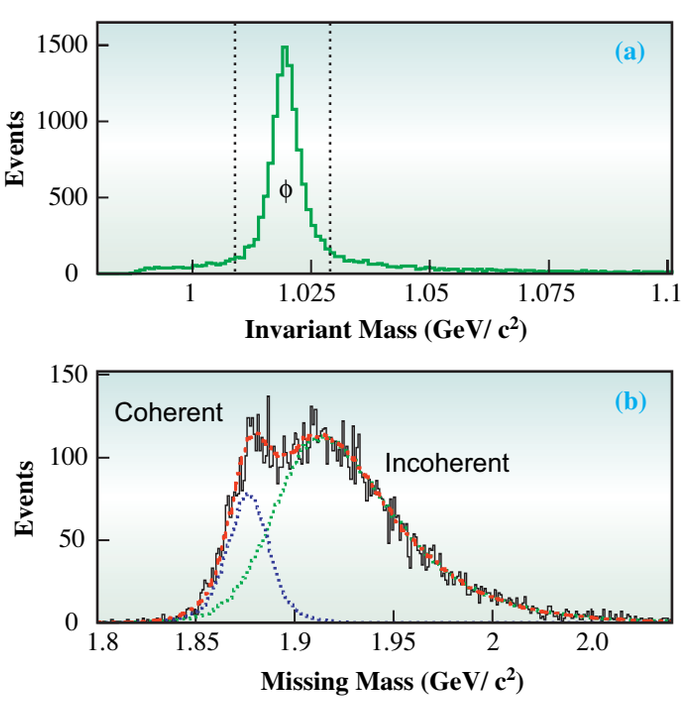

Fig. 1. **(a)** The distributions of invariant mass for the events with a K^+K^- pair. The two dashed lines on the distribution of invariant mass show the final cut to select the φ-meson events. **(b)** The missing mass spectrum together with fit of Monte-Carlo-simulated coherent and incoherent components.

degree as a function of beam energy were not consistent with the prediction of the conventional Pomeron model, shown in Fig. 2. Either a modified energy dependence for the Pomeron trajectory or additional natural-parity processes beyond Pomeron exchange in the near-threshold region would be compatible with our measurement. This measurement will serve as an important constraint on the theoretical modeling of Pomeron trajectory and additional exotic channels in the low-energy regime and help to understand the strong coupling region of Quantum Chromodynamics.

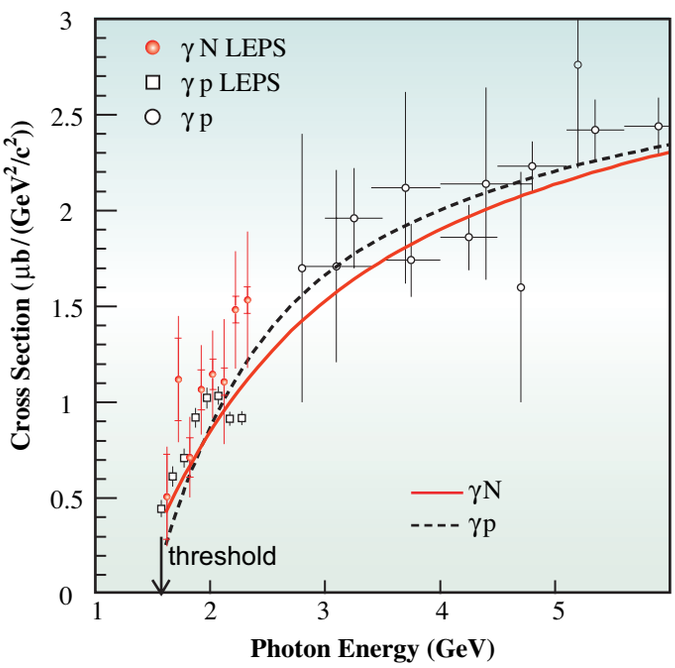

Fig. 2. Data of the cross section of ϕ-meson photoproduction from nucleons by iso-scalar t-channel exchange processes deduced from coherent production from deuterons in this work and the existing data of γp→ϕp up to photon energy equal to 6 GeV. The solid and dashed lines represent the predictions of conventional theoretical model including Pomeron and π-η exchange processes.

Wen-Chen Chang for the LEPS Collaboration

Institute of Physics, Academia Sinica, Taiwan

E-mail: changwc@phys.sinica.edu.tw

References

[1] *W.C. Chang, K. Horie, S. Shimizu, M. Miyabe, D.S. Ahn, J.K. Ahn, H. Akimune, Y. Asano, S. Daté, H. Ejiri, S. Fukui, H. Fujimura, M. Fujiwara, S. Hasegawa, K. Hicks, T. Hotta, K. Imai, T. Ishikawa, T. Iwata, Y. Kato, H. Kawai, Z.Y. Kimi, K. Kino, H. Kohri, N. Kumagai, P.J. Lin, S. Makino, T. Matsuda, T. Matsumura, N. Matsuoka, T. Mibe, Y. Miyachi, M. Morita, N. Muramatsu, T. Nakano, M. Niiyama, M. Nomachi, Y. Ohashi, H. Ohkuma, T. Ooba, D.S. Oshuev, C. Rangacharyulu, A. Sakaguchi, T. Sasaki, P.M. Shagin, Y. Shiino, A. Shimizu, H. Shimizu, Y. Sugaya, M. Sumihama, Y. Toi, H. Toyokawa, A. Wakai, C.W. Wang, S.C. Wang, K. Yonehara, T. Yorita, M. Yoshimura, M. Yosoi, R.G.T. Zegers: Phys. Lett. B* ***658*** *(2008) 209.*

Backward-angle Photoproduction of π^0 Mesons on Proton at BL33LEPS

The photoproduction of π^0 mesons from the proton ($\gamma p \rightarrow p\pi^0$) has been measured in order to study the resonances of nucleons (protons or neutrons), which consist of three quarks. Pion photoproduction has been well studied both experimentally and theoretically in the spectroscopy of nucleon resonances. Many nucleon resonances were found and their characteristics were determined at the total energy $W < 1.7$ GeV [1]. However, many higher-mass resonances are still not well established, and the identification of these missing resonances is important for understanding the quark structure of a nucleon. Some weakly excited resonances are obscured by other strong resonances with large decay widths, making it difficult to demonstrate their existence only from cross section data. Alternatively, polarization observables like photon beam asymmetries are useful to extract the missing resonances. At very backward angles, the production mechanism is expected to be dominated by contributions of u-channels, where a proton or a nucleon resonance is exchanged. The data obtained at the LEPS facility provide a good means of understanding the reaction mechanism with u-channel kinematics.

An experiment was carried out at the Laser-Electron Photon beamline **BL33LEPS** [2]. A multi-GeV photon beam was produced by backward Compton scattering (BCS) from the head-on collision between argon ion laser photons with 351-nm wavelength and circulating 8-GeV electrons in the storage ring. The photon energy of the tagged photons ranged from 1.5 GeV to 2.4 GeV. A liquid hydrogen target with a thickness of 5.6 cm was used. The beam intensity was about 10^6 photons/sec. Protons from the target were detected using a forward LEPS spectrometer. Charged particles were momentum analyzed using information from a silicon vertex detector and three drift chambers. The particle mass was determined using the momentum, path length and time-of-flight. π^0 mesons were identified using the missing mass spectrum as the mass of X in the $\gamma p \rightarrow pX$ reaction. Differential cross sections and photon beam asymmetries were obtained. Figure 1 shows the obtained differential cross sections as a

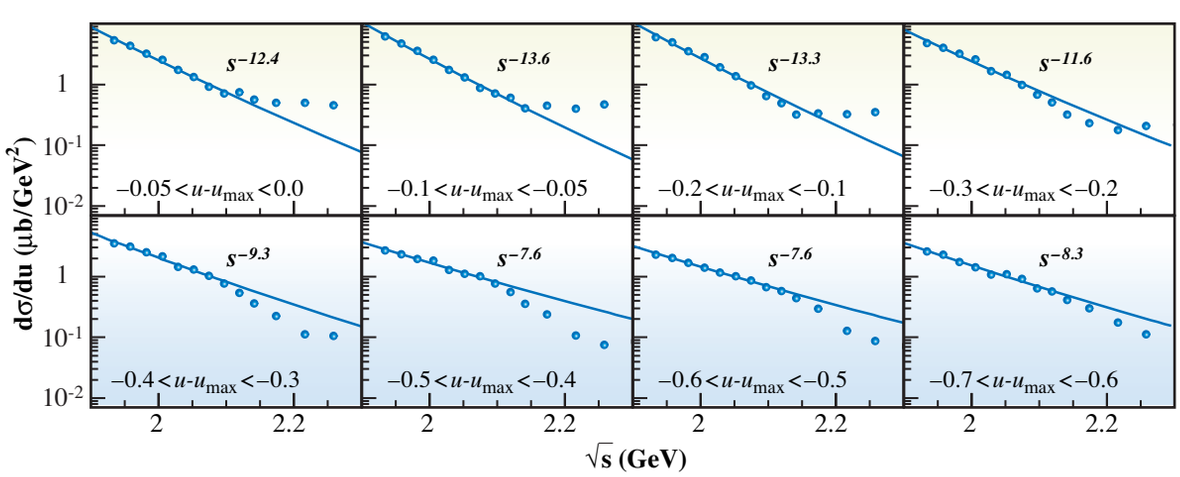

Fig. 1. Differential cross sections as a function of total energy of reaction.

function of the total energy of the reaction. The energy dependent slopes determined by fitting the data are indicated in Fig. 1. The differential cross sections sharply decrease at a total energy below 2.1 GeV. However, above 2.1 GeV, the cross sections do not agree with the fitting curves. To explain the current data in the u-channel kinematics, new mechanisms would be necessary.

Figure 2 shows photon beam asymmetries. Above 2.0 GeV, a dip structure is found around $\cos\Theta_{c.m.}$ =-0.8. Such a strong angular distribution cannot be explained using currently existing theoretical models. In order to explain this structure, we surmise that new high-mass resonances combined with u-channel diagrams are required. The present data were published [3].

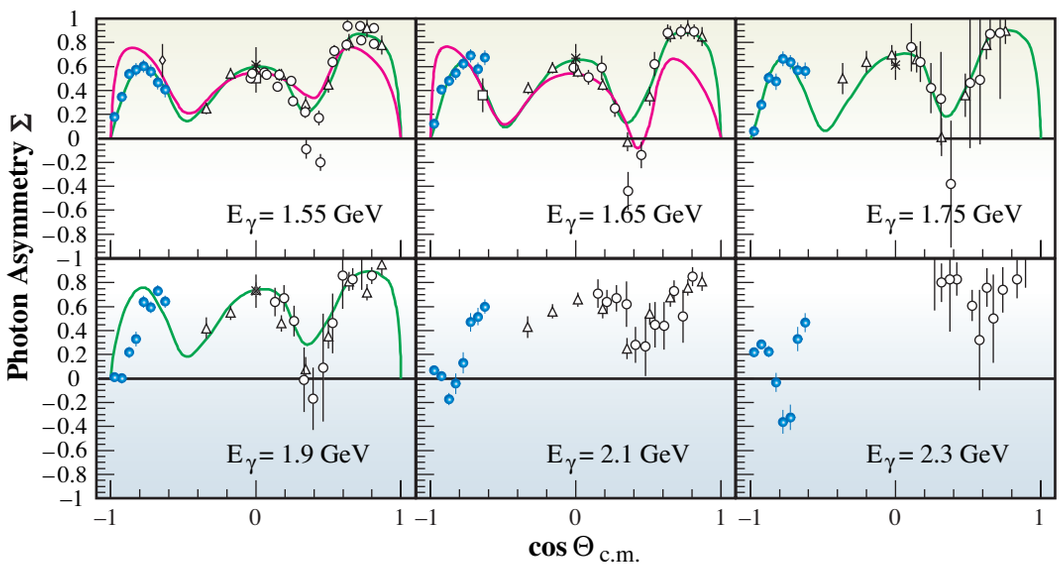

Fig. 2. Photon beam asymmetries. Above 2.0 GeV, a dip structure is found around $\cos\Theta_{c.m.} = -0.8$.

M. Sumihama for the LEPS Collaboration

Research Center for Nuclear Physics (RCNP), Osaka University

E-mail: sumihama@rcnp.osaka-u.ac.jp

References

[1] Particle Data Group, http://pdg.lbl.gov.
[2] T. Nakano: Nucl. Phys. A **721** (2003) C112.
[3] *M. Sumihama, J.K. Ahn, H. Akimune, Y. Asano, W.C. Change, S. Daté, H. Ejiri, H. Fujimura, M. Fujiwara, K. Hicks, T. Hotta, K. Imai, T. Ishikawa, T. Iwata, H. Kawai, Z.Y. Kim, K. Kino, H. Kohri, N. Kumagai, S. Makino, T. Matsumura, N. Matsuoka, T. Mibe, M. Miyabe, Y. Miyachi, M. Morita, N. Muramatsu, T. Nakano, M. Niiyama, M. Nomachi, Y. Ohashi, H. Ohkuma, T. Ooba, D.S. Oshuev, C. Rangacharyulu, A. Sakaguchi, T. Sato, P.M. Shagin, Y. Shiino, H. Shimizu, Y. Sugaya, H. Toyokawa, A. Wakai, C.W. Wang, S.C. Wang, K. Yonehara, T. Yorita, M. Yosoi, R.G.T. Zegers: Phys. Lett. B **657** (2007) 32.*

Accelerators & Beamlines Frontiers

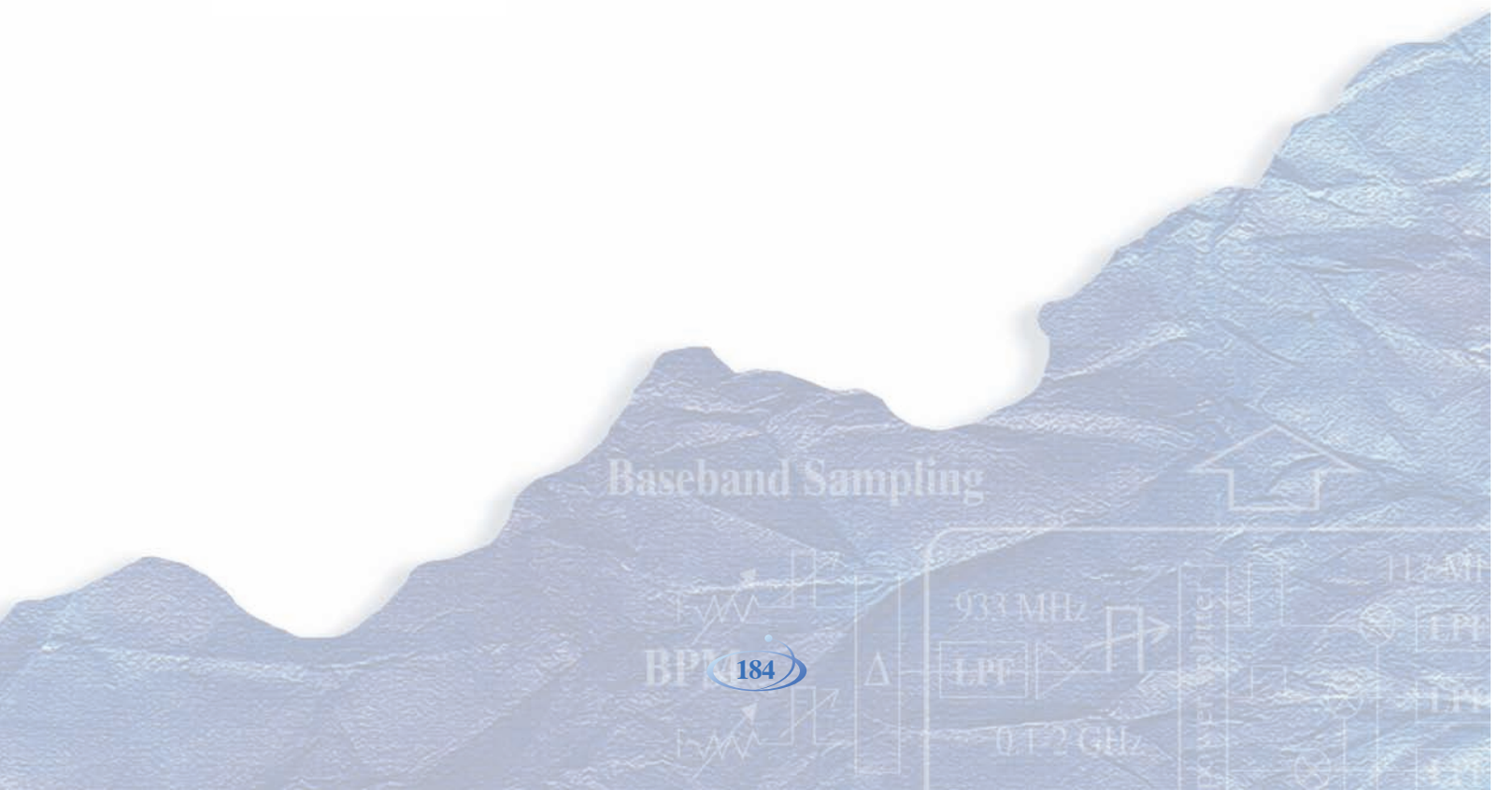

Beam Performance

Developments and Upgrades of Storage Ring

Improvement of Current Stability in Top-up Operation

The top-up operation of the SPring-8 storage ring started in September 2004 with the purpose of improving the average brilliance and stabilizing the stored current and the source intensity. Since the beginning of the top-up operation a stability of the stored current of 0.1% (100 μA) has been achieved. For example, Fig. 1 shows a typical trend of the stored current in October 2007. This high regularity of the stored current is profitable for user experiments, particularly for those requiring precision [1,2].

In the top-up operation of SPring-8 the injected current per shot is fixed to 30 μA to maintain the uniformity of the bunch currents of the several-bunch filling mode. In contrast, due to user requirements, the interval between the beam injections is fixed to 1 minute for the several-bunch filling mode and 5 minutes for the multi-bunch filling mode. Hence, the injected current of 30 μA does not compensate the decrease in stored current, and the shot number at each beam injection is unsettled and varies from 1 to 3. Thus, the deviation of the stored current becomes 0.1% (100 μA), although the injected beam current is 30 μA. Since the stored beam oscillation at injection is now well suppressed by machine tuning [3-5], users do not need to know the timing of the beam injection. In November 2007 we hence decided to reduce the interval between beam injections to improve the stored current stability.

In the new top-up mode the interval between beam injections is variable so that just one shot is injected at each injection. We call the new top-up operation the current prior mode and the old operation the interval prior mode. Figure 2 shows the trend of the stored beam current in the new mode. The deviation of the stored current is 30 μA, which corresponds to the injected current, as expected. At the time of measurement the beam lifetime was around 18 hours, so the average interval between beam injections was 20 seconds. Figure 3 shows the stored current distributions over 8 hours in both modes, which clearly shows that a current stability of the SPring-8 storage ring of 0.03% is achieved. We expect that this high stability of the stored current will contribute to the improvement of user experiments.

Development of Remote Tilt-Control System for Injection Bump Magnet of the Storage Ring

In the top-up operation mode, it is important to suppress the oscillation of the stored beam at beam injection. To generate a bump orbit, four bump magnets (BP1 - BP4) are excited with pulsed current by four different power supplies. These pulses are synchronized to the timing of the beam injection. The waveform of the excitation current is a half-sinusoidal shape with a pulse width of 8 μsec. If not all the pulses are the same shape, the stored beam is oscillated in the horizontal direction by the bump magnets. Furthermore, if the bump magnets have an alignment error in their rotation around the beam axis (tilt), the stored beam is also oscillated in the vertical direction.

To reduce the oscillation amplitude of the stored beam, we measured the beam oscillation using a turn-by-turn beam position monitor (BPM). By using the measured beam position data of the horizontal oscillation, we can estimate error kicks by the bump magnets and adjust their pulse height and timing. The vertical oscillation can also be reduced by estimating

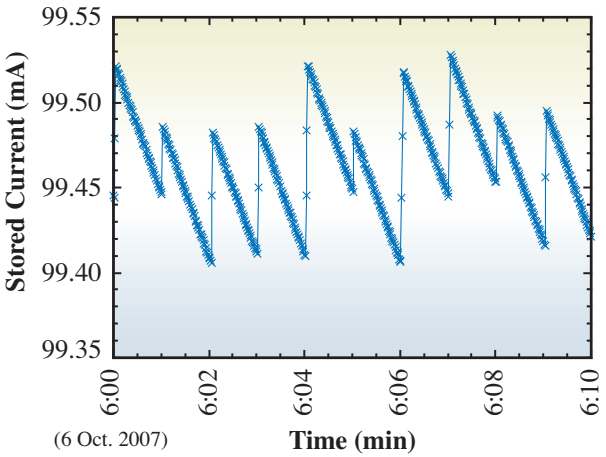

Fig. 1. Trend of the stored current over 10 minutes before the mode change of the top-up operation.

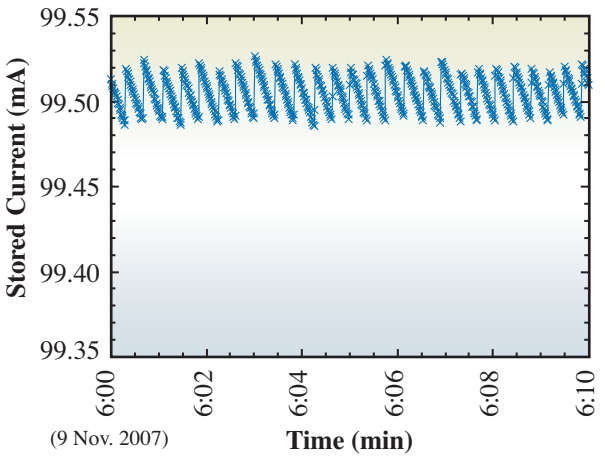

Fig. 2. Trend of the stored current over 10 minutes after the mode change of the top-up operation.

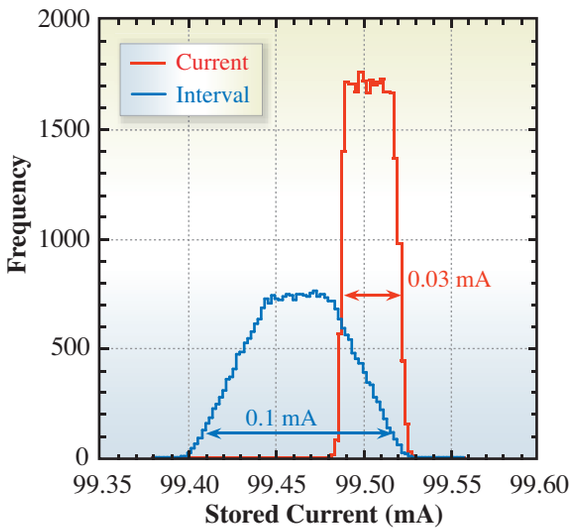

Fig. 3. Distributions of the stored current over 8 hours in both top-up operation modes.

the tilt of the bump magnets with the turn-by-turn beam position data. The process of adjusting the tilt is not easy and the oscillation measurement and tilt adjustment must be repeated two or three times [3]. We then developed a remote tilt-control system to ensure smooth realignment. The power machinery of the system is shown in Fig. 4. A bump magnet is placed on a stainless-steel plate. A stepper motor is attached to one side of the plate through a 1/30 warm gear. The other side of the plate is supported at two fixed points. The bump magnet is tilted in the clockwise direction if the stepper-motor side is moved upward. The range of adjustment is ±4 mrad with a resolution of 8.74 μrad / 1000 pulses.

The system was initially installed for one bump magnet (BP4). To confirm the response of the system, the tilt and rotation around the x-axis (pitch) were measured using a leveling instrument placed on top of the bump magnet. The stage was moved clockwise, then counterclockwise and then clockwise (see Fig. 5). As a result, the obtained backlash of the system was 0.827 mrad. The reproducibility was 6.4 μrad when the tilt was increased or decreased monotonically in the same direction. The measured tilt agreed with the set tilt within 5%. The change in the pitch upon controlling the tilt was less than 3%.

Figure 6 shows the rms amplitude of the measured vertical beam oscillation before and after adjusting the tilt of the bump magnets. The solid black line is the oscillation amplitude before turn-by-turn adjustment using the BPMs. In this measurement, the beam was stored in one RF bucket and the bump magnets were excited without injection. Using this data, we estimated the tilt errors of BP1 and BP4. The tilt of BP1 was adjusted manually on the site and that of BP4 was adjusted using the newly developed remote control system. The result is shown in Fig. 6 by the solid red line. The amplitude was well reduced to the level of resolution of the turn-by-turn BPM system. In the future, we will install the same tilt-control system for BP1 - BP3 for the complete on-beam reduction of the vertical oscillation.

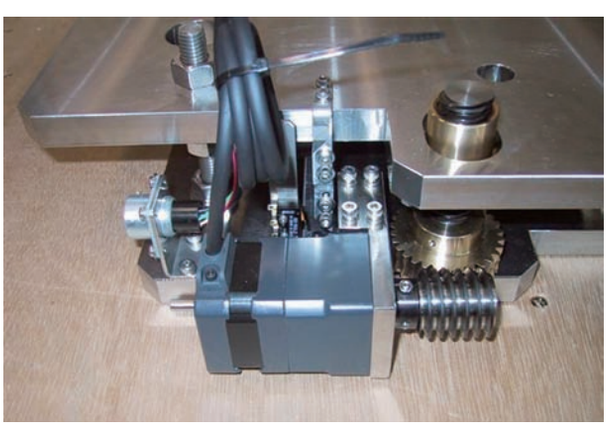

Fig. 4. Power machinery of a remote tilt-control system. A stepper motor (shown in the center of the picture) adjusts the tilt of the stage for a bump magnet. The bump magnet was placed on the stage. The beam travels from right to left in this figure. A rotary encoder was also attached to measure the number of rotations of the motor.

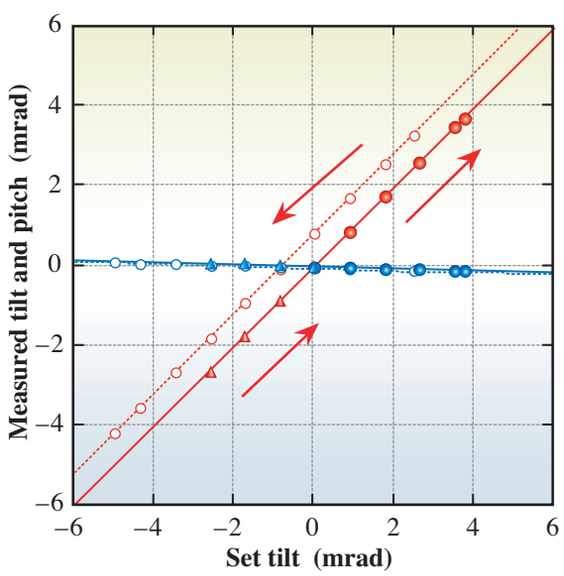

Fig. 5. Measured tilt and pitch of the bump magnet BP4 at various set values of the tilt. Solid red circles and open red circles indicate the measured tilt under clockwise and counterclockwise changes, respectively. Solid red triangles indicate the measured tilt under the subsequent clockwise change. Solid black circles and open black circles indicate the measured pitch under clockwise and counterclockwise changes, respectively.

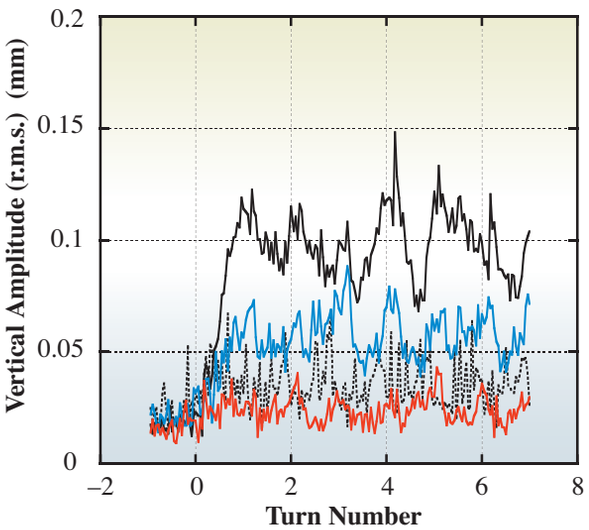

Fig. 6. Amplitude of the vertical oscillation of a stored beam induced by bump magnets. Measured values of r.m.s. amplitude are plotted as a function of the turn number (revolutions of the beam). The solid black, blue and red lines indicate the amplitude before adjustment, after BP4 remote adjustment and after BP1 and BP4 adjustment, respectively. The broken black line indicates the amplitude before installing the remote tilt-control system.

Linear Resonance Coupling Correction

The betatron coupling is one of the most important parameters of storage rings for a high brilliant light source, since it generates the vertical spread of the stored beam and hence reduces the brilliance of the radiated photon beam. By the precise alignment of the magnets [6] and the proper COD correction [7], we have succeeded in achieving very small linear betatron coupling without skew quadrupole corrector magnets since the commissioning phase of the SPring-8 storage ring. As the linear coupling is essential for the light source, we have routinely observed the resonance coupling. The method of observing the resonance coupling is as follows. The operation point of the SPring-8 storage ring is (β_x, β_y) = (40.15, 18.35); thus, the nearest linear resonance $\nu_x - \nu_y = 22$ has the greatest effect on the beam dynamics. The perturbation theory with single resonance approximation implies that the vertical beam size σ_y in the vicinity of the resonance is described as [8]

$$\sigma_y{}^2 = \frac{\frac{1}{2}|C|^2}{|C|^2 + \Delta^2}\beta_y \varepsilon_0 , \qquad (1)$$

where C is the coupling driving term, $\Delta(= \nu_x - \nu_y - 22)$ is the distance from the resonance, β_y is the vertical betatron function and ε_0 is the natural emittance. The coupling driving term is given by the integration of the error skew quadrupole magnetic field over the circumference, and reflects the performance of the machine. Hence, the more we reduce the coupling driving term, the smaller we can make the vertical beam size. From Eq. (1), we find that the vertical beam size has a Lorentzian-like variation with the distance from the resonance and that the width of the resonance is given by the strength of the coupling driving term. Figure 7 shows the trend of the measured vertical beam size near the resonance. In Fig. 7, "Ac" means the achromat optics, and "LE" represents the low emittance optics. Before September 2005 the storage ring was operated using the achromat optics with 6.6 nmrad emittance, and since then the low emittance optics with an emittance of 3.4 nmrad. Hence, the peak at the resonance, i.e., the maximum vertical beam size, is reduced after this change in optics.

From Fig. 7 one immediately finds that the coupling strength has grown year after year since 2004. Thus, we decided to correct the resonance coupling to improve the machine performance. Since the resonance coupling possesses two degrees of freedom, we correct it using two sets of skew quadrupole magnets, which have been installed in the SPring-8 storage ring. One set is installed at the arc section of every two normal cells, and the other is installed close to the entry and exit of each long straight section. The phase difference of these two families with respect to the linear resonance is almost 90°, which is favorable for the coupling correction. The coupling correction was carried out near the resonance $\Delta = 0.03$ for easy the observation of the response of the vertical beam size against the change in strength of the skew quadrupole magnets. The process of coupling correction is shown in Fig. 8, where the red

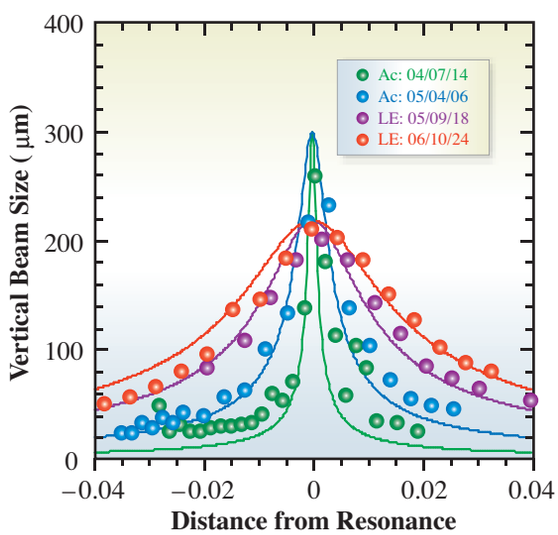

Fig. 7. Trend of the behavior of the vertical beam size in the vicinity of the nearest linear resonance.

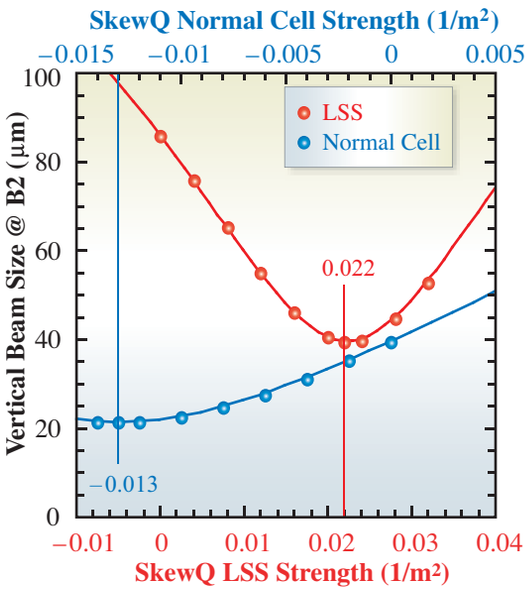

Fig. 8. Correction of the resonance coupling using the skew quadrupole magnet.

circles denote the response to the tuning of the skew quadrupole magnets at the long straight sections and the blue ones denote those at the normal cells. The lower ordinate in Fig. 8 denotes the total strength of the skew quadrupole magnets at the long straight sections and the upper ordinate represents that at the normal cells. By minimizing the vertical beam size, as shown in Fig. 8, we correct the resonance coupling. After the coupling correction, we observe the resonance coupling to confirm the performance of the correction, whose result is shown in Fig. 9. The strengths of the resonance coupling are estimated to be 0.012 and 0.001, respectively, before and after the correction, and thus we can correct the resonance coupling effectively. Although the operation point in user time is sufficiently far from the resonance, i.e., Δ = 0.2, it is observed that the coupling correction improves the vertical beam size by a few percent.

Installation of Counter-Sextupole Magnets in the Storage Ring

In the SPring-8 storage ring there are four magnet-free long straight sections of about 30 m length. These long straight sections were realized in 2000 by locally rearranging quadrupole and sextupole magnets. At that time we maintained the periodicity of the cell structure, especially that of sextupole field distribution along the ring. To keep the periodicity high and hence the dynamic aperture large when modifying the optics, we adopted a scheme in which "betatron phase matching" and "local chromaticity correction" are combined. In this scheme the dynamic aperture for on-momentum electrons is kept by the phase matching and that for off-momentum electrons is enlarged by the local chromaticity correction with weak sextupoles (SFL).

To further improve the symmetry of the ring, we installed "counter-sextupole magnets" in every long straight section in 2007. These magnets are placed 180° apart from SFL in the horizontal betatron phase. The counter-sextupole magnets can minimize the harmful effect of nonlinear kick due to the SFL [9]. After the beam tuning we confirmed that the dynamic aperture and the momentum acceptance were indeed improved.

Figure 10 shows the Touschek beam lifetime measured at the stored current of 1 mA/bunch with and without the counter-sextupole magnets. The Touschek

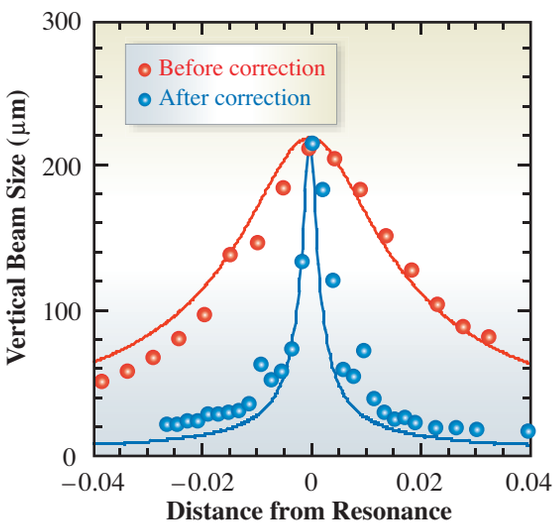

Fig. 9. Vertical beam size in the vicinity of the linear resonance before and after the coupling correction.

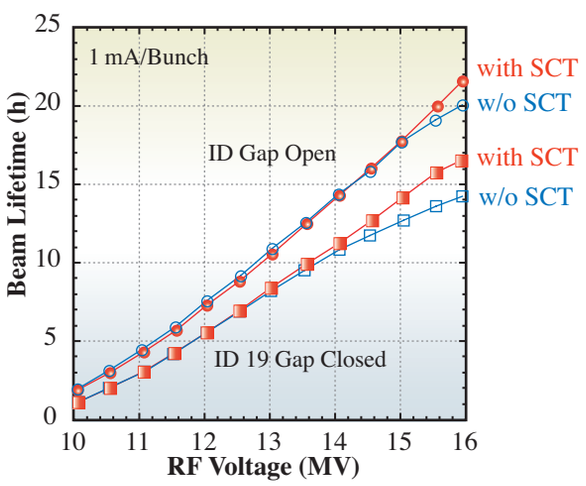

Fig. 10. Touschek beam lifetime at 1 mA/bunch as a function of RF accelerating voltage measured in the optics with and without the counter-sextupole magnets (SCT).

beam lifetime is an index of the momentum acceptance, and a longer beam lifetime at high RF accelerating voltages means larger momentum acceptance. From the figure we see that when the counter-sextupole magnets are used, the beam lifetime becomes longer at high RF voltages and hence the momentum acceptance becomes larger. This tendency in the Touschek beam lifetime can be seen more clearly when the gap of the 25-m-long in-vacuum undulator is closed, as also shown in the figure.

In Fig. 11 we plot the injection efficiency as a function of the horizontal position of an injected beam at the end of a beam transport line from the booster. The injection efficiency is higher when the counter-sextupole magnets are used. This means that the storage ring has a larger dynamic aperture, and beam loss during injection is reduced.

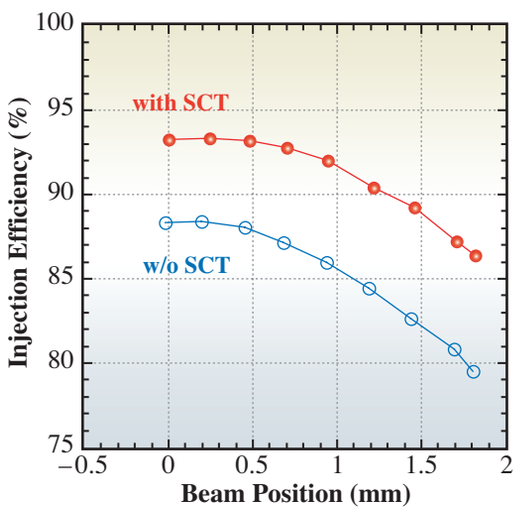

Fig. 11. Injection efficiency as a function of the horizontal position of an injected beam at the end of a beam transport line. The origin of the abscissa is the nominal beam position and a positive value corresponds to a position further away from the stored beam orbit.

Elimination of the Filling Pattern Dependence of the BPM Signal Processing Circuits

The signal processing electronics of the storage ring beam position monitors (BPMs) were replaced during the summer shutdown of 2006, as reported in Research Frontiers 2006 [10]. As a result, the speed and resolution of the closed-orbit distortion (COD) measurements improved. However, the differences of the COD data between different filling patterns reached over 100 μm, although the actual orbits were expected to be the same.

Some typical filling patterns of the SPring-8 storage ring are listed in Table 1. From the list, it is shown that current in a bunch varies by more than two orders of magnitude, and hence the voltage signal amplitude at the circuit inputs can change by the same amount according to the change of the filling pattern.

However, the intensity of the RF acceleration frequency component and its harmonics in the beam signal spectrum are independent of the filling pattern; the RF harmonics depend on the stored beam current and the shape of bunch pulse. The change of the filling pattern varies the intensities of the revolution frequency harmonics except for the RF harmonics. This intensity variation contributes to the large change of the voltage signal amplitude. To avoid the influence of the change of the filling pattern, we arranged the signal processing circuits of the BPM so that only the RF acceleration frequency component in the beam signal was detected.

Nevertheless, large differences of COD data with the change of the filling patterns resulted. The cause of the differences was attributed to the nonlinear response of the diodes used for protecting the multiplexers from electrostatic discharges. The filter-switch module, which is in the front part of the circuits, contains the low-pass filters, the RF switch and the diodes to protect the switch IC from excessive voltages, as shown in Fig. 12. This part is upstream of the place where the RF frequency component is selected; hence, the change of the filling pattern induces the large variation of the voltage signal amplitude at the diodes. When a large voltage signal was input to the circuit, the protective diodes were partially conductive, which resulted in the nonlinear response of the circuits. This nonlinearity induced by the diodes caused the filling pattern dependence.

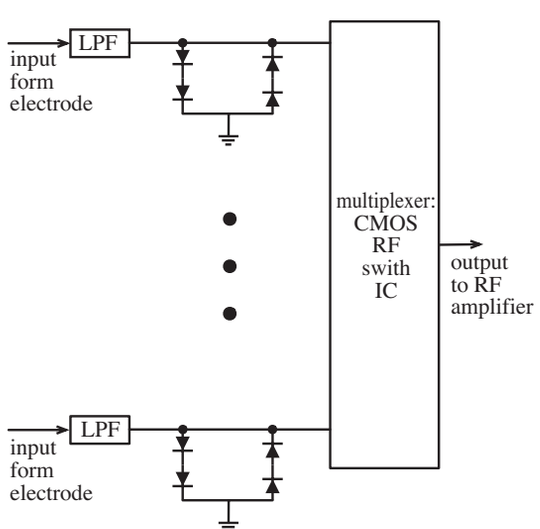

Fig. 12. Schematic diagram of the filter-switch module that is composed of the low pass filters (LPF) with 700 MHz cutoff frequency, CMOS RF switch IC and the diodes between them to protect the switch IC from excessive voltages.

Table 1. Examples of typical filling patterns of the SPring-8 storage ring

	Pattern name	Explanation
pattern 1	multi-bunches	(160-bunch train + 43-empty bucket train) × 12 with 50 μA/bunch
pattern 2	203 bunches	203 equally spaced bunches with about 0.5 mA/bunch
pattern 3	1/12 filling + 10 singles	203-bunch train with total of 82 mA + 10 equally spaced isolated bunches with about 1.8 mA/bunch
pattern 4	single bunch	Only one bucket is filled with electrons: 10 mA/bunch

* The harmonic number of the storage ring is 2436; 1/12 × 2436 = 203, etc.

One of the practical countermeasures used to eliminate the filling pattern dependence is to place additional band pass filters (BPFs) whose center frequency is the detection frequency of the circuits, i.e., the RF acceleration frequency, at the inputs of the filter-switch modules. The filters reduce the time domain signal amplitude by restricting unnecessary frequency components while keeping the detection frequency component unchanged. The effect of the amplitude reduction of the BPF is different for the isolated bunches and the bunch train parts. For example, in the hybrid filling patterns such as pattern 3 in Table 1, the amplitudes of the isolated bunches were larger than those of the train part for the signals before the BPF. On the contrary, the amplitude of the train part was larger than those of the isolated bunches for the signals after passing the BPF with 10 MHz bandwidth, because the RF acceleration frequency component contributed significantly in the train part spectrum, whereas components other than the RF acceleration frequency component had a large contribution in the isolated bunch spectrum. To remove the filling pattern dependence, the maximum amplitude must be smaller than the level of the onset of diode conduction after passing the BPF in any possible filling pattern, whether the maximum originates from a train part or from an isolated bunch with a large current.

The elimination of filling pattern dependence for actual beams had to be confirmed before the adoption of the method. For the BPF bandwidth selection, we had several BPF with 10 MHz bandwidth, and the results of some preliminary tests and calculations seemed to be promising. We made additional samples of the 10-MHz-bandwidth BPF and performed measurements to evaluate the effectiveness of the filters by using actual beams in the storage ring. The storage ring was operated in the filling patterns listed in Table 1 for the evaluation. The COD data were compared between the different filling patterns.

From the obtained data, the root-mean-square (rms) values of the differences of COD data between the different filling patterns were calculated. They are listed in Table 2, which shows that the COD differences were all within about 10 μm. The BPF were found to be effective in removing the filling pattern dependence. An example of the differences of the COD data between the different filling patterns is shown in Fig. 13. The BPF were attached to the BPM with serial numbers from 1 through 30. As shown in the figure, the effectiveness of the BPF is evident; the COD data of the BPM with the BPF were reproduced within 10 μm, whereas differences in the COD data of other BPM extended to more than 100 μm.

In accordance with the result, we will produce a sufficient number of BPF to cover the whole storage ring, i.e., more than 1000 pieces, and attach them to

Table 2. Summary of the measurements: rms of COD differences between different filling patterns. All the data are in the unit of μm, δx are in the horizontal and δy are in the vertical direction

Compared pattern	with BPF		without BPF	
	δx_{rms}	δy_{rms}	δx_{rms}	δy_{rms}
(203 bunches) – (multi-bunches)	1.5	4.4	41	51
(1/12filling + 10 singles) – (203 bunches)	6.2	4.1	28	60
(single bunch) – (multi-bunches)	9.0	10.7	2100	3072

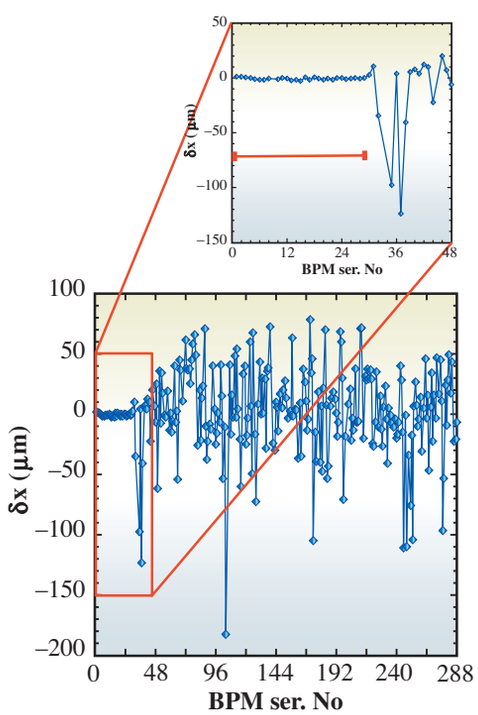

Fig. 13. Example of the COD differences in the horizontal direction between two different filling patterns: the 203 bunches and the multi-bunches. The data of the serial numbers from 1 to 48 are zoomed in the upper plot. The BPF were attached only to the BPM of serial numbers 1 to 30 indicated by the red line in the zoomed plot.

the inputs of filter-switch modules in the summer shutdown of 2008. We expect that, after the summer shutdown, we will be able to operate the storage ring in any filling pattern with a reproducibility of the closed orbit of about 10 μm.

Development of Bunch-by-bunch Feedback

Bunch-by-bunch feedback for filling with high contrast bunch current

The filling of the storage ring with a few high current singlet bunches and trains of low current bunches are requested by users and, for such requests, the ratio of maximum to minimum bunch current is nearly 10. Bunch-by-bunch feedback was installed to suppress transverse beam instabilities. The signal of a bunch from a BPM for feedback, or the gain of feedback, is proportional to the bunch current and the position shift of the bunch and, with the limited dynamic range of the components of feedback and feedback gain, it is difficult for the feedback to handle bunches with such a wide range of bunch current. To overcome this difficulty, we developed a bunch-by-bunch attenuation system, which automatically attenuates the signal from bunches with high bunch current to reduce the contrast of the bunch current (Fig. 14). This attenuator is composed of a fast discriminator that detects the bunch current and produces a gate signal, FPGA, for generating a one-turn delay of the gate signal, and mixers for attenuation driven by the gate signal. Using this attenuator, we could simultaneously store several singlet bunches with bunch current 3 mA/bunch and a bunch train with bunch current 0.6 mA/bunch.

RF direct sampling

For the operation of the bunch-by-bunch feedback since 2007, we have employed the scheme of RF direct sampling for the front-end circuit. The concept of RF direct sampling is shown in Fig. 15. With this scheme, we can eliminate the base-band conversion stage that requires mixers, an LO signal, filters and amplifiers, and simplify the system with fewer tuning points and low cost, as shown in Fig. 16. To perform the RF direct sampling, we chose the Analog Devices AD9433 ADC for the second version of the SPring-8 feedback processor, which was completed in 2005. The analog bandwidth of AD9433 extends up to 750 MHz (full power) and covers the required frequency range for the RF direct sampling, from 250 MHz to 750 MHz, with a bunch rate of 508 MHz.

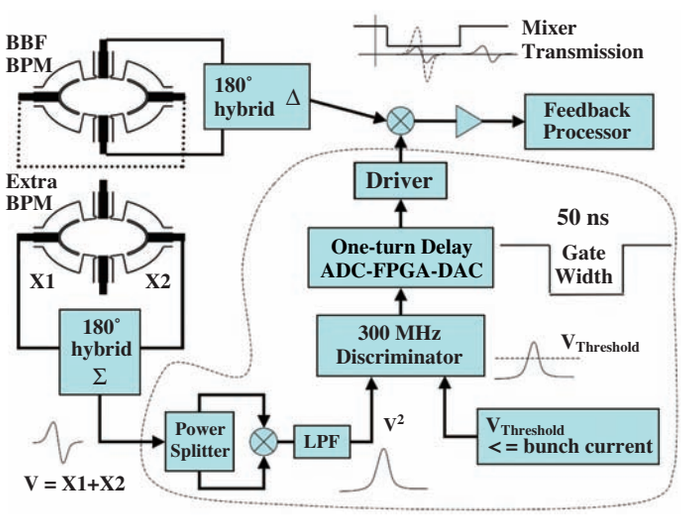

Fig. 14. Block diagram of bunch-current-sensitive automatic attenuation system. The threshold current above which the attenuation is large is controlled by the threshold voltage of the discriminator.

International Collaboration

In 2006, a single-loop two-dimensional transverse bunch-by-bunch feedback unit was successfully installed at SOLEIL storage ring in Paris, France, based on collaboration between JASRI and SOLEIL with the SPring-8 feedback processor. Also in 2006, the digital transverse feedback unit was tested in the Hefei light source at the National Synchrotron Radiation Laboratory (NSRL), University of Science and Technology of China (USTC), Hefei, China, using the feedback unit developed by JASRI during the visit of a researcher from JASRI as part of the collaboration between JASRI and NSRL/USTC.

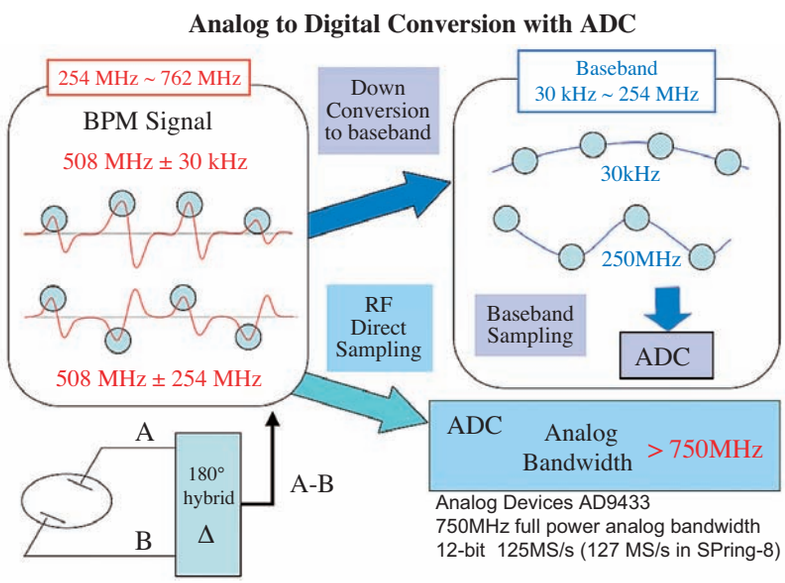

Fig. 15. Concept of RF direct sampling. Base-band conversion and base-band sampling are also shown.

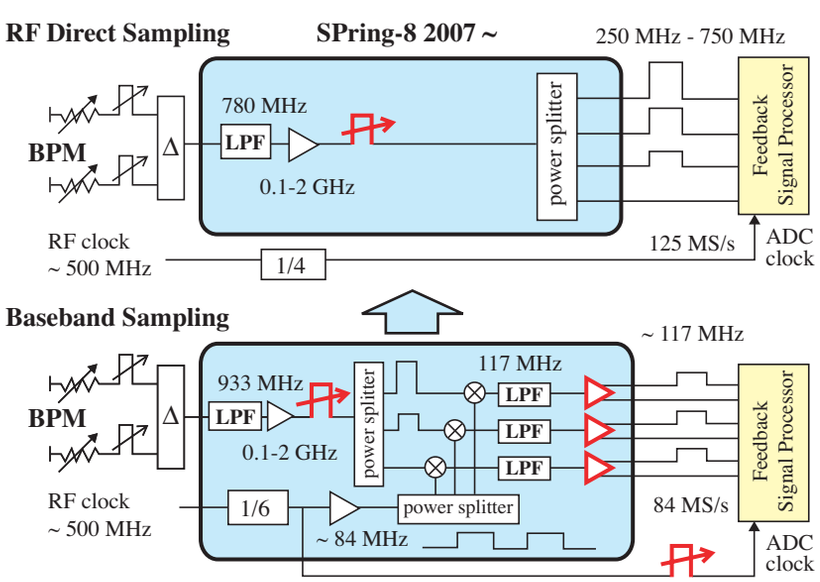

Fig. 16. RF front-end circuit for RF direct sampling in SPring-8. The circuits for base-band conversion and base-band sampling are also shown.

Development of Accelerator Diagnosis Beamlines

At accelerator diagnosis beamline I (BL38B2), a bunch purity monitor has been continuously monitoring the purity of isolated main bunches of several-bunch user operation modes. It is based on the gated photon counting method utilizing two fast Pockels cells as light shutters operating in the visible light region, and can successfully detect parasitic satellite bunches as low as 10^{-9} times the intensity of the main bunches [11]. An example of the evolution of bunch purity during a topping-up user operation measured using the monitor is shown in Fig. 17.

At accelerator diagnosis beamline II (BL05SS), the so-called edge radiation from the bending magnets upstream and downstream of the ID straight section of the beamline can be utilized in optics hutch I. By observing the microwave component of the edge radiation, burst coherent synchrotron radiation originating from instabilities of the intense single bunch beam was surveyed and promising preliminary results were obtained. Figure 18 shows an example of an oscilloscope trace of the output signal obtained from a microwave detector. A significant repeated signal above the noise level at the revolution frequency was observed sporadically for a beam current larger than about 10 mA. By irradiating the X-ray component of the edge radiation to a vacuum gauge head, misreading of a Bayard-Alpert ionization vacuum pressure gauge was studied experimentally [12].

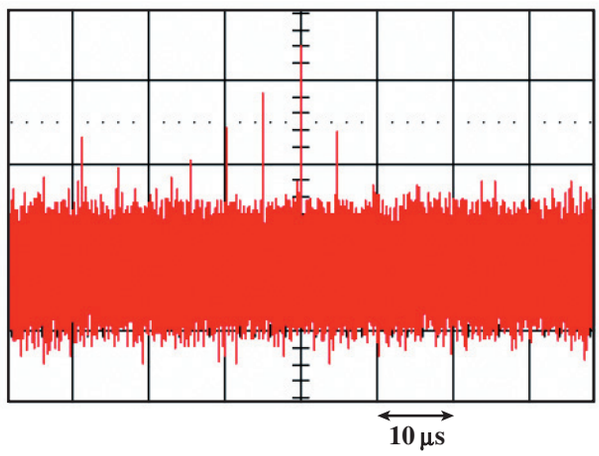

Fig. 18. Example of an oscilloscope trace of output from a microwave detector operating in the 75-110 GHz frequency range. The current of the single bunch was 12 mA. The horizontal scale is 10 μs per division and the revolution period of the bunch is 4.8 μs. A repeated signal above the noise level was observed at the revolution frequency.

The development and installation of the vacuum components of optics hutches I and II of the diagnosis beamline II have been completed (Fig. 19). The first light of the ID was successfully delivered to optics hutch I in May 2007. Optics hutch II has a double crystal monochromator based on the SPring-8

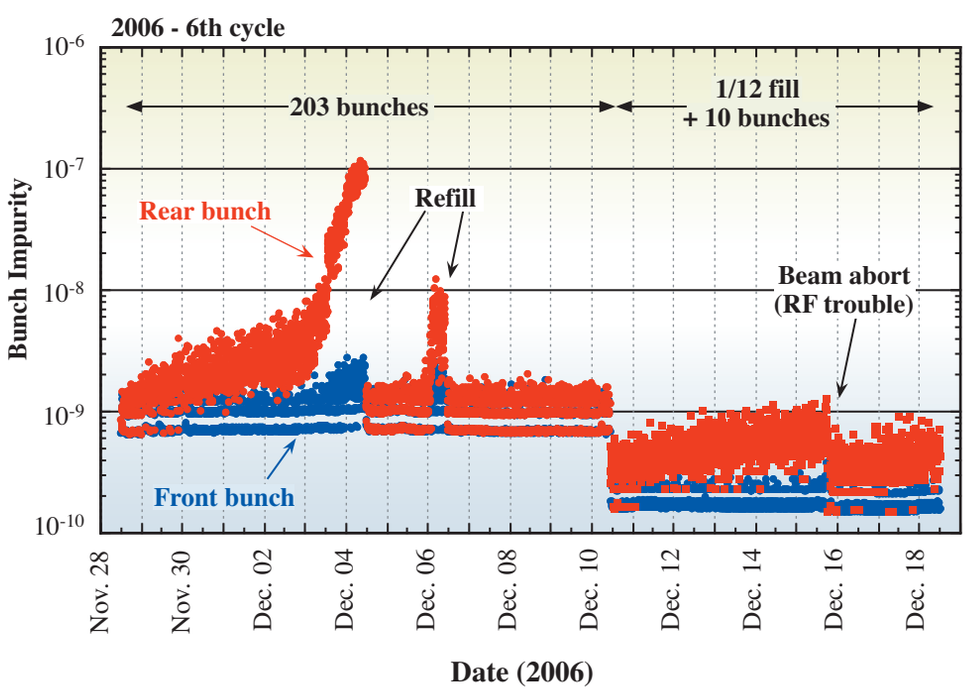

Fig. 17. Example of evolution of bunch purity. The red circles stand for the nearest satellite bunches preceding the main bunches and the blue ones stand for those behind the main bunches. On 4th and 6th December, abortion and refill of the beam were performed, respectively, because of an unacceptable increase of the bunch impurity.

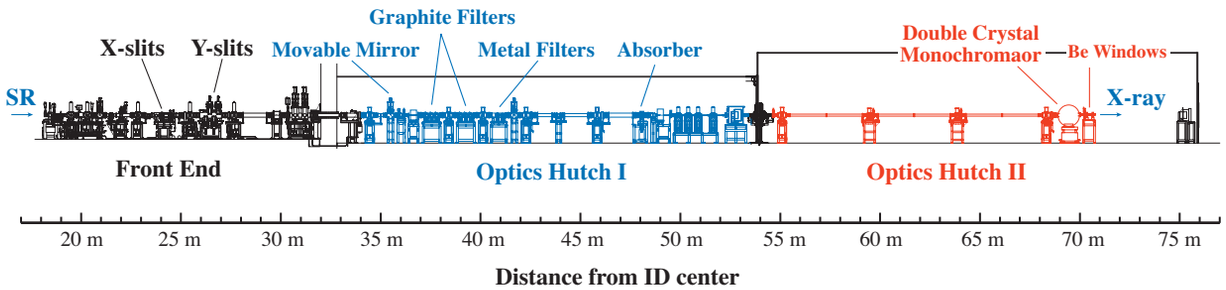

Fig. 19. Schematic layout of accelerator diagnosis beamline II (BL05SS).

standard type. The crystals of the monochromator are cooled by liquid nitrogen. The x- and y-slits used to shape the input X-ray beam of the monochromator have also been installed in the front end. The delivery of the first light of the ID to optics hutch II is planned early in 2008.

Research and Development of 10-T Superconducting Wiggler –Field Measurement–

If a high-field superconducting wiggler (SCW) is installed in the SPring-8 storage ring, it can generate synchrotron radiation with energy of MeV order [13], which is very useful for nuclear astrophysics and other experiments. The SCW consists of one central magnetic pole (main pole) and two side poles. The side poles are excited with opposite polarity to the main pole (see Fig. 20). The maximum field of the main pole is designed to be 10 T in the vertical direction (B_y). The beam orbit deflection in the horizontal plane can be closed within the SCW by adjusting the excitation currents of the main pole and side poles. For orbit stability of less than 1 μm, the field fluctuation must be less than 10^{-6} because the field of the main pole is one order higher than that of the normal dipole magnets. Accurate field measurement is then required. Furthermore, to estimate the total effect on the stored beam, it is necessary to measure not only the main component of the magnetic field B_y but also the minor component in the horizontal direction (B_x) and longitudinal direction (B_s). We then need to measure these components on three-dimensional mesh points to extract the quadrupole and higher multipole fields. For this purpose, we designed a stage for the field measurement of the SCW. Since the beam chamber of the SCW is narrow and long (65 mm in width, 20 mm in height and 1.5 m in length), it is difficult to access the central part of the chamber. We thus

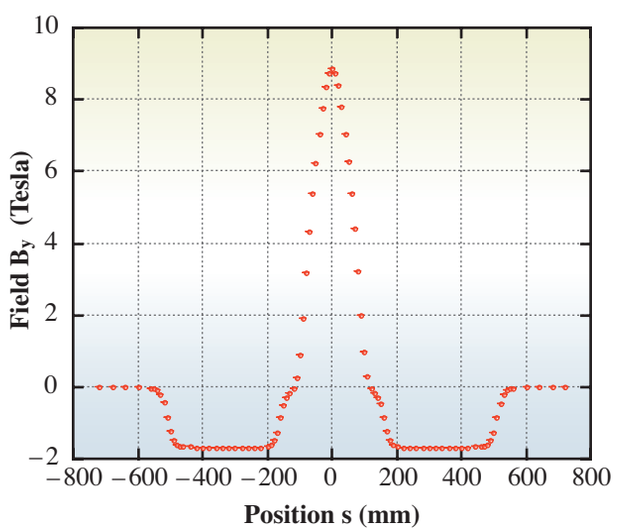

Fig. 20. Longitudinal distribution of the vertical field B_y (measured x = y = 0 mm on the s-axis). The field of the main pole was set to 9 T. The main pole and side poles are located at s = -100 mm ~ +100 mm, s = -500 mm ~ -150 mm and s = +150 mm ~ +500 mm, respectively. Error bars indicate one standard deviation of ten measurements.

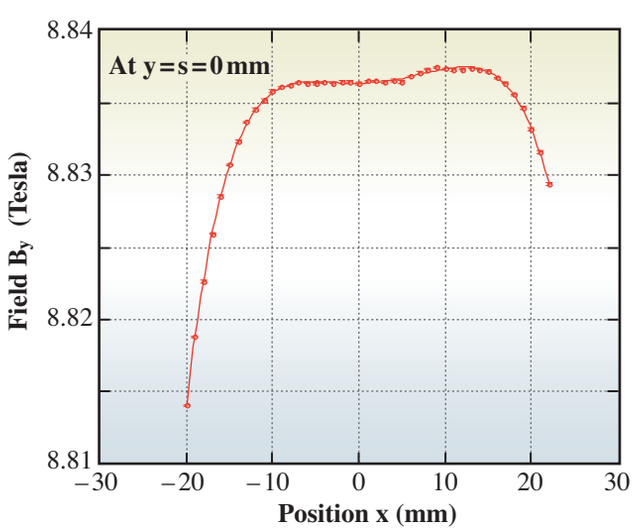

Fig. 21. Horizontal distribution of the vertical field B_y at the position y = s = 0 mm. The field of the main pole was set to 9 T. The solid line indicates the result of least-squares fitting with a polynomial of degree six in x. Error bars indicate one standard deviation of ten measurements.

passed a timing belt through the chamber, on which a three-dimensional hall probe was fixed. The belt forms a loop through the chamber with two gears at both ends. A gear on one side is pulled with a tension of 10^3 N to minimize the bending of the belt. To adjust the longitudinal position of the probe, the belt is rotated by a stepper motor, and to adjust the horizontal and vertical positions, the belt is moved manually using x-y stages set at both ends.

Examples of field measurements are shown in Figs. 20 and 21. In Fig. 20, the longitudinal distribution of the vertical field B_y (measured at x = y = 0 mm on the s-axis) is shown when the peak field was set to 9 T. The horizontal distribution of field B_y at the position y = s = 0 mm is shown in Fig. 21. The longitudinal distribution was consistent with the designed value. To estimate the strengths of the multipole components, the horizontal distribution was fitted by the least-squares method with a polynomial of degree six in x (Fig. 21, solid line). We found that the strengths of the multipole components could not be neglected and were asymmetric to the x-axis and the y-axis. By exciting the SCW several times, we also evaluated the reproducibility of the field and found that it was less than the error of the measurement.

In the future, a three-dimensional field will be measured automatically using automatic x-y stages in the range of x = ±20 mm, y = ±5 mm and s = ±720 mm. The measurement will be carried out with a 1 T step of the peak field. The field measurement data will be used for designing dipole, quadrupole, sextupole and, if necessary, higher multipole corrector magnets for compensating the SCW error field to suppress the effect on the stored beam.

Research and Development of Femto-second Pulse X-ray Generation

The principle of femtosecond pulse X-ray (FSX) generation studied at SPring-8 is as follows: RF deflectors installed in the storage ring vertically kick the head and tail of a stored bunch in opposite directions. Thus, the bunch is tilted and emits a tilted photon bunch in the undulator downstream. A slit further downstream slices the photon bunch to form a short pulse light. The plan to achieve FSX generator under consideration and its design parameters are detailed in a previous report [14].

In this report we presents performance achievable by the short X-ray generator. In the following discussion, we assume that all electron and photon bunches have Gaussian distributions. Note that the symbol "σ" meaning pulse width corresponds to a standard deviation of a Gaussian distribution.

Photon flux density and extraction efficiency

We have studied two types of undulators operating at SPring-8, the minipole undulator [15] and the standard-type undulator. The parameters of the undulators designed for FSX generation are listed in Table 3.

Table 3. Parameters of undulators designed for FSX generation

Type of Undulator	Period Length	Gap	K Value	Total Period
Mini-Pole Type	10 mm	5 mm	0.92	101
Standard Type	32 mm	10 mm	2	140

The above minipole undulator has the advantage of a smaller diffraction-limited spot size than the standard type. The photon flux density from the minipole undulator at a stored current of 100 mA is shown in Fig. 22. The photon energy and flux density of the first peak are 10.7 keV and 8.48×10^{17} photons/(sec·mrad^2·0.1% BW·100 mA) at an electron beam energy of 4GeV, and 42.5keV and 8.48×10^{17} at 8 GeV, respectively. The brilliance of the first peak corresponds to 5.34×10^{20} Photons/ (sec·mm^2·mrad^2·0.1% BW·100 mA) for 4 GeV and 1.62×10^{20} for 8 GeV.

Although the operating energy of the SPring-8 storage ring is 8 GeV, low energy operation at 4 GeV is being considered to improve the beam emittance. The dashed lines in Fig. 22 show the first peak shift as the K value approaches zero.

The extraction efficiency η, defined as the ratio of the X-ray flux sliced by the slit to the total flux emitted

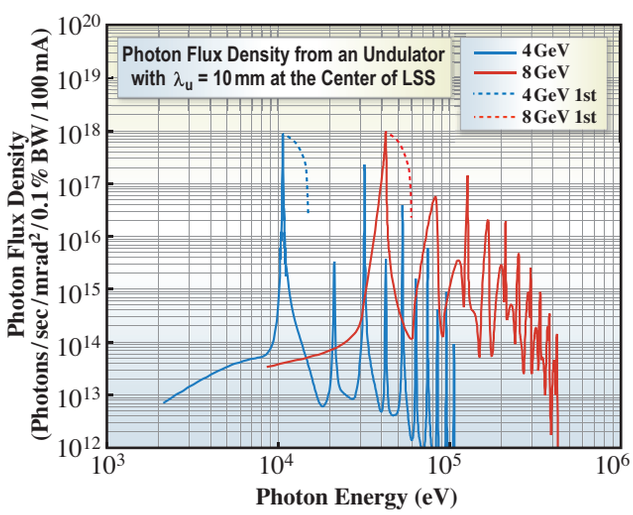

Fig. 22. Spectrum of photon flux density from the minipole undulator suitable for short-pulse generation. The intensities correspond to 100% extraction efficiency.

from the entire bunch, is approximated by

$$\eta \cong \frac{2W}{\sqrt{2\pi}\sigma_t c\tan\theta_{tilt}} , \qquad (1)$$

where $2W$ is the full width of the slit, σ_t is the longitudinal bunch length in time and $\tan\theta_{tilt}$ is the bunch tilt. Figure 22 corresponds to the case of $\eta = 1$, or 100% efficiency.

Pulse width

The extracted X-ray pulse width σ_p is described by

$$\sigma_p^2 \cong \sigma_{p0}^2 + \left(\frac{W}{\sqrt{6}c\tan\theta_{tilt}}\right)^2 , \qquad (2)$$

where σ_{p0} is the minimum X-ray pulse width attained by the FSX generator, given by

$$\sigma_{p0} = \sqrt{\sigma_y^2 + \sigma_r^2} \Big/ c\tan\theta_{tilt} , \qquad (3)$$

where σ_y is the vertical bunch size given by the emittance and β function, and σ_r is the diffraction limited spot size. This formula implies that we require smaller σ_y and σ_r and larger $\tan\theta_{tilt}$ to realize a shorter pulse width, where σ_y is dominated by the accelerator parameters and σ_r is mainly dominated by the insertion device parameters.

RF deflector – the crab cavity –

The bunch tilt $\tan\theta_{tilt}$ is given by

$$c\tan\theta_{tilt} = \frac{2\pi f_{def} L_{drift} eV_{\perp}}{E_{electron}} , \qquad (4)$$

where f_{def} and $V_{\perp}$ are the deflecting frequency and the voltage of the RF deflector, respectively. L_{drift} is the length of the drift space between the RF deflectors and $E_{electron}$ is the electron beam energy. In our design, L_{drift} is 7 m. From Formulae (2), (3) and (4) we find that a larger deflecting voltage is required to obtain a shorter X-ray pulse.

We employed a superconducting crab cavity developed at KEK [16] as a deflector, which has achieved a maximum deflecting voltage 2.7 MV for CW operation at 4.2 K, and its resonant frequency of 508.887 MHz is almost as same as that of 508.58 MHz of the SPring-8 storage ring. The crab cavity is operated in the TM_{110} mode and the bunch is kicked vertically by its horizontal magnetic field. The magnetic path integral in the cavity is converted into the effective deflecting voltage. In this paper we conservatively assumed the old value of 1.67 MV as the deflecting voltage of the cavities, and consequently obtained a bunch tilt $c\tan\theta_{tilt}$ of 13.3 μm/psec at 4 GeV (and 6.67 μm/psec at 8 GeV) for the 7 m drift space.

Performance of FSX – pulse width and extraction efficiency –

We evaluated the performance of the FSX sliced from the first peak X-ray. From Formulae (1) to (4) the relation between the sliced light pulse width and the extraction efficiency can be obtained for the minipole undulator (λ_u = 10 mm) and the standard-type undulator (λ_u = 32 mm) as shown in Fig. 23. In this calculation the diffraction effect was considered and the beam emittance was assumed to be $\varepsilon_y = 0.75 \times 10^{-12}$ m·rad at 4 GeV and $\varepsilon_y = 3 \times 10^{-12}$ m·rad at 8 GeV. If we assume the extraction efficiency to be 1% at 4 GeV operation, we can obtain a pulse width of 600 fs in two standard deviations. As the pulse width approaches the attainable minimum σ_{p0}, the extraction efficiency falls drastically.

According to Fig. 23, the minimum light pulse widths are determined by the parameters of the undulators in the case of 4 GeV operation, whereas they are almost unique in the case of 8 GeV operation. That is, the diffraction limited spot size is dominant at 4 GeV, as indicated by Formula (3), and therefore, it is effective to introduce the minipole undulator. On the other hand, the standard-type undulator operates satisfactorily at 8 GeV, as the vertical beam size given by the emittance is dominant at this beam energy.

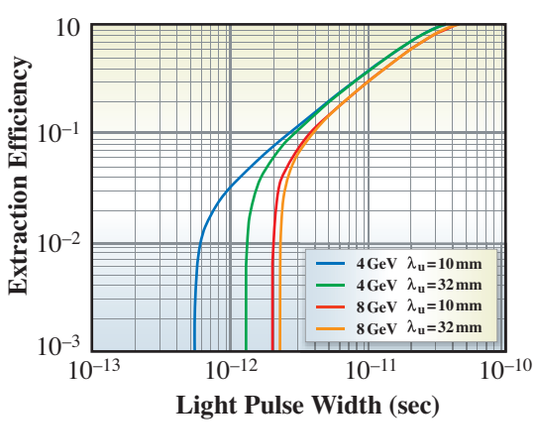

Fig. 23. Relation between the pulse width and the extraction efficiency. The pulse width is the value representing two standard deviations.

Developments and Upgrades of Linac

Improvement of Electron Gun System

The SPring-8 linac has been equipped with only one electron gun system, i.e., a high-voltage inverter-type pulse power supply, a pulse transformer, a high-voltage deck and an electron gun. That is, when any of these parts fail, the linac cannot inject beams into the booster synchrotron until the failure is fixed. In particular, the replacement of a cathode assembly requires at least three days to complete the processes of mounting a new cathode assembly, and the evacuation and activation of the cathode. Therefore, the construction of a backup system has been an important issue for enhancing the reliability of the electron gun system and to reduce the downtime of the beam injection in the case of a gun failure.

We have thus carried out the following improvements:

1) Development of a reliable high voltage pulse power supply.
2) Composition of a twin electron gun system.

New high voltage pulse power supply

The previous pulse power supply often caused discharges at the high-voltage terminal of the inverter power supply. In addition, it was difficult to maintain the pulse power supply because it was designed many years ago. The new power supply was completed in 2005 and it has been operated in a test stand for almost one year to confirm its performance and reliability. At the end of 2006, we replaced the previous power supply system with the new one. Figure 24 shows the pulse transformer tank and the high-voltage deck installed in the accelerator room.

The new system has the following features:

1) A pulse transformer with a step-up ratio of 1:30 decreases the primary voltage and accordingly solves the discharge problem. The inverter power supply now feeds a voltage of only 12 kV to the PFN to generate a pulse voltage of 180 kV at the terminal of the electron gun.
2) The FL-net, which is a standard universal network used in factory automation, was adopted as a new network connecting PLCs with a higher-level control system. All the linac PLCs used for local control of devices will be connected to the FL-net instead of the current network.
3) A larger high-voltage deck was installed to enhance functionality, expandability and serviceability.

The high-voltage pulse applied to the electron gun has a long rise/fall time of approximately 3 μs because the large step-up ratio enlarges the stray capacitances of the secondary circuit. However, the short flat top of the pulse caused by the long rise/fall time does not limit operation since in practice we use short pulse beams with pulse widths of less than 40 ns. The voltage stability of the inverter power supply is about 0.05% rms, which is sufficiently stable for the injector linac.

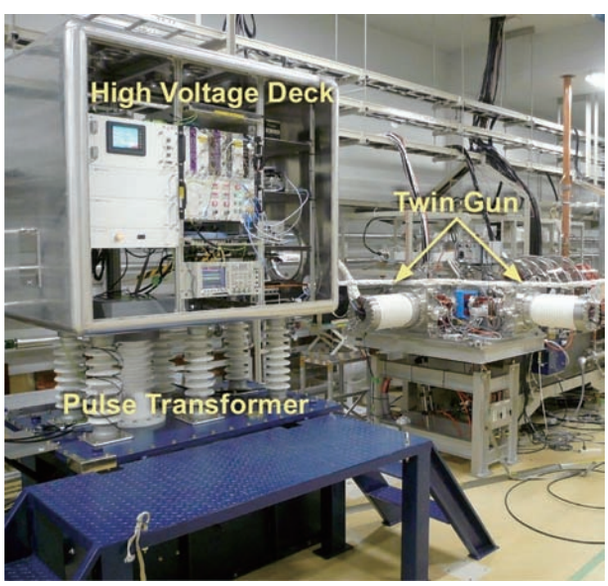

Fig. 24. New high-voltage station installed in the accelerator room.

Twin electron gun system

We had considered a couple of ideas that could realize a twin gun system: duplicating the present electron gun or doubling the present injector part including the gun and the buncher system, for example. We eventually decided to build only a backup gun and its power supply as early as possible. The following issues were taken into account in designing the backup gun.

1) The original performance of the main gun has to be maintained after the installation of the backup gun, whereas the performance of the backup gun for temporary operation, the beam current for example, can be inferior to that of the main gun.
2) The cathode of the backup gun has to be being pre-heated during the linac operation to immediately generate electron beams in case a failure of the main gun occurs.

A 90° bending magnet was installed to inject beams from the backup gun orthogonally mounted to the main gun, which was relocated upstream to make space for the bending magnet. The pole pieces of the bending magnet were designed to focus beams from the backup gun. A magnetic lens was installed for each gun to reduce the beam divergence caused by the space charge effects. A beam profile monitor and a coaxial type beam absorber to measure beam currents have also been installed for diagnosis of the backup gun's beam. Figure 25 shows the almost completed twin electron gun.

The backup gun will be soon tested and be ready for operation. The additional high-voltage power supply system for the backup gun will be constructed in 2008; hence, the complete twin gun system will start operation in 2009.

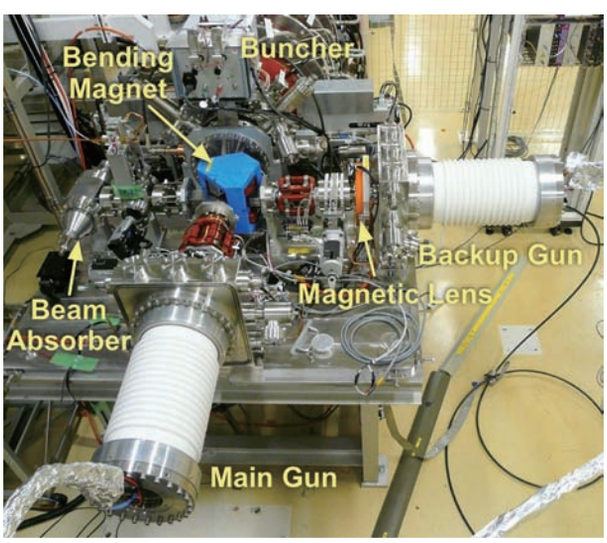

Fig. 25. Twin electron gun.

Haruo Ohkuma*, Hiroto Yonehara, Hirofumi Hanaki

SPring-8 / JASRI

*E-mail: ohkuma@spring8.or.jp

References

[1] H. Tanaka *et al.*: Proc. EPAC2004, Lucerne, Switzerland, p.222.
[2] H. Tanaka *et al.*: Proc. EPAC2006, Edinburgh, Scotland, p.3359.
[3] T. Ohshima *et al.*: Proc. EPAC2004, Lucerne, Switzerland, p.414.
[4] H. Tanaka *et al.*: Proc. EPAC2004, Lucerne, Switzerland, p.1330.
[5] H. Tanaka *et al.*: Nucl. Instrum. Meth. A **539** (2005) 547.
[6] H. Tanaka *et al.*: Nucl. Instrum. Meth. A **313** (1992) 529.
[7] K. Soutome *et al.*: Nucl. Instrum. Meth. A **459** (2001) 66.
[8] M. Takao: Phys. Rev. ST Accel. Beams **9** (2006) 084002.
[9] SPring-8 Research Frontiers 2006, p.179.
[10] SPring-8 Research Frontiers 2006, p.180.
[11] K. Tamura, T. Aoki: Proc. 1st Annual Meeting of Particle Accelerator Society of Japan and 29th Linear Accelerator Meeting in Japan, Funabashi, 2004, p.581.
[12] M. Oishi *et al.*: J. Vac. Soc. Jpn. **51** (2008) (in Japanese) - to be published.
[13] K. Soutome *et al.*: Proc. PAC2003, Portland, U.S.A., p.250; See also http://www.spring8.or.jp/en/about_us/organization/ acc_project/scw/
[14] SPring-8 Research Frontiers 2006, p183.
[15] T. Bizen *et al.*: Proc. 8th International Conf. on Synchrotron Rad. Instrumentation, San Francisco, CA, (2003) p.175.
[16] K. Hosoyama *et al.*: Proc. 12th International Workshop on RF Superconductivity, Cornell Univ., Ithaca, NY, (2005) - to be published.

CONTROLS & COMPUTING

Virtualization of the Operator Consoles on Beamline Control System

The control system is the nerve center of SPring-8. Upgrades of the control system increase the efficiency of experimental studies at beamlines. Since fiscal 2006, we upgraded the operator consoles of the beamline control system. At that time, nearly 50 high-performance workstations were being operated around the beamlines as operator consoles for experimental users. The proliferation of the workstations made it difficult to keep them in continous operation. Some computers occasionally malfunctioned, stopping users' experiments during exchange to new workstation. There have been over 20 instances of hardware trouble since 2000. A downtime of several hours was needed to exchange workstation and set up the replacement workstation. The increase in the number of workstations caused the total cost of ownership (TCO) to increase rapidly. To solve the above problems, we integrated the operator consoles of the beamlines into four enterprise-class server computers by applying virtualization technology, which enabled us to consolidate a large number of computers to a few host computers, thus reducing system maintenance costs drastically. Figure 1 shows the virtualization host server computers. We adopted an HP c-class blade system that has hot-swap functionality of all the modules without any interference with each other. A CPU module has two dual-core AMD Opteron processors and 8 GB memory. Over 50 operating systems are now running on only four server computers. The availability of the blade system, which has redundant power supplies and cooling fans, is high. In addition, one CPU module is a hot standby for emergencies. We adopted Xen as the virtualization environment. Xen has a live migration capability that can transfer a running guest operating system from one CPU module to another nearly instantaneously. We can maintain a CPU module with the control system in coutinuous operation. Two types of thin client systems, SunRay and VNC, were introduced as user control terminals to replace the previous X-terminals. Because these have no breakable boot devices such as a hard drive, the client systems are quite stable. Both systems boot up from a boot server. When a problem occurrs in the thin client, restoration becomes very easy. Previous workstations had another function of data acquisition for the interlock system. We have recently introduced

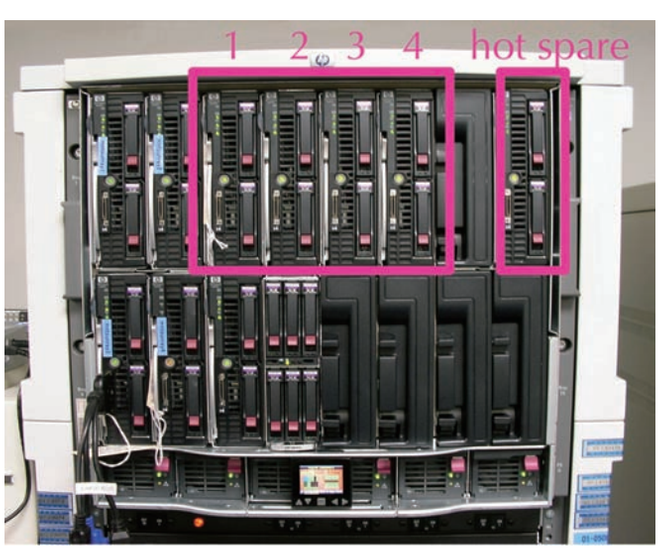

Fig. 1. Virtualization host server computers. Only four CPU modules cover all the operator consoles of the SPring-8 beamline.

an alternative data acquisition computer system, Armadillo. Armadillo is an ultrasmall embeded computer for uninterrupted operation. We used it as a serial-ethernet converter to communicate with the PLC of the interlock system. This contributes to the stablilization of the control system with the above-mentioned thin client systems. Figure 2 shows an overview of the new beamline control system.

The introduction of the virtualization system has resulted in many benefits. One is that the serviceability of the system has improved. The resources of CPU, memory and storage are consolidated at one location, and thus can be managed efficiently. Also, reliability has improved. We have had no serious trouble with the operator consoles since the update. During one year of operation there has been no downtime due to the live-migration function even though a hardware failure occurred in the host server. It is notable that the control response is faster than the previous system of high-performance workstations. The communication overhead between the control systems was observed to be shorter by up to about 64% as a result of the actual experimental study at the beamline.

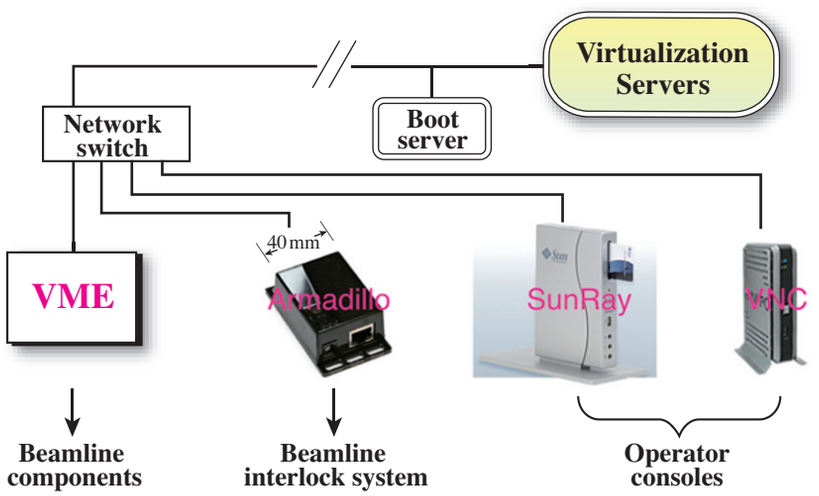

Fig. 2. Overview of newly installed beamline control system. Each beamline has VME, Armadillo, SunRay and VNC systems.

Toru Ohata

SPring-8 / JASRI

E-mail: ohata@spring8.or.jp

Network Security in SPring-8

The network system is one of the most important infrastructures that enable the continuous operation of SPring-8. Not only SPring-8 staff but also many experimental users from outside access various network services provided by SPring-8. A secure network system contributes to the stable operation of SPring-8. We will discuss the outline of the SPring-8 network system in this text.

The SPring-8 network system consists of three network zones: a public network for office work, a beamline user network and a control network. Figure 1 shows an overview of the network system of SPring-8. The public network provides services such as mail servers, web servers and a wireless network system. We constructed the wireless network and the guesthouse network under an authentication system. When users access the wireless or guesthouse network, only authorized users can access the public network and the Internet through the authentication system. We have several access policies for each access point. For instance, the access from the guesthouse to unauthorized network resources is restricted. To maintain the security of the access points, we have recently installed a wireless network-monitoring tool, using which we can detect network abuse such as rogue access points.

The beamline user network was constructed for users' experiments. Various experimental control and data acquisition systems are operated on the network. As shown in Fig. 2, the beamline user network is isolated from external networks such as the Internet and the public network by using NAT (network address translation). We introduced VLAN (virtual local area network) technology to build a logically independent and flexible network system. The access from one VLAN to other VLANs is restricted by IP filtering through a core switch. Additionally, by introducing an IPS (intrusion protection system) we can remove network threats that are caused by computer worms. When the IPS detects malicious activity, it prevents the spread of worms by dropping or rejecting the unauthorized connection.

The control network is used for the operation of accelerators and beamlines. The network is strictly protected because its importance to SPring-8 by a firewall system. However, if a recovery procedure from outside SPring-8 is needed in the case of machine trouble, we must access the control network

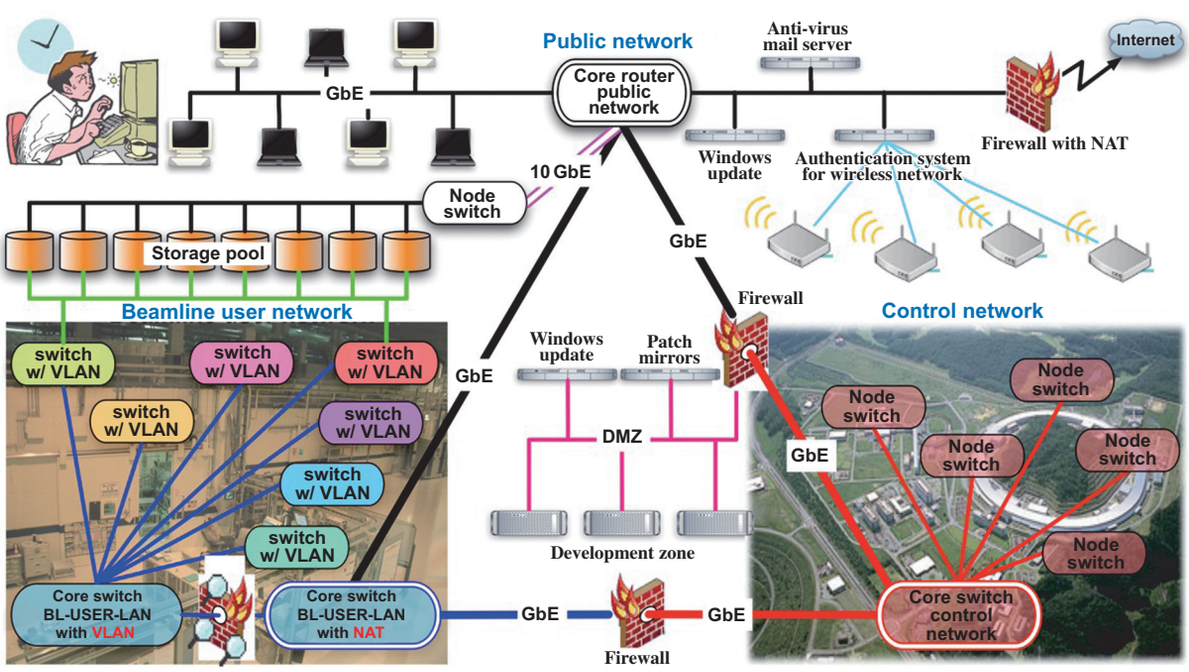

Fig. 1. Schematic view of the SPring-8 network system. The network is divided into three networks: a public network, a beamline user network and a control network.

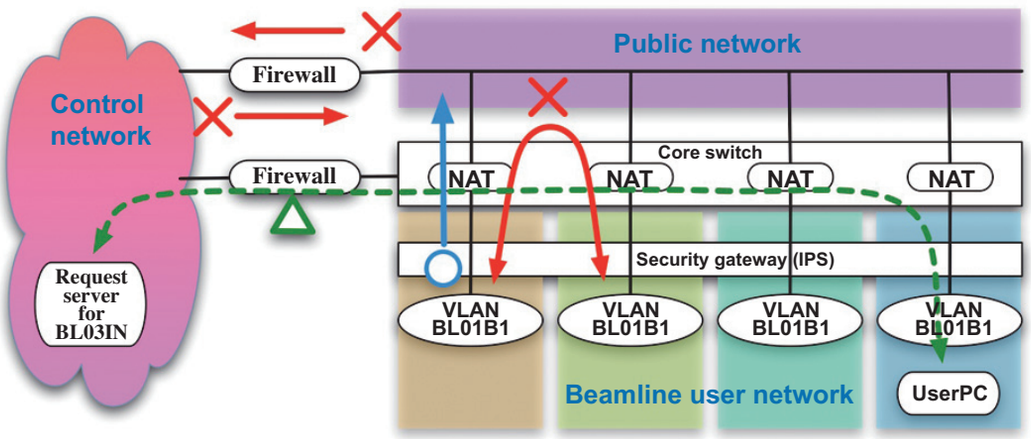

Fig. 2. Beamline user network isolated by using NAT and VLAN. The IPS prevents computer worms from spreading.

from outside. Thus, we constructed a remote maintenance mechanism, WARCS (wide area remote control system), which is able to access the higher-security control network. Figure 3 shows an overview of WARCS. WARCS comes under the scrutiny of the shift leader of the SPring-8 operators. WARCS is implemented by a network tunneling application, Zebedee, to bypass the firewalls system. The shift leader can control and monitor the access of WARCS. For a security reasons a one-time password is used to access the control network. By introducing WARCS we have acquired a safe remote maintenance scheme. The ability to conduct remote beamline experiments will be advanced on the basis of the technology of WARCS.

Network technology has progressed rapidly in recent years, during which many security threats have developed then been fixed, which has created a vicious circle of network development. It is difficult to achieve a good balance between security and user friendliness. At SPring-8, we are maintaining a secure network by conducting advanced research on network technology.

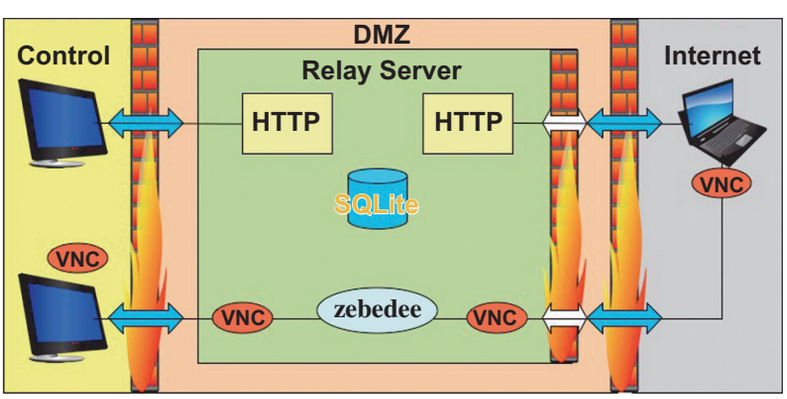

Fig. 3. Overview of WARCS, which realizes safe remote access by using the network tunneling technique.

Toru Ohata* and Miho Ishii

SPring-8 / JASRI

*E-mail: ohata@spring8.or.jp

New Apparatus & Upgrades

Undulator Update in 2007

Two major updates on light sources in existing beamlines were performed during the summer shutdown in 2007, with the aim of achieving better optical performance. The first update was the swapping of devices. The insertion device originally installed in BL10XU (ID10) was exchanged with that in BL46XU (ID46) to take the greatest advantage of the optical properties obtained by these two light sources, especially the photon energy region available with fundamental radiation. The periodic length of ID46/ID10, which is now installed in BL10XU/BL46XU, is 24mm/32 mm and can provide higher/lower photon energy with fundamental radiation, which is required from the users of each beamline. A variety of experiments using the photons in the new energy range are expected to be performed at both beamlines. The second update was to install a new system for helicity switching in BL23SU, which is basically the same as that in BL25SU. What should be noted is that the undulators are the in-vacuum type to reduce the periodic length and increase the number of periods. The layout of the kicker system installed in BL23SU is schematically shown in Fig. 1.

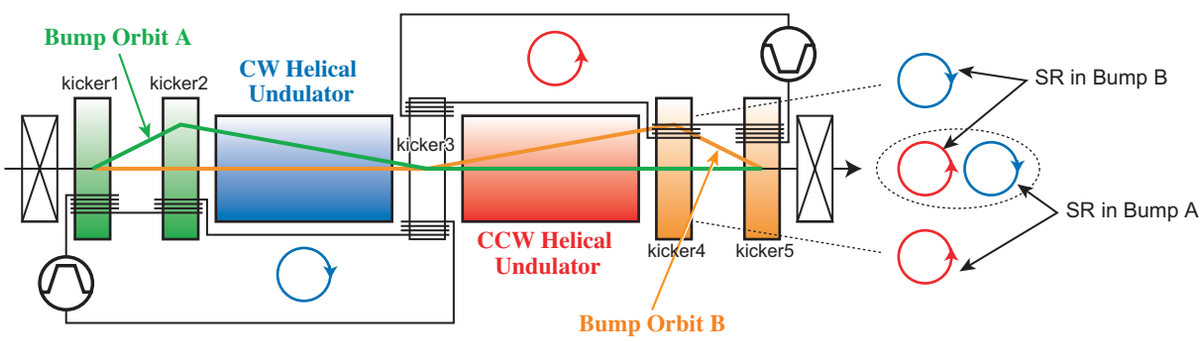

Fig. 1. The kicker magnet system used to change the helicity quickly. The maximum switching speed is expected to be up to 10 Hz, as in the case of BL25SU.

Takashi Tanaka

SPring-8 / RIKEN

E-mail: ztanaka@spring8.or.jp

Development of SAXS Apparatus Equipped at Hyogo Prefectural Beamline BL08B2

Hyogo prefectural beamline, **BL08B2**, has been constructed for industrial research [1]. The experimental hutches have been designed for XAFS, small-angle X-ray scattering (SAXS), monochromatic X-ray topography, and high-resolution powder X-ray diffraction measurements, which are utilized in key industries such as the semiconductor, catalyst, pharmaceutical and polymer industries.

SAXS has been particularly utilized for the study of hard and soft condensed materials in many industrial applications to survey the variation in density or the distribution of dispersed particles in nanocomposite materials with the aim of revealing the relation between the function or performance of the material and the nano-order structure (morphology and/or distribution). To satisfy these demands, standard SAXS and ultra-SAXS (U-SAXS) apparatuses have been installed in BL08B2 experimental hutch, and the system is now open for such industrial research.

The beamline optics was designed after consultation with reference to beamline BL01B1. A schematic view of the arrangement of the optics is shown in Fig. 1. Using a bending magnet source and a silicon double-crystal monochromator, photon energy is tunable from 6 to 70 keV. For the SAXS experiments, an energy range from 8 to 20 keV is mostly used with the aim of overcoming the limitation of SAXS resolution. A Rh-coated double mirror has the role of rejecting the higher harmonics and focusing the beam both vertically and horizontally. The monochromator and the upstream mirror are used to achieve a high energy resolution ($dE/E < 10^{-4}$). Using another mirror equipped downstream of the monochromator, the X-ray beam of a single wavelength can be focused at the SAXS detector position.

In the SAXS configuration, the focusing mirror is a source of diffuse scattering. Therefore, 5 sets of quadrant slits have been arranged to eliminate parasitic scattering. The slits were designed with blade to improve the efficiency of the suppression of diffuse scattering.

Owing to the very long focal length of the focusing mirror (placed about 30 m from the light source) and the effective use of the guard slits, highly parallel and small X-ray beams are available for SAXS experiments. The typical beam formation conditions are as follows. The beam size at the sample position is 200 μm × 200 μm, and the beam flux is about 10^{10} photons/sec.

A SAXS camera for BL08B2 (KOHZU and Daitoseiki, as shown in Fig. 2) has been designed to cover the wide range of surveying scales. The sample-to-detector distance (camera length) can be varied from 300 to 6000 mm depending on the SAXS resolution. A mechanical adjustment system consisting of several pre-aligned vacuum tubes was realized using long guide rails. The system enables

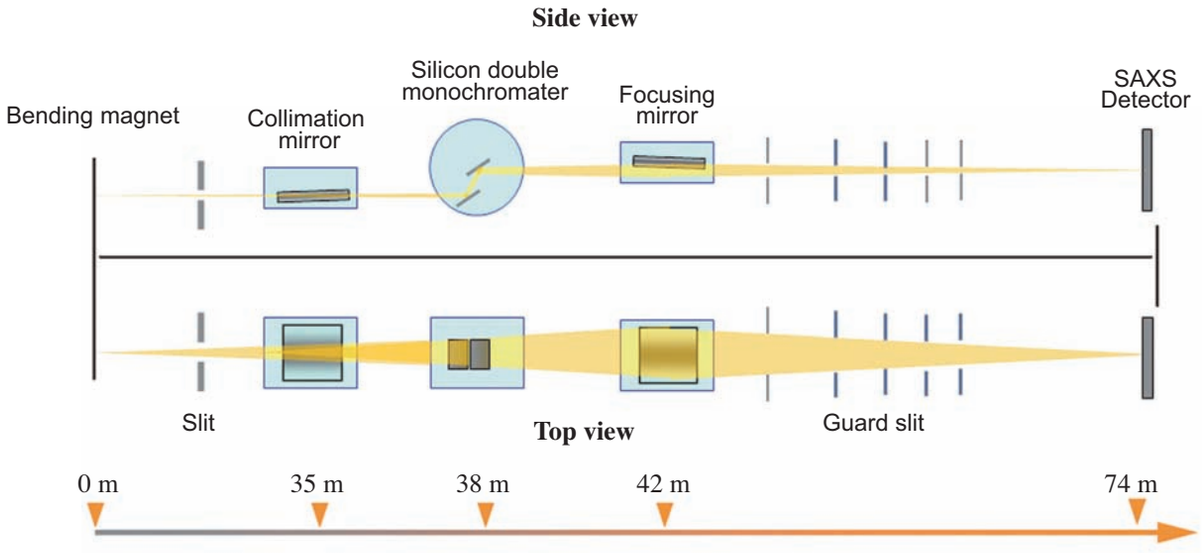

Fig. 1. Schematic view of BL08B2 optics.

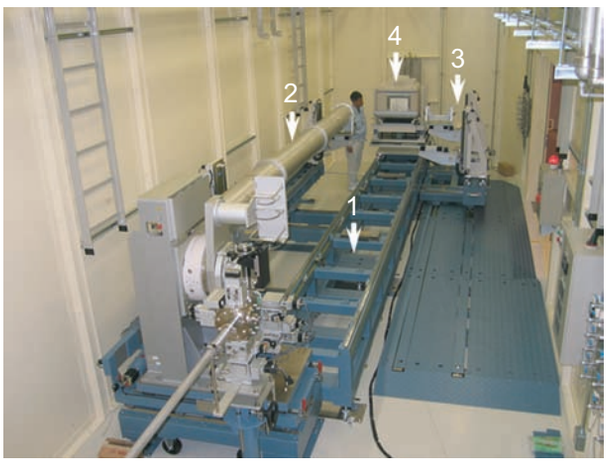

Fig. 2. Photograph of the SAXS camera in BL08B2 experimental hutch 2: (1) guide rail, (2) long vacuum tube (6 m camera length), (3) carrier stage for middle- or short-length vacuum path, (4) SAXS detector.

us to furnish any tube between the sample and the SAXS detector depending upon the desired *q* value (Fig. 3). Sample stages are also loaded on the same guide rail to allow fine adjustment of the camera length. The sample can be set on the stages under a vacuum or ambient condition, and both transmitted and total-reflection (grazing incident) X-ray configurations are possible for the purpose of measuring bulk, liquid, and thin films. For *in situ* experiments, large sample preparation systems such as a high-shear mixer can be used.

Two types of two-dimensional detectors are available for signal recording. One is an imaging plate system (Rigaku R-AXIS IV++) with a detecting area of 300 mm × 300 mm and high space resolution (100 μm). A 14-bit cooled CCD camera combined with an X-ray image intensifier (4 inch diameter) allows us to measure high-speed phenomena (37 msec/frame) with a space resolution of about 90 μm.

To meet the demand for higher resolution SAXS experiments (U-SAXS), a special configuration with long camera length ranging from 15,000 to 17,000 mm, is available using two experimental hutches simultaneously.

We have evaluated the SAXS resolution, the *q* range of the standard SAXS, and that of U-SAXS at the BL08B2 SAXS station using some standard samples such as collagen, polystyrene latex, and silica particles in solution. For each sample measurement, the SAXS camera length was adjusted according to the sample size. The scattering profile for silica particles is shown in Fig. 4 and the performance of the *q* resolution is shown in Table 1.

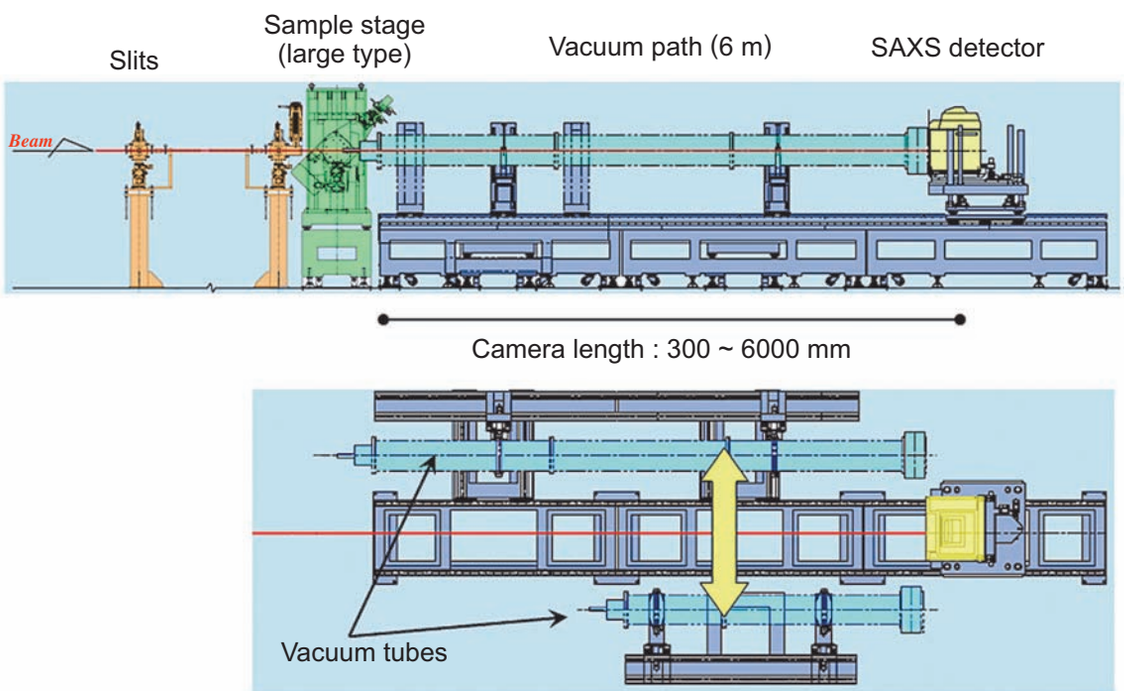

Fig. 3. Top view of guide rail system in BL08B2 SAXS camera.

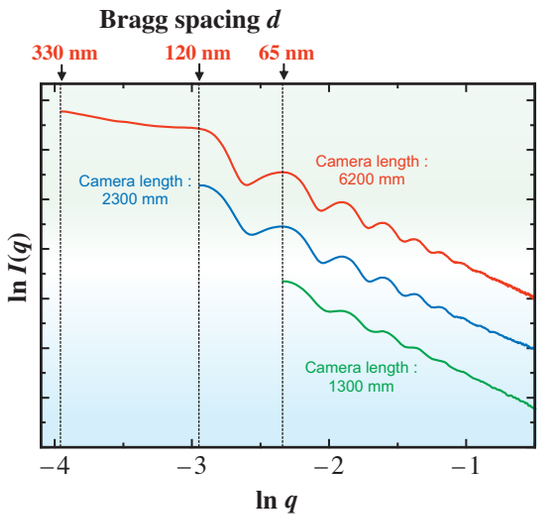

Fig. 4. Scattering profiles obtained from SiO_2 particles. The measurements were performed using a wavelength of 0.15 nm and the exposure time was 1.0 sec.

The results reveal that the performance of BL08B2 SAXS allow the observation of several hundred nm in a real space.

To perform valuable SAXS measurements of dispersion in solution, special sample cells are now being prepared, that can apply a shear stress to solution samples and induce the collapse of cluster structures.

For nanocomposite material applications, some experiments are planned to evaluate the dynamics of material structures such as the structural and morphological changes in materials caused by a catalyst and the simultaneous measurement of X-ray absorption fine structure (XAFS) and SAXS by the tuning and quick scanning of the photon energy near the absorption edge of the target element. This will enable us to realize the time-resolved observation of nanoscale structures.

Table 1. *q* range table of each camera length with IP detector

Camera length (mm)	*q* range (nm^{-1}) wave length = 0.15 nm	*d* spacing (nm)
500	0.260 ~ 11.4	0.55 ~ 24.2
1300	0.0966 ~ 4.30	1.46 ~ 65.0
2300	0.0527 ~ 1.50	4.18 ~ 119
6200	0.0189 ~ 0.963	6.52 ~ 332
15600	0.0081 ~ 0.246	25.5 ~ 781

These *q* range were estimated from the SAXS profile of standard samples, PS latex or SiO_2 particles.

Kazushi Yokoyama

Hyogo Science and Technology Association

E-mail: k_yokobe@spring8.or.jp

References

[1] *K. Yokoyama, T. Miyashita, S. Hiyama, S. Nose, M. Komatsu, Y. Urushihara, L. Li, S. Takeda, S. Kuwamoto, K. Nakamae and J. Matsui: in preparation.*

Upgrade of High Pressure Research Beamline BL10XU

Beamline **BL10XU** was one of the first public beamlines built at SPring-8, which was opened in 1997. It was designed for both high-pressure X-ray diffraction and high brilliance XAFS studies. In 2003, BL10XU was dedicated to high-pressure research using a diamond anvil cell (DAC). High-pressure X-ray diffraction experiments require high photon flux at high X-ray energies because of the limited opening angle for X-ray scattering and the high absorption by the diamond windows of the DAC. Moreover, a very intense and highly focused X-ray beam is indispensable for *in situ* X-ray diffraction experiments under extreme pressure-temperature conditions because of the very small sample size, typically 20 μm or smaller at multi-megabar pressures (> 200 GPa). Therefore, we proposed the optimization of a state-of-the-art high-pressure facility, and have upgraded the undulator and X-ray optics of BL10XU to make full use of the higher power and brilliance of SPring-8 and enhance high-pressure experiments with DAC techniques.

The X-ray source of beamline BL10XU was originally a SPring-8-standard 4.5-m-long in-vacuum X-ray undulator (32 mm periodic length and 140 periods) [1]. In summer 2007, the insertion device at BL10XU was exchanged for the in-vacuum X-ray hybrid undulator (24 mm and 186 period) installed at BL46XU in order to strongly enhance the flux in the 20-60 keV range, which is critical for high-pressure diffraction experiments (Fig. 1). The undulator upgrade included modifications to the existing front-end components.

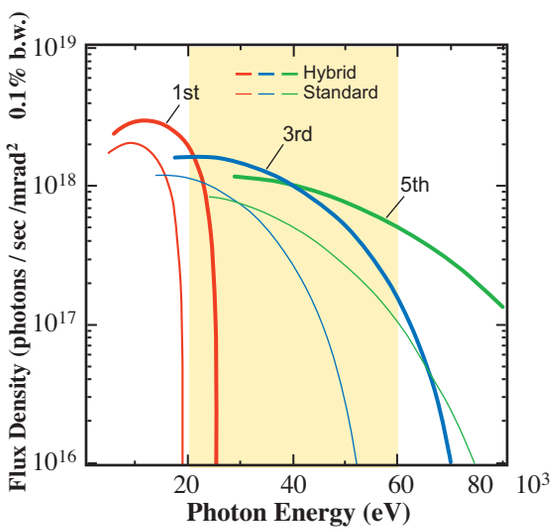

Fig. 1. Energy spectra of the on-axis flux density for standard and hybrid undulators at BL10XU. The spectra are calculated with SPECTRA [4].

The layout of the beamline BL10XU is shown in Fig. 2. The main X-ray optics components are the SPring-8-standard double-crystal monochromator

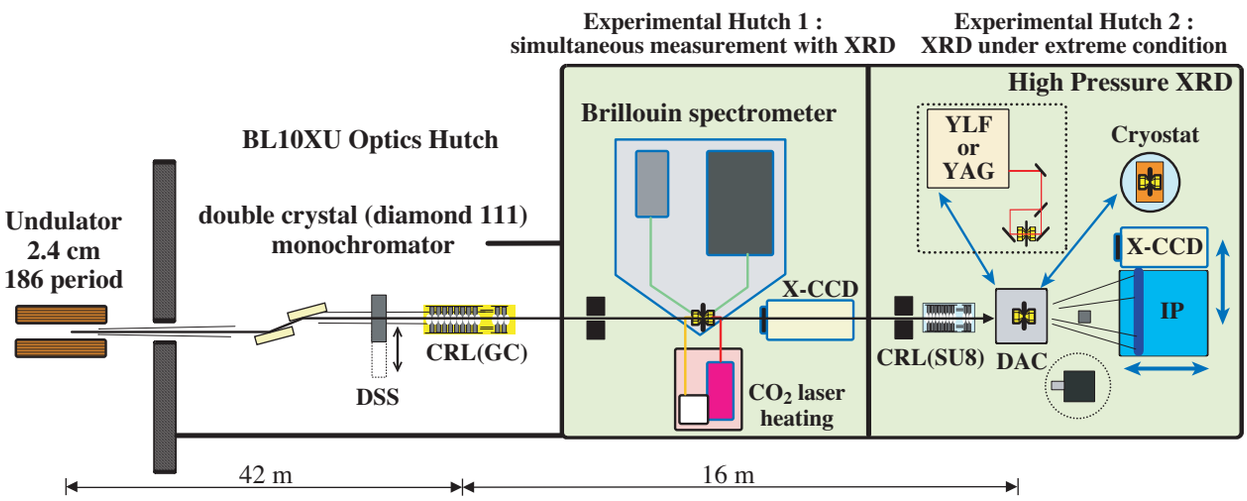

Fig. 2. Schematic layout of beamline BL10XU.

(DCM) located in the optics hutch 37.6 m from the source and an X-ray focusing lens in the optics and experimental hutches. The silicon 111 DCM had been previously operated in rotated-inclined geometry with pin-post cooling by water. To upgrade the beamline, a synthetic single-crystal diamond 111 DCM with indirect water-cooling was installed in 2006 [2]. The tunable photon energy now ranges from 8 to 58 keV using the diamond 111 reflection, in contrast with from 6 to 38 keV for the previous silicon 111 DCM.

X-ray focusing optics at high X-ray energies is essential in high-pressure experiments. At BL10XU, two types of new parabolic compound refractive lens (CRL) were installed in the upgrade. The upstream CRL is made from glassy carbon (GC) and is placed in the optics hutch at a distance of 42 m from the source. The GC-CRL is used as an X-ray collimating and/or focusing device for the high-energy beam (15-60 keV), resulting in photon density enhancement without increasing divergence of the X-ray beam due to its long focal distance (16 m). Another CRL made from SU-8 polymer [3] is installed in the experimental hutch 2 at a distance of 57.5 m from the source. The X-ray beam after passing through the DCM is collimated by the GC-CRL and is then focused to 10 μm by the SU-8 CRL. These upgrades of the undulator and X-ray optics at BL10XU allow us to collect high-quality X-ray diffraction data on materials subjected to extreme pressure of up to 400 GPa, corresponding to the conditions found at the center of our planet.

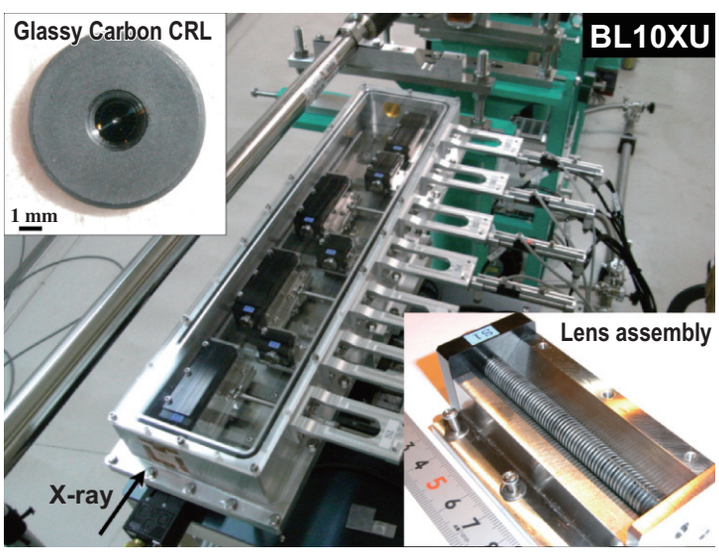

Fig. 3. Photographs of GC-CRL, lens assembly, and CRL device.

Naohisa Hirao and Yasuo Ohishi*

SPring-8 / JASRI

*E-mail: ohishi@spring8.or.jp

References

[1] H. Kitamura: J. Synchrotron Rad. **7** (2000) 121. For more information, http://www.spring8.or.jp/en(ja)/users/current_user/bl/source/
[2] M. Yabashi *et al.*: AIP Conf. Proc. **879** (2007) 922.
[3] V. Nazmov *et al.*: Proc. SPIE **5539** (2004) 235.
[4] T. Tanaka and H. Kitamura: J. Synchrotron Rad. **8** (2001) 1221.

Construction of a Side Beamline of BL12XU for HAXPES

Hard X-ray photoemission spectroscopy (HAXPES) has attracted much interest in recent years among the synchrotron radiation community in the world. SPring-8 has pioneered in developing suitable beamlines and end stations as well as advancing related sciences. The greatest advantage of using hard X-rays from several to above 10 keV over conventional VUV and soft X-rays to undertake photoemission spectroscopy is the increased electron inelastic mean free path of up to about 100 Å. This increased bulk sensitivity has made possible to probe the true bulk electronic structure in many strongly correlated systems in which the surface region has a markedly different electronic structure due to reduced coordination. In addition, the electronic structure of buried interfaces is of high interest but lacked a suitable probe in the past. HAXPES has thus attracted considerable attention for research on device applications. To explore research in these areas, NSRRC has teamed up with a research group at Cologne University in Germany to construct a side beamline at **BL12XU** with a dedicated end station since 2006.

Figure 1 shows the layout of the side beamline. We use a single-bounce diamond monochromator (DM) in the first optical hutch as the first optical component downstream of the front end. Diamond crystal is used because of its high thermal conductivity and low thermal expansion coefficient, so that a much simpler water cooling system can be used. Moreover, the high transmission of diamond would allow us to operate simultaneously the main beamline. Two modes of the DM are implemented. In the transmission Laue mode, a thin diamond (100) crystal is to produce a (111) reflection. The simultaneous use of photons at 10 keV, which are currently heavily used at the main beamline, is possible. In the reflection Bragg mode, a thicker diamond (111) crystal is used also for a (111) reflection, needed particularly for lower photon energies. In the latter mode the third harmonic radiation from the undulator is also available for the main beamline. An additional advantage of using diamond is its low absorption and high reflectivity at the top of the rocking curve for a perfect crystal; this basically increases the transmission efficiency within the intrinsic bandwidth as an optical device. Figure 2 shows the installed DM.

The upper right corner in Fig. 1 presents a schematic of the DM operation. The scattering angle 2θ ranges from 28 to 60 degrees, providing photons from 12.5 keV down to 6 keV. At all energies the diffracted beams converge to a single point inside the experimental hutch. Exactly at this convergence point is situated the pivot point of a rotational platform on which the remaining optical components and the end station are placed. To reduce the energy bandwidth from the output of the DM we adopt a channel-cut design for the high-resolution monochromator (HRM). Only one pair of Si channel-cut is used to minimize the flux loss due to the higher absorption of Si. A large range of photon energy can be used for a given pair of channel-cut providing a continuously tunable photon

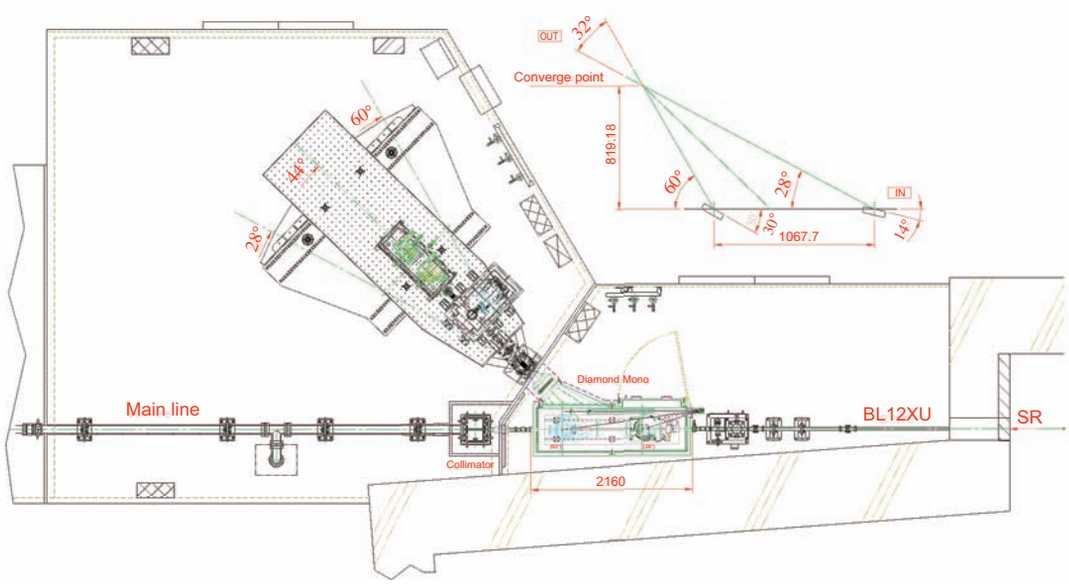

Fig. 1. Layout of the side beamline of BL12XU.

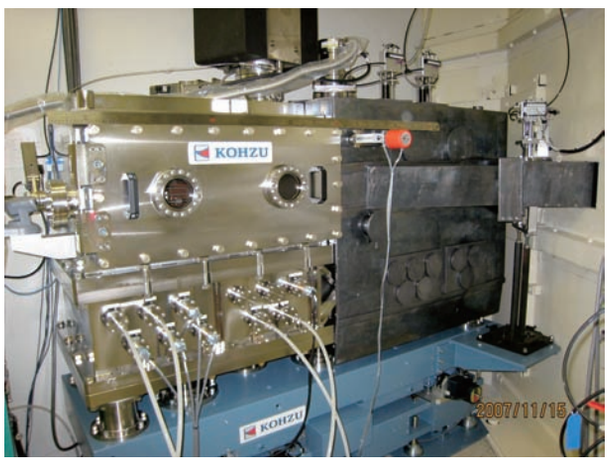

Fig. 2. Installed diamond monochromator in the first optical hutch.

energy for the measurement, at the expense of changing the beam height in addition to altering the platform angle. The former is compensated by applying motorized z-motion to the downstream optical components. In order to achieve sufficiently small beam spots to match the effective acceptance area of the electron energy analyzer we will install a pair of plane-elliptical KB mirrors to focus the beam to 30 × 30 μm^2 at the sample position in the end station. The sizes of 200 mm at 3 mrad grazing angle for the vertical focusing mirror and 400 mm at 5 mrad for the horizontal focusing mirror collect basically all beams from the undulator source. Both mirrors are coated with Rh to cut the higher harmonics above 12 keV. The whole photon beam from the DM to the end station will be placed under vacuum to eliminate the loss from absorption by air with only a few Be windows to separate chambers with different vacuum. The design concept is to minimize the loss or to maximize the transmission efficiency of all optical components. Figure 3 shows part of the side beamline inside the experimental hutch installed down to the HRM on the rotational platform. The commissioning of the side beamline will start in February 2008.

Fig. 3. High-resolution monochromator installed on the rotational platform in the experimental hutch.

Ku-Ding Tsuei*, Cheng-Chi Chen, Yong Cai and Chi-Yi Huang

National Synchrotron Radiation Research Center, Taiwan

*E-mail: tsuei@nsrrc.org.tw

High-resolution and Highly Stabilized Beamline BL17SU for Advanced Soft X-ray Spectroscopy

Beamline **BL17SU** was developed with the aim of carrying out spectroscopic studies for solid state physics as well as materials science. A novel insertion device, ID17, called a multi-polarization-mode undulator [1], has been developed to provide an intense soft X-ray (SX) beam. The ID17 consists of electromagnets and permanent magnets applying vertical and horizontal magnetic fields, respectively. By adjusting these magnetic fields to the specific operational mode, the ID17 can be operated as a helical or a pseudo-vertical undulator, and can also have a helicity switching capability that enables us to perform advanced SX spectroscopy. Recently, we have estimated the degree of circular polarization (CP) of the SX beam obtained from ID17 by magnetic circular dichroism in core-level X-ray absorption spectroscopy for a ferrimagnetic Gd-Fe-Co target [2]. The degrees of CP were deduced for all the available operational modes and compared with theoretical calculations, as shown in Fig. 1(c). As can be seen in the figure, the calculated degrees of CP are in reasonable agreement with the measurements. In Fig. 1(a), we also show the measured photon intensities, which are indicated as values of photocurrent (nA) measured using a Au flux monitor, as a function of energy.

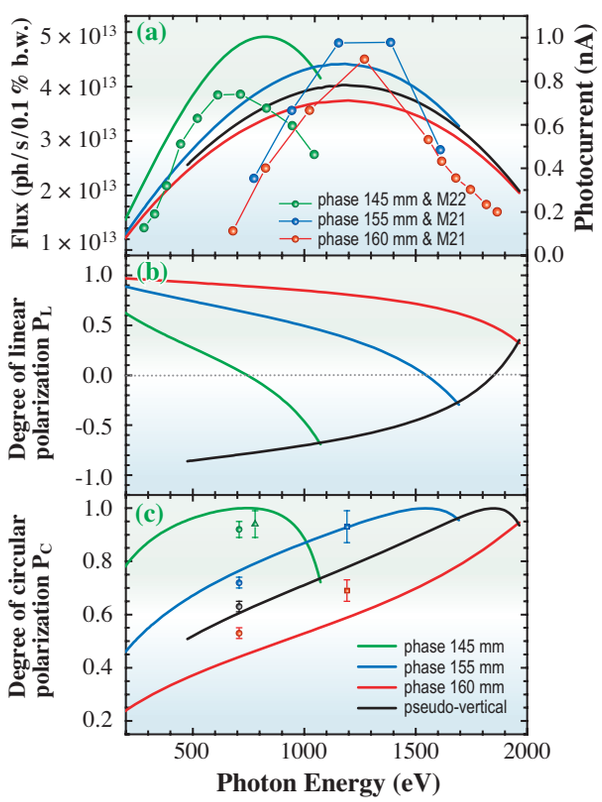

Fig. 1. Calculated and measured characteristic features of the SX beam from ID17.

BL17SU has been designed to have branched beamlines, which can be selected for exclusive use by using two sets of pre-focusing mirrors. Both branches have their own monochromator covering the energy range from 300 to 1800 eV [3]. Both branches have several experimental stations including one allowing high-resolution, angle-resolved photoemission spectrometry combined with laser molecular-beam epitaxy (E1a station) and one with high performance slit-less spectrometer for SX emission spectroscopy (E2a station). To achieve the ultimate performance of these experimental stations, a high-resolution and highly stabilized SX beam with a small spot-size is indispensable. Since the first ignition of ID17, we had been devoting much effort to satisfy such requirements.

We have housed the optical components in a temperature stabilization system (TSS) to improve the stability of a photon energy [4]. The system is composed of a thermal insulation booth and heaters controlled by a proportional-integral-derivative controller. The fluctuations in the photon energy, grating rotation angle, and the temperature of the support frame before the installation of the TSS were measured at 867 eV and are shown in Fig. 2(a). It is recognized that the fluctuation of the temperature difference ΔT of the support frame between upstream and downstream coincides exactly with that of the photon energy. This implies that the fluctuation of ΔT (0.15 °C/12 h) induces a slight variation in the angle of the optical element, which results in a corresponding energy drift (30 meV/12 h). Figure 2(b) shows the results measured after the installation of the TSS. By stabilizing the ambient temperature of the optical elements and their support frames to 0.01 °C/12 h, the photon energy stability is successfully improved to 10 meV/12 h as shown in Fig. 2(b).

To accomplish the small spot-size at the sample position, a set of refocusing mirrors with a Kirkpatrick-Baez configuration has been installed in each experimental station. A focal size of less than a few tens of microns was successfully achieved at each station. Figure 3 shows the focused beam profile at the E2a station measured by a two-dimensional scan of the pinhole. The vertical and horizontal focal sizes are 3 and 10 μm, respectively.

Using the high-resolution and highly stabilized SX beam, various advanced spectroscopic studies are being intensively carrying out at BL17SU.

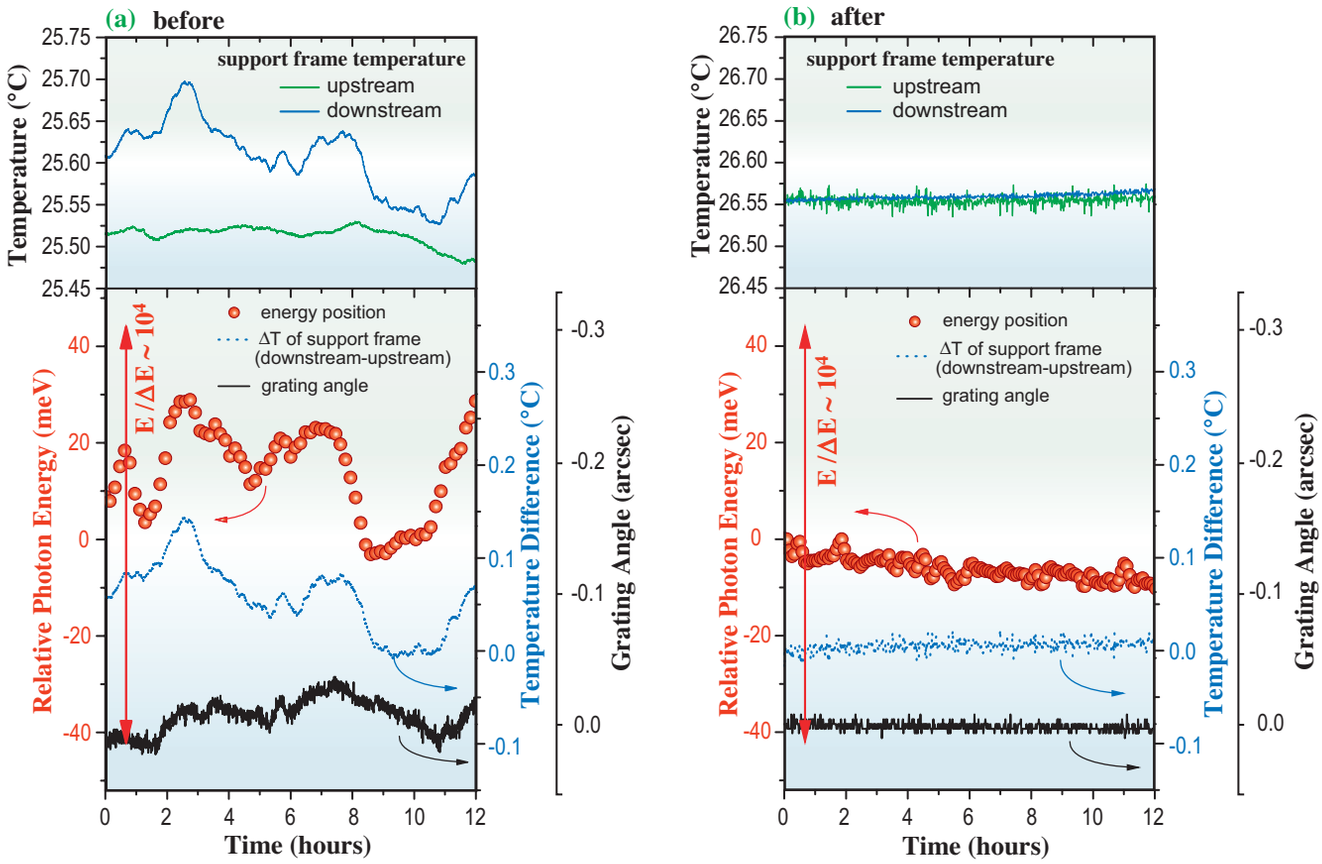

Fig. 2. Relative photon energy (red circles), grating rotation angle (black line), support frame temperature of the upstream (green line) and downstream (blue line), and the temperature difference of the support frame (blue dotted line) measured at 867 eV before **(a)** and after **(b)** installation of the TSS.

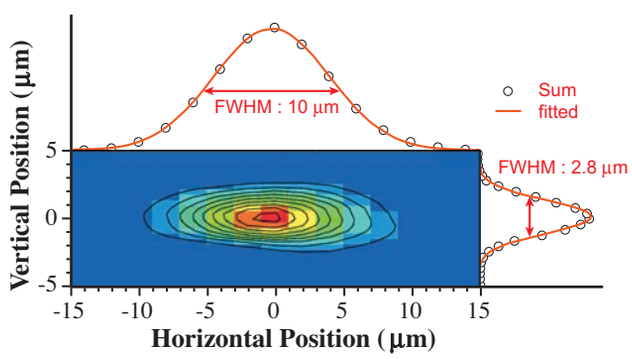

Fig. 3. Measured beam profile at E2a station.

Yasunori Senba [a], Haruhiko Ohashi [a,b] and Masaki Oura [b,*]

[a] SPring-8 / JASRI
[b] SPring-8 / RIKEN

*E-mail: oura@spring8.or.jp

References

[1] K. Shirasawa *et al.*: AIP Proc. **705** (2004) 203.
[2] *M. Oura, T. Nakamura, T. Takeuchi, Y. Senba, H. Ohashi, K. Shirasawa, T. Tanaka, M. Takeuchi, Y. Furukawa, T. Hirono, T. Ohata, H. Kitamura and S. Shin: J. Synchrotron Rad.* ***14*** *(2007) 483.*
[3] H. Ohashi *et al.*: AIP Proc. **879** (2006) 523.
[4] Y. Senba *et al.*: AIP Proc. **879** (2006) 718.

Facility Status

General

The 10th Anniversary

This year SPring-8 celebrated the 10th anniversary of its inauguration. During the last decade, SPring-8 has scientifically and technologically grown into maturity by evolving itself as one of the most advanced third generation synchrotron radiation facilities in the world, and has been successfully generating a vast number of high-level attainments in academic and industrial domains. Figure 1 shows the logos adopted to symbolize this important year in the history of SPring-8. All the events organized by SPring-8 were associated with these logos throughout this year, the list of which can be found in the sections of "Users Meeting" and "Conferences and Workshops" in this publication.

Fig. 1. The logos used to celebrate the 10th anniversary of SPring-8 inauguration.

The 10th anniversary was highlighted by the ceremony officially held October 19, 2007 in Himeji, and by the memorial symposium held in Harima Science Garden City on the following day. The ceremony hosted about 300 important guests from political, business, academic and local communities. The ceremony began by the welcome address given by Professor Ryoji Noyori, President of RIKEN. Mr. Yukihide Hayashi, Deputy Minister of Education, Culture, Sports, Science and Technology (MEXT), Mr. Toshizou Ido, Prefecture Governor of Hyogo, and Professor Ichirou Kanazawa, President of Science Council of Japan addressed, expressing their expectations to SPring-8 that would continuously play an important role in advancing science and technology in Japan as well as in contributing to the industry development with respect to its spectacular achievements established so far. The general introduction, the attainments in science and technology, industrial applications, and historical overview and outlook were presented by Dr. Akira Kira, Director General of Japan Synchrotron Radiation Research Institute (JASRI), Mr. Masayuki Nagata, Managing Executive Director of JASRI, and Professor Hiromichi Kamitsubo, Special Advisor of RIKEN, respectively. Mr. Tetsurou Kawakami, Chairman of JASRI gave a closing address for the successful ceremony.

The Memorial Symposium for the 10th Anniversary

The memorial symposium held on the following day consisted with two parts, i.e., the first one "The Past and Future of SPring-8," and the second one "Door to the next generation (the second part was doubled as The "2nd XFEL Symposium"). The opening remarks for the symposium were given by Dr. Akira Kira. The symposium had a pleasure of the company of Mr. Satoru Ohtake, Manager of basic and generic research division, MEXT, and of his complimentary address. The first part of the symposium was initiated by Professor Hiromichi Kamitsubo who gave an review talk on SPring-8 by looking its persistent progress in the past and by foreseeing its ultimate goal in future. Dr. Rafael Abela of PSI, Dr. J. Murray Gibson of APS, and Professor Keng S. Liang of NSRRC delivered congratulatory addresses on the 10th anniversary of SPring-8. The second part was opened by Professor Tetsuya Ishikawa, Director of RIKEN SPring-8 Center, who gave a review talk entitled "Compact X-ray Free Electron Laser at SPring-8." Professor John N. Galayda of SLAC, Professor Jerome B. Hastings of SLAC, and Professor Jochen R. Schneider of DESY made review talks introducing their free electron laser projects. Professor Hiroyoshi Suematsu, Director of RIKEN Harima Institute, gave a closing address for the successful symposium.

Reviews Conducted

Interim Assessment by MEXT

In July, MEXT released the interim assessment of SPring-8. The assessment reported that SPring-8 had been playing an important role by expanding academic user distributions in materials science, life science, and other fields of science and technology, and by establishing the advanced applications in industrial domain as well. Having reported the excellent status of SPring-8, the assessment indicated the guideline as follows:

(1) By designing systematic programs for operation and maintenance, the accelerator complex of SPring-8 should be stably operated with an annual operation time of 5000 hours, at least, eventually reaching 5500 hours.

(2) It is important to continuously conduct R&D for accelerators as well as for high brilliance SR sources.

(3) With conducting high-level research activities by an appropriate number of in-house staff, it is highly required for SPring-8 to establish a user support system that efficiently and effectively promote research outcome.

Following the interim assessment, Minister of MEXT issued an amended policy as well as a guideline for the promotion of the public utilization of SPring-8 at the beginning of October, with newly emphasizing the following points:

- The enhancement of human resources in order to continuously update the SPring-8, and to maintain the high-level research capability of the user-supporting organization.
- The importance of generating a decent number of eminent research attainment in order to appropriately respond to society.

Review of Medical Biology Trail Use

JASRI formed a review committee for evaluating "Medical Biology Trail Use," which was introduced to exploit potential users from medical-biology domain. The committee reviewed the proposal selection process, the user support system, and the research activities. The committee highly evaluated this program and strongly recommended its continuation, by pointing out that the program had succeeded in exploiting new users nationwide, of which research subjects were considered to be scientifically novel and well advanced.

Recommendation of Advisory Committee for Industry-academia-government Collaboration

The committee established by JASRI for promotion of industry-academia-government collaboration at SPring-8 recommended that JASRI should actively develop and introduce such a utilization scheme that would facilitate industrial applications at SPring-8 by

(1) promoting the innovation-oriented industry-academia-government collaborative projects,

(2) introducing group utilization scheme targeting common achievements among participating parties,

(3) enhancing the quality of user support system with charging its cost to users such as mail-in service, and

(4) making the barrier as low as possible in utilizing SPring-8 for new users.

Machine Operation

The operation statistics since the facility was opened to users are shown in Fig. 2. In 2007, the total operation time of the accelerator complex was 5027.9 hours. The operation time of the storage ring was 5019.2 hours, of which 77.7% (3900 hours) was made available to the users. The downtime resulting from failure accounted for 0.7% (27.6 hours) of the operation time of the storage ring; in 2007, no considerable loss of user time exceeding several hours occurred. Since 2004, there has been no injection time because top-up injection was introduced. Concerning user service operation, the high availability (ratio of net user time to planned user time) achieved, e.g., 99.1% in 2007. The total tuning and study time of 1100.3 hours was used for machine tuning, and the study of the linac, booster synchrotron and storage ring, and also for the beamline tuning and study.

Operations in three different filling modes were provided for the following user time: percentages 17% in the multi-bunch mode, 51.9% in the several bunch mode, such as the 203-bunch mode (203 equally spaced bunches) and 31.1% in the hybrid filling mode such as a 1/7- partially filled multi-bunch with 5-isolated bunches. In 2007, several bunch mode was the dominant filling mode. In particular, the 203-bunch mode reached 31.7% of the total user time. For the hybrid filling mode, 1.0 mA, 1.4 mA, 1.6 mA, or 3.0 mA is stored in each isolated bunch. An isolated bunch purity better than 10^{-10} is routinely maintained in the top-up operation. Table I shows a summary of the beam filling patterns.

Table II shows a summary of the useful beam parameters of the storage ring.

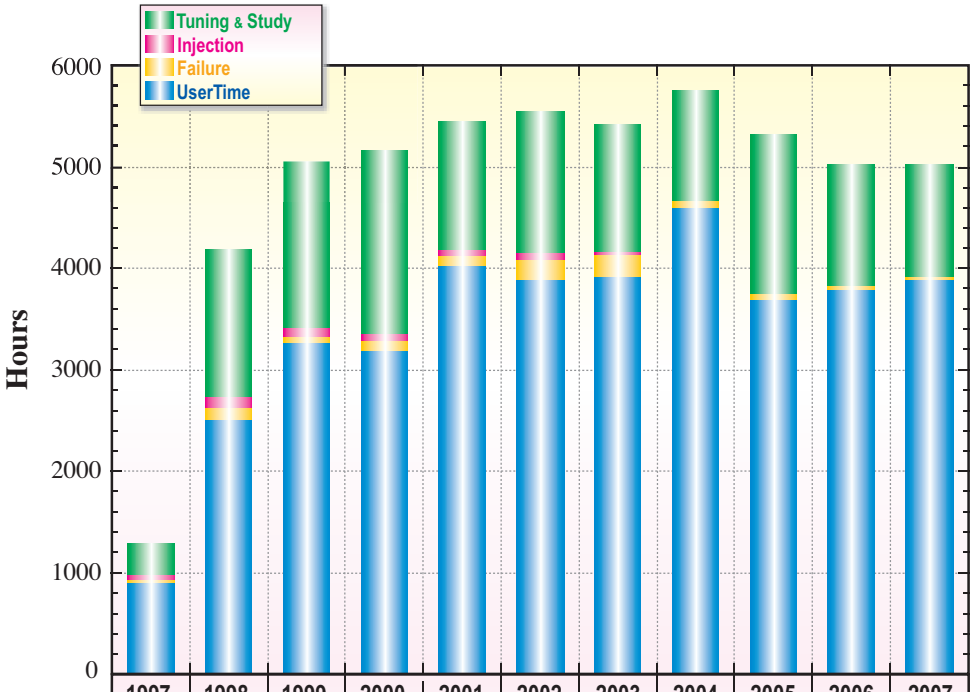

	1997	1998	1999	2000	2001	2002	2003	2004	2005	2006	2007
Accelerator Operation Time	1286.0	4189.6	5051.6	5167.5	5456.1	5542.9	5419.5	5759.2	5317.1	5026.2	5027.9
Storage Ring Operation Time	1270.6	4135.4	4863.9	4972.9	5340.6	5484.1	5328.5	5736.7	4781.3	5008.5	5019.2
Tuning & Study (Acc. & BL)	304	1457.6	1624.2	1815	1276.5	1394.9	1245.8	1085.9	1559.2	1193.6	1100.3
Injection	50	110	95.2	70.4	59.3	60.8	39.2	0	0	0	0
Failure	26	110	57.2	88.7	87.1	190.5	208.5	82.4	59.7	42.5	27.6
User Time	906	2512	3275	3193.4	4033.2	3896.7	3926	4590.9	3698.2	3790.1	3900
Planned Time	984	2712	3432	3352	4176	4152	4176	4680	3762	3840	3936
Availability (%)	97.2	96.7	98.2	97.4	98	95.3	95	98.1	98.3	98.7	99.1

Fig. 2. Operation statistics since the facility became available to users.

Table I. Filling patterns

	bunch current	life time
Multi-bunch (160 bunch-train × 12)	0.05 mA	~ 200 hr
203 bunches	0.5 mA	25 ~ 30 hr
4 bunch-train × 84	0.3 mA	35 ~ 50 hr
11 bunch-train × 29	0.3 mA	35 ~ 50 hr
1/7 - filling + 5 single bunches	3.0 mA (single)	18 ~ 25 hr
1/14 - filling + 12 single bunches	1.6 mA (single)	18 ~ 25 hr
2/29 - filling + 26 single bunches	1.4 mA (single)	18 ~ 25 hr
4/58 - filling + 53 single bunches	1.0 mA (single)	18 ~ 25 hr

Table II. Beam parameters of SPring-8 storage ring

Energy [GeV]	8
Number of buckets	2436
Tunes (ν_x / ν_y)	40.15 / 18.35
Current [mA]:	
single bunch	12
multi-bunch	100
Bunch length (σ) [psec]	13
Horizontal emittance [nm·rad]	3.4 *
Vertical emittance [pm·rad]	6.8 *
Coupling [%]	0.2
RF Voltage [MV]	16
Momentum acceptance [%]	±3 (= ±240 MeV)
Beam size [μm]: (σ_x /σ_y)* [μm]	
Long ID section	294 / 10
ID section	301 / 6
BM section	107 / 13
Beam divergence [μrad]: ($\sigma_{x'}$ /$\sigma_{y'}$)* [μrad]	
Long ID section	13 / 0.7
ID section	12 / 1.1
BM section	56 / 0.6
Operational chromaticities: (ξ_x /ξ_y)	+2 / +2 **
Lifetime [hr]:	
100 mA (multi-bunch)	~ 200
1 mA (single bunch)	~ 20
Horizontal dispersion [m]:	
Long ID section	0.103
ID section	0.107
BM section	0.032
Fast orbit stability (0.1 – 200 Hz)[μm]:	
horizontal (rms)	~ 4
vertical (rms)	~ 1

* Assuming 0.2% coupling for "Low Emittance Optics"
** With bunch-by-bunch feedback

Beamlines

The electron storage ring of the SPring-8 accelerator complex can potentially accommodate sixty-two beamlines (34 insertion devices, 4 long undulators, 23 bending magnets and 1 infrared). Currently, 49 beamlines are operational, reaching 75% of its full capacity as shown in the beamline map (Fig. 3) and list of beamlines (Table III). The beamlines are categorized into the following four groups:

(1) public beamlines,
(2) contract beamlines,
(3) RIKEN beamlines, and
(4) accelerator beam diagnostic beamlines.

The portfolio of SPring-8 beamlines is significantly increasing its variation. A new public beamline called "Engineering Science Research II (BL14B2)" became in operation since last autumn in order to appropriately respond to those users coming from industrial domain for XAFS experiments. In addition, there have been four contact beamlines approved, which are "LEPS2 (BL31IS)," "Univ-of-Tokyo (BL07LSU)," "TOYOTA (BL33XU)," and "Frontier Soft Matter (BL03XU). Furthermore, RIKEN has decided to construct a new beamline called "RIKEN Targeted Proteins (BL32XU)." At the time of writing this report, there are 26 public beamlines in operation: 11 BM beamlines, 14 ID beamlines (12 hard X-ray beamlines and 2 soft X-ray beamlines), and one infrared beamline. As for contract beamlines, 14 beamlines are operational and three beamlines are under construction. Among the eight RIKEN beamlines, seven of them are operational and the last one under construction. There are two accelerator diagnostic lines, both in operation. In order to effectively and efficiently promote the priority industrial application proposals started in April 2007, "R&D Beamline (BL46XU)" has become specialized in industrial applications, and its name was changed to "Engineering Science Research III" from 2007B.

The contract beamlines are installed, owned, operated and maintained by universities, companies, and other organizations for exclusive use by

contractors. Currently, there are 14 contract beamlines in operation and three new contract beamlines are scheduled for construction as mentioned above. The experimental stations of BL22XU and BL23SU are located at JAEA's RI Laboratory and are dedicated to research utilizing radioactive isotopes and actinide materials. The National Synchrotron Radiation Research Center of Taiwan (NSRRC) was the first foreign organization to construct contract beamlines at SPring-8, i.e., BL12B2 and BL12XU.

There are 7 RIKEN beamlines for their exclusive use to promote RIKEN's research activities, although 20% of the beamtime is reserved for public use. RIKEN BL19LXU is the only beamline equipped with a long undulator, realizing the highest degree of brilliance. BL26B1 and BL26B2 are the beamlines used for high-throughput protein crystallography, a method used in the human genome project. BL29XU has two experimental stations, one located in the experimental hall and the other at the end of the 1 km beamline.

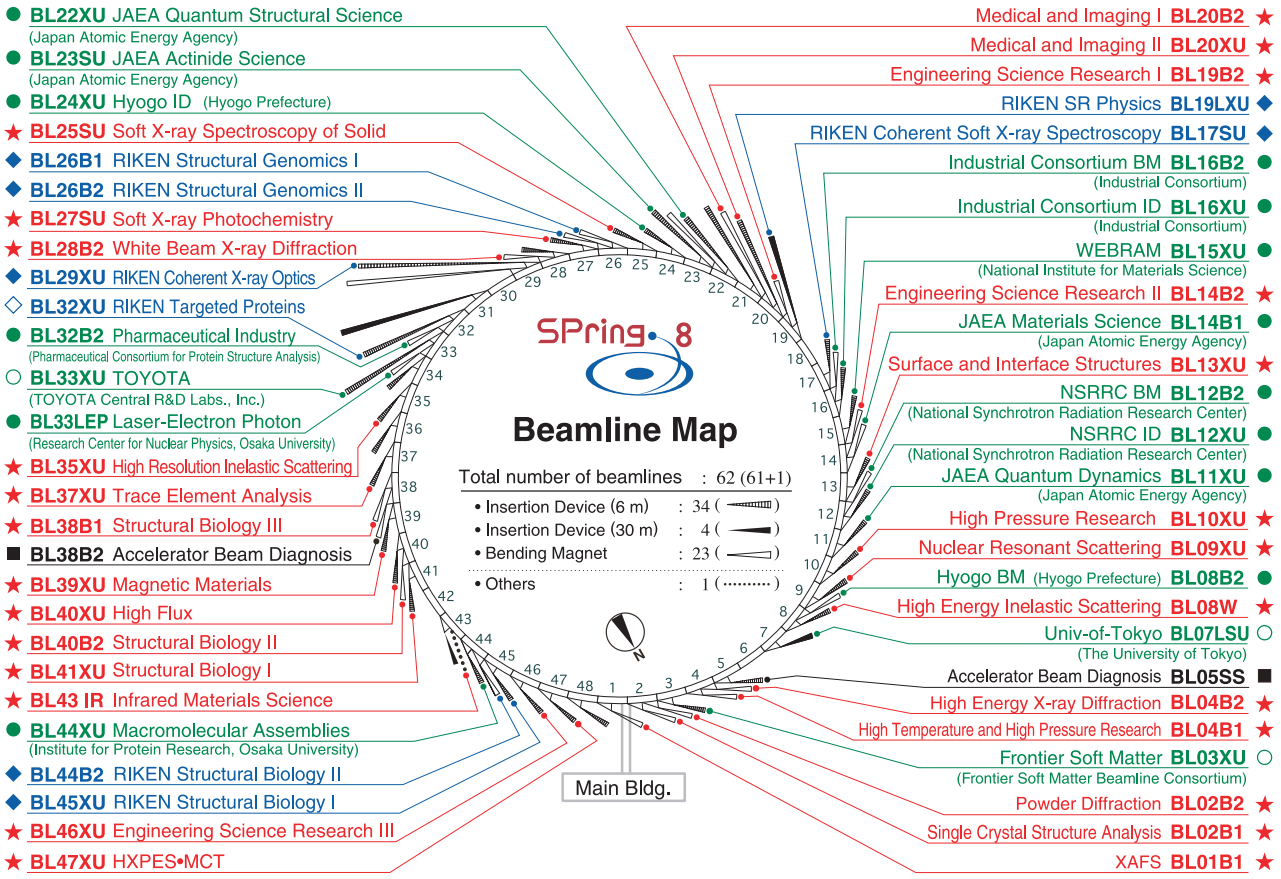

BL: Beamline
B1, B2: Bending Magnets
XU: X-ray Undulator
SU: Soft X-ray Undulator
W: Wiggler

IR: Infrared Radiation
LEP: Laser-Electron Photon
LXU: Long-length X-ray Undulator
LSU: Long-length Soft X-ray Undulator
SS: Straight Section

WEBRAM: Wide Energy Range Beamline for Research in Advanced Materials
NSRRC: National Synchrotron Radiation Research Center, Taiwan

HXPES•MCT: Hard X-ray Photoelectron Spectroscopy, Micro-Tomography

★ : Public Beamlines
● : Contract Beamlines
◆ : RIKEN Beamlines
■ : Accelerator Beam Diagnostic Lines
○ ◇ : Planned or Under Construction

Fig. 3. Beamline map.

Table III. List of beamlines

(September, 2007)

BL #	Beamline Name	(Public Use)	Areas of Research
★ Public Beamlines			
BL01B1	XAFS	(Oct. 1997)	XAFS in wide energy region (3.8 to 113 keV). XAFS of dilute systems and thin films.
BL02B1	Single Crystal Structure Analysis	(Oct. 1997)	Structure physics using single crystal analysis. Precise structure analysis of photo-excited state.
BL02B2	Powder Diffraction	(Sept. 1999)	Accurate structure analysis of crystalline materials using powder diffraction data by Rietveld refinements and MEM (maximum entropy method).
BL04B1	High Temperature and High Pressure Research	(Oct. 1997)	Mineral physics at high temperature and high pressure. Energy-dispersive X-ray diffraction and X-ray radiography using the large-volume press.
BL04B2	High Energy X-ray Diffraction	(Sept. 1999)	Structural analysis of glass, liquid, and amorphous materials. X-ray diffraction under ultra high-pressure. Precise single crystal structure analysis
BL08W	High Energy Inelastic Scattering	(Oct. 1997)	Magnetic Compton scattering. High-resolution Compton scattering. High-energy Bragg scattering. High-energy fluorescent X-ray analysis.
BL09XU	Nuclear Resonant Scattering	(Oct. 1997)	Time domain Mössbauer spectroscopy. Lattice dynamics study using nuclear resonant scattering.
BL10XU	High Pressure Research	(Oct. 1997)	Structure physics and earth science under ultra high pressure using DAC.
BL13XU	Surface and Interface Structures	(Sept. 2001)	Atomic-scale structure analysis of an ultra-thin film, nanostructure and surface, using in-air measurements (room temperature to 500 °C) and in-vacuum measurements (20 to 1300 K).
BL14B2	Engineering Science Research II	(Sept. 2007)	Medium-length hard X-ray bending magnet beamline designed for engineering science researches. X-ray absorption spectroscopy.
BL19B2	Engineering Science Research I	(Nov. 2001)	Industrial application using XAFS in wide energy region, residual stress measurement, structural analysis of thin film, surface and interface, powder diffraction, and X-ray imaging.
BL20XU	Medical and Imaging II	(Sept. 2001)	Medical application: Microangiography, refraction-enhanced imaging. / Microimaging: Scanning microscopy, imaging microscopy, microtomography, X-ray holography and X-ray optics. / Ultra-small angle scattering.
BL20B2	Medical and Imaging I	(Sept. 1999)	Medical application: Microradiography, micro-tomography and refraction-enhanced imaging. / Microimaging: R&D of optical elements for novel imaging techniques.
BL25SU	Soft X-ray Spectroscopy of Solid	(Apr. 1998)	High resolution photoemission spectroscopy. Photoelectron diffraction and holography. Magnetic circular dichroism (MCD). Photoelectron emission microscope (PEEM).
BL27SU	Soft X-ray Photochemistry	(May 1998)	Industrial research of functional material. Atomic and molecular spectroscopy by high resolution electron spectroscopy. Surface analysis and solid state physics.
BL28B2	White Beam X-ray Diffraction	(Sept. 1999)	White X-ray diffraction. Time-resolved energy-dispersive XAFS (DXAFS) .
BL35XU	High Resolution Inelastic Scattering	(Sept. 2001)	Material dynamics on ~ meV energy scales using inelastic X-ray scattering (IXS) and nuclear resonant scattering (NRS).
BL37XU	Trace Element Analysis	(Nov. 2002)	X-ray microbeam spectrochemical analysis. Ultra trace element analysis. High energy X-ray fluorescence analysis.
BL38B1	Structural Biology III	(Oct. 2000)	XAFS. R&D of optics and detector. Macromolecular crystallography.
BL39XU	Magnetic Materials	(Oct. 1997)	X-ray magnetic circular dichroism (XMCD) spectroscopy. Element-specific magnetometry. X-ray emission spectroscopy and its magnetic circular dichroism. Resonant or non-resonant magnetic scattering.
BL40XU	High Flux	(Apr. 2000)	Time-resolved diffraction and scattering experiments. X-ray speckle. X-ray fluorescence trace analysis.
BL40B2	Structural Biology II	(Sept. 1999)	Macromolecular crystallography. Small angle X-ray (solution) scattering.
BL41XU	Structural Biology I	(Oct. 1997)	Biological macromolecular crystallography.
BL43IR	Infrared Materials Science	(Apr. 2000)	Infrared microspectroscopy. Magneto-optical spectroscopy. Infrared surface science. Absorption and reflection spectroscopy. Time-resolved experiments with pulsed laser and SR (pump and probe).
BL46XU	R&D	(Nov. 2000)	Insertion devices R&D. Resonant and non-resonant magnetic scattering structural analysis.
BL47XU	HXPES・MCT	(Oct. 1997)	R&D of microtomography and microbeam technique. High energy photoemission spectroscopy.

(September, 2007)

BL #	Beamline Name (First Beam)	Areas of Research
	● Contract Beamlines	
BL08B2	**Hyogo BM** (Hyogo Prefecture) (Jun. 2005)	XAFS in a wide energy region. Small angle X-ray scattering for structural analyses of polymer and nano-composite materials. X-ray topography. Imaging. Powder diffraction with a high angular resolution.
BL24XU	**Hyogo ID** (Hyogo Prefecture) (May 1998)	Structure analysis of small bio-crystals for industry. Surface/interface analysis for industry by fluorescent X-ray analysis, strain measurements and grazing incidence X-ray diffraction. Microbeam formation studies for materials and life sciences.
BL12XU	**NSRRC ID** (National Synchrotron Rad. Res. Center) (Dec. 2001)	High resolution non-resonant or resonant inelastic X-ray scattering. High resolution near-edge X-ray Raman scattering. Phase transitions under high-pressure, low and high temperatures. High-resolution X-ray absorption and emission spectroscopy. X-ray physics and optics.
BL12B2	**NSRRC BM** (National Synchrotron Rad. Res. Center) (Oct. 2000)	X-ray absorption spectroscopy. Powder X-ray diffraction. High resolution X-ray scattering. Protein crystallography.
BL15XU	**WEBRAM** (National Institute for Materials Science) (Jan. 2000)	High resolution X-ray photoemission microscopy. High energy excitation X-ray photoelectron spectroscopy. High resolution X-ray emission spectroscopy. Highly precise X-ray powder diffraction and ultra-small angle scattering.
BL16XU	**Industrial Consortium ID** (Industrial Consortium) (Oct. 1998)	Characterization of thin films for ULSI and magnetic devices, catalysts, functional materials, and structural materials by X-ray diffraction, fluorescence X-ray analysis, X-ray magnetic circular dichroism, and imaging with X-ray microbeam.
BL16B2	**Industrial Consortium BM** (Industrial Consortium) (Oct. 1998)	Characterization of industrial materials, such as metal and oxide films, semiconductor crystals by XAFS, topography and other methods.
BL32B2	**Pharmaceutical Industry** (Pharmaceutical Consortium for Protein Structure Analysis) (Apr. 2002)	Protein structure analysis for structure-based drug design: Design and optimization of new leading compounds based on pharmacodynamic action mechanism elucidated at the molecular level which obtained from a detailed interaction analysis of receptor-drug complexes.
BL33LEP	**Laser-Electron Photon** (RCNP, Osaka University) (Jun. 1999)	Meson photoproduction from nucleon and nucleus. Photoexcitation of hyperons, nucleon resonances, and other exotic states. Photonuclear reactions. Beam diagnoses. Test and calibration of detectors with GeV photon beam.
BL44XU	**Macromolecular Assemblies** (IPR, Osaka University) (May 1999)	Crystal structure analysis of biological macromolecular assemblies (e.g. membrane complexes, protein complexes, protein-nucleic acid complexes, and viruses).
BL11XU	**JAEA Quantum Dynamics** (Oct. 1998)	Nuclear resonant scattering. Surface and interface structure with MBE. Inelastic scattering. XAFS.
BL14B1	**JAEA Materials Science** (Dec. 1997)	Materials science at high pressure. Structure physics.
BL22XU	**JAEA Quantum Structural Sci.** (May 2002)	Materials science at high pressure. Resonant X-ray scattering (activity at RI laboratory).
BL23SU	**JAEA Actinide Science** (Feb. 1998)	Surface chemistry with supersonic molecular beam. Biophysical spectroscopy. Photoelectron spectroscopy (activity at RI laboratory). Magnetic circular dichroism (activity at RI laboratory).
	◆ RIKEN Beamlines	
BL17SU	**RIKEN Coherent Soft X-ray Spectroscopy** (Sept. 2003)	Spectroscopy of multiply charged ions. Angle-resolved photoemission spectroscopy (ARPES). Soft X-ray emission spectroscopy.
BL19LXU	**RIKEN SR Physics** (Oct. 2000)	Any research field requiring the highly brilliant X-ray beam.
BL26B1/B2	**RIKEN Structural Genomics I & II** (Apr. 2002)	Structural genomics research based on single crystal X-ray diffraction.
BL29XU	**RIKEN Coherent X-ray Optics** (Dec. 1998)	X-ray optics, especially coherent X-ray optics.
BL44B2	**RIKEN Structural Biology II** (Feb. 1998)	Macromolecular crystallography.
BL45XU	**RIKEN Structural Biology I** (Jul. 1997)	Macromolecular crystallography. Time-resolved structures of non-crystalline biological materials using small-angle scattering and diffraction technique.
	■ Accelerator Beam Diagnosis	
BL05SS	**Accelerator Beam Diagnosis** (Mar. 2004)	Accelerator beam diagnostics. R&D of accelerator components.
BL38B2	**Accelerator Beam Diagnosis** (Sept. 1999)	Accelerator beam diagnostics. R&D of accelerator components. Production of MeV γ-ray photons.

Proposal Schemes, Utilization Statistics and Research Outcome

Overview

JASRI invites General Proposals twice a year. Submitted proposals are reviewed by the SPring-8 Proposal Review Committee (PRC). In the General Proposal scheme, the PRC approved 329 of 570 proposals in 2006B and 572 of 842 in 2007A. There was only "Medical Trial Use" conducted in the Priority Field Proposal scheme in the period of 2006B and 2007A, where 213 proposals were adopted from 297 in 2006B, and 11 adopted from 16 in 2007A. In total, 4,035 hours of beamtime was allocated to users from 2006B through 2007A.

SPring-8 user operation statistics for the period from 1997B to 2007A are shown in Table IV. This table summarizes the beamtime available to users, the number of users and the number of experiments conducted at both public and contract beamlines, which are also illustrated in Fig. 4. The number of experiments conducted in the reserved beamtime at RIKEN beamlines and the number of Priority Research Proposals are included in the number of Public BL experiments in the table and figure.

In 2006B and 2007A, SPring-8 provided users with 1,587 and 2,448 hours of beamtime in three and four operation cycles, respectively. As for 2006B, 3,513 individuals utilized the public beamlines in 548 independent experiments, while 1,487 individuals utilized the contract beamlines in 199 experiments. In 2007A, 4,999 individuals utilized the public beamlines in 780 independent experiments, while 2,282 individuals utilized the contract beamlines in 260 experiments. From October 1997, when SPring-8 was opened to the public, through 2007A, a total of 77,847 users conducted 11,567 experiments at public and contract beamlines.

Figures 5 and 6 indicate the number of approved experiments along with the affiliated number of users and the research fields from 1997B to 2007A. In Fig. 6,

Table IV. SPring-8 user operation results

Research Term	User Time (hours)	Public BL		Contract BL	
		Experiments	Users	Experiments	Users
1997B: 1997.10 - 1998.03	1,286	94	681		
1998A: 1998.04 - 1998.10	1,702	234	1,252	7	
1999A: 1998.11 - 1999.06	2,585	274	1,542	33	467
1999B: 1999.09 - 1999.12	1,371	242	1,631	65	427
2000A: 2000.02 - 2000.06	2,051	365	2,486	100	794
2000B: 2000.10 - 2001.01	1,522	382	2,370	88	620
2001A: 2001.02 - 2001.06	2,313	473	2,915	102	766
2001B: 2001.09 - 2002.02	1,867	486	3,277	114	977
2002A: 2002.02 - 2002.07	2,093	543	3,246	110	1,043
2002B: 2002.09 - 2003.02	1,867	538	3,508	142	1,046
2003A: 2003.02 - 2003.07	2,246	632	3,777	164	1,347
2003B: 2003.09 - 2004.02	1,844	548	3,428	154	1,264
2004A: 2004.02 - 2004.07	2,095	568	3,756	161	1,269
2004B: 2004.09 - 2004.12	1,971	554	3,546	146	1,154
2005A: 2005.04 - 2005.08	1,880	560	3,741	146	1,185
2005B: 2005.09 - 2005.12	1,818	619	4,032	187	1,379
2006A: 2006.03 - 2006.07	2,202	722	4,809	227	1,831
2006B: 2006.09 - 2006.12	1,587	548	3,513	199	1,487
2007A: 2007.03 - 2007.07	2,448	780	4,999	260	2,282
TOTAL	36,748	9,162	58,509	2,405	19,338

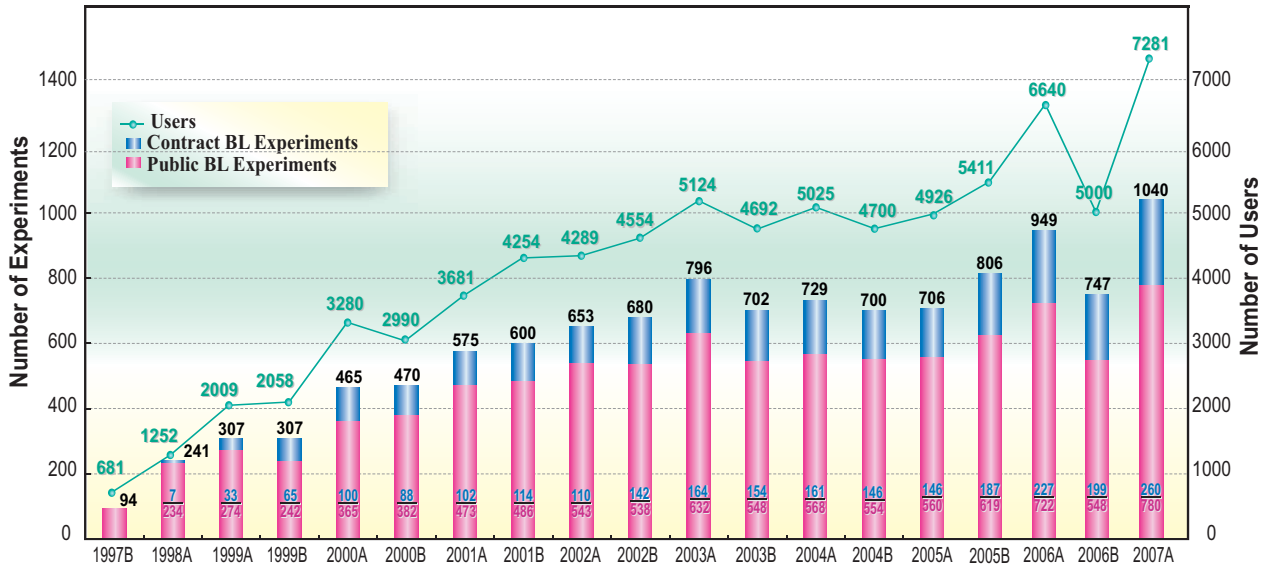

Fig. 4. Numbers of users and experiments conducted.

three types of research, namely, those performed under Advanced Large-Scale Research Facilities Strategic Program, Power User Proposal, Strategy Proposal, which have their own original peer review systems, are separated from the other general research fields. The percentages of experiments conducted by foreign users were 5.1% for 2006B and 5.2% for 2007A.

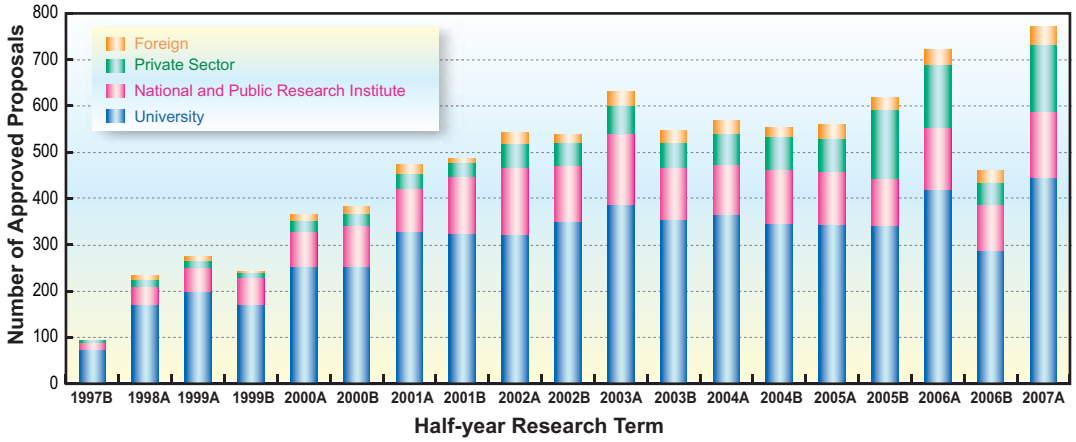

Fig. 5. Number of approved proposals by affiliation of applicants (public beamlines).

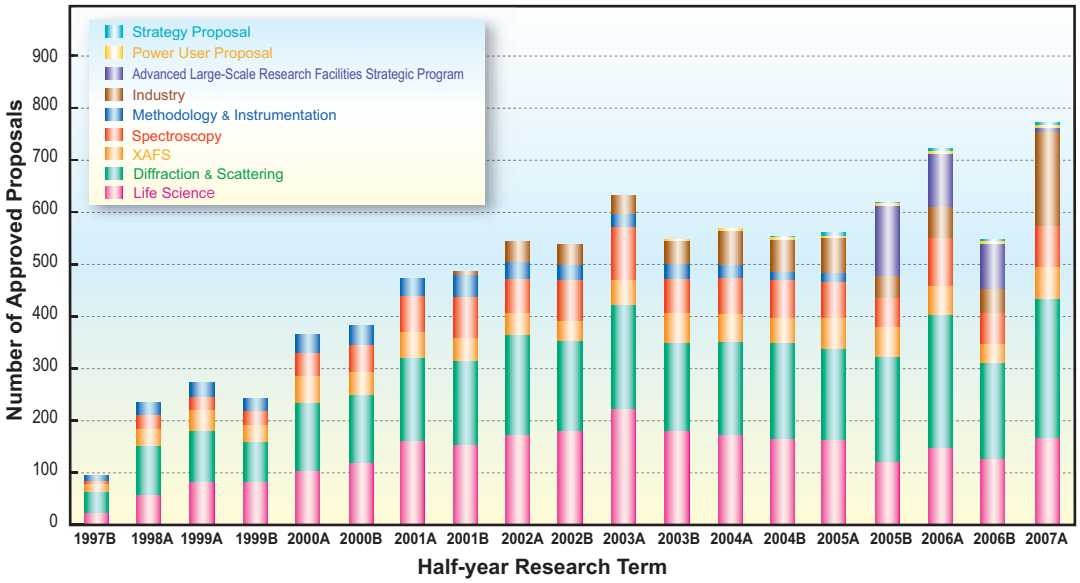

Fig. 6. Number of approved proposals by research fields (public beamlines).

Long-term Proposal

Independent of the General Proposals, JASRI has developed a novel scheme for the long-term use of beamlines, in which beam access is guaranteed for up to three years. This system aims to further promote research that is expected to produce outstanding results in the field of science and technology to pave the way for new research areas and research methodologies and to significantly help improve the technology for the industrial base by making the best use of the characteristics of SPring-8. Two proposals were selected from 4 submitted in 2006B and 2 was submitted and selected in 2007A. Eleven proposals were carried out by the end of 2007A.

Urgent Proposal

In 1999A, an Urgent Proposal scheme was established in order to adequately respond to urgent requests for conducting experiments as soon as possible. Upon receiving an Urgent Proposal of non-proprietary use, the Proposal Review Committee promptly reviews it electronically in terms of its necessity and urgency as well as on the basis of the criteria for General Proposals of non-proprietary use.

Proprietary Research Proposal

Users can conduct proprietary research by paying the beamtime fee, 480,000 yen/shift (8 hours) in 2007B. Proprietary research is essential when users have commercially confidential information in their experiment or samples and do not wish to disclose their research results. In 2006B, 31 proprietary experiments were performed at public beamlines and 26 were performed at contract beamlines (22 at BL32B2, 3 at BL24XU and BL08B2, and 1 at BL16B2). In 2007A, 42 experiments were conducted at public beamlines and 24 experiments were conducted at contract beamlines (22 at BL32B2, and 2 at BL16B2). From 1999B, when the system was introduced, to 2007A, a total of 554 proprietary experiments were carried out at both public and contract beamlines. The Pharmaceutical Consortium spent most of their beamtime on proprietary research at their contract beamline BL32B2 in 2006B and 2007A.

Proprietary Time-designated Proposal

In 1999B, JASRI established a utilization scheme for those who wish to take sole possession of their results and perform experiments during a specific time period by paying a beamtime fee with an increase in price of 50% compared with that charged for public beamlines as premium, 720,000 yen/shift. In this utilization scheme, users can specify the preferred time period in their Proprietary Time-designated Proposal, which will be promptly reviewed once submitted. During the period of 2007A, there have been 11 experiments conducted with a total shifts of 34.75 in this scheme.

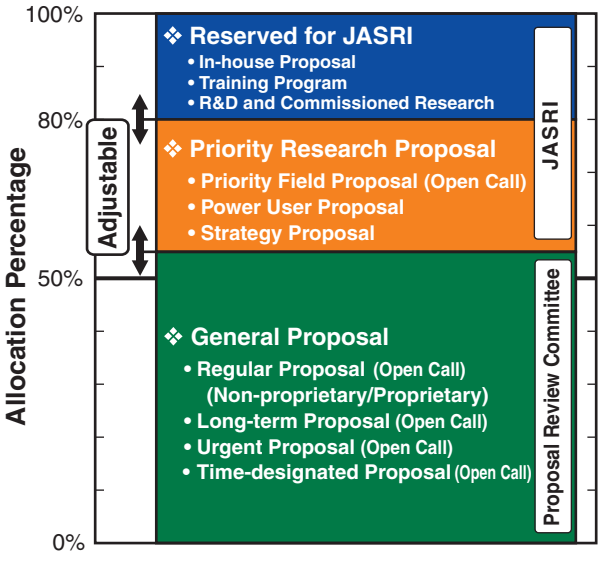

Fig. 7. Beamtime allocation scheme for public beamlines.

Priority Research Proposal

In FY2003, a new scheme for the management of public beamlines was established on the basis of a report on SPring-8 by the governmental review committee. The report called for SPring-8 to further promote the use of public beamlines to produce more research results. The most important point of the scheme was its launching of the Priority Research Program. The new scheme is shown in Fig. 7. As can be seen from the figure, beamtime not exceeding 50% is allocated to Priority Research Proposals and proposals using beamtime reserved for JASRI; thus, more than 50% of the total user beamtime is guaranteed for General and Long-term proposals. The Priority Research Program scheme is intended to make the best use of SPring-8 and to produce more research results. Priority Research Proposals are tentatively categorized into the following three groups: (1) Priority Field Proposal, (2) Power User Proposal, and (3) Strategy Proposal.

Priority Field Proposal

In this particular proposal scheme, JASRI strategically designates research fields in order to promote excellent research results from those areas in scientific and/or industrial domains with high strategic significance. The Priority Field Proposals are further categorized into three subgroups: Nanotechnology Support, Industrial Use and Medical Bio Trial Use. These proposals are reviewed before General Proposals at the review committees designated for each priority field. The outline of each priority research field is as follows.

Nanotechnology Support

This priority research field was developed to support developments in nanotechnology, using 12 beamlines at SPring-8. Nanotechnology Support at SPring-8 had already started in 2002 under the Nanotechnology Researchers Network Project (Nanonet Project) of MEXT, and was consolidated into the Priority Research Program in FY2003. In 2005B and 2006A, a total of 106 proposals were selected from 211 submitted proposals. This Project will be in effect until the end of FY2006.

Industrial Use

In relation to industrial use, the Trial Use Program originally ran from 2001B to 2002A for the purpose of attracting new users to SPring-8 mainly from industries, and was restarted as one of the Priority Field Proposals in 2003A. In 2005B, 4 from 6 proposals were selected and the Trial Use program for industrial use was successfully completed. In the

same period, the Advanced Large-Scale Research Facilities Strategic Utilization Program, which is mainly focused on enhancing industrial use, was launched as a national project. There were 101 proposals submitted, of which 72 were approved to be conducted in 2006B and 2007A, respectively.

Medical Biology

Since November 2005, JASRI has further designated Medical Biology as a priority field to expand the number of users in this field by organizing a trial use from 2006A. In 2006B, 9 from 11 proposals were selected.

Power User Proposal

The Power User Proposal category refers to proposals of user groups who have a complete understanding of beamline instrumentation, and are highly likely to produce excellent research results in the future. Such user groups are designated as Power Users (PUs) by JASRI and expected to provide support for general users. In return for their support, up to 20% of beamtime of relevant beamlines can be used by the PUs. Five groups were designated as PUs in May 2003. There have been 10 research subjects executed including five running subjects from 2006B and 2007A.

Strategy Proposal

Strategy Proposals are expected to contribute to the promotion of research at SPring-8, including the development of new technologies necessary for the operation of the facility. JASRI will conduct such research by itself or jointly with other organizations. Designated strategies research subject were:

- Analysis of Nanocomposite Materials (designated in May 2004)
- X-ray Pinpoint Structure Measurements (designated in January 2005)
- Observations of Biomolecular Structural Recognition Process from Highly Accurate Individual Single Molecular Movies (designated in October, 2006)

Beamtime Reserved for JASRI

Twenty percent of the total beamtime is reserved for JASRI to conduct its own research programs, to flexibly accept the Urgent Proposals mentioned above, to modify and adjust the instruments according to the users' requests, and to maintain the beamlines.

Industrial Research

In addition to the promotion of research activities in the field of basic science, the contribution to the reinforcement of the technological base in industry has been one of the main pillars of the SPring-8 Project. In 2005, JASRI established the Industrial Application Division by promoting the Industrial Application & Utilization Support Group. The division had intensively carried out the Advanced Large-Scale Research Facilities Strategic Utilization Program of MEXT, and has succeeded in doubling the number of new users conducting experiments at SPring-8.

Public beamline BL19B2, Engineering Science Research Beamline was the primary beamline used for the Trial Use Program. Currently, there are three public beamlines assigned for industrial application, which are Engineering Science Research I (BL19B2), II (BL14B2), and III (BL46XU), as shown in Fig. 3. The total number of proposals adopted for industrial applications accounts for more than 20% of the entire use. In addition to these public ones, there are three contract beamlines constructed by the Industrial Consortium and Pharmaceutical Consortium for use by consortium members.

The coordinator system, which was introduced in FY2000 to support industrial use mainly through consultation, continues to play a crucial role in exploring and acquiring new users from industrial domains. The Trial Use Program has made a significant contribution to industries by revitalizing local industries and creating and promoting new industries. There have been workshops and training courses organized to introduce a variety of research fields and SR instrumentation.

Research Outcome

Under the new utilization system established in 2006, SPring-8 users are charged only the expenditure fee for non-proprietary research, provided that they submit an experiment report within sixty days after their experiments. When their results are disclosed in scientific journals or any other form of publication, the project leaders are required to report to JASRI and have their results registered with JASRI. As of November 30, 2007, the cumulative number of refereed publications (journals, proceedings and dissertations) was 3,612, of which 2,847 were attributed to public use, 553 were attributed to contract beamlines and 559 were attributed to RIKEN beamlines; here, publications related to two or more beamlines are counted separated for each beamline. Figure 8 shows the number of refereed publications annually counted.

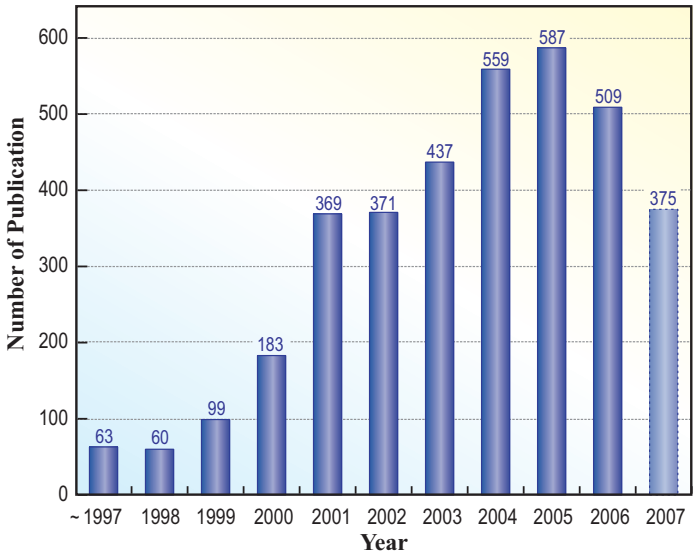

Fig. 8. Annual record of refereed publications as of September 30, 2007.

Budget and Personnel

After becoming open to public use in 1997, SPring-8 was managed by the three-party system of RIKEN, JAERI, and JASRI in a unified manner until September 30, 2005, when JAERI relinquished responsibility for SPring-8 management. Since JAERI withdrew, SPring-8 has been managed by the remaining two-party system of RIKEN and JASRI, although JASRI had a legal status transition during FY2006. Figures 9 and 10 display the variations in the total budgets allocated to SPring-8 and the numbers of staff members on the SPring-8 campus each year from FY1997 up to the current fiscal year. It should be noted here that, the figure is subject to some inaccuracy, partially because of this framework transition and partially because of the phase changing from construction to utilization, although the general trend is certainly represented. The total budget allocated to SPring-8 for FY2007 is almost the same as that of FY2006, maintaining the recent trend. In FY2007, the total number of JASRI staff members was 557. The total number of SPring-8 staff members amounts to ~1,200, when the numbers of staff members at the JAEA Kansai Research Establishment and the RIKEN Harima Institute are combined with the number of JASRI staff members. The numbers of staff members categorized by the types and fields of employment are illustrated in Fig. 10.

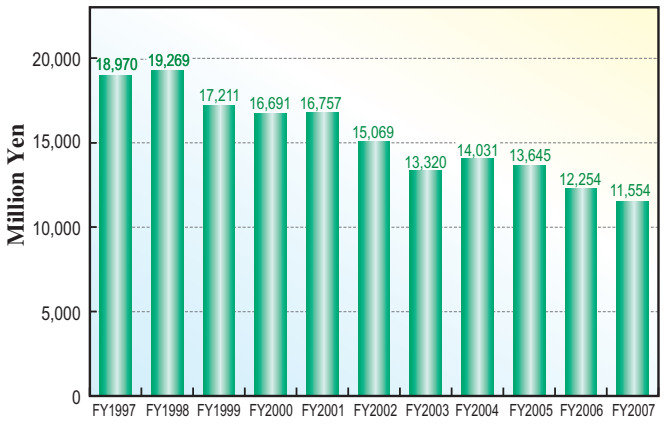

Fig. 9. Budget at SPring-8.

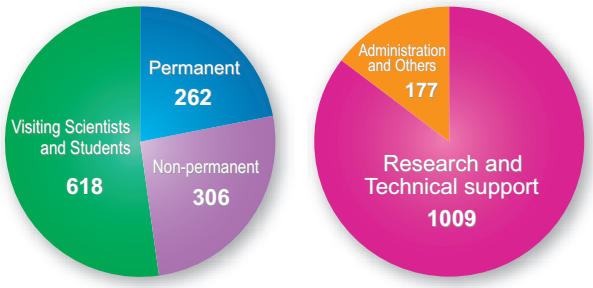

	by Type			by Field		Total
	Permanent	Non-permanent	Visiting Scientists and Students	Research and Technical Support	Administration and Others	
JASRI	212	155	190	414	143	557
RIKEN	50	148	421	588	31	619
XFEL	0	3	7	7	3	10
	262	306	618	1009	177	1186

Fig. 10. Personnel at SPring-8: JASRI, RIKEN and XFEL (FY2007).

Research Complex

As a center of excellence, SPring-8, XFEL, SCSS, and New SUBARU form a research complex for synchrotron radiation science and technology, being composed of JASRI, the RIKEN Harima Institute, and the JAEA Synchrotron Radiation Research Center, Laboratory of Advanced Science and Technology for Industry, together with various universities and institutes, as illustrated in Fig. 11. The two major bodies of the COE are the RIKEN Harima Institute and JASRI, the organization charts of which are shown in Fig. 12 and Fig. 13, respectively.

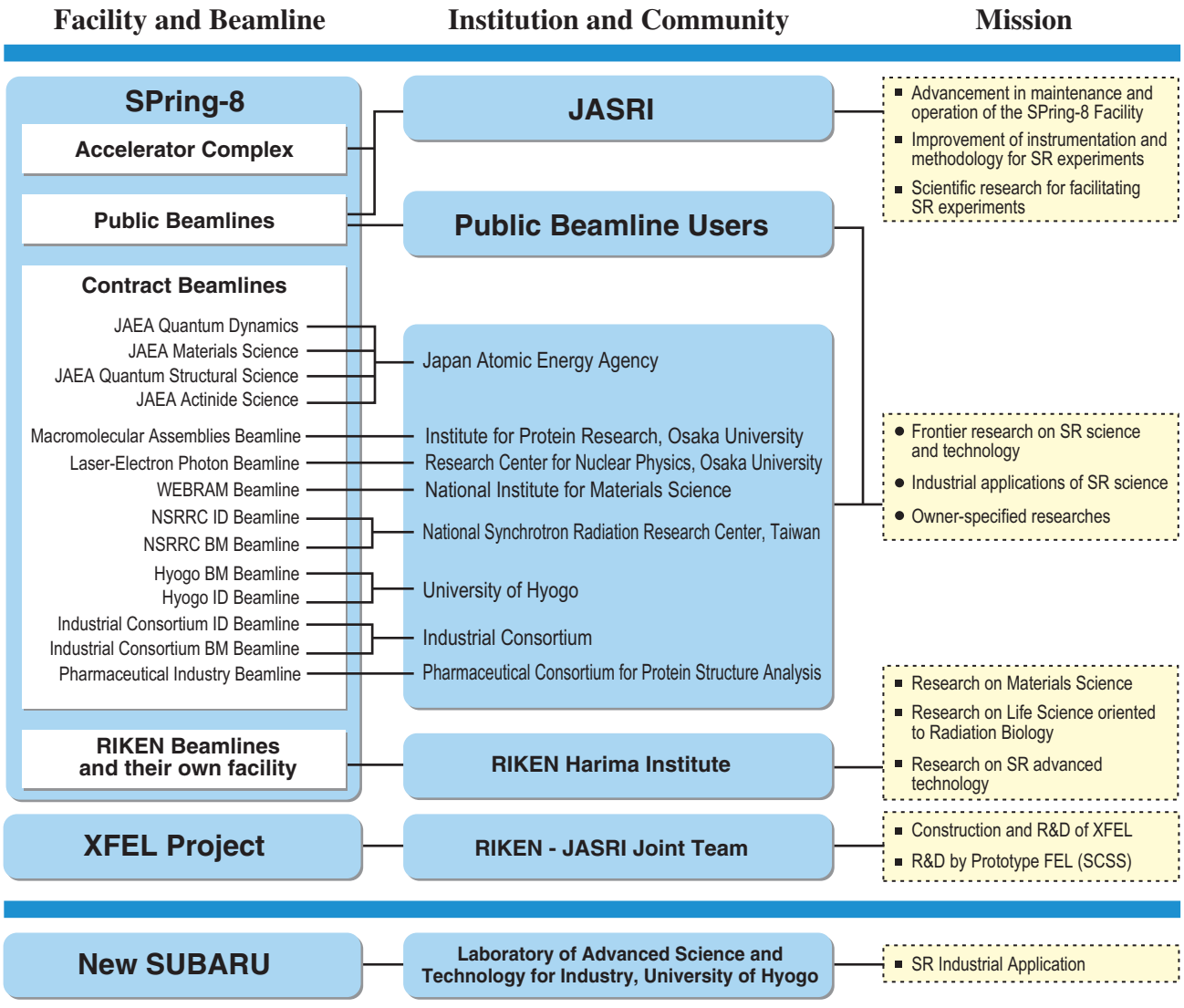

Fig. 11. SPring-8 research complex.

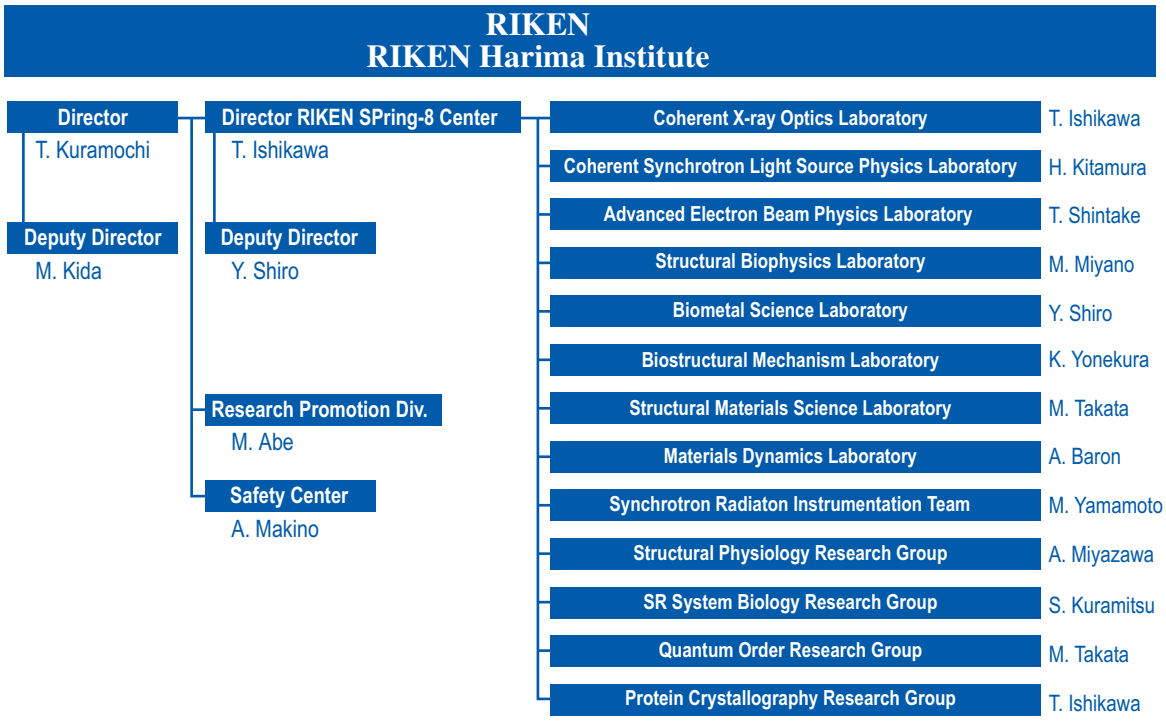

Figure 12

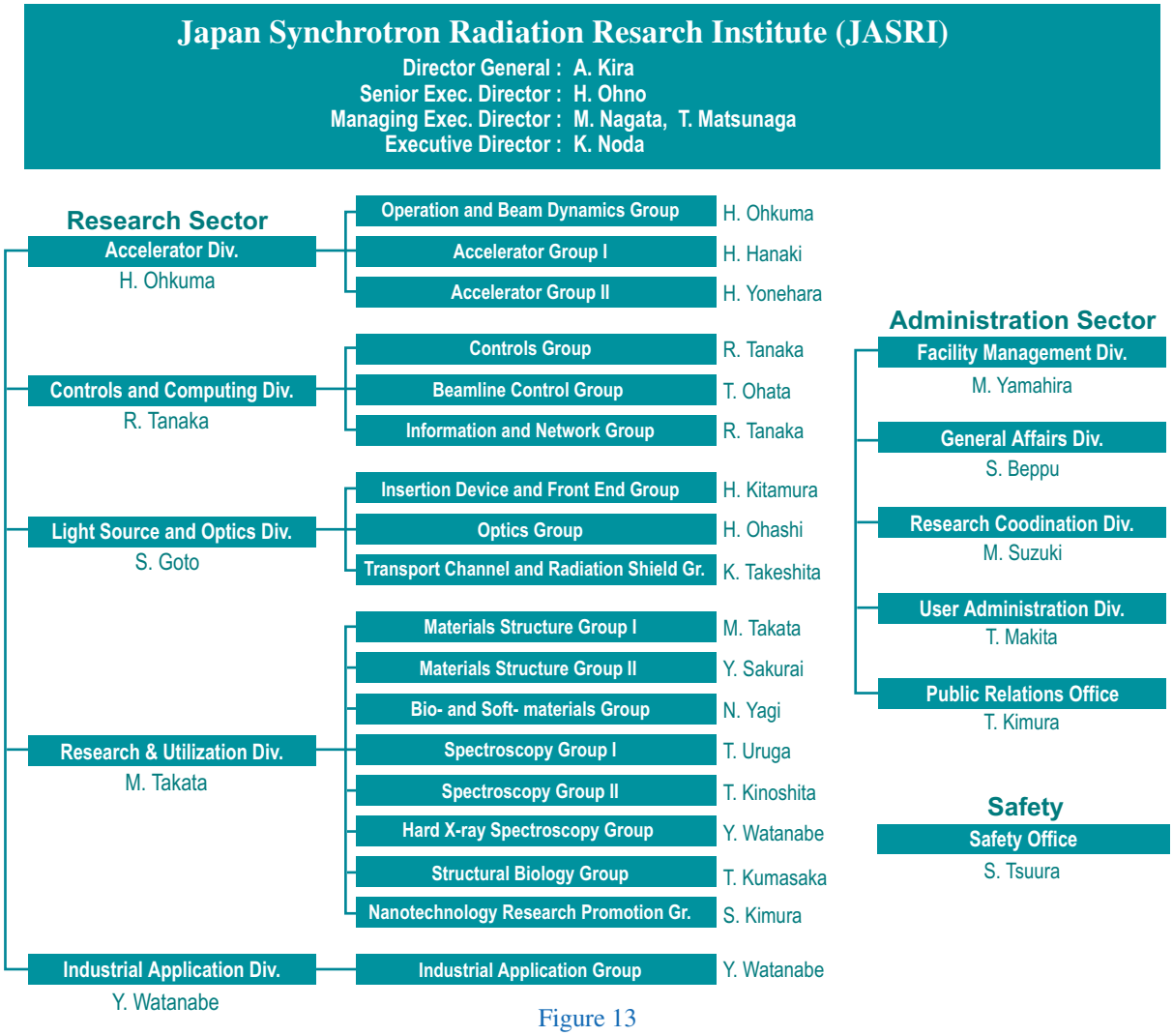

Figure 13

SPring-8 Users Societies

In order to advance the research activities of users at SPring-8, the **SPring-8 Users Society** was established in May 1993 in such a way that the users can cooperate in the upgrading, facilitation and promotion of SPring-8 utilization. For the purpose the Users Society is divided into 34 working groups to be able to communicate and exchange information with specialists and with the facility. Projects at the initial stage, which have been carried out for two years, will be completed in March 2008. Renewed programs of these research groups for new projects and relating meeting schedules for two years will be presented in April 2008 to further develop SPring-8 activities. The number of the members in the Society reached 1468 as of April 2008.

To promote utilization by the industrial users of SPring-8, the **SPring-8 Industrial User Society** was established in September 1990, and has been investigating and deliberating the feasibility of making improvement on the SPring-8 utilization system and on SPring-8 utilization by the industry and making recommendations. Eight workshops have been organized on various utilization topics, such as practical catalysis and stress analysis. The activities of this Society have played important roles in promoting communication between industrial uses and JASRI and/or MEXT. The number of companies and corporations joining the Society reached 71 as of April 2008.

Users Meeting

- SPring-8 Users Society Meeting, January 12-14, 2007 - International Conference Center, Hiroshima
- The 11th SPring-8 Symposium, October 29-30, 2007 - Public Relation Center, SPring-8, Hyogo
- The 4th Report Meeting on SPring-8 Industrial Application, September 11-12, 2007
  - Souhyo Kaikan, Tokyo
- Lectures on the Possibility of Industrial Application of SR, November 5, 2007
  - Nagoya Bankers Association, Nagoya

Conferences and Workshops

The Conferences and Workshops organized/sponsored by SPring-8 (JASRI and RIKEN), including with other organizations, in 2007 are listed below.

- The 2nd Medical Biology Workshop, January 25, 2007 - Public Relation Center, SPring-8.
- Result Report Symposium of SPring-8 Medical-biology Trial Use in FY2007, January 26, 2007 - Public Relation Center, SPring-8
- The 3rd Nanotechnology Support Project Workshop, February 19, 2007 - Public Relation Center, SPring-8
- The 6th International Conference on Inelastic X-ray Scattering, May 7-11, 2007 - Awaji Yumebutai International Conference Center, Hyogo
- International Workshop on Nuclear Resonant Inelastic Scattering International, May 14-15, 2007 - Annex of Material Science Research Facility, SPring-8
- Workshop on Organic and Polymeric Materials Science being led by Female Scientists, The Present and Future for Synchrotron Radiation Utilization, June 1, 2007 - Public Relation Center, SPring-8
- The 1st XFEL Application Workshop, June 7, 2007 - RIKEN Tokyo Office, Tokyo
- SPring-8 Workshop on Microstructural Observation of Metals and Steels by Synchrotron X-ray, July 20, 2007 - Campus Innovation Center Tokyo, Tokyo
- International Workshop on Infrared Microscopy and Spectroscopy with Accelerator Based Sources (WIRMS2007), September 25-29, 2007 - Awaji Yumebutai International Conference Center, Hyogo
- SPring-8 10th Anniversary Symposium, October 20, 2007 - Center for Advanced Science & Technology HYOGO, Hyogo
- The 2nd XFEL Symposium, October 20, 2007 - CAST, Hyogo
- Three Way Workshop for X-Ray Free Electron Laser, October 21-22, 2007 - SPring-8

Other Activities

- SPring-8 Open House, April 22, 2007
- The 7th SPring-8 Summer School, July 6-9, 2007 - Auditorium, SPring-8
- The 1st AOFSRR Summer School - Cheiron School 2007, September 10-20 - Public Relation Center, SPring-8

Project XFEL

For many years, scientists have used basic laser technology to generate shorter wavelength coherent radiation to explore the nano-world. But scientists have long dreamed of a new generation of laser-like X-rays to further their exploration. Although research to attain shorter wavelength lasers was initiated soon after the invention of visible lasers in the 1960s, scientists found it extremely difficult to adapt conventional laser technologies (based on atomic or molecular energy levels) to reach the X-ray region. Free electron lasers (FEL), initially proposed in the 1970s, were regarded as a potential technology for producing X-ray lasers. But the difficulty in devising an optical cavity with high reflectivity mirrors in the X-ray region prevented scientists from developing a working model. In the 1990s, the discovery of the SASE (self-amplified spontaneous emission) concept provided a promising breakthrough.

At the end of the last decade, a project for constructing an X-ray coherent light source (now known as a Linac Coherent Light Source, or LCLS) at the SLAC, was proposed. Another project proposed in Germany was based on superconducting linac technology. During the planning stages of these projects, SPring-8 scientists were asked to participate in the workshops because SPring-8 had just completed a 1-km beamline for coherent hard X-rays and a 27-m long undulator, both of which might prove useful for providing a SASE source. At the workshops we found a unique means of producing SASE-XFEL by using the in-vacuum undulator developed at the SPring-8. The shorter magnetic period achievable by using the in-vacuum undulator would help us to produce hard X-rays with relatively lower electron energy, potentially reducing the linac length. Using a higher frequency (C-band) high gradient accelerator unit could lead to even further reduction of the linac length.

We proposed a new type of SASE-XFEL source called the "SPring-8 Compact SASE Source" (SCSS), based on the concept of the lower energy and the higher gradient linac working together with the shorter undulator to contribute to significant reduction of the facility length. During 2001-2003, we developed critical components for the SCSS including a low-emittance thermionic e-gun. In 2004, we published a conceptual design report for XFEL and in 2005, we began construction of a 1/32 scale prototype of an FEL.

Our project was selected as one of Japan's five Key Technologies of National Importance. An XFEL based on an 8 GeV linac is now under construction with completion expected in 2010. RIKEN and JASRI set up a joint project team for the construction of the XFEL. Comprehensive discussions on applications for the XFEL are currently underway, under the initiative of MEXT, which includes many potential users of the XFEL.

Tetsuya Ishikawa

Progress of the XFEL Project at SPring-8

The X-ray free electron laser (XFEL) project started in FY2006 as one of the key technologies of national importance. The 8 GeV XFEL facility is being constructed along the 1-km-long beamline of SPring-8 (Fig. 1). The construction project is favorably progressing toward completion in FY2010 (Fig. 2).

At the first stage, XFEL radiation is generated based on a self amplified spontaneous emission (SASE) scheme. The radiation properties are characterized by fully spatial coherence, an ultra-short pulse of less than 100 fs, and peak brilliance that is 10^9 times higher than that of a typical undulator at SPring-8. The shortest target wavelength is 0.6 Å in the hard X-ray region.

The machine, which has a total length of 710 m, is much compact than LCLS at SLAC or the European XFEL at DESY. This compactness is realized by a unique system, which is composed of a low emittance injector with a single crystal thermionic gun, C-band accelerators, and in-vacuum undulators [1,2]. For performing the R&D of the whole FEL system, the SCSS test accelerator was constructed in 2005, and the lasing of EUV light was successfully achieved in June 2006. In September 2007, we achieved the saturation of radiation power in the extreme ultraviolet (EUV) region. The test operation for user experiments started in October 2007.

1. Status of XFEL Construction

In FY2006 the design of the accelerator was carefully investigated on the basis of the results obtained by operation at the SCSS test accelerator. Figure 3 shows the arrangement of the main components together with schematic diagrams of beam acceleration and pulse compression. The 500 keV pulsed thermionic gun generates uniform and cylindrical electron beams with a sharp edge [3]. This condition approximately satisfies a Kapchinskij-Vladimirskij (KV) distribution, which leads to a perfect linear space-charge force within the beam radius that well conserves the electron beam emittance through the following bunch compression process under reasonable transversal focusing and beam handling. By efficient nonlinear chirp correction, the peak current of the electron beam is increased from 1 A up to more than 3 kA through velocity bunching and a

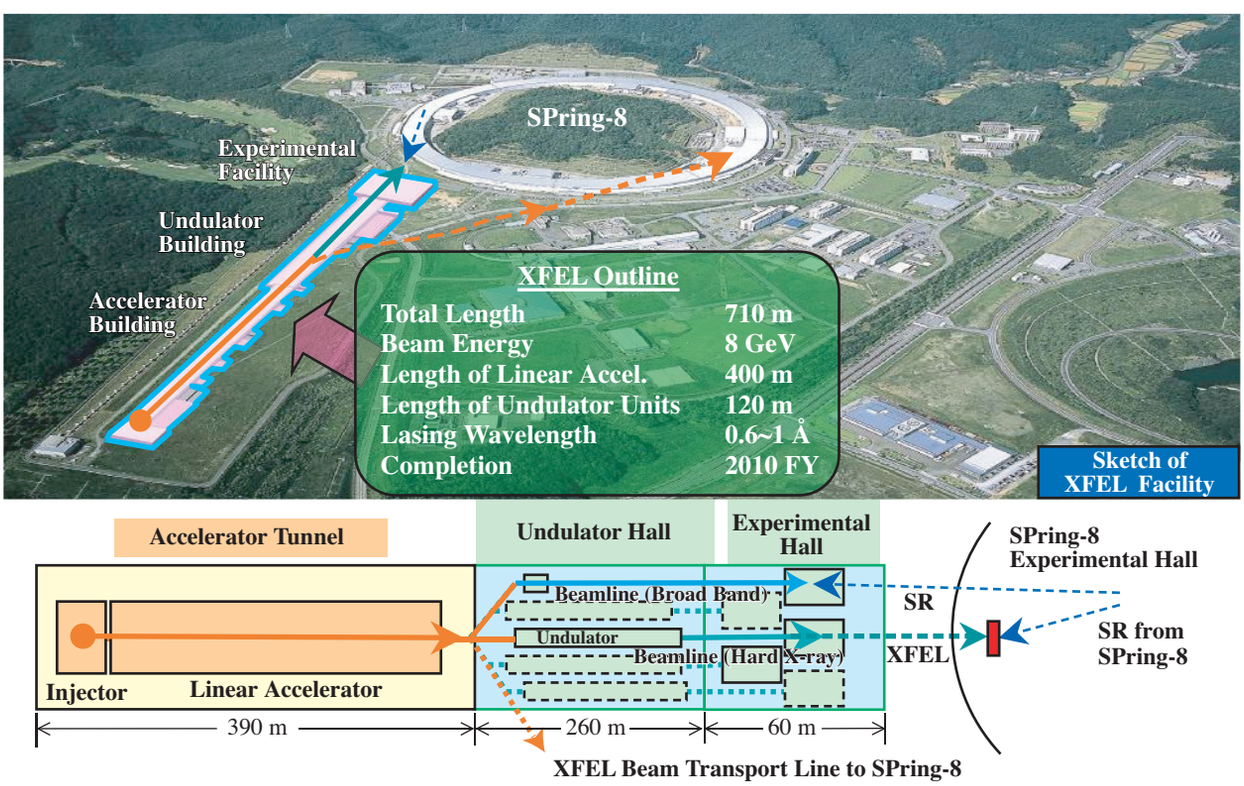

Fig. 1. Aerial photograph of the XFEL/SPring-8 facility (upper) and schematic layout (lower).

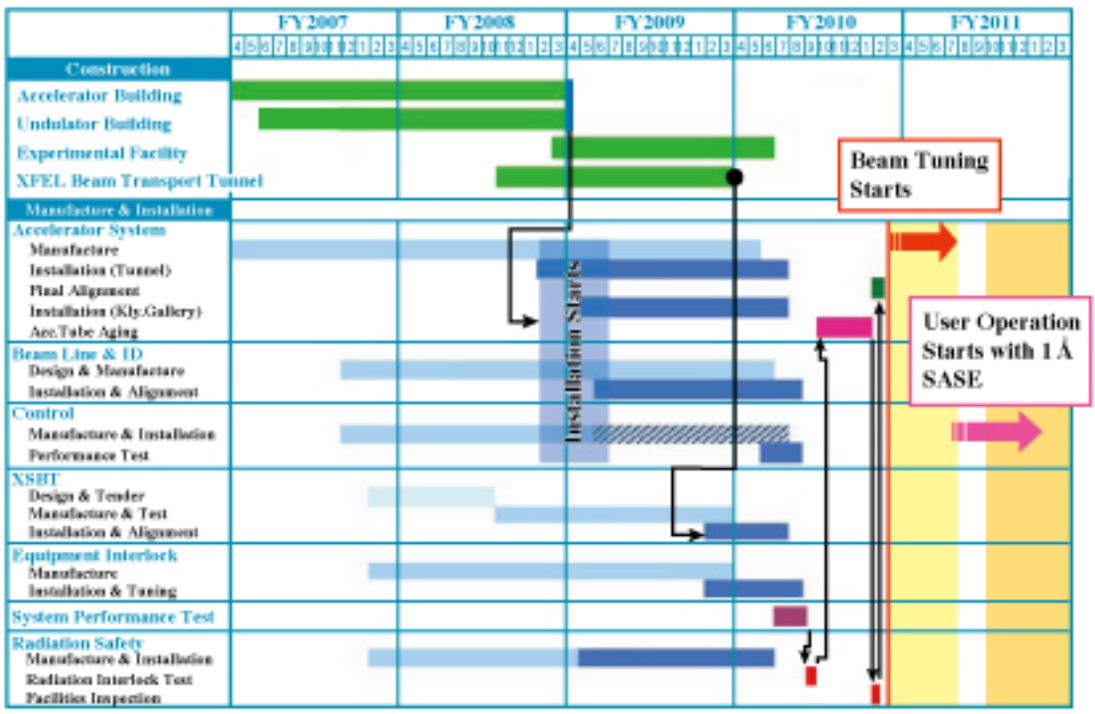

Fig. 2. XFEL/SPring-8 construction schedule.

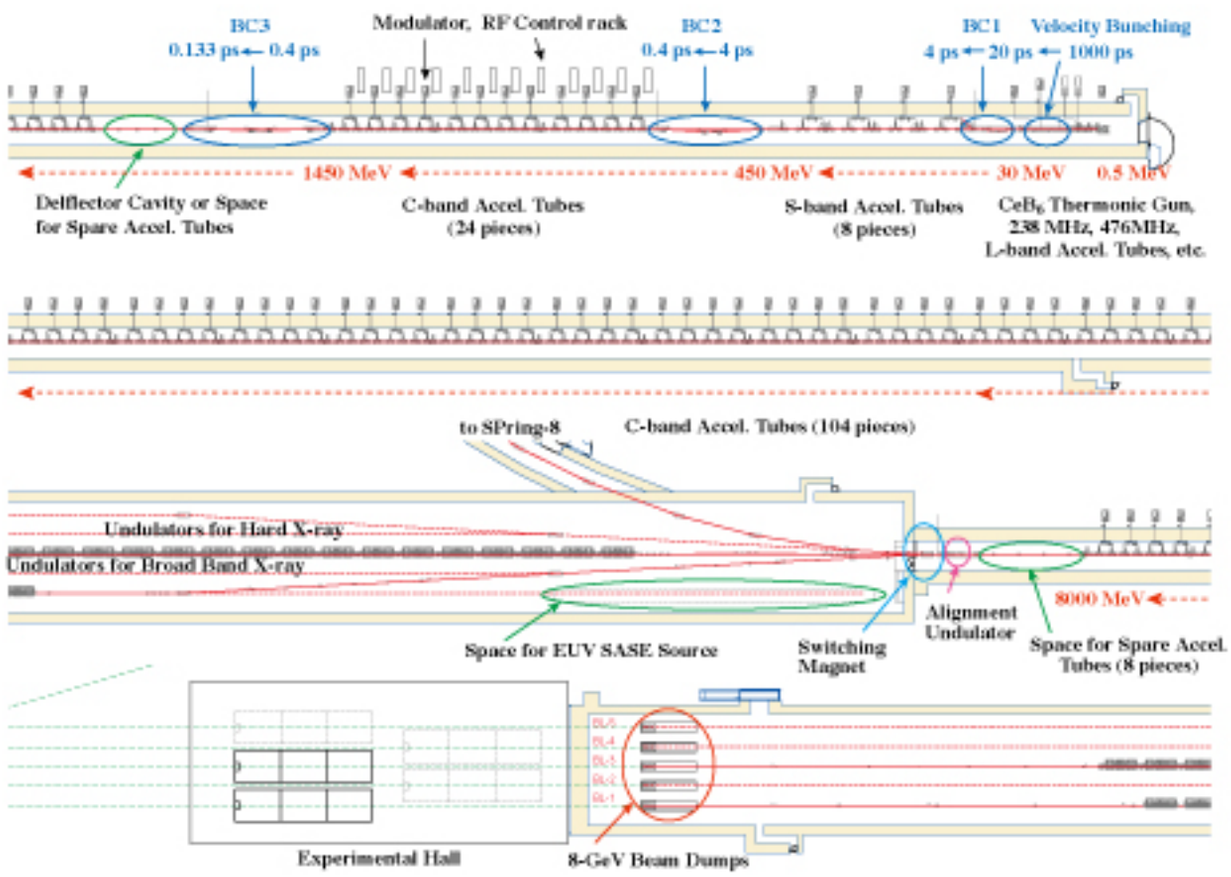

Fig. 3. Arrangement of the main accelerator and insertion device components with schematic diagrams of beam acceleration (red numbers with red dashed arrows) and pulse compression (blue numbers with blue dashed arrows).

three-stage bunch compression system based on magnetic chicanes. The stability requirements of RF voltages and phases for every RF component were evaluated. The key factors for achieving stable bunch compression have been studied to reduce the sensitivity of the peak current against RF voltage and phase errors.

In FY2007, intensive R&D was continued in order to meet the stability requirement. Inverter power supplies for an electron gun and klystrons have been developed for achieving extremely high stability. Although this was initially thought to be one of most difficult targets, a peak-to-peak voltage stability of 0.0045%, which surpasses the target value of 0.01%, has been achieved. A new compact modulator, which contains a klystron and a modulator in a single oil tank (Fig. 4), was developed for reducing RF noise and avoiding troubles with high-voltage cables. A high-power test was successfully completed to verify the noise reduction and reliable operation. Purchase orders for all accelerator components will be finished by FY2007.

The design of the undulator was revised, because the operation of the test accelerator revealed that one of the two undulators based on the original design [2] generated significant multipole error fields, which seriously degraded the beam quality. The new design (Table I) is expected to minimize the error components. A prototype undulator based on this design was manufactured. The field quality and its correction scheme will be studied using this prototype. We are developing a new technique of *in situ* field measurement, which aims to measure the field distribution even after the installation of undulators in the undulator hall.

Fig. 4. Photograph of the developed compact modulator.

Table I. List of new parameters of the XFEL undulator

Magnet Structure	Hybrid type
Material	NdFeB
Length (m)	5
Period Length (mm)	18
Number of Periods	277
Minimum Gap (mm)	3
Maximum K	2.2
Gap @ 1Å (mm)	4.5
K @ 1 Å	1.9

The piling for the foundations of the accelerator tunnel has been completed. Since the tunnel floor stability is quite important for the XFEL, piles with a maximum length of 50 m were used so that all piles reach the stable semi-hard rock bed, of which the ground vibration is sufficiently low, of nm order. Figure 5 shows the distribution of piling depth along the accelerator building. The construction of the concrete floor and wall casting for the accelerator tunnel is also in progress. The ground stability at the undulator building will be improved by replacing the earth method with crushed stones.

A basic plan of the experimental facility was investigated in FY2007. This facility is located on a stable ground. The experimental hall (56 × 30 m^2) contains five beamlines. Several rooms designed for experimental preparation, computer analysis, and remote control of instruments are adjacent to the hall.

The design of the photon beamline was investigated. A radioprotective consideration requires the elimination of energetic γ-rays from XFEL radiation for experimental utilization. For this purpose, two optical devices are installed in the optics hutch: a pair of plane mirrors and a double-crystal monochromator.

The former works as a low-pass filter for photon energies smaller than ~15 keV, while the latter sets a narrow band-pass in a photon energy range of 4 to 30 keV with a resolution of 10^{-4}. The qualitiy of the optical components should be severely controlled to avoid unwanted speckles under coherent illumination. The exit beam positions of these devices are designed to remain fixed during operation. The optics hutch also contains monitors, a beam shutter, collimators, and a pumping system for maintaining the ultrahigh-vacuum condition.

The XFEL beam is transported to experimental hutches, which contain experimental equipment, as well as to beam-conditioning devices such as a Kirkpatrick-Baez (K-B) mirror system for nano-focusing. Optical lasers, which are synchronized with FEL pulses, are introduced for pump-probe experiments.

X-ray diagnostic systems play a key role in the initial commissioning stage. In particular, the precise tuning of undulators is crucial for efficient lasing. We have investigated the effectiveness of several tuning methods. Semi-transparent monochromators are useful for checking the straightness of the electron-beam trajectory over undulator segments. A dispersive spectrometer is introduced to monitor the undulator spectra with single-shot detection for the precise tuning of *K*-parameters between the segments.

2. Saturation Achieved at the SCSS Test Accelerator

In summer 2007, the RF system in the injector section was stabilized to increase the lasing power. To reduce the fluctuation sources, (i) the temperature of the cooling water supplied to the RF cavities was stabilized, and (ii) the resolution of feedback loops for the RF phase and voltage was improved by adopting a time-resolved method for parameter setting. The attained phase and amplitude variations are 0.02 deg. and 0.03% in STD, respectively, which almost reach the target performance for the XFEL machine. Under the achieved stable condition, the machine parameters for RF, focusing, and steering were optimized. The precise tuning strongly enhanced the amplification gain.

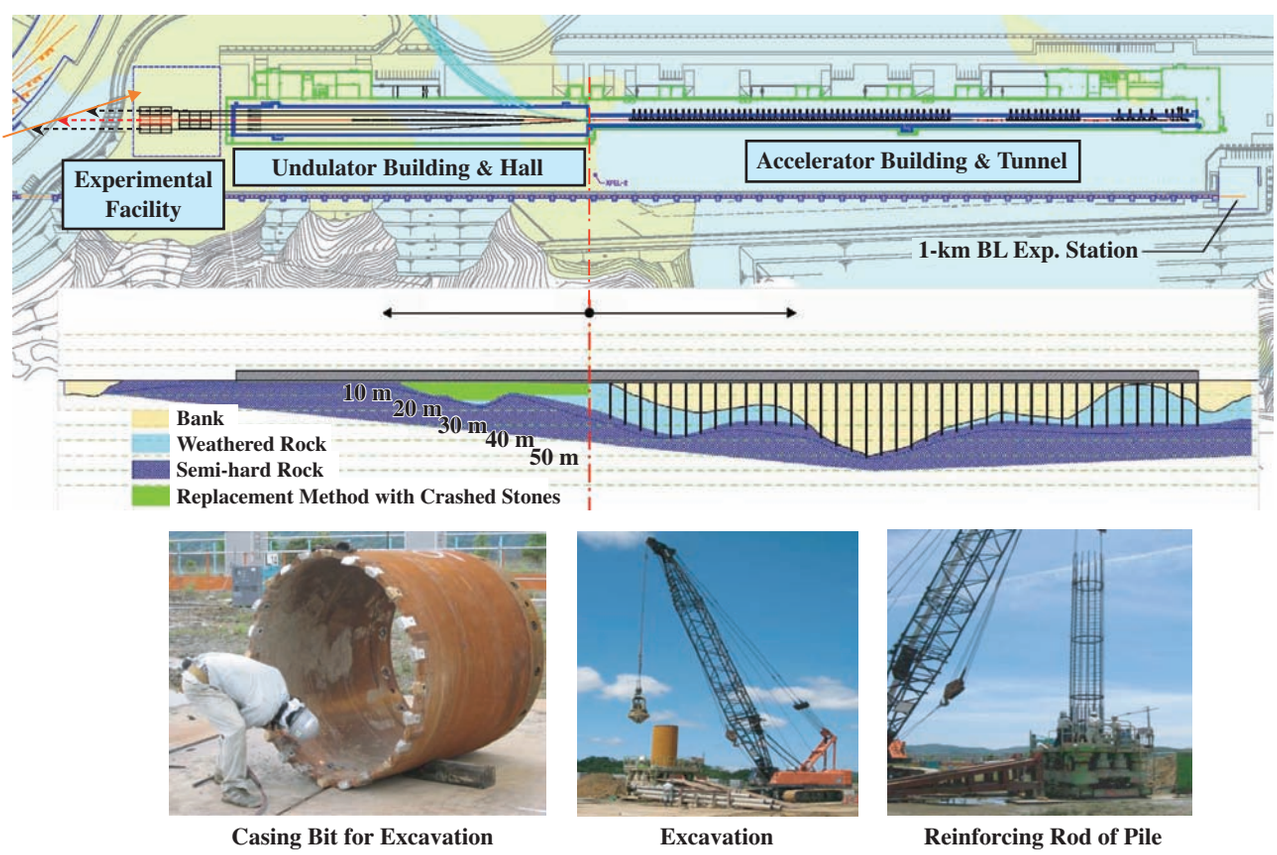

Fig. 5. Distribution of piling depth along the XFEL/SPring-8 facility (upper) and photograph of piling operation (lower).

In September 2007, the second undulator, which did not sufficiently contribute to the first lasing because of the large multipole field errors, was replaced by the new one. This enabled the successful observation of continuous SASE saturation at a wavelength ranging from 50 to 60 nm in late September. A pulse energy of 30 uJ is now routinely obtained at 60 nm with a repetition of 10 Hz and a small intensity fluctuation of ~10%. Figure 6 shows the fluctuation of the saturated SASE pulse energy over 40 min.

For user experiments, an experimental building was constructed in March 2007. A beam transport system, which includes a couple of mirrors, monitors, and vacuum pumps, were succeedingly installed. The beamlines in the experimental building are under construction. A transparent intensity monitor, focusing systems, an optical laser, and a data acquisition system will be installed. User operation is scheduled to start in spring of 2008.

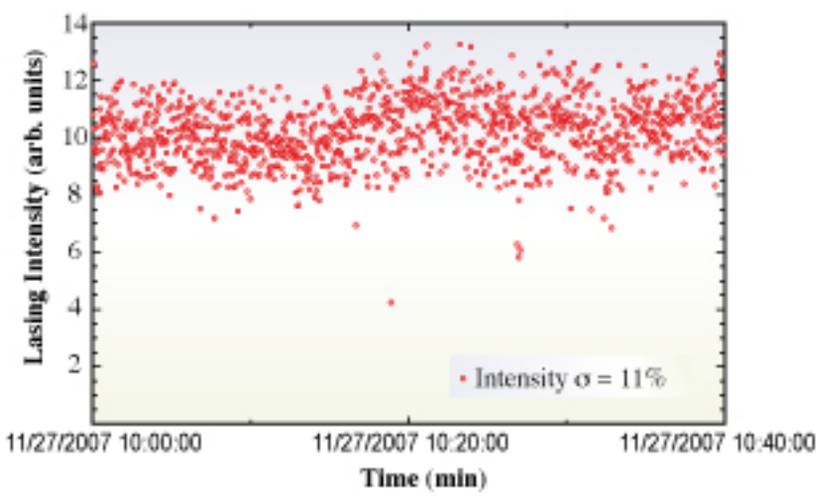

Fig. 6. Achieved intensity stability of SASE lasing.

SPring-8 Joint-Project for XFEL

E-mail: Project-XFEL@riken.jp

References

[1] T. Shintake *et al.*: Proc. SPIE **4500** (2001) 12.
[2] SCSS X-FEL Conceptual Design Report, RIKEN (2005).
[3] K. Togawa *et al.*: Phys. Rev. ST Accel. Beams **10** (2007) 020703.

NewSUBARU

A 1.5 GeV synchrotron radiation ring named NewSUBARU is the main facility of the Laboratory of Advanced Science and Technology for Industry (LASTI) at University of Hyogo. NewSUBARU is at the site of SPring-8 and can provide light beams from IR to soft X-ray. Significant progress has been achieved in upgrading the accelerator and in operations. We have succeeded in storing 500 mA at 1 GeV and 200 mA at 1.5 GeV. The beam lifetime has increased to 14 hours for storing 100 mA at 1.5 GeV. The missions of NewSUBARU at the LASTI are to research on synchrotron radiation and its applications and to prepare a base of advanced engineering in the local area in collaboration with various industries.

At present, NewSUBARU has five bending section beamlines (BL-2, BL-3, BL-6, BL-10, BL-11), two short undulator beamlines (BL-7a, BL-7b), a long undulator beamline (BL-9) and an optical-klystron beamline (BL-1), as shown in Fig. 1. Using these beamlines, many research activities have been performed as follows, (1) BL-3: extreme ultra-violet lithography (EUVL) and the evaluation of a mask used in a future ULSI fabrication technology, (2) BL-2 and BL-11: micro-nano manufacturing technologies including the LIGA process for fabricating three-dimensional structures, (3) BL-6 and BL-7: surface modification of new materials by SR exposure and photoelectron spectroscopy, (4) BL-9: a high precision measurement technique and an EUV interferometer using coherent X-rays from the long undulator, and (5) developments instrumentation and techniques. Many of these activities are being carried out in collaboration with industries. For the advancement of evaluation and analysis by industry, a new analysis beamline will be constructed at BL-5.

NewSUBARU research activities for this year include the first demonstration of nuclear transmutation by a laser Compton backscattered gamma-ray beam and the development of high-performance EUV photo-resist material. The demonstration of nuclear transmutation was made using natural iodine. Radioactive isotopes of iodine have a long lifetime and, in addition they are soluble in water, thus it is relatively difficult to confine them for a long period. The γ-n cross-section of an iodine isotope is expected to be almost equal to that of stable natural iodine. The development of EUV photo-resist is successfully in progress. The photo-resist has been demonstrated to have a low exposure energy and low line-edge roughness. The new resist material may have a strong impact on EUVL technology.

Most of our research activities are being conducted in collaboration with industries, government research institutes and other universities. We will continue to respond to their requirements by offering new technologies.

Takayasu Mochizuki
Director of LASTI, University of Hyogo

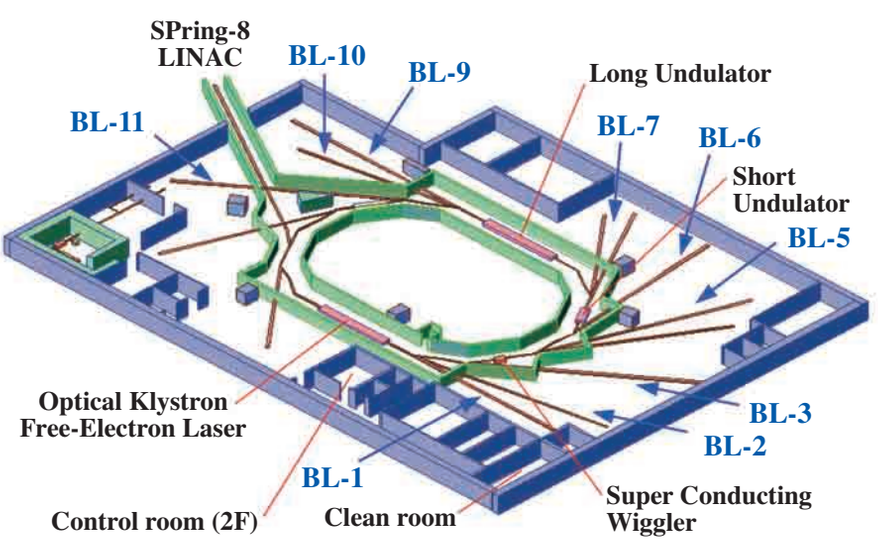

Fig. 1. Beamline arrangement in NewSUBARU.

Surveying Nanosize Particle and Flaw – Mask Defect Inspection System in Extreme Ultraviolet Lithography for Next-Generation Lithography –

Extreme ultraviolet lithography (EUVL) [1] is a most promising lithographic technology for the next-generation lithography of the 32 nm node around 2011. Defect-free mask fabrication is one of the critical issues in the use of EUVL technology in the high-volume production of semiconductor devices. According to the International Technology Roadmap for Semiconductors (ITRS) [2], a defect-free mask with no defect size greater than 25 nm is required for the 32 nm node. There are two types of EUVL mask defects. As shown in Fig. 1, one is an amplitude defect and another is a phase defect. Amplitude defects are either particles on the surface of a multilayer film or flaws in the multilayer film. These defects can be detected directly by measuring the reflected light intensity of deep ultraviolet (DUV) light from the mask surface. On the other hand, phase defects are produced when a multilayer film is deposited over a bump or pit on the substrate. The width (W) and height (H) of phase defects is shown in Fig. 1. Since these phase defects are swellings and depressions on the surface of the multilayer film, they cannot be inspected with a commercial tool using a DUV source. Thus, defect inspection can be carried out only by an inspection tool exposure using EUV light. As for defects on mask blanks, they can be detected using EUV dark-field actinic inspection systems at MIRAI and SEMATECH [3,4]; however, these systems cannot obtain an aerial image of mask absorber patterns because of its detection principle. Therefore, we developed an EUV microscope [5,6] that can observe an aerial image of mask absorber patterns for the criteria of defect size and height of multilayer phase defects to be printable.

Figure 2 shows the configuration and a photograph of the actinic EUV microscope installed at the BL-3 beamline in the NewSUBARU synchrotron radiation (SR) facility. It consists of Schwarzschild optics, a Mirau interferometer for phase-shift interference measurement, an X-Y sample stage, a focus detector, an X-ray zooming tube connected to a CCD camera, and an image processing computer. It was installed in a vacuum chamber evacuated to 1×10^{-5} Pa, and the vacuum chamber was set on a vibration isolation table.

The numerical aperture (NA) and magnification of Schwarzschild optics are 0.3 and 30, respectively. Our simulation predicted that the system can resolve a 10-nm-wide isolated line. The figure error and midfrequency surface roughness of the mirrors was less than 0.4 nm and less than 0.15 nm, respectively. The substrate material of the mirrors is Zerodur and is fabricated by ASML Tinsley. Mo/Si multilayer films were coated on these optics by an X-ray instrument company in Russia. A d-space matching of less than 0.01 nm was achieved at a wavelength of 13.5 nm. The wave-front error (WFE) of the Schwarzschild optics after assembly and alignment was measured by a Fizeau-type interferometer (ZYGO GPI) and found to be is approximately 2 nm (rms). The optics is installed in an optical housing made of invar to prevent the thermal expansion effect.

The mask image is projected to the X-ray zooming tube (Kawasaki Heavy Industries) with

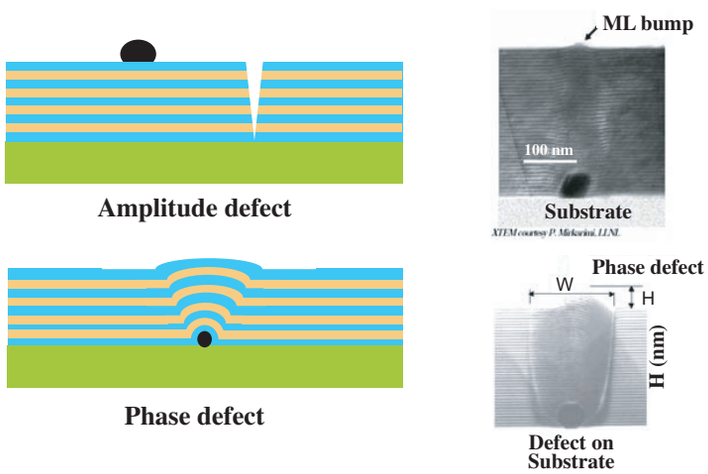

Fig. 1. Amplitude defect and phase defect of EUVL mask blanks.

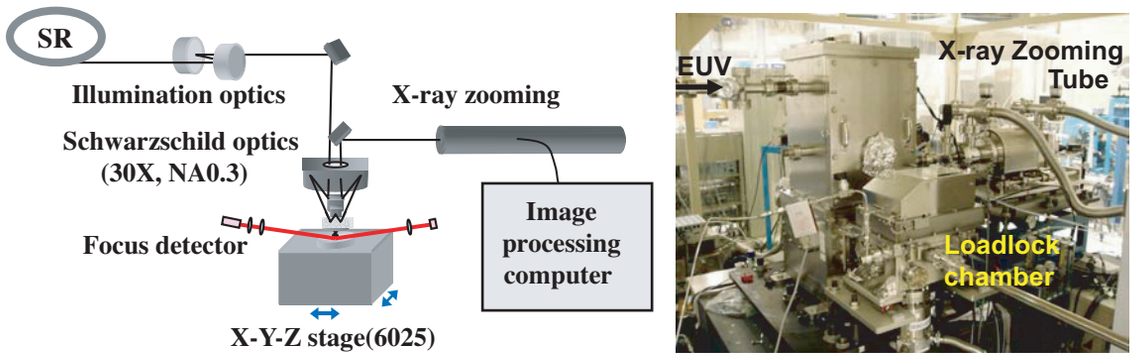

Fig. 2. Configuration and photograph of actinic EUV microscope.

electromagnetic lenses that can be adjusted to vary their magnification in the range from 10 to 200. Therefore, considering the magnification of the Schwarzschild optics, the total magnification range of the microscope system is from 300X to 6000X. The resolution of the X-ray zooming tube is 300 nm on a CsI photocathode. Defects of 10 nm size are magnified by the Schwarzschild optics to greater than 300 nm. Thus, the resolution of the X-ray zooming tube is sufficient to enable the detection of 10 nm defects and to produce resolution-limited Schwarzschild images of mask patterns. The X-ray zooming tube has a field of view of 1.5 × 1.5 mm^2 in the CsI photocathode, which corresponds to 50 × 50 μm^2 on the sample surface. The electron image generated by photoelectric transfer on the photocathode is magnified by the electrostatic lenses and focused on a microchannel plate (MCP). The magnified EUVM images are taken with the CCD camera and displayed on the screen of the image processing computer, and image data are stored in the computer.

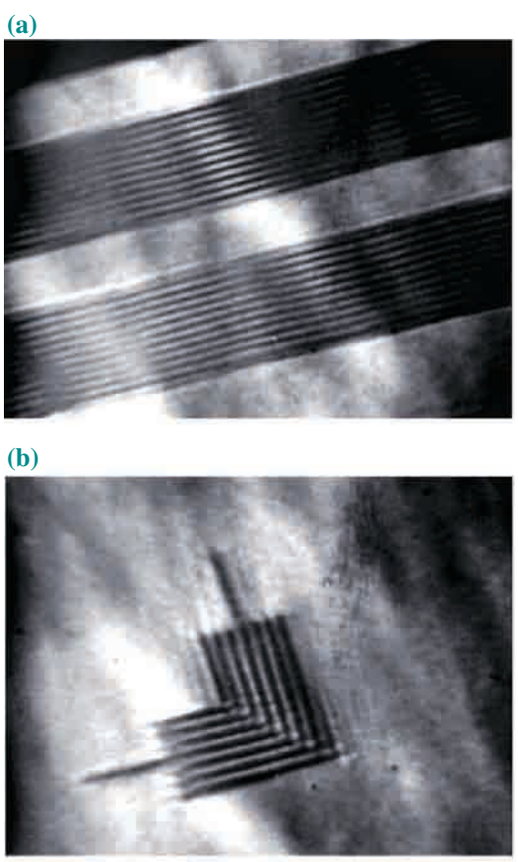

Fig. 3. EUVM images of mask with **(a)** 300-nm-wide isolated lines and **(b)** 400 nm-wide elbow patterns.

A finished EUVL mask was observed using the EUV microscope. The mask with a 6025-format substrate (ULE glass, Corning) was fabricated by HOYA Corporation. Figure 3 shows EUVM images of the mask with a 300-nm-wide line and space (L&S) pattern and a 400-nm L&S elbow pattern. The white part is the Si surface of the Mo/Si multilayer film and the dark part is the absorber material of TaBN. The resolution of the observation system is determined by the NA of the optics and is determined by the magnifying power of the zooming tube used. Assuming a resolution rage from 25 to 75% of the slope of a light intensity profile at the knife edge the total resolution of EUVM was 50 nm.

The following is the fabrication process of programmed phase defects [7]: 1) The glass substrate was coated with ZEP520A resist and a coated charge-up preventer thin film was coated on the resist. 2) The substrate was subject to electron beam exposure using an electron beam writing tool, followed by development of the resist. 3) Selective dry etching of the glass substrate was carried out by masking a resist pattern. 4) The remaining resist was removed. Finally, a Mo/Si multilayer film was deposited using a DC or RF magnetron sputtering

system, and programmed phase defects were formed on the glass substrate.

Figure 4 shows the observation result of a pit-patterned programmed defect with a shallow line pit. The pattern widths are 350 nm, 250 nm, 150 nm, 100 nm, and 75 nm. Programmed defects with a line width larger than 100 nm and a pit depth larger than 2.5 nm were clearly observed using the EUV microscope. However, no programmed defects with a 75 nm width and a 1.5 nm depth could be observed.

Figure 5 shows a summary of the printability results for pit line defects in both simulation and EUV microscopy. The horizontal axis is the width and the vertical axis is the depth of a pit line pattern. Star marks show the size of a pit line defect pattern observed using the EUV microscope. A printable region was calculated by computer simulation, which we previously reported. A programmed line pit phase defect with a 20 nm width and a 2 nm depth is the minimum printable size, as shown in the computer simulation. As observation results obtained using the EUV microscope, with a pit line depth of 2.5 nm, a line pit phase defect with a width larger than 100 nm is printable. Furthermore, a line pit with a 40 nm width and a 10 nm depth is also printable. Line pit phase defects could be observed here. Thus, we confirmed that this region is a printable region. However, no line pit defect with a 75 nm width and a 1.5 nm depth were observed using the EUV microscope. We thus confirmed that this area is unprintable.

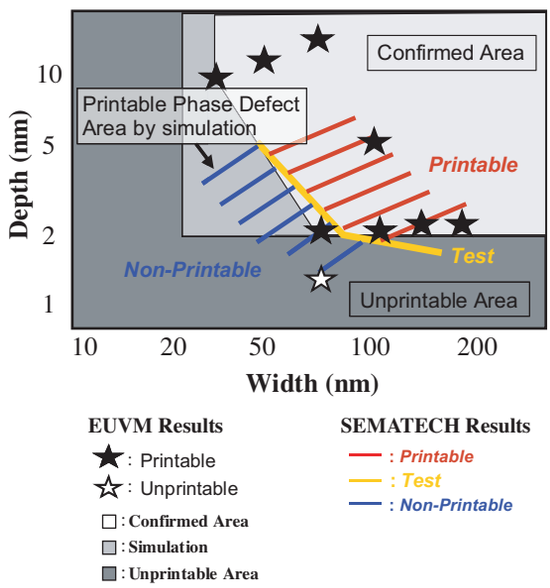

Fig. 5. Summary of printability results for pit line defects in both simulation and EUVM observation.

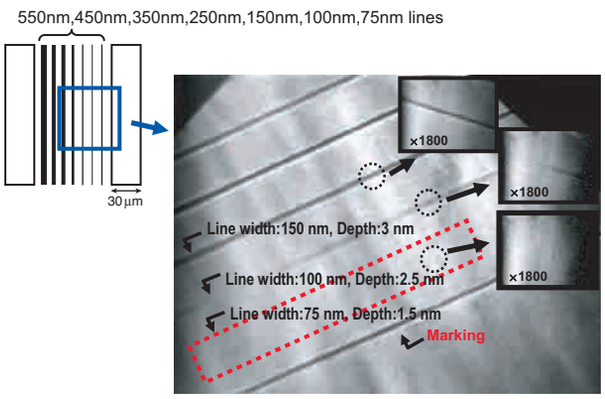

Fig. 4. EUVM image of pit defects.

Hiroo Kinoshita [a,c,*], Takeo Watanabe [a,c] and Kazuhiro Hamamoto [b,c]

[a] LASTI, University of Hyogo
[b] R&D Center, HOYA Corporation
[c] CREST, JST

*E-mail: kinoshita@lasti.u-hyogo.ac.jp

References

[1] H. Kinoshita *et al.*: J. Vac. Sci. Technol. B **7** (1989) 1648.
[2] International Technology Roadmap for Semiconductors 2006 Update edition.
[3] Y. Tezuka *et al.*: Proc. SPIE **6517** (2007) 65172M.
[4] K.A. Goldberg *et al.*: J. Vac. Sci. Technol B **24** (2006) 2824.
[5] H. Kinoshita *et al.*: J. Vac. Sci. Technol. B **22** (2004) 264.
[6] K. Hamamoto *et al.*: J. Vac. Sci. Technol. B **23** (2005) 2852.
[7] *T. Yoshizumi, T. Sugiyama, T. Uno, T. Watanabe and H. Kinoshita: J. Vac. Sci. Technol. B (2007) - in press.*

Editor
Seishi Kikuta
SPring-8 / JASRI

Editing & Layout
Marcia M. Obuti-Daté
SPring-8 / JASRI

Printing
Ono Printing Co.

J A S R I
Library and Information
Users Administration Division

1-1-1 Kouto, Sayo-cho, Sayo-gun
Hyogo 679-5198 • JAPAN
Tel. +81-(0)791 58-2797 Fax. +81-(0)791 58-1869

frontiers@spring8.or.jp
http://www.spring8.or.jp/

July 2008

SPring-8

Japan Synchrotron Radiation Research Institute
1-1-1 Kouto, Sayo-cho, Sayo-gun, Hyogo 679-5198 JAPAN
http://www.spring8.or.jp